Single Molecule Kinetic and Thermodynamic Studies of Molecular Crowding and Extreme Pressure Effects on Nucleic Acid Conformations

by

Hsuan-Lei Sung

B.S., National Taiwan University, 2011

A thesis submitted to the
Faculty of the Graduate School of the
University of Colorado in partial fulfillment
of the requirements for the degree of
Doctor of Philosophy
Chemistry
2022

Committee Members:
David Nesbitt, Chair
Meredith Betterton
Joseph Falke
J. Mathias Weber
Daniel Schwartz

Sung, Hsuan-Lei (Ph.D. Chemistry)

Single-Molecule Kinetic Studies of Nucleic Acid Folding: Insights from Temperature and Pressure Dependence

Thesis directed by Professor David J. Nesbitt

Biochemical activity of proteins and nucleic acids is strongly dependent on three-dimensional shape. As a result, upon synthesis biomolecules often undergo a series of secondary and tertiary folding transitions to achieve a spatial configuration crucial to biochemical function. This dissertation describes detailed studies on the folding dynamics of small RNA/DNA nucleic acid oligomers and RNA riboswitches at the single molecule level. In particular, our focus is on both equilibrium and real time kinetic characterization of two physical phenomena that can greatly impact the stability of a specific nucleic acid structure: “molecular crowding” and pressure-induced denaturation.

Nucleic acids have evolved to function inside cells. The intracellular environment is highly concentrated (> 20% by weight) with various solutes (mono/divalent cations, anions, peptides, nucleotides, fatty acids, osmolytes, metabolites, etc.) and thus is quite different from the dilute buffer conditions in which biochemical studies are traditionally performed. A predictive understanding of such spatial crowding effects on nucleic acid conformation is therefore key to unambiguous interpretation of *in vitro* data in terms of predicted *in vivo* behavior. Single molecule Fluorescence Resonance Energy Transfer (smFRET) measurements obtained with precise control of temperature allows us to measure equilibrium and kinetic properties as a function of temperature, which permits deconstruction of free energy changes in terms of enthalpic and entropic components. Significantly, this work reveals that stabilization of

nucleic acid structure with biochemically inert polymer PEG (polyethylene glycol) is essentially entirely entropic, i.e., consistent with excluded volume as the primary origin of nucleic acid molecular crowding. Furthermore, clean separation of the enthalpic and entropic chemical contributions in such temperature studies permits the dependence of crowding on molecular size to be revealed, with the surprising result that *smaller crowders* (at constant w%, percentage by weight) promote nucleic acid folding *more effectively*.

Due to the rapid pressure increase as a function of ocean depth, marine life can experience significant fluctuations in pressure. Moreover, marine organisms in deep sea regions (such as the Marianas trench) are constantly exposed to extreme pressures up to a thousand bars. In order to better understand how deep sea organisms adapt to extreme pressures at the molecular level, studies of the pressure-dependent effects on biomolecular structures (both protein and nucleic acids) are thus essential. In this work, our single molecule confocal microscope is coupled to a pressure generating system to explore the pressure response of nucleic acid folding. The pressure dependent equilibria reveal that nucleic acids effectively take up more volume than its unfolded conformation upon folding, which is at least initially counterintuitive to the commonly held physical picture of a folded conformation being more compact. The studies also demonstrated that the osmolyte trimethylamine N-oxide (TMAO), which is found to accumulate in deep sea fish, efficiently increases the pressure stability of nucleic acids both by promoting folding equilibrium and reducing the denaturing sensitivity to external hydrostatic pressure.

Acknowledgements

First, I would like to acknowledge my advisor David Nesbitt for providing me the research opportunities at CU/JILA and helping me become a better scientist. David is a great teacher, generous with both knowledge and time. He's not only taught me things about science but also encouraged me to clearly communicate my research in both speaking/writing, which has benefitted me tremendously. I would also like to thank the current and past members of the Nesbitt group: Andrea Menendez, David Nicholson and Abhigyan Sengupta for sharing interest in biophysics; Tim Livingston-Large, Jake Pettine and Mikhail Ryazanov for experimental advice and assistance; Erik Holmstrom and Mario Vieweger for helping me start with the single molecule experiment and teaching me the nucleic acid techniques; and all the rest of the group members that I had the pleasure and honor to work with.

I would like to thank all the JILA staff for keeping our research going: Brian Lynch, Jennifer Erickson, Randall Holliness, Daniel Lewis and Karen Lichtfuss in the supply office for helping me shop lab supplies and equipment; Hans Green, Todd Asincar, Kyle Thatcher and Calvin Schwadron in the JILA instrument shop for assisting me with the high-pressure experiment setup and fabrication of the capillary sample holders; Jim McKown and Eric Alvarado from the computing group for taking care of our old computers in the lab; Agnieszka Lynch of JILA human resources for hiring me and her advice on all the student and visa issues. People from the Chemistry department need acknowledgement too: Cora Fagan, Julia Shipman and many other graduate program managers in the past years for keeping me informed of department and graduate school updates. I would also like to thank my classmates in the Physical Chemistry program: Jonathan Church, Hayden Hamby and Jose Luis Falla for their friendship

and support. I am genuinely extremely grateful for everyone at CU who had been part of my doctoral journey.

In the end, I would like to thank my aunts Li-Ru Fu and Hsiao-Chuan Fu for their continuous support for me and my family in Taiwan. I would like to acknowledge my brother Hsing-Lei Sung for taking care of our mother and many other things at home while I am away. I wouldn't have the privilege to continue my study in the US without him. I would like to thank my mother Ya-Nan Fu for everything she had done for me and the family. There are no words to describe how grateful I am for her unconditional love and support to make me who I am today. Last, but certainly not least I would like to thank my best friend Ross Kenneth Thomas, not only for his friendship and company but also for motivating/encouraging me to become a better person. Ross was always nice to everyone and genuinely care about people in need. Ross's friendship is the best thing to have happened to me.

Table of Contents

List of Tables

List of Figures

Chapter 1

Introduction

1.1 Nucleic acids

Nucleic acids are large biopolymers that play essential roles in all forms of life and non-living biochemical machines such as viruses. The fundamental building blocks of nucleic acids are the nucleotides, consisting of three covalently attached components: a five-carbon sugar, a phosphate group, and a nucleobase (Figure 1.1).[1] The two principal categories of naturally occurring nucleic acids are ribonucleic acid (RNA) and deoxyribonucleic acid (DNA), formed from ribonucleotide and deoxyribonucleotide subunits, respectively. The only major difference between these two subunits is the presence (ribonucleotides) or absence (deoxyribonucleotides) of a hydroxyl group on the 2' carbon of the 5-carbon sugar.[2]

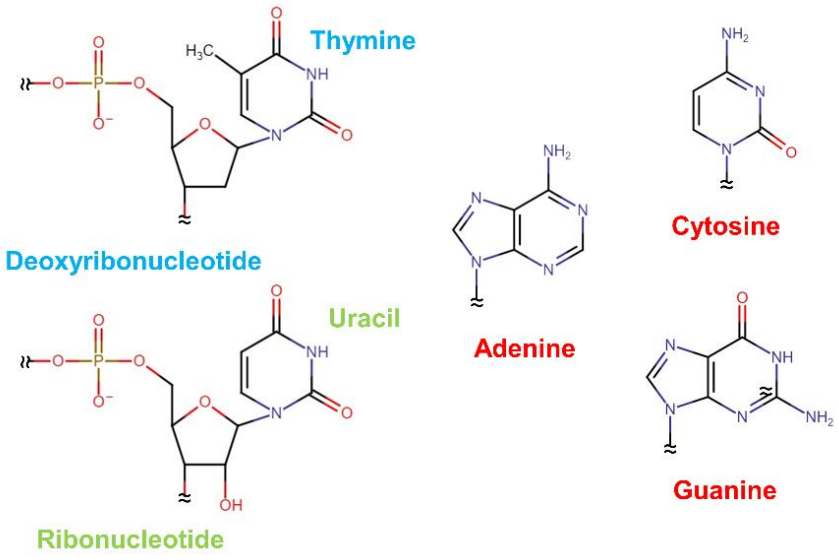

Figure 1.1 Chemical structures of deoxyribonucleotide/ribonucleotide and the corresponding nitrogenous bases.

1.1.2 Nucleic acid structure and function

There are four different nucleobases: guanine (G), cytosine (C), adenine (A), and thymine (T) for deoxyribonucleic acid (DNA), and guanine (G), cytosine (C), adenine (A), and uracil (U) for ribonucleic acid (RNA), respectively (Figure 1.1). The nucleotides are linked by phosphodiester bonds between the phosphate groups and hydroxyl groups on the 5-carbon sugars to form a linear polymeric chain,[1] where the specific sequence of nucleotides defines the primary (1^o) structure of the nucleic acid strand. The genetic information encoded in the DNA nucleic acid primary sequence (and in turn the transcribed messenger mRNA sequence) contains instructions for synthesis of proteins that facilitate most cellular function and ultimately allow organisms to thrive.

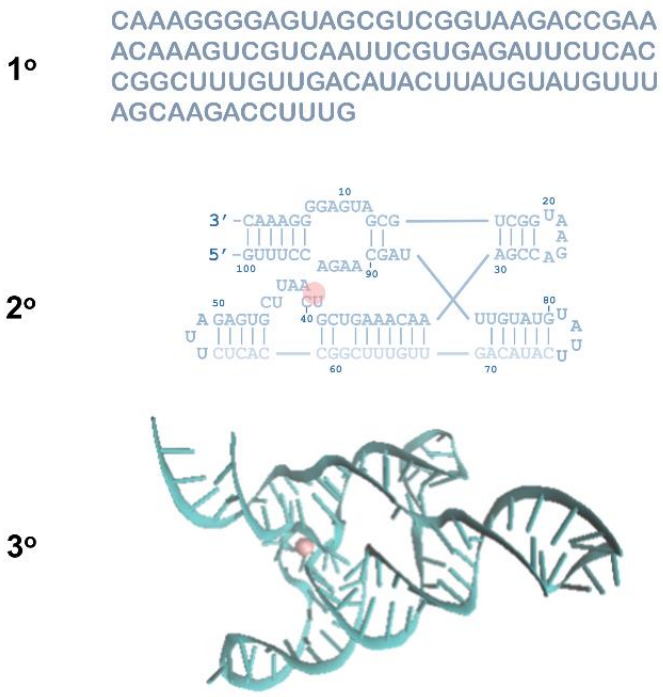

Figure 1.2 Example of RNA hierarchical folding: (from top to bottom) 1^o, 2^o and 3^o structure of the manganese (Mn^{2+}) riboswitch. (PDB 4Y1I)

Although the most fundamental genetic information in DNA and RNA is contained in the 1^{o} structure, the biochemical function of nucleic acids depends famously on the subsequent development of higher order oligomeric structures (Figure 1.2).[3] Specific combinations of nucleobases in DNA (RNA) can hydrogen bond with one another to form stable Watson–Crick pairs, with G pairing with C (for both DNA/RNA) and A pairing with T (for DNA) or U (for RNA) through hydrogen bonding, which are crucial for the secondary (2^{o}) structure formation. Double helix formation in double-stranded DNA (dsDNA) is arguably the best known and most prevalent 2^{o} nucleic acid structure,[4] formed by intermolecular Watson–Crick base pairing between two complementary DNA strands and allowing efficient storage and readout of important genetic information. By way of contrast, RNA typically tends to be single-stranded, but can also form relatively short double helix-like 2^{o} structures ("stems") between self-complimentary regions through intramolecular G-C and A-U base pairing. Most importantly, the regions of unpaired and/or mismatched sequences in single stranded RNA (ssRNA) permit the formation of a much wider variety of 2^{o} structures, such as junctions, loops, and bulges, each element allowing for much higher conformational flexibility.[5-6] Indeed, it is this larger library of 2^{o} motifs that allows RNA to be more functionally "creative", with folding interactions among these 2^{o} motifs allowing for formation of more complex tertiary (3^{o}) structures essential for biochemically competent catalytic and/or sensing RNAs:[7] As one CU-centric Nobel prize winning example, discovery in the 1980s of self-splicing activity by the group I intron[8] and RNase P[9] followed by the hammerhead ribozyme[10] demonstrated the enormous potential of ribonucleic acids as enzymatically active species. The 3^{o} interactions among stems, loops and bulges are each found to play important roles in forming and stabilizing such functional RNA structures,[11] the biophysics of which represents a primary goal of this thesis work.

1.1.2 Nucleic acid conformational transition

With the help of helicases, even the highly thermodynamically stable DNA double helix unwinds during replication.[12] This suggests that nucleic acid "structure" must or at least can be highly dynamic and thus biochemical reactions may require a series of conformational transitions[13-14] each occurring on a characteristic time scale. A detailed knowledge of nucleic acid conformational kinetics therefore represents a fundamental goal for any predictive understanding of such biochemical processes.

In this thesis, we explore the kinetics of the elemental structural transition, 1^o to 2^o and 2^o to 3^o as well as the more complicated folding of the complete RNA riboswitch (Figure 1.3). One model transformation system we have studied in detail is 2^o structure formation in the DNA hairpin construct, which consists of two short (7 to 9 nucleotide) complimentary sequences separated by a 40-adenine linker.[15-16] for which the two complimentary strands are joined by Watson–Crick base pairing to form a closed stem-loop configuration. Such 2^o folding is not only the primary structural interaction motif in the DNA double helix but is also essential for the widely prevalent stem/stem-loop formation in all RNA constructs. Another common RNA structural motif is the tertiary interaction between 2^o elements such as the loop (tetraloop) and bulge (tetraloop receptor), which is ubiquitously found in RNA 3D crystal structures and can serve as a nice test construct for study of 3^o folding kinetics.[17-18] Indeed, the specific tetraloop-tetraloop receptor docking construct we have chosen to explore is one of the key structural sequences that modulate catalytic activity for self-splicing in the group I intron.[17]

Riboswitches are noncoding RNA elements that sometimes appear in the 5' advance region of a gene which are therefore transcribed first and can undergo structural rearrangement in response to the presence or absence of specific ligands in the cell. Such ligand-induced

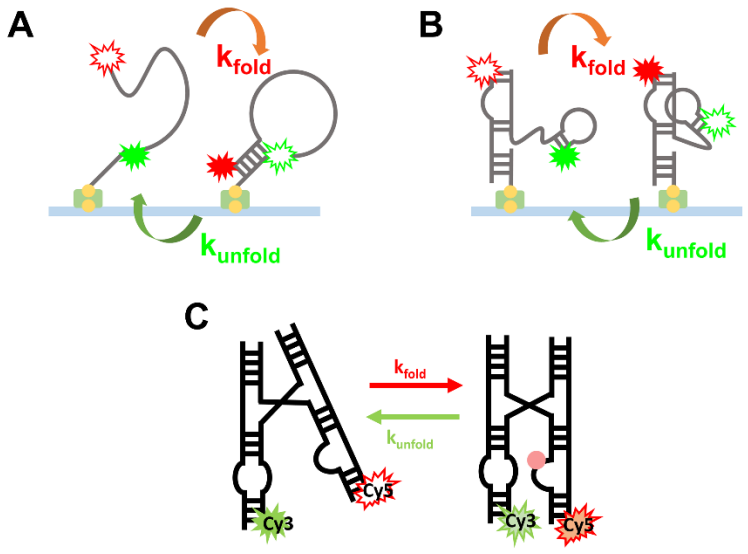

Figure 1.3 Examples of nucleic acid structural transition explored in this thesis. (A) 1° → 2° DNA hairpin formation. (B) 2° → 3° loop-bulge interaction between tetraloop and tetraloop receptor. (C) Full manganese riboswitch aptamer folding, which involves the Mn^{2+}-facilitated loop-loop folding and the rearrangement of the four-way junction as well as the attached stems.

rearrangements in effect permit regulation of gene expression by sensing of cell environment.[19-20] As a result, the thermodynamics of riboswitch folding are therefore of particular importance to gene regulation.[21] Of particular dynamic interest, this nascent mRNA begins to form stable aptamer sensing structures ("aptamer domain") synchronous with transcription until the complete riboswitch sequence is produced.[22-23] Such a "fold-upon-synthesis" process, often termed "co-transcriptional folding",[24] is therefore heavily impacted by the kinetics of RNA folding.[25] It is therefore a crucial evolutionary strategy for the riboswitch to fold into the correct conformation in response to ligand binding and in turn generate the desired genetic response. In this thesis, we study the folding kinetics and thermodynamics of a variety of riboswitches. One of the most extensively studied structures is the manganese riboswitch,[26-27] which conformationally responds to the presence/absence of Mn^{2+} and thereby regulate the transcription to form a protein responsible for Mn^{2+} homeostasis. Although such a conformational transition in the riboswitch is

primarily regulated by a Mn^{2+}-promoted 3^o loop-loop interaction, allosteric control of Mg^{2+} binding, rearrangement of the junctional loop and associated stems also play an important part in the overall folding event.[28]

1.2 Single molecule FRET kinetics

Traditional ensemble studies measure quantities that average over ~ 10^{23} molecules. Because the bulk system is often in rapid dynamic equilibrium due to both forward and backward reaction pathways, an ensemble experiment typically permits only observation of equilibrium properties, obscuring any detailed kinetics of the forward/backward folding reactions. To obtain kinetic information from such ensemble studies requires "molecular synchronization", for example, measuring the effective unimolecular rate constant for a non-equilibrium system returning to equilibrium, where the non-equilibrium state might be caused by rapid change in temperature/pressure (i.e., T-jump and pressure jump experiments) or buffer conditions (e.g., stopped-flow methods).[29-30] Despite a rich history, widespread use, and considerable generality, such synchronization methods often require additionally restrictive kinetic assumptions, for example, independent knowledge of fast vs. slow kinetic processes to deconstruct forward and reverse rate constants. Moreover, one additional assumption intrinsic to ensemble measurements (and perhaps the most critical to biomolecule conformational transitions) is that all the molecules are exactly identical. In fact, the presence of kinetic heterogeneity in biomolecule samples is a known issue,[31] for which study of the resulting kinetics requires observation of single molecules, one at a time.[32-33]

For much of the 20th century, the prospect of studying kinetics at the single molecule level was thought to be simply a dream. In fact, the underlying physical techniques (lasers,

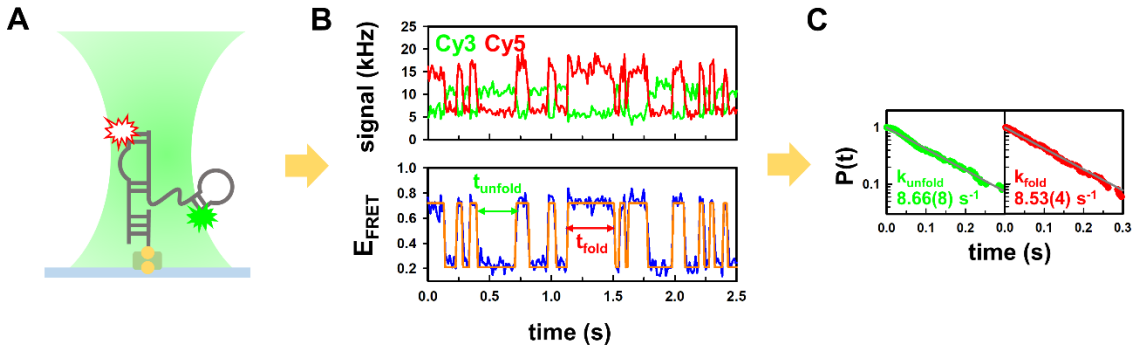

Figure 1.4 Schematic of single molecule FRET kinetic measurements and sample data. (A) the immobilized nucleic acid construct at the laser focus for extended fluorescence observation. (B) Sample fluorescent signal time trace (upper panel) and the resulting FRET transfer efficiency E_{FRET} trajectory (lower panel). (C) Dwell time analysis; the linearity in the semi-log plots indicates the folding and unfolding processes are well described by the first order kinetics.

photomultipliers, high NA microscopes, etc.) to achieve this ultimate sensitivity goal had arguably existed since the 1960s, requiring only particularly intrepid scientists to turn this into a reality. Indeed, such single molecule observations in early 1990s were first realized by W. E. Moerner in cryogenic crystals,[34-35] with the techniques greatly improved in the next several decades with the help of more versatile lasers, faster detectors, and brighter fluorophores. It was later extended to biological samples in coupling with various fluorescence methods including Foster resonance energy transfer (FRET).[36-37] FRET describes the energy transfer between two chromophores (light-absorbing molecules), where the dipole-dipole transfer efficiency is found to strongly depend ($1/R^6$) on the distance. It is therefore commonly used in structural studies with a pair of fluorophores to inform on distance between the labeled folding motifs within molecule(s) of interest. In this thesis, we utilize FRET between Cy3 and Cy5 fluorophore pair to visualize the folding of nucleic acids, whereby the change in distance between Cy3 and Cy5 during conformational transition results in different colors (Cy3 (green) vs Cy5 (red)) in fluorescence. Furthermore, with the confocal microscope setup,[38] the tightly focused laser allows

us to obtain the fluorescent signal from a single molecule at a time (Figure 1.4A). With surface-immobilized molecules, direct observation of folding/unfolding dynamics of nucleic acid structures can be realized by the prolonged observation of FRET from a single fluorophore-labeled construct (Figure 1.4B). The resulting kinetic information on the folded vs unfolded status of a single nucleic acid can therefore be obtained by analyzing the time dependent fluorescent traces for a single molecule (Figure 1.4C).

In addition to measurements of nucleic acid folding/unfolding rate constants, we are also interested in the response of these rate constants to mono/divalent salts, osmolytes, and riboswitch ligands. In particular, we can apply kinetic models to ligand-induced riboswitch folding (see Chapter 3 and 4 in this thesis), which reveal that folding in the presence of increasing magnesium shifts from a ligand binding-induced conformational change (i.e., "bind-then-fold" or induced fit: IF) mechanism to that of a pre-formed riboswitch structure successfully stabilized by subsequent binding of the ligand (i.e., "fold-then-bind" or conformation selection: CS).[39] Moreover, the recognition of multiple conformations (and thus FRET states) is also made possible with single molecule study. With such smFRET tools, we have successfully resolved three different conformational states for the Ni^{2+}/Co^{2+}-sensing riboswitch (see Chapter 5),[40-41] and can directly monitor the folding of each step promoted by mono/divalent cations and the relevant riboswitch ligands, respectively.[42]

1.3 Thermodynamics of nucleic acid structural transition

In thermodynamics, the Gibbs free energy determines the spontaneity of a reaction (e.g. conformational transition). It measures the maximum amount of work available from a reaction:

$$\Delta G = \Delta G^0 + RTlnQ, \qquad \text{Eq. 1.1}$$

where ΔG^0 is the change in free energy under standard state conditions (1 atm for ideal gases, 1M for ideal solutes), R the gas constant, and Q the reaction quotient. For a system in equilibrium, we have $\Delta G = 0$ and $Q = K_{eq}$ (equilibrium constant), which from Eq. 1.1 can be rewritten as

$$\Delta G^0 = -RTlnK_{eq}, \quad \text{Eq. 1.2}$$

which denotes the relation between the Gibbs free energy and the equilibrium constant.

1.3.1 Temperature as a variable

Conformational transitions in nucleic acids involve base stacking, hydrogen bond formation and disruption, as well as change in hydration including cation association and water reorganization.[43] Each of these interactions contribute to changes in enthalpy (ΔH) and entropy (ΔS) of the overall nucleic acid folding.[44] According the thermodynamic definition of the standard Gibbs free energy

$$\Delta G^0 = \Delta H^0 - T\Delta S^0, \quad \text{Eq. 1.3}$$

Eq. 1.2 can be rearranged into the van't Hoff equation

$$lnK_{eq} = \frac{-\Delta G^0}{RT} = \frac{1}{T}\left(\frac{-\Delta H^0}{R}\right) + \frac{\Delta S^0}{R}, \quad \text{Eq. 1.4}$$

which permits the deconstruction of the free energy into enthalpy and entropy contributions by temperature dependence of the folding equilibrium constant.

Our single molecule microscope is equipped with heating (and cooling) devices to achieve precise and tunable temperature control of the sample.[45] Temperature dependent folding experiments have revealed valuable biophysical insights:[46] In particular, we are able to identify the stabilization effects of PEG (polyethylene glycol) on nucleic acid 2º and 3º structures to be predominantly entropic (see Chapter 6 and 7),[47-49] which is entirely consistent with the crowding

effect originating from the pure excluded volume interaction.[50-51] Therefore, the steric constraint of the crowded intracellular environment may be effectively simulated by PEG to enhance the applicability of the in vitro studies to in vivo observations.[52] This successful incorporation of temperature control can also be extended to single molecule kinetics by Erying transition state analysis[53]

$$\ln(k) = -\frac{\Delta H^{\ddagger}}{R}\frac{1}{T} + \frac{\Delta S^{\ddagger}}{R} + \ln \nu, \qquad \text{Eq. 1.5}$$

where $\Delta H^{\ddagger}$ and $\Delta S^{\ddagger}$ are the enthalpic and entropic difference between the transition state and the folded/unfolded conformations, and ν is the attempt frequency for the system to cross the transition barrier.[54-55] The resulting detailed thermodynamic characterization allows us to deconstruct free energy contributions at the folding transition state into both enthalpic and entropic components, achieving even higher levels of insight into the free energy landscape topology.

1.3.2 Pressure as a variable

Pressure is another thermodynamic variable that drives biochemical reactions, including biomolecule folding. Although the effect of air pressure is rather negligible, hydraulic pressure can change quite rapidly in the ocean environment, at the rate of approximately 1 bar per 10 meters in depth. Marine organisms, especially deep-sea species, thus experience quite high pressures, with values up to ≈ 1.1 kilobars at the deepest part of the ocean/Mariana Trench.[56] It is therefore reasonable to speculate that conformational folding of biomolecules (e.g. proteins and nucleic acids) in deep-sea species must have evolved to adapt to such extreme pressure environments. Although there have been several efforts to study pressure effects on biomolecular folding in the early 1980s,[57-58] it is fair to say that the understanding of pressure-induced conformational change at the molecular level is still in its infancy.[59] Specifically, while various

protein species are found to unfold at high pressures[60-61] (i..e, pressure-induced denaturation),[62] the corresponding pressure-dependent response for nucleic acid structures is much less well understood, with the studies to date largely limited to 2º structure formations.[63-65] Since biomolecular function is strongly tied to structure, the kinetic and thermodynamic conformational response of nucleic acids to pressure would appear to be critical for evolutionary strategies adapting to extreme ocean depths.

Recently, single molecule FRET has been incorporated with high pressure systems to characterize the pressure response of nucleic acid folding (see Chapter 9 and 10).[66-67] In these experiments, the excitation laser is focused into the solution to record the fluorescent signal of molecules diffusing through the focal region,[68] allowing direct observation of folded vs. unfolded populations differentiated by FRET efficiency and photon color.[69-70] According to the thermodynamic relation between free energy and pressure, the volume change during folding (ΔV^0) can be obtained from pressure dependence of the equilibrium constant[60-61]

$$\left(\frac{\partial lnK_{eq}}{\partial P}\right)_T = \frac{-\Delta V^0}{RT}. \qquad \text{Eq. 1.6}$$

Interestingly, according to Eq. 1.6, the fact that pressure commonly induces unfolding (denaturation) indicates that biomolecules (such as proteins, nucleic acids) effectively take up more volume as it folds, despite ostensibly achieving a more compact folded conformation. Although not yet completely understood, this volume increase during folding is thought to result from nanoscopic voids/cavities formed in the folded conformation.[71-73] These cavities may either exclude the water molecules or disrupt the water network, resulting in a less compact water structure due to spatial confinement.[74] Another possible cause of the larger volume folded state may be the change in hydration,[75-76] with the less exposed charged surfaces and (cat)ion

recruitment result in the surrounding water molecules becoming less aligned by the charged folded biomolecule. Clearly, the key to resolving such counterintuitive volume change is to include the surrounding solvent into the physical picture of folding.[43, 77]

In this thesis, we have extended the high pressure single molecule equilibrium studies to kinetic measurements with surface immobilized nucleic acid constructs (see Chapter 11 and 12).[78] The resulting pressure dependent rate constants now inform on the volume changes associated with the folded, unfolded, and transition state conformations,[60] and thus provide particularly novel opportunities for detailed characterization of the volume change along the nucleic acid folding coordinate. We have determined the volume of nucleic acid monotonically increases along the nucleic acid folding ($V_U < V_{TS} < V_F$).[78] Moreover, we have found ΔV to be highly sensitive to cation association; the resulting detailed volumetric information of the folding landscapes is shown to complement the kinetic modeling performed at ambient pressure, providing additional insights into cation-nucleic acid interactions.

1.4 Thesis overview

In this thesis, we use single molecule FRET spectroscopy incorporated with temperature and pressure control to investigate several important topics in biophysics. Chapter 2 describes the single molecule FRET measurement in detail with special focus on development of the high pressure experimental apparatus. In Chapters 3 to 5, we study metal cation (Mn^{2+}, Ni^{2+}, and Co^{2+}) sensing riboswitches folding with emphasis on temperature dependent single molecule kinetics. Specifically, in Chapter 3 and 4, kinetic modeling reveals that the presence of magnesium cation shifts the predominant folding pathway for the manganese (Mn^{2+}) riboswitch between two kinetic paradigms of an induced-fit (IF, bind-then-fold) to a conformational

selection (CS, fold-then-bind) mechanism.[28, 39] In Chapter 5, the effects of magnesium induced pre-folding is again evidenced in the nickel/cobalt (Ni^{2+}/Co^{2+}) riboswitch, which now exhibits three distinctive FRET states.[42] Simply summarized, sequential folding kinetics of the nickel/cobalt riboswitch reveals that magnesium significantly promotes the formation of this pre-folded intermediate, but cannot achieve the final folded conformation without obligate Ni^{2+} or Co^{2+} binding. In Chapter 6, we explore the effects of "molecular crowding" on conformational folding with single molecule kinetic and thermodynamic studies.[48] These studies reveal not only that stabilization of nucleic acid structure by PEG is predominantly entropic (and well described by excluded volume models), but rather more surprisingly that this effectiveness (on a w% basis) increases with decreasing PEG size. Both of these observations are consistent with molecular crowding effect, in which the excluded volume is the predominant interaction. Chapter 7 explores and reveals the significant additional enthalpic effects of polysaccharides (i.e., dextran and Ficoll, common protein crowding agents) on nucleic acid folding, in strong contrast with the predominantly entropic effects of crowding by PEG.[49] The effect of molecular crowding on the lysine riboswitch has been explored in Chapter 8,[79] for which kinetic analysis reveals that PEG promotes riboswitch folding primarily by enhancement in the lysine ligand affinity. In Chapter 9 and 10, we develop and exploit high pressure single molecule FRET methods to study the pressure dependent folding equilibrium of the DNA hairpin[69] and lysine riboswitch,[70] respectively. Of special importance, the studies reveal that the osmolyte TMAO (trimethylamine N-oxide), which has been found to accumulate in deep-sea fish,[80] effectively protects the lysine riboswitch from pressure-induced denaturation by not only the stabilization of the folding event but also a reduced sensitivity to external pressure ($\Delta\Delta V^0_{TMAO} < 0$). In Chapter 11 and 12, we demonstrate the ability to extend these high pressure experiments from equilibrium studies of

freely diffusing molecules into the time domain by direct monitoring folding kinetics for single molecule constructs tethered to the inside surface of a high pressure capillary. With this new capability, we are able to achieve high pressure kinetic measurements of the folding/unfolding kinetics for both secondary (40A DNA hairpin)[78] and tertiary (manganese riboswitch) structure formation, and thereby infer the "free volume landscape" between unfolded, transition state, and folded configurations. Indeed, our experimental methods can be taken one step further from pressure dependent folding studies of the riboswitch measured over a series of Mn^{2+} concentrations, from which we are able to deduce *differential* changes in the free volume change for folding upon binding of the ligand Mn^{2+} (ΔV^0_{bind}). Interestingly, our measurements reveal such differential volume effects to be negative ($\Delta V^0_{bind} < 0$), which implies that ligand binding is favored with increasing pressure. Coming full circle back to deep sea organisms, such a negative pressure dependence for ligand binding may help mitigate the positive pressure-induced unfolding effects on the overall riboswitch structure ($\Delta V^0_{fold} > 0$) and thereby preserve riboswitch function over wider extremes of pressure.

1.5 References

1. Miller, P. S., A Brief Guide to Nucleic Acid Chemistry. *Bioconjugate Chem.* **1990,** *1* (3), 187-191.

2. Minchin, S.; Lodge, J., Understanding Biochemistry: Structure and Function of Nucleic Acids. *Essays Biochem.* **2019,** *63* (4), 433-456.

3. Belmont, P.; Constant, J.-F.; Demeunynck, M., Nucleic Acid Conformation Diversity: from Structure to Function and Regulation. *Chem. Soc. Rev.* **2001,** *30* (1), 70-81.

4. Watson, J. D.; Crick, F. H. C., Molecular Structure of Nucleic Acids: A Structure for Deoxyribose Nucleic Acid. *Nature* **1953,** *171* (4356), 737-738.

5. and, P. B.; Westhof, E., Hierarchy and Dynamics of RNA Folding. *Annu. Rev. Biophys. Biomol. Struct.* **1997,** *26* (1), 113-137.

6. Schroeder, R.; Barta, A.; Semrad, K., Strategies for RNA Folding and Assembly. *Nat. Rev. Mol. Cell Biol.* **2004,** *5* (11), 908-919.

7. Cech, T. R.; Bass, B. L., Biological Catalysis by RNA. *Annu. Rev. Biochem.* **1986,** *55* (1), 599-629.

8. Kruger, K.; Grabowski, P. J.; Zaug, A. J.; Sands, J.; Gottschling, D. E.; Cech, T. R., Self-Splicing RNA: Autoexcision and Autocyclization of the Ribosomal RNA Intervening Sequence of Tetrahymena. *Cell* **1982,** *31* (1), 147-157.

9. Guerrier-Takada, C.; Gardiner, K.; Marsh, T.; Pace, N.; Altman, S., The RNA Moiety of Ribonuclease P is the Catalytic Subunit of the Enzyme. *Cell* **1983,** *35* (3, Part 2), 849-857.

10. Cech, T. R.; Zaug, A. J.; Grabowski, P. J., *In vitro* Splicing of the Ribosomal RNA Precursor of Tetrahymena: Involvement of a Guanosine Nucleotide in the Excision of the Intervening Sequence. *Cell* **1981,** *27* (3), 487-496.

11. Noller, H. F., Structure of Ribosomal RNA. *Annu. Rev. Biochem.* **1984,** *53* (1), 119-162.

12. Gefter, M. L., DNA Replication. *Annu. Rev. Biochem.* **1975,** *44* (1), 45-78.

13. Tinoco, I.; Bustamante, C., How RNA Folds. *J. Mol. Biol.* **1999,** *293* (2), 271-281.

14. Mott, M. L.; Berger, J. M., DNA Replication Initiation: Mechanisms and Regulation in Bacteria. *Nat. Rev. Microbiol.* **2007,** *5* (5), 343-354.

15. Sengupta, A.; Sung, H.-L.; Nesbitt, D. J., Amino Acid Specific Effects on RNA Tertiary Interactions: Single-Molecule Kinetic and Thermodynamic Studies. *J. Phys. Chem. B* **2016,** *120* (41), 10615-10627.

16. Nicholson, D. A.; Sengupta, A.; Sung, H.-L.; Nesbitt, D. J., Amino Acid Stabilization of Nucleic Acid Secondary Structure: Kinetic Insights from Single-Molecule Studies. *J. Phys. Chem. B* **2018,** *122* (43), 9869-9876.

17. Adams, P. L.; Stahley, M. R.; Gill, M. L.; Kosek, A. B.; Wang, J.; Strobel, S. A., Crystal Structure of a Group I Intron Splicing Intermediate. *RNA* **2004,** *10* (12), 1867-1887.

18. Wu, L.; Chai, D.; Fraser, M. E.; Zimmerly, S., Structural Variation and Uniformity among Tetraloop-Receptor Interactions and Other Loop-Helix Interactions in RNA Crystal Structures. *PLOS ONE* **2012,** *7* (11), e49225.

19. Sherwood, A. V.; Henkin, T. M., Riboswitch-Mediated Gene Regulation: Novel RNA Architectures Dictate Gene Expression Responses. *Annu. Rev. Microbiol.* **2016,** *70* (1), 361-374.

20. Pavlova, N.; Kaloudas, D.; Penchovsky, R., Riboswitch Distribution, Structure, and Function in Bacteria. *Gene* **2019,** *708*, 38-48.

21. Haller, A.; Soulière, M. F.; Micura, R., The Dynamic Nature of RNA as Key to Understanding Riboswitch Mechanisms. *Acc. Chem. Res.* **2011,** *44* (12), 1339-1348.

22. Lai, D.; Proctor, J. R.; Meyer, I. M., On the Importance of Cotranscriptional RNA Structure Formation. *RNA* **2013,** *19* (11), 1461-1473.

23. Meyer, I. M.; Miklós, I., Co-Transcriptional Folding is Encoded within RNA Genes. *BMC Mol. Biol.* **2004,** *5* (1), 10.

24. Schärfen, L.; Neugebauer, K. M., Transcription Regulation Through Nascent RNA Folding. *J. Mol. Biol.* **2021,** *433* (14), 166975.

25. Lutz, B.; Faber, M.; Verma, A.; Klumpp, S.; Schug, A., Differences between Cotranscriptional and Free Riboswitch Folding. *Nucleic Acids Res.* **2013,** *42* (4), 2687-2696.

26. Dambach, M.; Sandoval, M.; Updegrove, Taylor B.; Anantharaman, V.; Aravind, L.; Waters, Lauren S.; Storz, G., The Ubiquitous *yybP-ykoY* Riboswitch Is a Manganese-Responsive Regulatory Element. *Mol. Cell* **2015,** *57* (6), 1099-1109.

27. Price, Ian R.; Gaballa, A.; Ding, F.; Helmann, John D.; Ke, A., Mn^{2+}-Sensing Mechanisms of *yybP-ykoY* Orphan Riboswitches. *Mol. Cell* **2015,** *57* (6), 1110-1123.

28. Sung, H.-L.; Nesbitt, D. J., Novel Heat-Promoted Folding Dynamics of the *yybP-ykoY* Manganese Riboswitch: Kinetic and Thermodynamic Studies at the Single-Molecule Level. *J. Phys. Chem. B* **2019,** *123* (26), 5412-5422.

29. Krüger, H., Techniques for the Kinetic Study of Fast Reactions in Solution. *Chem. Soc. Rev.* **1982,** *11* (3), 227-255.

30. Eccleston, J. F.; Martin, S. R.; Schilstra, M. J., Rapid Kinetic Techniques. In *Methods in Cell Biology*, Academic Press: 2008; Vol. 84, pp 445-477.

31. Greenfeld, M.; Solomatin, S. V.; Herschlag, D., Removal of Covalent Heterogeneity Reveals Simple Folding Behavior for P4-P6 RNA *J. Biol. Chem.* **2011,** *286* (22), 19872-19879.

32. Bokinsky, G.; Zhuang, X., Single-Molecule RNA Folding. *Acc. Chem. Res.* **2005,** *38* (7), 566-573.

33. Kowerko, D.; König, S. L. B.; Skilandat, M.; Kruschel, D.; Hadzic, M. C. A. S.; Cardo, L.; Sigel, R. K. O., Cation-Induced Kinetic Heterogeneity of the Intron-Exon Recognition in Single Group II Introns. *Proc. Natl. Acad. Sci. U.S.A.* **2015,** *112* (11), 3403-3408.

34. Moerner, W. E.; Kador, L., Optical Detection and Spectroscopy of Single Molecules in a Solid. *Phys. Rev. Lett.* **1989,** *62* (21), 2535-2538.

35. Orrit, M.; Bernard, J., Single Pentacene Molecules Detected by Fluorescence Excitation in a p-terphenyl Crystal. *Phys. Rev. Lett.* **1990,** *65* (21), 2716-2719.

36. Ha, T.; Zhuang, X.; Kim, H. D.; Orr, J. W.; Williamson, J. R.; Chu, S., Ligand-Induced Conformational Changes Observed in Single RNA Molecules. *Proc. Natl. Acad. Sci. U.S.A.* **1999,** *96* (16), 9077-9082.

37. Zhuang, X.; Bartley, L. E.; Babcock, H. P.; Russell, R.; Ha, T.; Herschlag, D.; Chu, S., A Single-Molecule Study of RNA Catalysis and Folding. *Science* **2000,** *288* (5473), 2048-2051.

38. Hodak, J. H.; Fiore, J. L.; Nesbitt, D. J.; Downey, C. D.; Pardi, A., Docking kinetics and equilibrium of a GAAA tetraloop-receptor motif probed by single-molecule FRET. *Proc. Natl. Acad. Sci. U.S.A.* **2005,** *102* (30), 10505-10510.

39. Sung, H.-L.; Nesbitt, D. J., Single-Molecule FRET Kinetics of the Mn^{2+} Riboswitch: Evidence for Allosteric Mg^{2+} Control of "Induced-Fit" vs "Conformational Selection" Folding Pathways. *J. Phys. Chem. B* **2019,** *123* (9), 2005-2015.

40. Furukawa, K.; Ramesh, A.; Zhou, Z.; Weinberg, Z.; Vallery, T.; Winkler, Wade C.; Breaker, Ronald R., Bacterial Riboswitches Cooperatively Bind Ni^{2+} or Co^{2+} Ions and Control Expression of Heavy Metal Transporters. *Mol. Cell* **2015,** *57* (6), 1088-1098.

41. Xu, J.; Cotruvo, J. A., Reconsidering the *czcD* (NiCo) Riboswitch as an Iron Riboswitch. *ACS Bio Med Chem Au* **2022,** *2* (4), 376-385.

42. Sung, H.-L.; Nesbitt, D. J., Sequential Folding of the Nickel/Cobalt Riboswitch Is Facilitated by a Conformational Intermediate: Insights from Single-Molecule Kinetics and Thermodynamics. *J. Phys. Chem. B* **2020,** *124* (34), 7348-7360.

43. Westhof, E., Water: An Integral Part of Nucleic Acid Structure. *Annu. Rev. Biophys. Biophys. Chem.* **1988,** *17* (1), 125-144.

44. Lane, A. N.; Jenkins, T. C., Thermodynamics of Nucleic Acids and Their Interactions with Ligands. *Q. Rev. Biophys.* **2000,** *33* (3), 255-306.

45. Fiore, J. L.; Holmstrom, E. D.; Nesbitt, D. J., Entropic origin of Mg^{2+}-facilitated RNA folding. *Proc. Natl. Acad. Sci. U.S.A.* **2012,** *109* (8), 2902-2907.

46. Holmstrom, E. D.; Nesbitt, D. J., Biophysical Insights from Temperature-Dependent Single-Molecule Förster Resonance Energy Transfer. *Annu. Rev. Phys. Chem.* **2016,** *67* (1), 441-465.

47. Dupuis, N. F.; Holmstrom, E. D.; Nesbitt, D. J., Molecular-Crowding Effects on Single-Molecule RNA Folding/Unfolding Thermodynamics and Kinetics. *Proc. Natl. Acad. Sci. U.S.A.* **2014,** *111* (23), 8464-8469.

48. Sung, H.-L.; Sengupta, A.; Nesbitt, D., Smaller Molecules Crowd Better: Crowder Size Dependence Revealed by Single-Molecule FRET Studies and Depletion Force Modeling Analysis. *J. Chem. Phys.* **2021,** *154* (15), 155101.

49. Sung, H.-L.; Nesbitt, D. J., Effects of Molecular Crowders on Single-Molecule Nucleic Acid Folding: Temperature-Dependent Studies Reveal True Crowding vs Enthalpic Interactions. *J. Phys. Chem. B* **2021,** *125* (48), 13147-13157.

50. Sasahara, K.; McPhie, P.; Minton, A. P., Effect of Dextran on Protein Stability and Conformation Attributed to Macromolecular Crowding. *J. Mol. Biol.* **2003,** *326* (4), 1227-1237.

51. Kilburn, D.; Roh, J. H.; Guo, L.; Briber, R. M.; Woodson, S. A., Molecular Crowding Stabilizes Folded RNA Structure by the Excluded Volume Effect. *J. Am. Chem. Soc.* **2010,** *132* (25), 8690-8696.

52. Gnutt, D.; Ebbinghaus, S., The Macromolecular Crowding Effect – from in vitro into the Cell. *Biol. Chem.* **2016,** *397* (1), 37-44.

53. Zhou, H.-X., Rate Theories for Biologists. *Q. Rev. Biophys.* **2010,** *43* (2), 219-293.

54. Szabo, A.; Schulten, K.; Schulten, Z., First Passage time Approach to Diffusion Controlled Reactions. *J. Chem. Phys.* **1980,** *72* (8), 4350-4357.

55. Zwanzig, R.; Szabo, A.; Bagchi, B., Levinthal's Paradox. *Proc. Natl. Acad. Sci. U.S.A.* **1992,** *89* (1), 20-22.

56. Aristides Yayanos, A., Deep-Sea Piezophilic Bacteria. In *Methods in Microbiology*, Academic Press: 2001; Vol. 30, pp 615-637.

57. Cocker, J. E., Adaptations of Deep Sea Fishes. *Environ. Biol. Fishes* **1978,** *3* (4), 389-399.

58. Jannasch, H. W.; Taylor, C. D., Deep-Sea Microbiology. *Annu. Rev. Microbiol.* **1984,** *38* (1), 487-487.

59. Jannasch, H. W.; Wirsen, C. O., Variability of Pressure Adaptation in Deep Sea Bacteria. *Arch. Microbiol.* **1984,** *139* (4), 281-288.

60. Gross, M.; Jaenicke, R., Proteins under Pressure. *Eur. J. Biochem.* **1994,** *221* (2), 617-630.

61. Mozhaev, V. V.; Heremans, K.; Frank, J.; Masson, P.; Balny, C., High Pressure Effects on Protein Structure and Function. *Proteins* **1996,** *24* (1), 81-91.

62. Roche, J.; Royer, C. A., Lessons from Pressure Denaturation of Proteins. *J. R. Soc. Interface* **2018,** *15* (147), 20180244.

63. Najaf-Zadeh, R.; Wu, J. Q.; Macgregor, R. B., Effect of Cations on the Volume of the Helix-Coil Transition of poly[d(A-T)]. *Biochim. Biophys. Acta. Gene Struct. Expr.* **1995,** *1262* (1), 52-58.

64. Wu, J. Q.; Macgregor Jr., R. B., Pressure Dependence of the Helix–Coil Transition Temperature of poly[d(G-C)]. *Biopolymers* **1995,** *35* (4), 369-376.

65. Takahashi, S.; Sugimoto, N., Effect of Pressure on Thermal Stability of G-Quadruplex DNA and Double-Stranded DNA Structures. *Molecules* **2013,** *18* (11), 13297-13319.

66. Patra, S.; Anders, C.; Erwin, N.; Winter, R., Osmolyte Effects on the Conformational Dynamics of a DNA Hairpin at Ambient and Extreme Environmental Conditions. *Angew. Chem.* **2017,** *56* (18), 5045-5049.

67. Patra, S.; Anders, C.; Schummel, P. H.; Winter, R., Antagonistic Effects of Natural Osmolyte Mixtures and Hydrostatic Pressure on the Conformational Dynamics of a DNA Hairpin Probed at the Single-Molecule Level. *Phys. Chem. Chem. Phys.* **2018,** *20* (19), 13159-13170.

68. Schneider, S.; Paulsen, H.; Reiter, K. C.; Hinze, E.; Schiene-Fischer, C.; Hübner, C. G., Single Molecule FRET Investigation of Pressure-Driven Unfolding of Cold Shock Protein A. *J. Chem. Phys.* **2018,** *148* (12), 123336.

69. Sung, H.-L.; Nesbitt, D. J., DNA Hairpin Hybridization under Extreme Pressures: A Single-Molecule FRET Study. *J. Phys. Chem. B* **2020,** *124* (1), 110-120.

70. Sung, H.-L.; Nesbitt, D. J., High Pressure Single-Molecule FRET Studies of the Lysine Riboswitch: Cationic and Osmolytic Effects on Pressure Induced Denaturation. *Phys. Chem. Chem. Phys.* **2020,** *22* (28), 15853-15866.

71. Frye, K. J.; Royer, C. A., Probing the Contribution of Internal Cavities to the Volume Change of Protein Unfolding under Pressure. *Protein Sci.* **1998,** *7* (10), 2217-2222.

72. Cioni, P., Role of Protein Cavities on Unfolding Volume Change and on Internal Dynamics under Pressure. *Biophys. J.* **2006,** *91* (9), 3390-3396.

73. Roche, J.; Caro, J. A.; Norberto, D. R.; Barthe, P.; Roumestand, C.; Schlessman, J. L.; Garcia, A. E.; García-Moreno E., B.; Royer, C. A., Cavities Determine the Pressure Unfolding of Proteins. *Proc. Natl. Acad. Sci. U.S.A.* **2012,** *109* (18), 6945-6950.

74. Knight, A. W.; Kalugin, N. G.; Coker, E.; Ilgen, A. G., Water Properties under Nano-Scale Confinement. *Sci. Rep.* **2019,** *9* (1), 8246.

75. Grigera, J. R.; McCarthy, A. N., The Behavior of the Hydrophobic Effect under Pressure and Protein Denaturation. *Biophys. J.* **2010,** *98* (8), 1626-1631.

76. Royer, C.; Winter, R., Protein Hydration and Volumetric Properties. *Curr. Opin. Colloid Interface Sci.* **2011,** *16* (6), 568-571.

77. Mitra, L.; Rouget, J.-B.; Garcia-Moreno, B.; Royer, C. A.; Winter, R., Towards a Quantitative Understanding of Protein Hydration and Volumetric Properties. *ChemPhysChem* **2008,** *9* (18), 2715-2721.

78. Sung, H.-L.; Nesbitt, D. J., Single-Molecule Kinetic Studies of DNA Hybridization under Extreme Pressures. *Phys. Chem. Chem. Phys.* **2020,** *22* (41), 23491-23501.

79. Sung, H.-L.; Nesbitt, D. J., Synergism in the Molecular Crowding of Ligand-Induced Riboswitch Folding: Kinetic/Thermodynamic Insights from Single-Molecule Spectroscopy. *J. Phys. Chem. B* **2022,** *126* (34), 6419-6427.

80. Yancey, P. H.; Gerringer, M. E.; Drazen, J. C.; Rowden, A. A.; Jamieson, A., Marine Fish May be Biochemically Constrained from Inhabiting the Deepest Ocean Depths. *Proc Natl Acad Sci U S A* **2014,** *111* (12), 4461-5.

Chapter 2

Methods

2.1 Single molecule confocal microscope

Observation of single molecule fluorescence is facilitated by a home-built confocal microscope.[1] The microscope system was first set up by a former postdoctoral researcher, Dr. Jose Hodak, with assistance from a former graduate student, Dr. Julie Fiore, and later modified by Dr. Erik Holmstrom. In addition to the microscope setup described in this section, both theses of Dr. Julie Fiore and Dr. Erik Holmstrom are great resources.

2.1.1 Laser excitation path

The excitation source of the single molecule experiment is a 532 nm frequency-doubled Nd:YAG laser pulsed at 20 MHz. The wavelength is chosen to efficiently excite the FRET donor Cy3 (absorption λ_{max} = 555 nm) and facilitate the spectral filtering of the resulting Cy3/Cy5 fluorescence (emission λ_{max} = 570/670 nm). The laser output is first polarized by a half wave plate and a polarizing beam splitter. The 1 mm diameter ($1/e^2$) beam is then expanded by a Keplerian telescope consisting a pair of lenses with focal lengths 25 mm and 300 mm, respectively. Before being directed to the back port of the inverted microscope (Olympus IX70), the beam is attenuated by an array of neutral density filters in adjustment of the optical power for single molecule fluorescence experiments. Inside the microscope (Figure 2.1), the beam is reflected upward by a custom two-color dichroic mirror to a 1.2 N.A. water immersion objective. With the back aperture ($d_{aperture}$ = 9.25 mm) overfilled by the collimated beam, the objective can effectively focus the laser into a diffraction-limited spot ($d_{x\text{-}y}$ = 260 nm) for excitation and collection of the single molecule fluorescence.

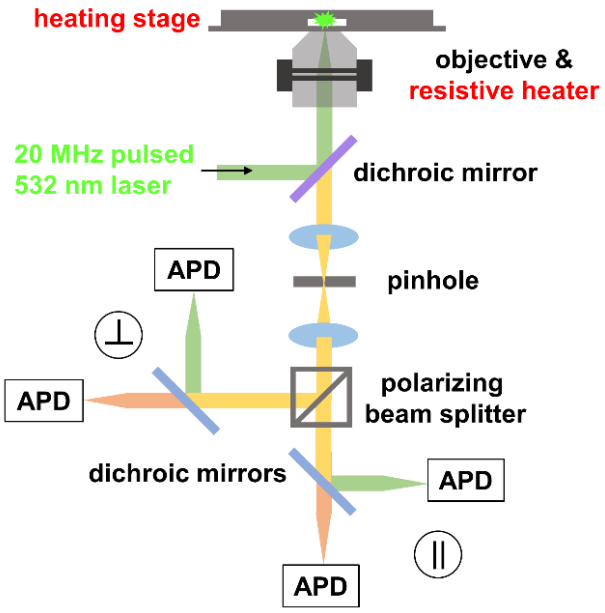

Figure 2.1 Schematic of the confocal microscope excitation/emission paths. The temperature control units are indicated in red.

2.1.2 Fluorescence emission path and detection

During single molecule fluorescence experiments, the emitted photons within the laser focus are collected by the same objective, directed through a dichroic mirror, and focused by a tube lens (f = 80 mm) before exiting the microscope side port (Figure 2.1). The resulting focused beam is subsequently filtered by a 50 µm pinhole to reject out-of-focus photons and directed to the detection unit, which contains a tree of four avalanche photodiodes (APDs, SPCM-ARQ-14, Excelitas). The photons are first spatially separated by polarization with a polarizing beam cube, and then by color with dichroic mirrors (645DCXR, Chroma Technology). Prior to detection, photons are filtered by band pass (long pass) filters to reject the photons from excitation source and ensure only Cy3 (Cy5) fluorescence reaches the green (red) APDs.

2.2 Temperature Control

Temperature as an experimental variable enables the deconstruction of the free energy into enthalpy and entropy contributions (e.g., via the van't Hoff analysis).[2] Moreover, in conjunction with the kinetic information obtained from the single molecule measurements, temperature dependence helps characterize the thermodynamic property of the transition state, and in turn construct the energy landscape in both enthalpic and entropic components. Such abundance of thermodynamic information allows us to readily identify physical phenomena such as ligand binding and the molecular crowding effect as described later in the thesis.

The temperature control is achieved by sample heating (Figure 2.1). In temperature dependent experiments, the sample is placed in the chamber of the enclosed heating stage (Instec) with vacuum grease to increase thermal contact. Moreover, the resistively heated wire-based collar heater (Bioptechs) is used to warm up the microscope objective to minimize the heat flow across the sample. With simultaneous heating both the sample and objective, the sample temperature can be precisely controlled with minimal thermal fluctuation (± 0.1 ℃). It is important to note due to the delicate nature of optical elements inside the microscope objective, the maximum heating temperature is limited to 50 ℃ with a relatively slow temperature ramp of 1 ℃/min. The system is allowed to equilibrate for 10 minutes prior to each temperature-controlled experiment. Although the 20 to 50 ℃ heating range is sufficient to explore most of the thermodynamic properties of our interest (i.e., nucleic acid folding), it's worth noting that an infrared-based laser heating method is developed by a former graduate student, Dr. Erik Holmstrom to expand the heading capability (up to 90 ℃) in our lab.[3] For more experiment details, please refer to his thesis.

2.3 Sample preparation

We use FRET (Forster resonance energy transfer) to visualize the conformation changes of biomolecules. To enable FRET observation, biomolecules of interest are doubly labeled with the Cy3-Cy5 FRET pair, and often with biotin modification to allow surface immobilization measurements (2.4.2).

2.3.1 Single molecule construct

The doubly fluorophore-labeled construct design is perhaps the most important step for the single molecule FRET experiment. The goal is to generate a biologically-relevant structure that i) undergoes conformational transition and ii) generate sufficient contrast in FRET efficiency, E_{FRET}. The selection of the fluorophore-labeling positions is therefore particularly crucial in construct design. Fortunately, it can be efficiently assisted by known structural data, especially the crystal structure of the protein/nucleic acid of interest in its native folded state. Since the characteristic length R_0 of the Cy3-Cy5 FRET pair is ≈ 50 Å, E_{FRET} is extremely sensitive to the change in distance between Cy3 and Cy5 ($\sim r^6$) when $r \approx R_0$ (Figure 2.2). Therefore, the general approach is to label Cy3 and Cy5 on each of the stems that are most likely to undergo conformational transition at a distance that is roughly 5 to 10 Å below R_0 according to the structural data of the folded conformation. In that case, we usually obtain a folded/native conformation with a mid to high E_{FRET} value, and would expect a sharp decrease in E_{FRET} when the construct unfolds and brings Cy3 and Cy5 further apart. However, the structure and consequently the E_{FRET} of the unfolded conformation is much less predictable due to lack of structural characterization. The unsuccessful design may result from insufficient E_{FRET} change upon unfolding or simply the fact that the targeted interaction might not be sensitive to the solute of interest (e.g., salts, osmolytes, and related ligands) at the physiologically relevant range.

In the surface immobilization experiments (2.4.2), the construct is tethered to the surface through biotin-streptavidin interaction, and therefore also needs to be biotin-labeled. Due to the constraint from the labeling site, we often apply the "flagpole" method to reduce the synthetic complexity of the oligomers, and provide reliable tethering without significant perturbation from the surface. Specifically, we attach a biotinylated DNA/RNA flagpole to the dangling extension strand of the readily fluorophore-labeled construct.[1] The rigid double-stranded flagpole ensure the minimal interaction between the construct and the protein-passivated surface.

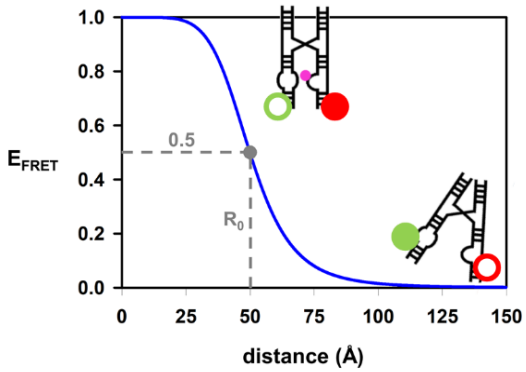

Figure 2.2 FRET energy transfer efficiency (E_{FRET}) as a function of distance between Cy3 and Cy5 (R_0 = 50 Å).

With extensive use of the flagpole strategy, our nucleic acid constructs are often assemblies of two or more oligomers. To prepare the multicomponent construct, the oligomers are first heat annealed, followed by high performance liquid chromatography (HPLC) purification. The purified product is stored at -70 ℃ in 50 mM HEPES buffer with 0.1 mM EDTA to prevent cleavage of the nucleic acid catalyzed by the divalent cation, e.g. Mg^{2+}. For use in day to day experiments, aliquot of the stock is dilute to 25 nM and may be stored at -20 ℃.

2.3.2 Sample of interest

Both the feely diffusing (2.4.1) and the surface immobilization (2.4.2) single molecule FRET measurements can be performed directly on the glass coverslip under the open-air condition. However, the data collection often required a extended experiment time. Therefore, the sandwich style sample holder is preferred in order to minimize the sample evaporation. To prepare the sandwich style sample holder, two stripes of double-sided sticky tape (3M) are apply parallelly across the glass slide with a ≈ 5 mm spacing. The space between the double-sided sticky tapes is subsequently topped with a coverslip to create a channel with the height of ≈ 80 μm, which allows us to flush through the desired solution via the capillary effect. In the single molecule experiment, the sandwich style sample holder can be directly supported by the microscope stage with the coverslip side down. In the temperature dependent experiment, the glass slide support is trimmed down to 25 mm × 25 mm in size by a diamond glass scriber pen in order to fit in the enclosed chamber of the heating stage (2.2).

For the feely diffusing (see 2.4.1 for more details) experiment, the nucleic acid stock is diluted in the imaging buffer to obtain the sample solution with 100 pM nucleic acid. The resulting sample solution can be directly flowed into the sandwich style sample holder for feely diffusing single molecule study. The imaging buffer contains buffer and background salts, solute(s) of interest, and the enzymatic oxygen scavenging system (PCA/PCD/TROLOX)[4] to catalytically remove oxygen and increase the photostability of the fluorophores.

Sample for the surface immobilization (2.4.2) single molecule measurement requires additional steps to decorate the surface of the coverslip with nucleic acid constructs via the biotin streptavidin interaction. First the surface of the coverslip is passivated by flushing the channel of the sandwich sample holder by a 10% biotinylated BSA (bovine serum albumin) solution (10 mg/mL). The BSA surface is negatively charged and therefore efficiently repels the nucleic acid

construct to prevent nonspecific surface attachment. The sample holder is then consecutively incubated with the streptavidin (200 μg/mL) and the biotinylated construct (≈ 25 pM) solutions with a 10-minute incubation time for each. Prior to each experiment, the sample holder is flushed by the imaging buffer with the desired experiment condition.

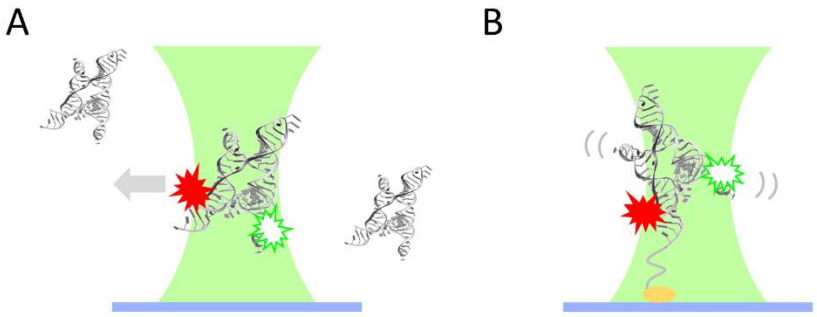

Figure 2.3 Two common strategies of the single molecule FRET experiment: A) freely diffusing and (B) surface immobilization. The construct in (B) is tethered to the glass surface through the biotin-streptavidin interaction.

2.4 Single molecule FRET experiment

The two strategies of the single molecule experiment are illustrated in Figure 2.3. The freely diffusing method offers a simple way to directly observe the FRET efficiency E_{FRET} from a doubly fluorophore-labeled construct diffusing though the confocal volume, and the results are free of surface perturbation. The surface immobilization method, on the other hand allows monitoring the single molecule E_{FRET} as a function of time and therefore generate valuable kinetic information.

2.4.1 Freely diffusing method

To perform the single molecule experiment, the nucleic acid construct is allowed to freely diffuse in the solution (Figure 2.3A). The excitation laser is focused into the solution and record the fluorescence signal each time a fluorophore-labeled construct passing through. To ensure

each fluorescent event comes from a single nucleic acid construct, its concentration needs to be sufficiently low so only one construct is in the focus at a time. With the present microscope setup, the $1/e^2$ focus region (termed as confocal volume) is measured as ≈ 0.20 fL. The concentration to have approximately 1 construct per 0.20 fL is calculated to be ≈ 10 nM. We therefore work with lower construct concentrations ≈100 pM to ensure majority of the fluorescence events coming from a single construct, while being able to acquire sufficient statistics of fluorescence events within reasonable experiment time.

In practice, the source of Cy3 emission event ($E_{FRET} \approx 0$) can be complex, including the doubly fluorophore-labeled construct in the low E_{FRET} conformation, construct with photobleached Cy5, incomplete construct with Cy3 only, and free Cy3 molecule. Therefore, a 635 nm laser is incorporated into the freely diffusing experiment to selectively excite Cy5 (λ_{max} = 650 nm) via the alternating laser excitation scheme (ALEX).[5] The intervening excitation of Cy3 and Cy5 allows us to confirm the fluorescent event comes from a doubly fluorophore-labeled construct by examining the signal correlation between the 532 nm and 635 nm excitation channels.

2.4.2 Surface immobilization method

Surface immobilization permits prolonged observation of the fluorescent signal from a single nucleic acid construct (Figure 2.3B). To achieve that, a surface scan of the excitation laser is performed to locate the fluorophore-labeled construct. With extended laser illumination, the time-dependent fluorescence of the located molecule can be used to calculate the time trajectory of E_{FRET} for further kinetic analysis (Figure 2.4). With the in-house analysis software written by Dr. Vasiliy Fomenko, the bin time of the resulting trajectory can be adjusted post-acquisition to improve the signal-to-noise level in trade of the temporal resolution. A simple thresholding

method can be used to determine the dwell time for each E_{FRET} state when the two E_{FRET} populations are widely separated with respected to their spread (Figure 2.4B). Specifically, an E_{FRET} threshold between two E_{FRET} populations is applied to distinguish the state of the nucleic acid construct at each bin. From that, a collection of dwell time—time spent in a particular state—can be obtained and further used to acquire the kinetic information (Figure 2.4C). In cases when the cumulative distribution of dwell time can be well-fit to a single exponential decay function, the process can be sufficiently described by a first order kinetic constant.

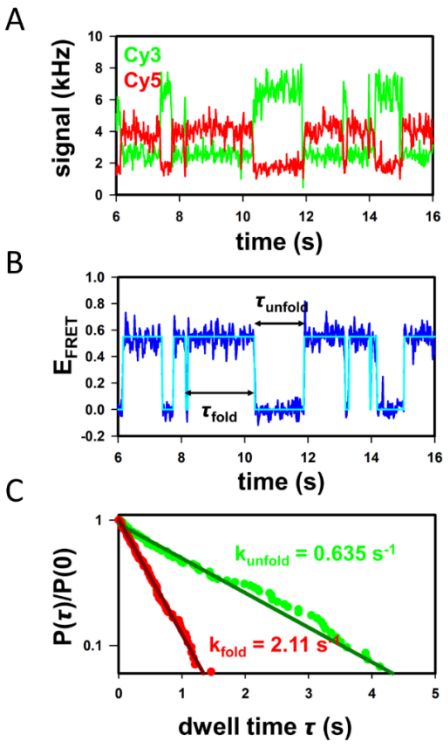

Figure 2.4 Sample surface immobilization single molecule FRET data. (A) fluorescence signal from Cy3 (green) and Cy5 (red) as a function of time. (B) the resulting time trajectory of E_{FRET}, where the high and low E_{FRET} states corresponding to the folded and unfolded conformation, respectively. (C) dwell time distributions (plotted in reverse cumulative distribution functions) for each state. The data are well-fit to a single exponential decay function to obtain the first order folding and unfolding rate constants k_{fold} and k_{unfold}, respectively. Typically, each set of data contains 20 to 50 molecules throughout this thesis.

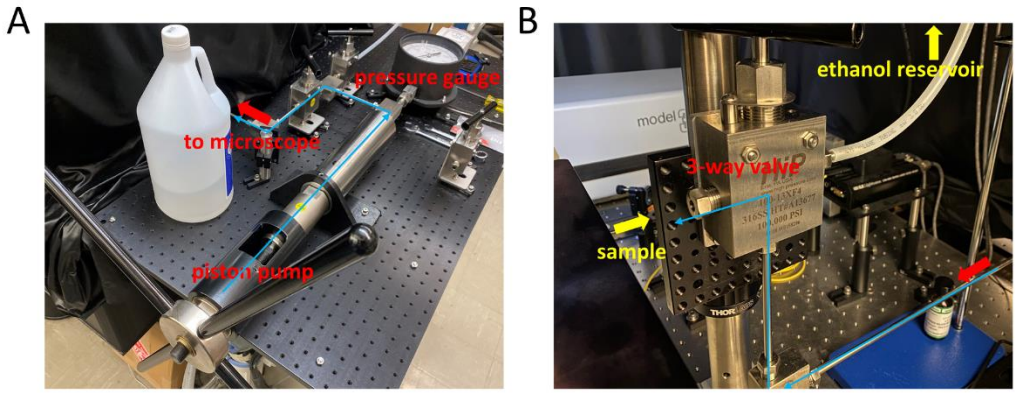

Figure 2.5 Images of the high pressure generating system. (A) The manually operated piston screw pump and the pressure gauge mounted on the extended surface outside the laser curtain. (B) The three-way control valve mounted to the optical breadboard that allows vertical translation of the sample holder. The blue lines/arrows indicate the direction of pressure transmitting through the high pressure tubing.

2.5 High pressure single molecule experiment

Besides temperature, pressure is another thermodynamic variable that plays an important role in biomolecule conformational change.[6] The single molecule experiment is herein incorporated with a pressure generating system to facilitate the exploration of the pressure dependent nucleic acid folding.

2.5.1 Pressure generation and transmission

The source of high pressure is a manually operated piston screw pump (Figure 2.5A, High Pressure Equipment), which is connected through high-pressure stainless-steel tubing to a bourdon tube pressure gauge for pressure measurements (accuracy ≈ 25 bar).[7-8] The liquid reservoirs contain ethanol as pressure transmitting fluid in use to remove air bubbles in the stainless-steel tubing manifold to increase the pressuring efficiency. The pressure is directed to a three-way control valve for coupling with the high pressure sample cell (Figure 2.5B). Note that

the control valve is mounted onto an optical breadboard with an adjustable post clamp to allow the vertical translation along the metal post for sample alignment with the microscope.

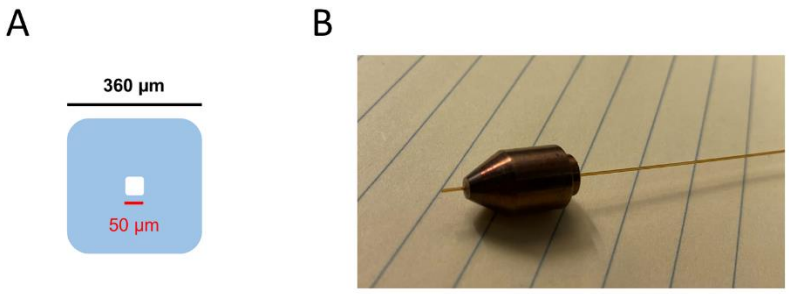

Figure 2.6 Capillary sample holder for the high pressure single molecule experiments. (A) the cross section of the square capillary. (B) the capillary end glued into the metal plug for coupling to the high pressure system.

2.5.2 Sample preparation for high pressure measurements

The high pressure sample holder is made from a glass capillary with a square cross section (Polymicro) while the inner and outer dimensions are measured as 50 µm and 360 µm, respectively (Figure 2.6A). The small surface area permits the capillary cell to sustain pressure up to ≈ 4 kilobars. Moreover, the flat surfaces and wall thickness (155 µm) allow it to behave like a regular coverslip in standard microscope imaging. To prepare the sample holder, one end of the capillary is first glue to a metal plug with a 450 µm diameter hole for further coupling to the high pressure system (Figure 2.6B). To create an optical window for fluorescence observation, about 1 to 2 inches of the nontransparent polyimide coating is burned away with a propane torch. Note that the location of the exposed capillary has to align with the objective after plugged into the control valve, about 17.5 cm away from the metal plug end in current instrument configuration.

In high pressure freely diffusing experiments, the capillary is filled with the imaging buffer containing the doubly fluorophore-labeled construct through the capillary effect simply by dipping the metal plug-attached open end into the sample solution. The same end of the capillary is then dipped into the low-viscosity silicon oil to create a thin film (≈ 25 to 50 μm) inside the capillary to prevent the sample contamination from the pressure transmitting fluid ethanol. Before high pressure experiment, the distal end (from the metal plug) of the capillary is sealed with an oxy-propane torch.

For high pressure surface immobilization experiments,[9] the sample is prepared by consecutively flushing the capillary cell with the following solutions: i) 10% biotinylated BSA (10 mg/mL), ii) streptavidin (200 μg/mL), iii) nucleic acid construct (≈ 25 pM), and iv) the imaging buffer (2.3.2). With a mechanical micropipette (Eppendorf) to continuously push the solutions through the capillary at the flow rate measured as ≈ 2 μL/min, the exposure time for each solution is approximately 2 minutes. After the interior surface of the capillary is decorated with nucleic acid in the desired buffer solution, the metal-plug end is then dipped into the silicon oil, followed by sealing the distal end with an oxy-propane torch prior to coupling to the high pressure system.

2.6 References

1. Fiore, J. L.; Hodak, J. H.; Piestert, O.; Downey, C. D.; Nesbitt, D. J., Monovalent and Divalent Promoted GAAA Tetraloop-Receptor Tertiary Interactions from Freely Diffusing Single-Molecule Studies. *Biophys. J.* **2008,** *95* (8), 3892-3905.

2. Holmstrom, E. D.; Nesbitt, D. J., Biophysical Insights from Temperature-Dependent Single-Molecule Förster Resonance Energy Transfer. *Annu. Rev. Phys. Chem.* **2016,** *67* (1), 441-465.

3. Holmstrom, E. D.; Nesbitt, D. J., Localized Heating of Single Oligonucleotides using Infrared Light. *Biophys. J.* **2012,** *102* (3), 180a.

4. Aitken, C. E.; Marshall, R. A.; Puglisi, J. D., An Oxygen Scavenging System for Improvement of Dye Stability in Single-Molecule Fluorescence Experiments. *Biophys. J.* **2008,** *94* (5), 1826-1835.

5. Lee, N. K.; Kapanidis, A. N.; Wang, Y.; Michalet, X.; Mukhopadhyay, J.; Ebright, R. H.; Weiss, S., Accurate FRET Measurements within Single Diffusing Biomolecules Using Alternating-Laser Excitation. *Biophys. J.* **2005,** *88* (4), 2939-2953.

6. Mozhaev, V. V.; Heremans, K.; Frank, J.; Masson, P.; Balny, C., High Pressure Effects on Protein Structure and Function. *Proteins* **1996,** *24* (1), 81-91.

7. Patra, S.; Anders, C.; Erwin, N.; Winter, R., Osmolyte Effects on the Conformational Dynamics of a DNA Hairpin at Ambient and Extreme Environmental Conditions. *Angew. Chem.* **2017,** *56* (18), 5045-5049.

8. Sung, H.-L.; Nesbitt, D. J., DNA Hairpin Hybridization under Extreme Pressures: A Single-Molecule FRET Study. *J. Phys. Chem. B* **2020,** *124* (1), 110-120.

9. Sung, H.-L.; Nesbitt, D. J., Single-Molecule Kinetic Studies of DNA Hybridization under Extreme Pressures. *Phys. Chem. Chem. Phys.* **2020,** *22* (41), 23491-23501.

Chapter 3

Single Molecule FRET Kinetics of the Mn^{2+} Riboswitch: Evidence for Allosteric Mn^{2+} Control of "Induced-Fit" vs. "Conformational Selection" Folding Pathways

---

3.1 Abstract

Gene expression in bacteria is often regulated dynamically by conformational changes in a riboswitch upon ligand binding, a detailed understanding of which is very much in its infancy. For example, the manganese riboswitch is a widespread RNA motif that conformationally responds in regulating bacterial gene expression to μM levels of its eponymous ligand, Mn^{2+}, but the mechanistic pathways are poorly understood. In this work, we quantitatively explore the dynamic folding behavior of the manganese riboswitch by single molecule FRET spectroscopy (smFRET) as function of cation/ligand conditions. From detailed analysis of the kinetics, the Mn^{2+} is shown to fold the riboswitch by a "bind-then-fold" (i.e., "induced-fit," IF) mechanism, whereby the ligand binds first and then promotes folding. On the other hand, the data also clearly reveal the presence of a folded yet ligand free structure predominating due to addition of physiological Mg^{2+} to a non-selective metal ion binding site. Of particular kinetic interest, such a Mg^{2+} "pre-folded" conformation of the riboswitch is shown to exhibit a *significantly increased affinity* for Mn^{2+} and further stabilization by subsequent binding of the ligand, thereby promoting efficient riboswitch folding by a "fold-then-bind" (i.e., "conformational selection," CS) mechanism. Our results not only demonstrate Mg^{2+} controlled switching between IF and CS riboswitch folding pathways, but also suggest a novel heterotropic allosteric control in the manganese riboswitch activity co-regulated by Mg^{2+} binding.

*This chapter is adapted from: Sung, H.-L.; Nesbitt, D. J. Single Molecule FRET Kinetics of the Mn^{2+} Riboswitch: Evidence for Allosteric Mg^{2+} Control of "Induced Fit" vs. "Conformational Selection" Folding Pathways. *J. Phys. Chem. B* **2019**, *123*, 2005-2015.

3.2 Introduction

Riboswitches are *cis*-acting regulatory RNA strands typically encoded in the 5' upstream untranslated regions of the genes which they regulate[1-4]. These structured RNA elements consist of i) an aptamer domain and ii) an expression platform, whereby the aptamer structurally binds a cognate ligand, inducing the expression platform to undergo conformational change in response[5-6]. This conformational shift, in turn, achieves a desired biochemical goal, such as blocked initiation of the translational event, premature termination of gene transcription, or controlled cleavage of the mRNA[4-5]. Such regulatory mechanisms of ligand responsive riboswitches are widely adopted by the bacterial kingdom. Many classes of both translational and transcriptional riboswitches have been identified and structurally characterized to date, responding to variety of molecular ligands, including enzymatic cofactors[7-11], nucleotide derivatives[12-13], and amino acids[14-16], but also simple atomic ions such as F^- [17-18], Mg^{2+} [19], Ni^{2+}/Co^{2+} [20] and Mn^{2+} [21-22].

The manganese (Mn^{2+}) responsive riboswitch (commonly denoted as the *yybP-ykoY* riboswitch) is now known to be extensively distributed among many bacterial phyla. However, even simple confirmation of the ligand identity was obtained only recently[21-22], due primarily to lack of characterization of the associated genes (*yybP* and *ykoY*) in *Bacillus subtilis* where the RNA motif was first discovered[23]. The aptamer domain of the manganese riboswitch comprises a four-way junction connecting four helices, which in the ligand-bound crystal structure (Figure 3.1A)[21] coaxially align in pairs to generate a tight hairpin-like conformation. The two helices (P1 and P3) then dock into highly conserved internal loop regions (L1 and L3), forming an elaborate interface stabilized by two coordinated divalent metal ion sites evident in the crystal structure (Figure 3.1B). Of these two metal binding sites, the first exhibits a very high specificity for Mn^{2+} over Mg^{2+}, whereas the second shows little cation selectivity and is largely occupied by Mg^{2+}

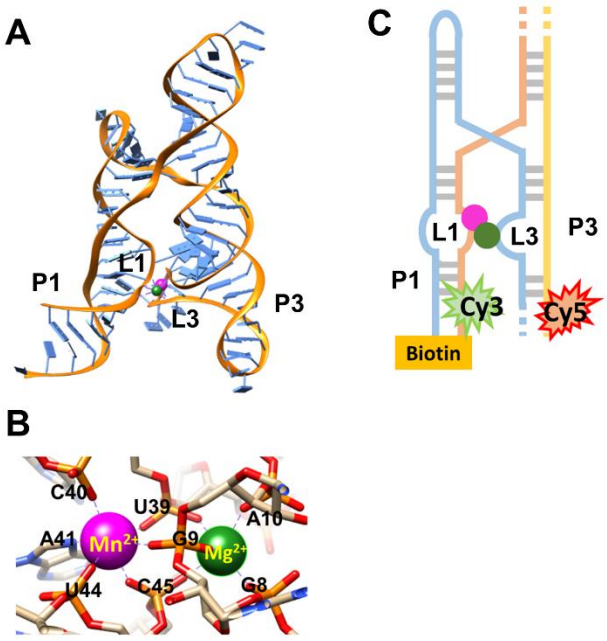

Figure 3.1 Structure of *L. lactis yybP-ykoY* manganese riboswitch (A) Overall crystal structure reconstructed from X-ray diffraction data (PDB 4Y1I) (B) Structure of M^{2+} binding sites with adjacent nucleotides (C) RNA construct design for smFRET experiment.

under physiological conditions. In fact, it is rather remarkable that this RNA riboswitch responds so preferentially to Mn^{2+} over Mg^{2+}, as both cations are similar in size, charge and coordination complex geometry[24], particularly with cellular Mg^{2+} concentrations[25] 10-100 fold higher than Mn^{2+}[26]. From previous mutational studies, it has been demonstrated that the origin of this high Mn^{2+} selectivity is preferential coordination between manganese and nitrogen (N7) in A41 (Figure 3.1B)[21, 24, 27] as Mg^{2+} is only known directly coordinated in RNA to oxygen.

Despite detailed crystallographic knowledge of the ligand-bound (i.e. fully-folded) riboswitch conformation, the dynamics and mechanisms for ligand-aptamer recognition and folding processes has remained elusive. By way of introduction, ligand promoted folding mechanisms can generally be classified into two categories, either i) induced-fit (IF) or ii)

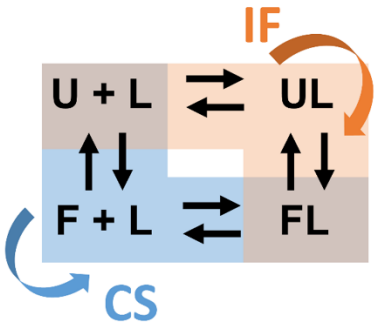

Figure 3.2 Schematic illustration of induced-fit (IF) and conformational selection (CS) pathways in the context of a four-state kinetic model.

conformational selection (CS)[28-32] (See Figure 3.2). In the induced-fit (IF) mechanism, the ligand binds to the unfolded conformation and triggers the folding event ("bind-then-fold"), whereas via conformational selection (CS), the structure dynamically rearranges into a "pre-folded" state that is subsequently further stabilized by the ligand ("fold-then-bind"). Despite obvious physical differences between these two kinetic pathways, it has proven quite challenging to distinguish between them in equilibrium ensemble experiments. With single-molecule methods, by way of contrast, conformational changes in response to the ligand can be probed at the single construct level, which in recent studies has enabled the identification of these two distinct IF and CS folding pathways for both proteins[33-34] and nucleic acids[35-40].

In this present work, the folding dynamics of the manganese riboswitch are monitored directly by single-molecule FRET (smFRET) spectroscopy, for which energy transfer (E_{FRET}) between covalently attached Cy3 and Cy5 dyes provides a probe of RNA conformational changes in real time at the single molecule level (Figure 3.1C). The resulting time dependent E_{FRET} trajectories provide direct kinetic information on the folding (k_{fold}) and unfolding (k_{unfold}) kinetic rate constants, as well as the overall folding equilibrium behavior ($K_{eq} = k_{fold}/k_{unfold}$). Of particular relevance to the present study, the ligand dependence of the folding/unfolding rate

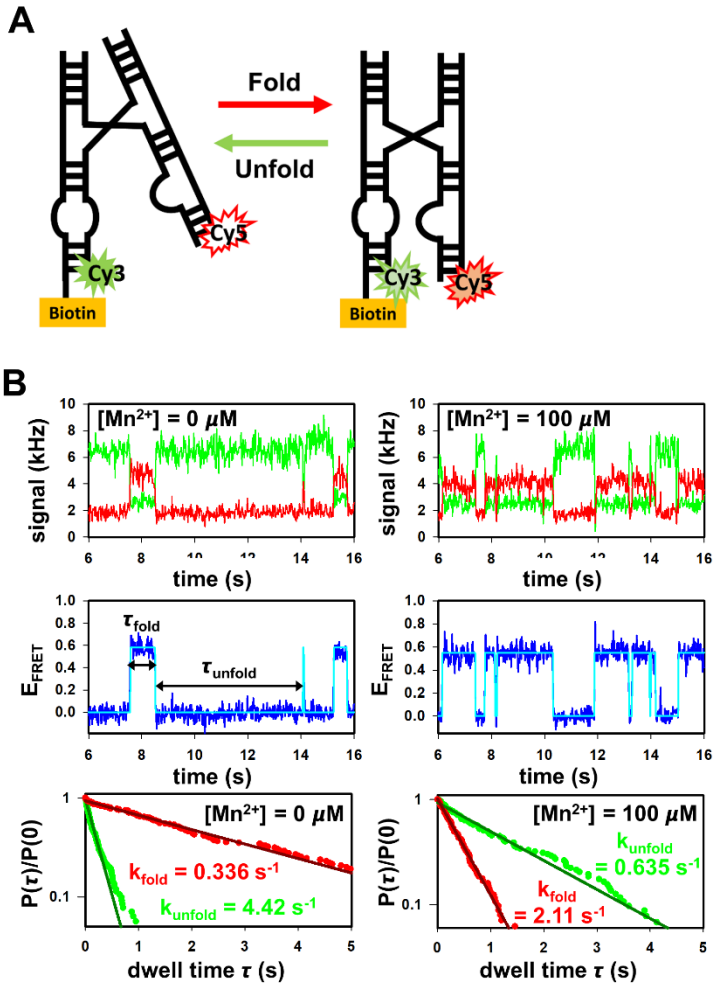

Figure 3.3 Sample smFRET experimental data; both with background 0.5 mM $MgCl_2$ and total 125 mM monovalent cation (A) Visual representation of manganese riboswitch folding changing the distance between Cy3 and Cy5 (B) (from top to bottom) Fluorescence time traces of signals from Cy3 and Cy5, the corresponding E_{FRET} trajectories, cumulative distribution function of dwell time analysis.

constants allows the aptamer recognition and folding mechanisms to be kinetically isolated and characterized individually.

In this investigation of manganese riboswitch folding, we build kinetic models and fit the smFRET data as a function of $[Mn^{2+}]$ and $[Mg^{2+}]$ to explicitly demonstrate which of the two (IF or CS) folding pathways is chosen under a specific cation environment. Interestingly, the work

reveals that manganese riboswitch folding can be impacted by either [Mn^{2+}] or [Mg^{2+}]. On the one hand, detailed kinetic analysis of the smFRET data reveals a 100-fold greater binding affinity for Mn^{2+} vs Mg^{2+}, which lends support to the simple Mn^{2+} ligand-promoted "induced-fit" folding mechanism. However, a parallel Mg^{2+} mediated folding process has also been identified, specifically in which Mg^{2+} promotes formation of a transient Mn^{2+} ligand-free (apo) pre-folded state, which then provides a subsequent binding platform for Mn^{2+} to further stabilize the conformation. We note that such Mg^{2+} control of the kinetic mechanism is strongly reminiscent of allostery commonly seen in enzymes, whereby binding of an "effector" species can alter the overall conformation and thereby regulate ligand affinity at a remote binding site.[41-43]. As explicitly shown in the current smFRET data, the ability of Mg^{2+} to facilitate riboswitch sampling states of more fold-like character provides an intriguing example of "RNA allostery."[44-46] Simply stated, the presence or absence of physiological Mg^{2+} is able to modulate the Mn^{+2} riboswitch folding pathway from that of induced-fit ("bind-then-fold") to conformational selection ("fold-then-bind").

3.3 Experiment

3.3.1 RNA construct design and preparation for single-molecule study

The aptamer domain of manganese riboswitch is a hairpin-like structure rearranged with four helices joined by a four-way junction (see Figure 3.1A). As shown in this crystal structure [21], folding between loops L1 and L3 can be stabilized by one Mn^{2+} and one Mg^{2+} (or a second Mn^{2+}) through metal coordination. The smFRET RNA construct (Figure 3.1C) is designed to probe the interaction between L1 and L3 that are not only considered as the major structural

change during riboswitch folding but also have been identified as crucial elements for ligand recognition and binding[21-22].

The manganese riboswitch in this work is constructed from the sequence of *Lactococcus lactis* that has been structurally characterized in previous studies.[21] To achieve surface immobilization and dye labeling, the riboswitch construct is formed by annealing three chemically modified RNA oligos from Integrated DNA Technologies (IDT, Coralville, IA): (i) Biotinylated strand 1, 5'-biotin- GUG UGU GUG UGU GUG GCA AAG GGG AGU AGC GUC GGG AAA CCG AAA CAA AGU CGU CAA UUC GUG AGC GCA CUC GUC UGA G-3'; (ii) Cy3 labeled strand 2, 5'-GGU ACG CAC GUA CGG UAU GUU UAG CAA GAC CU-Cy3- UUG CCA CAC ACA CAC ACA C-3'; and (iii) Cy5 labeled strand 3, 5'-Cy5-CUC AGA CGA GUG CGC UCA CCG GCU UUG UUG ACA UAC CGU ACG UGC GUA CC-3' (Figure 3.1C). Each end of the open helix is extended from its native sequence by 14 base pairs to stabilize the RNA trimer construct under all experimental cation conditions of interest. The FRET pair Cy3 and Cy5 are labeled at the end of P1 and P3 respectively with distance between them estimated from crystal structure plots to be ~45 Å[21]. For the characteristic Forster length of the Cy3 and Cy5 FRET pair (R_0 ~50 Å), we expect an intermediate E_{FRET} (~ 0.5) state for the folded conformation, which will drop to FRET values near zero in the unfolded state due to the rapid ~$1/R^6$ dependence on distance. (Figure 3.3).

The RNA molecules for smFRET studies are tethered on the surface of glass coverslip by biotin-streptavidin interactions. Sample preparation is accomplished by successively flushing the sample holder in the following solution order to obtain ~50 RNAs per 100 μm^2 surface coverage: (i) 10 mg/mL bovine serum albumin (BSA) with 10% biotinylated BSA, (ii) 200 µg/mL streptavidin solution, (iii) ~ 25 pM of the biotin/dye labeled and annealed RNA riboswitch

construct, with the samples allowed to incubate for 10 mins between each step. Immediately prior to a specific smFRET data run, the sample holder is then flushed by a buffer containing (i) 50 mM hemisodium HEPES buffer (pH 7.5), (ii) enzymatic oxygen scavenger cocktail (PCD/PCA/Trolox) to catalytically remove oxygen, (iii) 100 mM NaCl to provide background monovalent salt, and (iv) sufficient $MgCl_2$ and/or $MnCl_2$ to tune the divalent cation concentrations over the desired dynamic range.

3.3.2 Single-molecule FRET spectroscopy and data analysis

A 532 nm beam from a pulsed Nd:YAG laser (10 ps pulses at a 20 MHz repetition rate) is directed onto a sample through an inverted confocal microscope with a 1.2 N.A. water immersion objective. The beam is collimated with lenses in the backplane to overfill the limiting microscope aperture, resulting in a diffraction limited laser excitation/collection spot ($r_{x\text{-}y}$ ~250 nm). For the smFRET experiments, the laser illuminates the surface of coverslip with sub-femtoliter confocal volume control to allow observation of single fluorophore-labeled RNA constructs. The resulting fluorescence signal is then collected through the same objective and split by i) color (green/red) and ii) polarization (horizontal/vertical) before detection on four single photon avalanche photodiodes (APDs). For each photon detection event, 4 bits of information (color, polarization, wall clock time (± 50 ns) and microtime with respect to the laser pulse (± 50 ps)) are recorded with a time-correlated single-photon counting (TCSPC) module.

The donor/acceptor fluoresence photon arrivals as a function of wall clock time are analyzed with in-house software to generate background and cross talk corrected E_{FRET} = I(red)/(I(green) + I(red)) trajectories with 20-ms bin time resolution (Figure 3.3B). Since populations for the two distinct riboswitch conformations are quite separated in E_{FRET} value, a

simple thresholding routine can be used to obtain dwell time distributions for the ensemble of time durations spent in the folded (docked) vs. unfolded (undocked) state between transitions. The folding (docking) equilibrium constant ($K_{eq} \approx$ [fold]/[unfold]) can be accurately measured by i) ratios of total dwell times for folded and unfolded states, but with far more detailed information on the folding/unfolding kinetic rate constants obtained from ii) analyzing cumulative distribution functions (CDFs) for the individual dwell times ($P(\boldsymbol{\tau})/P(0)$)[47]. The resulting plots of ln [$P(\boldsymbol{\tau})/P(0)$] vs. low FRET and high FRET dwell times are linear (see Figure 3.3B, lower panel), corresponding to single exponential decays that yield first order docking and undocking rate constants (k_{dock} and k_{undock}), respectively.

3.4 Results and analysis

3.4.1 Manganese riboswitch folding kinetics with Mg^{2+} alone

Structural changes in the manganese riboswitch construct are signaled by the labeled Cy3/Cy5 FRET dye pair, with FRET energy transfer clearly evident in the anti-correlated red and green fluorescent signals as function of time (Figure 3.3B upper panel). The resulting E_{FRET} time trajectories indicate that the manganese riboswitch oscillates between two states with distinct E_{FRET} values ~ 0.5 and 0, consistent with predictions based on the construct geometry. The high E_{FRET} state corresponds to a fully folded conformation with the two L1 and L3 loops mutually docked onto each other, while the low E_{FRET} state corresponds to an unfolded conformation with the two loops substantially further apart.

In these smFRET experiments, the presence of either Mg^{2+} or Mn^{2+} divalent metal cation is required for folding of the manganese riboswitch. Specifically, no folding events are seen at background (125 mM) monovalent salt levels. However, as evident in the trajectories in Figure

3.3B, transitions between high and low E_{FRET} states are readily observed already at 0.5 mM Mg^{2+}, with the low E_{FRET} state more dominant and the RNA mostly unfolded. On the other hand, with addition of only 100 μM Mn^{2+} (right panels of Figure 3.3B), the high E_{FRET} population becomes significantly more prominent, indicating that the overall stability of the folded manganese riboswitch is promoted by its eponymous ligand Mn^{2+}. Note that from E_{FRET} values, the folded states promoted by Mn^{2+} and Mg^{2+} alone are indistinguishable, consistent with Mg^{2+} alone being capable of facilitating L1 and L3 docking and promoting transcriptional readthrough in previous *in vitro* transcription assay at relatively high concentration (> 10 mM)[21].

We first explore the Mg^{2+} concentration dependence of manganese riboswitch folding in absence of ligand ($[Mn^{2+}] = 0$), explicitly probing the equilibrium folded fraction as a function of $[Mg^{2+}]$. The sample data in Figure 3.4A make it clear that Mg^{2+} promotes folding and the data exhibit minimal cooperativity, as evidenced by a nearly linear increase in folded fraction at low $[Mg^{2+}]$. The results can be fit to a modified Hill equation[48-53]:

$$\text{fraction folded} = F_0 + (1 - F_0) \times F_s \left(\frac{[M^{2+}]^n}{K_D{}^n + [M^{2+}]^n} \right), \qquad \text{Eq. 3.1}$$

where F_0 and F_s are attributed to folding under $[Mg^{2+}] = 0$ and saturation conditions respectively. The effective binding constant K_D is determined as 1.1(2) mM for Mg^{2+} with a Hill coefficient of n ≈1.3(2). In general, the Hill coefficient n indicates the number of associated ligands (Mg^{2+}) during folding. As a result, n could moderately depend on $[Mg^{2+}]$ since, as $[Mg^{2+}]$ increases, more Mg^{2+} ions may preferentially surround the negatively charged RNA to facilitate folding.[54] However, within the limited range of $[Mg^{2+}]$ explored, as well as with sufficient background monovalent cations (> 100 mM), n can be treated as a constant in our study.[54-56] The n = 1.3(2) indicates a negligible level of cooperativity in Mg^{2+}-mediated folding. Despite n is not always equivalent to the binding stoichiometry, one nearly fully (5-fold) coordinated Mg^{2+} has been

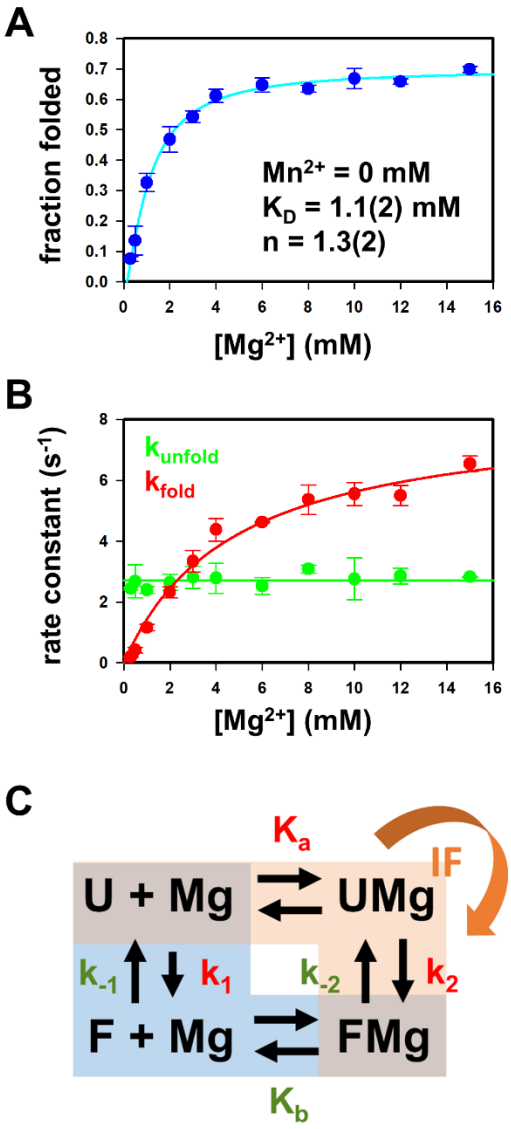

Figure 3.4 Mg^{2+} dependence of manganese riboswitch folding (A) equilibrium fraction folded as a function of [Mg^{2+}] (B) Mg^{2+} dependence of rate constants at [Mn^{2+}] = 0 mM (C) A four-state model for Mg^{2+} facilitated manganese riboswitch folding kinetics.

found crucial to stabilize the L1 and L3 folding interface of the manganese riboswitch in previous structural study (consistent with n = 1).[21] We therefore simplify our kinetic analysis with a model of single Mg^{2+} binding. The deviation of n = 1.3(2) from 1 may indicate the weak association of the divalent cation Mg^{2+} accumulated around the negatively charged RNA. As we

shall see, this non-cooperativity (n = 1) of Mg^{2+} raises the intriguing possibility that occupancy of the non-selective site by Mg^{2+} can promote conformational changes in manganese riboswitch, in particular shifting the mechanistic folding pathway from an induced fit (IF) kinetic paradigm to one of conformational selection (CS).

In addition to the above equilibrium results, the smFRET time traces also permit direct measurement of the folding/unfolding rate constants k_{fold} and k_{unfold} as a function of [Mg^{2+}] (Figure 3.4B). The near-linear dependence of k_{fold} at low [Mg^{2+}] again suggests the folding process to be non-cooperative with effectively only single Mg^{2+} binding. We thus restrict our analysis of the kinetic data to a single binding site (n = 1), which, assuming rapid equilibration between Mg^{2+} associated/dissociated species, is equivalent to the well-known four-state model (folded vs. unfolded and Mg^{2+} bound vs. unbound), used in previous studies[47, 57-58] and shown schematically in Figure 3.4C. In such a four-state model, the apparent single exponential folding/unfolding rate constants can be analytically derived to be:

$$k_{fold/unfold} = \frac{k_{1/-1}+k_{2/-2}K_{a/b}[Mg^{2+}]}{1+K_{a/b}[Mg^{2+}]} \qquad \text{Eq. 3.2}$$

(where subscripts designate folding and unfolding pathways, respectively) and used to least squares fit the folding/unfolding kinetic data in Figure 3.4B. First of all, k_{fold} at [Mg^{2+}] = 0 (Figure 3.4C, Table 3.1) is indistinguishable from zero and indeed yields zero folding events in the absence of any divalent cations. To limit the number of free parameters and parameter correlation, we set $k_1 \approx 0$, though the results are in fact insensitive to whether k_1 is left freely floating in the least squares fits. Physically this would imply that all riboswitch folding events occur from the Mg^{2+} *bound* construct (i.e., k_2), which also explains the kinetic saturation behavior achieved at high $Mg^{2+} >> 1/K_a$ = 4.7(8) mM.

	k_1 (s^{-1})	k_2 (s^{-1})	$1/K_a$ (mM)
3-parameter fit	-0.3(4)	7.7(4)	3.4(7)
k_1 fixed	0*	8.3(6)	4.7(8)

Table 3.1 Least squares fit results of the smFRET kinetics for Mg^{2+} promoted folding of the Mn^{2+} riboswitch.

In dramatic contrast, the unfolding rate constant, $k_{unfold} \approx 2.7\ s^{-1}$, shows essentially no dependence on [Mg^{2+}] over nearly two orders of magnitude (300 μM to 15 mM). In the context of a 4 state-kinetic model, this would be consistent with either (i) K_b strongly *favoring* Mg^{2+} binding to the folded riboswitch (F) and thus only the rate constant $k_{unfold} \approx k_1$ is measured even at the lowest Mg^{2+} levels, or (ii) $k_{unfold} \approx k_{-1} \approx k_{-2}$ and the unfolding results are therefore perfectly *insensitive* to Mg^{2+}. Furthermore, no smFRET transitions are observed at [Mg^{2+}] = 0, which again implies that $k_1 \approx 0$ within experimental uncertainty. Since k_1/k_{-1}= [F]/[U] requires [F] << [U], the kinetic analysis for k_{unfold} becomes completely insensitive to k_{-1} due to [F] << [FMg] ≈ [U]. Simply stated, the effective unfolding rate constant $k_{unfold} \sim 2.7\ s^{-1}$ can be ascribed entirely to k_{-2}, with FMg as the dominant folded species at our lowest possible [Mg^{2+}] ≈ 300 μM and unimolecular unfolding from FMg to UMg as the predominant unfolding channel. In essence, the independence of k_{unfold} on Mg^{2+} signals facile Mg^{2+} binding to the folded riboswitch ($1/K_b$ << 300 μM), which prevents probing smFRET kinetics at sufficiently low Mg^{2+} to accurately sample the [Mg^{2+}] = 0 unfolding rate pathway.

As a unifying theme, we return to characterizing the Mg^{2+} promoted folding/unfolding pathways in terms of the “induced fit” vs “conformational selection” kinetic limits, which can be visually distinguished by either *counterclockwise* (blue arrow) vs *clockwise* (orange arrow) pathways around the 4-state kinetic model (see Figure 3.4C). The purely Mg^{2+} promoted folding/unfolding

kinetics for the Mn^{2+} riboswitch clearly follows the "induced-fit" paradigm, i.e., whereby Mg^{2+} binding to the riboswitch is a prerequisite for folding. (Indeed, the dramatic insensitivity of k_{unfold} to Mg^{2+} follows directly from an induced-fit mechanism.) Specifically, this implies for our riboswitch a predominantly *clockwise* kinetic pathway (Figure 3.4C, orange) from the unfolded (U) to the Mg^{2+}-bound and folded (FMg) state, without corresponding evidence for a *counterclockwise* pathway (Figure 3.4C, blue) involving a Mg^{2+}-free folded (F) riboswitch state.[32, 40]

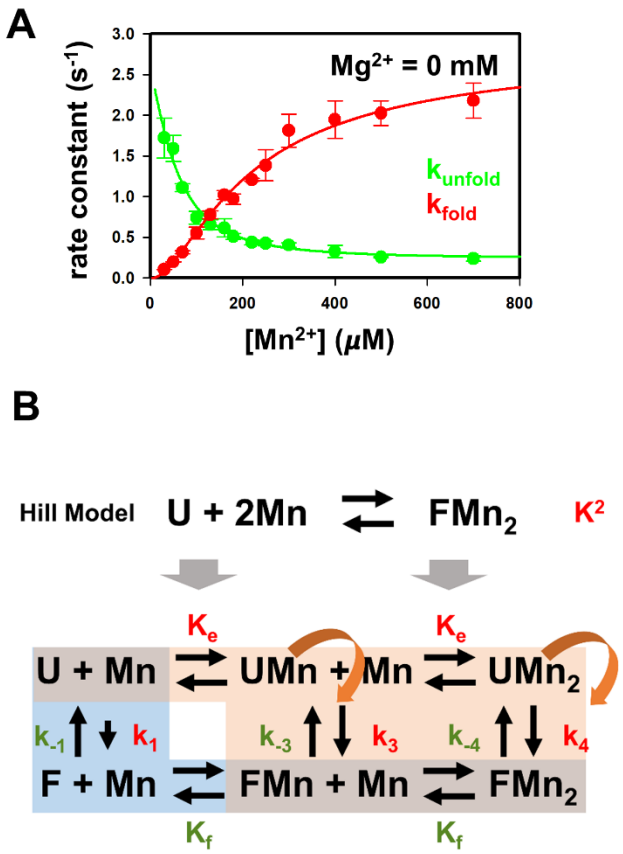

Figure 3.5 Kinetics of Mn^{2+} promoted manganese riboswitch folding (A) Mn^{2+} dependent k_{fold} and k_{unfold} (B) Scheme of extended Hill model into six-state kinetic model (least squares fit results summarized Table 3.2).

3.4.2 Manganese riboswitch folding kinetics with Mn^{2+} alone

As a next step up in kinetic complexity, we have similarly investigated the smFRET kinetics of Mn^{2+} mediated folding of the riboswitch in absence of Mg^{2+}, with the kinetic data summarized in Figure 3.5A. Note that such conditions now allow the cognate ligand Mn^{2+} to occupy both highly selective and non-selective binding sites on the riboswitch, from which we might anticipate strong cooperativity in a Hill kinetic analysis at sufficiently low Mn^{2+}. Fortunately, the effective folding rate constant k_{fold} is clearly measurable by smFRET methods even at $[Mn^{2+}] > 30$ μM, which is sufficient for multiple folding events to be observed within the experimental photobleaching time window. As expected, the rate constant k_{fold} increases supralinearly at low $[Mn^{2+}]$ and eventually approaches an asymptotic value, consistent with sigmoidal growth kinetics and a positive cooperativity (i.e., Hill coefficient $n > 1$). Conversely, k_{unfold} *decreases* rapidly with increasing Mn^{2+}, also gradually reaching an asymptotic rate constant at saturating Mn^{2+} conditions.

From a least squares fit analysis of k_{fold} (Figure 3.5A) and the fraction folded (Figure 3.6A), the Hill cooperativity is found to be $n \approx 2.0(3)$ and 2.1(2), respectively. This is consistent with the presence of two Mn^{2+} ions associated with the riboswitch during the folding process and as confirmed by x-ray crystallography.[21] To appropriately include the effects of these two divalent cations, we therefore must expand our previous 4-state model into a more detailed kinetic model with $n = 2$ (see Figure 3.5B). Such a 6-state kinetic treatment incorporates folding and unfolding processes between each of the RNA conformations associated with zero, one and two Mn^{2+} cations, which requires a large number of model kinetic parameters. To limit parameter correlation and make such a multistate treatment mathematically tractable, therefore, we have assumed that the Mn^{2+} association/dissociation processes for the unfolded (K_e) and

folded (K_f) states are both rapid and insensitive to number of Mn^{2+} (i.e., $K_e \approx K_f$). In this kinetic limit, the apparent k_{fold} and k_{unfold} rate constants can be analytically expressed in terms of rate and equilibrium constants as:

$$k_{fold/unfold} = \frac{k_{1/-1}+k_{3/-3}K_{e/f}[Mn^{2+}]+k_{4/-4}K_{e/f}^2[Mn^{2+}]^2}{1+K_{e/f}[Mn^{2+}]+K_{e/f}^2[Mn^{2+}]^2}, \quad \text{Eq. 3.3}$$

which can be least squares fit to the smFRET kinetic dwell times. Sample kinetic data are shown in Figure 3.5A, with least square fitted results from the Mn^{2+} dependent studies summarized in Table 3.2, where the docking rate constant in the absence of Mn^{2+} ($k_1 \approx 0$) is fixed at zero as per experimental observation. Interestingly, the binding constant [$(K_{e/f})^{-1}$] is found to be ≈ 2-fold smaller for the folded vs. unfolded state, reflecting a higher ligand affinity riboswitch conformation when the binding site is pre-organized by docking of L1 and L3. In addition, the data reveals a systematic speed up of the folding rate processes (e.g. $k_4 > k_3 > k_1$), as well as a corresponding slowing down of the unfolding rate processes ($k_{-1} > k_{-3} \sim k_{-4}$) with incremental Mn^{2+} association.

	k_1 (s^{-1})	k_3 (s^{-1})	k_4 (s^{-1})	K_e (μM)
4-parameter	0.3(5)	-1.0(17)	2.87(15)	115(53)
k_1 fixed	0*	0.1(5)	2.89(14)	151(32)
	k_{-1} (s^{-1})	k_{-3} (s^{-1})	k_{-4} (s^{-1})	K_f (μM)
4-parameter	2.6(3)	0.2(12)	0.24(18)	84(47)

Table 3.2 Least squares fit results of the smFRET kinetics for Mn^{2+} promoted folding of the Mn^{2+} riboswitch.

Once again, the prerequisite of one or both Mn^{2+} ligands for folding of the manganese riboswitch is consistent with a predominantly "induced-fit" (IF) mechanism. Indeed, the least squares fit indicates that the overall folding rate for the riboswitch is dominated by the doubly

Mn^{2+} associated unfolded state (k_4). However, the data are agnostic whether or not folding can be achieved with only a single Mn^{2+}, due to residual uncertainty in $k_3 = 0.1(5)$. If k_3 is finite, folding could be induced by a single Mn^{2+} occupying one of the two metal binding sites, with the folded conformation further stabilized by sequential binding of a second Mn^{2+}. Indeed, this proves to be the case for tandem Mg^{+2} and Mn^{+2} promoted folding, as explored in detail below.

3.4.3 Synergistic folding in the presence of both Mn^{2+} and Mg^{2+}

Armed with this information on individual Mg^{2+} and Mn^{2+} promoted folding pathways, we can now tackle the more complex yet biologically relevant "multi-cation" kinetic nature of this riboswitch. As mentioned in the introduction, previous structural studies have demonstrated that the manganese riboswitch contains two highly coordinated divalent metal binding sites: one with a more than 200-fold selectivity for Mn^{2+} over Mg^{2+} and the other with essentially no preference between the two cations[21]. Consequently, manganese riboswitch folding is therefore dependent on the simultaneous occupancy of both selective and non-selective binding sites. To address the role of such heterogeneous binding sites, we have studied the equilibrium folding behavior and its dependence on $[Mn^{2+}]$ for a series of different Mg^{2+} concentrations.

The resulting equilibrium folding fractions are fit to the modified Hill equation (Eq. 3.1), with the results summarized in Figure 3.6A, B, and C. In the absence of Mg^{2+} (Figure 3.6A), the presence of Mn^{2+} promotes efficient fractional folding from 0.0 to ~ 0.9 with an effective K_D = 111(4) $\boldsymbol{\mu}$M. The clear, sigmoidal nature of this curve is again indicative of a strong positive cooperativity, which can be least squares fit with a Hill coefficient of n = 2.1(2). Interestingly, the Hill coefficient for Mn^{2+} systematically drops from n = 2.1(2) to 1.0(3) as $[Mg^{2+}]$ increases from 0 to 2 mM (Figure 3.6A to 3.6C). This would be consistent with a simple kinetic picture

whereby, of the two metal binding sites, one is exclusively reserved for Mn^{2+} binding, while the other could be equally well occupied by Mn^{2+} or Mg^{2+} under near physiological conditions. Moreover, it also suggests that the occupancy of the non-Mn^{2+} selective site by Mg^{2+} is responsible for "pre-folding" conformational kinetics promoted by Mg^{2+} alone, as previously described in Section 3.4.1.

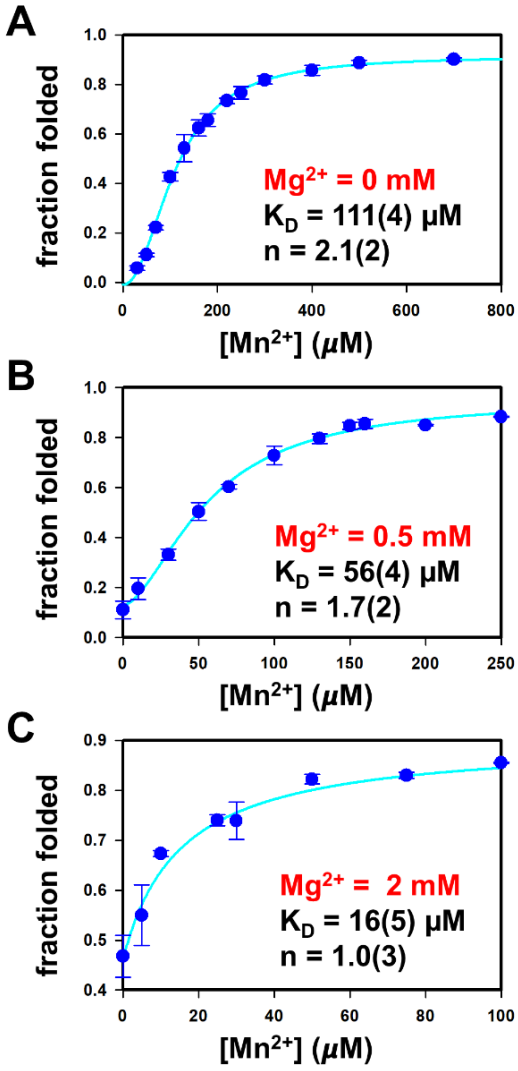

Figure 3.6 Equilibrium Mn^{2+}-dependent fraction folded studied at different [Mg^{2+}] (A) [Mg^{2+}] = 0 mM (B) 0.5 mM (C) 2 mM.

Besides providing a source of cation competition for the non-selective binding site, another clear effect of Mg^{2+} in Figure 3.6A, 3.6B, 3.6C is that it *dramatically lowers* the effective K_D for Mn^{2+} facilitated folding from 111(4) to 16(5) μM. Similar synergistic effects have been observed in other riboswitches, where the presence of Mg^{2+} is shown to significantly enhance ligand affinity [50, 59-61]. Since the ligand-free "pre-folded" conformation of the manganese riboswitch is promoted solely by Mg^{2+}, it is likely that such a structure has higher Mn^{2+} ligand affinity due to formation of a new binding site.

3.5 Discussion

3.5.1 Induced fit vs. conformational selection mechanisms: dependence on Mn^{2+}/Mg^{2+} alone

We have presented extensive smFRET kinetic data for folding and unfolding of the manganese riboswitch, which has two binding sites (on Mn^{2+} and Mg^{2+}) and therefore generates a complex parameter space of concentrations to explore. In this discussion, we present evidence that even in such complex kinetic folding landscapes, we can be guided by simple considerations of a few limiting kinetic mechanisms and pathways. There are two commonly proposed (and often debated) biophysical mechanisms (see Figure 3.2) for ligand-promoted folding of a biomolecule, either by "induced-fit" or "conformational selection" processes.[28-32] In the induced-fit ("bind-then-fold") mechanism, the ligand (L) binds tightly to an initially unfolded structure (U), changes some folding transition state barrier/rate constant, which in turn kinetically facilitates formation of a ligand bound folded state (FL). In the simplifying kinetic framework pictured in Figure 3.2, this would be represented by the *clockwise*, orange path. Conversely, in the conformational selection paradigm ("fold-then-bind"), the unfolded state dynamically

searches over a large ensemble of folded/unfolded conformations (U_i), with the ligand preferentially binding to states with more fold-like character (F_j) and thus driving the equilibrium towards the folded state (FL). In the context of Figure 3.2, this would be represented by the *counterclockwise,* blue path. As shown in previous smFRET kinetic studies of riboswitch folding[40], the dependence of k_{unfold} on ligand concentration can clearly distinguish between these two mechanisms. For a conformational selection (CS) process, k_{unfold} should depend strongly on ligand concentration due to rapid equilibration between ligand-free (fold-like) and ligand-bound (folded) states. For the induced-fit (IF) mechanism, on the other hand, k_{unfold} will be relatively insensitive to ligand concentration, since the dominant pathway is unfolding of the ligand-bound state. On the other hand, the requirement of ligand binding prior to folding and the linear response of k_{fold} on ligand concentration both support the IF mechanism. However, there could be potential ambiguity about whether or not the lifetime of the "pre-folded" state (which could be quite dynamic) is long enough to be detected under experimental conditions. The actual folding mechanism is therefore not determined by k_{fold} alone but more by the integrated kinetic picture.

We first consider the folding kinetics in the absence of the Mn^{2+} ligand, i.e., pure Mg^{2+} controlled folding. From Figure 3.4B, k_{unfold} is clearly independent of $[Mg^{2+}]$. Moreover, the fact that k_{fold} vanishes at $[Mg^{2+}] \approx 0$ indicates that binding of the Mg^{2+} ligand is crucial for folding. Both of the above statements strongly support an *induced-fit mechanism* for riboswitch folding with respect to a single Mg^{2+}. Thus, despite the fact that Mg^{2+} is not cognate for the manganese riboswitch, it can still act as a ligand to promote folding through an induced-fit mechanism. This folding pathway is already illustrated in the upper half diagonal subset of the 4 state kinetic model presented in Figure 3.2 and Figure 3.4C, by which Mg^{2+} predominantly associates with

the unfolded riboswitch (UMg), which then folds to form FMg ("bind-then-fold"). Conversely, exponential decay of the folded conformation occurs simply via unimolecular unfolding from the cation bound FMg state, which would explain why k_{unfold} is kinetically independent of Mg^{2+} concentration.

Similarly, for riboswitch folding kinetics observed solely in the presence of Mn^{2+} (i.e., $[Mg^{2+}] = 0$, see Figure 3.5A), the folding rate constant i) vanishes in the limit of $[Mn^{2+}] = 0$ and ii) exhibits a strong positive cooperativity (n = 2.0(3)). Both of these observations signal an induced-fit mechanism for ligand promoted folding of the manganese riboswitch, as explicitly demonstrated by fitting rate constants to the six-state kinetic model (Figure 3.5B, upper half diagonal and Table 3.2). However, in contrast to Mg^{2+} dependent folding, k_{unfold} now depends significantly on Mn^{2+}, decreasing rapidly at low concentration to a saturation value. As shown in the kinetic model, the folded species can associate up to two Mn^{2+} and each state may exhibit a distinct unfolding rate. Since we are able to probe manganese riboswitch folding at sufficiently low $[Mn^{2+}]$ (≈ 30 μM), the rapid equilibrium between the three folded conformations with different numbers of bound Mn^{2+} cations can explain the Mn^{2+} dependence in k_{unfold}.

3.5.2 Mg^{2+} mediated manganese riboswitch folding under physiological conditions

The folding of the manganese riboswitch in the presence of Mn^{2+} and Mg^{2+} alone have been determined by the above kinetic analysis to proceed by an induced-fit mechanism. However, under more physiologically relevant cation conditions, the presence of both Mn^{2+} and Mg^{2+} need to be considered. Indeed, typical Mg^{2+} concentrations inside bacterial cells are already at the few millimolar level, while Mn^{2+} concentrations range from only ten to hundreds of micromolar[25-26]. Furthermore, Mg^{2+} is known to be a particularly relevant cation for formation

and maintenance of RNA tertiary structure, as well as to promote pre-folded structures relevant to the conformational selection mechanism. In fact, it has been suggested in previous studies that conformational selection is the preferred pathway for Mg^{2+} promoted riboswitch folding and that [Mg^{2+}] may be responsible for shifting the folding mechanism from induced-fit to conformational selection[36, 38, 40, 50].

In the current smFRET experiments, the ligand-free "pre-folded" riboswitch structure is directly observable in the presence of Mg^{2+} alone and, according to E_{FRET} value, is structurally indistinguishable from the ligand-bound folded state. It has also been shown that magnesium effectively promotes formation of a ligand-free folded species under physiologically relevant concentrations of Mg^{2+} ($K_D \approx 1.1$ mM). It is worth remembering that ligand (Mn^{2+}) facilitated folding of the manganese riboswitch in the absence of Mg^{2+} proceeds via an induced-fit (IF) mechanism. The ligand-free folded structure achieved with single site Mg^{2+} binding can therefore results in a "kinetic shift" toward the conformational selection (CS) folding pathway, due to a selectively available Mn^{2+} vacant site as well as increased cognate ligand affinity in the pre-folded state. In the presence of Mn^{2+}, this pre-folded structure can be stabilized by ligand

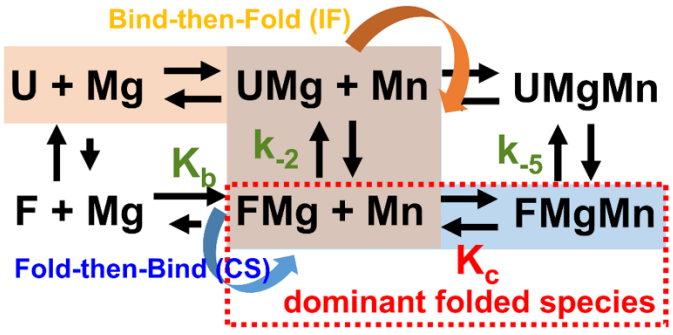

Figure 3.7 The dominant folding pathways and equilibriums in the extended kinetic model with both Mg^{2+} and Mn^{2+} present.

association, further shifting the equilibrium towards a fully folded riboswitch conformation (Figure 3.7).

To provide further experimental validation for such a Mg^{2+} induced switch between induced fit (IF) and conformational selection (CS) mechanisms, we must include additional pathways in our kinetic model (Figure 3.7), whereby the Mg^{2+} associated yet ligand-free pre-folded state can further accommodate a Mn^{2+} cation. In Section 3.4.1, we demonstrated that the Mg^{2+}-bound pre-folded structure FMg is the dominant folded species in presence of physiological magnesium. With K_b = [FMg]/[F] >>1 largely favoring the FMg state, it is clear under physiological [Mg^{2+}] (~2 mM) that the dominant folded species are in rapid equilibrium between FMg and FMgMn. This makes K_c the key driver of the pre-folded (FMg) structure towards a ligand-bound fully folded state (FMgMn) through conformational selection. Since there are only two species differing by absence or presence of Mn^{2+}, the apparent k_{unfold} can be written as:

$$k_{unfold} = \frac{k_{-2}+k_{-5}K_c[Mn^{2+}]}{1+K_c[Mn^{2+}]}, \qquad \text{Eq. 3.4}$$

which of course closely parallels the kinetics of unfolding with single Mn^{2+} association in the four-state model. (djn) The model is then applied to the [Mn^{2+}] dependence of k_{unfold} (Figure 3.8A, k_{unfold} decay from [Mn^{2+}] = 0 to saturation [Mn^{2+}]), revealing that the effective Mn^{2+} binding constant K_D (= $(K_c)^{-1}$) is reduced to 14(2) μM from 84 μM, approximately 6 times enhancement in Mn^{2+} affinity for the Mg^{2+}-bound ligand-free folded state. Therefore, we not only isolate the ligand-free pre-folded manganese riboswitch with Mg^{2+}-mediated folding but also demonstrate such pre-folded structure can effectively associate one Mn^{2+} into its fully folded state with even higher ligand affinity, indicating Mg^{2+} is the key to shifting the folding mechanism from induced-fit to conformational selection.

It is worth noting that such binding-promoted change in conformation and ligand affinity by Mg^{2+} resembles the allosteric control strategy widely adopted in the regulation of enzymes[41-43]. In allosteric regulation, a specific molecule ("effector") binds to a site removed from the active site to induce conformational changes that either promote or inhibit enzymatic activity. In the manganese riboswitch, Mg^{2+} binding facilitates the sampling of states with more fold-like character (e.g. L1-L3 docking), which enhances Mn^{2+} affinity and thus biochemical competence for promoting gene expression. It is worth noting that one of the gene products of this riboswitch is the manganese efflux pump[62-64], a transporter protein that actively removes Mn^{2+}. Thus, one control loop for Mn^{2+} transport would be that physiological [Mg^{2+}] conditions lead to greater activation of the manganese riboswitch, resulting in more efflux pump proteins produced, which in turn promote removal of excess Mn^{2+}. Conversely, under reduced [Mg^{2+}] conditions, fewer Mn^{2+} transporters are synthesized and thus more Mn^{2+} remains to maintain cellular function. Though the actual metal homeostasis pathways may be more complicated, the data suggest that allosteric modulation of the manganese riboswitch by Mg^{2+} is designed to confer evolutionary advantage.

The concept of "RNA allostery" has been discussed previously in the literature, though some could argue that all riboswitches are modulated by ligand-induced conformational changes and thus operate allosterically.[65-66] If we focus on cases where riboswitch functionality is activated by multiple copies of the same ligand[43], several systems (e.g., Ni^{2+}/Co^{2+} [20] and tetrahydrofolate riboswitches[67]) may be regarded as examples of homotropic RNA allostery, with behavior often identified by cooperativity in Hill plots.[43] The more distinctive case of heterotropic allostery (i.e., conformational activation of ligand binding by a different ligand), on

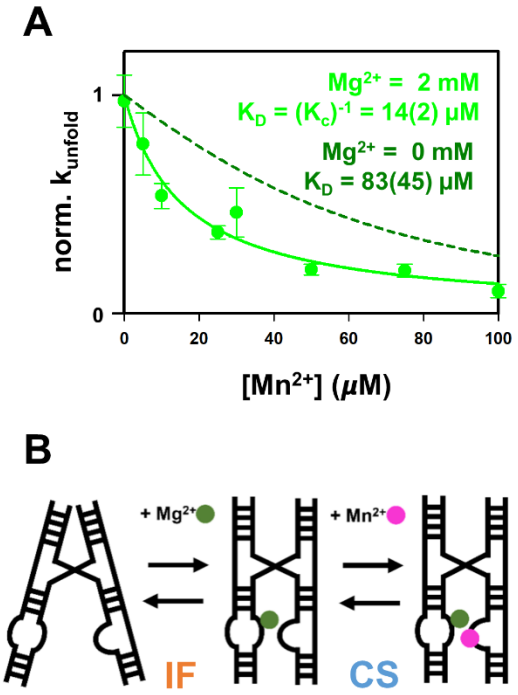

Figure 3.8 Manganese riboswitch folding under near physiological condition with both Mg^{2+} and Mn^{2+} (A) Decay of normalized k_{unfold} from $[Mn^{2+}]$ = 0 to saturation condition suggests Mg^{2+} enhances the ligand (Mn^{2+}) affinity. (B) Schematic of dominant folding pathway indicating that Mg^{2+} pre-folds the RNA via an induced-fit (IF) mechanism and then Mn^{2+} stabilizes the folded conformation by a conformational selection (CS) mechanism.

the other hand, would appear to be far less common in RNA. Indeed, to date, the c-di-GMP-II riboswitch-ribozyme is the only known system with well-characterized heterotropic RNA allostery. In this system, cyclic-di-GMP binds to a pseudo knot to stabilize the folded aptamer structure in the riboswitch, exposing a downstream ribozyme core domain which then binds with GTP to promote self-splicing activity.[68-69] In this work, we report another example of heterotropic allostery in the RNA world, where the conformation of the manganese riboswitch responds to the presence of Mg^{2+}, which in turn enhances riboswitch activity by increased affinity for a remote, highly selective cognate Mn^{2+} ligand. Considering that cations are known to in general promote RNA structure formation, one might speculate whether or not Mg^{2+} facilitates manganese riboswitch folding through some more universal cation effect. However,

the distinct 5-fold coordination of the Mg^{2+} binding site and the correlation between [Mg^{2+}] and manganese riboswitch function suggests a designated allosteric control loop that could play a role in metal ion homeostasis inside cells. Finally, the smFRET data explicitly reveals that Mg^{2+} promotes a dynamical sampling of more fold-like configurations of the manganese riboswitch, which suggests a case where allostery kinetically observed under ensemble conditions may reflect a more dynamic rather than fully stabilized structural effect.[44-46]

3.6 Summary and Conclusion

The equilibrium and kinetics of manganese riboswitch folding have been studied with smFRET microscopy as a function of divalent Mn^{2+} and Mg^{2+} concentrations. It has been shown that the folded riboswitch structure is promoted by the presence of Mn^{2+} and Mg^{2+}, alone as well as in tandem. In single molecule studies of the folded fraction (FF) under equilibrium conditions, Hill analysis suggests that two Mn^{2+} ions are cooperatively associated with folding of the riboswitch, consistent with the presence of two different M^{2+} binding sites with a 200 fold difference in selectivity to the cognate Mn^{2+} ligand.[21] Magnesium concentration dependent studies indicate that Mg^{2+} does not occupy the Mn^{2+} specific binding site, with Hill analysis of the kinetics confirming that only a single Mg^{2+} associates with the riboswitch during folding. Both the Mg^{2+} and Mn^{2+} kinetic results can be well fit to 4- and 6-state kinetic models, respectively, with rate constants indicating that prior binding of the cations is a prerequisite to subsequent folding of the manganese riboswitch, as per an induced-fit ("bind-then-fold") mechanism. By way of contrast, our analysis of riboswitch folding kinetics in the presence of *both* Mn^{2+} and Mg^{2+} indicates that the most relevant equilibrium is between a Mn^{+2} ligand-free "pre-folded" structure (containing one Mg^{2+}) and the corresponding Mn^{2+} ligand-bound folded structure, where Mn^{2+} binding to the

ligand-free pre-folded structure represents the rate limiting pathway for stabilization of the folded riboswitch. Such a kinetic process corresponds to a conformational selection ("fold-then-bind") mechanism, with the shift between induced fit (IF) and conformational selection (CS) pathways mediated by cellular levels of Mg^{2+}. Moreover, the ability to directly observe and isolate such Mg^{2+} induced structures in a smFRET experiment provides support for the widespread notion that Mg^{2+} promotes formation of ligand-free "pre-folded" structures in a conformational selection pathway. In fact, such Mg^{2+} induced changes in riboswitch conformation and subsequent cognate ligand affinity is analogous to the allosteric regulation behavior commonly noted in protein enzymes, suggesting that a similar regulatory strategy may be adopted by both RNAs and proteins.

3.7 References

1. Nahvi, A.; Sudarsan, N.; Ebert, M. S.; Zou, X.; Brown, K. L.; Breaker, R. R., Genetic Control by a Metabolite Binding mRNA. *Chem. Biol.* **2002,** *9* (9), 1043-1049.

2. Tucker, B. J.; Breaker, R. R., Riboswitches as versatile gene control elements. *Curr. Opin. Struct. Biol.* **2005,** *15* (3), 342-348.

3. Breaker, R. R., Riboswitches and the RNA World. *Cold Spring Harbor Persp. Biol.* **2012,** *4* (2), 1-15.

4. Serganov, A.; Nudler, E., A Decade of Riboswitches. *Cell* **2013,** *152* (1), 17-24.

5. Roth, A.; Breaker, R. R., The Structural and Functional Diversity of Metabolite-Binding Riboswitches. *Annu. Rev. Biochem.* **2009,** *78* (1), 305-334.

6. Garst, A. D.; Edwards, A. L.; Batey, R. T., Riboswitches: Structures and mechanisms. *Cold Spring Harbor Persp. Biol.* **2011,** *3* (6), a003533.

7. Montange, R. K.; Batey, R. T., Structure of the S-adenosylmethionine riboswitch regulatory mRNA element. *Nature* **2006,** *441*, 1172.

8. Serganov, A.; Polonskaia, A.; Phan, A. T.; Breaker, R. R.; Patel, D. J., Structural basis for gene regulation by a thiamine pyrophosphate-sensing riboswitch. *Nature* **2006,** *441*, 1167.

9. Thore, S.; Leibundgut, M.; Ban, N., Structure of the Eukaryotic Thiamine Pyrophosphate Riboswitch with Its Regulatory Ligand. *Science* **2006,** *312* (5777), 1208-1211.

10. Gilbert, S. D.; Rambo, R. P.; Van Tyne, D.; Batey, R. T., Structure of the SAM-II riboswitch bound to S-adenosylmethionine. *Nat. Struct. Molec. Biol.* **2008,** *15*, 177.

11. Lu, C.; Smith, A. M.; Fuchs, R. T.; Ding, F.; Rajashankar, K.; Henkin, T. M.; Ke, A., Crystal structures of the SAM-III/SMK riboswitch reveal the SAM-dependent translation inhibition mechanism. *Nat. Struct. Molec. Biol.* **2008,** *15*, 1076.

12. Serganov, A.; Yuan, Y.-R.; Pikovskaya, O.; Polonskaia, A.; Malinina, L.; Phan, A. T.; Hobartner, C.; Micura, R.; Breaker, R. R.; Patel, D. J., Structural Basis for Discriminative Regulation of Gene Expression by Adenine- and Guanine-Sensing mRNAs. *Chem. Biol.* **2004,** *11* (12), 1729-1741.

13. Batey, R. T.; Gilbert, S. D.; Montange, R. K., Structure of a natural guanine-responsive riboswitch complexed with the metabolite hypoxanthine. *Nature* **2004,** *432*, 411.

14. Mandal, M.; Lee, M.; Barrick, J. E.; Weinberg, Z.; Emilsson, G. M.; Ruzzo, W. L.; Breaker, R. R., A Glycine-Dependent Riboswitch That Uses Cooperative Binding to Control Gene Expression. *Science* **2004,** *306* (5694), 275-279.

15. Serganov, A.; Huang, L.; Patel, D. J., Structural insights into amino acid binding and gene control by a lysine riboswitch. *Nature* **2008,** *455*, 1263.

16. Serganov, A.; Patel, D. J., Amino acid recognition and gene regulation by riboswitches. *Biochim. Biophys. Acta* **2009,** *1789* (9), 592-611.

17. Baker, J. L.; Sudarsan, N.; Weinberg, Z.; Roth, A.; Stockbridge, R. B.; Breaker, R. R., Widespread Genetic Switches and Toxicity Resistance Proteins for Fluoride. *Science* **2012,** *335* (6065), 233-235.

18. Ren, A.; Rajashankar, K. R.; Patel, D. J., Fluoride ion encapsulation by Mg^{2+} ions and phosphates in a fluoride riboswitch. *Nature* **2012,** *486*, 85.

19. Dann, C. E.; Wakeman, C. A.; Sieling, C. L.; Baker, S. C.; Irnov, I.; Winkler, W. C., Structure and Mechanism of a Metal-Sensing Regulatory RNA. *Cell* **2007,** *130* (5), 878-892.

20. Furukawa, K.; Ramesh, A.; Zhou, Z.; Weinberg, Z.; Vallery, T.; Winkler, Wade C.; Breaker, Ronald R., Bacterial Riboswitches Cooperatively Bind Ni^{2+} or Co^{2+} Ions and Control Expression of Heavy Metal Transporters. *Mol. Cell* **2015,** *57* (6), 1088-1098.

21. Price, I. R.; Gaballa, A.; Ding, F.; Helmann, J. D.; Ke, A., Mn^{2+}-Sensing Mechanisms of *yybP-ykoY* Orphan Riboswitches. *Mol. Cell* **2015,** *57* (6), 1110-1123.

22. Dambach, M.; Sandoval, M.; Updegrove, Taylor B.; Anantharaman, V.; Aravind, L.; Waters, Lauren S.; Storz, G., The Ubiquitous *yybP-ykoY* Riboswitch Is a Manganese-Responsive Regulatory Element. *Mol. Cell* **2015,** *57* (6), 1099-1109.

23. Barrick, J. E.; Corbino, K. A.; Winkler, W. C.; Nahvi, A.; Mandal, M.; Collins, J.; Lee, M.; Roth, A.; Sudarsan, N.; Jona, I., et al., New RNA motifs suggest an expanded scope for riboswitches in bacterial genetic control. *Proc. Natl. Acad. Sci. USA* **2004,** *101* (17), 6421-6426.

24. Harding, M. M.; Hsin, K.-Y., Mespeus—A Database of Metal Interactions with Proteins. In *Structural Genomics: General Applications*, Chen, Y. W., Ed. Humana Press: Totowa, NJ, 2014; pp 333-342.

25. Grubbs, R. D., Intracellular magnesium and magnesium buffering. *BioMetals* **2002,** *15* (3), 251-259.

26. Helmann, J. D., Specificity of Metal Sensing: Iron and Manganese Homeostasis in Bacillus subtilis. *J. Biol. Chem.* **2014**.

27. Chen, Y.; Li, X.; Gegenheimer, P., Ribonuclease P Catalysis Requires Mg^{2+} Coordinated to the *pro*-R_P Oxygen of the Scissile Bond. *Biochem.* **1997,** *36* (9), 2425-2438.

28. Leulliot, N.; Varani, G., Current Topics in RNA−Protein Recognition: Control of Specificity and Biological Function through Induced Fit and Conformational Capture. *Biochem.* **2001,** *40* (27), 7947-7956.

29. Boehr, D. D.; Nussinov, R.; Wright, P. E., The role of dynamic conformational ensembles in biomolecular recognition. *Nat. Chem. Biol.* **2009,** *5*, 789.

30. Stelzer, A. C.; Kratz, J. D.; Zhang, Q.; Al-Hashimi, H. M., RNA Dynamics by Design: Biasing Ensembles Towards the Ligand-Bound State. *Angew. Chem. Int. Ed.* **2010,** *49* (33), 5731-5733.

31. Haller, A.; Soulière, M. F.; Micura, R., The Dynamic Nature of RNA as Key to Understanding Riboswitch Mechanisms. *Acc. Chem. Res.* **2011,** *44* (12), 1339-1348.

32. Weikl, T. R.; Fabian, P., Conformational selection in protein binding and function. *Protein Sci.* **2014,** *23* (11), 1508-1518.

33. Kim, E.; Lee, S.; Jeon, A.; Choi, J. M.; Lee, H.-S.; Hohng, S.; Kim, H.-S., A single-molecule dissection of ligand binding to a protein with intrinsic dynamics. *Nat. Chem. Biol.* **2013,** *9*, 313.

34. Gouridis, G.; Schuurman-Wolters, G. K.; Ploetz, E.; Husada, F.; Vietrov, R.; de Boer, M.; Cordes, T.; Poolman, B., Conformational dynamics in substrate-binding domains influences transport in the ABC importer GlnPQ. *Nat. Struct. Mol. Biol.* **2014,** *22*, 57.

35. Brenner, M. D.; Scanlan, M. S.; Nahas, M. K.; Ha, T.; Silverman, S. K., Multivector Fluorescence Analysis of the *xpt* Guanine Riboswitch Aptamer Domain and the Conformational Role of Guanine. *Biochem.* **2010,** *49* (8), 1596-1605.

36. Haller, A.; Rieder, U.; Aigner, M.; Blanchard, S. C.; Micura, R., Conformational capture of the SAM-II riboswitch. *Nat. Chem. Biol.* **2011,** *7*, 393.

37. Wood, S.; Ferré-D'Amaré, A. R.; Rueda, D., Allosteric Tertiary Interactions Preorganize the c-di-GMP Riboswitch and Accelerate Ligand Binding. *ACS Chem. Biol.* **2012,** *7* (5), 920-927.

38. Haller, A.; Altman, R. B.; Soulière, M. F.; Blanchard, S. C.; Micura, R., Folding and ligand recognition of the TPP riboswitch aptamer at single-molecule resolution. *Proc. Natl. Acad. Sci. USA* **2013,** *110* (11), 4188-4193.

39. Xia, T.; Yuan, J.; Fang, X., Conformational Dynamics of an ATP-Binding DNA Aptamer: A Single-Molecule Study. *J. Phys. Chem. B* **2013,** *117* (48), 14994-15003.

40. Suddala, K. C.; Wang, J.; Hou, Q.; Walter, N. G., Mg^{2+} Shifts Ligand-Mediated Folding of a Riboswitch from Induced-Fit to Conformational Selection. *J. Am. Chem. Soc.* **2015,** *137* (44), 14075-14083.

41. Monod, J.; Changeux, J.-P.; Jacob, F., Allosteric proteins and cellular control systems. *J. Mol. Biol.* **1963,** *6* (4), 306-329.

42. Perutz, M. F., Mechanisms of cooperativity and allosteric regulation in proteins. *Q. Rev. Biophys.* **1989,** *22* (2), 139-237.

43. Peselis, A.; Gao, A.; Serganov, A., Cooperativity, allostery and synergism in ligand binding to riboswitches. *Biochimie* **2015,** *117*, 100-109.

44. Kern, D.; Zuiderweg, E. R. P., The role of dynamics in allosteric regulation. *Curr. Opin. Struct. Biol.* **2003,** *13* (6), 748-757.

45. Motlagh, H. N.; Wrabl, J. O.; Li, J.; Hilser, V. J., The ensemble nature of allostery. *Nature* **2014,** *508*, 331.

46. Thayer, K. M.; Lakhani, B.; Beveridge, D. L., Molecular Dynamics–Markov State Model of Protein Ligand Binding and Allostery in CRIB-PDZ: Conformational Selection and Induced Fit. *J. Phys. Chem. B* **2017,** *121* (22), 5509-5514.

47. Sengupta, A.; Sung, H.-L.; Nesbitt, D. J., Amino Acid Specific Effects on RNA Tertiary Interactions: Single-Molecule Kinetic and Thermodynamic Studies. *J. Phys. Chem. B* **2016,** *120* (41), 10615-10627.

48. Fiegland, L. R.; Garst, A. D.; Batey, R. T.; Nesbitt, D. J., Single-Molecule Studies of the Lysine Riboswitch Reveal Effector-Dependent Conformational Dynamics of the Aptamer Domain. *Biochem.* **2012,** *51* (45), 9223-9233.

49. Schroeder, Kersten T.; Daldrop, P.; Lilley, David M. J., RNA Tertiary Interactions in a Riboswitch Stabilize the Structure of a Kink Turn. *Structure* **2011,** *19* (9), 1233-1240.

50. Hennelly, S. P.; Novikova, I. V.; Sanbonmatsu, K. Y., The expression platform and the aptamer: cooperativity between Mg^{2+} and ligand in the SAM-I riboswitch. *Nucleic Acids Res.* **2013,** *41* (3), 1922-1935.

51. Lamichhane, R.; Daubner, G. M.; Thomas-Crusells, J.; Auweter, S. D.; Manatschal, C.; Austin, K. S.; Valniuk, O.; Allain, F. H.-T.; Rueda, D., RNA looping by PTB: Evidence using FRET and NMR spectroscopy for a role in splicing repression. *Proc. Natl. Acad. Sci. USA* **2010,** *107* (9), 4105-4110.

52. Fragata, M.; Dudekula, S., Nonlinear Enhancement of Oxygen Evolution in Thylakoid Membranes: Modeling the Effect of Light Intensity and β-Cyclodextrin Concentration. *J. Phys. Chem. B* **2005,** *109* (30), 14707-14714.

53. Moyon, N. S.; Mitra, S., Luminol Fluorescence Quenching in Biomimicking Environments: Sequestration of Fluorophore in Hydrophobic Domain. *J. Phys. Chem. B* **2011,** *115* (33), 10163-10172.

54. Leipply, D.; Draper, D. E., Dependence of RNA Tertiary Structural Stability on Mg2+ Concentration: Interpretation of the Hill Equation and Coefficient. *Biochem.* **2010,** *49* (9), 1843-1853.

55. Grilley, D.; Soto, A. M.; Draper, D. E., Mg^{2+}–RNA interaction free energies and their relationship to the folding of RNA tertiary structures. *Proc. Natl. Acad. Sci. USA* **2006,** *103* (38), 14003-14008.

56. Leipply, D.; Lambert, D.; Draper, D. E., Ion–RNA Interactions: Thermodynamic Analysis of the Effects of Mono- and Divalent Ions on RNA Conformational Equilibria. In *Methods Enzymol.*, Academic Press: 2009; Vol. 469, pp 433-463.

57. Fiore, J. L.; Holmstrom, E. D.; Fiegland, L. R.; Hodak, J. H.; Nesbitt, D. J., The Role of Counterion Valence and Size in GAAA Tetraloop–Receptor Docking/Undocking Kinetics. *J. Mol. Biol.* **2012,** *423* (2), 198-216.

58. Kim, H. D.; Nienhaus, G. U.; Ha, T.; Orr, J. W.; Williamson, J. R.; Chu, S., Mg^{2+}-dependent conformational change of RNA studied by fluorescence correlation and FRET on immobilized single molecules. *Proc. Natl. Acad. Sci. USA* **2002,** *99* (7), 4284.

59. Baird, N. J.; Inglese, J.; Ferré-D'Amaré, A. R., Rapid RNA–ligand interaction analysis through high-information content conformational and stability landscapes. *Nature Comm.* **2015,** *6*, 8898.

60. Leipply, D.; Draper, D. E., Effects of Mg^{2+} on the Free Energy Landscape for Folding a Purine Riboswitch RNA. *Biochem.* **2011,** *50* (14), 2790-2799.

61. Yamauchi, T.; Miyoshi, D.; Kubodera, T.; Nishimura, A.; Nakai, S.; Sugimoto, N., Roles of Mg^{2+} in TPP-dependent riboswitch. *FEBS Lett.* **2005,** *579* (12), 2583-2588.

62. Waters, L. S.; Sandoval, M.; Storz, G., The *Escherichia coli* MntR Miniregulon Includes Genes Encoding a Small Protein and an Efflux Pump Required for Manganese Homeostasis. *J. Bacteriol.* **2011,** *193* (21), 5887-5897.

63. Veyrier, F. J.; Boneca, I. G.; Cellier, M. F.; Taha, M.-K., A Novel Metal Transporter Mediating Manganese Export (MntX) Regulates the Mn to Fe Intracellular Ratio and *Neisseria meningitidis* Virulence. *PLoS Path.* **2011,** *7* (9), e1002261.

64. Li, C.; Tao, J.; Mao, D.; He, C., A Novel Manganese Efflux System, YebN, Is Required for Virulence by *Xanthomonas oryzae* pv. *oryzae*. *PLOS ONE* **2011,** *6* (7), e21983.

65. Winkler, W. C.; Dann III, C. E., RNA allostery glimpsed. *Nat. Struct. Mol. Biol.* **2006,** *13*, 569.

66. Mandal, M.; Breaker, R. R., Gene regulation by riboswitches. *Nature Rev. Molec. Cell Biol.* **2004,** *5*, 451.

67. Trausch, Jeremiah J.; Ceres, P.; Reyes, Francis E.; Batey, Robert T., The Structure of a Tetrahydrofolate-Sensing Riboswitch Reveals Two Ligand Binding Sites in a Single Aptamer. *Structure* **2011,** *19* (10), 1413-1423.

68. Lee, E. R.; Baker, J. L.; Weinberg, Z.; Sudarsan, N.; Breaker, R. R., An Allosteric Self-Splicing Ribozyme Triggered by a Bacterial Second Messenger. *Science* **2010,** *329* (5993), 845-848.

69. Chen, A. G. Y.; Sudarsan, N.; Breaker, R. R., Mechanism for gene control by a natural allosteric group I ribozyme. *RNA* **2011,** *17* (11), 1967-1972.

Chapter 4

Novel Heat-Promoted Folding Dynamics of the *yybP-ykoY* Manganese Riboswitch: Kinetic and Thermodynamic Studies at the Single Molecule Level

---

4.1 Abstract

Riboswitches are highly structured RNA elements that regulate gene expressions by undergoing conformational changes in response to their cognate ligands. Such regulatory strategies are particularly prevalent among bacteria, which need to be evolutionarily responsive to thermal fluctuations in the surrounding environment, for example, generating extremophiles evolved to survive anomalously high or low temperatures. As a consequence, the response of such riboswitches to thermal stress becomes of considerable interest. In this study, the temperature-dependent folding kinetics and thermodynamics of the manganese riboswitch (*yybP-ykoY*) is studied by single-molecule FRET spectroscopy under external thermal control. Surprisingly, the *folding* of the manganese riboswitch is found to be strongly *promoted* by temperature. Detailed thermodynamic analysis of the equilibrium and forward/reverse kinetic rate constants reveal folding to be a strongly endothermic process ($\Delta H > 0$) made feasible by an overall entropic lowering ($-T\Delta S < 0$) in free energy. This is in contrast to a more typical picture of RNA folding achieving a more compact, highly ordered state ($\Delta S < 0$) and clearly speaks to the significant role of solvent/cation reorganization in the folding thermodynamics. With the help of transition state theory, free energy landscapes for the manganese riboswitch are constructed from the temperature-dependent kinetic data, revealing two distinctive folding mechanisms promoted

*This chapter is adapted from: Sung, H.-L.; Nesbitt, D. J. Novel Heat-Promoted Folding Dynamics of the yybP-ykoY Manganese Riboswitch: Kinetic and Thermodynamic Studies at the Single Molecule Level. *J. Phys. Chem. B* **2019**, *123*, 5412-5422.

dependence for folding of the manganese riboswitch may reflect evolution of bacterial gene regulation strategies to survive environments with large temperature variations.

4.2 Introduction

Riboswitches are noncoding mRNA elements that regulate gene expression by undergoing conformational change upon ligand binding[1-3]. These riboswitches are particularly widely exploited in bacterial gene regulation, responding to a wide variety of ligands including small molecule metabolites and atomic ions[4-5]. The structure of a riboswitch is typically comprised of an aptamer domain and an expression platform[5-6]. The aptamer domain of a riboswitch structurally conforms to selectively capture its cognate ligand, while the expression platform adopts a distinctive folding structure in response to the aptamer. Such complex conformational transitions result in clear "on" and "off" states of a riboswitch [6], which can structurally regulate downstream gene expression. Common regulatory strategies include premature transcriptional termination and blocked translation initiation[4-5].

Temperature is known to significantly influence biomolecular structure and, consequently, biochemical function. Folding into a more ordered RNA structure typically results in a state of lower entropy[7-8] ($-T\Delta S > 0$) with the net folding enthalpically driven ($\Delta H < 0$) by interactions such as hydrogen bonding and charge neutralization[9-10]. By Le Chatelier's principle, such enthalpically driven processes give rise to strongly temperature dependent equilibrium and kinetic behavior. The requisite exothermicity for such structure formation, in turn, is routinely observed and confirmed in many examples of thermal denaturation, whereby biomolecules unfold from their native structures with elevated temperature[11-12]. However, in contrast to these more conventional pictures of folding, some biomolecules are found to *unfold* with *decreasing*

temperature, i.e., so called “heat-promoted folding” or, equivalently, “cold denaturation”[13-14]. Such reversal in the normal paradigmatic behavior can arise, for example, from changes in the solvent configurations dominated by hydrophobic and hydrophilic interactions, which also contribute significantly to the overall free energy and thereby influence the thermal sensitivity of biomolecular folding[7, 15-16]. In the case of cold denaturation, it is the entropic gain in solvent configuration which overcomes any entropic penalty associated with a more compact structure, thus providing a predominantly entropic driving force for biomolecular folding.

Unlike many proteins which function from a native folded state, riboswitches regulate gene expression dynamically by switching between on and off configurations in response to cellular environment and ligand association. As the two different conformational states result in opposite biochemical outcomes, it is reasonable to expect gene regulation by riboswitches to be modulated by temperature. However, exactly how a riboswitch reacts to thermal stress remains unclear, due to the fact that both on and off state conformations each contain complex secondary and tertiary structural motifs. This provides important motivation for exploring temperature dependent dynamics of riboswitch folding as well as consideration of any potential evolutionary advantages. Given that bacteria can experience significant temperature fluctuations in their environment and indeed some may even endure high or low extremes[17-19], it is not surprising that they may have evolved to incorporate thermal stress as an important element in gene regulation strategies[20-23]. In fact, some temperature-responsive RNA motifs commonly referred to as “RNA thermometers” have been discovered[22-23]. Similar to riboswitches, they often regulate genes related to heat shock response by a thermally responsive conformational change. The results of the present study take this concept one step further, suggesting that temperature modulation

might be a common feature of riboswitch gene regulation and thus potentially a more general protective mechanism for bacteria under thermal fluctuations and/or biochemical distress.

As the particular focus of this work, the manganese riboswitch is found extensively distributed in the noncoding regions of bacterial mRNA[24-26]. It responds to micromolar of cellular Mn^{2+} and regulates the expression of genes responsible for metal homeostasis, including the manganese efflux pump, a transport protein that removes excessive Mn^{2+} from the cell[27-29]. The aptamer domain of manganese riboswitch consists of four helices tethered by a four-way junction (Figure 4.1A and 4.1C). In the ligand-bound folded state identified in previous x-ray studies[25] (Figure 4.1A), the four helices coaxially align into a tight hairpin-like structure with docking between two highly conserved loops L1 and L3. The docking interface formed by L1 and L3 contains one Mn^{2+} specific binding site and one non-selective divalent cation M^{2+} (M = Mn or Mg) binding site that is predominantly occupied by Mg^{2+} due to natural physiological abundance (Figure 4.1B). Regulation of gene expression can therefore be activated by single metal ion (M^{2+}) binding, followed by L1 and L3 docking.

In this study, thermal response of the manganese riboswitch is studied by single-molecule FRET (smFRET) spectroscopy and kinetics under external temperature control (± 0.1 ^{o}C), where conformational folding of a single RNA molecule is monitored by FRET energy transfer efficiency (E_{FRET}) as a function of time. The resulting E_{FRET} time trajectories not only explicitly recapitulate the *equilibrium* folding behavior but also contain detailed information on single molecule *kinetics* for further analysis of the unimolecular folding/unfolding rate processes. Indeed, it has long been recognized that "co-transcriptional formation" of the natively folded riboswitch structure is a crucial strategic element in real time gene regulation[1, 30-31]. Thus, the kinetic time scales for both manganese riboswitch folding and unfolding become particularly

important to ensuring an adequate temporal window for both i) metabolite recognition and ii) conformational change with respect to the gene transcription regulated event.

In our investigation of such temperature-dependent manganese riboswitch dynamics, we find that the folding kinetics is strongly sensitive to and increases dramatically with temperature. Thermodynamic analysis of the single molecule data as a function of temperature allows us to decompose the folding free energy into entropic and enthalpic contributions, revealing that manganese riboswitch folding is surprisingly endothermic and compensated by favorable entropic gain. With the help of such thermodynamic and kinetic data, a detailed energy landscapes of manganese riboswitch folding can be reconstructed from transition state theory, highlighting several intriguing observations consistent with our previous kinetic study of manganese riboswitch folding mechanisms[32]. Specifically, the manganese riboswitch is found to respond to Mg^{2+} primarily during the early stages of folding and prior to surmounting the transition state barrier. This is in agreement with a "bind-then-fold" (i.e., induced fit or IF) mechanism, whereby folding is directly promoted by Mg^{2+} association. Mn^{2+}, on the other hand, changes free energies in both early and late stages of folding, implying different M^{2+} (M = Mn or Mg) occupancies can be adopted in the folded manganese riboswitch. This is in support of the "fold-then-bind" (i.e. conformation selection or CS) mechanism, whereby the ligand binds to and thermodynamically stabilizes an already preorganized fold-like structure[30, 32-33].

4.3 Experiment

4.3.1 RNA construct design and preparation for single-molecule study

The ligand-bound folded state of manganese riboswitch has been determined in previous x-ray studies to be a hairpin-like structure formed from four jointed helices (Figure 4.1A)[25]. The

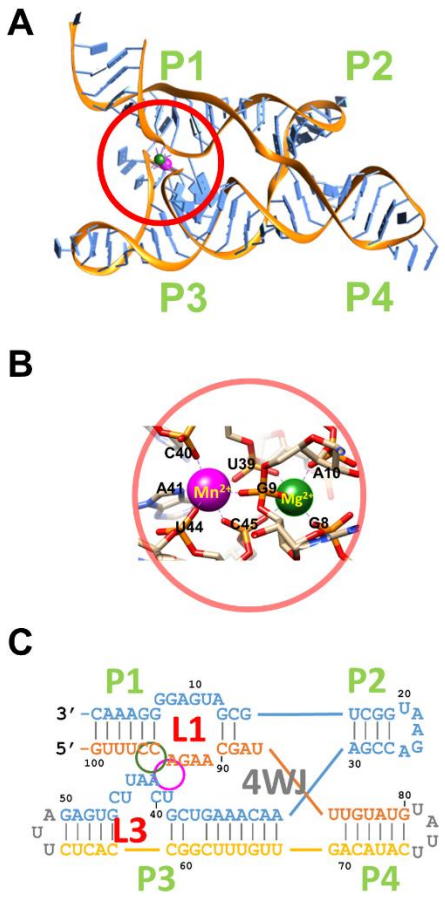

Figure 4.1 Structure of *L. lactis yybP-ykoY* manganese riboswitch: (A) Overall crystal structure (PDB 4Y1I); (B) Close-up details on the cation M^{2+} binding sites with adjacent nucleotides; (C) Manganese riboswitch sequence in a secondary structure representation.

major docking interaction between L1 and L3 directly responds to M^{2+} ligand binding, which is crucial to stabilizing the folded conformation. Therefore, we have designed a smFRET RNA construct sensitive to the distance between L1 and L3 as a proxy for conformational change[32]. In this smFRET construct design, the cyanine dyes Cy3 and Cy5 are covalently labeled on P1 and P3 stems respectively to achieve two distinct distance-dependent energy transfer states distinguished by RNA folding/unfolding (Figure 4.2A). A biotin modification is introduced to the P1 end so that the RNA construct can be tethered on a coverslip surface by biotin-streptavidin interactions for study at the single molecule level. The Mn^{2+} aptamer domain is

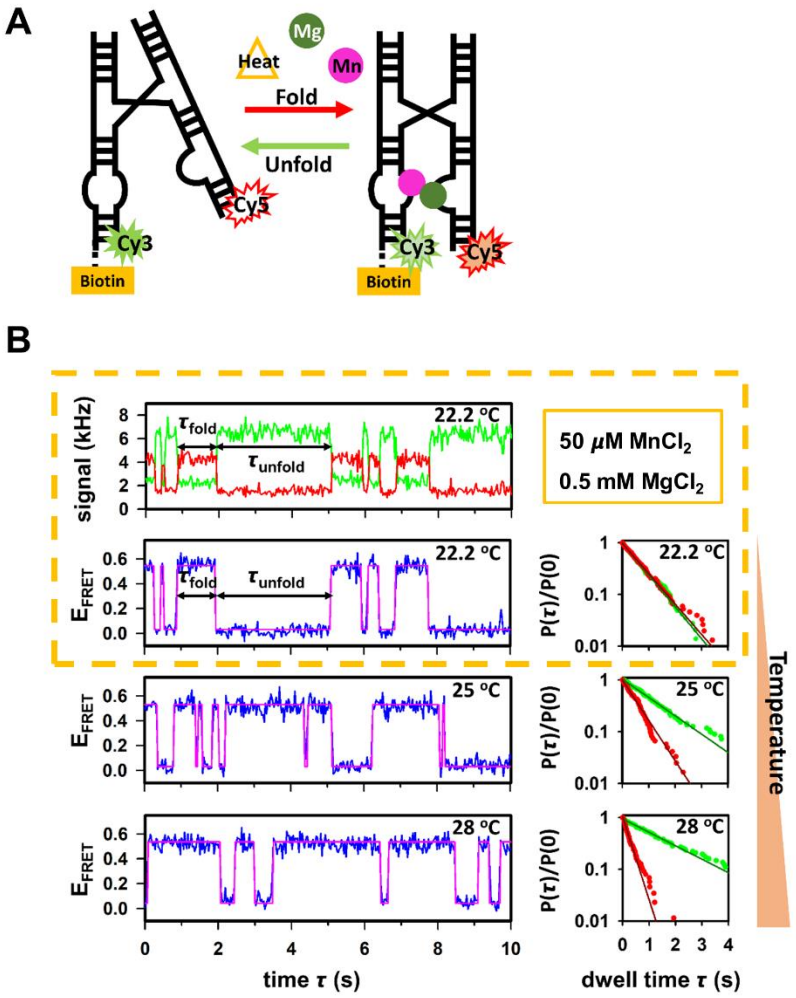

Figure 4.2 Sample smFRET experiment data: (A) Cartoon depiction of how manganese riboswitch folding changes the distance between Cy3 and Cy5; (B) Sample time trace of Cy3 and Cy5 fluorescence (22.2 C, top left), the corresponding E_{FRET} trajectory (lower left), and a series of E_{FRET} trajectories (lower left) and dwell time distributions (lower right) as a function of increasing temperature (22.2 C-28.0C). Note that a small increase in temperature dramatically increases the folded time distributions, consistent with strongly endothermic folding ($\Delta H > 0$).

reconstructed from the RNA sequence in *Lactococcus lactis*, as structurally characterized in previous studies[25, 32]. The final smFRET manganese riboswitch construct is synthesized by annealing three chemically modified RNA oligos purchased from Integrated DNA Technologies (IDT, Coralville, IA), followed by HPLC purification. Detailed construct design and explicit oligo sequences can be found in our previous work[32].

By way of sample preparation for these smFRET experiments, the sample holder is flushed in sequential order with: (i) 10 mg/mL BSA (bovine serum albumin) with 10% biotinylation for surface pacification, (ii) 200 μg/mL streptavidin for surface tethering, and (iii) ~ 25 pM of the biotinylated RNA construct. Each flushing step is followed by a 10-minute incubation period, which yields a consistent, reliable surface coverage of ~50 RNAs per 100 μm^2. In addition to the specified Mn^{2+} ($MnCl_2$) and Mg^{2+} ($MgCl_2$) divalent cation concentrations, the smFRET buffer solution also contains (i) 50 mM hemisodium HEPES (pH 7.5), (ii) an enzymatic oxygen scavenger system (PCD/PCA/TROLOX), and (iii) 100 mM NaCl background salt.

4.3.2 Single-molecule FRET spectroscopy

Single-molecule fluorescence imaging capabilities are achieved in a homebuilt confocal microscope system described in previous papers [34-35]. In short, a 532 nm pulsed Nd:YAG laser is collimated by a Keplerian beam expander before being directed into an inverted microscope water immersion objective (1.2 N.A), resulting in a diffraction limited laser excitation spot of ~250 nm lateral dimension. In smFRET experiments, the dye-labeled RNA molecules are located by scanning the coverslip surface under conditions where RNA coverage is sufficiently low to ensure observation of one RNA molecule at a time in the sub-femtoliter confocal volume. The fluorescence photon from a single dye-labeled RNA is collected for each pulse through the same microscope objective and split into color (green/red) and polarization (horizontal/vertical) channels before detection by four single photon avalanche photodiodes (APDs). For each photon event, the color, polarization, wall clock time (± 50 ns) and time respect to the laser pulse (± 50 ps) are recorded by a time-correlated single-photon counting (TCSPC) module[35-36]. For temperature controlled studies, thermal equilibrium at a desired temperature (± 0.1 ^oC) is achieved by heating both sample and microscope objective simultaneously, with details of the

commercial stage and objective heater setup presented in previous work[34-36]. Before each experimental temperature run, samples remain in contact with the objective for > 15 mins to ensure complete thermal equilibrium.

4.4 Results and analysis

4.4.1 Temperature-promoted folding revealed by smFRET

The smFRET RNA construct is doubly labeled with fluorophores Cy3 and Cy5 so that the conformational change can be visualized by distance-dependent FRET energy transfer (E_{FRET})[32]. In the sample fluorescence signal time trace (Figure 4.2B upper panel), the clearly anti-correlated switching between the donor (green) and acceptor (red) signals unambiguously reflects folding/unfolding events and energy transfer between Cy3 and Cy5, from which the corresponding time dependent E_{FRET} trajectory can be calculated. The resulting time trace for E_{FRET} (see Figure 4.2B) reveals that the RNA construct switches between two distinct states with well separated E_{FRET} values of ~ 0.55 and ~ 0. As expected from the construct geometry[32] and crystal structure data[25], the high E_{FRET} state (E_{FRET} ~ 0.55) corresponds to a compact folded conformation of the manganese riboswitch with loops L1 and L3 docking onto each other. Conversely, the low E_{FRET} is consistent with the two loops much further apart, corresponding to a non-compact, unfolded conformation.

From the E_{FRET} trajectory, the folding equilibrium constant (K_{eq}) can be readily obtained from the ratio of total time spent in the high E_{FRET} (folded) versus low E_{FRET} (unfolded) state. More revealingly, however, direct observation of the dynamic folding/unfolding behavior also permits the rate constants (k_{fold} and k_{unfold}) to be determined by analysis of the corresponding dwell time distributions (Figure 4.2B right panels)[32, 35]. Specifically, semi-logarithmic plots of

the resulting cumulative distribution functions ($P(\boldsymbol{\tau})/P(0)$) vs. dwell times are quite linear, and thus appropriately fit to a single exponential decay function to extract the first order folding/unfolding rate constants (k_{fold} and k_{unfold}).

In the temperature dependent studies, the temperature is controlled (± 0.1 ^{o}C) by simultaneously heating the sample and the optical objective. A representative temperature response of the manganese riboswitch is illustrated in the series of E_{FRET} trajectories obtained at increasing thermal stress (Figure 4.2B from top to bottom), for which the RNA clearly spends more time in the high E_{FRET} (i.e., folded) state. Indeed, the approximately 5-fold increase in K_{eq} for $\Delta T = +\ 5.8\ ^{o}C$ indicates that folding of the manganese riboswitch is both highly sensitive to temperature and favored by heat. In addition, the dwell time analysis (Figure 4.2B right) reveals the kinetic origin of such "heat-promoted folding" behavior arising from a temperature dependent *increase* in k_{fold} and *decrease* in k_{unfold}, respectively.

4.4.2 Mg^{2+} effects on the temperature dependence of folding

Previous studies have shown that docking between the loops L1 and L3 of the manganese riboswitch requires binding of at least one divalent cation M^{2+} (Mg^{2+} or Mn^{2+})[25, 32]. It has also been shown that Mg^{2+} alone promotes manganese riboswitch folding by only occupying the non-selective binding site, leaving the Mn^{2+}-specific site open for further ligand association (Figure 4.1). According to previous detailed kinetic analysis[32], the fold-like structure achieved with Mg^{2+}-binding plays a crucial role in opening a conformational selection ("fold-then-bind") pathway by enhancing the Mn^{2+} ligand affinity. It is therefore useful to further explore the formation of the this Mn^{2+} ligand-free folded state with single molecule thermodynamic techniques.

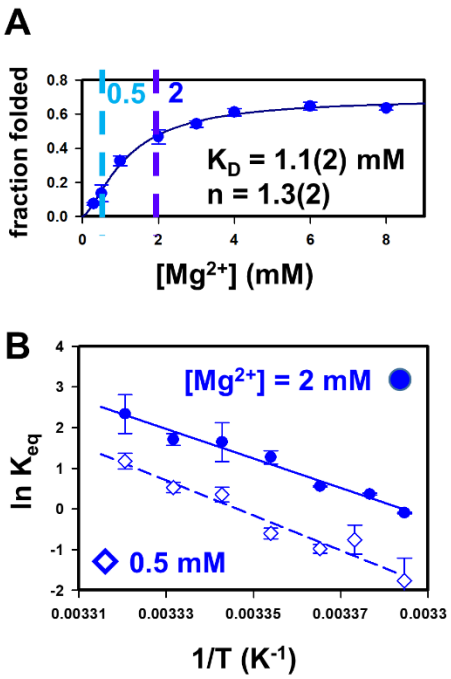

Figure 4.3 Mg^{2+} dependence of the manganese riboswitch folding under equilibrium conditions: (A) Folded fraction as a function of $[Mg^{2+}]$; (B) van't Hoff plot for the temperature dependent behavior of the manganese riboswitch equilibrium constant ($K_{eq} = k_{fold}/k_{unfold}$) at $[Mn^{2+}] = 0$.

From the $[Mg^{2+}]$ dependent studies, folding of the manganese riboswitch is known to be effectively promoted by millimolar levels of Mg^{2+} (Figure 4.3A). By visual inspection, the fraction folded increases monotonically with $[Mg^{2+}]$, gradually reaching a saturation value. The nearly linear increase of fraction folded at low $[Mg^{2+}]$ indicates only a minimal Hill cooperativity (n ~ 1). More quantitatively, the data can be fit to the normalized Hill equation in the form of[32, 37-39]

$$\text{fraction folded} = F_0 + (1 - F_0) \times F_s \left(\frac{[M^{2+}]^n}{K_D{}^n + [M^{2+}]^n} \right), \qquad \text{Eq. 4.1}$$

where F_0 and F_s are fractions of the riboswitch folded at 0 and saturation $[M^{2+}]$ (M = Mg or Mn), respectively. The Hill coefficient n is readily determined to be 1.3(2), suggesting that folding is effectively promoted by a singly occupied 5-fold coordination Mg^{2+} binding site, in agreement

with characterization in previous structural studies[25]. It is worth noting that the Hill coefficient indicates the number of ligands (Mg^{2+}) that become associated during the folding event and need not necessarily equal the binding stoichiometry[40]. Indeed, the minor deviation of n from unity could reflect increased number of Mg^{2+} ions surrounding the riboswitch during folding, for which the effective Mg^{2+} binding constant is found to be K_D = 1.1(2) mM. To explore the thermodynamics of subsequent Mn^{2+} binding, we therefore choose to study the temperature dependence of manganese riboswitch folding at two representative [Mg^{2+}] concentrations of i) relatively low ([Mg^{2+}] = 0.5 mM < K_D) and ii) near saturation ([Mg^{2+}] = 2 mM > K_D) levels.

The results are summarized in a van't Hoff analysis (see Figure 4.3B), where K_{eq} is plotted logarithmically vs. reciprocal temperature (1/T, T in Kelvin). The negative slopes in the data immediately reveal that folding of the manganese riboswitch is promoted by increasing temperature. In particular, the data indicate approximately 20- and 10-fold increase in the equilibrium folding constant (K_{eq}) over a temperature change of only 10 ^{o}C, at 0.5 and 2 mM Mg^{2+}, respectively, signaling an unusually strong dependence of riboswitch conformation on temperature. More quantitatively, linear least squares fit of such van't Hoff data to:

$$\ln(K_{eq}) = -\frac{\Delta H^0}{R}\frac{1}{T} + \frac{\Delta S^0}{R}, \qquad \text{Eq. 4.2}$$

allows one to deconstruct overall free energies into enthalpic and entropic contributions; corresponding to $-\Delta H^0/R$ and $\Delta S^0/R$, respectively. The negative slope is consistent with $\Delta H^0 > 0$, meaning the folding is endothermic process and thus promoted by heat; whereas the positive intercept suggests a strong increase in entropy ($\Delta S^0 > 0$) upon folding. Such heat promoted-folding (or "cold-denaturation") behavior is relatively unusual, as we more conventionally expect the folding into a more order compact state to be entropically unfavored ($\Delta S^0 < 0$) and enthalpically driven ($\Delta H^0 < 0$) by interactions such as hydrogen bonding and metal coordination.

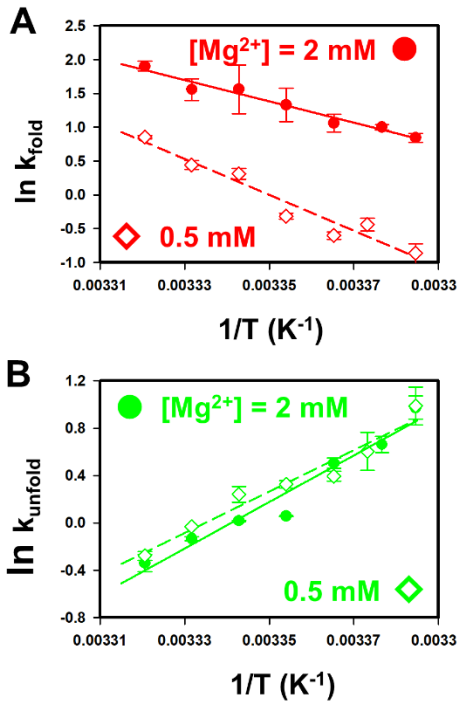

Figure 4.4 Kinetic effects of Mg^{2+} in an activated complex/transition state theory analysis of (A) k_{fold} and (B) k_{unfold}.

Furthermore, the [Mg^{2+}] dependence of this van't Hoff plot shows moderate changes in slope and intercept, indicating that the Mg^{2+} dependence of folding occurs by mildly lowering the enthalpic cost ($\Delta\Delta H^0 < 0$) while increasing the overall entropic gain ($\Delta\Delta S^0 > 0$) (Figure 4.3B).

At the kinetic level, we can trace the impact of temperature on equilibrium constants from the corresponding folding and unfolding rate constants. If we associate purely single exponential kinetic behavior with a single rate limiting transition state, the detailed thermodynamic properties of this transition state can be obtained from an activated transition state/Eyring analysis of ln(k_{fold}) or ln(k_{unfold}) vs 1/T (see Figure 4.4):

$$\ln(k) = -\frac{\Delta H^{\ddagger}}{R}\frac{1}{T} + \frac{\Delta S^{\ddagger}}{R} + \ln \nu \,. \qquad \text{Eq. 4.3}$$

In Eq. 4.3, $\Delta H^{\ddagger}$ and $\Delta S^{\ddagger}$ represent differences in enthalpy and entropy between the transition state and the folded (or unfolded) state, while ν is the so called "attempt frequency" to access the

transition barrier along the reaction coordinate [34-35, 41-43]. One challenge of such an activated transition state analysis is that ν is generally not known *a priori* and often simply estimated to be of order 10^{12} -10^{14} s^{-1}, though the inferred entropy of the transition state ($\Delta S^{\ddagger}$) depends only logarithmically on ν. However, it is worth noting that any cation induced *changes* in this entropic barrier (i.e., $-\Delta[T\Delta S^{\ddagger}]$) exactly cancel even this weak logarithmic sensitivity and become rigorously independent of the choice of ν[34-35].

The results of such an Eyring analysis immediately reveal several interesting features. First of all, a temperature rise promotes folding of the manganese riboswitch by both *increasing* k_{fold} and *decreasing* k_{unfold}, as clearly evident from the negative and positive slopes in Figure 4.4A and 4.4B, respectively. Secondly, the negative slopes for k_{fold} implies that overall folding of the manganese riboswitch is an *endothermic* process, in contrast with the more usual *exothermic* folding behavior due to formation of additional stabilizing hydrogen bonding networks. Thirdly, increasing Mg^{2+} from 0.5 to 2 mM increases the riboswitch stability (K_{eq}) significantly, but almost entirely by dramatic enhancement in k_{fold} (Figure 4.4A) with relatively little change on k_{unfold} (Figure 4.4B). However, even though k_{fold} is uniformly larger under high [Mg^{2+}] conditions, it is also much less temperature sensitive than at low [Mg^{2+}]. Conversely, the temperature dependence of k_{unfold} is almost completely insensitive to [Mg^{2+}], which echoes a similar lack of [Mg^{2+}] dependence to unfolding rate constants observed from previous study at room temperature [32]. Simply summarized, these results suggest that Mg^{2+} promotes the stability of the folded riboswitch structure predominantly by *lowering* both the folded and transition state free energies by equivalent amounts, thereby permitting k_{fold} and k_{unfold} to be strongly *increased* and *largely unaffected*, respectively.

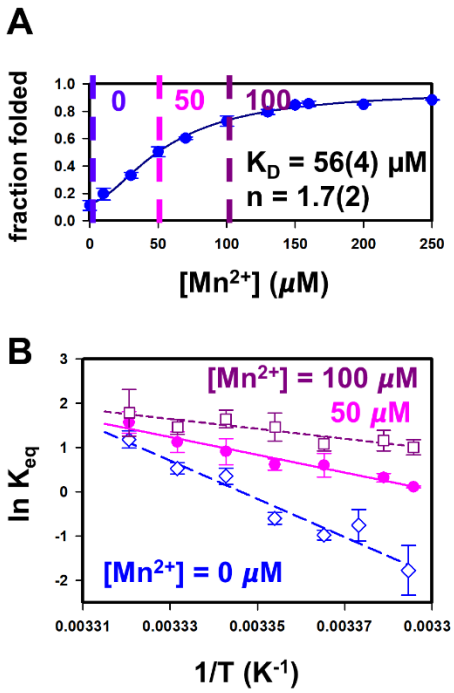

Figure 4.5 Mn^{2+} effects on manganese riboswitch folding under equilibrium conditions: (A) Folded fraction as a function of [Mn^{2+}]; (B) van't Hoff plot of temperature dependent manganese riboswitch folding at [Mg^{2+}] = 0.5 mM.

4.4.3 Mn^{2+} effects on the temperature dependence of folding

The [Mn^{2+}] dependent folding data suggests a positive cooperativity of Mn^{2+}, whereby the fraction folded increases nearly quadratically at low [Mn^{2+}] and gradually reaches saturation (Figure 4.5A). By Hill analysis, the cooperativity is found to be n = 1.7(2), consistent with the presence of two M^{2+} binding sites determined by x-ray structural studies[25]. Deviation of the Hill coefficient from 2 can be understood as arising from the non-selective cation site already being partially occupied by Mg^{2+} under near physiological conditions ([Mg^{2+}] ≈ 0.5 mM)[32]. More importantly, the effective binding constant K_D for Mn^{2+} is determined to achieve a much tighter value of 56(4) μM. We thus choose to explore the temperature dependent rate processes at three representative [Mn^{2+}] conditions corresponding to folding at i) far below (0 μM), ii) comparable with (50 μM), and iii) above (100 μM) the value of K_D, respectively.

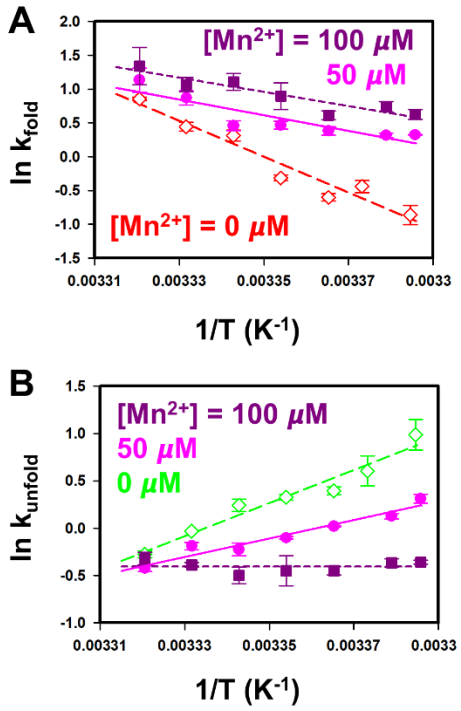

Figure 4.6 Kinetic dependence of Mn^{2+} in an activated complex/transition state theory analysis of (A) k_{fold} and (B) k_{unfold}.

From van't Hoff analyses summarized in Figure 4.5B, the folding equilibria under all three cation conditions are clearly shown to be endothermic (negative slopes) and thereby promoted by increasing temperature. Furthermore, the positive intercepts indicate that folding increases the overall entropy ($\Delta S^0 > 0$) of the system. However, the manganese riboswitch reveals an unconventional heat-promoted folding behavior with a surprising sensitivity to $[Mn^{2+}]$. Specifically as $[Mn^{2+}]$ *increases*, the magnitudes of both the van't Hoff slopes and intercepts *decrease*. The net effect of Mn^{2+} on manganese riboswitch folding would therefore appear to be a simultaneous *reduction* in ΔH^0 and ΔS^0. Though more work need to be done, this would at least be consistent with a more common physical scenario of cation binding resulting in enthalpic stabilization ($\Delta\Delta H^0 < 0$) and yet added entropic cost ($\Delta[-T\Delta S^0] > 0$), largely caused by loss in translational entropy of the ligand[44-46].

From the corresponding temperature dependent folding/unfolding kinetics summarized in Figure 4.6, a rise in temperature promotes the overall manganese riboswitch folding once again by increasing k_{fold} and decreasing k_{unfold}. From the Eyring plots, k_{fold} (Figure 4.6A) becomes less sensitive to temperature, with the overall rate constant increasing but slope magnitudes decreasing dramatically with increasing $[Mn^{2+}]$. This would be consistent with any enthalpic barrier between the unfolded state and transition state being lowered by increasing Mn^{2+}. The intercept, on the other hand, also decreases ($\Delta[-T\Delta S^0] > 0$) with increasing Mn^{2+}, suggesting that any entropy gain achieved during folding is mitigated by Mn^{2+}. Finally, both Eyring analysis slopes and intercepts for k_{unfold} are observed to decrease with increasing $[Mn^{2+}]$ conditions. In summary, the effect of Mn^{2+} on the kinetics would appear to lower the enthalpic barrier to folding and yet also contribute to entropically destabilizing the folded configuration.

4.5 Discussion

4.5.1 Unconventional temperature response of manganese riboswitch folding

The combination of hydrogen bonding, coulombic interactions (both attractive and repulsive), and water hydration often cause nucleic acid biomolecules to spontaneously rearrange into a more ordered and compact conformation[7-8]. As a result, the conventional thermodynamic paradigm for RNA folding is an enthalpically driven process ($\Delta H^0 < 0$) but with appreciable increase in free energy due to entropic penalty in the final state ($-T\Delta S^0 > 0$). In the current studies, folding of the manganese riboswitch has been shown to be strongly promoted by increasing temperature. The negative slopes and positive intercepts in the van't Hoff plots under all Mg^{2+} and Mn^{2+} conditions indicate that folding occurs spontaneously, made possible by *entropic gain* competing against an unfavorable *enthalpic penalty*. Though such temperature-

promoted folding ("cold denaturation") seems at first counterintuitive, such behavior has nonetheless been discovered in many proteins, with the phenomenon often linked to change in solvent exposed area during folding[47-49], for which largely entropically driven hydrophobic and hydrophilic interactions play the dominant role.

The thermodynamic analysis of Section 4.4.2 and 4.4.3 clearly reveals that both enthalpy and entropy of the *system* (i.e., RNA construct *plus* surrounding solvent environment) increase with folding of the manganese riboswitch, with a large entropic contribution ($-T\Delta S$) compensating and even dominating free energy stabilization of the more structured conformation. Previous studies indicate that variation in solvent exposure along the folding

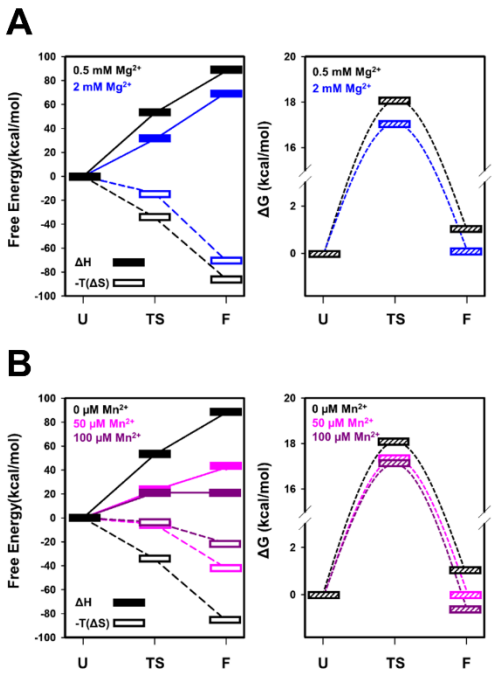

Figure 4.7 Folding free energy landscapes of the manganese riboswitch: (A) Mg^{2+} effects on enthalpic and entropy contributions (left) and the overall free energy (right); (B) Mn^{2+} effects on enthalpic and entropy contributions (left) and the overall free energy (right). Note that although there is no information on change in absolute free energies with cation conditions, the unfolded state (U) is conventionally referenced to zero free energy in both plots.

coordinate plays an important role in cold denaturation[47-49], which in turn results in significant solvent impact on the equilibrium behavior. In the manganese riboswitch, the two M^{2+} binding sites are rich in phosphate groups and highly negatively charged (Figure 4.1B). When such a charged species is placed in aqueous solution, the water molecules orient to lower the enthalpy ($\Delta H^0 < 0$), with water ordering resulting in a large entropy decrease for the solvent system ($\Delta S^0 > 0$), a process known as hydration[50-51]. When the manganese riboswitch folds, the highly charged regions of RNA become less accessible to water due to partial neutralization by counterions. Thus, the reverse "dehydration" process can occur during the folding event due to water expulsion around the highly charged binding sites. If such dehydration effects predominate over intramolecular hydrogen bonding in the RNA construct, this could thereby result in i) a large enthalpic cost ($\Delta H^0 > 0$) balanced by ii) entropically driven folding ($\Delta S^0 < 0$). Since the manganese riboswitch folds into a more order state upon metal binding, we would expect both ΔH^0 and ΔS^0 for the construct to be less than zero. However, it is the total enthalpies and entropies of the system (RNA plus buffer solution) that is observed, likely dominated by the hydration process and solvent reorganization. For Mn^{2+} binding to the Mn^{2+}-specific site[25, 32], the process can therefore quite understandably result in lowering both the enthalpic cost and entropic gain ($\Delta(\Delta H^0) < 0$, $\Delta(\Delta S^0) < 0$), consistent with our observations in Figure 4.7B.

4.5.2 Temperature response of RNA

Although cold denaturation (or heat-promoted folding) has been widely explored in proteins, it is a much less commonly observed in RNA. One such RNA system known to exhibit heat-promoted folding is the hammerhead ribozyme[47-48], for which temperature-dependent folding of the three way junction has been investigated with circular dichroism (CD) over a wide range of temperature. Interestingly, the studies reveal that the three way junction folded structure

is stabilized with increasing temperature at relatively low temperature, but that this thermal stabilization of folding reverses at a critical temperature. In another recent study of the adenine-sensing riboswitch, it was shown by NMR spectroscopy that achievement of the ligand-free folded conformation is also promoted by temperature increase[52]. Despite only relatively few direct measurements of temperature responsive RNA folding, the thermodynamic parameters for ligand-mediated riboswitch folding can be estimated from isothermal titration calorimetry (ITC) as well as other temperature-dependent binding studies, since ligand binding is always accompanied by conformational change in the RNA riboswitch. From literature search over 17 classes of riboswitches/ribozymes that responding to various ligands and substrates[38, 53-77], nine appear to exhibit entropically favored binding ($\Delta S^0 > 0$) [53-62], indicating that configurational entropy of the solvent can dominate the folding entropy of the riboswitch construct. Furthermore, four out of these nine are also found to be endothermic ($\Delta H^0 > 0$)[53-58], similar to the manganese riboswitch behavior. Thus, one is led to speculate that cold denaturation might not actually be so uncommon for a tertiary binding/folding strategy in RNA. In fact, RNAs are structurally polyanion electrolytes that interact strongly with water; as a result, thermodynamic free energies for RNA folding might reflect even greater sensitivity to the solvent and buffer system than for proteins[7, 15-16]. This would appear likely to have evolutionary consequences. Bacteria in the wild experience significant temperature fluctuations, with some thriving under extreme temperature conditions[17-19]. It is thus perhaps not surprising that temperature sensitivity may have been evolutionarily integrated into riboswitch function.

It is also possible to take this analysis further toward understanding the biochemical role of temperature in gene regulation. For example, Mn^{2+} is known to catalyze formation of reactive oxidative species (ROS) that are particularly damaging to cells[78-79]. In this study, we have seen

that the manganese riboswitch at higher temperatures transcriptionally promotes gene expression of a Mn^{2+} efflux protein, essentially by folding into "on" conformation. Due to more active production and higher reactivity of ROS at high temperature[80-82], such a temperature dependence could be advantageous for bacteria survival as a protective mechanism reducing cellular [Mn^{2+}]. Indeed, bacteria have been shown to exploit temperature control in gene regulation, as evident in so called "RNA thermometers," [22-23] i.e., small mRNA elements that structurally respond to temperature in regulation of translational efficiency. Since RNA structures are highly responsive to temperature, it is interesting to speculate that *cation* plus *environmental temperature* modulation of a specific RNA conformation could reflect a more general strategic example of *multicomponent sensitivity* in riboswitch gene regulation.

4.5.3 Reconstructing folding free energy landscapes from temperature-dependent kinetics

The thermodynamic/kinetic parameters obtained from the current van't Hoff and Eyring analyses can provide particularly invaluable information on pieces of the overall free energy landscape for folding of the manganese riboswitch. For example, Figure 4.7A immediately reveals that the enthalpic (ΔH) and entropic ($-T\Delta S$) contributions to the free energy (ΔG) for both the transition (TS) and folded (F) state confirmations move synchronously up/down with increasing Mg^{2+} in a clearly anticorrelated fashion. This notable level of synchrony suggests that the impact of Mg^{2+} is primarily on the enthalpy/entropy of the unfolded state (U), as shifts in only U would maintain all relative free energy spacings between the TS and F conformations. Such a strong dependence of unfolded structure free energies on [Mg^{2+}] can be rationalized as arising from differential Mg^{2+} occupancy at the non-selective M^{2+} binding site, as these experiments are performed at Mg^{2+} concentrations appreciably below (0.5 mM) and above (2 mM) the effective binding affinity (K_D =1.1 mM). Simply stated, since M^{2+} binding is essential

for riboswitch folding[32], the free energy differences between the anticorrelated TS and F states are insensitive to [Mg^{2+}] due to the fact that they are both associated with one Mg^{2+}. Thus, the Mg^{2+}-mediated manganese riboswitch folding thermodynamics plots in Figure 4.7A reveal that Mg^{2+} binding must occur while the construct is still mostly *unfolded*. In agreement with the previous kinetic studies, therefore, this is consistent with an induced-fit (i.e., "bind-then-fold") mechanism[30, 32-33], whereby prior binding of the ligand is required to achieve the correct folding behavior. We note that such information can be gleaned from the plots even in the absence of any knowledge about absolute free energies (e.g., the free energy for the U state is kept at zero by convention)

Similarly, for [Mn^{2+}] dependent riboswitch folding (Figure 4.7B), the entropy and enthalpy of the TS and F states are both significantly shifted with increasing Mn^{2+} concentration. Overall, as [Mn^{2+}] increases, the enthalpic (ΔH) and entropic ($-T\Delta S$) contributions bifurcate systematically. Such effects are in agreement with ligand binding models, where the enthalpic gain (from Mn^{2+} coordination) is accompanied by entropic loss (largely translational entropy of ligand and higher degree of ordering at the binding site[44-46]. Interestingly, however, there is also a strongly non-linear saturation dependence of these effect on [Mn^{2+}]. For example, the transition state (TS) free energy changes significantly between 0 and 50 μM of Mn^{2+} and yet remains essentially constant with an additional aliquot of 50 μM Mn^{2+} (100 μM in total). This behavior is likely due to the fact that Mn^{2+} promotes achievement of the TS state via different occupancies of the two M^{2+} binding sites. Indeed, the largest free energy effects between conditions of 50 and 100 μM Mn^{2+} appear in the folded (F) state, but now with negligible changes in the TS and U conformations. Much as invoked above for Mg^{2+} dependence, this can be simply rationalized by the folded state existing with two different metal occupancies of the two binding sites: one M^{2+}

(M = Mn or Mg) binding or two M^{2+} binding with at least one Mn^{2+}. The Mn^{2+} effect of $\Delta(\Delta H^0) < 0$ and $\Delta(\Delta S^0) < 0$ is again consistent with increased Mn^{2+} binding. Although the manganese riboswitch is known to fold via an induced-fit (IF, bind-then-fold) mechanism with at least one M^{2+} binding in the unfolded state[32], the ability of Mn^{2+} to directly bind to a (pre-)folded conformation and thereby stabilize the folding equilibrium is consistent with a conformational selection (CS, fold-then-bind) mechanism[30, 32-33], whereby the RNA dynamically samples many different configurations while the ligand binds only to those constructs with a preformed Mn^{2+} binding site. To summarize, the thermodynamic analysis of the rate and equilibrium data reveals that the manganese riboswitch folds through an induced-fit mechanism via early Mg^{2+} association with U. Conversely, Mn^{2+} binds to a pre-folded ligand-free riboswitch structure to stabilize the folding equilibrium (i.e., in support of a conformation selection mechanism), as evidenced by selective effects of $Mn^{2+} > 50$ μM on the free energy of the folded (F) configuration. Finally it is worth emphasizing that such Mn^{2+} and Mg^{2+} ligand binding shifts in the enthalpic and entropic contributions are all anticorrelated and very finely balanced to yield only relatively small differences (or order 1 kcal/mol) in the overall free energies for the folded vs unfolded states of the riboswitch. This allows for strong environmental regulation of the kinetic rates and time constants for riboswitch folding, with only relatively small changes in the overall folding stability. Such a cationic modulation of the folding time constant behavior could be relevant in co-transcriptional folding dynamics and gene regulation strategies.[30-31]

4.6 Summary and conclusion

The temperature dependence of manganese riboswitch folding has been explored in detail by confocal smFRET experiments. The folded manganese riboswitch conformation is found to

be strongly stabilized by temperature, which from a kinetic perspective occurs via simultaneous increase (decrease) in the folding (k_{fold}) (unfolding) (k_{unfold}) unimolecular rate constants, respectively. A thermal Van't Hoff analysis of the equilibrium constant reveals that folding is strongly disfavored enthalpically ($\Delta H > 0$), while favored with significant and closely balanced entropic contributions ($-T\Delta S < 0$) to yield an overall $\Delta G < 0$. This is in clear contrast with the more conventional behavior of ligand-promoted folding behavior of entropically disfavored folding into a compact state driven by enthalpic energy release[9-10]. Such temperature-promoted folding (or equivalently, cold denaturation) can result from change in ionic hydration/dehydration and hydrophilic/hydrophobic interactions, highlighting the crucial importance of *solvent* contributions to the overall free energy change in an RNA folding event. Moreover, we speculate that such a less conventional thermophilic response of the manganese riboswitch may provide an additionally useful survival mechanism for successful bacterial proliferation in a fluctuating temperature environment, suggesting a mechanism by which temperature may be more widely incorporated into riboswitch gene regulation. In Mg^{2+}-mediated folding, Mg^{2+} is found to mainly affect the free energy of the unfolded (U) state, consistent with the unfolded structure having 0 or 1 Mg^{2+} occupancy and yet with the ones binding to a single Mg^{2+} able to access the transition state and thereby achieve a fully folded structure. Such binding of a single Mg^{2+} prior to the transition state supports the predominant existence of an induced-fit ("bind-then-fold") mechanism for Mg^{2+}-promoted folding. For Mn^{2+} mediated folding, by way of contrast, Mn^{2+} is found to significantly shift the relative free energies of *both* the transition (TS) and folded (F) states. This sensitivity to $[Mn^{2+}]$ is consistent with the folded state of the riboswitch associating different numbers of Mn^{2+} into its two (selective and non-selective) binding sites, which would provide support for a conformational selection ("fold-then-bind")

pathway. Such a combined thermal and cation sensitivity to modulation of the riboswitch folding pathway offers a distinctly new opportunities for evolutionary adaptation and flexibility of the manganese riboswitch to variable environmental conditions.

4.7 References

1. Mironov, A. S.; Gusarov, I.; Rafikov, R.; Lopez, L. E.; Shatalin, K.; Kreneva, R. A.; Perumov, D. A.; Nudler, E., Sensing Small Molecules by Nascent RNA: A Mechanism to Control Transcription in Bacteria. *Cell* **2002,** *111* (5), 747-756.

2. Nahvi, A.; Sudarsan, N.; Ebert, M. S.; Zou, X.; Brown, K. L.; Breaker, R. R., Genetic Control by a Metabolite Binding mRNA. *Chem. Biol.* **2002,** *9* (9), 1043-1049.

3. Tucker, B. J.; Breaker, R. R., Riboswitches as versatile gene control elements. *Curr. Opin. Struct. Biol.* **2005,** *15* (3), 342-348.

4. Serganov, A.; Nudler, E., A Decade of Riboswitches. *Cell* **2013,** *152* (1), 17-24.

5. Roth, A.; Breaker, R. R., The Structural and Functional Diversity of Metabolite-Binding Riboswitches. *Annu. Rev. Biochem.* **2009,** *78* (1), 305-334.

6. Garst, A. D.; Edwards, A. L.; Batey, R. T., Riboswitches: Structures and mechanisms. *Cold Spring Harbor Persp. Biol.* **2011,** *3* (6), a003533.

7. Brady, G. P.; Sharp, K. A., Entropy in protein folding and in protein—protein interactions. *Curr. Opin. Struct. Biol.* **1997,** *7* (2), 215-221.

8. Onuchic, J. N.; Wolynes, P. G., Theory of protein folding. *Curr. Opin. Struct. Biol.* **2004,** *14* (1), 70-75.

9. Draper, D. E., Strategies for RNA folding. *Trends Biochem. Sci.* **1996,** *21* (4), 145-149.

10. Dill, K. A., Dominant forces in protein folding. *Biochem.* **1990,** *29* (31), 7133-7155.

11. Schildkraut, C.; Lifson, S., Dependence of the melting temperature of DNA on salt concentration. *Biopolymers* **1965,** *3* (2), 195-208.

12. Donovan, J. W.; Mapes, C. J.; Davis, J. G.; Garibaldi, J. A., A differential scanning calorimetric study of the stability of egg white to heat denaturation. *J. Sci. Food Agric.* **1975,** *26* (1), 73-83.

13. Privalov, P. L., Cold Denaturation of Protein. *Crit. Rev. Biochem. Mol. Biol.* **1990,** *25* (5), 281-306.

14. Hatley, R. H. M.; Franks, F., Cold destabilisation of enzymes. *Faraday Discuss.* **1992,** *93* (0), 249-257.

15. Makhatadze, G. I.; Privalov, P. L., Contribution of Hydration to Protein Folding Thermodynamics: I. The Enthalpy of Hydration. *J. Mol. Biol.* **1993,** *232* (2), 639-659.

16. Privalov, P. L.; Makhatadze, G. I., Contribution of Hydration to Protein Folding Thermodynamics: II. The Entropy and Gibbs Energy of Hydration. *J. Mol. Biol.* **1993,** *232* (2), 660-679.

17. Kurr, M.; Huber, R.; König, H.; Jannasch, H. W.; Fricke, H.; Trincone, A.; Kristjansson, J. K.; Stetter, K. O., *Methanopyrus kandleri*, gen. and sp. nov. represents a novel group of hyperthermophilic methanogens, growing at 110°C. *Arch. Microbiol.* **1991,** *156* (4), 239-247.

18. Takai, K.; Nakamura, K.; Toki, T.; Tsunogai, U.; Miyazaki, M.; Miyazaki, J.; Hirayama, H.; Nakagawa, S.; Nunoura, T.; Horikoshi, K., Cell proliferation at 122°C and isotopically heavy CH_4 production by a hyperthermophilic methanogen under high-pressure cultivation. *Proc. Natl. Acad. Sci. USA* **2008,** *105* (31), 10949-10954.

19. Mykytczuk, N. C. S.; Foote, S. J.; Omelon, C. R.; Southam, G.; Greer, C. W.; Whyte, L. G., Bacterial growth at −15 °C; molecular insights from the permafrost bacterium *Planococcus halocryophilus* Or1. *The Isme Journal* **2013,** *7*, 1211.

20. Hurme, R.; Rhen, M., Temperature sensing in bacterial gene regulation — what it all boils down to. *Mol. Microbiol.* **1998,** *30* (1), 1-6.

21. Konkel, M. E.; Tilly, K., Temperature-regulated expression of bacterial virulence genes. *Microb. Infect.* **2000,** *2* (2), 157-166.

22. Narberhaus, F., Translational control of bacterial heat shock and virulence genes by temperature-sensing mRNAs. *RNA Biology* **2010,** *7* (1), 84-89.

23. Kortmann, J.; Narberhaus, F., Bacterial RNA thermometers: molecular zippers and switches. *Nat. Rev. Microbiol.* **2012,** *10*, 255.

24. Barrick, J. E.; Corbino, K. A.; Winkler, W. C.; Nahvi, A.; Mandal, M.; Collins, J.; Lee, M.; Roth, A.; Sudarsan, N.; Jona, I.; Wickiser, J. K.; Breaker, R. R., New RNA motifs suggest an expanded scope for riboswitches in bacterial genetic control. *Proc. Natl. Acad. Sci. USA* **2004,** *101* (17), 6421-6426.

25. Price, Ian R.; Gaballa, A.; Ding, F.; Helmann, John D.; Ke, A., Mn^{2+}-Sensing Mechanisms of *yybP-ykoY* Orphan Riboswitches. *Mol. Cell* **2015,** *57* (6), 1110-1123.

26. Dambach, M.; Sandoval, M.; Updegrove, Taylor B.; Anantharaman, V.; Aravind, L.; Waters, Lauren S.; Storz, G., The Ubiquitous *yybP-ykoY* Riboswitch Is a Manganese-Responsive Regulatory Element. *Mol. Cell* **2015,** *57* (6), 1099-1109.

27. Waters, L. S.; Sandoval, M.; Storz, G., The *Escherichia coli* MntR Miniregulon Includes Genes Encoding a Small Protein and an Efflux Pump Required for Manganese Homeostasis. *J. Bacteriol.* **2011,** *193* (21), 5887-5897.

28. Veyrier, F. J.; Boneca, I. G.; Cellier, M. F.; Taha, M.-K., A Novel Metal Transporter Mediating Manganese Export (MntX) Regulates the Mn to Fe Intracellular Ratio and *Neisseria meningitidis* Virulence. *PLoS Path.* **2011,** *7* (9), e1002261.

29. Li, C.; Tao, J.; Mao, D.; He, C., A Novel Manganese Efflux System, YebN, Is Required for Virulence by *Xanthomonas oryzae* pv. *oryzae*. *PLOS ONE* **2011,** *6* (7), e21983.

30. Haller, A.; Soulière, M. F.; Micura, R., The Dynamic Nature of RNA as Key to Understanding Riboswitch Mechanisms. *Acc. Chem. Res.* **2011,** *44* (12), 1339-1348.

31. Garst, A. D.; Batey, R. T., A switch in time: Detailing the life of a riboswitch. *Biochimica et Biophysica Acta (BBA) - Gene Regulatory Mechanisms* **2009,** *1789* (9), 584-591.

32. Sung, H.-L.; Nesbitt, D. J., Single Molecule FRET Kinetics of the Mn^{2+} Riboswitch: Evidence for Allosteric Mg^{2+} Control of "Induced Fit" vs. "Conformational Selection" Folding Pathways. *J. Phys. Chem. B* **2019**.

33. Leulliot, N.; Varani, G., Current Topics in RNA−Protein Recognition: Control of Specificity and Biological Function through Induced Fit and Conformational Capture. *Biochem.* **2001,** *40* (27), 7947-7956.

34. Fiore, J. L.; Holmstrom, E. D.; Nesbitt, D. J., Entropic origin of Mg^{2+}-facilitated RNA folding. *Proc. Natl. Acad. Sci. USA* **2012,** *109* (8), 2902-2907.

35. Sengupta, A.; Sung, H.-L.; Nesbitt, D. J., Amino Acid Specific Effects on RNA Tertiary Interactions: Single-Molecule Kinetic and Thermodynamic Studies. *J. Phys. Chem. B* **2016,** *120* (41), 10615-10627.

36. Nicholson, D. A.; Sengupta, A.; Sung, H.-L.; Nesbitt, D. J., Amino Acid Stabilization of Nucleic Acid Secondary Structure: Kinetic Insights from Single-Molecule Studies. *J. Phys. Chem. B* **2018,** *122* (43), 9869-9876.

37. Fiegland, L. R.; Garst, A. D.; Batey, R. T.; Nesbitt, D. J., Single-Molecule Studies of the Lysine Riboswitch Reveal Effector-Dependent Conformational Dynamics of the Aptamer Domain. *Biochem.* **2012,** *51* (45), 9223-9233.

38. Schroeder, Kersten T.; Daldrop, P.; Lilley, David M., RNA Tertiary Interactions in a Riboswitch Stabilize the Structure of a Kink Turn. *Structure* **2011,** *19* (9), 1233-1240.

39. Hennelly, S. P.; Novikova, I. V.; Sanbonmatsu, K. Y., The expression platform and the aptamer: cooperativity between Mg^{2+} and ligand in the SAM-I riboswitch. *Nucleic Acids Res.* **2013,** *41* (3), 1922-1935.

40. Leipply, D.; Draper, D. E., Dependence of RNA Tertiary Structural Stability on Mg^{2+} Concentration: Interpretation of the Hill Equation and Coefficient. *Biochem.* **2010,** *49* (9), 1843-1853.

41. Szabo, A.; Schulten, K.; Schulten, Z., First passage time approach to diffusion controlled reactions. *J. Chem. Phys.* **1980,** *72* (8), 4350-4357.

42. Zwanzig, R.; Szabo, A.; Bagchi, B., Levinthal's paradox. *Proc. Natl. Acad. Sci. USA* **1992,** *89* (1), 20-22.

43. Zhou, H.-X., Rate theories for biologists. *Q. Rev. Biophys.* **2010,** *43* (2), 219-293.

44. Murphy, K. P.; Xie, D.; Thompson, K. S.; Amzel, L. M.; Freire, E., Entropy in biological binding processes: Estimation of translational entropy loss. *Proteins: Struct. Funct. Bioinform.* **1994,** *18* (1), 63-67.

45. Mario, A. L., Loss of translational entropy in binding, folding, and catalysis. *Proteins: Structure, Function, and Bioinformatics* **1997,** *28* (2), 144-149.

46. Lu, B.; Wong, C. F., Direct estimation of entropy loss due to reduced translational and rotational motions upon molecular binding. *Biopolymers* **2005,** *79* (5), 277-285.

47. Mikulecky, P. J.; Feig, A. L., Cold Denaturation of the Hammerhead Ribozyme. *J. Am. Chem. Soc.* **2002,** *124* (6), 890-891.

48. Mikulecky, P. J.; Feig, A. L., Heat capacity changes in RNA folding: application of perturbation theory to hammerhead ribozyme cold denaturation. *Nucleic Acids Res.* **2004,** *32* (13), 3967-3976.

49. Cooper, A.; Johnson, C. M.; Lakey, J. H.; Nöllmann, M., Heat does not come in different colours: entropy–enthalpy compensation, free energy windows, quantum confinement, pressure perturbation calorimetry, solvation and the multiple causes of heat capacity effects in biomolecular interactions. *Biophys. Chem.* **2001,** *93* (2), 215-230.

50. Lumry, R.; Rajender, S., Enthalpy–entropy compensation phenomena in water solutions of proteins and small molecules: A ubiquitous property of water. *Biopolymers* **1970,** *9* (10), 1125-1227.

51. Schmid, R.; Miah, A. M.; Sapunov, V. N., A new table of the thermodynamic quantities of ionic hydration: values and some applications (enthalpy–entropy compensation and Born radii). *Phys. Chem. Chem. Phys.* **2000,** *2* (1), 97-102.

52. Reining, A.; Nozinovic, S.; Schlepckow, K.; Buhr, F.; Fürtig, B.; Schwalbe, H., Three-state mechanism couples ligand and temperature sensing in riboswitches. *Nature* **2013,** *499*, 355.

53. McConnell, T. S.; Cech, T. R., A positive entropy change for guanosine binding and for the chemical step in the Tetrahymena ribozyme reaction. *Biochem.* **1995,** *34* (12), 4056-4067.

54. Kuo, L. Y.; Cech, T. R., Conserved thermochemistry of guanosine nucleophile binding for structurally distinct group I ribozymes. *Nucleic Acids Res.* **1996,** *24* (19), 3722-3727.

55. Huang, L.; Serganov, A.; Patel, D. J., Structural Insights into Ligand Recognition by a Sensing Domain of the Cooperative Glycine Riboswitch. *Mol. Cell* **2010,** *40* (5), 774-786.

56. Trausch, Jeremiah J.; Ceres, P.; Reyes, Francis E.; Batey, Robert T., The Structure of a Tetrahydrofolate-Sensing Riboswitch Reveals Two Ligand Binding Sites in a Single Aptamer. *Structure* **2011,** *19* (10), 1413-1423.

57. Burnouf, D.; Ennifar, E.; Guedich, S.; Puffer, B.; Hoffmann, G.; Bec, G.; Disdier, F.; Baltzinger, M.; Dumas, P., kinITC: A New Method for Obtaining Joint Thermodynamic and Kinetic Data by Isothermal Titration Calorimetry. *J. Am. Chem. Soc.* **2012,** *134* (1), 559-565.

58. Baird, N. J.; Ferré-D'Amaré, A. R., Modulation of quaternary structure and enhancement of ligand binding by the K-turn of tandem glycine riboswitches. *RNA* **2013,** *19* (2), 167-176.

59. Gilbert, S. D.; Rambo, R. P.; Van Tyne, D.; Batey, R. T., Structure of the SAM-II riboswitch bound to S-adenosylmethionine. *Nat. Struct. Molec. Biol.* **2008,** *15*, 177.

60. Ren, A.; Rajashankar, K. R.; Patel, D. J., Fluoride ion encapsulation by Mg^{2+} ions and phosphates in a fluoride riboswitch. *Nature* **2012,** *486*, 85.

61. Ren, A.; Patel, D. J., c-di-AMP binds the *ydaO* riboswitch in two pseudo-symmetry–related pockets. *Nat. Chem. Biol.* **2014,** *10*, 780.

62. Ren, A.; Rajashankar, K. R.; Patel, D. J., Global RNA Fold and Molecular Recognition for a *pfl* Riboswitch Bound to ZMP, a Master Regulator of One-Carbon Metabolism. *Structure* **2015,** *23* (8), 1375-1381.

63. Stoddard, C. D.; Gilbert, S. D.; Batey, R. T., Ligand-dependent folding of the three-way junction in the purine riboswitch. *RNA* **2008,** *14* (4), 675-684.

64. Wickiser, J. K.; Cheah, M. T.; Breaker, R. R.; Crothers, D. M., The Kinetics of Ligand Binding by an Adenine-Sensing Riboswitch. *Biochem.* **2005,** *44* (40), 13404-13414.

65. Gao, A.; Serganov, A., Structural insights into recognition of c-di-AMP by the *ydaO* riboswitch. *Nat. Chem. Biol.* **2014,** *10*, 787.

66. Wood, S.; Ferré-D'Amaré, A. R.; Rueda, D., Allosteric Tertiary Interactions Preorganize the c-di-GMP Riboswitch and Accelerate Ligand Binding. *ACS Chem. Biol.* **2012,** *7* (5), 920-927.

67. Kang, M.; Eichhorn, C. D.; Feigon, J., Structural determinants for ligand capture by a class II preQ$_1$ riboswitch. *Proc. Natl. Acad. Sci. USA* **2014,** *111* (6), E663.

68. Wickiser, J. K.; Winkler, W. C.; Breaker, R. R.; Crothers, D. M., The Speed of RNA Transcription and Metabolite Binding Kinetics Operate an FMN Riboswitch. *Mol. Cell* **2005,** *18* (1), 49-60.

69. Baird, N. J.; Ferré-D'Amaré, A. R., Idiosyncratically tuned switching behavior of riboswitch aptamer domains revealed by comparative small-angle X-ray scattering analysis. *RNA* **2010,** *16* (3), 598-609.

70. Batey, R. T.; Gilbert, S. D.; Montange, R. K., Structure of a natural guanine-responsive riboswitch complexed with the metabolite hypoxanthine. *Nature* **2004,** *432*, 411.

71. Gilbert, S. D.; Stoddard, C. D.; Wise, S. J.; Batey, R. T., Thermodynamic and Kinetic Characterization of Ligand Binding to the Purine Riboswitch Aptamer Domain. *J. Mol. Biol.* **2006,** *359* (3), 754-768.

72. Edwards, A. L.; Reyes, F. E.; Héroux, A.; Batey, R. T., Structural basis for recognition of S-adenosylhomocysteine by riboswitches. *RNA* **2010,** *16* (11), 2144-2155.

73. Pikovskaya, O.; Polonskaia, A.; Patel, D. J.; Serganov, A., Structural principles of nucleoside selectivity in a 2'-deoxyguanosine riboswitch. *Nat. Chem. Biol.* **2011,** *7*, 748.

74. Wilson, R. C.; Smith, A. M.; Fuchs, R. T.; Kleckner, I. R.; Henkin, T. M.; Foster, M. P., Tuning Riboswitch Regulation through Conformational Selection. *J. Mol. Biol.* **2011,** *405* (4), 926-938.

75. Müller, M.; Weigand, J. E.; Weichenrieder, O.; Suess, B., Thermodynamic characterization of an engineered tetracycline-binding riboswitch. *Nucleic Acids Res.* **2006,** *34* (9), 2607-2617.

76. Li, Y.; Bevilacqua, P. C.; Mathews, D.; Turner, D. H., Thermodynamic and activation parameters for binding of a pyrene-labeled substrate by the Tetrahymena ribozyme: docking is not diffusion-controlled and is driven by a favorable entropy change. *Biochem.* **1995,** *34* (44), 14394-14399.

77. Kulshina, N.; Edwards, T. E.; Ferré-D'Amaré, A. R., Thermodynamic analysis of ligand binding and ligand binding-induced tertiary structure formation by the thiamine pyrophosphate riboswitch. *RNA* **2010,** *16* (1), 186-196.

78. Ali, S. F.; Duhart, H. M.; Newport, G. D.; Lipe, G. W.; Slikker, W., Manganese-induced reactive oxygen species: Comparison between Mn^{+2} and Mn^{+3}. *Neurodegeneration* **1995,** *4* (3), 329-334.

79. Brenneman, K. A.; Cattley, R. C.; Ali, S. F.; Dorman, D. C., Manganese-induced developmental neurotoxicity in the CD rat: is oxidative damage a mechanism of action? *Neurotoxicology* **1999,** *20* (2-3), 477-487.

80. Sairam, R. K.; Deshmukh, P. S.; Shukla, D. S., Tolerance of Drought and Temperature Stress in Relation to Increased Antioxidant Enzyme Activity in Wheat. *J. Agron. Crop Sci.* **1997,** *178* (3), 171-178.

81. Sairam, R. K.; Srivastava, G. C.; Saxena, D. C., Increased Antioxidant Activity under Elevated Temperatures: A Mechanism of Heat Stress Tolerance in Wheat Genotypes. *Biol. Plant.* **2000,** *43* (2), 245-251.

82. Lushchak, V. I.; Bagnyukova, T. V., Temperature increase results in oxidative stress in goldfish tissues. 2. Antioxidant and associated enzymes. *Comp. Biochem. Physiol. C* **2006,** *143* (1), 36-41.

Chapter 5

Sequential Folding of the Nickel/Cobalt Riboswitch is Facilitated by a Conformational Intermediate: Insights from Single-Molecule Kinetics and Thermodynamics

---

5.1 Abstract

The present work presents first single molecule Fluorescence Resonant Energy Transfer (smFRET) studies of the nickel/cobalt (NiCo) riboswitch, with temperature dependent, single molecule confocal microscopy to provide comprehensive kinetic and thermodynamic information on folding into a biochemically competent structure. The results indicate that the NiCo riboswitch first folds into a more compact "prefolded" conformation, with a preorganized binding pocket partially stabilized under physiological conditions by non-cognate monovalent/divalent cations. Such a prefolded intermediate then has opportunity to fold further into a tightly ligand-bound structure, in response to the cognate ligands, Ni^{2+} or Co^{2+}, with sub-micromolar affinities. Such stepwise ligand-induced folding represents a particularly clean example of a conformational selection ("fold-then-bind") mechanism, whereby a configuration dynamically accessible by thermal fluctuation is stabilized into the final folded state by ligand association. In addition, we observe a strong positive cooperativity in the ligand-induced folding kinetics with respect to both Ni^{2+} and Co^{2+} ligands. This provides maximal sensitivity in riboswitch conformational response near $[Ni^{2+}]$ or $[Co^{2+}] \approx K_d$, which facilitates more accurate biochemical probing of the cell environment and therefore bioregulation of gene expression. Temperature dependent kinetics at the single molecule level have also been explored, which

*This chapter is adapted from: Sung, H.-L.; Nesbitt, D. J. Sequential Folding of the Nickel/Cobalt Riboswitch is Facilitated by a Conformational Intermediate: Insights from Single-Molecule Kinetics and Thermodynamics. *J. Phys. Chem. B* **2020**, *124*, 7348–7360.

permit free energies to be deconstructed into enthalpic and entropic components along the folding coordinate. In the absence of the cognate ligand, a predominantly enthalpic barrier between the unfolded riboswitch (U) and the prefolded intermediate (I) suggests a rearrangement of the hydrogen bonding network, whereas in the presence of the cognate ligand, a large entropic penalty ($-T\Delta S^0 > 0$) in forming the folded riboswitch conformation (F) is almost perfectly counterbalanced by equivalent enthalpic gain ($\Delta H^0 < 0$) to yield $\Delta G^0 \approx 0$. The thermodynamic results are therefore consistent with a simple physical picture of RNA folding, whereby association of the cognate ligand is strongly stabilized by Coulombic attraction, while forming an entropically more ordered structure around the binding site.

5.2 Introduction

Riboswitches are highly structured cis-regulatory elements commonly found in the 5' untranslated region of mRNA.[1-2] Part of the highly conserved structure, known as the aptamer domain, functions as a metabolite sensor that folds to selectively capture the cognate ligand molecule. The rest of the riboswitch sequence comprises the expression platform which undergoes conformational transitions in response to the aptamer.[2] As a result, the overall riboswitch construct often adopts two mutually exclusive conformations corresponding to "on" and "off" states that structurally regulate expression of the downstream gene.[2-3] Such a regulatory mechanism has been widely exploited in bacteria[3-4], with riboswitches found to respond to a variety of ligands including small-molecule metabolites and even simple atomic ions.[5]

Heavy metals can be highly cytotoxic, forming complexes with proteins and catalyzing the production of reactive oxidative species damaging to cells.[6-7] However, heavy metals are also essential to cellular function, as they often serve a crucial role in enzymes and enzyme cofactors.[8-9] Ni^{2+}, for example, is a common component of almost all hydrogenases, while Co^{2+} is an essential constituent of vitamin B_{12}. As a result, tight control over intracellular metal ion concentrations is clearly desirable, with sensing and regulatory feedback mechanisms highly evolved to maintain ions at just the right level to support biochemical function while minimizing toxic side effects. In bacteria, for example, genetic expression of membrane transporters and traffic proteins for heavy metals are known to be predominantly controlled by a suite of metalloregulatory proteins.[10-11] The exact role of RNA in maintaining this heavy metal homeostasis is not entirely clear but changing rapidly. Indeed, the possibility of RNA *selectively responding* to heavy metal ions might at first have been dismissed as unlikely due to the limited types of functional groups available for metal coordination and the well-known association of RNA with physiological Mg^{2+}, the predominant divalent cation in cells.[12-13] By way of contrast, however, riboswitches have recently been identified that respond with remarkably high specificity to manganese (Mn^{2+})[14-15] and nickel/cobalt (Ni^{2+}/Co^{2+})[16], which in turn regulate the genetic expression of the corresponding protein transporters for these cations. This strongly suggests that metalloregulation is not the exclusive domain of proteins but also cooperatively involves some form of RNA-based sensor of the cellular metal ion environment.

The NiCo riboswitch has been previously referred to as the czcD motif,[16] which resides upstream of czcD genes encoding a subfamily of metal export and resistance proteins.[17-19] The capability of this riboswitch motif for atomic cation Ni^{2+}/Co^{2+} sensing has been recently validated,[16] and furthermore confirmed by detection of an explicitly Co^{2+}-bound crystal structure

in companion high resolution x-ray diffraction studies (PDB: 4RUM, Figure 5.1A). The Ni^{2+}/Co^{2+} sensing aptamer domain in this riboswitch consists of a four-way junction, with four helices coaxially-stacked in pairs to form a twisted H conformation. As a point of particular relevance to the present study, the NiCo riboswitch construct lacks the long-range tertiary interactions commonly found in other known riboswitches.[16] As a result, the conformation of the junctional loop responds directly to ligand binding, in turn signaling the on- vs off- state of the gene expression mechanism. Moreover, among the four Co^{2+} ions resolved in the crystal structure (Figure 5.1A), three form a strong coordination network primarily between the highly conserved guanines at the junction. It is believed that the coordination between Co^{2+} and the guanine nitrogen (N7) provides the source of metal ion selectivity, since Mg^{2+} prefers to coordinate with oxygens in the RNA phosphate backbone rather than nitrogens in the nucleobases.[13, 16] In terms of the gene regulation mechanism, the NiCo riboswitch controls RNA polymerase activity by termination of the transcription event.[16] Upon ligand binding, the four-way junction, particularly the stem P1, is stabilized by the Ni^{2+}/Co^{2+} coordination network to prevent the expression platform from forming a self-annealed terminator hairpin that in turn disrupts the RNA polymerase transcription complex. As a result, in the presence of excess Ni^{2+}/Co^{2+}, the polymerase complex proceeds to transcribe the mRNA which encodes for the metal transporter protein.

Riboswitches are highly dynamic in structure with the ability to switch between different conformations in response to ligand to achieve gene regulation.[1] Moreover, upon transcription, the nascent mRNA must fold in real time ($t \approx 1/k_{fold}$) and thereby participate in conformational search over the downstream DNA, a competitive kinetic process known as cotranscriptional folding.[20-21] During transcription, only a limited time window is therefore allowed for the

riboswitch to dynamically sample the on- vs. off-configurations and thereby achieve the desired ligand response.[22] Consequently, both ligand recognition and conformational folding rates are crucially important to achieving the requisite regulatory effect.[23-25] Over the past decade, single-molecule techniques have been applied to study biomolecular folding and unfolding kinetics. In particular, single-molecule Fluorescence Resonance Energy Transfer (smFRET) microscopy has been extensively utilized,[26-27] whereby the conformational change can be visualized in real time by monitoring energy transfer efficiency (E_{FRET}) between the fluorophore pair. Moreover, in contrast to bulk fluorescence measurements where the observed E_{FRET} is averaged over many trillions of replicates, smFRET at the single molecule level is in principle able to identify multiple conformations from distinct E_{FRET} values to elucidate a more comprehensive folding mechanism.[28-30] Furthermore, precise thermal control is incorporated into the smFRET measurements to facilitate study of the kinetics as a function of temperature. Monitoring the thermal dependence of the NiCo riboswitch kinetics allows us to deconstruct the folding free energies into enthalpic and entropic contributions,[31-32] from which we can generate detailed energy diagrams explicitly demonstrating changes in each of the thermodynamic variables along the folding coordinate.[33-34]

The organization of this paper is as follows. First, the experimental design including the sample preparation and smFRET experimental setup is presented in Section 5.3. Folding of the NiCo riboswitch is then systematically explored at the single molecule level as a function of (i) monovalent (Na^+), (ii) divalent (Mg^{2+}), (iii) target ligand (Ni^{2+} and Co^{2+}) cation concentrations, and (iv) sample temperature, with results presented in Section 5.4.1 to 5.4.5. Of particular interest, we find that the NiCo riboswitch exhibits three distinct E_{FRET} states, with a “prefolded”

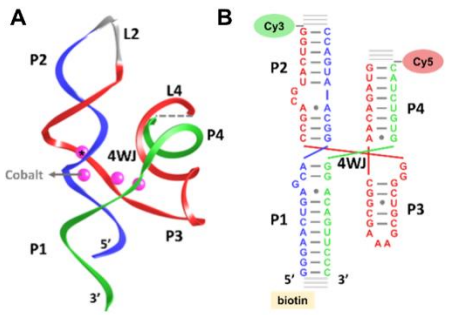

Figure 5.1 Structure of *E. bacterium* NiCo riboswitch. (A) Overall crystal structure (PDB: 4RUM). (B) Riboswitch sequence in secondary structure representation. The oligomers forming the ternary smFRET construct are indicated in red, green and blue, respectively.

intermediate structure identified to play a crucial role in ligand recognition and riboswitch folding. Such behavior is consistent with a conformational selection ("fold-then-bind") mechanism,[35-37] where the biomolecule spontaneously samples a prefolded structure prior to ligand association and stabilization. This novel combination of i) stepwise folding and ii) unique cation response of a riboswitch observed at the single molecule level is noteworthy and provides material for further discussion in Section 5.5.1 and 5.5.2, respectively. In addition, the thermodynamic variables obtained from our temperature dependent studies are utilized in Section 5.5.3 to reconstruct a detailed free energy diagram of the NiCo riboswitch folding pathway. Finally, Section 5.6 summarizes the work and points to directions for future exploration.

5.3 Experiment

5.3.1 NiCo riboswitch construct design and sample preparation

The aptamer domain of the NiCo riboswitch consists of four helices joined by a four-way junctional loop (see Figure 5.1).[16] In the cobalt-bound crystal structure (Figure 5.1A), the two

sets of coaxially-stacked helices adopt a twisted H conformation with three out of the four resolved Co^{2+} ions in direct contact with the junctional loop. The fourth Co^{2+} ion peripheral to the junction (indicated by * in Figure 5.1A) shows only relatively low anomalous density in the X-ray diffraction data and appears to make fewer contacts with any of the conserved nucleotides.[16] It is therefore presumed that this final Co^{2+} ion does not play a critical role in NiCo riboswitch folding and might be substitutable by other cations such as physiological Mg^{2+}.

Although not the first example of conformational change in a riboswitch induced by ligand-binding to a junctional loop,[38-40] the NiCo riboswitch is of particular interest in its own right due to two unique structural features:[16] First of all, the suite of 3-4 Co^{2+} ions occupying the junction loop region and located by anomalous X-ray dispersion data forms an strongly interacting network and suggests that the ligand binding kinetics might be highly cooperative. Secondly, the NiCo riboswitch lacks the long-range tertiary interaction motifs and close helical packing which are relatively common features found in other riboswitches. In combination, this provides a relatively novel opportunity for probing cooperative ligand induced conformational response in a riboswitch, but probed by the relative orientation between minimally interacting helices.

The NiCo riboswitch in this work is constructed from the *Erysipelotrichaceae bacterium* (*E. Bacterium*) sequence that has been well characterized in previous study.[16] To achieve surface immobilization and fluorophore labeling, the ternary smFRET construct is assembled by annealing three chemically modified RNA oligomers (Integrated DNA Technologies, Coralville, IA), followed by high-performance liquid chromatography (HPLC) purification, with detailed oligomer sequences and fluorophore-labeled positions illustrated in Figure 5.1B. (Note: companies are mentioned for explicit information and not by way of commercial product

support) In particular, the P1 stem has been extended by 8 base pairs and modified with a terminal biotin to tether the single molecule RNA construct onto the biotin-BSA surface through biotin-streptavidin interactions. The Cy3 and Cy5 FRET fluorophores are labeled at the distal ends of P2 and P4 (Figure 5.1B), respectively, corresponding to loops L2 and L4 in the native structure. According to previous structural characterization,[16] L2 and L4 do not respond to ligand binding and are not part of the conserved sequence essential for ligand sensing and riboswitch function. Thus, we reasonably do not expect our choice of dye labelling sites to interfere with the overall riboswitch conformation. Finally, the distance between Cy3 and Cy5 of the folded NiCo riboswitch is estimated to be $R \approx 45$ Å,[16] which is close to the characteristic Forster length for the Cy3 and Cy5 FRET pair ($R_0 \approx 50$ Å). Due to the extremely rapid ($1/R^6$) dependence of Forster energy transfer, we therefore expect high sensitivity in E_{FRET} values to any changes in the Cy3-Cy5 distance upon conformational unfolding.

To achieve prolonged observation of fluorescent signals from a single RNA molecule, the smFRET NiCo riboswitch constructs are immobilized on the surface of a glass coverslip through biotin-streptavidin interaction. The sample is prepared by successively flushing the sample holder with the following solutions to obtain a typical ≈ 50 RNA molecules per 100 μm^2 surface coverage:[37, 41] (i) 10 mg/mL bovine serum albumin (BSA) with 10% biotinylated BSA, (ii) 200 μg/mL streptavidin solution, (iii) ≈ 25 pM of the smFRET NiCo riboswitch construct, with a 10-minute incubation time between each step. Prior to each smFRET experiment, the sample is flushed with an imaging buffer containing (i) 50 mmol/L hemipotassium HEPES buffer (pH 7.5), (ii) Trolox/PCA/PCD enzymatic oxygen scavenger system to catalytically remove oxygen, (iii) 100 mmol/L NaCl and 0.5 mmol/L $MgCl_2$ to provide background salt (unless otherwise

specified), and (iv) sufficient $NiCl_2$ and $CoCl_2$ to achieve desired cation concentration conditions.

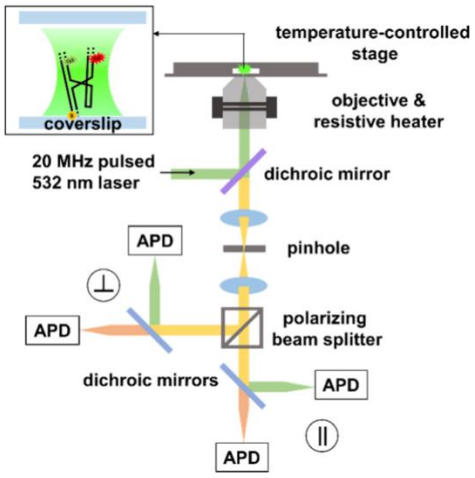

Figure 5.2 Schematic of the single-molecule confocal fluorescence microscope. Inset: Cartoon representation of a doubly fluorophore labeled smFRET construct tethered on the surface of a glass coverslip for the single-molecule fluorescence observation.

5.3.2 Single-molecule FRET spectroscopy and temperature control

The single-molecule FRET experiment in this work is based on a homebuilt confocal microscope system adapted for additional temperature control (Figure 5.2).[34, 41-42] In brief, a 532 nm collimated beam from a high repetition rate (50 MHz) pulsed Nd:YAG laser is directed onto the sample through an inverted confocal microscope. The beam is tightly focused by a 1.2 N.A. water immersion objective into a diffraction limited laser excitation/collection spot ($1/e^2$ radius ≈ 310(30) nm), allowing for diffraction limited observation of one fluorophore-labeled RNA at a time. The resulting fluorescence photons are collected through the same objective and then separated with dichroics by (i) color (green/red) and (ii) polarization (horizontal/vertical) before detection on single-photon avalanche photodiodes. For each photon detection event, four bits of information (color, polarization, "wall clock" time (sorted into 50 ns bins), and microtime with respect to the laser pulse (50 ps resolution)) are recorded with a fast router, time to amplitude

converter (TAC), and a time-correlated single-photon counting modules. In this work, we focus primarily on the photon color and arrival time information, with which we can calculate a time-dependent E_{FRET} trajectory.

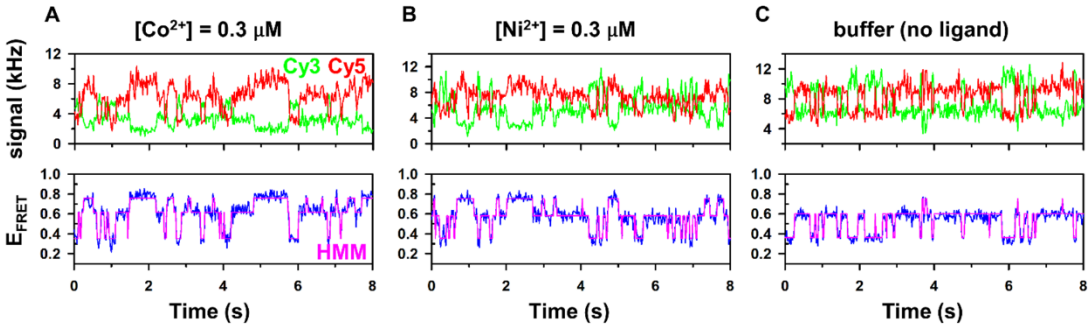

Figure 5.3 Sample fluorescence time traces of Cy3 and Cy5 signal (upper panel) and corresponding EFRET time trajectories (lower panel) obtained with (A) $[Co^{2+}]$ = 0.3 μmol/L, (B) $[Ni^{2+}]$ = 0.3 μmol/L and (C) neat buffer (background $[Mg^{2+}]$ = 0.5 mmol/L and $[Na^{+}]$ = 100 mmol/L).

For temperature-controlled experiments, the temperature is precisely servo loop stabilized by heating the sample and the microscope objective simultaneously.[31, 43] Specifically, the sample holder is mounted to a thermal stage (Instec, Boulder, CO) that regulates the sample temperature by responsive heating and cooling. In addition, a resistive collar (Bioptechs, Butler, PA) is used to simultaneously heat the objective to the desired temperature, minimizing thermal gradients throughout the sample and thereby increasing the servo loop bandwidth and temperature stability. Prior to each experiment, the system is allowed to equilibrate for > 15 minutes to achieve steady sample temperatures with ± 0.1 ℃ precision and accuracy.

5.3.3 Single-molecule E_{FRET} trajectory and data analysis

The donor/acceptor fluorescent signals are analyzed with in-house software to generate background and cross talk corrected E_{FRET} = I(red)/(I(green) + I(red)) trajectories with 20-ms bin

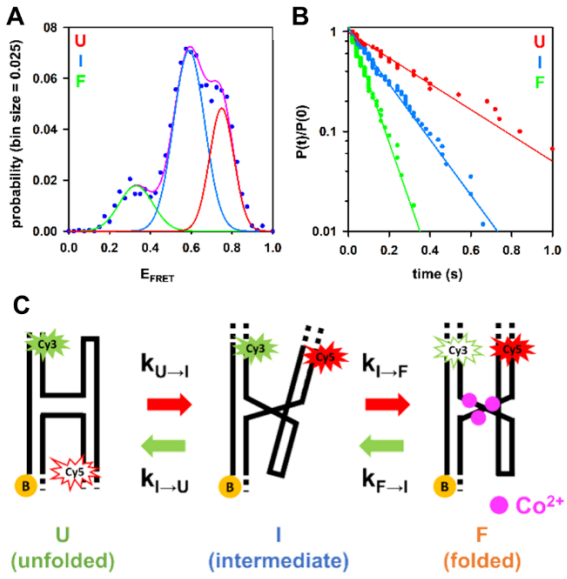

Figure 5.4 Sample data analysis of the 3-state folding system. (A) E_{FRET} histogram fit to 3 Gaussian functions corresponding to unfolded (U), intermediate (I) and folded (F) subpopulations of the NiCo riboswitch. (B) Exponential decays of the dwell time distributions presented in a semi-logarithm plot, indicating that folding and unfolding of the NiCo riboswitch follow first order kinetics. (C) Schematic representation of detailed NiCo riboswitch smFRET construct folding and unfolding. Note that the cartoon representation of the unfolded state (U) suggests a more relaxed/less structured state, which does not necessarily represent the average configuration.

time resolution (Figure 5.3).[31] From visual inspection of sample data in Figure 5.3, the resulting E_{FRET} trajectories indicate that the NiCo riboswitch exists in three states with distinct E_{FRET} values, which are also clearly evident in the corresponding E_{FRET} histograms (Figure 5.4A). Due to the fact that the three E_{FRET} distributions are partially overlapping, the traditional methods of dwell time analysis with thresholding prove challenging to implement due to shot noise fluctuations in the fluorescence signals.[31, 44] To facilitate the data analysis and improve the reliability of the extracted rate constant information, we have implemented Hidden Markov modeling (HMM) methods based on maximum likelihood estimation, which have been widely applied to study time-dependent single-molecule data.[45-48] Simply summarized, HMM presumes a given kinetic model and optimizes (by changing these model parameters) the likelihood of predicting E_{FRET} values/distributions that correctly match the actual E_{FRET} time trajectory data.[48]

Such an approach proves extremely useful in obtaining estimates of E_{FRET} values, number of states, and kinetic rate constants. As one of many powerful attributes, HMM analysis provides access to explicit time trajectory predictions with which to compare to experimental E_{FRET} data (e.g., the dark blue line in Figure 5.3).

As yet another advantage, HMM analysis allows one to include and rigorously examine the statistical possibility that the system is better described by more than three E_{FRET} distributions[48]. Interestingly, HMM analysis rejects this and consistently predicts three states in the E_{FRET} trajectories (Figure 5.3, lower panels), corresponding to $E_{FRET} \approx 0.35$, 0.60 and 0.75. The high E_{FRET} state ($E_{FRET} \approx 0.75$) agrees well with our prediction of the folded NiCo riboswitch from the crystal structure.[16] Furthermore, we find virtually all transitions (> 98 %) between the lowest ($E_{FRET} \approx 0.35$) and highest ($E_{FRET} \approx 0.75$) states exhibit a "pause" at the intermediate $E_{FRET} \approx 0.60$ value, strongly suggesting that the subpopulation with $E_{FRET} \approx 0.60$ corresponds to a folding intermediate (denoted herein as I) that represents a stable transition point between fully folded (F) and unfolded (U) conformations (more details in Section 5.4). We therefore assign the three E_{FRET} populations to be the folded (F, $E_{FRET} = 0.75$), intermediate (I, $E_{FRET} = 0.6$) and unfolded (U, $E_{FRET} = 0.35$) conformations of the NiCo riboswitch, described by a simple kinetic model with 4 corresponding unimolecular rate constants ($k_{U\rightarrow I}$, $k_{I\rightarrow U}$, $k_{I\rightarrow F}$, $k_{F\rightarrow I}$) illustrated schematically in Figure 5.4C. In Figure 5.4B, the conventional dwell time analysis of the predicted E_{FRET} trace supports that each folding process is effectively described by a first order rate constant, with the cumulative dwell time distributions well fit to exponential decay functions, and yielding HMM predictions of the rate constants summarized in Table 5.1. We can also extend these kinetic results in a few ways. For example, according to the kinetic model, the

	$k_{U\rightarrow I}$ (s^{-1})	$k_{I\rightarrow U}$ (s^{-1})	$k_{I\rightarrow F}$ (s^{-1})	$k_{I\rightarrow F}$ (s^{-1})
HMM analysis	13.0	4.90	1.55	2.89
Dwell time analysis	13.5(4)	4.82(9)	1.58(4)	3.05(11)

Table 5.1 Rate constants obtained from HMM and traditional dwell time analysis**.** Error bars in parentheses represent 1σ standard deviations of the mean.

decay rate constant of the dwell time distribution for state I should be the sum of $k_{I\rightarrow U}$ and $k_{I\rightarrow F}$ due to parallel I → U and I → F pathways. The individual values of $k_{I\rightarrow U}$ and $k_{I\rightarrow F}$ can thus be extracted by multiplying the total decay rate constant by the branching ratio for each transition. For instance, the decay rate constant for I is determined to be k = 6.40(12) s^{-1} (Figure 5.4B, blue line), with numbers of independently observed I → U and I → F transitions as $N_{I\rightarrow U}$ = 64 and $N_{I\rightarrow U}$ = 21, from which $k_{I\rightarrow U}$ and $k_{I\rightarrow F}$ can be readily calculated to be 4.82 s^{-1} and 1.58 s^{-1}, respectively. Finally, due to limited statistics on sampling of all three states with limited observation times due to photobleaching, the dwell time data for the HMM analyses are collectively analyzed for each experimental sample run consisting of N ≈ 30 single molecules separated into n = 3 separate samples. This parsing of the data allows us to obtain HMM rate constants independently for each of the three samples, yielding meaningful statistical averages and standard deviations of the mean.

5.4 Results and analysis

5.4.1 Co^{2+}-promoted NiCo riboswitch folding

From previous study of the NiCo riboswitch surveying a wide range of metal cations,[16] the Ni^{2+} and Co^{2+} were alone found to influence the structure of the four-way junction, which in turn correlates with the relative orientation between the 4 helices. As a result, we can hope to monitor

the effects of Ni^{2+} and Co^{2+} binding to the 4-way junction loop via time-dependent E_{FRET} trajectories (Figure 5.3). Since the Co^{2+} ion positions are most clearly resolved from X-ray crystal structures,[16] we first systematically explore the folding kinetics of the NiCo riboswitch as a function of $[Co^{2+}]$. Specifically, HMM methods are used to analyze E_{FRET} trajectories for a statistically significant sample (three independent sets of $N \approx 10$ molecules) of NiCo riboswitch constructs, to obtain the 4 kinetic rate constants ($k_{U\to I}$, $k_{I\to U}$, $k_{I\to F}$, $k_{F\to I}$) connecting the unfolded (U), intermediate (I), and folded (F) conformational manifolds. The results from such an analysis are summarized in a plot of rate constants (Figure 5.5A) as a function of Co^{2+}, with the equilibrium fraction of U, I, F states at each ion concentration depicted in Figure 5.5B. From the bottom panel, it is clear that the overall complex equilibrium shifts systematically from unfolded

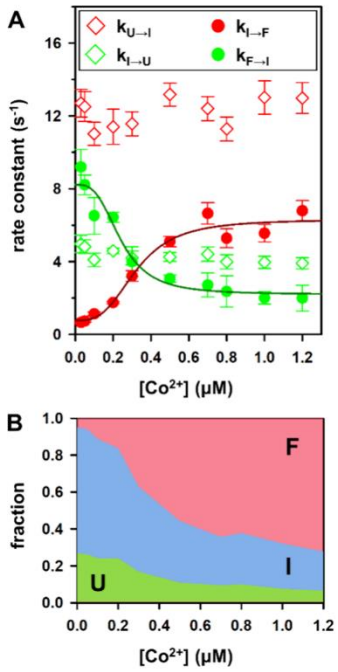

Figure 5.5 Co^{2+} dependence of NiCo riboswitch folding. (A) Rate constants $k_{U\to I}$ (red empty diamonds), $k_{I\to U}$ (green empty diamonds), $k_{I\to F}$ (red solid circles) and $k_{F\to I}$ (green solid circles) as a function of $[Co^{2+}]$. (B) Equilibrium fraction as a function of $[Co^{2+}]$ (green: U, blue: I, red: F). Solid lines represent fits to the Hill equation (Eq. 5.1). Error bars represent 1σ standard deviations of the mean.

	k_0 (s^{-1})	k_1 (s^{-1})	K_d (μM)	n
$k_{I\rightarrow F}$ (Co^{2+})	0.8(3)	6.3(5)	0.32(4)	3.1(11)
$k_{F\rightarrow I}$ (Co^{2+})	8.2(4)	2.2(3)	0.24(3)	3.1*
$k_{I\rightarrow F}$ (Ni^{2+})	0.9 (2)	2.6(2)	0.26(7)	1.8(10)
$k_{F\rightarrow I}$ (Ni^{2+})	7.7(8)	1.8(4)	0.17(6)	1.8*

Table 5.2 Fitting results from Hill analysis. (* indicates parameters fixed in the fit). Error bars in parentheses represent 1σ standard deviations of the mean.

(≈ (U + I)) to predominantly folded (≈ F) at increasing [Co^{2+}] with sub-micromolar affinities. However, parsed in terms of individual rate constant contributions, the kinetics become even more interesting, as displayed in Figure 5.5A. For example, the major contributor to such conformational transformation appears to be the forward/reverse rate processes between I and F (solid circles), with the successful folding of the NiCo riboswitch (U → F) promoted by a simultaneous [Co^{2+}]-dependent *increase in* $k_{I\rightarrow F}$ (I → F transition) and *decrease in* $k_{F\rightarrow I}$ (F → I transition), respectively. Of particular relevance, the rate of increase in $k_{I\rightarrow F}$ for low [Co^{2+}] is *supralinear*, which suggests that conformational change from I to F is driven by the *cooperative* presence of multiple Co^{2+}.[49] This can be further quantified by least squares fits of the rate constants to a Hill equation[37, 50-51]

$$k_{\mathrm{I}\rightarrow\mathrm{F}} = k_0 + (k_1 - k_0)\left(\frac{[\mathrm{M}^{2+}]^{\mathrm{n}}}{K_{\mathrm{d}}{}^{\mathrm{n}} + [\mathrm{M}^{2+}]^{\mathrm{n}}}\right), \qquad \text{Eq. 5.1}$$

where k_0 represents the value of $k_{I\rightarrow F}$ at [Co^{2+}] = 0, k_1 represents the saturated value of $k_{I\rightarrow F}$ at high [Co^{2+}], K_d is the apparent dissociation constant, and n is the Hill coefficient. The fits yield a Hill coefficient of n = 3.1(11) for Co^{2+}-promoted folding (Table 5.2), again indicating a strong positive cooperativity and in good agreement with previous in-line probing assays.[16] Conversely,

the unfolding rate constant $k_{F\rightarrow I}$ decreases as a function of increasing $[Co^{2+}]$. Since the range of $[Co^{2+}]$ explored (0-1.2 μM) is 2-3 orders of magnitude lower than the background $[Mg^{2+}]$ (≈ 0.5 mmol/L), this monotonic decrease in $k_{F\rightarrow I}$ cannot result from purely cationic stabilization of the aptamer domain by Co^{2+}. Indeed, $k_{F\rightarrow I}$ has already been shown (Section 5.4.3) to be insensitive to $[Na^{+}]$ and $[Mg^{2+}]$ in the absence of Ni^{2+} or Co^{2+}, which indicates that $k_{F\rightarrow I}$ primarily depends on ligand association. Thus, the strong dependence of $k_{F\rightarrow I}$ on $[Co^{2+}]$ suggests that the NiCo riboswitch unfolds at distinctive rates from each sub-population (F_i) with different numbers of Co^{2+} ions, and with the equilibrium between each state $F_{i=1,2,3}$ modulated by $[Co^{2+}]$,[37] thus naturally leading to a strongly $[Co^{2+}]$-dependent unfolding. In order to model the decrease in

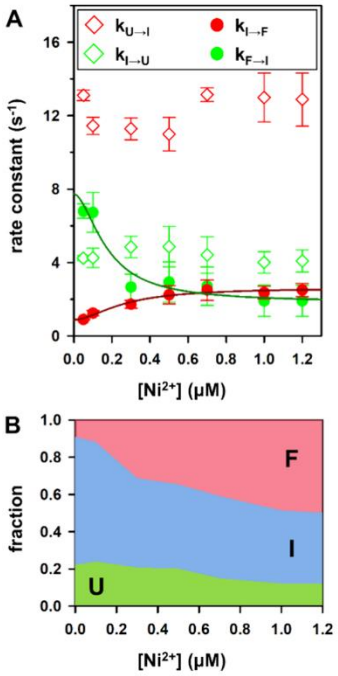

Figure 5.6 Ni^{2+} dependence of NiCo riboswitch folding. (A) Rate constants $k_{U\rightarrow I}$ (red empty diamonds), $k_{I\rightarrow U}$ (green empty diamonds), $k_{I\rightarrow F}$ (red solid circles) and $k_{F\rightarrow I}$ (green solid circles) as a function of $[Ni^{2+}]$; (B) equilibrium fraction as a function of $[Ni^{2+}]$ (green: U, blue: I, red: F). Solid lines represent fits to the Hill equation (Eq. 5.1). Error bars represent 1σ standard deviations of the mean.

$k_{F\rightarrow I}$ with Co^{2+}, the kinetic data in Figure 5.5A are similarly fit to the Hill equation (Eq. 5.1) with n fixed at 3.1 value from analysis of $k_{I\rightarrow F}$ (Table 5.2).

By way of contrast, the conformational kinetics sampling transitions between the unfolded (U) and intermediate (I) states is insensitive to [Co^{2+}] (Figure 5.5A, empty diamonds), with $k_{U\rightarrow I} \approx 13\ s^{-1}$ and $k_{I\rightarrow U} \approx 4\ s^{-1}$, respectively. This implies that the NiCo riboswitch is actively sampling the "prefolded" intermediate state with a similar rate constant under all buffer conditions here. As these "prefolding" rate constants are on the order of or larger than the subsequent (I → F) folding rate constants, the fractional split between [U] and [I] (see Figure 5.5B) remains relatively constant over the full dynamic range of [Co^{2+}] explored. However, since I folds efficiently upon Co^{2+} binding, the overall concentration [U + I] is significantly depleted with increasing [Co^{2+}] as the overall equilibrium is driven towards [F] (Figure 5.5B).

5.4.2 Ni^{2+}-promoted NiCo riboswitch folding

The NiCo riboswitch has been shown to respond to Ni^{2+} as well as Co^{2+} in previous structural studies and *in vitro* transcription assays.[16] Although the x-ray crystal structure of the Ni^{2+}-bound NiCo riboswitch is currently unavailable, previous in-line probing studies have revealed similar cleavage patterns in response to Ni^{2+} and Co^{2+} ions, suggesting that both ligands induce a similar conformational change. Experimentally (see Figure 5.3 and 5.6), the present studies show remarkably similar single molecule folding kinetics as a function of either [Ni^{2+}] or [Co^{2+}]. For example, time dependent E_{FRET} trajectories for the NiCo riboswitch construct in the presence of Ni^{2+} (Figure 5.3) also exhibit three distinct states (U, I, and F), indeed with the same E_{FRET} values (0.35, 0.6, 0.75) seen in the presence of Co^{2+}. Also consistent with the [Co^{2+}] dependence, the rate constants for folding ($k_{U\rightarrow I}$) and unfolding ($k_{I\rightarrow U}$) from U to the "prefolded" intermediate I remain relatively constant over the range of [Ni^{2+}] studied (Figure 5.6A, empty

diamonds), with the equilibrium driven toward the F conformation by a simultaneous increase and decrease in $k_{I\rightarrow F}$ and $k_{F\rightarrow I}$, respectively (Figure 5.6A, solid circles). The only quantitative differences in the rate analyses can be seen in the Ni^{2+} vs. Co^{2+} dependence of $k_{I\rightarrow F}$. Specifically, $k_{I\rightarrow F}$ increases less superlinearly with $[Ni^{2+}]$ than $[Co^{2+}]$, which is consistent with a lower (albeit finite) Hill cooperativity and a significantly lower saturation rate constant in $k_{I\rightarrow F}$. Indeed, least squares Hill fits of k_0, k_1, K_d, and n to Eq. 5.1 yield $k_0 = 0.9(2)\ s^{-1}$, $k_1 = 2.6(2)\ s^{-1}$, $K_d = 0.26(7)$ μM and n = 1.8(10), respectively (Table 5.2). Note that Ni^{2+}-promoted folding of the NiCo riboswitch construct still exhibits positive cooperativity (n > 1), though with lower levels than Co^{2+}.[16]

5.4.3 Physiological cation (Na^+/Mg^{2+}) effects on the NiCo riboswitch structure

Counterions (cations) are essential for RNA folding due to charge neutralization and electrostatic screening.[52-53] Cations in the cellular environment are quite abundant, with monovalent (Na^+ and K^+) and divalent (Mg^{2+}) cation concentrations at the ~100 mmol/L and few-mmol/L levels, respectively. It is thus useful to probe NiCo riboswitch conformational kinetics and dynamics under physiological cation conditions in the complete absence of Ni^{2+} or Co^{2+} cognate ligand. We first explore the NiCo riboswitch as a function of $[Na^+]$ without divalent cations, i.e. $[Mg^{2+}] = 0$ (Figure 5.7A). It is important to note that we still see clear evidence in the E_{FRET} trajectories for the three conformational states (U, I and F) even in the absence of ligands (see Figure 5.3C), which indicates the robustness of the prefolded intermediate and motivates a similar HMM analysis of the rate constants (see Figure 5.7A and 5.7B). Interestingly, three of the four rate constants show little dependence on monovalent $[Na^+]$, with the only significant response that the rate constant for unfolding of the intermediate ($k_{I\rightarrow U}$)

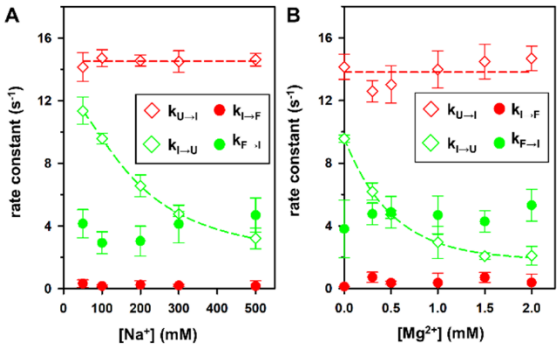

Figure 5.7 General monovalent/divalent background cation dependence of NiCo riboswitch folding. Rate constants $k_{U\rightarrow I}$ (red empty diamonds), $k_{I\rightarrow U}$ (green empty diamonds), $k_{I\rightarrow F}$ (red solid circles) and $k_{F\rightarrow I}$ (green solid circles) are studied as a function of (A) $[Na^+]$ and (B) $[Mg^{2+}]$ concentration. Dashed lines are added to highlight the change in k (or lack thereof) as a function of cation concentration. Error bars represent 1σ standard deviation of the mean.

is reduced by Na^+ (Figure 5.7A). Stated alternatively, increase in $[Na^+]$ primarily enhances the fractional concentration of the prefolded intermediate [I]/[U] by *decelerating* the rate of I → U *unfolding*. This is in dramatic contrast to the behavior noted previously for the cognate ligand cations, which impact only the rate constants for final folding from I to F ($k_{I\rightarrow F}$) or vice versa ($k_{F\rightarrow I}$) with negligible impact on the corresponding U to I initial folding/unfolding steps ($k_{I\rightarrow U}$ and $k_{U\rightarrow I}$). Also surprisingly, the high E_{FRET} folded state (F) is observable over the entire range of $[Na^+]$ explored, though formed with a much lower rate constant (i.e., $k_{I\rightarrow F} \approx 0.2\ s^{-1}$) and equilibrium probability ($K_{I\leftrightarrow F} \approx 0.05$), with both $k_{I\rightarrow F}$ and $k_{F\rightarrow I}$ exhibiting no systematic dependence on $[Na^+]$. These results indicate that the NiCo riboswitch can dynamically sample the fully folded conformation even without cognate ligand binding to stabilize the final biochemically competent state.

Similar effects are also observed in studies of the Mg^{2+}-dependent folding/unfolding kinetics at a constant monovalent background $[Na^+]$ = 100 mmol/L (Figure 5.7B), except that

reduction in the unfolding rate constant ($k_{I\rightarrow U}$) is now > 100-fold more sensitive to Mg^{2+} and responds at the sub-millimolar level. Therefore, both Na^{+} and Mg^{2+} background levels efficiently promote the intermediate population (I) by decelerating the unfolding rate constant $k_{I\rightarrow U}$ without significant impact on unimolecular folding to the final folded state $k_{I\rightarrow F}$. Differential response to the two cationic species and cognate ligands in terms of folding of the NiCo riboswitch may therefore be sorted into two separate contributions (see Figure 5.4): (i) prefolding from U to I promoted by universal (i.e., non-selective) counterion stabilization effects (both Na^{+} and Mg^{2+}) and (ii) folding from I to F promoted by selective cognate ligand binding. Although Na^{+} and Mg^{2+} do not by themselves promote the fully folded state (F), they do nevertheless facilitate formation of the NiCo riboswitch by encouraging a "fold-like" conformation (I) and effectively suppressing the unfolded state (U). As a result, the overall fraction of the fully folded state can still be enhanced by background [Na^{+}] and [Mg^{2+}]. We note that such cation effects to promote a

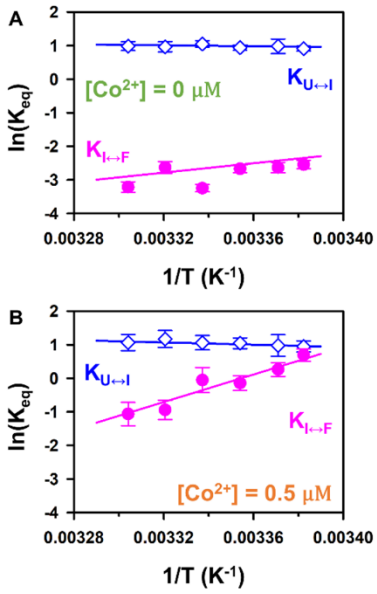

Figure 5.8 Temperature dependence of equilibrium constants presented in van't Hoff plots at (A) [Co^{2+}] = 0 µmol/LM and (B) [Co^{2+}] = 0.5 µmol/L (blue empty diamonds: $K_{U\leftrightarrow I}$, pink solid circles: $K_{I\leftrightarrow F}$). Data fits with linear regression yield detailed thermodynamic information (i.e. ΔH^0 and ΔS^0) by Eq. 5.2. Error bars represent 1σ standard deviations of the mean.

fold-like state in preparation for folding have been observed in multiple riboswitch systems with Mg^{2+}.[29, 36-37] It is also not surprising that cations like Na^{+} yield stabilization effects at higher concentration, as monovalent-ion-promoted folding has been demonstrated with fundamental RNA tertiary folding motifs such as the kink turn,[54] four-way junction[55] and tetraloop-receptor[44, 56] commonly found in fully functional RNA.

5.4.4 Temperature dependent folding equilibrium: Van't Hoff analysis

Temperature has significant impact on biomolecular structure, as the folding/unfolding kinetics depend exponentially on enthalpic and/or entropic contributions to the overall free energy differences. Indeed, the temperature dependence of biomolecular folding contains crucial thermodynamic information that helps provide a clearer physical picture of the folding dynamics.[33] Toward that end, NiCo riboswitch folding kinetics at the single molecule level has been studied as a function of temperature (T ≈ 20–30 °C), with and without the primary cognate ligand ($[Co^{2+}]$ = 0.0 and 0.5 μM), and analyzed by HMM methods described in Section 5.3.3. As a first stage of analysis, we focus on the two temperature dependent equilibrium constants, $K_{U\leftrightarrow I}(T) = k_{U\rightarrow I}/k_{I\rightarrow U} = [I]_{eq}/[U]_{eq}$ and $K_{I\leftrightarrow F}(T) = k_{I\rightarrow F}/k_{F\rightarrow I} = [F]_{eq}/[I]_{eq}$, which are extracted from the HMM modeling and displayed in a conventional van't Hoff plot in Figure 5.8. This allows us to deconstruct the two folding free energy differences (U → I and I → F) into changes in enthalpy (ΔH^0) and entropy (ΔS^0) via a linear fit to the standard van't Hoff expression

$$\ln\left(K_{eq}\right) = -\frac{\Delta H^0}{R}\frac{1}{T} + \frac{\Delta S^0}{R}. \qquad \text{Eq. 5.2}$$

In the absence of Co^{2+} (Figure 5.8A), $K_{U\leftrightarrow I}$ shows only a weak dependence on the temperature (i.e., slope m ≈ 0 within experimental uncertainty), indicating therefore a negligible enthalpic contribution ($\Delta H^0_{U\rightarrow I}$ = 1.4(13) kcal/mol ≈ 0). Conversely, we can extrapolate Eq. 5.2 in the high temperature limit to yield a positive intercept that reveals U → I folding to be dominated by only

modest entropic gain ($\Delta S^0_{U\rightarrow I}$ = 7(4) cal/mol/K). The second stage (I ↔ F) folding equilibrium constant ($K_{I\leftrightarrow F}$) exhibits a more pronounced dependence on temperature, now with an overall positive slope consistent with a mildly exothermic process ($\Delta H^0_{I\rightarrow F}$ = -14(8) kcal/mol) and a negative intercept indicating an overall entropic penalty to folding ($\Delta S^0_{I\rightarrow F}$ = -52(26) cal/mol/K). Thermodynamic data obtained from these van't Hoff analyses are summarized in Table 5.3.

	$\Delta G^0_{U\rightarrow I}$ (kcal/mol)	$\Delta G^0_{I\rightarrow F}$ (kcal/mol)	$\Delta H^0_{U\rightarrow I}$ (kcal/mol)	$\Delta H^0_{I\rightarrow F}$ (kcal/mol)	$\Delta S^0_{U\rightarrow I}$ (cal/mol/K)	$\Delta S^0_{I\rightarrow F}$ (cal/mol/K)
$[Co^{2+}]$ = 0 mM	-0.54(4)	1.49(7)	1.4(13)	-14(8)	7(4)	-52(26)
$[Co^{2+}]$ = 0.5 mM	-0.56(9)	-0.41(10)	4.1(15)	-44(6)	16(4)	-146(21)

Table 5.3 Thermodynamic values obtained from a van't Hoff analysis of the equilibrium constant data, where ΔG^0 is calculated from K_{eq} at T = 22.5 °C. Error bars in parentheses represent 1σ standard deviations of the mean.

In the presence of 0.5 μM Co^{2+} (Figure 5.8B), the temperature dependence of the first stage ($K_{U\leftrightarrow I}$) is virtually identical to that at 0.0 μM. This is of course consistent with our previous room temperature observations, whereby "prefolding" from U → I showed no sensitivity to the presence or absence of the cognate ligand. However, a much more dramatic effect of Co^{2+} on NiCo riboswitch folding is indicated by the rapid decrease of the second stage ($K_{I\leftrightarrow F}$) with increasing temperature, which now yields a strongly positive slope (m > 0) and a more negative intercept in the van't Hoff plot, corresponding to a substantial increase in both exothermicity ($\Delta H^0_{I\rightarrow F}$ = –44(6) vs -14(8) kcal/mol) and entropic loss ($\Delta S^0_{I\rightarrow F}$ = -146(21) vs -52(26) cal/mol/K) at 0.5 vs 0.0 μM. As a plausible physical picture, this would be consistent with the cognate ligand preferentially captured by a prefolded (I) vs unfolded (U) riboswitch via

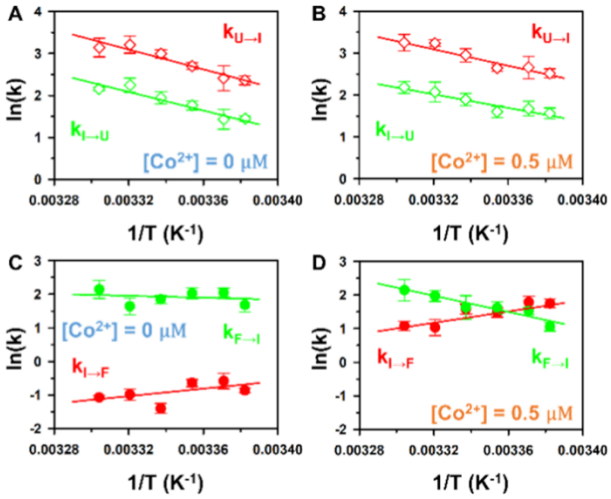

Figure 5.9 Temperature dependence of rate constants presented in Eyring plots: $k_{U\rightarrow I}$ (red empty diamonds) and $k_{I\rightarrow U}$ (green empty diamonds) at (A) [Co^{2+}] = 0 μmol/L and (B) [Co^{2+}] = 0.5 μmol/L; $k_{I\rightarrow F}$ (red solid circles) and $k_{F\rightarrow I}$ (green solid circles) at (C) [Co^{2+}] = 0 μmol/L and (D) [Co^{2+}] = 0.5 μmol/L. Data fits with linear regression yield detailed thermodynamic information (i.e. $\Delta H^{\ddagger}$ and $\Delta S^{\ddagger}$) by Eq. 5.3. Error bars represent 1σ standard deviation of the mean.

exothermic coordination of the Co^{2+}, resulting in a more highly ordered ligand-bound configuration and thus a significant loss in translational entropy.[57-58]

5.4.5 Temperature dependent folding kinetics: transition state theory (TST) analysis

Further information can be obtained from the corresponding temperature dependence of the forward/reverse kinetics, which can be deconstructed with Eyring/transition state theory (TST) analysis to yield isolated enthalpic and entropic contributions to the transition state barrier. Specifically, the thermodynamics of the transition state can be obtained from a standard Eyring plot of ln(k) vs 1/T:[31, 34, 41]

$$\ln(k) = -\frac{\Delta H^{\ddagger}}{R}\frac{1}{T} + \frac{\Delta S^{\ddagger}}{R} + \ln \nu \,. \qquad \text{Eq. 5.3}$$

In Eq. 5.3, $\Delta H^{\ddagger}$ and $\Delta S^{\ddagger}$ represent enthalpy and entropy differences between the transition state and the initial (or final) state, while ν represents an "attempt frequency" sampling the free energy

barrier along the folding coordinate[59-60] and often treated as a low frequency skeletal vibration with $\nu \approx 10^{13}$ s^{-1}.[61-62] It is worth noting that $\Delta S^{\ddagger}$ depends only quite weakly (i.e., logarithmically) on the choice of ν and, furthermore, any differential (e.g., Co^{2+} induced) changes in the transition state entropy ($\Delta\Delta S^{\ddagger}$) are rigorously independent of ν.

Eyring plots of Eq. 5.3 for the two conformational transformations U ↔ I and I ↔ F (forward and reverse) are presented in Figure 5.9 and reveal several interesting features. First of all, by visual comparison of Figure 5.9A and 5.9B, the plots for the U ↔ I kinetics indicate Co^{2+} to have only quite modest effects on the forward (folding) and reverse (unfolding) rate constants $k_{U\rightarrow I}$ and $k_{I\rightarrow U}$. This insensitivity to Co^{2+} in both the forward/reverse rate and equilibrium constants for this prefolding step implies negligible changes in the first transition state barrier ($TS_{U\leftrightarrow I}$) with cognate ligand. Indeed, the negative slopes observed for both $k_{U\rightarrow I}$ and $k_{I\rightarrow U}$ indicate a strong but equally endothermic process ($\Delta H^{\ddagger}_{U\rightarrow I}$ = 23(3) kcal/mol, $\Delta H^{\ddagger}_{I\rightarrow U}$ = 22(3) kcal/mol) to cross the transition barrier from either direction.

By way of contrast, the cognate ligand effects on the second stage I ↔ F conformational kinetics are clearly much more significant. In the absence of Co^{2+} (Figure 5.9C), both the forward ($k_{I\rightarrow F}$) and reverse ($k_{F\rightarrow I}$) folding rate constants depend only weakly on temperature, with slopes corresponding to $\Delta H^{\ddagger}_{I\rightarrow F}$ = -11(8) kcal/mol and $\Delta H^{\ddagger}_{F\rightarrow I}$ = 3(6) kcal/mol, respectively. Moreover, by Eq. 5.3, the entropic penalties of accessing the transition state are determined as $\Delta S^{\ddagger}_{I\rightarrow F}$ = -98(27) cal/mol/K and $\Delta S^{\ddagger}_{F\rightarrow I}$ = -46(22) cal/mol/K). However, in the presence of 0.5 μM Co^{2+}, the rate constant changes dramatically (cf. Figure 5.9C vs Figure 5.9D). The first effect is an increased slope in the rate constant for folding ($k_{I\rightarrow F}$) with decreasing experimental temperature, consistent with a more exothermic folding in the presence of the cognate ligand Co^{2+} ($\Delta H^{\ddagger}_{I\rightarrow F}$ = -20(4) vs -11(8) kcal/mol). This increased slope results in a more

negative y-intercept, therefore predicting an even *greater entropic penalty* for Co^{2+}-induced folding ($\Delta S^{\ddagger}_{I\rightarrow F}$ = -123(14) vs -98(27) cal/mol/K). Simply summarized, the forward folding step (I → F) experiences a more significant entropic penalty ($-T\Delta\Delta S^{\ddagger}_{I\rightarrow F} > 0$) which is counterbalanced by increased enthalpic stabilization ($\Delta\Delta H^{\ddagger}_{I\rightarrow F} < 0$) in the presence of 0.5 μM Co^{2+}. The reverse folding step (F → I), on the other hand (see Figure 5.9D), now becomes noticeably more temperature sensitive. From fits to Eq. 5.3, the riboswitch needs to cross a more significant enthalpic barrier to fold ($\Delta H^{\ddagger}_{F\rightarrow I}$ = 24(4) vs 3(6) kcal/mol), with the effects strongly mitigated by entropic gain ($\Delta S^{\ddagger}_{F\rightarrow I}$ = 24(13) vs -46(22) cal/mol/K) in the presence and absence of the cognate ligand (see Table 5.4).

	$\Delta H^{\ddagger}_{U\rightarrow I}$ (kcal/mol)	$\Delta H^{\ddagger}_{I\rightarrow U}$ (kcal/mol)	$\Delta H^{\ddagger}_{I\rightarrow F}$ (kcal/mol)	$\Delta H^{\ddagger}_{F\rightarrow I}$ (kcal/mol)	$\Delta S^{\ddagger}_{U\rightarrow I}$ (cal/mol/K)	$\Delta S^{\ddagger}_{I\rightarrow U}$ (cal/mol/K)	$\Delta S^{\ddagger}_{I\rightarrow F}$ (cal/mol/K)	$\Delta S^{\ddagger}_{F\rightarrow I}$ (cal/mol/K)
$[Co^{2+}]$ = 0 mM	23(3)	22(3)	-11(8)	3(6)	24(11)	18(11)	-98(27)	-46(22)
$[Co^{2+}]$ = 0.5 mM	20(2)	16(2)	-20(4)	24(4)	14(9)	-1(8)	-123(14)	24(13)

Table 5.4 Thermodynamic values obtained from an Eyring/TST analysis. Error bars in parentheses represent 1σ standard deviations of the mean.

5.5 Discussion

5.5.1 Cations facilitate formation of a prefolded NiCo riboswitch intermediate

The combination of FRET, time correlated single photon counting methods, and high NA confocal microscopy have permitted monitoring of conformational kinetics of the NiCo riboswitch construct at the single molecule level. The results indicate that folding proceeds via a two-step process between three conformations with three distinct E_{FRET} values (Figure 5.3), specifically identified as unfolded (U) and folded (F) states, with a stable "prefolded"

intermediate conformation (I) directly along the U → F folding pathway (Figure 5.4). The cognate ligands (Co^{2+} and Ni^{2+}) are found to efficiently promote the formation of F from the prefolded intermediate I with sub-micromolar affinities by simultaneously increasing and decreasing $k_{I\rightarrow F}$ and $k_{F\rightarrow I}$, respectively. In sharp contrast, however, kinetic rates and overall equilibrium constants between the unfolded (U) and prefolded intermediate (I) conformations show zero dependence on cognate ligand concentrations up to micromolar levels. Finally, we find the first stage of folding/unfolding (U ↔ I) to be strongly stimulated by near physiological levels of monovalent (Na^{+}) and divalent (Mg^{2+}) cations (Figure 5.7). This collective behavior suggests that the NiCo riboswitch intermediate (I) is a prefolded structure stabilized by cations through charge neutralization and screening of the phosphate groups,[52-53] with an intermediate E_{FRET} value indicating that the helices are partially aligned toward the folded conformation due to preorganization of the junctional loop aptamer domain. Indeed, this would be consistent with previous studies, whereby a more fold-like conformation of riboswitches can be promoted by physiological levels of Mg^{2+} to increase the aptamer ligand affinity in a "fold-then-bind" mechansim.[29, 36-37] Moreover, the present work has shown that monovalent cations (Na^{+}) exhibit similar stabilization effects for the intermediate state, requiring higher but still physiologically relevant concentrations. Such "fold-then-bind" behavior represents a classic example of conformational selection, whereby a biomolecule spontaneously samples many thermodynamically accessible configurations, but preferentially locking into an optimal "target" structure due to enhanced binding for the cognate ligand.[35] In this study, the prefolded NiCo riboswitch intermediate (I) is sufficiently long lived to be identified by its distinct E_{FRET} value. As a novel result of the intermediate (I) being along the folding pathway and distinguishable from the unfolded (U) and folded states (F), we are able to follow the folding/binding process in

single molecule detail and thereby provide direct evidence for a “fold-then-bind” mechanism without any underlying kinetic model assumptions.[36-37]

5.5.2 Folding is induced by ligand binding to the conformational intermediate

Ni^{2+} and Co^{2+} cognate ligands of the NiCo riboswitch have been shown to effectively promote conformational transformation from a prefolded intermediate I to the fully folded state F with sub-micromolar affinities. Furthermore, it achieves this while maintaining a fixed [U]/[I] ratio through cationic stabilization effects dominated by physiological monovalent (Na^{+}) and divalent (Mg^{2+}) salt conditions. As a function of increasing [Co^{2+}] (Figure 5.5), the NiCo riboswitch is stabilized in the folded state (F) both by increasing the folding ($k_{I\rightarrow F}$) and decreasing the unfolding ($k_{F\rightarrow I}$) rate constant. The supralinear increase of $k_{I\rightarrow F}$ at low [Co^{2+}] indicates the Co^{2+}-induced folding to be highly cooperative, consistent with previous in-line probing results.[16] The cooperativity for $k_{I\rightarrow F}$ is determined from a Hill analysis to be n = 3.1(11) (Table 5.2), in good agreement with the three bound Co^{2+} ions resolved in the crystal data.[16] One should stress that Hill coefficients can differ from the number of bound ligands and are not always equivalent to the exact ligand stoichiometry.[63-64] Instead, the data indicate a consistency with complete folding (i.e. change in E_{FRET}) of the NiCo riboswitch upon association of the three Co^{2+} ions.

This cooperativity makes the NiCo riboswitch particularly sensitive to cognate ligand at concentrations in the transition region near [Co^{2+}] ≈ K_d = 0.32(4) μM and thus yielding a much sharper threshold response.[65-66] Cooperative Co^{2+} response of the NiCo riboswitch may therefore be advantageous by allowing cellular [Co^{2+}] to be maintained near K_d, but where high cytotoxicity requires any additional Co^{2+} to be immediately removed.[6-7] Note that while the present K_d values are in quantitative agreement with the recent studies of NiCo riboswitch-based

fluorescent sensors titrated in citrate buffer,[67] they are roughly an order of magnitude lower (i.e., *more* sensitive) than previous in-line probing results.[16] We do not know the reason for these differences, but can speculate that the presence of high [Mg^{2+}] in the in-line probing studies may interfere with ligand recognition/binding. Indeed, since Mg^{2+} is the dominant divalent cation in cells and is known to strongly interact with RNA, either synergy or competition between Mg^{2+} and the cognate ligands would be a natural possibility. This would suggest the value of future studies into Mg^{2+} cooperativity/anticooperativity effects on riboswitch response and metal ion toxicity.

The second cognate ligand Ni^{2+} promotes the NiCo riboswitch folding in a way qualitatively similar to Co^{2+}, with $k_{I\rightarrow F}$ and $k_{F\rightarrow I}$ systematically increasing and decreasing, respectively as a function of [Ni^{2+}] (Figure 5.6). There are, however, important differences between the two ligands. Specifically, the increase in $k_{I\rightarrow F}$ at low [Ni^{2+}] indicates a lower cooperativity (n = 1.8(10)) for Ni^{2+}-promoted folding, yet which is compensated by an even tighter ligand affinity (K_d = 0.26(7) μM) (Table 5.2).[67] The results suggest that the NiCo riboswitch has evolved to trigger at lower levels of cognate ligand but more gradually toward removal of excess Ni^{2+}. A second difference in the NiCo riboswitch behavior can be seen in the saturation value of $k_{I\rightarrow F}$, which is nearly 3 times lower for Ni^{2+} than Co^{2+} and therefore predicts only ≈ 50 % of the folded population under saturating [Ni^{2+}] conditions. Such incomplete folding behavior, however, may not be characteristic of NiCo riboswitch *in vivo*, where more complete folding may be aided by molecular crowding and excluded volume interactions in the intracellular environment.[68-69]

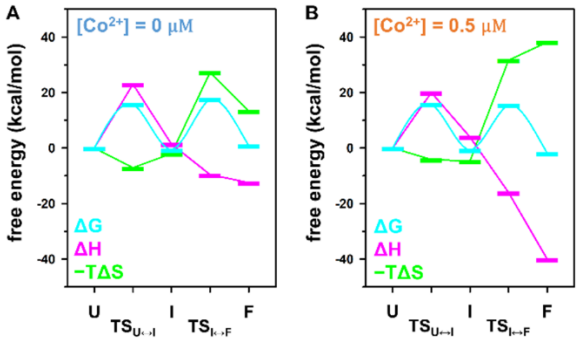

Figure 5.10 Detailed energy diagram of NiCo riboswitch folding at (A) [Co^{2+}] = 0 µmol/L and (B) [Co^{2+}] = 0.5 µmol/L, with the unfolded state (U) as reference zero (blue: ΔG, red: ΔH, green: −T(ΔS) at T = 22.5 °C).

5.5.3 Detailed thermodynamics for folding of the NiCo riboswitch

NiCo riboswitch folding at the single molecule level has been examined with temperature controlled measurements to obtain detailed information on relative free energies (ΔG^0) for each of the three conformational states (U, I and F) and two transition state barriers ($TS_{U\leftrightarrow I}$, $TS_{I\leftrightarrow F}$) as well as thermodynamic deconstruction of these free energies into enthalpic (ΔH) and entropic (−TΔS) contributions. These unusually rich free energy landscapes are presented in Figure 5.10, where the single arbitrary reference energy is chosen to be zero for the unfolded state (U). First, we focus on the limit of ligand-free folding, i.e. [Co^{2+}] = 0 (Figure 5.10A). In the prefolding transition (U → I), the system encounters an enthalpic barrier ($\Delta H^{\ddagger}_{U\rightarrow I}$ = 23(3) kcal/mol) that is only partially mitigated by small entropic gain corresponding to a free energy contribution $-T(\Delta S^{\ddagger}_{U\rightarrow I})$ ≈ -7(3) kcal/mol at T = 22.5 °C. Furthermore, after crossing the transition state ($TS_{U\leftrightarrow I}$), the riboswitch reaches the intermediate prefolded state (I) with a free energy surprisingly close to the unfolded conformation (U), despite a large 15 kcal/mol transition state barrier. The net near zero change in both $\Delta H^0_{U\rightarrow I}$ (1.4(13) kcal/mol) and $-T\Delta S^0_{U\rightarrow I}$ (-2.0(12)

kcal/mol) would be consistent with the absence of significant cation association in the U → I step, which in contrast would be highly enthalpically favored and accompanied by large entropic loss due to reduced cation mobility. This suggests that the major structural transition from U → I instead involves modest rearrangement of the solvent (water) configuration and hydrogen bonding around the RNA junction that successively re-orientates the four helices and results in the observed E_{FRET} change. A predominantly enthalpic barrier would thus be consistent with the simple physical picture that, during rearrangement, only some of the hydrogen bond structure is restored at the transition state ($TS_{U\leftrightarrow I}$). Furthermore, after crossing the transition barrier, hydrogen bond reformation enthalpically stabilizes the system and effectively brings down the free energy level of the intermediate state I, as illustrated in Figure 5.10A.

The second stage of folding (I → F) is more complex. In the absence of cognate ligand (Figure 5.10A), the free energy transition state barrier ($TS_{I\rightarrow F}$) is dominated by entropic loss of the system ($-T(\Delta S^{\ddagger}_{I\rightarrow F})$ = 29(8) kcal/mol) partially mitigated by a relatively small exothermicity ($\Delta H^{\ddagger}_{I\rightarrow F}$ = -11(8) kcal/mol). Moreover, the final folded state F is stabilized by a further decrease in enthalpy ($\Delta H^{0}_{I\rightarrow F}$ = -14(8) kcal/mol), while destabilized by entropy loss ($-T(\Delta S^{0}_{I\rightarrow F})$ = 15(7) kcal/mol), with respect to the intermediate conformation (I). Such changes in the thermodynamics would be consistent with Coulomb repulsion of the phosphate groups partially neutralized by associated monovalent/divalent cations. We note that in the kinetic analysis, folding and unfolding between I and F conformations have been shown insensitive to Na+/Mg2+ concentrations. While the cation association and neutralization are clearly indicated in the thermodynamic analysis, we therefore suspect the cation effects may saturate at relatively low concentrations. Alternatively stated, stabilizing cations are readily attracted to the 4-way junction

at relatively low concentrations. Therefore, cation stabilization effects and cation-insensitive folding are independently observed in thermodynamic and kinetic analysis, respectively.

In the presence of cognate ligand [Co^{2+}] = 0.5 μM (Figure 5.10B), the free energy changes in the initial folding process (U → I) are quite similar to those at [Co^{2+}] = 0 μM (see also Table 5.3 and Table 5.4). This is again consistent with our previous observation (Figure 5.5A) of an insensitivity in U → I folding pathway to Co^{2+}. The more dramatic Co^{2+} effects are seen in the (I ↔ F) transition between the prefolded and fully folded state. At the second transition state ($TS_{I\leftrightarrow F}$), the presence of Co^{2+} results in an increased entropic barrier ($-T(\Delta S^{\ddagger}_{I\rightarrow F})$ = 36(4) kcal/mol vs 29(8) kcal/mol at [Co^{2+}] = 0), accompanied by a 2x greater enthalpic stabilization ($\Delta H^{\ddagger}_{I\rightarrow F}$ = -20(4) kcal/mol vs -11(8) kcal/mol). Furthermore, the Co^{2+} effects are even stronger for the overall I → F changes in free energy due to enthalpy ($\Delta H^{0}_{I\rightarrow F}$ = -44(6) vs -14(8) kcal/mol) and entropic ($-T(\Delta S^{0}_{I\rightarrow F})$ = 43(6) vs 15(7) kcal/mol) for 0.5 μm and 0.0 μm, respectively. Both this increased entropic penalty and enthalpic stabilization along the folding coordinate are consistent with strong binding of the cognate ligand to the binding site to form a more ordered structure with loss in mobility.[58] In contrast with the monovalent/divalent cation effects at [Co^{2+}] = 0, the greater enthalpic stabilization of Co^{2+} due to the metal coordination overcomes the entropic loss, resulting an overall free energy change in slight favor of the folded (F) conformation ($\Delta G^{0}_{I\rightarrow F}$ = -0.41 vs +1.49(7) kcal/mol at [Co^{2+}] = 0). In fact, such thermodynamic shifts induced by ligand association are routinely observed in both ligand-binding protein[70] and nucleic acid[34, 71] systems. Our results thus provide additional thermodynamic support for cognate ligand Co^{2+} binding to the prefolded conformation (I) directly promoting and stabilizing the folded structure (F) in a “bind-then-fold” conformational selection mechanism.

As a parting comment, it is noteworthy that the enthalpic (ΔH^0) and entropic ($-T(\Delta S^0)$) contributions to the overall free energy change are large in magnitude and of opposing signs. Such a counterbalance between the enthalpic/entropic effects is known as entropy-enthalpy compensation.[58, 72] In folding of the NiCo riboswitch, such enthalpy-entropy compensation effects are seen to occur multiple times, as highlighted in Figure 5.10 by the relatively modest shifts in ΔG^0 values contrasting with the order of magnitude larger ΔH^0 and $-T\Delta S^0$ values. As one example, the free energy $\Delta G^0_{I\rightarrow F}$ for I → F folding in the presence of Co^{2+} is only -0.41(10) kcal/mol, despite the fact that each of the entropic penalty and enthalpic stabilization effects are larger by 2 orders of magnitude (> 40 kcal/mol). Similarly, in the absence of Co^{2+}, $\Delta G^0_{I\rightarrow F}$ is +1.49(7) kcal/mol while the enthalpic stabilization as well as entropic destabilization components are 10x higher (> 15 kcal/mol). Such a biological propensity to achieve nearly equally balanced free energy contributions in $-T\Delta S^0$ and ΔH^0 for conformational change offers one way to modulate the temperature sensitivity of RNA folding and conformational stability of a biologically competent species with only small changes in the overall free energy ΔG^0.

5.6 Summary and conclusion

The present work reports on the single molecule kinetics and thermodynamics of folding of the NiCo ribowitch construct as a function of (i) cognate ligand (Ni^{2+}, Co^{2+}), (ii) background monovalent (Na^+) and divalent (Mg^{2+}) concentrations, and (iii) temperature (T = 20-30K). Although the aptamer domain structure of the NiCo riboswitch is built on a 4-way junction with no long-range tertiary stem-stem or loop-loop interactions, evidence from the present single molecule study reveals it to be more complex and kinetically interesting than a simple two-state folder. Specifically, the NiCo riboswitch has been shown to dynamically fluctuate between three

stable conformations (unfolded U, folded F and intermediate I) and exhibit three distinct E_{FRET} values. Of particular relevance, the overwhelming majority (> 98%) of all transitions between unfolded (U) and folded (F) conformations sample this third conformation (I), which therefore acts as a long-lived, prefolded intermediate through which overall folding proceeds by two distinct steps (U → I and I → F). This intermediate I proves particularly crucial for selective cognate ligand recognition and ligand-induced folding, as clearly evidenced by the fact that Ni^{2+}/Co^{2+} strongly promote the I → F folding step, while Mg^{2+}/Na^{+} has little effect even at 3-5 orders of magnitude higher concentrations. As a result, the first stage of this NiCo riboswitch folding (U → I) can be facilitated by $[Na^{+}]$ and $[Mg^{2+}]$ present at physiological levels, whereas the second stage of folding is controlled with high selectivity by submicromolar concentrations of the cognate ligand. The overall folding pathway thus follows a classic "bind-then-fold" conformational selection mechanism, whereby the binding site on the prefolded intermediate captures cognate ligands with high selectivity and thereby stabilizes the overall folding event. Furthermore, both Ni^{2+} and Co^{2+} are shown from a Hill analysis to *cooperatively* promote folding of the NiCo riboswitch, with cation selective signatures in Hill cooperativity, K_d affinity, and saturation kinetics. As a result, these unique signatures could offer the NiCo riboswitch a mechanism for discriminating between Ni^{2+} and Co^{2+} to optimize gene-regulation efficiency and *in vivo* management of metal ion cytotoxicity. Finally, detailed free energy landscapes have been reconstructed from van't Hoff and Eyring analysis of the temperature dependent equilibrium and kinetic data. The results highlight a complete insensitivity of the first prefolding step (U → $TS_{U\leftrightarrow I}$ → I) to cognate ligand, with both dramatic entropy-enthalpy compensation and cognate ligand sensitivity effects along the second step (I → $TS_{I\leftrightarrow F}$ → F) for folding the NiCo riboswitch into biochemically competent shape.

5.7 References

1. Barrick, J. E.; Breaker, R. R., The Distributions, Mechanisms, and Structures of Metabolite-Binding Riboswitches. *Genome Biol.* **2007,** *8* (11), R239.

2. Garst, A. D.; Edwards, A. L.; Batey, R. T., Riboswitches: Structures and Mechanisms. *Cold Spring Harb. Perspect. Biol.* **2011,** *3* (6), a003533.

3. Nudler, E.; Mironov, A. S., The Riboswitch Control of Bacterial Metabolism. *Trends Biochem. Sci.* **2004,** *29* (1), 11-17.

4. Winkler, W. C.; Breaker, R. R., Regulation of Bacterial Gene Expression by Riboswitches. *Annu. Rev. Microbiol.* **2005,** *59* (1), 487-517.

5. McCown, P. J.; Corbino, K. A.; Stav, S.; Sherlock, M. E.; Breaker, R. R., Riboswitch Diversity and Distribution. *RNA* **2017,** *23* (7), 995-1011.

6. Valko, M.; Morris, H.; Cronin, M. T. D., Metals, Toxicity and Oxidative Stress. *Curr. Med. Chem.* **2005,** *12* (10), 1161-1208.

7. Jaishankar, M.; Tseten, T.; Anbalagan, N.; Mathew, B. B.; Beeregowda, K. N., Toxicity, Mechanism and Health Effects of Some Heavy Metals. *Interdiscip. Toxicol.* **2014,** *7* (2), 60-72.

8. Andreini, C.; Bertini, I.; Cavallaro, G.; Holliday, G. L.; Thornton, J. M., Metal Ions in Biological Catalysis: from Enzyme Databases to General Principles. *J. Biol. Inorg. Chem.* **2008,** *13* (8), 1205-1218.

9. Hausinger, R. P., Nickel Utilization by Microorganisms. *Microbiol. Rev.* **1987,** *51* (1), 22-42.

10. Chen, P. R.; He, C., Selective Recognition of Metal Ions by Metalloregulatory Proteins. *Curr. Opin. Chem. Biol.* **2008,** *12* (2), 214-221.

11. Reyes-Caballero, H.; Campanello, G. C.; Giedroc, D. P., Metalloregulatory Proteins: Metal Selectivity and Allosteric Switching. *Biophys. Chem.* **2011,** *156* (2), 103-114.

12. Pyle, A., Metal ions in the structure and function of RNA. *J. Biol. Inorg. Chem.* **2002,** *7* (7), 679-690.

13. Saunders, A. M.; DeRose, V. J., Beyond Mg^{2+}: Functional Interactions Between RNA and Transition Metals. *Curr. Opin. Chem. Biol.* **2016,** *31*, 153-159.

14. Price, Ian R.; Gaballa, A.; Ding, F.; Helmann, John D.; Ke, A., Mn^{2+}-Sensing Mechanisms of *yybP-ykoY* Orphan Riboswitches. *Mol. Cell* **2015,** *57* (6), 1110-1123.

15. Dambach, M.; Sandoval, M.; Updegrove, Taylor B.; Anantharaman, V.; Aravind, L.; Waters, Lauren S.; Storz, G., The Ubiquitous *yybP-ykoY* Riboswitch Is a Manganese-Responsive Regulatory Element. *Mol. Cell* **2015,** *57* (6), 1099-1109.

16. Furukawa, K.; Ramesh, A.; Zhou, Z.; Weinberg, Z.; Vallery, T.; Winkler, Wade C.; Breaker, Ronald R., Bacterial Riboswitches Cooperatively Bind Ni^{2+} or Co^{2+} Ions and Control Expression of Heavy Metal Transporters. *Mol. Cell* **2015,** *57* (6), 1088-1098.

17. Anton, A.; Große, C.; Reißmann, J.; Pribyl, T.; Nies, D. H., CzcD Is a Heavy Metal Ion Transporter Involved in Regulation of Heavy Metal Resistance in *Ralstonia* sp. Strain CH34. *J. Bacteriol.* **1999,** *181* (22), 6876-6881.

18. Große, C.; Anton, A.; Hoffmann, T.; Franke, S.; Schleuder, G.; Nies, D. H., Identification of a Regulatory Pathway that Controls the Heavy-Metal Resistance System Czc via Promoter czcNp in *Ralstonia metallidurans*. *Arch. Microbiol.* **2004,** *182* (2), 109-118.

19. Bouzat, J. L.; Hoostal, M. J., Evolutionary Analysis and Lateral Gene Transfer of Two-Component Regulatory Systems Associated with Heavy-Metal Tolerance in Bacteria. *J. Mol. Evol.* **2013,** *76* (5), 267-279.

20. Frieda, K. L.; Block, S. M., Direct Observation of Cotranscriptional Folding in an Adenine Riboswitch. *Science* **2012,** *338* (6105), 397-400.

21. Watters, K. E.; Strobel, E. J.; Yu, A. M.; Lis, J. T.; Lucks, J. B., Cotranscriptional Folding of a Riboswitch at Nucleotide Resolution. *Nat. Struct. Mol. Biol.* **2016,** *23* (12), 1124-1131.

22. Tolić-Nørrelykke, S. F.; Engh, A. M.; Landick, R.; Gelles, J., Diversity in the Rates of Transcript Elongation by Single RNA Polymerase Molecules. *J. Biol. Chem.* **2004,** *279* (5), 3292-3299.

23. Wickiser, J. K.; Winkler, W. C.; Breaker, R. R.; Crothers, D. M., The Speed of RNA Transcription and Metabolite Binding Kinetics Operate an FMN Riboswitch. *Mol. Cell* **2005,** *18* (1), 49-60.

24. Lemay, J.-F.; Desnoyers, G.; Blouin, S.; Heppell, B.; Bastet, L.; St-Pierre, P.; Massé, E.; Lafontaine, D. A., Comparative Study between Transcriptionally- and Translationally-Acting Adenine Riboswitches Reveals Key Differences in Riboswitch Regulatory Mechanisms. *PLoS Genet.* **2011,** *7* (1), e1001278.

25. Lutz, B.; Faber, M.; Verma, A.; Klumpp, S.; Schug, A., Differences Between Cotranscriptional and Free Riboswitch Folding. *Nucleic Acids Res.* **2013,** *42* (4), 2687-2696.

26. Zhuang, X.; Bartley, L. E.; Babcock, H. P.; Russell, R.; Ha, T.; Herschlag, D.; Chu, S., A Single-Molecule Study of RNA Catalysis and Folding. *Science* **2000,** *288* (5473), 2048-2051.

27. Roy, R.; Hohng, S.; Ha, T., A Practical Guide to Single-Molecule FRET. *Nat. Methods* **2008,** *5* (6), 507-516.

28. Guo, Z.; Karunatilaka, K. S.; Rueda, D., Single-Molecule Analysis of Protein-Free U2–U6 snRNAs. *Nat. Struct. Mol. Biol.* **2009,** *16* (11), 1154-1159.

29. McCluskey, K.; Boudreault, J.; St-Pierre, P.; Perez-Gonzalez, C.; Chauvier, A.; Rizzi, A.; Beauregard, P. B.; Lafontaine, D. A.; Penedo, J. C., Unprecedented Tunability of Riboswitch Structure and Regulatory Function by Sub-Millimolar Variations in Physiological Mg^{2+}. *Nucleic Acids Res.* **2019,** *47* (12), 6478-6487.

30. Lu, M.; Ma, X.; Castillo-Menendez, L. R.; Gorman, J.; Alsahafi, N.; Ermel, U.; Terry, D. S.; Chambers, M.; Peng, D.; Zhang, B., et al., Associating HIV-1 Envelope Glycoprotein Structures with States on the Virus Observed by smFRET. *Nature* **2019,** *568* (7752), 415-419.

31. Fiore, J. L.; Holmstrom, E. D.; Nesbitt, D. J., Entropic origin of Mg^{2+}-Facilitated RNA Folding. *Proc. Natl. Acad. Sci. U.S.A.* **2012,** *109* (8), 2902-2907.

32. Nicholson, D. A.; Sengupta, A.; Sung, H.-L.; Nesbitt, D. J., Amino Acid Stabilization of Nucleic Acid Secondary Structure: Kinetic Insights from Single-Molecule Studies. *J. Phys. Chem. B* **2018,** *122* (43), 9869-9876.

33. Holmstrom, E. D.; Nesbitt, D. J., Biophysical Insights from Temperature-Dependent Single-Molecule Förster Resonance Energy Transfer. *Annu. Rev. Phys. Chem.* **2016,** *67* (1), 441-465.

34. Sung, H.-L.; Nesbitt, D. J., Novel Heat-Promoted Folding Dynamics of the yybP-ykoY Manganese Riboswitch: Kinetic and Thermodynamic Studies at the Single-Molecule Level. *J. Phys. Chem. B* **2019,** *123* (26), 5412-5422.

35. Vogt, A. D.; Pozzi, N.; Chen, Z.; Di Cera, E., Essential Role of Conformational Selection in Ligand Binding. *Biophys. Chem.* **2014,** *186*, 13-21.

36. Suddala, K. C.; Wang, J.; Hou, Q.; Walter, N. G., Mg^{2+} Shifts Ligand-Mediated Folding of a Riboswitch from Induced-Fit to Conformational Selection. *J. Am. Chem. Soc.* **2015,** *137* (44), 14075-14083.

37. Sung, H.-L.; Nesbitt, D. J., Single-Molecule FRET Kinetics of the Mn^{2+} Riboswitch: Evidence for Allosteric Mg^{2+} Control of "Induced-Fit" vs "Conformational Selection" Folding Pathways. *J. Phys. Chem. B* **2019,** *123* (9), 2005-2015.

38. Serganov, A.; Yuan, Y.-R.; Pikovskaya, O.; Polonskaia, A.; Malinina, L.; Phan, A. T.; Hobartner, C.; Micura, R.; Breaker, R. R.; Patel, D. J., Structural Basis for Discriminative Regulation of Gene Expression by Adenine- and Guanine-Sensing mRNAs. *Chem. Biol.* **2004,** *11* (12), 1729-1741.

39. Garst, A. D.; Héroux, A.; Rambo, R. P.; Batey, R. T., Crystal Structure of the Lysine Riboswitch Regulatory mRNA Element. *J. Biol. Chem.* **2008,** *283* (33), 22347-22351.

40. Serganov, A.; Huang, L.; Patel, D. J., Coenzyme Recognition and Gene Regulation by a Flavin Mononucleotide Riboswitch. *Nature* **2009,** *458* (7235), 233-237.

41. Sengupta, A.; Sung, H.-L.; Nesbitt, D. J., Amino Acid Specific Effects on RNA Tertiary Interactions: Single-Molecule Kinetic and Thermodynamic Studies. *J. Phys. Chem. B* **2016,** *120* (41), 10615-10627.

42. Holmstrom, E. D.; Nesbitt, D. J., Single-Molecule Fluorescence Resonance Energy Transfer Studies of the Human Telomerase RNA Pseudoknot: Temperature-/Urea-Dependent Folding Kinetics and Thermodynamics. *J. Phys. Chem. B* **2014,** *118* (14), 3853-3863.

43. Sung, H.-L.; Nesbitt, D. J., DNA Hairpin Hybridization under Extreme Pressures: A Single-Molecule FRET Study. *J. Phys. Chem. B* **2020,** *124* (1), 110-120.

44. Fiore, J. L.; Holmstrom, E. D.; Fiegland, L. R.; Hodak, J. H.; Nesbitt, D. J., The Role of Counterion Valence and Size in GAAA Tetraloop–Receptor Docking/Undocking Kinetics. *J. Mol. Biol.* **2012,** *423* (2), 198-216.

45. Qin, F.; Auerbach, A.; Sachs, F., A Direct Optimization Approach to Hidden Markov Modeling for Single Channel Kinetics. *Biophys. J.* **2000,** *79* (4), 1915-1927.

46. Andrec, M.; Levy, R. M.; Talaga, D. S., Direct Determination of Kinetic Rates from Single-Molecule Photon Arrival Trajectories Using Hidden Markov Models. *J. Phys. Chem. A* **2003,** *107* (38), 7454-7464.

47. Schröder, G. F.; Grubmüller, H., Maximum Likelihood Trajectories from Single Molecule Fluorescence Resonance Energy Transfer Experiments. *J. Chem. Phys.* **2003,** *119* (18), 9920-9924.

48. McKinney, S. A.; Joo, C.; Ha, T., Analysis of Single-Molecule FRET Trajectories Using Hidden Markov Modeling. *Biophys. J.* **2006,** *91* (5), 1941-1951.

49. Forsén, S.; Linse, S., Cooperativity: over the Hill. *Trends Biochem. Sci.* **1995,** *20* (12), 495-497.

50. Schroeder, Kersten T.; Daldrop, P.; Lilley, David M. J., RNA Tertiary Interactions in a Riboswitch Stabilize the Structure of a Kink Turn. *Structure* **2011,** *19* (9), 1233-1240.

51. Fiegland, L. R.; Garst, A. D.; Batey, R. T.; Nesbitt, D. J., Single-Molecule Studies of the Lysine Riboswitch Reveal Effector-Dependent Conformational Dynamics of the Aptamer Domain. *Biochemistry* **2012,** *51* (45), 9223-9233.

52. Draper, D. E.; Grilley, D.; Soto, A. M., Ions and RNA Folding. *Annu. Rev. Biophys. Biomol. Struct.* **2005,** *34* (1), 221-243.

53. Woodson, S. A., Metal Ions and RNA Folding: a Highly Charged Topic with a Dynamic Future. *Curr. Opin. Chem. Biol.* **2005,** *9* (2), 104-109.

54. Goody, T. A.; Melcher, S. E.; Norman, D. G.; Lilley, D. M. J., The Kink-Turn motif in RNA is Dimorphic, and Metal Ion-Dependent. *RNA* **2004,** *10* (2), 254-264.

55. Hohng, S.; Wilson, T. J.; Tan, E.; Clegg, R. M.; Lilley, D. M. J.; Ha, T., Conformational Flexibility of Four-way Junctions in RNA. *J. Mol. Biol.* **2004,** *336* (1), 69-79.

56. Holmstrom, E. D.; Fiore, J. L.; Nesbitt, D. J., Thermodynamic Origins of Monovalent Facilitated RNA Folding. *Biochemistry* **2012,** *51* (18), 3732-3743.

57. Irudayam, S. J.; Henchman, R. H., Entropic Cost of Protein−Ligand Binding and Its Dependence on the Entropy in Solution. *J. Phys. Chem. B* **2009,** *113* (17), 5871-5884.

58. Zhou, H.-X.; Gilson, M. K., Theory of Free Energy and Entropy in Noncovalent Binding. *Chem. Rev.* **2009,** *109* (9), 4092-4107.

59. Kramers, H. A., Brownian Motion in a Field of Force and the Diffusion Model of Chemical Reactions. *Physica* **1940,** *7* (4), 284-304.

60. Grote, R. F.; Hynes, J. T., The Stable States Picture of Chemical Reactions. II. Rate Constants for Condensed and Gas Phase Reaction Models. *J. Chem. Phys.* **1980,** *73* (6), 2715-2732.

61. Szabo, A.; Schulten, K.; Schulten, Z., First Passage Time Approach to Diffusion Controlled Reactions. *J. Chem. Phys.* **1980,** *72* (8), 4350-4357.

62. Zwanzig, R.; Szabo, A.; Bagchi, B., Levinthal's Paradox. *Proc. Natl. Acad. Sci. U.S.A.* **1992,** *89* (1), 20-22.

63. Weiss, J. N., The Hill Equation Revisited: Uses and Misuses. *FASEB J.* **1997,** *11* (11), 835-841.

64. Leipply, D.; Draper, D. E., Dependence of RNA Tertiary Structural Stability on Mg^{2+} Concentration: Interpretation of the Hill Equation and Coefficient. *Biochemistry* **2010,** *49* (9), 1843-1853.

65. Goldbeter, A.; Koshland, D. E., An Amplified Sensitivity Arising from Covalent Modification in Biological Systems. *Proc. Natl. Acad. Sci. U.S.A.* **1981,** *78* (11), 6840-6844.

66. Ralston, D. M.; O'Halloran, T. V., Ultrasensitivity and Heavy-Metal Selectivity of the Allosterically Modulated MerR Transcription Complex. *Proc. Natl. Acad. Sci. U.S.A.* **1990,** *87* (10), 3846-3850.

67. Xu, J.; Cotruvo, J. A., The czcD (NiCo) Riboswitch Responds to Iron(II). *Biochemistry* **2020,** *59* (15), 1508-1516.

68. Minton, A. P., Macromolecular Crowding and Molecular Recognition. *J. Mol. Recognit.* **1993,** *6* (4), 211-214.

69. Zhou, H.-X.; Rivas, G.; Minton, A. P., Macromolecular Crowding and Confinement: Biochemical, Biophysical, and Potential Physiological Consequences. *Annu. Rev. Biophys.* **2008,** *37* (1), 375-397.

70. Reynolds, C. H.; Holloway, M. K., Thermodynamics of Ligand Binding and Efficiency. *ACS Med. Chem. Lett.* **2011,** *2* (6), 433-437.

71. Marchand, A.; Rosu, F.; Zenobi, R.; Gabelica, V., Thermal Denaturation of DNA G-Quadruplexes and Their Complexes with Ligands: Thermodynamic Analysis of the Multiple States Revealed by Mass Spectrometry. *J. Am. Chem. Soc.* **2018,** *140* (39), 12553-12565.

72. Gallicchio, E.; Kubo, M. M.; Levy, R. M., Entropy−Enthalpy Compensation in Solvation and Ligand Binding Revisited. *J. Am. Chem. Soc.* **1998,** *120* (18), 4526-4527.

Chapter 6

Smaller Molecules Crowd Better: Crowder Size Dependence Revealed by Single-Molecule FRET Studies and Depletion Force Modeling Analysis

---

6.1 Abstract

The cell is an extremely crowded environment which is known to have profound impact on the thermodynamics, functionality, and conformational stability of biomolecules. Speculations from recent theoretical molecular dynamics studies suggest an intriguing size dependence to such purely entropic crowding effects, whereby small molecular weight crowders under constant enthalpy conditions are more effective than larger crowders on a per volume basis. If experimentally confirmed, this would be profoundly significant, as the cellular cytoplasm is also quite concentrated in smaller molecular weight solutes such as inorganic ions, amino acids, and various metabolites. The challenge is to perform such studies isolating entropic effects under isoenthalpic conditions. In this work, we present first results from single molecule FRET spectroscopy (smFRET) on the molecular size-dependent crowding stabilization of a simple RNA tertiary motif (the GAAA tetraloop-tetraloop receptor), indeed providing evidence in support of the surprising notion in the crowding literature that "smaller is better." Specifically, systematic smFRET studies as a function of crowder solute size reveal that smaller molecules both significantly *increase the RNA tertiary folding rate* and yet simultaneously *decrease the unfolding rate*, predicting strongly size dependent stabilization of RNA tertiary structures under crowded cellular conditions. The size dependence of these effects has been

*This chapter is adapted from: Sung, H.-L.; Sengupta, A.; Nesbitt, D. J. Smaller Molecules Crowd Better: Crowder Size Dependence Revealed by Single-Molecule FRET Studies and Depletion Force Modeling Analysis. *J. Chem. Phys.* **2021***, 154,* 155101*.*

explored via systematic variation of crowder size over a broad range of molecular weights (90 amu to 3000 amu). Furthermore, corresponding temperature dependent studies indicate the systematic changes in the folding equilibrium to be predominantly entropic in origin, i.e., consistent with a fundamental picture of entropic molecular crowding without additional enthalpic interactions. Most importantly, all trends in the single molecule crowding data can be quantitatively recapitulated by a simple analytic depletion force model, whereby excluded volume interactions represent the major thermodynamic driving force towards folding. Our study thus not only provides experimental evidence and theoretical support for small molecule crowding but also predicts further *enhancement of* crowding effects for *even smaller molecules* on a per volume basis.

6.2 Introduction

RNA plays a crucially important role in multiple cellular processes, with particular relevance in protein translation and gene regulation pathways.[1] Due to the crucial dependence of biochemical competence on correct nucleic acid conformation, many studies have focused on RNA folding,[2] with experiments traditionally performed in relatively dilute buffers with typical solute concentrations of less than 1% by weight.[3] This differs quite dramatically from the typical intracellular environment, where cytoplasmic mass comprises approximately 20 to 30 % solute.[4-5] Such concentrations of solute result in extremely “crowded” environments that could significantly alter the thermodynamics, kinetics, and tertiary folding stabilities of small RNA oligos, which in turn can directly impact biochemical activity.[5-7] As a result, the deeper understanding of such macroscopic crowding effects on the kinetics and thermodynamics of RNA conformation remains a crucial element to establishing a predictive first principles

connection between *in vitro* experimental results and *in vivo* observation under physiological conditions.

Molecular crowding effects on biomolecular folding in nucleic acid systems have been demonstrated by many studies.[8-13] In most of those crowding studies, the common observation is that high molecular weight crowders (i.e. polyethylene glycol (PEG) or dextran with molecular weights greater than 1000 amu) *enhance* thermodynamic stability of the more compact state and therefore promote nucleic acid folding.[8-13] Note that this implicitly assumes zero solute-induced change in enthalpic contributions to folding, which would also shift the relative free energies. The origin of such purely entropic crowding effects is thought to arise from excluded volume interactions,[6, 14-15] whereby a folded biomolecule takes on a more compact conformation and therefore allows the rest of the system to (entropically) sample a larger pool of microstates. From a simple hard sphere perspective, one might think of this additional volume as arising from excluded interstitial spaces between the crowder particles. One might therefore naturally anticipate a characteristic length scale (ζ) to exist for a given biomolecular size, that allows it to fit (or not) in the unoccupied interstitial volume. For crowders with a size scale smaller than ζ, there would be insufficient room to "hide" the biomolecule, which could translate into more intense crowding effects. From this perspective, one would predict an asymptotically flat crowding response above a certain crowder size, but with a rapid increase in crowding effects as the crowder scale size becomes comparable to that of the biomolecule.

To date, most studies have focused on crowding effects induced by relatively large molecular weight polymer crowders (e.g. MW > 1000 amu), often referred to as *macromolecular* crowding.[5-6] By way of contrast, the potential crowding effects caused by lower molecular weight species (e.g. MW < 1000 amu) has remained relatively unexplored, particularly with

respect to effects on RNA folding. This fundamental question of whether small molecule crowders have significant impact on biomolecular structural stabilities remains unsettled,[10, 16-18] despite the fact that all species exhibit excluded volume effects regardless of size. Recently, small molecule crowding (and the size dependence thereof) has been studied in detail by theoretical simulations of biomolecular folding in polypeptides and nucleic acids,[19-23] with additional size dependent predictions made based on hard sphere models.[24-25] As one particularly interesting prediction, the stabilization due to small crowders in some of these studies was demonstrated to exceed that of higher molecular weight crowders under constant volume fraction conditions.[20-22, 25] Despite these theoretical predictions for small molecule crowding, the experimental evidence to support these predictions has remained elusive: There has been some work studying small molecules such as TMAO (trimethylamine N-oxide)[26] and TFE (trifluoroethanol)[27] and which attributes the stabilization effects to crowding. However, these solutes also contain strong dipole moments and reactive functional groups, and thus, the bimolecular interaction between these small crowders and protein/nucleic acid polymers can be quite complex, with both enthalpic and entropic contributions to the overall folding thermodynamics. This in turn makes it challenging to isolate pure entropic crowding from a more generic enthalpic steering toward/away from a specific folded configuration.

In the present work, the crowding effect on RNA tertiary folding is studied by PEG and DME crowders with various molecular weights. PEG is a class of synthetic polymer with tunable length and well known for its inert biochemical properties. Of particular relevance, PEG has been shown in previous studies to promote the RNA folding primarily through changes in entropy,[11] consistent with a predominantly excluded volume picture of crowding.[14-15] Therefore, with PEG as a crowding agent, we can hope to isolate these entropic crowding interactions from

the more complex enthalpic contributions such as preferential binding and hydrogen bond formation. To systematically explore potential crowding effects induced by even smaller crowders, we then turn to 1, 2-dimethoxyethane (DME, MW = 90 amu) as the smallest repeating unit of PEG, and its higher molecular weight analogs (MW = 134 and 222 amu), motivated by the structural similarity to PEG (Figure 6.1).[28] DME contains a polyether backbone identical to PEG, which is considered a key reason for its low biochemical interference. Finally, the methoxy substituted end groups in DME avoid undesired enthalpic hydrogen bonding interactions with the crowded biomolecules, but also with other crowder molecules in solution, thus minimizing crowding effects by clusters of poorly defined size.[29-31]

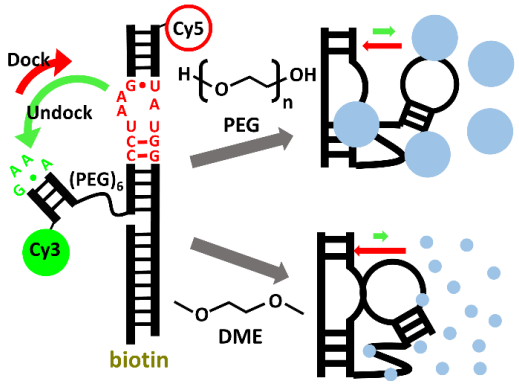

Figure 6.1 Schematic representation of RNA TL-TLR docking/undocking in the presence of large (PEG) or small (DME) crowders. The RNA sequences color coded in green/red indicate the tetraloop/tetraloop receptor folding motifs.

Single-molecule FRET spectroscopy (smFRET) is utilized to explore the kinetics of RNA conformational folding as a function of crowding conditions. We exploit the RNA tetraloop-tetraloop receptor (TL-TLR; Figure 6.1) as a model test system to explore the influence of crowding, since it is a ubiquitous tertiary binding motif in the 3D folding of many RNA oligos into biocompetent structures (e.g. ribozymes, riboswitches) and has been extensively

characterized in biophysical studies at the single-molecule level.[32-34] The TL-TLR RNA construct is doubly labeled with fluorescent dyes to provide dynamic structural information through FRET, with a biotin extension to allow tethering of the RNA construct to the coverslip surface for extended single molecule fluorescence observation. The docking (folding) behavior of TL-TLR is visualized by monitoring the FRET energy transfer efficiency (E_{FRET}) in real time, and thus the time-dependent E_{FRET} trajectory contains the information on both docking/undocking equilibria and kinetics (Figure 6.2). Most relevantly, by supplementing these studies with temperature dependent kinetic and equilibrium measurements, we are able to decompose the free energy change into entropic and enthalpic contributions.[33, 35] Knowledge of the underlying thermodynamics of crowding allows us to identify the predominantly entropic effects of PEG/DME molecules on RNA folding and therefore provide additional quantitative insights/interpretations into crowding phenomena from an excluded volume perspective.

As a natural extension and second major thrust of this paper, we present a simple physical model based on excluded volume/depletion force to account for the *size dependent* PEG and DME crowding phenomena observed at the single molecule level. In such a model, the purely entropic depletion force is generated by osmotic pressure differences arising from an uneven distribution of solute crowders due to excluded volume effects.[36-38] Based on a simplified picture of TL-TLR docking as arising from two RNA motif surfaces drawn into intimate contact, we find that the size dependence of PEG/DME crowding can be quantitatively well described by predictions from a depletion force model. Of special relevance, this model predicts small molecule crowding to be significantly more effective than larger crowders under constant volume fraction (i.e. % weight) concentrations. The excellent agreement between our experimental observations and theoretical studies[20-22, 25] not only provides direct evidence for

"small molecule crowding" and predictions of crowder size dependence, but also highlights the important role of depletion forces in biomolecule folding.[37]

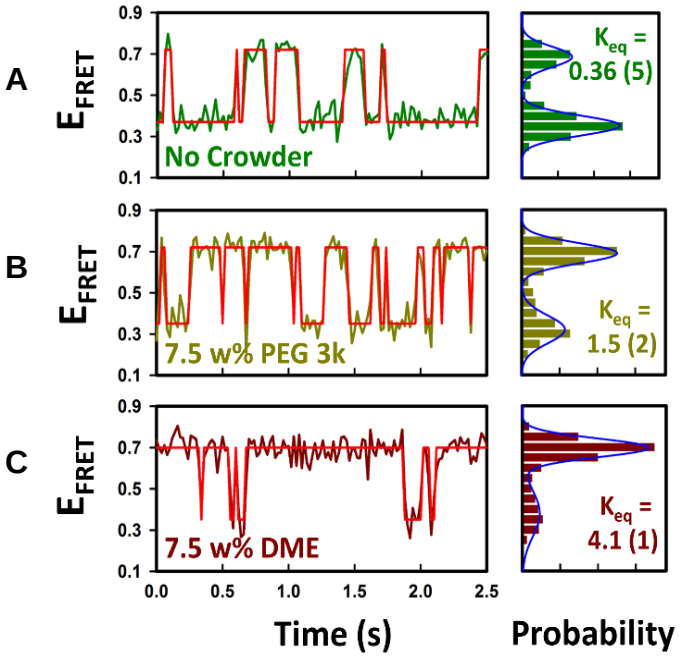

Figure 6.2 Sample data of single molecule time-dependent E_{FRET} trajectories (left panel) and E_{FRET} distributions (right panel) under different crowding conditions: (A) no crowder, (B) 7.5 w% PEG 3k, and (C) 7.5 w% DME.

6.3 Experiment

6.3.1 RNA construct design and sample preparation

A schematic of the TL-TLR folding mechanism is illustrated in Figure 6.1, where Cy3 and Cy5 indicate the positions of the labelled cyanine dyes and the colored coded sequences correspond to the tetraloop (green) and the tetraloop receptor (red), respectively. The TL-TLR construct consists of three nucleic acid oligomers:[34] (i) a DNA surface tether strand conjugated with biotin, 5'-biotin-CGC ACT CGT CTG AG-3'; (ii) a Cy3 labeled RNA strand, 5'-Cy3-GGC GAA AGC C-PEG_6-CGU GUC GUC CUA AGU CGG C-3'; and (iii) a Cy5 labeled RNA strand, 5'-Cy5-GCC GAU AUG GAC GAC ACG CCC CUC AGA CGA GUG CG-3' (all

purchased from Integrated DNA Technologies, Coralville, IA). Once annealed, the product is then purified with high-performance liquid chromatography (HPLC) to isolate the full TL-TLR ternary construct for single molecule studies.

In smFRET experiments, the TL-TLR molecules are immobilized on the coverslip surface through biotin-streptavidin interactions for prolonged single molecule fluorescence observations. The imaging buffer contains: (i) 50 mM hemisodium HEPES buffer (pH 7.5) with 0.1 mM EDTA, (ii) the PCD/PCA/Trolox enzymatic oxygen scavenger system to increase the dye photostability,[39] (iii) 20 mM NaCl (for temperature controlled experiments), and (iv) 0 to 10 w% PEG or DME crowder.

6.3.2 Temperature controlled single-molecule FRET spectroscopy

The smFRET experiment is performed with a home-built inverted confocal microscope:[34, 40] The collimated 532 nm pulsed laser is tightly focused by a 1.2 N.A. water immersion objective onto a single surface-tethered TL-TLR construct. The resulting fluorescent photons are collected by the same objective, and then sorted by colors (green/red) and polarizations (horizontal/vertical) before detection by a series of single photon avalanche photodiodes (APDs). The arrival time of each photon, both wall-clock "macrotime" time (50 ns precision) and "microtime" (50 ps precision) with respect to the corresponding excitation pulse, is recorded by the time-correlated single-photon counting (TCSPC) module and stored for later analysis. For the temperature dependent studies, control is achieved by heating both coverslip sample and microscope objective at the same time to minimize thermal gradients and maintain thermal equilibrium at the desired absolute temperature and precision (± 0.1 ^{o}C). Setup details for the presently used stage and objective heater can be found in previous work.[33, 40]

6.4 Results

6.4.1 RNA tertiary folding is promoted by PEG and small molecule DME

The TL-TLR binding motif consists of non-canonical hydrogen bond formation and base stacking interactions between a loop and bulge, representing one of the most common distinguishing features of RNA tertiary structure.[33, 41] In the present smFRET study, the docking of the TL-TLR is visualized by time-dependent E_{FRET} trajectories, sample data from which are shown in Figure 6.2. The data clearly indicate 2-state toggling behavior of the TL-TLR between two distinct E_{FRET} values, corresponding to docked (E_{FRET} ~ 0.7) and undocked (E_{FRET} ~ 0.35) conformations. The docking equilibrium constant K_{eq} is most readily extracted from the ratio of the total time spent in the docked vs. undocked state. In the absence of crowding solute (Figure. 6.2A), the TL-TLR preferentially remains in the undocked state (K_{eq} = 0.36(5)), while at 7.5 w% PEG 3k (average molecular weight MW_{av} = 3000 amu, Figure 6.2B), K_{eq} increases by over 4-fold (K_{eq} = 1.5(2)). This confirms that crowding by PEG energetically favors the docked state of TL-TLR, consistent with previous studies indicating PEG promotes biomolecular folding.[11] Of particular relevance to the present work, however, even stronger stabilization of the TL-TLR tertiary folding motif is observed for the small molecule crowder DME (Figure 6.2C), which now achieves an additional 3-fold (i.e., for an order of magnitude net) increase in K_{eq} for the exact same 7.5 w% concentration of crowding solutes. In agreement with theoretical predictions,[20, 25] these results provide first indications for increasingly significant stabilization effects for RNA tertiary folding with smaller molecular crowders at constant volume fraction.

With these tethered constructs, we can obviously take this crowding analysis one step further. In addition to equilibrium information, the time-dependent E_{FRET} trajectories also report

on the forward/reverse kinetics of TL-TLR docking, with the rate constants obtained by analysis of the cumulative distribution functions (CDFs) of dwell times for each state.[42-44] As shown in

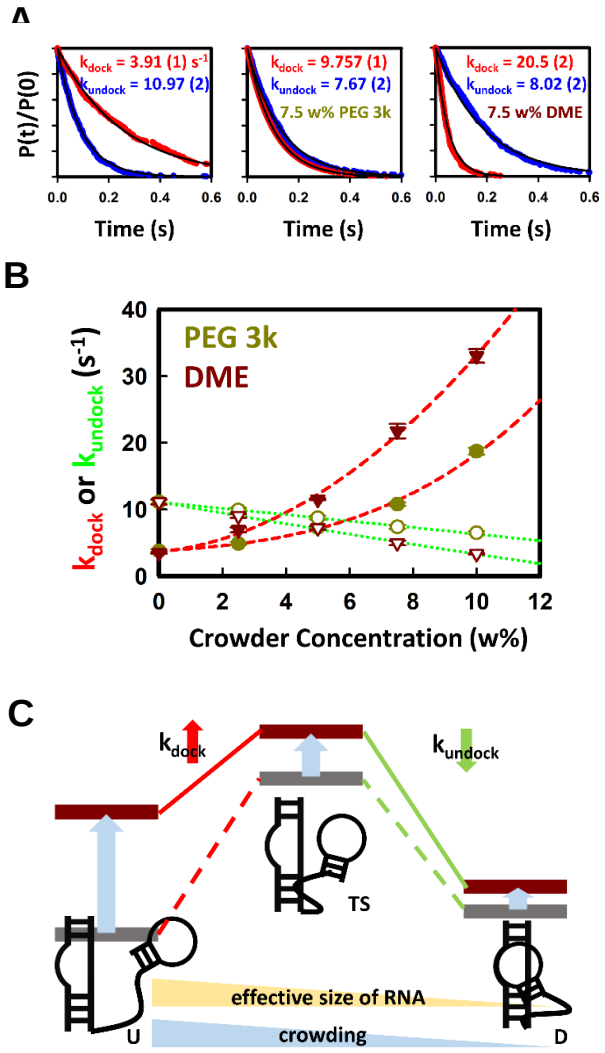

Figure 6.3 Crowder effects on the TL-TLR docking kinetics. (A) Cumulative distribution functions (CDFs) of docked and undocked dwell time well-characterized by single exponential decays (B) Crowder concentration dependence of rate constants k_{dock} and k_{undock} with overall trends highlighted in red dashed and green dotted lines, respectively (C) Crowding effects on rate constants illustrated in unequal free energy shifts in U (undocked), TS (transition) and D (docked) states. Error bars represent 1σ standard deviation of the mean.

the sample data in Figure 6.3A, the individual CDFs clearly exhibit single exponential decay, with the exponent yielding the first order TL-TLR docking or undocking rate constants (k_{dock} or k_{undock}). The effects of PEG 3k vs. DME on the rate kinetics of TL-TLR docking/undocking are explicitly summarized in Figure 6.3B. Both PEG and DME clearly promote formation of the TL-TLR tertiary motif, predominantly by a crowding induced *enhancement i*n k_{dock}, but also by commensurate *decrease* in k_{undock}. Once again, the results clearly reveal significant differences at constant w% between the 2 molecular crowding agents, with significantly stronger effects observed for the smaller (DME) molecular crowder.

These crowding-mediated variations in docking and undocking rate constants for RNA folding can be parsed within a simplified physical framework of activated complex or transition state theory (TST)[45-46] (Figure 6.3C). From transition state theory, the crowding dependence of these rate constants can be quantified in terms of the free energy differences between the transition state (TS) and either the docked or undocked state.[33-34] Simply stated, crowding must shift the free energies of the unfolded state upward (and folded state free energy downward) with respect to the TS, in order to achieve the observed increase (decrease) in k_{dock} (k_{undock}), respectively. Moreover, the transition state for RNA folding would be expected to be intermediate in size between the docked (i.e., most compact) and undocked state (i.e., most expanded). Given that crowding decreases the system entropy by reducing the number of accessible microstates, the more compact state is expected to be free energetically favored in a crowded environment. Since the undocked TL-TLR conformation is less compact than the transition state, k_{dock} would be predicted to *increase* under crowded conditions, in essence by lowering the free energy transition state barrier for docking. Conversely, the more compact folded state experiences a greater crowding-mediated stabilization with respect to the transition

state, thus yielding the observed crowding induced *decrease* in k_{undock}. To summarize, the rate constant changes induced by PEG 3k and DME are in already in good qualitative agreement with theoretical predictions of crowding on the folding kinetics. Of particular relevance, the larger shift for both docking/undocking rate constants with DME vs PEG 3k under constant w% conditions is consistent with the greater stabilization effects noted from equilibrium analysis, once again indicating the presence of stronger effects for *smaller molecular crowders* (i.e., DME vs PEG 3k).

6.4.2 Predominantly entropic stabilization confirmed by temperature dependence

The thermodynamic origin of PEG and DME crowding can be specified in greater detail by temperature dependent folding measurements, which permit the free energies to be broken down into enthalpic and entropic contributions. As a first example, we probe the effects of crowding on the overall equilibrium K_{eq} as a function of temperature. The free energy change for TL-TLR docking, ΔG^0 ($\Delta G^0 = \Delta G^0_{dock} - \Delta G^0_{undock}$) can be readily obtained from $\Delta G^0 = -RT \ln[K_{eq}]$, where R is the gas constant and T is temperature in Kelvin. These free energies can be further deconstructed into overall entropic ($-T\Delta S^0$) and enthalpic (ΔH^0) contributions by conventional van't Hoff analysis at the single molecule level.

$$\ln K_{eq} = -\frac{\Delta G^0_{dock}}{RT} = \frac{\Delta S^0}{R} - \frac{\Delta H^0}{RT}. \qquad \text{(Eq. 6.1)}$$

As demonstrated by sample data in Figure 6.4, a standard van't Hoff plot of $\ln[K_{eq}]$ vs. 1/T yields excellent straight line fits for each set of crowding conditions, with fitted slopes and intercepts corresponding to $(-\Delta H^0)/R$ and $\Delta S^0/R$, respectively. These lines are parallel within experimental uncertainty, implying that $\Delta(\Delta H^o) \approx 0$ and therefore the overall TL-TLR docking enthalpies are only minimally perturbed by both PEG 3k and DME molecular crowders. By way of contrast, the vertical offsets in these linear fits are strongly concentration- and molecular

crowder species-dependent, which unambiguously indicate that crowding of the TL-TLR docking event is predominantly driven by entropy ($\Delta(-T\Delta S^0) < 0$), though to dramatically different extents for PEG and DME crowders. These results confirm earlier observations that PEG crowding promotes RNA folding predominantly through entropic stabilization effects, with essentially negligible enthalpic contributions.[11, 15, 47] It is worth stressing that the predominance of entropy on these free energies is entirely consistent with molecular crowding arising from simple excluded volume (non-enthalpic) interactions,[14] which would predict a purely entropic origin.

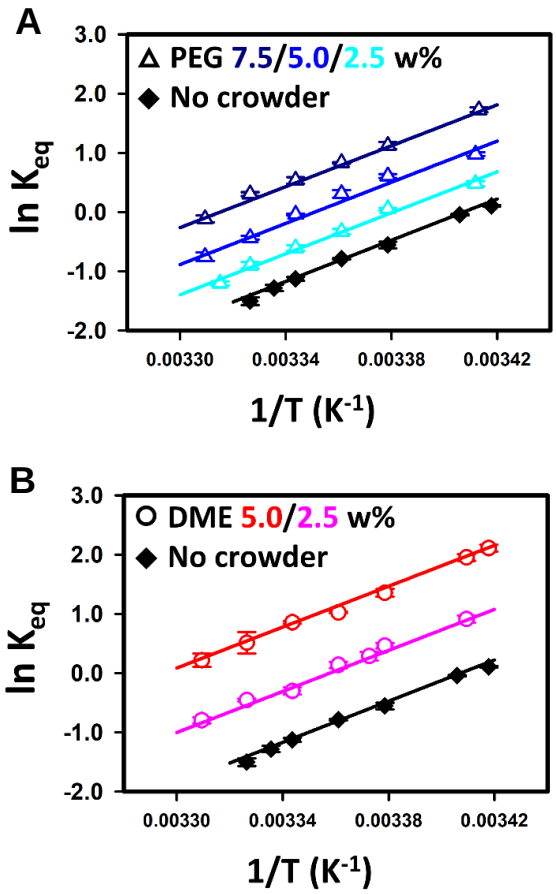

Figure 6.4 Temperature dependence of TL-TLR docking presented in van't Hoff plots at elevating (A) PEG 3k and (B) DME concentrations. Error bars represent 1σ standard deviation of the mean.

Quantitative thermodynamic results from the above van't Hoff analyses are summarized in Table I, which indicate a strongly exothermic yet entropically penalized folding event. The exothermicity of RNA folding arises from the non-canonical hydrogen bond formations and base stacking during the docking process[33]. The standard enthalpy changes (ΔH^o) reported in Table I are indistinguishable for dilute buffer vs. crowded solutions, again reinforcing the evidence for minimum differential enthalpic interactions between RNA with either PEG 3k or DME molecular solutes. Additionally, reliable predictions of the standard entropy changes (ΔS^0) can be achieved by simply requiring a globally fit exothermicity ($\Delta(\Delta H^0) \approx 0$), as summarized in the final column values for ΔS^0. The fact that ΔS^o is strongly negative in both the presence and absence of crowders, can be readily attributed to the presence of more highly organized loop and bulge configurations in the docked state. As more clearly indicated in Table I, however, this value of ΔS^0 increases systematically ($\Delta(\Delta S^0) > 0$) with crowding agents, indicating that docking of the TL-TLR is promoted by PEG and DME by *a reduction in entropic penalty* ($\Delta(-T(\Delta S^0)) < 0$) for folding. This conclusion is made more quantitatively by the final column of constrained

	ΔH^0 (kcal/mol)	ΔS^0 (kcal/mol/K)	ΔH^0 (kcal/mol)*	ΔS^0 (kcal/mol/K)*
No crowder	-34.6 (9)	-118 (3)	-34.5 (5)	-117.7 (17)
PEG 2.5 w%	-34.4 (7)	-117 (3)	-34.5 (5)	-116.6 (17)
PEG 5.0 w%	-34.8 (20)	-116 (8)	-34.5 (5)	-115.4 (17)
PEG 7.5 w%	-34.4 (10)	-114 (4)	-34.5 (5)	-114.1 (17)
DME 2.5 w%	-34.5 (14)	-116 (5)	-34.5 (5)	-115.6 (17)
DME 5.0 w%	-34.3 (9)	-113 (3)	-34.5 (5)	-113.5 (17)

Table 6.1 Thermodynamic parameters obtained from the van't Hoff analysis. *from global fit results.

fits to the entropy, which reveals a systematic and indeed approximately linear dependence on crowder w%/concentration. At least over the accessible dynamic range of 1/T probed, the results are in excellent agreement with the assertion that the mechanism of free energy stabilization of RNA tertiary folding events due to PEG and DME is predominantly entropic in nature, again consistent with a simple picture of molecular crowding without significant impacts due to differential enthalpies.

6.4.3 Stabilization free energies are greater for smaller molecular crowders

The distribution of solute sizes in cells is exceptionally broad, ranging from simple atomic ions, to moderately sized molecular metabolites, to larger macromolecules such as proteins and nucleic acids.[5] As a result, knowledge of the scaling dependence on crowder size is particularly crucial for any predictive understanding of cellular crowding. The previous sections have demonstrated that the effects of both i) polymer PEG 3k and its constituent subunit ii) DME on the kinetics and thermodynamics of TL-TLR folding are consistent with a simple physical picture of entropic crowding. In this next section, we explore the size dependence of such crowding phenomena over a wide range of molecular weights (MW), with 6 species between MW = 90 amu to MW = 3000 amu and as a function of crowder concentration. Moreover, the experimental conditions have been carefully restricted to a dilute regime where individual crowder molecules are diffusing independently (i.e., concentrations below which the polymer chains start to entangle),[16] and yet effects are still sufficiently pronounced to unambiguously reflect size dependence on the crowding species. By convention, we look for changes in the overall ΔG^0 ($\Delta\Delta G^0 = \Delta G^0_{crowded} - \Delta G^0_{dilute}$) as a measure of crowding stabilization on the TL-TLR tertiary structure, with size dependence of the results summarized in Figure 6.5A.

There are several notable features immediately visible in Figure 6.5A. First of all, for each crowder size, the stabilization free energy increases monotonically with increasing concentration, with a more nearly linear dependence observed at low molecular weight. Such an approximately linear dependence on concentration is mainly due to reduction in accessible volume and is directly proportional to the number density of crowders. We note that such a direct proportionality between $\Delta\Delta G^0$ and solute concentration is also quite commonly observed in several RNA-solute systems with preferential interactions (i.e., nonzero ΔH^0).[26, 48] For the data at hand, however, the case of such additional complicating contributions have been excluded by parallelism in the van't Hoff slopes exhibited in the temperature dependent analyses seen in Figure 6.4. Secondly, this free energy stabilization monotonically increases as a function of decreasing crowder size (i.e. $\Delta\Delta G^0$ becomes less negative), indicating the presence of *stronger crowding effects for smaller molecular weight crowders* at the same w%. Such an inverse dependence on crowder size is in excellent qualitative agreement with theoretical predictions from molecular dynamics simulations.[20-22, 25]

We can take this crowding analysis further in the context of a simple polymer model. Specifically, the scaling between PEG radius of gyration, R_g, and molecular weight (MW) in aqueous solution has been experimentally found to be approximately $R_g \sim MW^{\nu}$ with $\nu = 0.58$.[16, 49] The fact that this exponent is higher/faster than simple hard sphere scaling ($\nu_{HS} = 1/3$) implies that *larger* PEG crowders take up *more volume* than smaller PEGs under constant w% concentrations, whereas it is the *smaller* molecular weight crowders that promote RNA folding more efficiently, as the above studies have surprisingly revealed. These results highlight the important scaling synergy between number density and crowder size in crowding phenomena, which we will explore in greater detail in the discussion section. Furthermore, this dependence of

$\Delta\Delta G^0$ on crowder molecular weight is particularly sensitive in the low MW regime, as evident in Figure 6.5, with such crowding effects on free energy growing less sensitive to crowder concentration with increasing PEG molecular weight. Finally, these observations of enhanced crowding of nucleic acid folding as a function of decreasing molecular weight is one again qualitatively consistent with several previous theoretical predictions.[20-22, 25]

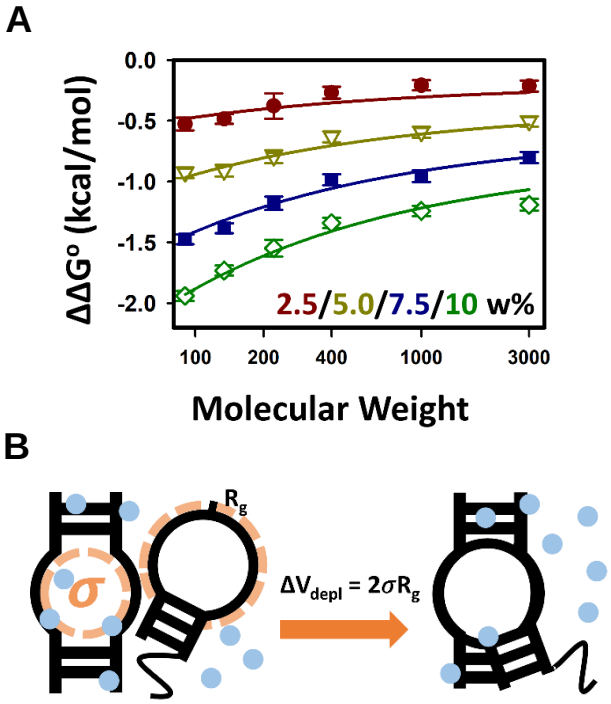

Figure 6.5 Crowder size dependence well described by the depletion force model. (A) Crowding stabilization effects as a function of crowder size at a series of w% concentrations. (B) Schematic representation of depletion force promoting TL-TLR folding. Error bars represent 1σ standard deviation of the mean. Solid lines represent fits to the depletion force model (see text for details).

6.5 Discussion

The depletion force and its intimate dependence on excluded volume is one of the most fundamental interactions in biology, becoming especially important in studies of biomolecular folding[37-38, 50]. From a hard sphere perspective, such depletion forces arise from a very simple guiding principle: solute molecules of a given size (*d*) cannot intervene between two folding

motifs coming into contact when the separation (*l*) becomes less than or equal to *d*. This generates a differential force pushing the two folding motifs together for $l \leq d$. A simple thermodynamic interpretation of this depletion force is that it reflects the osmotic pressure difference created by an uneven distribution of solutes on all sides of the folding motifs of interest. In the limit of a net zero enthalpic differential between solute/biomolecule and solute/solute interactions, such free energy crowding effects are predicted to be purely entropic, as indicated by the van't Hoff plots in Figure 6.4.

In a solution of a single spherical solute species of radius *r*, the center of a solute is excluded from the surface of any object by a distance *r* to avoid overlap. Such a solute inaccessible region is sometimes known as the depletion zone[51], with the volume directly proportional to the product of the total surface area of the object and the radius of the solute. Such depletion volume can be reduced by decreasing solvent/solute exposed surface area to maximize the system entropy. From an osmotic pressure point of view[37, 50], when two parallel plates are placed far apart in the solution, each plate creates a depletion zone of thickness r equivalent to the solute radius right above the surfaces. As they are brought closer to approximately < 2*r* away from each other, excluded volume requires that the space between the two plates contain no solute molecules, creating a depletion zone with zero osmotic pressure. For any nonzero osmotic pressure outside this depletion zone, the two plates will then be pushed into contact due to imbalance in the force. The net result is a reduction in the depletion zone by $\Delta V_{depl} = 2\sigma r$, where σ is the contact surface area. Since the depletion force increases the volume available for the solute to sample, it entropically favors the contacted vs separated states, for which the additional free energy of stabilization can be simply evaluated as $\Delta\Delta G_{depl}^{0} = -P_{osm} \Delta V_{depl}$, where P_{osm} is the osmotic pressure of the bulk solute[37].

In the present work, folding of TL-TLR RNA forms a docking interface by bringing two spatially separate RNA motifs (tetraloop and tetraloop receptor) into contact. Moreover, crowding conditions in this study are chosen such that crowder solute molecules are freely diffusing in solutions and can be approximated by hydrated spheres with an isotropic monomer distribution.[16] In the framework of a depletion force model, the total reduction in depletion volume due to TL-TLR folding is therefore $\Delta V_{depl} = 2\sigma R$, where σ is the contact area between tetraloop and tetraloop receptor and R is the radius of crowder. For PEG and PEG-like polymer molecules, this distance R is often approximated by the radius of gyration (R_g)[51]. Specifically, there is a well-established empirical scaling relation between molecular weight (MW) and radius of gyration given by $R_g = b(MW)^{\nu}$, with parameters b = 0.23 Å/(g/mol)$^{\nu}$ and $\nu = 0.58$ experimentally determined for aqueous PEG solutions[49] to recapitulate the MW dependence of R_g between 60 to 10k amu.[16] Note that the close proximity of $\nu \approx 0.58$ to 0.50 implies that PEG behaves in aqueous solution approximately like a diffusive random walk ($\nu_{diff} = 1/2$), with the $\nu - \nu_{diff} \approx 0.08$ differential reflecting contributions due to self-avoidance ($\nu_{self\text{-}avoid} = 0.6$ for a self-avoiding walk polymer model[52-53]). Furthermore, the fact that $\nu \approx 0.58$ considerably exceeds 0.33 indicates that the PEG molecules are highly hydrated and expand in size with increasing MW faster than predicted from a simple compact hard sphere model ($\nu_{hard\ sph} = 1/3$). Indeed, it is conjectured that this strong hydration sphere is what is responsible for the enthalpic inertness of PEG with RNA ($\Delta(\Delta H^0) = 0$)[54-55] and thus prospects for primarily entropic ($\Delta(\Delta S^0) > 0$) excluded volume contributions to the free energy. Finally, for relatively dilute PEG solutions, we can take osmotic pressures to be well approximated by $P_{osm} = nRT$ [56], where n is the crowder number density (in # solute particles/volume). In this limit, the depletion force contribution to the TL-TLR folding free energy can be expressed as

$$\Delta\Delta G^{o}_{depl} = -P_{osm}\Delta V_{depl}$$

$$= -(n\mathrm{RT})(2\sigma R_g)$$

$$= -(\mathrm{w\%}\frac{\rho}{MW}\mathrm{RT})(2\sigma b(MW)^{\nu})$$

$$= -(w\%)(2\sigma\rho b\mathrm{RT})(MW)^{\nu-1} \qquad \text{(Eq. 6.2)}$$

where $n = \frac{w\%}{MW}\rho$ is the solute number density required to interconvert between mass density (ρ) and weight percent (w%), the concentration unit most commonly used in crowding studies.[11-12] In Eq. 6.2, the solutions are still dilute enough to approximate the mass density to be ρ ≈ 1.0 (g/cm^3) for all crowder conditions reported in the present work.[57] With b, ν experimentally determined, Eq (2) represents a simple analytic model for predicting the depletion force contribution to crowding stabilization free energies, with the active area (σ) as the only free parameter.

As will become clear from fits to the data in Figure 6.5, Eq. 6.2 does not capture the complete story. Specifically, due to residual uncertainties in the experimentally measured ΔH^0 values, we cannot definitively rule out the possibility of additional small differential interactions between the TL-TLR construct and PEG and DME crowders. However, since the solute effects on biomolecular folding free energies are empirically found to exhibit a simple proportionality between $\Delta\Delta G^0$ and solute concentration[26, 48], we can therefore modify Eq. 6.2 by including an additive linear term in our model to correct for any additional solute induced free energy shifts ($\Delta\Delta G^0_{sol}$) beyond that from purely entropic crowding, i.e.

$$\Delta\Delta G^{o}_{sol} = m(w\%). \qquad \text{(Eq. 6.3)}$$

In Eq. 6.3, this multiplicative factor (m) can be readily interpreted as the m-value commonly utilized to characterize the strength of solute interactions per unit concentration[26, 48], in units of kcal/mol/w%. To include all contributions to the PEG crowder interaction, the depletion force model for the overall differential free energy change ($\Delta(\Delta G^0)$) is therefore simply expressed as the sum of the direct solute-RNA interaction free energy and depletion force contributions:

$$\Delta\Delta G^o = \Delta\Delta G^o_{sol} + \Delta\Delta G^o_{depl}$$

$$= (w\%)[(m - 2\sigma\rho bRT(MW)^{\nu-1})]. \qquad \text{(Eq. 6.4)}$$

From Eq. 6.4, the only molecular weight (MW) dependent contribution to these stabilization free energies arises from the depletion force entropies, with a much smaller but finite global dependence of the solute interaction on w% of crowder. Most importantly, since the exponent ν-1 = -0.42 < 0, this simple analytic expression does make the successful prediction of progressively stronger stabilization free energy effects for smaller molecular crowders under constant w% conditions, as theoretically predicted from molecular dynamics simulations.[20-22, 25]

For further testing this simple analytical model, we have explored crowding of the TL-TLR folding interaction for a systematic series of PEG molecular weight values ranging from 90 to 3000 amu with the corresponding experimentally observed differential changes in free energy plotted versus MW in Figure 6.5A. The experimental data clearly indicate a downward curvature in $\Delta\Delta G^0$ as a function of lower molecular weight crowders, in excellent qualitative agreement with Eq. 6.4. Furthermore, we have repeated these crowding studies over a systematic series of w% values (2.5% to 10%), which indicate a systematic decrease in the $\Delta\Delta G^0$ differential free energies with increasing w% over the experimentally explored range of 2.5% to 10% for each MW crowder. In addition, we have performed global least squares fits of Eq. 6.4 to the experimental results as a function of both w% and molecular weight (MW) of the PEG crowding

species. The results of these fits are shown as solid lines in Figure 6.5A and represent a quantitatively accurate characterization of the data over a remarkably wide range of molecular crowder sizes and concentrations. By globally fitting the depletion force model to the size dependence data with only two free parameters, σ (contact area of TL-TLR folding) and m (strength of solute interactions), it successfully captures all experimental trends in the MW and w% dependence of the crowding effect. Finally, the surface area for TL-TLR folding is determined from these fit to be σ = 447(30) $Å^2$, which is in excellent agreement with the actual size of the TL-TLR docking site (~ 500 $Å^2$) estimated from x-ray crystal structural studies.[11, 41]

Similarly, these same least squares fits also predict the $\Delta\Delta G^0_{sol}$ dependence on w% ("m-value") to be m ≈ – 0.081(5) kcal/mol per w%. This is small enough that even at the highest w% values explored, the least squares fitted m-value would correspond to $\Delta\Delta G^0_{sol}$ = -0.81 kcal/mol (10 w%). This is clearly non-zero and implies a relatively small but non-negligible differential solute interaction between PEG and TL-TLR, but well within the experimental uncertainties reported in Table 6.1. By way of establishing a more quantitative context, such small PEG solute free energy effects on the TL-TLR construct are some 1 to 2 orders of magnitudes lower than for urea (+4.2 kcal/mol per w%) and TMAO (Trimethylamine N-oxide; -6.4 kcal/mol per w%)[26], two well-studied osmolytes that influence RNA folding. Despite such nonzero solute effects, the model clear demonstrates that fundamental excluded volume and crowding effects dominate the size dependent thermodynamic stabilization of the RNA by PEG. In summary, the excellent least squares agreement in fits of the experimental data to our theoretical model predictions (Eq. 6.4) drives home the two key points. Specifically, i) there is a clear molecular size dependence to the effect of crowding on formation of a ubiquitous RNA tertiary finding motif, and ii) these crowding studies confirm long standing theoretical predictions[20-22, 25] that under constant w%

conditions, smaller molecular weight crowders exert a stronger impact on free energy stabilization for the folded species.

6.6 Summary and conclusion

The effects of size dependent molecular crowding on the folding of a model RNA tertiary interaction have been studied in detail at the single molecule level. Crowding by the small molecule PEG subunit such as dimethoxy ethane (DME) is found to promote TL-TLR docking more significantly than the much larger macromolecular crowder PEG 3k. Both the observed kinetic increase in k_{dock} and decrease in k_{undock} with crowder concentration are successfully predicted from transition state theory,[45-46] as well as provides simple physical pictures of the crowding phenomena. The predominant role of entropy in the free energy stabilization of folding is revealed by detailed temperature dependent study of the equilibrium constants, which identify the excluded volume and depletion forces as the primary source of crowding interactions between RNA and PEG/DME. Our results provide unambiguous evidence for the greater impact on RNA conformational stability by smaller vs larger molecular crowders under constant w% concentration conditions, in agreement with theoretical predictions from molecular dynamics simulations.[20-22, 25] The size dependence of these crowding effects on RNA folding has been further investigated by systematic study of crowders over a wide range of molecular weights (MW) and solute concentrations (w%). Of particular importance, these stabilization free energy effects are found to *increase* with *decreasing crowder MW*, indicating such crowding effects to be increasingly sensitive to crowder size in the low molecular weight regime. The work highlights the important role that relatively small solutes (e.g., inorganic ions, amino acids, and

various metabolites) may play in intracellular crowding, whose contributions appear to have been largely neglected to date.

6.7 References

1. Caprara, M. G.; Nilsen, T. W., RNA: Versatility in Form and Function. *Nat. Struct. Biol.* **2000,** *7* (10), 831-833.

2. Brion, P.; Westhof, E., Hierarchy and Dynamics of RNA Folding. *Annu. Rev. Biophys. Biomol. Struct.* **1997,** *26* (1), 113-137.

3. Draper, D. E.; Grilley, D.; Soto, A. M., Ions and RNA Folding. *Annu. Rev. Biophys. Biomol. Struct.* **2005,** *34* (1), 221-243.

4. Fulton, A. B., How Crowded is the Cytoplasm? *Cell* **1982,** *30* (2), 345-347.

5. Ellis, R. J., Macromolecular Crowding: Obvious but Underappreciated. *Trends Biochem. Sci.* **2001,** *26* (10), 597-604.

6. Minton, A. P., The Influence of Macromolecular Crowding and Macromolecular Confinement on Biochemical Reactions in Physiological Media. *J. Biol. Chem.* **2001,** *276* (14), 10577-10580.

7. Zhou, H.-X.; Rivas, G.; Minton, A. P., Macromolecular Crowding and Confinement: Biochemical, Biophysical, and Potential Physiological Consequences. *Annu. Rev. Biophys.* **2008,** *37* (1), 375-397.

8. Nakano, S.-i.; Karimata, H.; Ohmichi, T.; Kawakami, J.; Sugimoto, N., The Effect of Molecular Crowding with Nucleotide Length and Cosolute Structure on DNA Duplex Stability. *J. Am. Chem. Soc.* **2004,** *126* (44), 14330-14331.

9. Zheng, K.-w.; Chen, Z.; Hao, Y.-h.; Tan, Z., Molecular Crowding Creates an Essential Environment for the Formation of Stable G-Quadruplexes in Long Double-Stranded DNA. *Nucleic Acids Res.* **2010,** *38* (1), 327-338.

10. Knowles, D. B.; LaCroix, A. S.; Deines, N. F.; Shkel, I.; Record, M. T., Separation of Preferential Interaction and Excluded Volume Effects on DNA Duplex and Hairpin Stability. *Proc. Natl. Acad. Sci. U.S.A.* **2011,** *108* (31), 12699-12704.

11. Dupuis, N. F.; Holmstrom, E. D.; Nesbitt, D. J., Molecular-Crowding Effects on Single-Molecule RNA Folding/Unfolding Thermodynamics and Kinetics. *Proc. Natl. Acad. Sci. U.S.A.* **2014,** *111* (23), 8464-8469.

12. Paudel, B. P.; Rueda, D., Molecular Crowding Accelerates Ribozyme Docking and Catalysis. *J. Am. Chem. Soc.* **2014,** *136* (48), 16700-16703.

13. Baltierra-Jasso, L. E.; Morten, M. J.; Laflör, L.; Quinn, S. D.; Magennis, S. W., Crowding-Induced Hybridization of Single DNA Hairpins. *J. Am. Chem. Soc.* **2015,** *137* (51), 16020-16023.

14. Minton, A. P., Excluded Volume as a Determinant of Macromolecular Structure and Reactivity. *Biopolymers* **1981,** *20* (10), 2093-2120.

15. Kilburn, D.; Roh, J. H.; Guo, L.; Briber, R. M.; Woodson, S. A., Molecular Crowding Stabilizes Folded RNA Structure by the Excluded Volume Effect. *J. Am. Chem. Soc.* **2010,** *132* (25), 8690-8696.

16. Soranno, A.; Koenig, I.; Borgia, M. B.; Hofmann, H.; Zosel, F.; Nettels, D.; Schuler, B., Single-Molecule Spectroscopy Reveals Polymer Effects of Disordered Proteins in Crowded Environments. *Proc. Natl. Acad. Sci. U. S. A.* **2014,** *111* (13), 4874-4879.

17. Bai, J.; Liu, M.; Pielak, G. J.; Li, C., Macromolecular and Small Molecular Crowding Have Similar Effects on α-Synuclein Structure. *ChemPhysChem* **2017,** *18* (1), 55-58.

18. Das, N.; Sen, P., Size-dependent Macromolecular Crowding Effect on the Thermodynamics of Protein Unfolding Revealed at the Single Molecular Level. *Int. J. Biol. Macromol.* **2019,** *141*, 843-854.

19. Cho, S. S.; Reddy, G.; Straub, J. E.; Thirumalai, D., Entropic Stabilization of Proteins by TMAO. *J. Phys. Chem. B* **2011,** *115* (45), 13401-13407.

20. Denesyuk, N. A.; Thirumalai, D., Crowding Promotes the Switch from Hairpin to Pseudoknot Conformation in Human Telomerase RNA. *J. Am. Chem. Soc.* **2011,** *133* (31), 11858-11861.

21. Denesyuk, N. A.; Thirumalai, D., Entropic Stabilization of the Folded States of RNA Due to Macromolecular Crowding. *Biophys. Rev.* **2013,** *5* (2), 225-232.

22. Kang, H.; Pincus, P. A.; Hyeon, C.; Thirumalai, D., Effects of Macromolecular Crowding on the Collapse of Biopolymers. *Phys. Rev. Lett.* **2015,** *114* (6), 068303.

23. Hilaire, M. R.; Abaskharon, R. M.; Gai, F., Biomolecular Crowding Arising from Small Molecules, Molecular Constraints, Surface Packing, and Nano-Confinement. *J. Phys. Chem. Lett.* **2015,** *6* (13), 2546-2553.

24. Lebowitz, J. L.; Helfand, E.; Praestgaard, E., Scaled Particle Theory of Fluid Mixtures. *J. Chem. Phys.* **1965,** *43* (3), 774-779.

25. Sharp, K. A., Analysis of the Size Dependence of Macromolecular Crowding Shows That Smaller is Better. *Proc. Natl. Acad. Sci. U.S.A.* **2015,** *112* (26), 7990-7995.

26. Holmstrom, E. D.; Dupuis, N. F.; Nesbitt, D. J., Kinetic and Thermodynamic Origins of Osmolyte-Influenced Nucleic Acid Folding. *J. Phys. Chem. B* **2015,** *119* (9), 3687-3696.

27. Culik, R. M.; Abaskharon, R. M.; Pazos, I. M.; Gai, F., Experimental Validation of the Role of Trifluoroethanol as a Nanocrowder. *J. Phys. Chem. B* **2014,** *118* (39), 11455-11461.

28. Verma, P. K.; Kundu, A.; Cho, M., How Molecular Crowding Differs from Macromolecular Crowding: A Femtosecond Mid-Infrared Pump–Probe Study. *J. Phys. Chem. Lett.* **2018,** *9* (22), 6584-6592.

29. Ydoshida, K.; Yamaguchi, T., Low-frequency Raman Spectroscopy of Aqueous Solutions of Aliphatic Alcohols. *Z. Naturforsch. A* **2001,** *56* (8), 529-536.

30. Roney, A. B.; Space, B.; Castner, E. W.; Napoleon, R. L.; Moore, P. B., A Molecular Dynamics Study of Aggregation Phenomena in Aqueous n-Propanol. *J. Phys. Chem. B* **2004,** *108* (22), 7389-7401.

31. Chodzińska, A.; Zdziennicka, A.; Jańczuk, B., Volumetric and Surface Properties of Short Chain Alcohols in Aqueous Solution–Air Systems at 293 K. *J. Solution Chem.* **2012,** *41* (12), 2226-2245.

32. Fiore, J. L.; Holmstrom, E. D.; Fiegland, L. R.; Hodak, J. H.; Nesbitt, D. J., The Role of Counterion Valence and Size in GAAA Tetraloop–Receptor Docking/Undocking Kinetics. *J. Mol. Biol.* **2012,** *423* (2), 198-216.

33. Fiore, J. L.; Holmstrom, E. D.; Nesbitt, D. J., Entropic Origin of Mg^{2+}-Facilitated RNA Folding. *Proc. Natl. Acad. Sci. U.S.A.* **2012,** *109* (8), 2902-2907.

34. Sengupta, A.; Sung, H.-L.; Nesbitt, D. J., Amino Acid Specific Effects on RNA Tertiary Interactions: Single-Molecule Kinetic and Thermodynamic Studies. *J. Phys. Chem. B* **2016,** *120* (41), 10615-10627.

35. Sung, H.-L.; Nesbitt, D. J., Novel Heat-Promoted Folding Dynamics of the yybP-ykoY Manganese Riboswitch: Kinetic and Thermodynamic Studies at the Single-Molecule Level. *J. Phys. Chem. B* **2019,** *123* (26), 5412-5422.

36. Asakura, S.; Oosawa, F., On Interaction between Two Bodies Immersed in a Solution of Macromolecules. *J. Chem. Phys.* **1954,** *22* (7), 1255-1256.

37. Marenduzzo, D.; Finan, K.; Cook, P. R., The Depletion Attraction: an Underappreciated Force Driving Cellular Organization. *J. Cell Biol.* **2006,** *175* (5), 681-686.

38. Trokhymchuk, A.; Henderson, D., Depletion Forces in Bulk and in Confined Domains: From Asakura–Oosawa to Recent Statistical Physics Advances. *Curr. Opin. Colloid Interface Sci.* **2015,** *20* (1), 32-38.

39. Aitken, C. E.; Marshall, R. A.; Puglisi, J. D., An Oxygen Scavenging System for Improvement of Dye Stability in Single-Molecule Fluorescence Experiments. *Biophys. J.* **2008,** *94* (5), 1826-1835.

40. Sung, H.-L.; Nesbitt, D. J., Sequential Folding of the Nickel/Cobalt Riboswitch Is Facilitated by a Conformational Intermediate: Insights from Single-Molecule Kinetics and Thermodynamics. *J. Phys. Chem. B* **2020,** *124* (34), 7348-7360.

41. Cate, J. H.; Gooding, A. R.; Podell, E.; Zhou, K.; Golden, B. L.; Kundrot, C. E.; Cech, T. R.; Doudna, J. A., Crystal Structure of a Group I Ribozyme Domain: Principles of RNA Packing. *Science* **1996,** *273* (5282), 1678-1685.

42. Sung, H.-L.; Nesbitt, D. J., Single-Molecule FRET Kinetics of the Mn2+ Riboswitch: Evidence for Allosteric Mg2+ Control of "Induced-Fit" vs "Conformational Selection" Folding Pathways. *J. Phys. Chem. B* **2019,** *123* (9), 2005-2015.

43. Hodak, J. H.; Fiore, J. L.; Nesbitt, D. J.; Downey, C. D.; Pardi, A., Docking Kinetics and Equilibrium of a GAAA Tetraloop-Receptor Motif Probed by Single-Molecule FRET. *Proc. Natl. Acad. Sci. U. S. A.* **2005,** *102* (30), 10505.

44. Sung, H.-L.; Nesbitt, D. J., Single-Molecule Kinetic Studies of DNA Hybridization Under Extreme Pressures. *Phys. Chem. Chem. Phys.* **2020,** *22* (41), 23491-23501.

45. Zhou, H.-X., Rate Theories for Biologists. *Quarterly Reviews of Biophysics* **2010,** *43* (2), 219-293.

46. Gorensek-Benitez, A. H.; Smith, A. E.; Stadmiller, S. S.; Perez Goncalves, G. M.; Pielak, G. J., Cosolutes, Crowding, and Protein Folding Kinetics. *J. Phys. Chem. B* **2017,** *121* (27), 6527-6537.

47. Kilburn, D.; Roh, J. H.; Behrouzi, R.; Briber, R. M.; Woodson, S. A., Crowders Perturb the Entropy of RNA Energy Landscapes to Favor Folding. *J. Am. Chem. Soc.* **2013,** *135* (27), 10055-10063.

48. Shelton, V. M.; Sosnick, T. R.; Pan, T., Applicability of Urea in the Thermodynamic Analysis of Secondary and Tertiary RNA Folding. *Biochemistry* **1999,** *38* (51), 16831-16839.

49. Devanand, K.; Selser, J. C., Asymptotic behavior and long-range interactions in aqueous solutions of poly(ethylene oxide). *Macromolecules* **1991,** *24* (22), 5943-5947.

50. Mitchison, T. J., Colloid Osmotic Parameterization and Measurement of Subcellular Crowding. *Mol. Biol. Cell* **2019,** *30* (2), 173-180.

51. Lee, H.-C.; Jiang, H.-R., Directed aggregation of carbon nanotube on curved surfaces by polymer induced depletion attraction. *AIP Adv.* **2017,** *7* (12), 125228.

52. McKenzie, D. S., Polymers and Scaling. *Phys. Rep.* **1976,** *27* (2), 35-88.

53. Pietronero, L., Critical Dimensionality and Exponent of the "True" Self-Avoiding Walk. *Phys. Rev. B* **1983,** *27* (9), 5887-5889.

54. Leung, B. O.; Yang, Z.; Wu, S. S. H.; Chou, K. C., Role of Interfacial Water on Protein Adsorption at Cross-Linked Polyethylene Oxide Interfaces. *Langmuir* **2012,** *28* (13), 5724-5728.

55. Leng, C.; Hung, H.-C.; Sun, S.; Wang, D.; Li, Y.; Jiang, S.; Chen, Z., Probing the Surface Hydration of Nonfouling Zwitterionic and PEG Materials in Contact with Proteins. *ACS Appl. Mater. Interfaces* **2015,** *7* (30), 16881-16888.

56. Money, N. P., Osmotic Pressure of Aqueous Polyethylene Glycols: Relationship between Molecular Weight and Vapor Pressure Deficit. *Plant Physiol.* **1989,** *91* (2), 766-769.

57. Gonzalez-Tello, P.; Camacho, F.; Blazquez, G., Density and Viscosity of Concentrated Aqueous Solutions of Polyethylene Glycol. *J. Chem. Eng. Data* **1994,** *39* (3), 611-614.

Chapter 7

The Effects of Molecular Crowders on Single Molecule Nucleic Acid Folding: Temperature Dependent Studies Reveal True Crowding vs. Enthalpic Interactions

---

7.1 Abstract

Biomolecular folding in cells can be strongly influenced by spatial overlap/excluded volume interactions (i.e., "crowding") with intracellular solute. As a result, traditional *in vitro* experiments with dilute buffers may not accurately recapitulate biomolecule folding behavior *in vivo*. In order to account for such ubiquitous excluded volume effects, biologically inert polyethylene glycols (PEG) and polysaccharides (dextran, Ficoll) are often used as *in vitro* crowding agents to mimic *in vivo* crowding conditions, with a common observation that high concentrations of these polymers stabilize the more compact biomolecule conformation. However, such an analysis can be distorted by differences in polymer interactions with the folded vs. unfolded conformers, requiring temperature dependent analysis of the thermodynamics to reliably assess competing enthalpic vs. entropic contributions and thus the explicit role of excluded volume. In this work, temperature-controlled single molecule fluorescence resonance energy transfer (smFRET) is used to characterize the thermodynamic interaction between nucleic acids and common polymer crowders PEG, dextran and Ficoll. The results reveal that PEG promotes secondary and tertiary nucleic acid folding by simultaneously increasing the folding rate while decreasing the unfolding rate, with temperature dependent studies confirming that the source of PEG stabilization is predominantly entropic and consistent

*This chapter is adapted from: Sung, H.-L.; Nesbitt, D. J. Effects of Molecular Crowders on Single-Molecule Nucleic Acid Folding: Temperature-Dependent Studies Reveal True Crowding vs Enthalpic Interactions. *J. Phys. Chem. B* **2021**, *125*, 13147-13157.

with a true excluded volume crowding mechanism. By way of contrast, neither dextran nor Ficoll induce any significant concentration dependent change in nucleic acid folding stability at room temperature, but instead, stabilization effects gradually appear with temperature increase. Such a thermal response indicates that both folding enthalpies as well as entropies are impacted by dextran and Ficoll. A detailed thermodynamic analysis of the kinetics suggests that, instead of true *entropic* molecular crowding, dextran and Ficoll associate preferentially with the unfolded vs folded nucleic acid conformer as a result of larger solvent accessible surface area (SASA), thereby skewing the free energy landscapes through both *entropic/enthalpic* contributions.

7.2 Introduction

The cell is an extremely crowded environment, with 20% of the mass taken up by various organic and biopolymer solutes such as proteins, nucleic acids, and small molecule metabolites.[1-2] This raises the real likelihood that biomolecules *in vivo* function differently from the *in vitro* behavior traditionally observed in biochemical assays under dilute buffer conditions.[3-4] Correct assessment of the impact of each solute species on biomolecular structure and function is extremely challenging to quantify, particularly under such highly concentrated, non-ideal solution conditions. However, these solutes do share one simplifying contribution in common: they all take up physical space in solution and therefore impose fundamental steric constraints on the biomolecule widely known as excluded volume interactions.[5-6] Simply stated, the presence of excess solute reduces the space available for a specific biomolecule to sample; as a result, the biomolecule is driven into a more compact configuration to maximize the accessible microstates for the overall biomolecule + solvent system.[3] In other words, excluded volume effects are

predicted to *entropically* promote biomolecule folding/compaction, with this critical yet ubiquitous stabilization mechanism commonly referred to as "molecular crowding".[7-9]

Experimentally, the effects of cellular crowding are often studied by adding polymeric macromolecules such as polyethylene glycol (PEG) or polysaccharides such as dextran and Ficoll into the buffers.[9-12] Such polymers have been shown to resist protein adhesion and are believed to be biologically inert.[13-14] They are thus often referred to as "crowders" due to the possible predominance of these excluded volume (entropic) effects over other (enthalpic) chemical interactions.[15-17] Indeed, in the presence of these crowders, enhanced biomolecular folding has often been observed, qualitatively consistent with predictions of excluded volume energetically favoring the more compact state.[18] Furthermore, early temperature dependent studies of dextran stabilized lysozyme folding have revealed that the melting transition temperatures (T_m) increase predominantly due to entropic interactions with dextran and yet with essentially negligible enthalpic contributions.[16] It is this predominance of entropic stabilization that is a robust and distinctive feature of the excluded volume mechanism and the resulting molecular crowding effects. Identification of crowding effects arising solely through entropic contributions with inert polymers has since been demonstrated for both proteins and nucleic acids, requiring detailed thermodynamic investigations as a function of variable temperature.[16-17, 19-21]

In intriguing contrast with these early crowding studies, more recent results have suggested that both PEG and polysaccharide crowders may also influence the net folding *enthalpies* for certain protein systems.[22-25] Indeed, it is not particularly surprising that such molecules could exhibit differential chemical interactions with folded vs unfolded biomolecules above and beyond simple excluded volume interactions. These studies highlight the simple fact

that chemical interactions can depend significantly on both structure/charge state of the biomolecule and the presence of specific moieties on the crowding polymer species.[19] It is worth noting that most of these previous thermodynamic studies have focused on folding/unfolding in proteins, with characterization of the corresponding molecular crowding effects with nucleic acids still very much in its infancy.[26-28]

To address this informational lacuna, we explore herein the effects of the most commonly used polymeric molecular crowders (i.e., PEG, dextran, and Ficoll) on both secondary and tertiary structures of nucleic acid constructs by temperature-controlled single molecule FRET

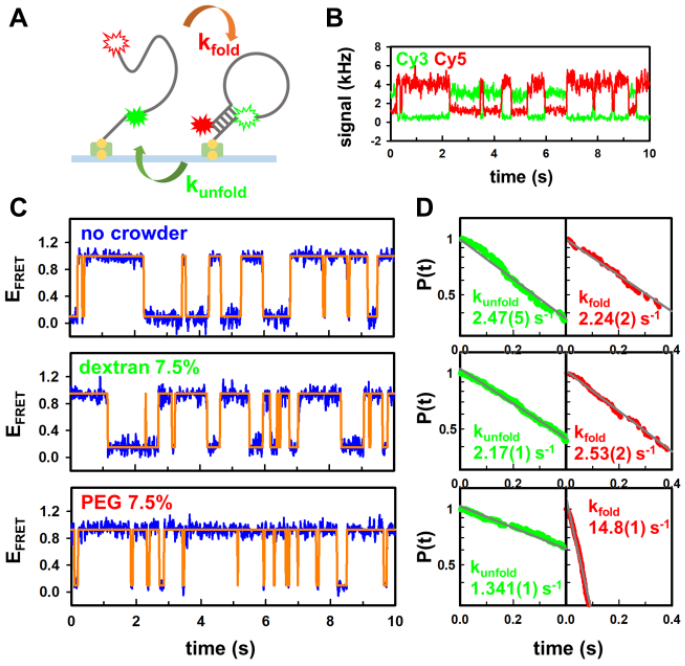

Figure 7.1 Sample smFRET experiment data. (**A**) Cartoon depiction of DNA hairpin secondary structure folding and (**B**) the resulting time-resolved single-molecule fluorescent signal from the donor, Cy3 (green) and acceptor, Cy5 (red). (**C**) Sample time-dependent E_{FRET} trajectories (blue) and the simulated time trace by the simple thresholding method (orange); (**D**) The corresponding dwell time distribution functions of the folded and unfolded conformations with (from top to bottom) 0 w% crowder, 7.5 w% dextran, and 7.5 w% PEG. Data are fit to a single exponential decay function to obtain the rate constants k_{fold}/k_{unfold}, with uncertainties evaluated from the fits.

spectroscopy (smFRET).[29-30] In this work, the folding/unfolding equilibria and kinetics are revealed at the single molecule level, with deconstruction of free energies into enthalpic and entropic components extracted from temperature-dependent crowding studies. The studies indeed reveal PEG stabilization of nucleic acid folded structures to be predominantly entropic, consistent with the simple picture of pure crowding dynamics originating from excluded volume effects.[16-17] More surprisingly, however, we find that the commonly used polysaccharide crowders dextran and Ficoll do not significantly impact either folding/unfolding kinetics or thermodynamic stability of nucleic acids, at least at room temperature. Interestingly, however, temperature dependent studies reveal this lack of crowding impact to be due to accidental cancellation between folding enthalpy (ΔH) and entropy ($-T\Delta S$) contributions at room temperature, where additional changes in the enthalpy result from the preferential binding of the polysaccharide molecules to the more solvent exposed unfolded conformation of the nucleic acid.

7.3 Experiment

7.3.1 Nucleic acid constructs and sample preparation

In order to study molecular crowding interaction on nucleic acids as a function of secondary vs. tertiary structure, we exploit a simple DNA hairpin (Figure 7.1) and the ubiquitous RNA tetraloop-tetraloop receptor tertiary folding domain (TL-TLR, Figure 7.2) as model systems, respectively. The DNA hairpin (with a 7 complimentary base pair stem and a 40 dA linker, see Figure 7.1A) is doubly dye-labeled (Cy3, Cy5), biotinylated for binding to a cover

slip surface, purchased in HPLC purified form (Integrated DNA technologies, Coralville, IA), and used as is.[31-32] The ternary TL-TLR construct comprises three smaller oligonucleotides, each singly-labeled with Cy3, Cy5, or biotin (Integrated DNA technologies, Coralville, IA), as described in detail elsewhere.[33] The full ternary construct is then prepared by heat-annealing the three oligomers together, followed by purification via high-performance liquid chromatography (HPLC).

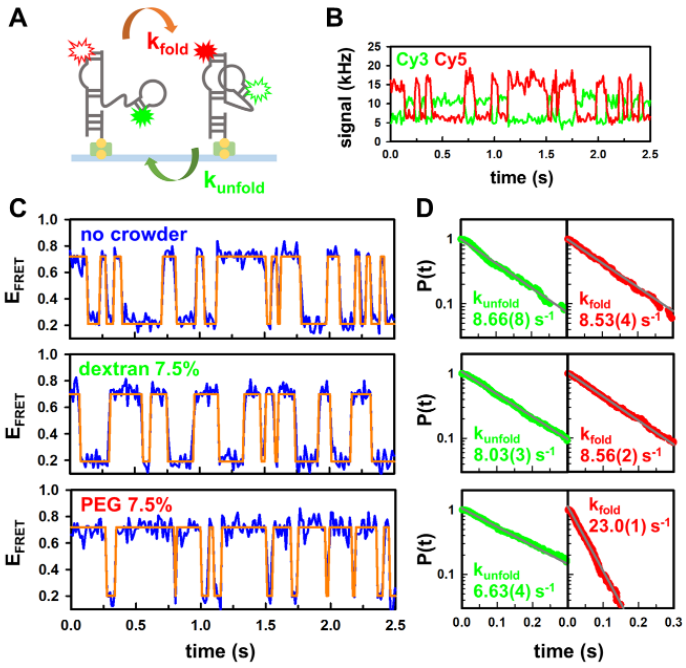

Figure 7.2 Sample smFRET experiment data. (**A**) Cartoon depiction of TL-TLR tertiary structure folding and (**B**) the resulting time-resolved single-molecule fluorescent signal from the donor, Cy3 (green) and acceptor, Cy5 (red). (**C**) Sample time-dependent E_{FRET} trajectories (blue) and the simulated time trace by the simple thresholding method (orange); (**D**) The corresponding dwell time distribution functions of the folded and unfolded conformations with (from top to bottom) 0 w% crowder, 7.5 w% dextran, and 7.5 w% PEG. Data are fit to a single exponential decay function to obtain the rate constants k_{fold}/k_{unfold}, with uncertainties evaluated from the fits.

The smFRET sample preparation is achieved by first coating the surface of a standard glass coverslip with an excess bovine serum albumin (BSA) and biotinylated BSA mixture, followed by incubation with streptavidin solution to generate a streptavidin-decorated surface with suitable surface densities. The resulting secondary and tertiary nucleic acid constructs are then immobilized on the surface of the coverslip through the highly stable biotin-streptavidin interactions, which permits prolonged observation of the folding/unfolding kinetics under single molecule conditions over several minutes to fractions of an hour. The smFRET imaging buffer consists of (i) 50 mM HEPES-KOH buffer (pH = 7.5), (ii) NaCl to provide background monovalent cation concentrations of $[M^+]$ = 100 or 150 mM for hairpin or TL-TLR construct, respectively, (iii) an enzymatic oxygen scavenger cocktail (PCD/PCA/Trolox) to increase fluorophore photostability,[34] and (iv) polymeric crowders PEG 6k, dextran 6k (MW = 6,000 amu), or Ficoll PM70 (MW = 70,000 amu), to achieve the desired concentration conditions.

7.3.2 Single-Molecule FRET spectroscopy and temperature control

The smFRET experiment in this work is performed with a home-built confocal microscope system,[35] based on a pulsed 532 nm Nd:YAG laser, collimated and directed onto the sample through an inverted confocal microscope. The beam is tightly focused into a diffraction limited spot by a 1.2 N.A. water immersion objective, achieving $\lambda/(2NA) \approx 220$ nm spatial resolution and allowing observation of one fluorophore-labeled construct at a time. The resulting emitted signal fluorescence is then collected through the same objective, with photons split into four different channels corresponding to red vs. green, horizontal vs. vertical polarizations before detection on four separate avalanche photon diodes (APD). For each detected photon, four bits of information: color, polarization, wall-clock time (in 50 ns bins), and microtime (with respect to

the laser pulse in 50 ps resolution) are recorded with fast time to amplitude conversion and/or time-correlated single-photon counting modules. In this work, we average over polarization effects by simply grouping all green (donor Cy3) and red (acceptor Cy5) photons to calculate FRET efficiency (E_{FRET}) as a function of time and thereby obtain the resulting E_{FRET} trajectories.

To achieve precise temperature control, the sample and the microscope objective are heated simultaneously to minimize thermal gradients.[36-37] Specifically, the sample holder is mounted to a thermal stage (Instec, Boulder, CO) which regulates the sample temperature by servo loop controlled heating and cooling. At the same time, the objective is heated by a commercially available resistive collar (Bioptechs, Butler, PA). Prior to each experiment, a 15 min incubation time is allowed to achieve steady sample temperature (± 0.1 °C).

7.3.3 Single molecule FRET data analysis

We calculate the background and cross-talk corrected FRET energy transfer efficiency E_{FRET} ($E_{FRET} = I_A / (I_D + I_A)$) at 10 ms bin time resolution to generate the time dependent E_{FRET} trajectories. Due to widely separated E_{FRET} values for folded (high E_{FRET}) and unfolded (low E_{FRET}) conformations (Figure 7.1C and 7.2C), a simple thresholding routine is adopted to determine the folding/unfolding states as well as the corresponding dwell time distributions.[35, 38] The folding equilibrium constant K_{eq} can be readily obtained by the ratios of total dwell times for the folded and unfolded states. Furthermore, our kinetic analysis is achieved by generating cumulative distribution functions of the dwell times for each state (see Figure 7.1D and 7.2D for sample data). For both constructs, the resulting folded/unfolded dwell time distributions P(t) are well fit to single exponential decay functions to extract rate constants k_{unfold}/k_{fold}, respectively,

confirming that the folding/unfolding processes can be satisfactorily characterized by first order kinetics.[39]

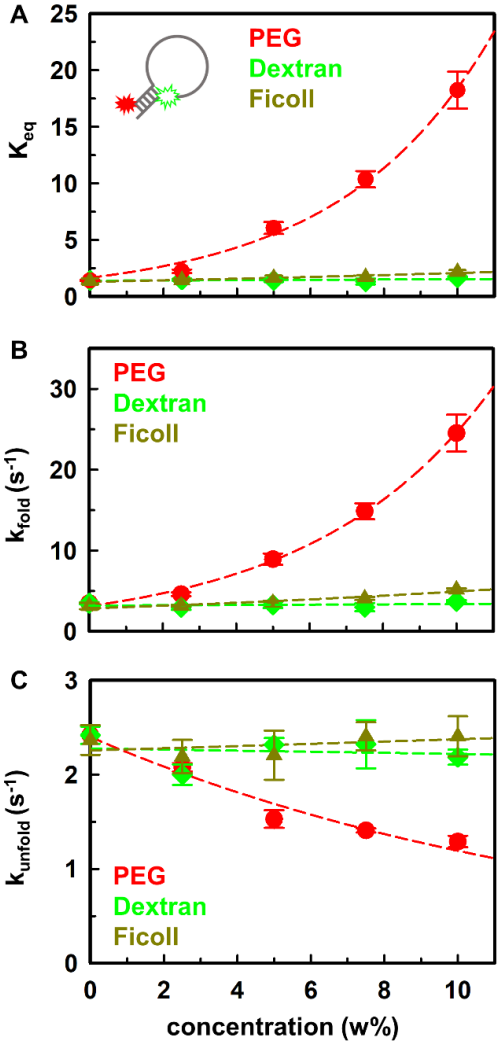

Figure 7.3 Crowder effects on DNA hairpin folding at constant room temperature (21 °C). Crowder concentration dependence of (**A**) K_{eq}, (**B**) k_{fold}, and (**C**) k_{unfold}. Error bars represent standard deviation of the mean (N = 3). Data are fit to a single exponential function based on the empirical observation of solute effects on the free energy change upon folding (see text for more details).

7.4 Results and analysis

7.4.1 Crowder effects on the DNA hairpin secondary folding kinetics

Folding of the 7-base pair DNA hairpin involves formation of secondary double helix structure essential for nucleic acid function. Its unimolecular design simplicity and easily tunable folding/unfolding rates make this an ideal model system for exploring nucleic acid secondary folding through single-molecule kinetic studies (Figure 7.1A).[38, 40-41] Herein, we explore the effects of three polymer crowders widely used in crowding studies: PEG, dextran, and Ficoll. These species have been consistently shown to stabilize the folded conformation of biomolecules,[9-12] primarily proteins, although the thermodynamic origin of this stabilization still remains debatable and probably structure-dependent.[19]

In the absence of crowders, the secondary folding equilibria of the DNA hairpin construct are adjusted by NaCl in the buffer to achieve $K_{eq} \approx 1$ conditions (at room temperature 21.0 ± 0.2 °C), in order to permit maximum dynamic range in ΔK_{eq} for shifts in either the folded or unfolded directions (Figure 7.1). In the presence of PEG (MW = 6,000 amu), the folding equilibrium K_{eq} is greatly enhanced, with a nearly 20-fold increase at the maximal PEG concentrations (10% by weight, or 10 w%) in this study (Figure 7.3A). Conversely, both polysaccharide crowders clearly exhibit much smaller effects, with only a 20% and 50% increase in K_{eq} for 10 w% dextran (MW = 6,000 amu) and Ficoll (MW = 70,000 amu), respectively. Furthermore, complementary kinetic information on folding/unfolding rate constants can be obtained by dwell time analysis of the single molecule E_{FRET} trajectories (Figure 7.1C and 7.1D). As clearly evident in Figure 7.3, PEG promotes the DNA hairpin folding by simultaneously increasing k_{fold} and decreasing k_{unfold}. Indeed, this effect is particularly significant for k_{fold}, which exhibits an order of magnitude increase with 10 w% PEG, with a relatively smaller but still quite noticeable 2-fold reduction observed for k_{unfold}. By way of contrast, similar w% concentrations of

the polysaccharide dextran and Ficoll increase $k_{fold,}$ by a relatively small amount (< 60%), with only negligible effects on k_{unfold} (< 10%) within experimental uncertainty.

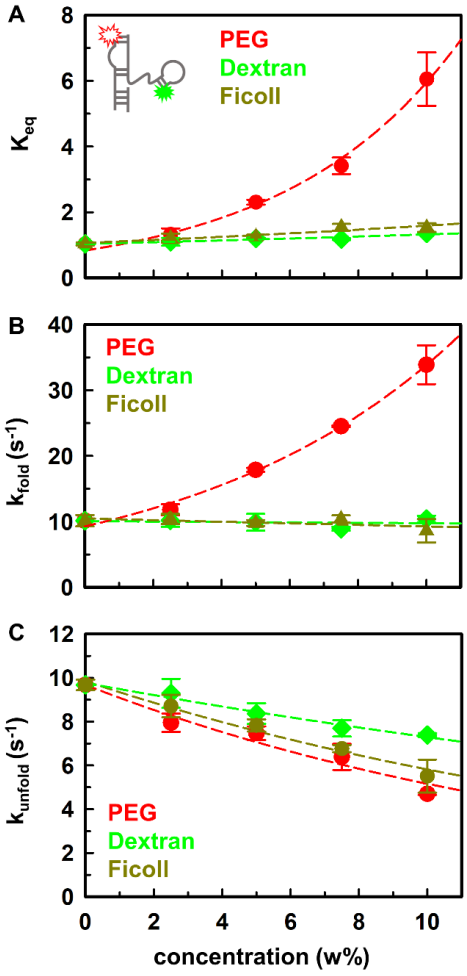

Figure 7.4 Crowder effects on RNA TL-TLR folding at constant room temperature (21 ℃). Crowder concentration dependence of (**A**) K_{eq}, (**B**) k_{fold} and (**C**) k_{unfold}. Error bars represent standard deviation of the mean (N = 3). Data are fit to a single exponential function based on the empirical observation of solute effects on the free energy change upon folding (see text for details).

7.4.2 Crowder effects on the RNA TL-TLR tertiary folding kinetics

TL-TLR is a ubiquitous folding element that is widely found in RNA tertiary structures (Figure 7.2A).[42] It has been extensively studied at the single molecule level[33] and its

kinetic/thermodynamic responses to PEG are found to be consistent with crowding effects reported in previous studies.[17, 43] Again by way of contrast, the potential crowding effects of dextran and Ficoll on such a common tertiary RNA folding motif have remained largely unexplored.

As a function of increasing concentration, PEG significantly promotes TL-TLR folding, with a more than 6-fold increase in K_{eq} at 10 w%, whereas dextran and Ficoll induce only much smaller increases in K_{eq} (< 50%, Figure 7.4A), very much consistent with the DNA hairpin results. Furthermore, kinetic analysis of the smFRET trajectories indicates k_{fold} for the TL-TLR to increase *exponentially* with PEG concentration, but remain surprisingly constant (< 20%) in response to dextran and Ficoll (Figure 7.3B). Interestingly, k_{unfold} for the TL-TLR construct is reduced comparably by all three crowders (Figure 7.3C), although the impact of PEG crowding is still the largest. It is also worth noting that the putative crowding dependences of K_{eq} and k_{fold}/k_{unfod} are well-fit (dashed lines in Figure 7.3 and 7.4) to exponential growth/decay functions, which would be entirely consistent with empirically observed linear relationships between folding free energy changes ($\Delta\Delta G$) and solute concentration.[44-45] Specifically, the strength of the solute interaction is often characterized by the so-called m-value,[46-48] which corresponds to exponents in exponential growth/decay fits of the concentration-dependent K_{eq} in Figure 7.3A and 7.4A. In the interest of completeness, the corresponding m-values of the crowder-TL-TLR interaction can be least squares fitted and found to be -0.115(6), -0.015(2) and -0.023(4) kcal mol^{-1} $w\%^{-1}$ for PEG, dextran and Ficoll, respectively. The m-value from PEG concentration dependence is therefore > 5 times larger than dextran/Ficoll, again highlighting the fact that the TL-TLR folding free energy is much more sensitive to PEG crowding. A similar crowder

concentration dependence is also observed for the DNA hairpin, with m-values for PEG, dextran and Ficoll determined to be -0.141(8), -0.005(6) and -0.027(4) kcal mol^{-1} $w\%^{-1}$, respectively.

Our results indicate that PEG promotes both nucleic acid secondary and tertiary folding by simultaneously increasing k_{fold} and decreasing k_{unfold}. However, the polysaccharide crowders, dextran and Ficoll show little to no effect on both nucleic acid folding equilibria and kinetics, i.e. corresponding to $\Delta\Delta G \approx 0$. This is already substantially different from results of several previous protein folding studies, where the prominent stabilization effects were observed and often attributed to crowding.[5] It is worth noting that the above differential results for the impact of dextran or Ficoll on nucleic acid folding could reflect two quite different scenarios. It could be that there is vanishingly small differential interaction enthalpy ($\Delta\Delta H^0 \approx 0$) between the solutes and the folded or unfolded biomolecule, in which case the observed $\Delta\Delta G^0 \approx 0$ would translate into $\Delta\Delta S^0 \approx 0$ and therefore no entropic crowding. However, $\Delta\Delta G^0 \approx 0$ could also reflect the coincidental balance between competing enthalpic and entropic contributions at a single temperature. Thus, an unambiguous determination of whether dextran and Ficoll have only minimal differential interactions with our folded/unfolded nucleic acid constructs requires additional van't Hoff and Arrhenius investigation of the temperature dependent equilibrium and kinetic behavior, as described below.

7.4.3 Crowding effects on DNA secondary structure folding thermodynamics

Conventional modelling of "pure" molecular crowding dynamics based on hard sphere excluded volume considerations explicitly ignores any chemical interactions between the crowder and the crowded species. As a result, such crowding dynamics automatically satisfy $\Delta(\Delta H^0) \approx 0$ (where

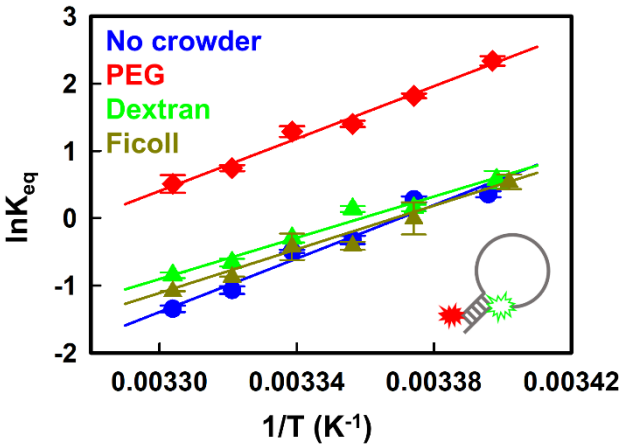

Figure 7.5 van't Hoff plot for the temperature dependent K_{eq} of the DNA hairpin construct at constant crowder concentrations (0 or 7.5 w%). Least squares fits of the data to Eq. 7.1 yield changes in overall enthalpies (ΔH^0) and entropies (ΔS^0).

the second Δ reflects the differential presence/absence of crowder) and should ideally contribute only entropically ($\Delta\Delta S^0 > 0$) to the overall folding free energy.[5, 17, 19] Herein we explore the temperature dependent response of nucleic acid folding to identify the thermodynamics of the solute-biomolecule crowder interactions. Specifically, van't Hoff analysis allows deconstruction of the folding free energies into entropy and enthalpy components via:

$$\ln(K_{eq}) = -\frac{\Delta G^0}{RT} = -\frac{\Delta H^0}{R}\frac{1}{T} + \frac{\Delta S^0}{R}. \qquad \text{Eq. 7.1}$$

From a standard $\ln(K_{eq})$ vs 1/T van't Hoff plot (e.g., see Figure 7.5), the slope and intercept permit independent quantitation of enthalpic ($-\Delta H^0/R$) and entropic ($\Delta S^0/R$) changes upon folding, respectively, which can be studied in the absence/presence of crowding agents.

In the absence of crowders, the DNA hairpin becomes less stable and unfolds with increasing temperature, consistent with temperature-induced melting/denaturation routinely observed for nucleic acid secondary structure.[49] Moreover, the linear van't Hoff plot reveals a

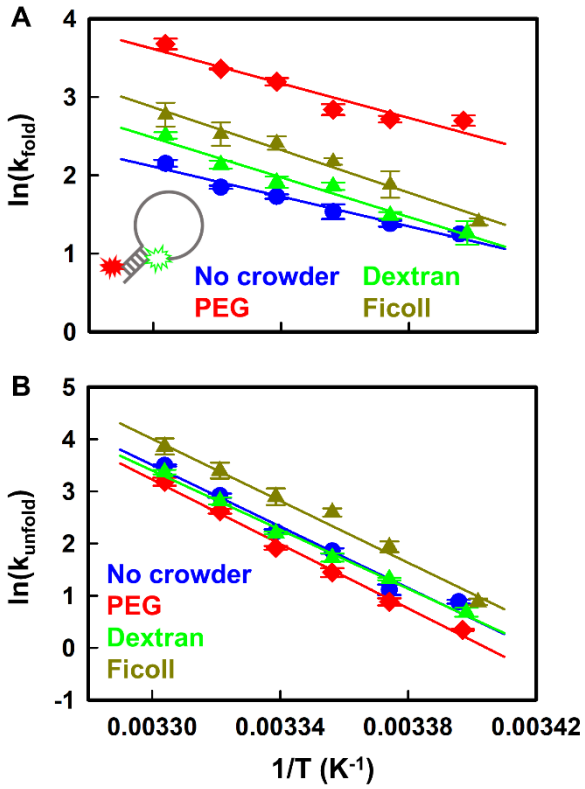

Figure 7.6 Eyring plot for the temperature dependent (**A**) k_{fold} and (**B**) k_{unfold} of the DNA hairpin construct at constant crowder concentrations (0 or 7.5 w%). Least squares fits of the data to Eq. 7.2 yield forward/reverse activation enthalpies ($\Delta H^{\ddagger}$) and entropies ($\Delta S^{\ddagger}$) for k_{fold}/k_{unfold}.

positive slope and a negative intercept (Figure 7.5), corresponding to negative folding enthalpy ($\Delta H^0 < 0$) and entropy ($\Delta S^0 < 0$) changes, respectively. Such free energy behavior agrees with the common physical picture of folding where biomolecules are enthalpically driven into the more order folded conformation.[33, 50] The presence of PEG vertically translates the linear fit upward with respect to zero-crowder conditions, suggesting a decrease in entropic penalty ($\Delta\Delta S^0 > 0$) with essentially unchanged enthalpic gain ($\Delta\Delta H^0 \approx 0$). Such predominantly entropic stabilization is of course consistent with crowding effects resulting from excluded volume.[5, 17, 19] By way of contrast, dextran and Ficoll clearly reveal a more complex temperature dependent

	ΔH^0 (kcal/mol)	ΔH^{0*} (kcal/mol)	ΔS^{0*} (cal/mol/K)	$\Delta H^{\ddagger}$ (kcal/mol)	$\Delta H^{\ddagger*}$ (kcal/mol)	$\Delta S^{\ddagger*}$ (cal/mol/K)
No crowder	-40 (3)	-40.1 (0.9)	-135 (2)	19.1 (1.5)	20.3 (0.6)	11 (2)
7.5 w% PEG	-39.7 (1.8)	-40.1 (0.9)	-131 (2)	21 (2)	20.3 (0.6)	16 (2)
7.5 w% Dextran	-31 (2)	-	-103 (9)	25 (2)	-	29 (7)
7.5 w% Ficoll	-32 (2)	-	-109 (7)	27.2 (1.8)	-	36 (5)

Table 7.1 Thermodynamic parameters of DNA hairpin folding obtained from van't Hoff and Eyring analyses**.** Asterisk (*) indicates results from global fits assuming a common slope (i.e., enthalpy change) between no crowder and 7.5 w% PEG data.

behavior, with a decrease in the slopes ($\Delta\Delta H^0 > 0$) and increase in the intercepts ($\Delta\Delta S^0 > 0$). Such non-zero enthalpic contributions clearly signal additional solute-specific chemical interactions, as well as changes in these interactions as a function of crowding environment.

In addition to these equilibrium results for K_{eq}, the folding rate constants k_{fold} and k_{unfold} also depend on temperature and contain equally valuable thermodynamic information. For secondary structure in the DNA hairpin, the data reveal a dramatic increase in both k_{fold} and k_{unfold} rate constants at elevated temperature (see Figure 7.6), signaling a significantly endothermic approach to the transition state from both folded/unfolded sides of the barrier. Based on results from other single molecule studies,[51] such an enthalpic penalty likely arises from competition between Coulomb repulsion of the negatively charged DNA strands and the lack of complete hydrogen bond formation in the transition state. The corresponding entropy changes can be obtained from the more sophisticated Eyring analysis of the temperature-dependent k_{fold}/k_{unfold} from the transition state expression:[52]

$$\ln(k) = -\frac{\Delta H^{\ddagger}}{R}\frac{1}{T} + \frac{\Delta S^{\ddagger}}{R} + \ln \nu, \qquad \text{Eq. 7.2}$$

where ν represents the attempt frequency sampling the free energy barrier along the folding coordinate. From such a standard Eyring plot of lnk vs 1/T (see Figure 7.6), the slopes and intercepts for $\ln k_{fold}$ or $\ln k_{unfold}$ correspond to the activation enthalpy ($-\Delta H^{\ddagger}/R$) and entropy ($\Delta S^{\ddagger}/R + \ln\nu$) from either the folded (F) or the unfolded (U) state, respectively. Since $\Delta S^{\ddagger}$ depends only weakly (logarithmically) on ν, it suffices in this work to simply estimate ν as a low frequency skeletal vibration with $\nu = 10^{13}$ s^{-1}.[29, 53] However, it is also worth noting that any reported changes in the activation entropy (i.e., $\Delta\Delta S^{\ddagger}$) are rigorously independent of this estimate for ν.

For the DNA hairpin, the presence or absence of PEG (red vs blue solid line, Figure 7.6) does not change the slopes in plots of both k_{fold} and k_{unfold}., with vertical shifts again signaling that PEG promotes secondary nucleic acid folding predominantly through "pure" crowding (i.e., entropic) effects. Furthermore, both the magnitude and sign of these uniform vertical displacements in $\ln k_{fold}$ vs. $\ln k_{unfold}$ are consistent with the PEG-dependent enhancement of folding stability observed at room temperature (Figure 7.2B and 7.2C). The polysaccharide crowders dextran and Ficoll, on the other hand, exhibit more complex behaviors, with the data now revealing significant changes in both slopes ($\Delta\Delta H^{\ddagger} > 0$) and intercepts ($\Delta\Delta S^{\ddagger} > 0$) in the Eyring plots for k_{fold}. Interestingly, however, these slope differences are much less evident for the unfolding step, which is consistent with polysaccharide solute effects primarily influencing the approach to the transition state from the unfolded conformation. Thermodynamic values (ΔH^0, ΔS^0, $\Delta H^{\ddagger}$, $\Delta S^{\ddagger}$) extracted from these plots for both PEG and polysaccharide solutes are quantitatively summarized in Table 7.1.

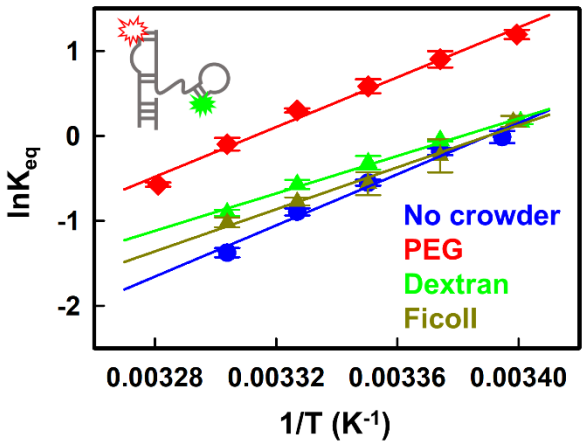

Figure 7.7 van't Hoff plot for the temperature dependent K_{eq} of the RNA -TL-TLR construct at constant crowder concentrations (0 or 7.5 w%). Least squares fits of the data to Eq. 7.1 yield changes in overall enthalpies (ΔH^0) and entropies (ΔS^0).

7.4.4 Crowding effects on RNA TL-TLR tertiary folding thermodynamics

As for many compact nucleic acid conformations, the TL-TLR tertiary binding motif weakens and unfolds with increasing temperature,[33] with the positive (negative) slope (intercept) in the van't Hoff plot (see Figure 7.7) indicating folding to be exothermically favored ($\Delta H^0 < 0$) and entropically penalized ($\Delta S^0 < 0$). Once again, the presence of PEG solute at high w% shifts the linear fits vertically upward without appreciable change in slope ($\Delta\Delta H^0 \approx 0$), which corresponds to a positive change in intercept ($\Delta\Delta S^0 > 0$). In other words, PEG *entropically* stabilizes the TL-TLR tertiary structure formation, consistent with a conventional excluded volume mechanism for molecular crowding.[17, 43] By way of contrast, the putative polysaccharide "crowders" dextran and Ficoll exhibit decreased slopes and increased intercepts in the van't Hoff plots, indicating significant solute-dependent differential enthalpic interactions, in addition to possible entropic crowding corresponding to a less exothermic ($\Delta\Delta H^0 > 0$) but more entropically favored ($\Delta\Delta S^0 > 0$) folding into the TL-TLR tertiary structure. It is particularly noteworthy that

the absence of polysaccharide "crowding" effects observed near room temperature for both the DNA hairpin and RNA TL-TLR constructs (Figure 7.3 and 7.4) is simply due to a fortuitous balance between entropic and enthalpic contributions. Indeed, the data in Figure 7.7 reveal that dextran and Ficoll at 7.5 w% can and do efficiently stabilize nucleic acid folding at higher (and presumably destabilize at lower) temperatures, but only via a temperature dependent imbalance in enthalpic and entropic contributions to the free energies. Such stabilization effects can be quite comparable to (and indeed easily mistaken for) pure entropic crowding if the temperature dependence is not also carefully explored and taken into account.

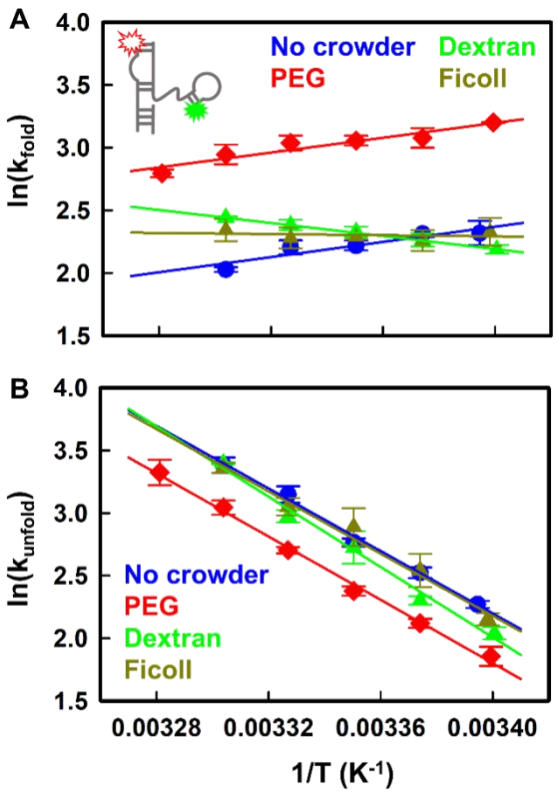

Figure 7.8 Eyring plots for the temperature dependent (**A**) k_{fold} and (**B**) k_{unfold} of the RNA TL-TLR construct at constant crowder concentrations (0 or 7.5 w%). Least squares fits of the data to Eq. 7.2 yield forward/reverse activation enthalpies ($\Delta H^{\ddagger}$) and entropies ($\Delta S^{\ddagger}$) for k_{fold}/k_{unfold}.

The temperature dependent kinetic data for k_{fold} and k_{unfold} again reiterate the predominantly entropic role of PEG stabilization on RNA tertiary folding, as indicated by parallel vertical shifts in the Eyring plots (Figure 7.8). Again, by way of contrast, dextran and Ficoll polysaccharides both show quite strong enthalpic and entropic effects on k_{fold}. Indeed, the Eyring plot slopes in Figure 7.8A for tertiary structure folding even change sign (from plus to minus), indicating that the presence of dextran and Ficoll transform a normally *exothermic* pre-folding approach into a significantly *endothermic* approach to the transition state ($\Delta H^{\ddagger} > 0$). Conversely, the temperature dependence of k_{unfold} (Figure 7.8B) for the TL-TLR construct is much less dramatic. Similar to the effects seen in k_{unfold} for secondary DNA hairpin structure, the presence/absence of polysaccharide solute for the TL-TLR generates much more subtle changes in the unfolding endothermicity during the U to TS transition. The list of parameters obtained from kinetic/thermodynamic analysis of the PEG vs polysaccharide solute dependence for tertiary TL-TLR folding/unfolding are summarized in Table 7.2.

	ΔH^0 (kcal/mol)	ΔH^{0*} (kcal/mol)	ΔS^{0*} (cal/mol/K)	$\Delta H^{\ddagger}$ (kcal/mol)	$\Delta H^{\ddagger*}$ (kcal/mol)	$\Delta S^{\ddagger*}$ (cal/mol/K)
No crowder	**-30 (2)**	**-29.5 (1.2)**	**-101 (4)**	**-6.0 (1.3)**	**-5.9 (0.7)**	**-75 (2)**
7.5 w% PEG	**-29.2 (1.6)**	**-29.5 (1.2)**	**-97 (3)**	**-5.9 (0.9)**	**-5.9 (0.7)**	**-72 (2)**
7.5 w% Dextran	**-21.9 (1.2)**	-	**-74 (3)**	**5.17 (0.11)**	-	**-37.6 (0.3)**
7.5 w% Ficoll	**-24.6 (1.7)**	-	**-83 (5)**	**0.5 (1.0)**	-	**-53 (3)**

Table 7.2 Thermodynamic parameters of RNA TL-TLR folding obtained from van't Hoff and Eyring analyses**.** Asterisk (*) indicates results from global fits assuming a common slope (i.e., enthalpy change) between no crowder and 7.5 w% PEG data.

7.5 Discussion

7.5.1 Crowder effects on nucleic acid folding kinetics

Crowders (or any solute) take up physical space in solution, reducing the volume and the corresponding number of microstates available for a nominally crowded biomolecule to sample.[3] For the same crowder/solute configuration, folded biomolecules (V_F) can generally sample more space than a non-compact unfolded (V_U) structure, where $V_U > V_F$;[2] thus, the presence of solute crowders entropically favors the more compact state of biomolecule.[21] Furthermore, if the transition state is considered as a partially folded conformation, we can further expect that $V_U > V_{TS} > V_F$. The crowding effect will favor the more compact TS state over U, thereby entropically lowering the free energy barrier for the U to TS transition and consequently increasing k_{fold}.[43] Similarly, k_{unfold} would be expected to decrease with added solute due to the compact F state being more efficiently stabilized by crowding with respect to the TS. In summary, molecular crowding is predicted to promote folding *entropically* by simultaneously increasing k_{fold} and decreasing k_{unfold}, which is entirely consistent with the PEG data for *exponential* enhancement of secondary and tertiary structure formation in nucleic acids (i.e., see Figure 7.3 and 7.4). By way of contrast, polysaccharides dextran and Ficoll at similar w% concentrations exhibit only quite modest effects on the folding/unfolding rate constants and equilibrium constants ($K_{eq} = k_{fold}/k_{unfold}$) for both the DNA hairpin and the RNA TL-TLR at room temperature. With respect to impact on nucleic acid folding/unfolding dynamics, the single molecule equilibrium/kinetic data reported herein indicate significant differential enthalpic interactions ($\Delta\Delta H \neq 0$) between the putative polysaccharide "crowders" dextran and Ficoll with nucleic acid constructs. We would argue that such behavior is inconsistent with conventional excluded volume model predictions, and thus dextran and Ficoll polysaccharides do not represent initiators of molecular crowding

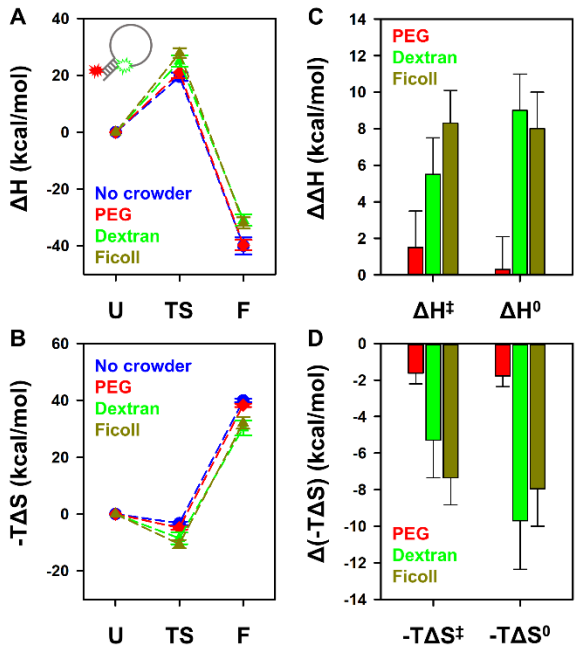

Figure 7.9 Folding free energy landscapes of the DNA hairpin construct. (**A**) Enthalpic and (**B**) entropic contributions along the folding coordinate, with the relative enthalpy/entropy of the unfold state, U conventionally referenced to zero. The corresponding (**C**) enthalpic and (**D**) entropic changes by the three crowders at 7.5 w%. Note that entropic contributions (-TΔS) to the free energies are estimated for room temperature conditions (21.0 °C).

phenomena for nucleic acids. Of course, this assessment depends on the nature of chemical interaction with the biomolecule being crowded. We cannot rule out the possibility that dextran and Ficoll have negligible differential chemical interactions between folded vs. unfolded proteins and therefore may act as truly entropic crowding agents.[16]

7.5.2 Predominantly entropic effects of PEG are consistent with pure crowding

Despite the fact that excluded volume effects are ubiquitous for all solutes, the resulting crowding can be buried in or dominated by additional solute- and/or biomolecule-specific enthalpic chemical interactions. The chemically and biologically inactive polymer PEG provides a valuable opportunity for us to identify and isolate pure crowding effects from these other more

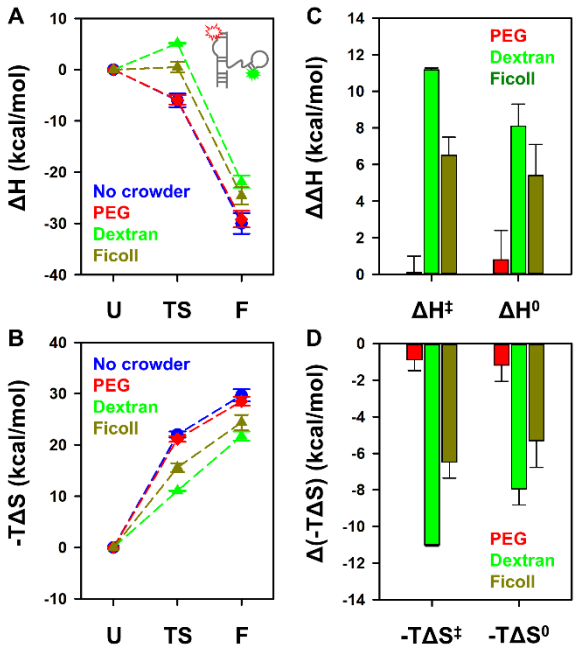

Figure 7.10 Folding free energy landscapes of the RNA TL-TLR construct. (**A**) Enthalpic and (**B**) entropic contributions along the folding coordinate with the relative enthalpy/entropy of the unfold state, U conventionally referenced to zero. The corresponding (**C**) enthalpic and (**D**) entropic changes by the three crowders at 7.5 w%. Note that entropic contributions (-TΔS) to the free energies are estimated for room temperature conditions (21.0 ℃).

complex solute-biomolecule interactions. The literature on this important topic is still evolving. To date, many studies have used PEG as the crowding agent and simply report the additional stabilization to be the result of crowding.[10, 40, 54-55] However, PEG has also been found to perturb folding enthalpies of some protein systems, implying the presence of solute-specific chemical interactions. [24-25] This differs yet again with multiple other studies on proteins[21] and nucleic acids[17, 20] claiming the effects of PEG to be primarily entropic and therefore reflect true crowding phenomena. Such a discrepancy would seem to indicate that crowding by PEG may depend significantly on the structure and chemical properties of the crowded biomolecules. This provides us with additional motivation for detailed characterization of the thermodynamic crowding effects of PEG, as applied to both secondary and tertiary structures of nucleic acids.

From the temperature dependent studies reported herein (Figure 7.5 to 7.8), we are able to deconstruct the folding free energy landscape into enthalpic and entropic contributions. Vertical shifts in the van't Hoff plots confirm that PEG only changes the folding entropy ($\Delta\Delta S^0 > 0$) and leaves the enthalpy unchanged ($\Delta\Delta H^0 \approx 0$) for both nucleic acid secondary (Figure 7.5) and tertiary (Figure 7.7) folding. The predominantly entropic stabilization effects of PEG are consistent with crowding originating from excluded volume interactions. Furthermore, from transition state analysis, the parallel nature of the Eyring plots for both k_{fold} and k_{unfold} again signal the predominantly entropic origins of PEG stabilization effects (Figure 7.6 and 7.8). It is worth noting that our ability to infer small enthalpic changes in these thermodynamic studies is limited by experimental uncertainties. We therefore cannot completely rule out the possibility of small interactions with PEG that could either weakly stabilize or destabilize the nucleic acid. Nevertheless, from previous work on RNA TL-TLR folding, the magnitude of such entropic effects[17] and their dependence on PEG polymer size[43] were successfully predicted by hard sphere models based purely on excluded volume interactions. Strengthened by additional confirming evidence for both nucleic acid secondary and tertiary folding from the temperature dependent kinetic studies, the data strongly suggest that the PEG crowding of nucleic acids can be largely attributed to true entropic crowding effects.

7.5.3 Enthalpic/entropic effects with polysaccharides suggest preferential binding

Polysaccharide crowders such as dextran and Ficoll are also commonly used in crowding studies, but primarily with proteins.[12] One early study found that lysozyme stability is entropically enhanced by the presence of dextran,[16] from which it was inferred that the effects on protein folding arose primarily from crowding. However, some recent studies have pointed out the additional presence of enthalpic interactions between dextran and Ficoll with certain protein

structures.[22-23, 56-57] This raises obvious questions for the role of such polysaccharides in the crowding of nucleic acid folding, which has received much less attention and remains poorly understood. This further motivates us to characterize the thermodynamic free energies, enthalpies, and entropies between model secondary and tertiary nucleic acid structure constructs and polysaccharides widely used in protein crowding studies, i.e., dextran and Ficoll.

For both secondary (DNA hairpin) and tertiary (RNA TL-TLR) nucleic acid structures, polysaccharide crowders dextran and Ficoll are found to significantly change enthalpic as well as the entropic contributions to the folding free energy landscape. From standard van't Hoff analysis (Figure 7.5 and 7.7), an increase in dextran and Ficoll concentration (0 to 7.5 w%) decreases the slope, indicating a reduction in overall exothermicity for folding ($\Delta\Delta H^0 > 0$), but with a corresponding increase in the intercept reflecting a reduction in entropic penalty ($\Delta\Delta S^0 > 0$). Moreover, from temperature dependent analysis (Figure 7.6 and 7.8), we find the effects of these polysaccharides on the folding kinetics to be primarily visible in the folding rate constant k_{fold}. Specifically, dextran and Ficoll are found to increase the folding activation enthalpy ($\Delta\Delta H^{\ddagger} > 0$), as well as the activation entropy ($\Delta\Delta S^{\ddagger} > 0$) during the approach from U to TS.

The overall folding free energy landscapes and the corresponding crowder-induced changes in the folding/activation enthalpies/entropies are conveniently summarized in Figure 7.9 and 10 for the secondary (DNA hairpin) and tertiary (RNA TL-TLR) structures, respectively. It is worth noting that along the folding coordinate, the enthalpic penalty ($\Delta\Delta H > 0$) is significant but competing with (and indeed, at room temperature, completely compensated by) a counterbalancing entropic stabilization ($\Delta(-T\Delta S) < 0$) (Figure 7.9A and 7.9B; Figure 7.10A and 7.10B), leading to a greatly reduced sensitivity in the folding kinetics and equilibrium to both dextran and Ficoll, at least at room temperature where all three Eyring and van't Hoff curves

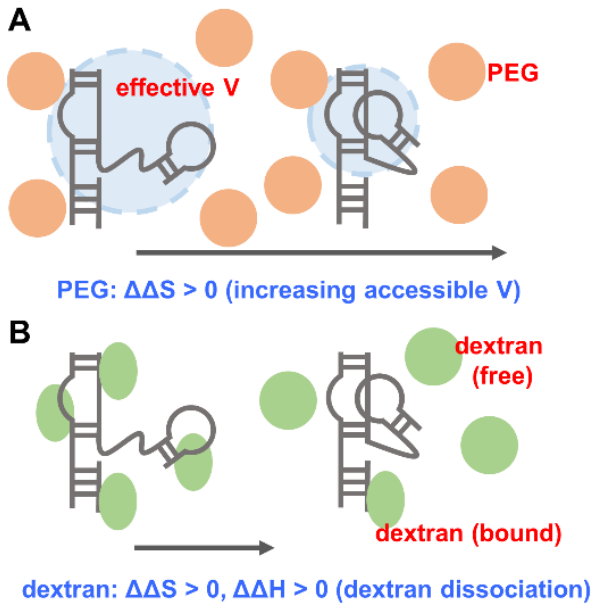

Figure 7.11 Schematic model for the effects of (**A**) PEG or (**B**) dextran on folding of the RNA TL-TLR, highlighting the differential entropic ($\Delta\Delta S > 0$) and enthalpic contributions ($\Delta\Delta H > 0$) due to binding of polysaccharide to the greater solvent accessible surface area (SASA) of the unfolded nucleic acid.

intersect in a single point. Such compensating tradeoffs in free energy between enthalpy and entropy[58] are of course quite ubiquitous in biophysics, but may provide a partial explanation for the mislabeling of polysaccharides as crowding agents for nucleic acids. In the present case, a potentially better qualitative interpretation for anticorrelation between enthalpic and entropic changes may be that the more enthalpically stabilized system is also more restrictive with respect to microstate-sampling: e.g. enthalpic binding of solute to the biomolecule diminishes the overall translational entropy of the solution system.[59]

Based on the thermodynamic evidence, we propose a simple binding model to account qualitatively for the simultaneous enthalpic destabilization ($\Delta\Delta H > 0$) and entropic stabilization ($\Delta(-T\Delta S) < 0$) effects of polysaccharides upon nucleic acid folding (Figure 7.11). First of all, we

expect the abundance of hydroxyl groups on the polysaccharide molecules to be overall attractive to the nucleic acid, in order to have significant impacts on the folding free energy. As a result, the polysaccharide solute will tend to accumulate on the accessible surface area of nucleic acid, enthalpically stabilizing the system at the cost of entropy primarily in the translational degrees of freedom of the bound polysaccharide and solvent reorganization. Upon folding, this solvent accessible surface area (SASA) of the nucleic acid decreases, requiring partial expulsion of the associated polysaccharide molecules. The net effect will be a less enthalpically stabilized folded structure ($\Delta\Delta H^0 > 0$) with entropic gain ($\Delta(-T\Delta S^0) < 0$) from freeing the polysaccharide molecules, much as reflected in the thermodynamic results summarized in Figure 7.9 and 7.10.

We can take this preferential binding model one step further to interpret the influence of polysaccharide crowders on the folding kinetics. Specifically, the transition state for TL-TLR folding has been previously characterized[29] as a tetraloop and tetraloop receptor in close proximity, but with unformed yet "pre-aligned" hydrogen bonds between the TL and TLR. This is clearly supported by the fact that the majority of the enthalpic stabilization occurs in the second half of the reaction coordinate as the TL-TLR evolves from the TS to the fully folded state (see Figure 7.10A). As a result, we would expect the majority of changes in SASA to take place as the two folding motifs are brought into contact along the approach from U to TS. By way of support, this would be entirely consistent with the fact that polysaccharide "crowders" primarily influence the temperature dependence of k_{fold}, rather than k_{unfold} (e.g., the slopes in Figure 7.8). Furthermore, as a result of limited changes in SASA between the TS and F states, the model also correctly predicts the unfolding rate constant (k_{unfold}) to be largely insensitive to differential enthalpic contributions from dextran and Ficoll binding, which is again nicely consistent with the temperature dependent data in Figure 7.8. Indeed, the similar impacts of all

three crowders revealed in Figure 7.8B signals the relatively minor role of enthalpic contributions on k_{unfold}. As a result, at least the *unfolding kinetics* for these secondary and tertiary nucleic acid constructs appear to be dominated by more purely entropic, excluded volume effects for both PEG and Ficoll/dextran polysaccharide polymers (Figure 7.4C).

7.6 Summary and conclusion

Temperature-controlled smFRET confocal microscopy has been used to study the kinetics of solute-biomolecule interactions for common molecular crowding agents, PEG, dextran and Ficoll, in order to explore/interpret the thermodynamics effects of crowding on nucleic acid secondary (DNA hairpin) and tertiary (RNA TL-TLR) structures. Room temperature kinetic analysis reveals that PEG promotes nucleic acid folding by simultaneously increasing k_{fold} and decreasing k_{unfold}, qualitatively consistent with predictions from purely entropic crowding effects due to excluded volume interactions. By way of contrast, polysaccharide crowders, dextran and Ficoll do not significantly impact either the equilibria or kinetics of nucleic acid folding at room temperature. From temperature dependent studies, this thermodynamic stabilization at 7.5 w% PEG is found to be predominantly entropic ($\Delta\Delta S > 0$) with only negligible enthalpic ($\Delta\Delta H \approx 0$) contributions, again perfectly consistent with excluded volume models of crowding. Again, by way of contrast, the presence of 7.5 w% dextran and Ficoll significantly influences both folding enthalpies as well as entropies, suggesting solute-specific chemical interactions which we attribute to preferential binding of polysaccharide with the larger solvent accessible surface area of the unfolded nucleic acid construct. The results indicate the presence of PEG promotes nucleic acid folding predominantly through purely

entropic crowding effects without enthalpic contributions. However, these studies also reveal dextran and Ficoll to perturb the folding free energy landscape for nucleic acid folding in more complicated ways, by differential enthalpic contributions to the folded vs unfolded conformations ($\Delta\Delta H \neq 0$) that compete with the purely entropic crowding effects ($\Delta\Delta S > 0$) arising from simple excluded volume models. The results highlight the power of temperature dependent single molecule FRET microscopy studies for access to and allowing systematic deconstruction of free energy landscapes into enthalpic and entropic contributions.

7.7 References

1. Fulton, A. B., How Crowded is the Cytoplasm? *Cell* **1982,** *30* (2), 345-347.

2. Ellis, R. J., Macromolecular Crowding: Obvious but Underappreciated. *Trends Biochem. Sci.* **2001,** *26* (10), 597-604.

3. Minton, A. P., The Influence of Macromolecular Crowding and Macromolecular Confinement on Biochemical Reactions in Physiological Media. *J. Biol. Chem.* **2001,** *276* (14), 10577-10580.

4. Gnutt, D.; Ebbinghaus, S., The Macromolecular Crowding Effect – from *in vitro* into the Cell. *Biol. Chem.* **2016,** *397* (1), 37-44.

5. Minton, A. P., Excluded Volume as a Determinant of Macromolecular Structure and Reactivity. *Biopolymers* **1981,** *20* (10), 2093-2120.

6. Gnutt, D.; Gao, M.; Brylski, O.; Heyden, M.; Ebbinghaus, S., Excluded-Volume Effects in Living Cells. *Angew. Chem.* **2015,** *54* (8), 2548-2551.

7. Cheung, M. S.; Klimov, D.; Thirumalai, D., Molecular Crowding Enhances Native State stability and Refolding Rates of Globular Proteins. *Proc. Natl. Acad. Sci. U.S.A.* **2005,** *102* (13), 4753.

8. Zheng, K.-w.; Chen, Z.; Hao, Y.-h.; Tan, Z., Molecular Crowding Creates an Essential Environment for the Formation of Stable G-Quadruplexes in Long Double-Stranded DNA. *Nucleic Acids Res.* **2009,** *38* (1), 327-338.

9. Miyoshi, D.; Sugimoto, N., Molecular Crowding Effects on Structure and Stability of DNA. *Biochimie* **2008,** *90* (7), 1040-1051.

10. Tokuriki, N.; Kinjo, M.; Negi, S.; Hoshino, M.; Goto, Y.; Urabe, I.; Yomo, T., Protein Folding by the Effects of Macromolecular Crowding. *Protein Sci.* **2004,** *13* (1), 125-133.

11. Denos, S.; Dhar, A.; Gruebele, M., Crowding Effects on the Small, Fast-Folding Protein λ_{6-85}. *Faraday Discuss.* **2012,** *157* (0), 451-462.

12. Politou, A.; Temussi, P. A., Revisiting a Dogma: the Effect of Volume Exclusion in Molecular Crowding. *Curr. Opin. Struct. Biol.* **2015,** *30*, 1-6.

13. Blümmel, J.; Perschmann, N.; Aydin, D.; Drinjakovic, J.; Surrey, T.; Lopez-Garcia, M.; Kessler, H.; Spatz, J. P., Protein Repellent Properties of Covalently Attached PEG Coatings on Nanostructured SiO2-Based Interfaces. *Biomaterials* **2007,** *28* (32), 4739-4747.

14. Schulz, A.; Woolley, R.; Tabarin, T.; McDonagh, C., Dextran-Coated Silica Nanoparticles for Calcium-Sensing. *Analyst* **2011,** *136* (8), 1722-1727.

15. Kilburn, D.; Roh, J. H.; Guo, L.; Briber, R. M.; Woodson, S. A., Molecular Crowding Stabilizes Folded RNA Structure by the Excluded Volume Effect. *J. Am. Chem. Soc* **2010,** *132* (25), 8690-8696.

16. Sasahara, K.; McPhie, P.; Minton, A. P., Effect of Dextran on Protein Stability and Conformation Attributed to Macromolecular Crowding. *J. Mol. Biol.* **2003,** *326* (4), 1227-1237.

17. Dupuis, N. F.; Holmstrom, E. D.; Nesbitt, D. J., Molecular-Crowding Effects on Single-Molecule RNA Folding/Unfolding Thermodynamics and Kinetics. *Proc. Natl. Acad. Sci. U.S.A.* **2014,** *111* (23), 8464.

18. Minton, A. P., Models for Excluded Volume Interaction between an Unfolded Protein and Rigid Macromolecular Cosolutes: Macromolecular Crowding and Protein Stability Revisited. *Biophys. J.* **2005,** *88* (2), 971-985.

19. Christiansen, A.; Wittung-Stafshede, P., Synthetic Crowding Agent Dextran Causes Excluded Volume Interactions Exclusively to Tracer Protein Apoazurin. *FEBS Lett.* **2014,** *588* (5), 811-814.

20. Kilburn, D.; Behrouzi, R.; Lee, H.-T.; Sarkar, K.; Briber, R. M.; Woodson, S. A., Entropic Stabilization of Folded RNA in Crowded Solutions Measured by SAXS. *Nucleic Acids Res.* **2016,** *44* (19), 9452-9461.

21. Halpin, J. C.; Huang, B.; Sun, M.; Street, T. O., Crowding Activates Heat Shock Protein 90. *J. Biol. Chem.* **2016,** *291* (12), 6447-6455.

22. Mukherjee, S.; Waegele, M. M.; Chowdhury, P.; Guo, L.; Gai, F., Effect of Macromolecular Crowding on Protein Folding Dynamics at the Secondary Structure Level. *J. Mol. Biol.* **2009,** *393* (1), 227-236.

23. Benton, L. A.; Smith, A. E.; Young, G. B.; Pielak, G. J., Unexpected Effects of Macromolecular Crowding on Protein Stability. *Biochem.* **2012,** *51* (49), 9773-9775.

24. Senske, M.; Törk, L.; Born, B.; Havenith, M.; Herrmann, C.; Ebbinghaus, S., Protein Stabilization by Macromolecular Crowding through Enthalpy Rather Than Entropy. *J. Am. Chem. Soc* **2014,** *136* (25), 9036-9041.

25. Das, N.; Sen, P., Shape-Dependent Macromolecular Crowding on the Thermodynamics and Microsecond Conformational Dynamics of Protein Unfolding Revealed at the Single-Molecule Level. *J. Phys. Chem. B* **2020,** *124* (28), 5858-5871.

26. Miyoshi, D.; Nakao, A.; Sugimoto, N., Molecular Crowding Regulates the Structural Switch of the DNA G-Quadruplex. *Biochem.* **2002,** *41* (50), 15017-15024.

27. Knowles, D. B.; LaCroix, A. S.; Deines, N. F.; Shkel, I.; Record, M. T., Separation of Preferential Interaction and Excluded Volume Effects on DNA Duplex and Hairpin Stability. *Proc. Natl. Acad. Sci. U.S.A.* **2011,** *108* (31), 12699.

28. Nakano, S.-i.; Miyoshi, D.; Sugimoto, N., Effects of Molecular Crowding on the Structures, Interactions, and Functions of Nucleic Acids. *Chem. Rev.* **2014,** *114* (5), 2733-2758.

29. Fiore, J. L.; Holmstrom, E. D.; Nesbitt, D. J., Entropic Origin of Mg^{2+}-Facilitated RNA Folding. *Proc. Natl. Acad. Sci. U.S.A.* **2012,** *109* (8), 2902.

30. Sung, H.-L.; Nesbitt, D. J., Novel Heat-Promoted Folding Dynamics of the *yybP-ykoY* Manganese Riboswitch: Kinetic and Thermodynamic Studies at the Single-Molecule Level. *J. Phys. Chem. B* **2019,** *123* (26), 5412-5422.

31. Nicholson, D. A.; Sengupta, A.; Sung, H.-L.; Nesbitt, D. J., Amino Acid Stabilization of Nucleic Acid Secondary Structure: Kinetic Insights from Single-Molecule Studies. *J. Phys. Chem. B* **2018,** *122* (43), 9869-9876.

32. Sung, H.-L.; Nesbitt, D. J., DNA Hairpin Hybridization under Extreme Pressures: A Single-Molecule FRET Study. *J. Phys. Chem. B* **2020,** *124* (1), 110-120.

33. Fiore, J. L.; Kraemer, B.; Koberling, F.; Edmann, R.; Nesbitt, D. J., Enthalpy-Driven RNA Folding: Single-Molecule Thermodynamics of Tetraloop−Receptor Tertiary Interaction. *Biochem.* **2009,** *48* (11), 2550-2558.

34. Aitken, C. E.; Marshall, R. A.; Puglisi, J. D., An Oxygen Scavenging System for Improvement of Dye Stability in Single-Molecule Fluorescence Experiments. *Biophys. J.* **2008,** *94* (5), 1826-1835.

35. Sengupta, A.; Sung, H.-L.; Nesbitt, D. J., Amino Acid Specific Effects on RNA Tertiary Interactions: Single-Molecule Kinetic and Thermodynamic Studies. *J. Phys. Chem. B* **2016,** *120* (41), 10615-10627.

36. Sung, H.-L.; Nesbitt, D. J., Sequential Folding of the Nickel/Cobalt Riboswitch Is Facilitated by a Conformational Intermediate: Insights from Single-Molecule Kinetics and Thermodynamics. *J. Phys. Chem. B* **2020,** *124* (34), 7348-7360.

37. Holmstrom, E. D.; Nesbitt, D. J., Biophysical Insights from Temperature-Dependent Single-Molecule Förster Resonance Energy Transfer. *Annu. Rev. Phys. Chem.* **2016,** *67* (1), 441-465.

38. Sung, H.-L.; Nesbitt, D. J., Single-Molecule Kinetic Studies of DNA Hybridization Under Extreme Pressures. *Phys. Chem. Chem. Phys.* **2020,** *22* (41), 23491-23501.

39. Fiore, J. L.; Holmstrom, E. D.; Fiegland, L. R.; Hodak, J. H.; Nesbitt, D. J., The Role of Counterion Valence and Size in GAAA Tetraloop–Receptor Docking/Undocking Kinetics. *J. Mol. Biol.* **2012,** *423* (2), 198-216.

40. Baltierra-Jasso, L. E.; Morten, M. J.; Laflör, L.; Quinn, S. D.; Magennis, S. W., Crowding-Induced Hybridization of Single DNA Hairpins. *J. Am. Chem. Soc* **2015,** *137* (51), 16020-16023.

41. Patra, S.; Schuabb, V.; Kiesel, I.; Knop, J.-M.; Oliva, R.; Winter, R., Exploring the Effects of Cosolutes and Crowding on the Volumetric and Kinetic Profile of the Conformational Dynamics of a Poly dA Loop DNA Hairpin: a Single-Molecule FRET Study. *Nucleic Acids Res.* **2018,** *47* (2), 981-996.

42. Vander Meulen, K. A.; Davis, J. H.; Foster, T. R.; Record, M. T.; Butcher, S. E., Thermodynamics and Folding Pathway of Tetraloop Receptor-Mediated RNA Helical Packing. *J. Mol. Biol.* **2008,** *384* (3), 702-717.

43. Sung, H.-L.; Sengupta, A.; Nesbitt, D., Smaller Molecules Crowd Better: Crowder Size Dependence Revealed by Single-Molecule FRET Studies and Depletion Force Modeling Analysis. *J. Chem. Phys.* **2021,** *154* (15), 155101.

44. Greene, R. F.; Pace, C. N., Urea and Guanidine Hydrochloride Denaturation of Ribonuclease, Lysozyme, *α*-Chymotrypsin, and *b*-Lactoglobulin. *J. Biol. Chem.* **1974,** *249* (17), 5388-5393.

45. Holmstrom, E. D.; Dupuis, N. F.; Nesbitt, D. J., Kinetic and Thermodynamic Origins of Osmolyte-Influenced Nucleic Acid Folding. *J. Phys. Chem. B* **2015,** *119* (9), 3687-3696.

46. Yi, Q.; Scalley, M. L.; Simons, K. T.; Gladwin, S. T.; Baker, D., Characterization of the Free Energy Spectrum of Peptostreptococcal Protein L. *Fold. Des.* **1997,** *2* (5), 271-280.

47. Shelton, V. M.; Sosnick, T. R.; Pan, T., Applicability of Urea in the Thermodynamic Analysis of Secondary and Tertiary RNA Folding. *Biochem.* **1999,** *38* (51), 16831-16839.

48. Auton, M.; Bolen, D. W., Predicting the Energetics of Osmolyte-Induced Protein Folding/Unfolding. *Proc. Natl. Acad. Sci. U.S.A.* **2005,** *102* (42), 15065.

49. Wartell, R. M.; Benight, A. S., Thermal Denaturation of DNA Molecules: A Comparison of Theory with Experiment. *Phys. Rep.* **1985,** *126* (2), 67-107.

50. Privalov, P. L., Thermodynamics of Protein Folding. *J. Chem. Thermodyn.* **1997,** *29* (4), 447-474.

51. Dupuis, Nicholas F.; Holmstrom, Erik D.; Nesbitt, David J., Single-Molecule Kinetics Reveal Cation-Promoted DNA Duplex Formation Through Ordering of Single-Stranded Helices. *Biophys. J.* **2013,** *105* (3), 756-766.

52. Zhou, H.-X., Rate Theories for Biologists. *Q. Rev. Biophys.* **2010,** *43* (2), 219-293.

53. Szabo, A.; Schulten, K.; Schulten, Z., First Passage Time Approach to Diffusion Controlled Reactions. *J. Chem. Phys.* **1980,** *72* (8), 4350-4357.

54. Paudel, B. P.; Rueda, D., Molecular Crowding Accelerates Ribozyme Docking and Catalysis. *J. Am. Chem. Soc* **2014,** *136* (48), 16700-16703.

55. Tyrrell, J.; Weeks, K. M.; Pielak, G. J., Challenge of Mimicking the Influences of the Cellular Environment on RNA Structure by PEG-Induced Macromolecular Crowding. *Biochem.* **2015,** *54* (42), 6447-6453.

56. Sharma, G. S.; Mittal, S.; Singh, L. R., Effect of Dextran 70 on the Thermodynamic and Structural Properties of Proteins. *Int. J. Biol. Macromol.* **2015,** *79*, 86-94.

57. Malik, A.; Kundu, J.; Mukherjee, S. K.; Chowdhury, P. K., Myoglobin Unfolding in Crowding and Confinement. *J. Phys. Chem. B* **2012,** *116* (43), 12895-12904.

58. Dunitz, J. D., Win Some, Lose Some: Enthalpy-Entropy Compensation in Weak Intermolecular Interactions. *Chem. Biol.* **1995,** *2* (11), 709-712.

59. Eftink, M. R.; Anusiem, A. C.; Biltonen, R. L., Enthalpy-Entropy Compensation and Heat Capacity Changes for Protein-Ligand Interactions: General Thermodynamic Models and Data for the Binding of Nucleotides to Ribonuclease A. *Biochem.* **1983,** *22* (16), 3884-3896.

Chapter 8

Synergism in the Molecular Crowding of Ligand-Induced Riboswitch Folding: Kinetic/Thermodynamic Insights from Single Molecule FRET Spectroscopy

---

8.1 Abstract

Conformational dynamics in riboswitches involves ligand binding and folding of the RNA, each of which can be influenced by excluded volume effects under "crowded" *in vivo* cellular conditions and thus incompletely characterized by *in vitro* studies under dilute buffer conditions. In this work, temperature-dependent single molecule FRET spectroscopy is used to characterize the thermodynamics of i) lysine ligand and ii) molecular crowders (PEG, polyethylene glycol) on folding of the *B. subtilis LysC* lysine riboswitch. With the help of detailed kinetic analysis, we isolate and study effects of PEG on lysine binding and riboswitch folding individually, from which we find that PEG crowding facilitates riboswitch folding primarily via a surprising *increase in affinity for the cognate ligand*. This is furthermore confirmed by temperature dependent studies which reveal that PEG crowding is not purely entropic and instead significantly impacts both enthalpic and entropic contributions to the free energy landscape for folding. The results indicate that PEG molecular crowding/stabilization of the lysine riboswitch is more mechanistically complex and requires extension beyond the conventional picture of purely repulsive solvent-solute steric interactions arising from excluded volume and entropy. Instead, the current experimental FRET data supports an alternative multistep mechanism whereby PEG first entropically crowds the unfolded riboswitch into a "pre-

*This chapter is adapted from: Sung, H.-L.; Nesbitt, D. J Synergism in the Molecular Crowding of Ligand-Induced Riboswitch Folding: Kinetic/Thermodynamic Insights from Single-Molecule Spectroscopy. *J. Phys. Chem. B* **2022**, *126*, 6419-6427.

folded" conformation, which in turn greatly increases the ligand binding affinity, and thereby enhances the overall equilibrium for riboswitch folding.

8.2 Introduction

Intracellular environments are highly concentrated with various kinds of solutes ranging from small molecule metabolites to macromolecule proteins and nucleic acids.[1] All these solutes impose ubiquitous steric constraints (such as excluded volume) that affect both biomolecular structure and function.[2-3] Simply summarized, the presence of solute limits the space available for the biomolecule to sample and thereby entropically favors any conformations that occupy smaller volume.[4] Such steric stabilization toward more compact biomolecule structures is often referred to as molecular crowding.[5-6]

Most biochemical studies are performed in dilute buffer, which differs significantly from the *in vivo* intracellular environment where biomolecules actually function. In order to correctly interpret these *in vitro* observations, therefore, it is crucial to characterize and understand the effects of crowding on biomolecular systems.[7-9] Experimentally, polymeric crowders such as PEG (polyethylene glycol) and dextran (polysaccharide) are often introduced into biological buffers to mimic the intracellular crowding environment.[10] Consistent with simple crowding expectations, the presence of such polymers favors the more compact biomolecular conformation.[11] Interestingly, many of these studies identified the origin of such polymer stabilization[12-14] to be largely entropic in nature, suggesting that the interaction between polymer crowders and a crowded biomolecule occurs predominantly via the effective "repulsion" due to pure excluded volume effects.[15]

Riboswitches are RNA elements that regulate gene expression in response to ligand concentrations in the cell.[16-17] In particular, folding of the lysine riboswitch is found to be facilitated by ligand through an induced-fit (IF, "bind-then-fold") mechanism,[18-19] whereby the presence of the lysine binding lowers the free energy activation barrier and thereby promotes subsequent folding of the riboswitch. As indicated in Figure 8.1A, the binding of lysine (with dissociation constant K_d) is prerequisite for the riboswitch folding; the lysine-associated riboswitch can then fold and unfold at the rate of k_{fold} and $k_{unfold,}$ respectively. Since molecular crowding effects can in principle impact both binding and folding steps,[20-24] this necessitates further study into kinetic and thermodynamic mechanisms for crowding and ligand-induced riboswitch folding, in order to deconstruct their respective influences on riboswitch function and resulting gene expression.

In this work, we explore the effects of PEG on the lysine riboswitch folding with single molecule FRET spectroscopy. In the context of simple nucleic acid constructs, PEG has been found to facilitate secondary and tertiary folding via predominantly entropic effects,[25] which would be consistent with a "hard sphere" physical picture of crowding. Specifically, previous PEG crowding studies as a function of temperature highlight the negligible role of differential enthalpic effects in RNA/DNA conformational change. From detailed kinetic analysis of the single molecule data, however, one can characterize the overall riboswitch folding by two sequential mechanistic pathways: i) ligand binding and ii) subsequent conformational change of the lysine riboswitch,[26] thereby motivating study of the impact of PEG crowding on each of these processes separately. Moreover, single molecule experiments as a function of temperature enable further deconstruction of free energies and free energy barriers into enthalpic and entropic contributions along the folding coordinate.[27] As a result, the work potentially provides new

thermodynamic and kinetic insights into the effect of molecular crowding on both RNA-small molecule binding and evolution of the lysine riboswitch from unfolded to "pre-folded" to folded confirmations.

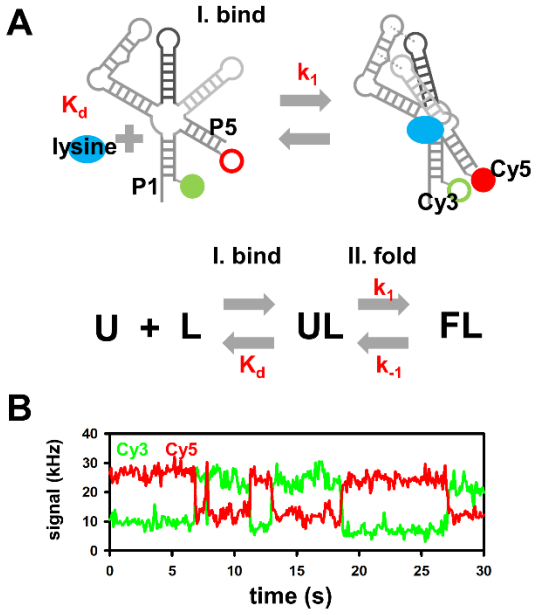

Figure 8.1 Schematic presentation of lysine riboswitch single molecule FRET construct folding. (A) The induced-fit mechanism of lysine riboswitch folding where I. lysine binding is followed by II. the riboswitch conformational change (U = unfolded riboswitch, F = folded riboswitch, and L = lysine). Note that folding brings Cy3 and Cy5 closer and thereby increases the FRET energy transfer efficiency (E_{FRET}). (B) Sample time dependent fluorescent signal. The conformational change is visualized by the anticorrelation between the Cy3 and Cy5 signal, which results in E_{FRET} changes.

8.3 Experiment

8.3.1 Lysine riboswitch construct and sample preparation

In this work, we use a modified *B. subtilis lysC* lysine riboswitch[28] as a model system to explore the effect of crowding on ligand-induced RNA folding. The doubly dye-labeled and biotinylated RNA construct is synthesized by annealing three strands of nucleic acid oligomers together (Figure 8.1A, the biotinylated P1 extension not shown).[18] The distal ends of stem P1 and P5 are labeled with the cyanine dyes Cy3 and Cy5, respectively to maximize the E_{FRET} (FRET

energy transfer efficiency) contrast during the conformational change in response to lysine.[29] Details of the RNA sequences and synthesis methods can be found in previous work.[18] We note that the conformational change of the model construct is consistent with the wild type riboswitch as the E_{FRET} values can be predicted from the crystal structure.[28] The ligand affinity of the model construct is about 1 to 2 orders of magnitudes lower than the wild type riboswitch, which has the dissociation constant $K_D \approx 1$ μM.[30] Such a discrepancy can be simply attributed to the typically higher Mg^{2+} concentration (20 mM) used in the structural analysis (e.g., in-line probing) of the wild type RNA.[30]

To prepare samples for single molecule experiments, the coverslip sample holder is first incubated with 10% biotinylated BSA (bovine serum albumin) to prevent non-specific binding. A second incubation step results in sufficient streptavidin attachment to the coverslip, with surface tethering of the riboswitch construct achieved by biotin-streptavidin association. Single molecule fluorescence experiments are performed under buffer conditions with (i) 50 mM HEPES (pH 7.5), 100 mM NaCl, 50 mM KCl and 0.5 mM $MgCl_2$ to provide sufficient background cations and maintain the buffer pH, (ii) Trolox/PCA/PCD oxygen scavenger system to enhance fluorophore photostability,[31] and (iii) additional lysine and PEG 3K (average molecular weight ≈ 3000 amu) to achieve desired experimental crowding conditions.

8.3.2 Temperature-controlled single molecule experiment and data analysis

The present single molecule FRET experiments have been performed with a through-objective total internal reflection fluorescence (TIRF) microscope, with details described elsewhere.[32] In brief, a 532 nm laser beam is directed through a high numerical aperture oil-immersion microscope objective, with a mirror set for parallel translation of the beam with respect to the objective axis to increase the incident angle and thereby achieve total internal

reflection illumination of fluorescent RNA constructs immobilized at the coverslip-water interface. The resulting fluorescence from the sample is then collected by the same wide-field objective, split by a dichroic mirror into Cy3 and Cy5 channels, and focused onto a charge-coupled device (CCD) video camera, with which data are collected in a video format at a 20 Hz acquisition framerate (Figure 8.1B).

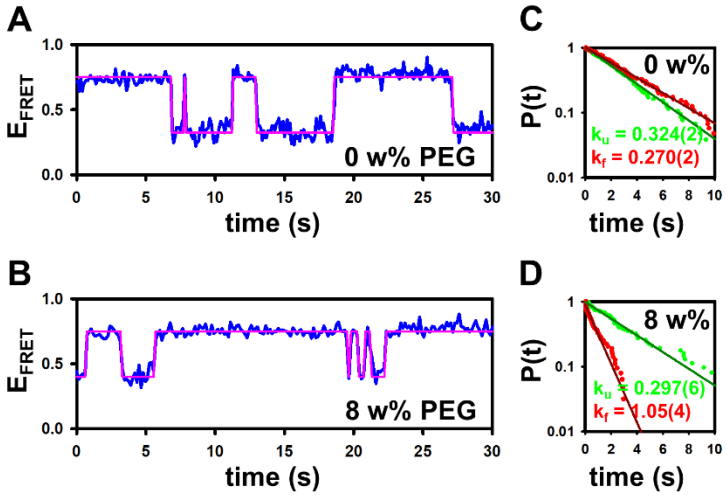

Figure 8.2 Sample E_{FRET} trajectories and dwell time analysis. (A) E_{FRET} trajectories without PEG. (B) E_{FRET} trajectories with 8 w% PEG. Note that the construct spends significantly more time in the high E_{FRET} state corresponding to the folded conformation. (C) Dwell time analysis without PEG. (D) Dwell time analysis with 8 w% PEG. The cumulative distribution function of the unfolded dwell time decays much more rapidly, corresponding to accelerated k_{fold}.

Single molecule fluorescent traces are obtained from the recorded movie by custom analysis software with background correction to generate the resulting E_{FRET} time trajectory (see sample data in Figure 8.2A and 8.2B). A standard hidden Markov modeling method is used to identify transitions between the folded (E_{FRET} ~ 0.7) and the unfolded (E_{FRET} ~ 0.3 to 0.4) conformations and thereby to acquire individual dwell times.[33] The folding equilibrium constant K_{fold} can be readily extracted as the ratio of total folding and unfolding dwell times ($K_{fold} = T_{fold}/T_{unfold}$), from which the folded fraction F_{fold} can be calculated ($F_{fold} = T_{fold}/(T_{fold} + T_{unfold})$).

The folding (k_{fold}) and unfolding (k_{unfold}) rate constants themselves can be obtained from analysis of the corresponding dwell time distributions for t_{unfold} and t_{fold} (see sample data in Figure 8.2C and 2D), respectively.[34] Cumulative distributions for both t_{fold} and t_{unfold} are well fit to single exponential decay functions, consistent with folding and unfolding of the lysine riboswitch well described by simple first order kinetics. Note that each cumulative distribution function (N = 3) consists of dwell times obtained from ≈ 10 individual molecules within 1 or 2 surface scans. The uncertainties (e.g., error bars in Figure 8.3 to 8.7) are reported as the standard deviation of the mean. We believe the major source of measurement uncertainties is the sample heterogeneity, along with minor contributions from fitting errors and temperature fluctuation.

The temperature-controlled single molecule studies are achieved with the help of thermoelectric cooling/heating modules under servo loop control, as described in previous work.[32] Both the sample and microscope objective are cooled/heated simultaneously to minimize any thermal gradients across the sample, with sample temperatures measured (to ± 0.1 ℃ accuracy) by a calibrated resistance thermometer.

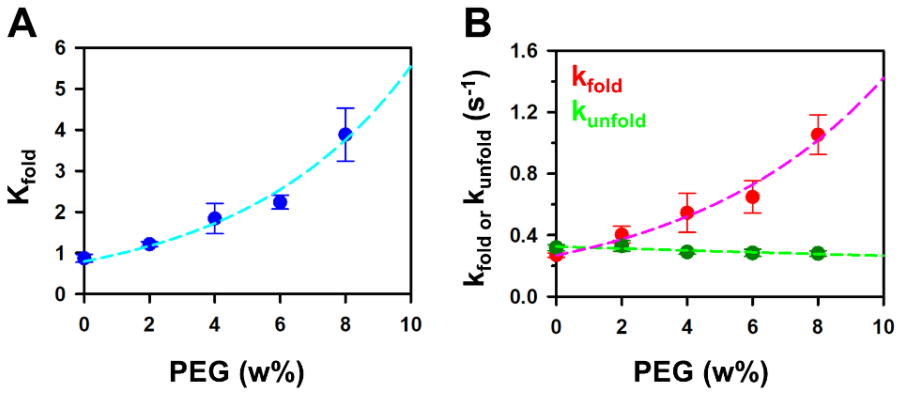

Figure 8.3 PEG-dependent lysine riboswitch folding at a constant lysine concentration (1 mM). (A) folding equilibrium and (B) kinetics as a function of PEG concentration. Data are fit to a single exponential function to highlight the rapid rise of K_{fold} and k_{fold} with increasing PEG concentration.

8.4 Results and analysis

8.4.1 Lysine riboswitch folding promoted by PEG

Previous studies have shown that folding kinetics of the lysine riboswitch follows an induced-fit (IF) mechanism,[18-19] whereby lysine binding is an essential prerequisite for the riboswitch to fold. Under 1.0 mM lysine conditions, the riboswitch spends roughly equal average amounts of time in the high E_{FRET} (E_{FRET} ~ 0.7) and low E_{FRET} (E_{FRET} ~ 0.3) states, corresponding to the folded and unfolded conformations, respectively (Figure 8.2A). Additional 8 w% (percentage by weight) of PEG significantly promotes equilibrium folding of the riboswitch, as evident in the greatly enhanced time durations the fluorescent construct spends in the high E_{FRET} state (Figure 8.2B). Furthermore, at constant 1 millimolar lysine concentration, K_{fold} increases monotonically (Figure 8.3A) with systematically increasing PEG, again consistent with crowding promotion of the folded riboswitch conformation under equilibrium conditions.

In addition to the above equilibrium data, however, an even greater wealth of information on single molecule biophysical kinetics is revealed in dwell time distributions for each fluorescence trajectory. In particular, kinetic information in these single molecule fluorescence trajectories can be obtained from logarithmic dwell time analysis of the cumulative probability distributions,[34] with sample data under low (0 w% PEG) and high (8 w% PEG) crowding conditions displayed in Figure 8.2C and 8.2D. These data make clear that PEG dramatically increases the folding rate (k_{fold}, in red) and decreases the unfolding rate (k_{unfold}, in green) of the lysine riboswitch (Figure 8.3B). In particular, the crowding effects are much stronger on the folding vs. unfolding step. Specifically, there is a nearly 400% increase in k_{fold} between 0 and 8 w% PEG concentrations, over which range k_{unfold} is reduced by only 10%.

8.4.2 PEG stabilization on lysine dependent folding illustrated by kinetic modeling

Here we implement a more detailed kinetic analysis to highlight the PEG effect on the ligand response of the riboswitch folding.[26] In previous work, folding of the lysine riboswitch was found to be initiated by ligand association, followed by RNA conformational change in a "bind-then-fold" induced fit (IF) mechanism.[18-19] The simplified IF folding pathway is illustrated in Figure 8.1A, where K_d reflects the dissociation constant of lysine and k_1/k_{-1} correspond to unimolecular forward/backward rate constants for overall conformational changes in the riboswitch construct.

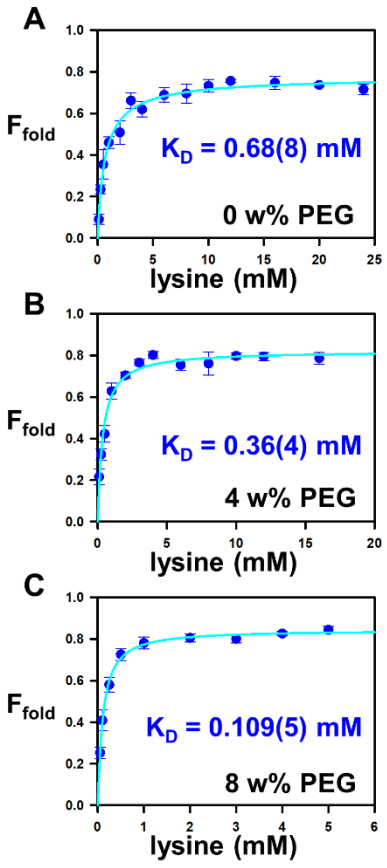

Figure 8.4 Lysine-dependent folding curves at a series of PEG concentrations. Folded fraction F_{fold} as a function of lysine with (A) 0 w%, (B) 4 w%, and (C) 8 w% PEG. Data are nonlinear least squares fit to the Hill equation (Eq. 8.1).

We first focus on the equilibrium folding behavior by studying the folded fraction $F_{fold} = \frac{T_{fold}}{T_{fold}+T_{unfold}}$ as a function of lysine at constant PEG concentration (Figure 8.4). As expected, the data indicate linear growth in F_{fold} at low ligand concentration and eventual saturation at high lysine. More surprising is the dependence of these curves on crowder, with the saturation plateau quite insensitive to PEG from 0 to 8 w%, yet with the lysine binding affinity increasing by nearly an order of magnitude over the same range of crowding conditions. Simply summarized, the main role of PEG as molecular crowder appears to be through promotion of the lysine-riboswitch binding interaction, which in turn facilitates subsequent folding of the riboswitch. It's worth noting that the enhancement of bimolecular association is expected from PEG crowding. To highlight more quantitatively the impact of PEG on lysine-induced riboswitch folding, the data can be fit to the Hill equation[35]

$$F_{fold} = F_{max} \times \frac{[lysine]^{n_1}}{K_D{}^{n_1}+[lysine]^{n_1}} \qquad \text{Eq. 8.1}$$

where n_1 is the Hill coefficient, K_D is the effective dissociation constant for lysine binding, and F_{max} corresponds to the maximal F_{fold} value under saturated lysine conditions. Since K_D corresponds to the lysine concentration for which $F_{fold} = F_{max}/2$, a smaller K_D value reflects a more effective lysine promotion of riboswitch folding. The fitting results are summarized in Table 8.1 for 0 to 8 w% PEG crowder conditions, over which K_D reduces from 0.68(8) mM from 0.109(5) mM, corresponding to an equivalent 7-fold efficiency increase in lysine promoted riboswitch folding with a $n_1 \approx 1$ (i.e., non-cooperative) Hill coefficient.

	K_D (mM)	n_1	F_{max}
0 w% PEG	0.68(8)	0.91(9)	0.77(2)
4 w% PEG	0.36(4)	1.02(12)	0.82(2)
8 w% PEG	0.109(5)	1.08(6)	0.843(10)

Table 8.1 Least squares fit results for the lysine-induced folding equilibria.

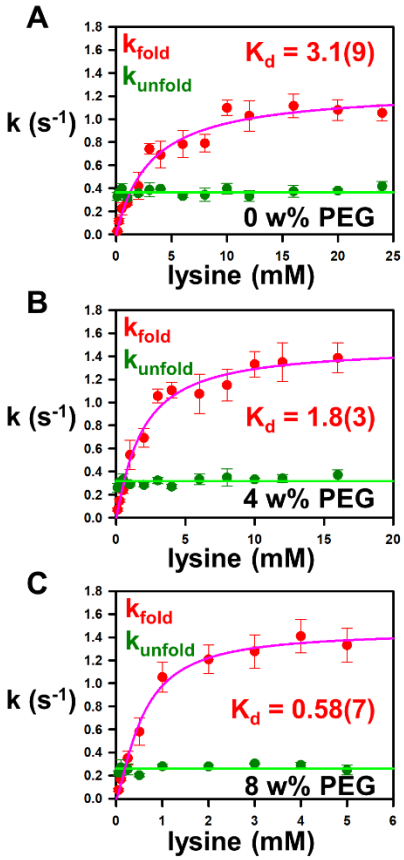

Figure 8.5 Lysine-dependent folding and unfolding rates at a series of PEG concentrations. Folding rate constants k_{fold}/k_{unfold} as a function of lysine with (A) 0 w%, (B) 4 w%, and (C) 8 w% PEG. The k_{fold} data are fit to the Hill-like kinetic equation (Eq. 8.2), while the lysine-independent k_{unfold} data are fit with a horizontal line.

The kinetic promotion of lysine-induced riboswitch folding can also be investigated via statistical analysis of the dwell time distributions (see Figure 8.5), for which the effective folding rate constant (k_{fold}) increases as a function of lysine and eventually reaches a saturation plateau. By way of contrast, the unfolding rate constant k_{unfold} is completely insensitive to lysine and remains constant over a wide range of ligand concentrations.[18] Such kinetic results are in fact entirely consistent with an induced-fit mechanism, whereby lysine promotes riboswitch folding through a "bind-then-fold" process.[18-19] Specifically for such a simplified kinetic model (see Figure 8.1A), increase in lysine concentration simply shifts the equilibrium toward a higher

fraction in the ligand bound state, thereby promoting the effective unimolecular folding rate k_{fold} up to the limiting velocity of k_1. Conversely, the effective unimolecular unfolding rate k_{unfold} simply reflects k_{-1} and remains independent of lysine concentration.[26] By solving the kinetic equations assuming rapid equilibration with respect to lysine binding, the data can be fit to an independent Hill equation for k_{fold}[26]

$$k_{fold} = k_1 \times \frac{[lysine]^{n_2}}{{K_d}^{n_2} + [lysine]^{n_2}} \qquad \text{Eq. 8.2}$$

where again n_2 is a Hill coefficient, K_d is the lysine dissociation constant and k_1 corresponds to the maximal k_{fold} value under saturating ligand conditions. Similar to the results discussed above for folding/unfolding equilibrium constant properties, we find that the addition of PEG crowder significantly increases the efficiency for lysine binding (i.e., reduces K_d) and in turn facilitates folding of the lysine riboswitch. Interestingly, by way of comparison only relatively modest PEG effects on the elemental folding/unfolding rate processes are observed, with 8 w% PEG concentrations increasing/decreasing the unimolecular folding (k_1)/unfolding (k_{-1}) rate constants by only 10%/40%, respectively. Such relatively modest changes in the intrinsic rates are consistent with crowding,[14] with fits of the kinetic data to Eq. 8.2 summarized in Table 8.2. However, it is worth stressing that the predominant impact of molecular crowding from this mechanistic perspective arises from a 7x decrease in K_d (i.e., 700% enhancement of ligand binding to the riboswitch).

	K_d (mM)	n_2	k_1 (s^{-1})	k_{-1} (s^{-1})
0 w% PEG	3.1(9)	1.00(19)	1.26(13)	0.367(8)
4 w% PEG	1.8(3)	1.12(17)	1.48(10)	0.317(9)
8 w% PEG	0.58(7)	1.34(17)	1.45(6)	0.262(11)

Table 8.2 Least squares fit results for the lysine-induced folding kinetics.

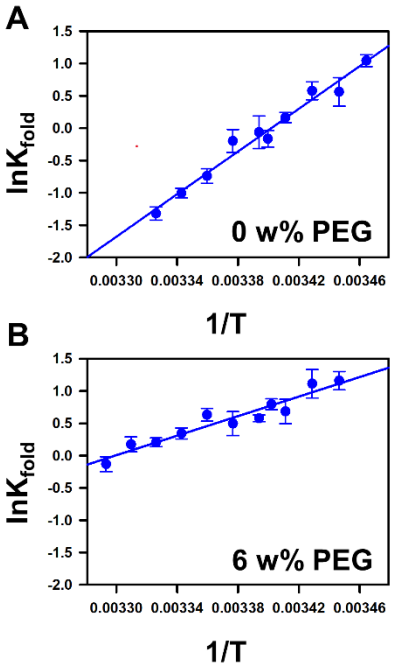

Figure 8.6 van't Hoff plots for the temperature dependent lysine riboswitch folding at (A) 0 w% PEG and (B) 6 w% PEG. [lysine] = 1 mM.

8.4.3 Temperature-dependent folding reveals both enthalpic and entropic PEG effects

We can take such equilibrium and kinetic analyses one important step further by performing temperature dependent smFRET folding experiments, which permit deconstruction of overall (ΔG^0) and transition state ($\Delta G^{\ddagger}$) free energies into enthalpic (ΔH) and entropic (ΔS) contributions as a function of PEG crowder concentrations. First of all, studies in absence of crowder reveal that unfolding of the lysine riboswitch is strongly favored with increasing temperature, specifically 10-fold reduction in the overall equilibrium constant K_{fold} over a modest 12 °C temperature range. Quantitative thermodynamic information for the corresponding folding enthalpy and entropies can be extracted from a simple van't Hoff analysis, i.e.,

$$lnK_{fold} = -\frac{\Delta H^0}{R}\frac{1}{T} + \frac{\Delta S^0}{R}. \qquad \text{Eq. 8.3}$$

As summarized in the sample data in Figure 8.6A, B, overall folding of the lysine riboswitch at both low (0 w%) and high (6 w%) crowder conditions is found to be exothermic (ΔH^0 = -32.8(18) and -15.0(14) kcal/mol, respectively) and yet entropically penalized ($-T\Delta S^0$ = -111(5) and -50(3) cal/mol/K), consistent with a simple physical picture of folding whereby biomolecules are enthalpically encouraged to fold into a more ordered (lower entropy) state.[36] Of particular interest, however, the addition of 6 w% PEG (Figure 8.6B) decreases and increases the slopes vs. intercepts, respectively, corresponding to incremental PEG-induced increase in *both* ΔH^0 and ΔS^0 ($\Delta\Delta H^0 > 0$ and $\Delta\Delta S^0 > 0$). Simply stated, the presence of PEG crowder reduces the thermodynamic advantage of folding exothermicity and yet also lowers the entropic penalty for folding of the lysine riboswitch. We will return to this important issue in the discussion section, but for the moment emphasize that such changes in overall exothermicity ($\Delta\Delta H^0 > 0$) with PEG

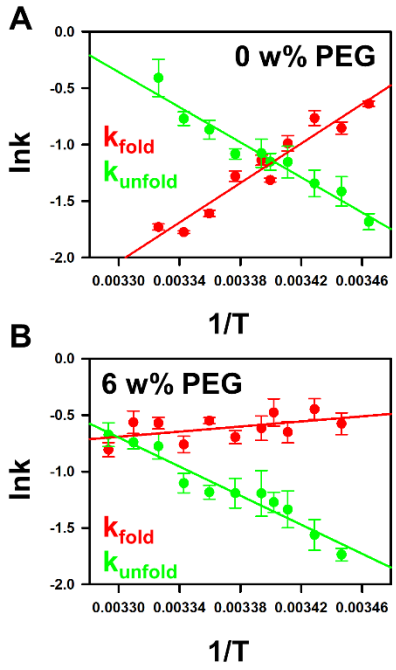

Figure 8.7 Eyring plots for the temperature dependent lysine riboswitch folding at (A) 0 w% PEG and (B) 6 w% PEG. [lysine] = 1 mM.

concentration *are inconsistent with a purely excluded volume interpretation of crowding*, for which the driving forces are predicted to be purely entropic ($\Delta\Delta S^0 > 0$).

There is of course additional thermodynamic information in the temperature-dependence of the kinetic rate constants themselves. Specifically, if we make the plausible assumption of a single rate-limiting transition state, we can similarly analyze the temperature-dependent kinetic data with transition state/Eyring theory[37-39]

$$lnk = -\frac{\Delta H^{\ddagger}}{R}\frac{1}{T} + \frac{\Delta S^{\ddagger}}{R} + \ln \nu \qquad \text{Eq. 8.4}$$

where $\Delta H^{\ddagger}$ and $\Delta S^{\ddagger}$ represent enthalpic and entropic differences, respectively, between the transition state and the folded/unfolded states of the riboswitch. In Eq 3, ν represents the attempt frequency (set to be 10^{13} s^{-1} in our analysis) to access the transition barrier along the folding/unfolding coordinate,[40] though the extracted value of $\Delta S^{\ddagger}$ is only logarithmically dependent on such a choice. Despite the fact that any absolute entropy change associated with surmounting the transition state barrier will depend weakly on the choice of ν, any differential changes in entropy ($\Delta\Delta S^{\ddagger}$) induced by PEG crowding remain rigorously independent of any such logarithmic offset.

As clearly evident in Figure 8.7A, the logarithmic rate constant from such an Arrhenius analysis for folding of the lysine riboswitch increases linearly with 1/T. The slope in Figure 8.7A (red line) implies that folding of the riboswitch releases heat ($\Delta H_{fold}^{\ddagger} \approx -17.3(16)$ kcal/mol) in accessing the transition state, while the negative intercept ($\Delta S_{fold}^{\ddagger} \approx -121(3)$ cal/mol/K) indicates an entropic TS barrier ($-T\Delta S_{fold}^{\ddagger} > 0$) in the absence of crowding conditions. In the presence of 6 w% PEG crowder (see Figure 8.7B), slope and intercept of the Eyring plot change rather dramatically for k_{fold}, corresponding to a significant differential decrease in both exothermicity ($\Delta\Delta H_{fold}^{\ddagger} > 0$) and entropic cost ($-T\Delta\Delta S_{fold}^{\ddagger} < 0$) for access to the folding

transition state. Of particular interest and in contrast with the riboswitch folding kinetics, however, the presence of 6 w% PEG molecular crowders results in very modest effects on the temperature dependence of k_{unfold}, with therefore only small crowding-induced changes in enthalpy ($\Delta\Delta H_{unfold}^{\ddagger} \approx 0$) and entropy ($(-T\Delta\Delta S_{unfold}^{\ddagger} \approx 0$) required to reach the transition state from the fully folded lysine riboswitch conformation.

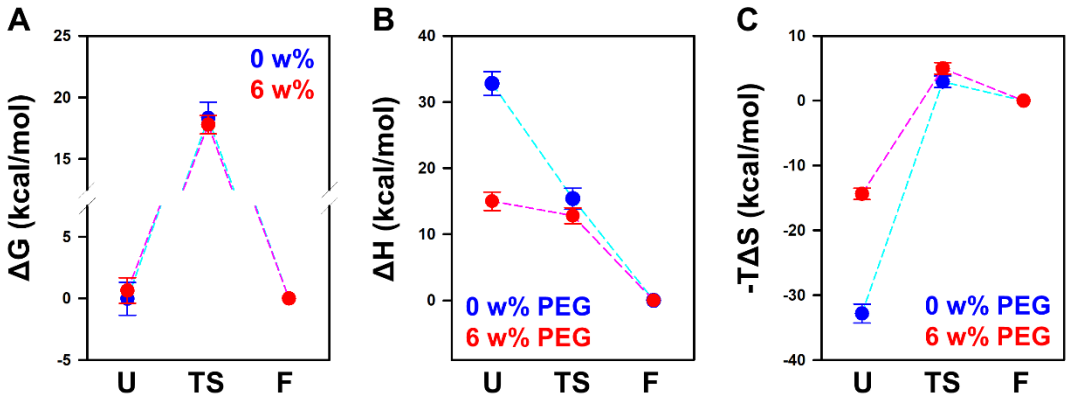

Figure 8.8 Free energy landscapes for lysine riboswitch folding. PEG effects on the (A) free energy, (B) enthalpic, and (C) entropic contributions along the folding coordinate (U = unfolded state, TS = transition state, and F = folded state). Values are arbitrarily referenced to zero for the folded state F.

8.5 Discussion

8.5.1 Kinetic vs. thermodynamic crowding data indicate conflicting solute interaction models

We have shown the lysine riboswitch folding can be promoted by increasing PEG concentration, which is entirely consistent with crowding effects, where the presence of PEG favors the more compact state.[13-14] From the perspective of the solute interaction model, such PEG-enhanced structure formation can simply result from generic repulsion between PEG and the RNA.[41] Specifically, the biomolecule might tend to adopt the more compact conformation in

order to reduce the solvent-accessible surface area (SASA) and in turn decrease overall unfavorable solute-biomolecule contact.[42-43] Taking these ideas one step further, if this repulsion were shown to be predominantly steric (i.e. entropic) in nature, it can be unambiguously attributed to the crowding effects originating from excluded volume.[13] However, the significant slope changes in the van' Hoff plots in Figure 8.6 signal differential enthalpic contributions and may suggest a more complex solute effect which we can explore further.

The thermodynamic parameters obtained from the temperature dependence are summarized in Figure 8.8, where the relative enthalpy and entropy of each state are plotted along the simplified folding coordinate, with the folded state F referenced to zero.[35] It is shown that PEG exerts effects (red vs blue) predominantly on the (forward) folding activation enthalpy ($\Delta H_{fold}^{\ddagger}$) and entropy ($\Delta S_{fold}^{\ddagger}$), while leaving the relative free energy contributions between the transition state and the folded state largely unperturbed (Figure 8.8B and 8.8C). Furthermore, the shifts in Figure 8.8 suggest the unfolded conformation is enthalpically stabilized and entropically destabilized by PEG with respect to the transition/folded states. From the physical picture of a simple solute interaction model, such a free energy change corresponds to increase in PEG association with the unfolded conformation of larger SASA.[25] In other words, our thermodynamic analysis reveals an overall attraction (favorable contact) between PEG and the riboswitch.

Indeed, solvent-solute interactions represent a simple yet efficient way to understand solute-promoted biomolecule folding/unfolding. However, the thermodynamic results for preferential PEG solvation of the unfolded state clearly contradict the general repulsion between PEG and RNA predicted from the PEG enhanced lysine riboswitch folding. It is in fact unusual for favorable PEG-RNA contacts to enhance folding, which requires increasing the area of the

RNA-RNA interface. Such discrepancies suggest solute interactions alone are insufficient to account for our present findings, with a much more likely hybrid folding mechanism required for the observed changes in both entropy and enthalpy with crowding conditions.

8.5.2 PEG prearranges the unfolded riboswitch to facilitate folding

Careful inspection of the E_{FRET} trajectories in Figure 8.2 show the low E_{FRET} state of the lysine riboswitch shifts to a slightly higher value (from ≈ 0.3 to 0.4, as illustrated in Figure 8.9) by PEG when the riboswitch becomes more folded. Such an observation indicates PEG may not only promote the overall riboswitch folding, but also alter the structure of the unfolded (relatively low E_{FRET}) state. Similar behavior is also observed in previous single molecule studies of the lysine riboswitch,[18, 29, 44] where the low E_{FRET} value increases in response to buffer conditions that promote folding. Moreover, one study is able to resolve the low E_{FRET} population of the same *lysC* riboswitch into (i) the fully unfolded, and (ii) the lysine-free pre-folded states.[44] We therefore suspect that equilibrium between the unresolved low E_{FRET} conformations may have significant impact on our thermodynamic analysis.

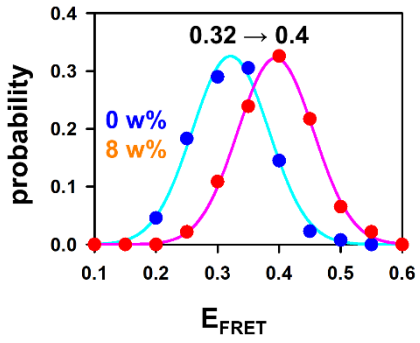

Figure 8.9 Normalized E_{FRET} distribution of the low E_{FRET} population with 0 w% PEG (blue) and 8 w% PEG (red). Bin size = 0.05.

Although we are unable to resolve, assign, and deconvolute these low E_{FRET} conformations in the kinetics, we can treat the low E_{FRET} state as an average of (1) the fully

unfolded and (2) the pre-folded conformations, as the simplest physical model to understand the thermodynamic consequence. The slightly elevated E_{FRET} value indicates PEG drives the equilibrium from the unfolded to a "pre-folded" lysine riboswitch, which is consistent with the common observation of PEG promoting the formation of structure. Since the low E_{FRET} state is already partially folded by PEG, we therefore expect a lower enthalpic gain accompanied by a lower entropic penalty for folding, with these predictions clearly confirmed in Figure 8.8. Moreover, the previous study has demonstrated that this pre-folded state has stronger lysine affinity and thus higher tendency to fold,[44] which agrees completely with the rapidly decreasing lysine dissociation constants (K_D and K_d) by PEG observed in our detailed kinetic analysis (Figure 8.4). It is worth noting that a similar mechanism of solute facilitating folding by "pre-organization" of the unfolded state has also been observed in several riboswitch systems.[26, 34, 45] The addition of a postulated pre-folded state provides a more reasonable and plausible mechanism with which to explain the present kinetic and thermodynamic data. Since the thermodynamics of lysine riboswitch folding is dominated by rapid equilibrium between the two low E_{FRET} (unfolded/prefolded) conformations, we lose the information on the PEG-RNA interaction except for the fact that PEG increases the overall riboswitch (pre-)folding. It's been previously shown that the interactions between PEG and nucleic acid secondary/tertiary structures are predominantly entropic and therefore consistent with crowding via fundamental excluded volume interactions.[25] In fact, it was surprising in this study to see any PEG-dependent differential enthalpy effects for lysine riboswitch folding, as we do not expect significant changes in thermodynamic properties between simple nucleic acid folding motifs to the more complex structure of a riboswitch.[46-47] With the partially folded state included as part of the low E_{FRET} population, we cannot rule out excluded volume effects as the predominant reason behind

any PEG-dependent changes in riboswitch conformation, despite significant enthalpic contributions to the overall thermodynamics. In fact, the observation that the lysine-saturated folding (k_1)/unfolding (k_{-1}) rate constants increase/decrease, respectively, as a function of PEG concentration is entirely consistent with simple crowding predictions.[14] This prompted our suggestion of an alternative albeit simple three-state (unfolded ⇌ "prefolded" ⇌ folded) kinetic mechanism whereby crowding is able to manifest itself via both enthalpic and entropic changes in the thermodynamics, in addition to recapitulating the physically correct kinetic and thermodynamic basis for PEG-promoted lysine riboswitch folding.

8.6 Summary and conclusions

We use the single molecule FRET methods to characterize the ligand-induced RNA folding motif in response to common crowding agent PEG, for which PEG promotes the overall RNA folding by increasing k_{fold} and decreasing k_{unfold} simultaneously. With detailed kinetic analysis, we find the most prominent PEG effect is to facilitate the lysine binding and thereby promote the overall structural change of the riboswitch. Such kinetic effects are consistent with a simple physical picture of repulsive interactions between PEG and the surface of the riboswitch and/or lysine. However, the reduced exothermicity and entropic penalty for folding observed in the temperature dependent studies suggests that PEG preferentially solvates the unfolded state due to its larger surface area.[48] Such a discrepancy suggests the PEG effects cannot be simply understood by the very common physical picture of purely "repulsive" solute-biomolecule interactions. Further motivated by additional structural information from small E_{FRET} shifts, we therefore propose a simple physical model with an additional "pre-folded" low E_{FRET} state that nicely accounts for both the thermodynamic and kinetic findings. In the model, PEG prearranges

the unfolded conformation of the riboswitch and shifts the E_{FRET} to slightly higher values, as evidence in our single molecule E_{FRET} trajectories. From our kinetic analysis, we find the more fold-like but ligand-free riboswitch has a much higher tendency to bind a lysine molecule and proceed to fold. On the other hand, the partially formed riboswitch structure also reduces the folding exothermicities and entropic penalties as seen in the temperature dependent studies. Furthermore, the proposed three-state model provides an alternative mechanism for purely entropic crowding to induce secondary changes in the overall RNA folding enthalpy that are consistent with experimental observation. Although this will require confirmation by additional single molecule temperature dependent studies, the net effect is an extension of simple excluded volume models that can correctly predict both entropic and enthalpic contributions to the crowding process occurring in cellular environment.

8.7 References

1. Fulton, A. B., How Crowded is the Cytoplasm? *Cell* **1982,** *30* (2), 345-347.

2. Minton, A. P., Excluded Volume as a Determinant of Macromolecular Structure and Reactivity. *Biopolymers* **1981,** *20* (10), 2093-2120.

3. Ellis, R. J., Macromolecular Crowding: Obvious but Underappreciated. *Trends Biochem. Sci.* **2001,** *26* (10), 597-604.

4. Minton, A. P., The Influence of Macromolecular Crowding and Macromolecular Confinement on Biochemical Reactions in Physiological Media. *J. Biol. Chem.* **2001,** *276* (14), 10577-10580.

5. Nakano, S.-i.; Miyoshi, D.; Sugimoto, N., Effects of Molecular Crowding on the Structures, Interactions, and Functions of Nucleic Acids. *Chem. Rev.* **2014,** *114* (5), 2733-2758.

6. Cheung, M. S.; Klimov, D.; Thirumalai, D., Molecular Crowding Enhances Native State Stability and Refolding Rates of Globular Proteins. *Proc. Natl. Acad. Sci. U.S.A.* **2005,** *102* (13), 4753-4758.

7. Gnutt, D.; Ebbinghaus, S., The Macromolecular Crowding Effect – from in vitro into the Cell. *Biol. Chem.* **2016,** *397* (1), 37-44.

8. Zhou, H.-X.; Rivas, G.; Minton, A. P., Macromolecular Crowding and Confinement: Biochemical, Biophysical, and Potential Physiological Consequences. *Annu. Rev. Biophys.* **2008,** *37* (1), 375-397.

9. Rivas, G.; Minton, A. P., Macromolecular Crowding In Vitro, In Vivo, and In Between. *Trends Biochem. Sci.* **2016,** *41* (11), 970-981.

10. Politou, A.; Temussi, P. A., Revisiting a Dogma: the Effect of Volume Exclusion in Molecular Crowding. *Curr. Opin. Struct. Biol.* **2015,** *30*, 1-6.

11. Minton, A. P., Models for Excluded Volume Interaction between an Unfolded Protein and Rigid Macromolecular Cosolutes: Macromolecular Crowding and Protein Stability Revisited. *Biophys. J.* **2005,** *88* (2), 971-985.

12. Sasahara, K.; McPhie, P.; Minton, A. P., Effect of Dextran on Protein Stability and Conformation Attributed to Macromolecular Crowding. *J. Mol. Biol.* **2003,** *326* (4), 1227-1237.

13. Dupuis, N. F.; Holmstrom, E. D.; Nesbitt, D. J., Molecular-Crowding Effects on Single-Molecule RNA Folding/Unfolding Thermodynamics and Kinetics. *Proc. Natl. Acad. Sci. U.S.A.* **2014,** *111* (23), 8464-8469.

14. Sung, H.-L.; Sengupta, A.; Nesbitt, D., Smaller Molecules Crowd Better: Crowder Size Dependence Revealed by Single-Molecule FRET Studies and Depletion Force Modeling Analysis. *Chem. Phys.* **2021,** *154* (15), 155101.

15. Kilburn, D.; Roh, J. H.; Guo, L.; Briber, R. M.; Woodson, S. A., Molecular Crowding Stabilizes Folded RNA Structure by the Excluded Volume Effect. *J. Am. Chem. Soc.* **2010,** *132* (25), 8690-8696.

16. Nudler, E.; Mironov, A. S., The Riboswitch Control of Bacterial Metabolism. *Trends Biochem. Sci.* **2004,** *29* (1), 11-17.

17. Mironov, A. S.; Gusarov, I.; Rafikov, R.; Lopez, L. E.; Shatalin, K.; Kreneva, R. A.; Perumov, D. A.; Nudler, E., Sensing Small Molecules by Nascent RNA: A Mechanism to Control Transcription in Bacteria. *Cell* **2002,** *111* (5), 747-756.

18. Fiegland, L. R.; Garst, A. D.; Batey, R. T.; Nesbitt, D. J., Single-Molecule Studies of the Lysine Riboswitch Reveal Effector-Dependent Conformational Dynamics of the Aptamer Domain. *Biochemistry* **2012,** *51* (45), 9223-9233.

19. Marton Menendez, A.; Nesbitt, D. J., Lysine-Dependent Entropy Effects in the *B. subtilis* Lysine Riboswitch: Insights from Single-Molecule Thermodynamic Studies. *J. Phys. Chem. B* **2021**.

20. Zimmerman, S. B.; Harrison, B., Macromolecular Crowding Increases Binding of DNA Polymerase to DNA: an Adaptive Effect. *Proc. Natl. Acad. Sci. U.S.A.* **1987,** *84* (7), 1871-1875.

21. Ralston, G. B., Effects of "Crowding" in Protein Solutions. *J. Chem. Educ.* **1990,** *67* (10), 857.

22. Qu, Y.; Bolen, D. W., Efficacy of Macromolecular Crowding in Forcing Proteins to Fold. *Biophys. Chem.* **2002,** *101-102*, 155-165.

23. Tokuriki, N.; Kinjo, M.; Negi, S.; Hoshino, M.; Goto, Y.; Urabe, I.; Yomo, T., Protein Folding by the Effects of Macromolecular Crowding. *Protein Sci.* **2004,** *13* (1), 125-133.

24. Batra, J.; Xu, K.; Qin, S.; Zhou, H.-X., Effect of Macromolecular Crowding on Protein Binding Stability: Modest Stabilization and Significant Biological Consequences. *Biophys. J.* **2009,** *97* (3), 906-911.

25. Sung, H.-L.; Nesbitt, D. J., Effects of Molecular Crowders on Single-Molecule Nucleic Acid Folding: Temperature-Dependent Studies Reveal True Crowding vs Enthalpic Interactions. *J. Phys. Chem. B* **2021,** *125* (48), 13147-13157.

26. Sung, H.-L.; Nesbitt, D. J., Single-Molecule FRET Kinetics of the Mn^{2+} Riboswitch: Evidence for Allosteric Mg^{2+} Control of "Induced-Fit" vs "Conformational Selection" Folding Pathways. *J. Phys. Chem. B* **2019,** *123* (9), 2005-2015.

27. Fiore, J. L.; Holmstrom, E. D.; Nesbitt, D. J., Entropic Origin of Mg^{2+}-Facilitated RNA Folding. *Proc. Natl. Acad. Sci. U.S.A.* **2012,** *109* (8), 2902-2907.

28. Garst, A. D.; Héroux, A.; Rambo, R. P.; Batey, R. T., Crystal Structure of the Lysine Riboswitch Regulatory mRNA Element *J. Biol. Chem.* **2008,** *283* (33), 22347-22351.

29. Sung, H.-L.; Nesbitt, D. J., High Pressure Single-Molecule FRET Studies of the Lysine Riboswitch: Cationic and Osmolytic Effects on Pressure Induced Denaturation. *Phys. Chem. Chem. Phys.* **2020,** *22* (28), 15853-15866.

30. Sudarsan, N.; Wickiser, J. K.; Nakamura, S.; Ebert, M. S.; Breaker, R. R., An mRNA Structure in Bacteria That Controls Gene Expression by Binding Lysine. *Genes Dev.* **2003,** *17* (21), 2688-2697.

31. Aitken, C. E.; Marshall, R. A.; Puglisi, J. D., An Oxygen Scavenging System for Improvement of Dye Stability in Single-Molecule Fluorescence Experiments. *Biophys. J.* **2008,** *94* (5), 1826-1835.

32. Nicholson, D. A.; Sengupta, A.; Nesbitt, D. J., Chirality-Dependent Amino Acid Modulation of RNA Folding. *J. Phys. Chem. B* **2020,** *124* (51), 11561-11572.

33. McKinney, S. A.; Joo, C.; Ha, T., Analysis of Single-Molecule FRET Trajectories Using Hidden Markov Modeling. *Biophys. J.* **2006,** *91* (5), 1941-1951.

34. Sung, H.-L.; Nesbitt, D. J., Sequential Folding of the Nickel/Cobalt Riboswitch Is Facilitated by a Conformational Intermediate: Insights from Single-Molecule Kinetics and Thermodynamics. *J. Phys. Chem. B* **2020,** *124* (34), 7348-7360.

35. Sung, H.-L.; Nesbitt, D. J., Novel Heat-Promoted Folding Dynamics of the *yybP-ykoY* Manganese Riboswitch: Kinetic and Thermodynamic Studies at the Single-Molecule Level. *J. Phys. Chem. B* **2019,** *123* (26), 5412-5422.

36. Privalov, P. L., Thermodynamics of Protein Folding. *J. Chem. Thermodyn.* **1997,** *29* (4), 447-474.

37. Winzor, D. J.; Jackson, C. M., Interpretation of the Temperature Dependence of Equilibrium and Rate Constants. *J. Mol. Recognit.* **2006,** *19* (5), 389-407.

38. Zhou, H.-X., Rate Theories for Biologists. *Q. Rev. Biophys.* **2010,** *43* (2), 219-293.

39. Sengupta, A.; Sung, H.-L.; Nesbitt, D. J., Amino Acid Specific Effects on RNA Tertiary Interactions: Single-Molecule Kinetic and Thermodynamic Studies. *J. Phys. Chem. B* **2016,** *120* (41), 10615-10627.

40. Szabo, A.; Schulten, K.; Schulten, Z., First Passage Time Approach to Diffusion Controlled Reactions. *Chem. Phys.* **1980,** *72* (8), 4350-4357.

41. Pegram, L. M.; Wendorff, T.; Erdmann, R.; Shkel, I.; Bellissimo, D.; Felitsky, D. J.; Record, M. T., Why Hofmeister Effects of Many Salts Favor Protein Folding But Not DNA Helix Formation. *Proc. Natl. Acad. Sci. U.S.A.* **2010,** *107* (17), 7716-7721.

42. Courtenay, E. S.; Capp, M. W.; Record Jr., M. T., Thermodynamics of Interactions of Urea and Guanidinium Salts with Protein Surface: Relationship Between Solute Effects on Protein Processes and Changes in Water-Accessible Surface Area. *Protein Sci.* **2001,** *10* (12), 2485-2497.

43. Capp, M. W.; Pegram, L. M.; Saecker, R. M.; Kratz, M.; Riccardi, D.; Wendorff, T.; Cannon, J. G.; Record, M. T., Interactions of the Osmolyte Glycine Betaine with Molecular Surfaces in Water: Thermodynamics, Structural Interpretation, and Prediction of m-Values. *Biochemistry* **2009,** *48* (43), 10372-10379.

44. McCluskey, K.; Boudreault, J.; St-Pierre, P.; Perez-Gonzalez, C.; Chauvier, A.; Rizzi, A.; Beauregard, P. B.; Lafontaine, D. A.; Penedo, J. C., Unprecedented Tunability of Riboswitch Structure and Regulatory Function by Sub-Millimolar Variations in Physiological Mg^{2+}. *Nucleic Acids Res.* **2019,** *47* (12), 6478-6487.

45. Suddala, K. C.; Wang, J.; Hou, Q.; Walter, N. G., Mg^{2+} Shifts Ligand-Mediated Folding of a Riboswitch from Induced-Fit to Conformational Selection. *J. Am. Chem. Soc.* **2015,** *137* (44), 14075-14083.

46. Paudel, B. P.; Rueda, D., Molecular Crowding Accelerates Ribozyme Docking and Catalysis. *J. Am. Chem. Soc.* **2014,** *136* (48), 16700-16703.

47. Kilburn, D.; Roh, J. H.; Behrouzi, R.; Briber, R. M.; Woodson, S. A., Crowders Perturb the Entropy of RNA Energy Landscapes to Favor Folding. *J. Am. Chem. Soc.* **2013,** *135* (27), 10055-10063.

48. Knowles, D. B.; LaCroix, A. S.; Deines, N. F.; Shkel, I.; Record, M. T., Separation of Preferential Interaction and Excluded Volume Effects on DNA Duplex and Hairpin Stability. *Proc. Natl. Acad. Sci. U.S.A.* **2011,** *108* (31), 12699-12704.

Chapter 9

DNA Hairpin Hybridization under Extreme Pressures: A Single-Molecule FRET Study

---

9.1 Abstract

Organisms have evolved to live in a variety of complex environments, which clearly has required cellular biology to accommodate to extreme conditions of hydraulic pressure and elevated temperature. In this work, we exploit single-molecule Forster resonance energy transfer (FRET) spectroscopy to probe structural changes in DNA hairpins as a function of pressure and temperature, which allows us to extract detailed thermodynamic information on changes in free energy (ΔG^0), free volume (ΔV^0), enthalpy (ΔH^0) and entropy (ΔS^0) associated with DNA loop formation and sequence dependent stem hybridization. Specifically, time correlated single photon counting experiments on freely diffusing 40A DNA hairpin FRET constructs are performed in a 50 μm x 50 μm square quartz capillary cell pressurized from ambient pressure up to 3 kbar. By pressure-dependent van't Hoff analysis of the equilibrium constants, ΔV^0 for hybridization of the DNA hairpin can be determined as a function of stem length (n_{stem} = 7-10) with single base pair resolution, which further motivates a simple linear deconstruction into additive stem ($\Delta V^0_{stem} = \Delta V^0_{bp} \times n_{stem}$) and loop ($\Delta V^0_{loop}$) contributions. We find that increasing pressure destabilizes the DNA hairpin stem region (ΔV^0_{bp} = +1.98(16) cm^3/mol/bp), with additional positive free volume changes (ΔV^0_{loop} = +7.0(14) cm^3/mol) we ascribe to bending and

*This chapter is adapted from: Sung, H.-L.; Nesbitt, D. J. DNA Hairpin Hybridization under Extreme Pressures: A Single-Molecule FRET Study. *J. Phys. Chem. B* **2020**, *124*, 110-120.

base stacking disruption of the 40A loop. From a van't Hoff temperature dependent analysis of the DNA 40A hairpin equilibria, the data support a similar additive loop/stem deconstruction of enthalpic ($\Delta H^0 = \Delta H^0_{loop} + \Delta H^0_{stem}$) and entropic ($\Delta S^0 = \Delta S^0_{loop} + \Delta S^0_{stem}$) contributions, which permits insightful comparison with predictions from nearest neighbor thermodynamic models for DNA duplex formation. In particular, the stem thermodynamics is consistent with exothermically favored ($\Delta H^0_{stem} < 0$) and entropically penalized ($\Delta S^0_{stem} < 0$) hydrogen bonding, but with additional enthalpic ($\Delta H^0_{loop} > 0$) and entropic ($\Delta S^0_{loop} > 0$) contributions due to loop bending effects and consistent with distortion of A base stacking in the 40A linker.

9.2 Introduction

Temperature and pressure are two intensive thermodynamic variables that play crucial roles in the folding of biomolecules into biologically competent structures [1-2]. Interestingly, while the thermal dependence of biomolecular conformational change has been thoroughly investigated, the effects of extreme hydraulic pressure have received much less attention. One justification for such disparate attentions is that pressure is a relatively constant variable in conventional biology, while temperature fluctuations are quite common and appreciated to be much more important[3]. However, improved sampling tools in the last two decades[4-5] has made extreme biological environments increasingly available for study. As one particularly relevant example, robotic deep sea exploration vehicles have revealed a plethora of thermophilic organisms thriving in hydrothermal vents where extreme pressures and elevated temperatures result from the rapid increase of hydraulic pressure with ocean depth (≈ 1 bar every 10 meters) and proximity to geothermal heat sources in the ocean bed. In fact, the much of the ocean bottom is 3500 meters below sea level (i.e., P = 350 bars), with the deepest point in the Marianas Trench

at 11km (i.e., P = 1.1 kbar). From such a perspective, high pressure biological environments are in fact ubiquitous, with the dynamic range of pressures spanning more than three orders of magnitude. This provides incentive for single molecule biophysical folding studies under extreme (P/T) conditions, with which to explore how biology successfully adapts to (and potentially even harnesses) such extreme variations in pressure and temperature[2-3] to influence conformational folding/unfolding and/or hybridization/dehybridization dynamics.

Pressure and temperature are particularly powerful intensive variables for such thermodynamic exploration. According to the Gibbs free energy differential expression,

$$d(\Delta G^0) = -\Delta S^0(dT) + \Delta V^0(dP) \qquad \text{(Eq. 9.1)}$$

the temperature dependence of an equilibrium process is determined by entropy change (ΔS^0), while the pressure dependent response is controlled by the free volume difference (ΔV^0) between folded and unfolded conformations[3-4]. In the past decade, spectroscopic methods have been coupled with high pressure techniques to study local/global changes of biomolecular structure[1, 3]. For example, proton exchange rates in solution phase NMR spectroscopy have been used to probe pressure dependent structure formation in proteins[6-7], while small-angle X-ray scattering experiments have allowed extraction of radii of gyration as a proxy for global compactness as a function of applied pressure[8-10]. The single-molecule FRET spectroscopy (smFRET, Figure 9.1) could be particularly useful in detecting conformational change of biomolecules, given the extremely rapid decrease in FRET energy transfer efficiency ($E_{FRET} \sim 1/(1+(r/r_0)^6)$) with distance between dye-labeled positions, which may therefore be sensitive to conformational compactness[1, 11], as well as overall folding of the biomolecule. Indeed, as external pressure can significantly skew the folding free energy landscape[12-13], biomolecules can adopt different

folding conformations under extreme vs. ambient conditions[11, 14], which one could hope to identify by E_{FRET} value in high pressure smFRET studies[11].

The present studies focus on pressure dependent hybridization/dehybridization of single molecule DNA hairpins, as a simple first introduction to high pressure smFRET. DNA hairpins play an important role in biological systems[15] and have been widely used as model constructs for duplex formation, as well as probing the nucleic acid response to cosolutes such as amino acids[16], osmolytes[11, 14, 17] and crowding agents[18-21]. The 40A DNA hairpin construct utilized in the present studies (Figure 9.2) is ideally suitable for smFRET investigation because i) folding is known to proceed by well-behaved, unimolecular 2-state kinetics[16, 18] and yet ii) the poly(dA) linker acts as a sufficiently long spacer to provide high E_{FRET} contrast between the folded and unfolded conformations. Free volume changes in smFRET DNA hairpin studies have been explored recently, suggesting that the fully hybridized DNA conformation is destabilized (i.e., *denatures*) with increasing pressure[11, 14, 18]. While these previous studies have focused on the free volume change (ΔV^0) in response to different crowding agents and cosolutes, the effects of sequence, specifically, the dependence of free volume on stem sequence length (n_{step}) and chemical identity (A, T, G, C), have remained largely unexplored. Furthermore, the process of DNA hairpin folding not only requires secondary structure formation in the *stem* region, but also forces the single-stranded DNA *loop* domain into a more compact ring-like conformation. Since both stem and loop regions represent ubiquitous structural elements in nucleic acid folding[22-23], the successful deconstruction and simple theoretical modelling of their free volume contributions could provide intriguing, new physical insight into the thermodynamics of nucleic acid structure.

In this work, we report on the development of new high pressure smFRET capabilities in our labs with access up to 5 kbar external pressure. We then perform “burst diffusion” smFRET

experiments over an extreme pressure (1-3000 bar) and a modest temperature ($\Delta T \approx 10K$) range, which permit one to extract thermodynamic properties for a series of fluorescently labelled 40A DNA hairpin constructs. For pressure dependence studies, a manual pressure generator is coupled to a square (50 μm x 50 μm) quartz capillary sample cell (Figure 9.1), which can sustain from 1 bar up to 5000 bar in pressure without shattering. Such large dynamic ranges in pressure enable measurement of free volume changes i) at the single molecule level and ii) with approximately single base pair resolution. Analysis of the nucleotide sequence dependent equilibrium constants for hybridization as well as comparison to nearest neighbor predictions[24-25] allow us to extract free volume (ΔV^0), enthalpy (ΔH^0), and entropy (ΔS^0) changes in *stem formation*, which both isolate and highlight additional contributions to *loop formation* for each thermodynamic quantity.

The organization of this paper is as follows. In Sec. 9.3, we present a detailed discussion of the smFRET apparatus, with capabilities for both extreme pressure (1-5000 bar) and modest temperature (20–40 ℃) control, with pressure/temperature and sequence dependent results on 40A DNA hairpin constructs reported in Sec. 9.4. In Sec. 9.5A we analyze and interpret the stem length and sequence dependence of the high pressure results and present a simple model for interpreting these data which permits systematic deconstruction of stem (ΔV_{stem}) and loop (ΔV_{loop}) free volume contributions. In Sec. 9.5B and 9.5C, we explore temperature dependence of 40A hairpin formation, specifically deconstruction of ΔG^0 into enthalpic and entropic contributions by van't Hoff analysis. The resulting thermodynamic contributions prove consistent with a simple physical picture of i) exothermic bonding ($\Delta H^0 < 0$) yet ii) base stacking in the duplex stem to achieve a more ordered ($\Delta S^0 < 0$) secondary structure[26]. The results are then compared to nearest neighbor (NN) model predictions (ΔH^{NN}_{stem}, ΔS^{NN}_{stem}) for DNA stem

formation[24-25], which intriguingly suggest 40A *loop formation* to be endothermic ($\Delta H_{loop} > 0$) and yet favored by entropic gain ($\Delta S_{loop} > 0$). Finally, main conclusions and directions for further experimental improvements are briefly summarized in Sec. 9.6.

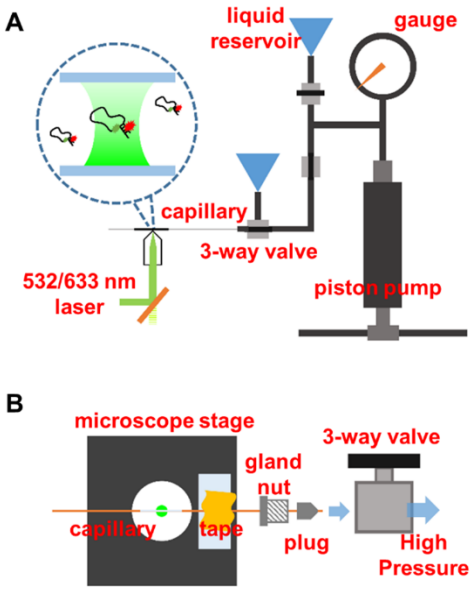

Figure 9.1 High pressure smFRET experiment setup: (A) High pressure generating system coupled to the confocal microscope for smFRET freely diffusing study; (B) Top view of the square capillary alignment to the microscope objective and the high pressure mechanical sealing strategy.

9.3 Experiment

9.3.1 High pressure microscopy cell and pressure control

The current high pressure smFRET experiments (Figure 9.1) have been performed by modification of a time correlated single photon counting confocal microscope to incorporate a high pressure glass capillary cell[27]. As one crucial design change, we use square instead of round capillary tubing made from fused silica, with 360 μm and 50 μm outer and inner diameter, respectively (Polymicro, Phoenix, AZ). This is used to contain the high pressure sample for microscope studies, with thickness and relatively flat surfaces to mimic a standard cover slip and thereby optimize collection of fluorescent photons[14]. Although studies have previously warned

that such square capillaries might fail at pressures over 2 kilobars[27], we find this not to be the case, working well beyond this limit and indeed up to nearly 5 kilobars without signs of fracturing. However, we have learned that sealing the capillary end with a oxy-propane torch can at times result in breakage at high pressure, likely due to unresolved strain in the fused silica due to intense heating (and cooling). In our experience, such problems are mitigated by a simple tempering of the glass capillary ends, as described below.

First of all, one end of the capillary is glued with epoxy adhesive into a modified stainless-steel pressure plug (High Pressure Equipment, Erie, PA) with a 450 μm hole drilled through the center (Figure 9.1B) and the opaque outer polymer coating of the capillary removed by a low temperature propane flame to create optical access for the fluorescent measurements. Loading of the low concentration DNA samples is then achieved by immersing one end of the capillary into the sample hairpin solution. Once the capillary is filled by capillary action, the free end opposite the plug is sealed with an oxy-propane torch. Since the mechanical strength of the fused silica can be compromised by heating/cooling, we utilize an extended heating time to create an inner channel tapered into a needle point in the interior of the glass, thereby reducing the contact surface area and thus the total force on the sealed end. Prior to coupling to the high pressure liquid source, the plug-attached open end of the capillary is dipped into low viscosity silicone oil to create a thin immiscible layer, which prevents contamination of the fluorescence capillary region by the pressure-transmitting fluid and yet still conducting the pressure effectively. The sample is then connected to the high pressure source system by tightening the high pressure plug and gland nut, during which the flat surface of the square capillary is visually aligned with the microscope objective eyepiece. Since the capillary rotates slightly with the gland nut while being tightened, a cover slip is attached to the capillary with tape to mark the

correct capillary orientation (Figure 9.1B). After tightening the gland nut, the cover slip is then rotated back to the desired flat surface orientation, gently torqueing the capillary to realign its flat surface with the microscope objective. Although this last step might seem practically equivalent to fixing the capillary orientation before tightening the gland nut, the sudden rotation tends to loosen the tape and misalign the capillary. Indeed, strong adhesives may also work well, though we find the tape method easier and faster to apply.

The source of high pressure is simply a manually operated piston screw pump (High Pressure Equipment) which can generate pressures up to 5 kilobars (Figure 9.1A). As adapted from previous work[27-28], the pressure generator is connected to the sample cell and a Bourdon pressure gauge via high pressure 1/4" stainless steel tubing (High Pressure Equipment), with the entire system filled with ethanol as the pressure-transmitting fluid. Residual air bubbles in the ethanol decrease the pressuring efficiency, which are removed by repeatedly flushing the system through liquid ethanol reservoirs (Figure 9.1A). The valves are then closed to isolate the fluid reservoirs, with simple mechanical rotation of the piston achieving a desired pressure (0-5 kbar), as indicated by the Bourdon pressure gauge.

9.3.2 Temperature control

Precise temperature control (± 0.1 °C) is achieved by simultaneously heating the capillary sample and microscope objective and stabilizing the temperature with electronic feedback loop. Prior to each temperature-controlled experiment, the sample holder is mounted on a stage heater (Instec, Boulder, CO) and stabilized via feedback control for more than 15 minutes to ensure complete thermal equilibrium. At the same time, the microscope objective is heated by a resistive collar (Bioptechs, Butler, PA) to the same temperature to prevent thermal gradients due to water immersion optics. Details of the resistive feedback heating system can be found elsewhere [29-30].

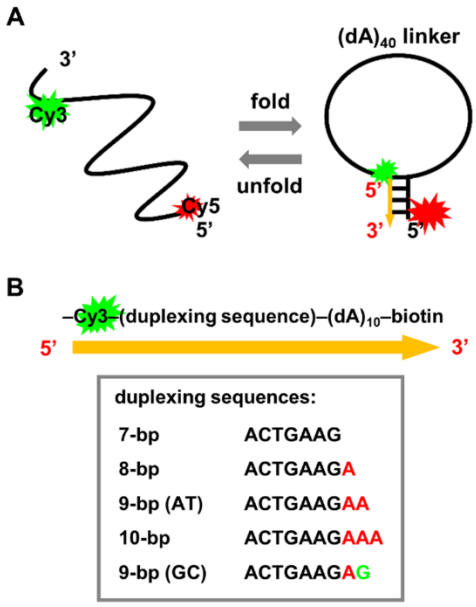

Figure 9.2 Details of the DNA hairpin smFRET constructs: (A) Schematic representation of DNA hairpin folding; (B) The structural details of the complementary strand, with systematic variations in the duplexing sequence beyond 7-bp denoted in red (A) and green (G). The location of Cy3 labeling with respective to the duplexing sequence at 3' end is highlighted in green, and Cy5 is chemically attached to the 5' end.

9.3.3 DNA 40A hairpin construct and sample preparation

All DNA hairpin constructs in this study contain the identical 40-nucleotide poly-adenine linker (designated as 40A Hairpin), with the number of base pairs within the stem varying from n_{stem} = 7-10. The overall construct design, doubly fluorophore-labeled positions, and stem sequences are described in Figure 9.2, with each of the DNA oligomers commercially available in HPLC purified forms (Integrated DNA Technologies, Coralville, IA). In the "folded" state of the hairpin, the stem is fully hybridized by complementary Watson-Crick base pairing, bringing the two fluorescent dyes Cy3 and Cy5 in close proximity to achieve the high E_{FRET} (~ 0.8) state. Conversely, dissociation of the duplex stem "unfolds" hairpin, which allows the covalently linked dye-labeled strands to diffuse to much larger (~ 80 Å) separations, resulting in a E_{FRET} state near zero. The observed range of E_{FRET} values are entirely consistent with predictions based

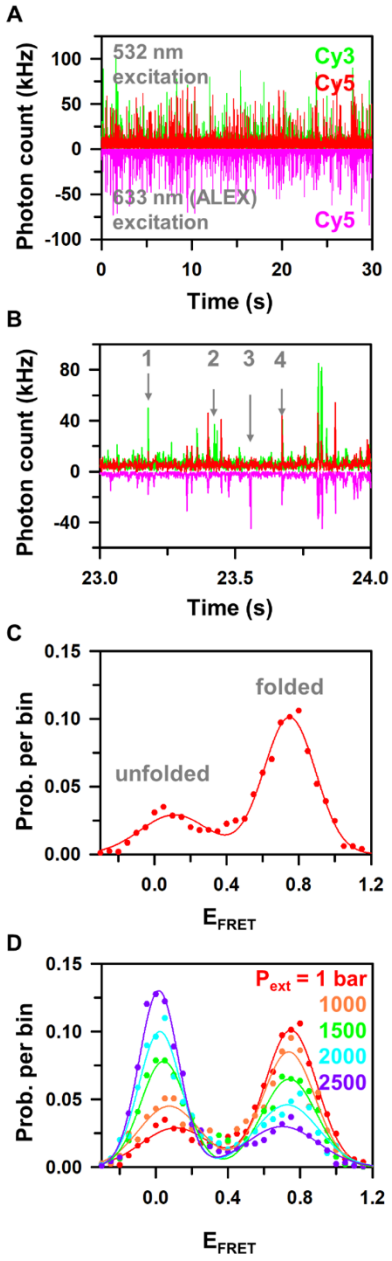

Figure 9.3 Sample data and analysis from the freely diffusing smFRET studies: (A) Sample time resolved fluorescent signals from 532 nm laser excitation, with upward green and red traces corresponding to Cy3 and Cy5 fluorescence channels, respectively. The pink trace due to 633 nm alternating laser excitation (ALEX) of the diffusing constructs is plotted downward for direct comparison with the 532 nm excitation signals, confirming the presence (or absence) of the Cy5 fluor. (B) Single events in the fluorescence traces, where arrows point at the fluorescent bursts corresponding to (1) an unfolded doubly-labeled hairpin, (2) a Cy3-only, (3) Cy5-only and (4) folded doubly-labeled construct. (C) Sample E_{FRET} histogram of the 9-bp (AT) hairpin folding at ambient pressure, fit to a superposition of two Gaussians. (D) Sample E_{FRET} histogram of the 9-bp hairpin folding at a series of external pressures, revealing a reversible propensity for unfolding with increasing P_{ext} (1-2500 bar).

on the Cy3/Cy5 Forster radius (R_0 = 55 Å), construct geometry, and results from previous surface-tethered smFRET experiments[16]. There is a 10A-biotin oligo extension on the 3' end after the duplexing sequence, designed for future attachment of the 40A hairpin constructs to a BSA surface by biotin-streptavidin interactions. For simplicity in these first high pressure experiments, however, we have simply chosen to allow the constructs to freely diffuse in solution through the laser beam, exploiting "burst fluorescence" methods to stochastically probe the single 40A hairpin oligos present in the confocal volume.

In preparation of the smFRET samples, the stock DNA solution has been diluted in imaging buffer to ~ 50 pM, such that fluorescent bursts result exclusively from single doubly-labeled DNA constructs diffusing through the confocal volume. The imaging buffer contains i) 50 mM hemipotassium HEPEs buffer (pH 7.5), ii) Trolox/PCA/PCD oxygen scavenger cocktail to catalytically remove oxygen[16, 30] and thereby increase Cy3/Cy5 dye photostability, with iii) sufficient NaCl to achieve total monovalent cation concentrations of $[M^+]$ = 100 mM.

9.3.4 Single-molecule FRET spectroscopy and data analysis

Details of the confocal smFRET experimental apparatus can be found in previous work[30-32]. In short, the output from a 532 nm Nd:YAG laser (10 ps pulses at a 20 MHz repetition rate) is beam expanded, collimated, and directed into an inverted confocal microscope with a 1.2 N.A. water immersion objective. The collimated beam overfills the limiting microscope aperture, resulting in a near diffraction limited excitation and collection spot size ($1/e^2$ radius ω_0 = 310(30) nm). In the current smFRET diffusion experiments (Figure 9.1A), the laser is focused into a solution of doubly dye labeled 40A DNA at sufficient dilution (~ 50 pM) to ensure that only a single DNA molecule diffuses through the observation window at a time, thereby generating typically an isolated ≈ 1 ms burst in fluorescent signal (Figure 9.3A and 9.3B). The resulting

photons are collected through the same objective, sorted by wavelength (green/red) and polarization (horizontal/vertical) before detection on four single photon avalanche photodiodes (APDs). A 50 μm pinhole spatial filter before the APD detection unit is used to restrict out of focus photons along the (z) photon propagation direction to achieve a sub-femtoliter detection volume. For each fluorescent burst above the 25 KHz photon/sec software adjustable count rate threshold (i.e., 10-fold higher than background noise in an equivalent 1 ms burst window), an E_{FRET} value is obtained from the number of green vs. red photon counts detected, after suitable correction for background and cross talk contributions with in-house software[31, 33]. Since the double fluorophore labelling efficiency for the DNA constructs is high but imperfect (> 90%), alternating laser excitation methods (ALEX) with interleaving green and red laser pulses are used to ensure only bursts from doubly-labeled DNA constructs are included in the E_{FRET} distributions[31, 34]. By way of example, the series of events flagged by arrows in Figure 9.3B and numbered from 1 to 4 can be unambiguously sorted into fluorescent bursts corresponding to 1) unfolded yet doubly labeled, 2) Cy3 only labeled, 3) Cy5 only labeled, and 4) folded doubly labeled DNA constructs, respectively.

Once the E_{FRET} value of each burst event from doubly-labeled DNA has been computed, an E_{FRET} histogram is generated (Figure 9.3C). Note that the E_{FRET} value is calculated as $I_A/(I_A + I_D)$, where $I_{A/D}$ is the total acceptor/donor signal after background fluorescence and detector crosstalk corrections. For the DNA hairpin constructs in this study, the E_{FRET} histograms exhibit two distinct populations with low E_{FRET} (~0) and high E_{FRET} (~0.8), corresponding to the unfolded and folded conformation, respectively[16]. The E_{FRET} distribution is then fit to a sum of two Gaussian functions, with the folding equilibrium constant readily calculated from the ratio of areas under each component[29, 31, 33-34]. We have observed for each hairpin construct the

maximum folded fraction to be around 80%. This actively folding fraction is consistent with our surface-tethered smFRET experiments, for which 80% of the DNA hairpin constructs actively fold/unfold, with the remainder are trapped in the low E_{FRET} configuration. Quantification of the non-folding subpopulation is thereby achieved by comparing surface-tethered results with freely diffusing studies[29, 33], with such subpopulations subtracted from the equilibrium constant calculation, as detailed in previous work[29, 33]. The resulting folding equilibrium constant (K_{fold}) is then obtained from this corrected data and used for further thermodynamic analyses.

9.4 Results and Analysis

9.4.1 Pressure dependence of DNA hairpin folding

The free volume taken up by a biomolecule will vary as a function of conformation, which in turn will control the effect of external pressure on biomolecular folding[3-4]. By differentiating the expression for Gibbs free energy, we can express the pressure dependence of the folding equilibrium constant as[3]

$$\left(\frac{\partial lnK_{fold}}{\partial P}\right)_T = \frac{-\Delta V^0}{RT}, \qquad \text{Eq. 9.2}$$

where R is the gas constant and ΔV^0 denotes the change in free volume upon folding: $\Delta V^0 = V_{fold} - V_{unfold}$. According to Eq. 9.2, folding is promoted by increasing pressure when $\Delta V^0 < 0$, and reduced by pressure when $\Delta V^0 > 0$. As expected from Le Chatelier's principle, stress due to increasing pressure is partially relieved by shifting the equilibrium toward the direction of smaller volume[3]. Eq. 9.2 can be integrated at constant T to predict the simple function dependence of K_{fold} on external pressure

$$\ln K_{fold}(P) = \frac{-P_{ext}\Delta V^0}{RT} + C \qquad \text{or} \qquad K_{fold}(P) = \exp\left(\frac{-P_{ext}\Delta V^0}{RT} + C\right), \qquad \text{Eq. 9.3}$$

where C is the integration constant. Note that C can be completely decoupled from the pressure-dependent term.

To explore the pressure dependence of DNA hairpin folding, smFRET experiments have been performed over a wide range of external pressures (P_{ext} = 1 bar to 3000 bar) inside fused silica square capillaries coupled to our high pressure compression apparatus. The sample E_{FRET} histogram reveals two distinct populations with $E_{FRET} \approx 0$ and ≈ 0.8 (Figure 9.3C), corresponding to unfolded and folded states of the DNA hairpin construct, respectively. As the external pressure rises, the folded (unfolded) population decreases (increase), respectively. This implies that increasing pressure favors the unfolded state of the DNA hairpin and thus a positive change in free volume ($\Delta V^0 > 0$) (Figure 9.3D). Such pressure induced unfolding or "denaturation" has been experimentally observed in previous bulk ensemble studies of nucleic acids[35] and proteins[3, 36]. However, the physical reason behind why $\Delta V^0 > 0$ is far from obvious, since one might at first expect nucleic acids and proteins to adopt more compact conformations upon folding. Though still controversial[36-39], one of the simplest interpretation would be that the folded structure generates more hydrophobic regions which exclude the solvent shell, generating "solvent voids" and therefore taking up greater volume; an equally plausible explanation is that the increase in solvent accessible surface area of the unfolded state facilitates solvation with a more compact solvent structure, which translates into $\Delta V^0 > 0$ and thus correctly predicts the pressure-induced denaturation of biomolecules[36-39].

The pressure dependences of DNA hairpin folding with different stem sequences are plotted in Figure 9.4A, which display the expected linear dependence (i.e., Eq. 9.3) of $\ln[K_{fold}]$ vs. P_{ext} and provides clear evidence that the 40A DNA hairpin constructs *unfold* with increasing pressure. Note the systematic upward shift in these curves with increasing stem sequence length,

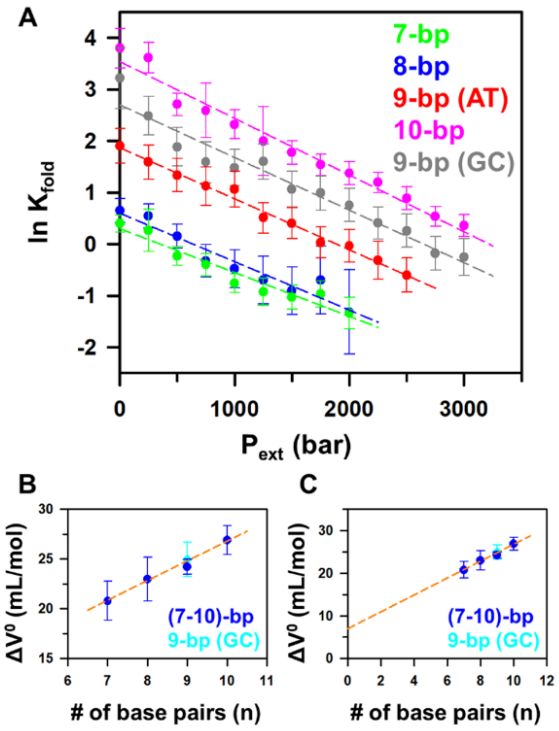

Figure 9.4 Pressure dependence of folding for a systematic series of DNA hairpins: (A) Pressure effects presented in a van't Hoff plot of ln[K_{fold}] versus P_{ext}, for which the slope yields the free volume change due to DNA stem hybridization ($\Delta V^0 = V^0_{fold} - V^0_{unfold}$). (B) Volume changes upon folding (ΔV^0) as a function of number of base pairs in the duplex stems, which reveal a remarkable linear dependence on n_{stem}; (C) Extrapolation of this linear dependence on stem length to $n_{stem} = 0$, thereby isolating free volume contributions (ΔV^0_{loop}) to DNA hybridization from formation of the 40A loop.

which is in almost all cases consistent with the exponential increase in K_{fold} predicted with additional free energy release due to incremental base pairing. The only exception to this trend is evident in the nearly overlapping K_{fold} trendlines for the 7-bp and 8-bp constructs, which occur because the additional stabilization due to the extra base pair (n_{stem} = 7 vs. 8) is counteracted by the terminal d(G-C) pair being replaced by the less stable d(A-T) (Figure 9.2B) in the 7-bp and 8-bp constructs, respectfully.

For nearly incompressible fluids, ΔV^0 remains approximately constant over wide pressure ranges[36]; hence the data for each stem sequence can be linearly fit to Eq. 9.3 in order to obtain

accurate free volume changes upon folding (ΔV^0) as a function of hybridization length. Although the slopes appear quite similar for each data set, upon closer inspection, systematic differences are visually apparent. By way of more quantitative comparison, least squares fitted slopes (ΔV^0) of Figure 9.4A have been plotted against the number of base pairs in Figure 9.4B and 9.4C. Though the slope uncertainties are appreciable, the overall trend in the data is quite clear; ΔV^0 increases smoothly and quasilinearly with number of base pairs within the duplex stem. This can be rationalized by a roughly linear growth in solvent-inaccessible "voids" and hydration volume with each additional DNA base pair in the stem sequence. Most importantly, pressure induced measurements of ΔV^0 exhibit a sensitivity to stem length that is clearly at the single base pair level of resolution.

If we interpret this quasilinearity as arising solely from solvent inaccessible regions in the stem, the data suggest a deconstruction of the free volume change into *a simple additive sum* of stem and loop contributions with a ΔV^0 resolution close to the single base pair difference, the average volume change per base pair $\Delta V_{stem} = \Delta V_{bp} * n_{stem}$ is determined to be $\Delta V_{bp} = 1.98(16)$ $cm^3/mol/bp$ (base pair), which is consistent with previous values ($\Delta V_{bp} = 2.1(4)$ $cm^3/mol/bp$) obtained from high-pressure UV melting experiments on poly[d(A-T)] DNA[40-42]. Moreover, despite the impressively small fractional uncertainties in ΔV^0 obtained from these least squares fits, the 9-bp hairpin with a *weaker* terminal d(A-T) base pair is experimentally indistinguishable from the 9-bp hairpin with a *stronger* terminal d(G-C). Thus, although the incremental free volume changes due to increasing stem length are unambiguously determined in this study, the corresponding effects due to a stronger d(G-C) or weaker d(A-T) terminal base pairing appear to be 5 to 10 fold smaller and obscure any finer differential effects at our current sensitivities due to single base pair variance.

9.4.2 Temperature dependence of DNA hairpin Folding

Temperature plays an equally crucial role in both the kinetics and thermodynamics of biochemical reactions, with nucleic acid structures known to be highly sensitive to temperature[43]. In general, nucleic acids fold into more ordered states driven by exothermic interactions such as hydrogen bonding and base stacking. Thus, by Le Chatelier's principle, folding in nucleic acids is generally but not exclusively unfavored by increasing temperature, with notable exceptions in systems where the free energy changes are dominated by solvent vs. solute contributions[32, 44-45]. The temperature dependent unfolding of the DNA hairpins is shown in a van't Hoff plot (Figure 9.5A), where $\ln[K_{fold}]$ is plotted as a function of reciprocal temperature (1/T). The data are well fit to linear functions which allow us to deconstruct the full folding free energy (ΔG^0) into enthalpic (ΔH^0) and entropic (ΔS^0) contributions:

$$lnK_{fold} = -\frac{1}{T}\frac{\Delta H^0}{R} + \frac{\Delta S^0}{R}. \qquad \text{Eq. 9.4}$$

Note that the fractional temperature vs. pressure changes required to see comparable effects in K_{fold} differ by orders of magnitude. This is due to the large change in entropy upon folding of a complex biomolecule, which results in much larger thermodynamic free energy contributions arising from $T\Delta S^0$ vs $P\Delta V^0$ under ambient physiological conditions. In the linear least squares fits in Figure 9.5A, the positive slopes signal folding of the 40A hairpin folding to be exothermic ($\Delta H^0 < 0$) and therefore penalized by heating. Conversely, the negative intercepts from these fits indicate a decrease in entropy ($\Delta S^0 < 0$) during hairpin formation, consistent with the canonical picture (stated above) of folding into a more ordered structure. However, one should always be mindful that the measured thermodynamic response is determined by free energy change for the entire system, which includes both structural effects from the biomolecules as well as the surrounding solvent[32, 46-47].

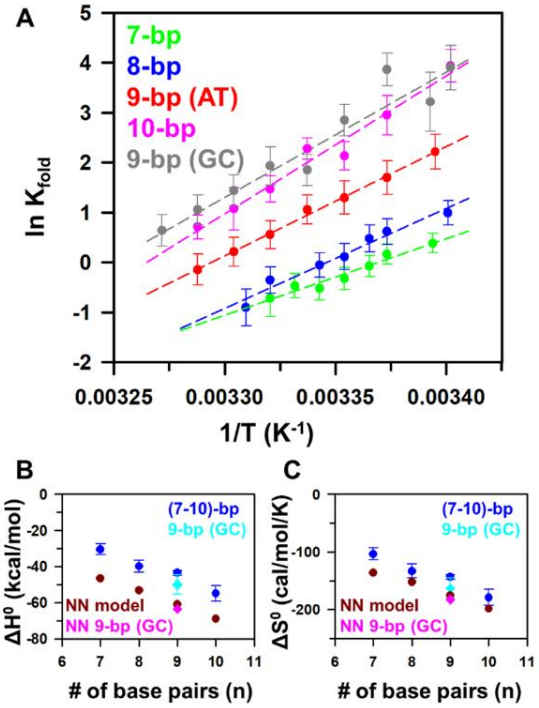

Figure 9.5 Temperature dependent folding response: (A) Temperature unfolding effects for a for the series of DNA hairpins presented as a standard van't Hoff plot, with the slope ($m = -\Delta H^0$) and intercept yielding the enthalpy and entropy changes upon folding; (B) Enthalpy change (ΔH^0) as a function of stem length (n_{stem}, dark blue), as well as predictions (dark red) from nearest neighbor model parameters; (C) Entropy change (ΔS^0) as a function of duplex stem length (dark blue), in comparison to the nearest neighbor model prediction for fully bimolecular stem formation (dark red). The two additional points in (B) and (C) (light blue) correspond to data for an alternate 9-bp construct with the 3' d(A-T) replaced by a stronger d(G-C) base pair. Corresponding enthalpy and entropy predictions from nearest neighbor model predictions for *bimolecular* stem formation are also shown (light red), which suggest a small increase in enthalpy and entropy change under *unimolecular* stem formation conditions for a hairpin construct.

Thermodynamic results for ΔH^0 and ΔS^0 from van't Hoff analysis for the n_{stem} = 7-10-bp and 9-bp (GC) series of constructs are summarized in Figure 9.5B and 9.5C, along with predictions of the same quantities by nearest neighbor models[24-25]. Interestingly, these plots explicitly demonstrate that ΔH^0 and ΔS^0 both decrease in approximately linearly fashion with the number of base pairs (n_{stem}) (Figure 9.5B), consistent with a heat release and change in disorder roughly proportional to hybridization length. Also worth emphasizing, the 9-bp hairpin with a

terminal G-C base pair exhibits a noticeably larger incremental decrease in both ΔH^0 and ΔS^0 than for the corresponding 9-bp hairpin sequence with a terminal d(A-T) base pair. This shift arises as a result of a stronger d(G-C) vs. d(A-T) base pairing interaction, as consistent with previous observations[24-25].

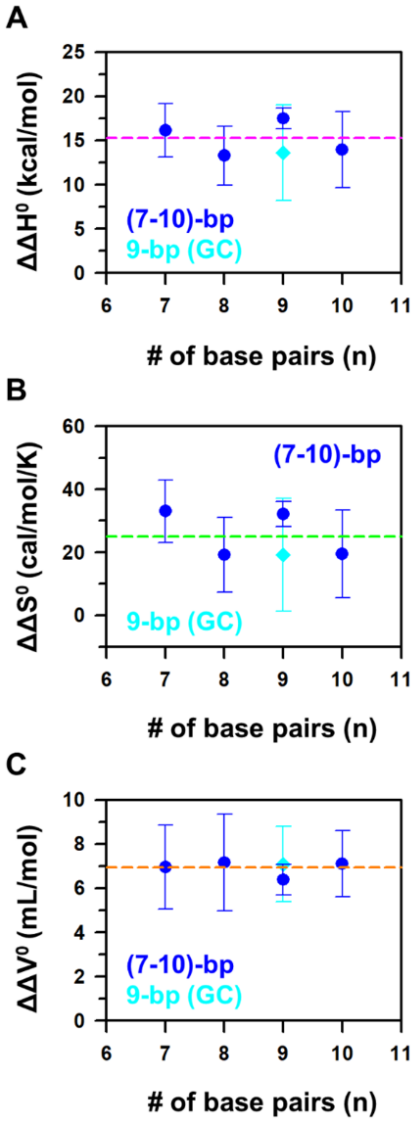

Figure 9.6 Subtraction of the stem length (n_{stem}) dependent contributions from DNA double-strand formation resulting in single-strand DNA looping (A) enthalpy (ΔH^0_{loop}), (B) entropy (ΔS^0_{loop}) and (C) free volume (ΔV^0_{loop}) changes. The data is consistent with a simple linear offset for these loop contributions, indicated by pink, green and orange dashed lines for enthalpy, entropy and free volume, respectively.

9.5 Discussion

9.5.1 Deconstructing free volume changes into DNA stem and loop formation

With the present experimental combination of i) high dynamic range of pressures and ii) quantitative smFRET measurements, we achieve single base pair resolution for the free volume changes (ΔV^0) incurred upon hybridization of a 40A DNA hairpin. Furthermore, when the analysis is repeated for a series of stem junction sequences (see Figure 9.2), the data follow a nearly linear trend with a slope ΔV^0_{bp} = 1.98(16) cm^3/mol/bp (Figure 9.4B), which is already consistent with a previously reported (albeit less precise) value of ΔV^0_{bp} = 2.1(4) cm^3/mol/bp for poly[d(A-T)] DNA hybridization obtained from high pressure UV melting experiments under comparable monovalent cation concentrations[40]. Although the effect of swapping a single base pair (i.e., 9-bp AT to 9-bp GC) is indistinguishable for the present selection of stem sequences, results from previous high pressure UV melting studies at a relatively low monovalent cation concentration for poly[d(A-T)], poly[d(G-C)][48], and poly[d(I-C)] (dI = 2'-deoxyinosine, a dG like derivative) yield unit base-pair slopes of ΔV^0_{bp} = 1.42 cm^3/mol/bp, 4.57 cm^3/mol/bp[41], and 4.8(6) cm^3/mol/bp[48], respectively. Specifically, the predicted free volume differences for single d(A-T) and d(G-C) swaps in poly[d(A-T)] and poly[d(G-C)] would be $\Delta\Delta V^0_{bp}$ = 3.4 cm^3/mol/bp. This is significantly higher (20-fold) than our experimental uncertainty, yet no change is seen for such an d(A-T) → d(G-C) single base-pair swap in our data. In contrast, a UV melting experiment of mixed-base pair DNA with G-C content similar to our complementary sequences has found ΔV^0_{bp} = 1.8(2) cm^3/mol/bp[42], in much improved agreement with our results. We therefore suspect that ΔV_{bp} may additionally depend upon interaction between neighboring base pairs, resulting in excess values of ΔV^0_{bp} for homonucleotide duplexes poly[d(G-C)] and

poly[d(I-C)], which appear to be moderated in DNA duplexes with more mixed-base-pair character.

If we extrapolate the linear relation between ΔV^0 and the number of base pairs, the vertical intercept is clearly positive, well within experimental uncertainty (Figure 9.4C). This indicates that there must be a free volume change ΔV^0 (0 bp) > 0 even in the absence of any base pairing of the stem sequence. A simple additive model for this behavior would suggest that the overall change in free volume is given by

$$\Delta V^0 = \Delta V^0_{stem} + \Delta V^0_{loop} = \Delta V^0_{bp} \times n + \Delta V^0_{loop} \qquad \text{Eq. 9.5}$$

where ΔV^0_{loop} represents a contribution generated from loop formation of the single-stranded poly(dA) DNA linker. Specifically, the results suggest *an increase* in the effective DNA volume (ΔV^0_{loop} = +7.0(14) cm^3/mol) when the DNA linker forms a loop structure[49-50], which at first seems counterintuitive. However, it is also well established that single stranded poly(dA) is appreciably structured due to spontaneous base stacking between adjacent adenine bases, a stacking which would be disrupted upon folding of the hairpin [51-55] due to loop distortion. The data therefore suggest that the closely stacked adenine bases occupy less volume than free bases, and therefore when the base stacking is disrupted, the effective volume occupied by the single-strand DNA increases, thus resulting in a positive volume change contributed from DNA linker looping ($\Delta V^0_{loop} > 0$).

Although positive ΔV^0_{bp} seems to imply the longer DNA double strand is more susceptible to pressure denaturation effects, we have found the free energy stabilization per base is more than an order of magnitude higher than the pressure-volume perturbation even at the bottom of the Marianas Trench (~ 1.1 kbar). Thus, it is true that the stability of DNA duplex is increased with the number of base pairs at any pressure in nature (on earth). However, such

pressure perturbation can significantly affect the local stability of a DNA double strand, especially when the DNA needs to unzip (partially melt) to participate in biochemical reactions such as DNA replication and transcription. Therefore, the deep sea species may alter the cellular osmolyte compositions to accommodate the high pressure environments[56]. It has been found deep sea fish accumulate high level of TMAO in their muscles[56-57], while TMAO is also shown to not only stabilize DNA secondary structures[58], but reduce ΔV^0 to mitigate the pressure effects[11, 18]. Moreover, high pressure may also destabilize RNA structures and greatly affect their biochemical functions. For example, the gene regulatory elements RNA riboswitches can be extremely sensitive to pressure, due to the fact that they dynamically fold into different conformations to control the gene expression. The deconstructed volume contributions from stem (ΔV^0_{stem}) and loop (ΔV^0_{loop}) determined in this work may help to predict the more complicated RNA folding in the future.

Although more work clearly needs to be done, our results suggest both the double-strand stem and the single-strand loop significantly contribute for the 40A hairpin construct to the pressure dependent response for the overall folding thermodynamics. Hairpin structures are ubiquitous in nucleic acids[15, 59], the response for which may help us understand pressure effects on more complex nucleic acid folding in extreme environments[23]. From our volumetric analysis, the positive ΔV^0_{loop} is consistent with the disruption of base stacking within the poly(dA) linker, indicating adjacent base stacking reduces the free volume of single-stranded DNA. On the other hand, the positive ΔV^0_{stem} suggests the DNA duplex formation increase the free volume. The two main forces that govern the structure of double-stranded DNA are inter-base-pair hydrogen bonding and base-stacking. The overall positive sign for ΔV^0_{stem} implies that inter-base-pair hydrogen bonding and perhaps higher-order structure formation (e.g., major and minor grooves)

reduce solvent accessibility to the DNA backbone and thus lead to larger free volume[60-62], completely dominating the volume reduction by base-stacking.

9.5.2 Deconstruction of stem (ΔH_{stem}) and loop (ΔH_{loop}) enthalpy changes

The enthalpy (ΔH^0) and entropy (ΔS^0) changes obtained from the temperature dependent study in Sec. 9.4B are summarized in Figure 9.5B and 9.5C, respectively. For comparison, the Figures 9.5B and 9.5C include predictions from the so-called nearest-neighbor models (NN), which take into account free energy contributions due to hydrogen bonding between single base pairs but also includes the additional base stacking and stabilization effects accrued due to neighboring base pairs. The model parameters have been significantly improved and extended beyond Watson-Crick pairs in the past two decades, and are now thought to provide reasonably accurate predictions of all thermodynamic parameters (ΔG, ΔH and ΔS) for DNA duplexing[24-25].

In Figure 9.5B, the experimental ΔH^0 values for hairpin folding and the nearest-neighbor predictions for duplex stem formation from two separate DNA strands (ΔH_{duplex}) clearly exhibit the same trend, specifically an increasing exothermicity with increasing number of base pairs. (Figure 9.5B). However, there would also appear to be an equally clear and nearly constant shift between the two data sets, with $\Delta H^0 - \Delta H_{duplex} \approx 15$ kcal/mol (Figure 9.5B and 9.6A). In a manner similar to linear deconstruction of free volume changes ($\Delta V^0 = \Delta V^0_{stem} + \Delta V^0_{loop}$) into stem and loop contributions, it is interesting to speculate how such an enthalpy shift could again arise by virtue of the loop formation. Specifically, the offset between the two experimental and theoretical enthalpy curves can be attributed to differences between i) full *bimolecular* formation of a stem (i.e., from separate ssDNA's) and ii) *unimolecular* diffusing of the two stems together to form a hairpin linked by the poly(dA) strand, the latter of which incurs additional enthalpic (and entropic, see Sec. 9.5C) contributions due to loop formation in the single-stranded DNA

linker. From this perspective, subtraction of ΔH^0_{stem} from ΔH^0 (Figure 9.6A) would correspond to the additional loop formation enthalpy ΔH^0_{loop}, which from the fits in Figure 9.5B can be estimated to be $\Delta H^0_{loop} \approx +15(2)$ kcal/mol. If we further assume this additional enthalpy penalty to be proportional to linker length, the looping enthalpy per nucleotide (ΔH^0_{loop}/40 nt $\approx +0.38(5)$ kcal/mol/nt) would be relatively close to previously reported scaling relations (ΔH^0_{loop} per nt $\sim$ +0.5 kcal/mol/nt) at comparable monovalent salt concentrations[51]. The source of such endothermicity could again be attributed to disrupted base stacking and distortion in the poly(dA) ssDNA loop[51-55]. Indeed, since a near-linear proportionality in incremental folding enthalpy has been observed in previous studies for constant stem lengths with linkers varying between 8 to 30 nucleotides[51], our 20% lower per nucleotide value can be rationalized as due to partial relaxation of these looping distortions for a longer (40A) linker. Moreover, different buffer conditions may also contribute to our low ΔH^0_{loop}; specifically, our experiments have been performed at lower monovalent cation concentration ($[M^+]$ = 100 mM vs 250 mM). This is quite relevant as base stacking is repressed at reduced $[M^+]$[52], thereby lowering the ΔH^0_{loop} enthalpic penalty and as consistent with our observations. It is worth noting that such positive ΔH^0_{loop} contributions again confirm that 40A loop formation is an endothermic process, enthalpically destabilizing the folded hairpin conformation.

9.5.3 Deconstruction of stem (ΔS_{stem}) and loop (ΔS_{loop}) entropy changes

We can take this analysis one step further and attempt to deconstruct the entropic contributions for hairpin formation into both loop and stem components. In an analogous fashion to the trends in ΔH^0 (Figure 9.5B), the experimental dependence of ΔS^0 on sequence length (Figure 9.5C) follows a similar trend to that of nearest neighbor model prediction[24-25], with ΔS^0 systematically decreasing with increasing number of base pairs. The experimental results are

again all shifted from model predictions by an approximately constant positive offset, which by a similar line of reasoning as in Sec. 9.5B may be taken to represent the entropic contribution due to poly(dA) loop formation, i.e., ΔS^0_{loop} = +25(7) cal/mol/K (Figure 9.6B). Such entropic favoring of the looping process would again appear to be counterintuitive, since constraining the ends in a random walk or worm like chain model would certainly lower the overall entropy[49-50]. However, in interpreting such an entropically favored loop formation, it is important to note that the poly(dA) linker contribution is more than simply structural. Specifically, the poly(dA) linker also plays a crucial role in raising the effective concentration of the one strand (S_2) with respect to its complement (S_1) and vice versa. Therefore, ΔS^0_{loop} may be usefully deconstructed into two further contributions: i) structural changes due to the biomolecule plus solvent system (ΔS^0_{struct}) and ii) unimolecular raising of the effective strand concentration (ΔS^0_{conc}), with $\Delta S^0_{loop} = \Delta S^0_{conc} + \Delta S^0_{struct}$.

More quantitatively, the difference between the *unimolecula*r folding equilibrium constant (K_{fold}) from covalently linked strands, i.e., what is experimentally measured, and a fully *bimolecular* duplex formation (K_{bimol}) from freely diffusing S_1, S_2 strands, i.e., what is predicted by the NN model, can be related as follows:

$$K_{bimol} = \frac{[S_1S_2]}{[S_1][S_2]} = \frac{[S_1S_2]}{[S_1]} \times \frac{1}{[S_2]} = K_{fold} \times \frac{1}{[S_2]}. \qquad \text{Eq. 9.6}$$

where $[S_1]$, $[S_2]$, and $[S_1S_2]$ are concentrations of the two strands and the full hairpin, respectively.

For experimental folding of the 40A hairpin, an additional term of $RTln[S_2]_0$ between *unimolecular* and *bimolecular* folding free energies can be immediately recognized from the Gibbs relation $\Delta G^0 = -RTlnK_{fold}$. Such concentration effects are purely entropic, as the linker provides a physical limit to the phase space which S_2 can sample. The effective $[S_2]_0$ can be

estimated from random walk theory, where the 40A linker is simplified into a collection of N (~ 9) "Kuhn segments," with the angular orientation of a given Kuhn segment taken as completely random and independent from adjacent units[63-65]. The per volume probability density of the end-to-end distance for a random-walk polymer P(**r**) is known to be well described by a Gaussian function[66], with P(r = 0) immediately recognized as the probability of S_1 and S_2 diffusing together. Therefore, the effective concentration is simply determined by matching the encounter probability P(0) with a bulk concentration $[S_2]_0$. With previously determined persistence lengths and sizes of a single nucleotide base[67-70], the effective concentration $[S_2]_0$ is calculated as 0.74(17) mM, corresponding to an additional entropy change of ΔS^0_{conc} = +14.7(5) cal/mol/K. The positive sign of ΔS^0_{conc} reflects the thermodynamic favoring of unimolecular over bimolecular folding due to entropic enhancement of the local strand concentration.

Consistent with our simple additive thermodynamic modeling, we can subtract this concentration entropy ΔS^0_{conc} from the average linker contribution (ΔS^0_{loop}) to infer an overall ΔS^0_{struct} = +10(7) cal/mol/K for structural change in the poly(dA) linker plus solvent system. The positive value for ΔS^0_{struct} implies an entropy increase when linear DNA turns into a loop via head-to-end connection. This entropy gain is at first counterintuitive, since looping structure would be expected to *restrict* conformational phase space with respect to a linear configuration[49-50]. However, looping can also disrupt the low entropy state achieved by base stacking effects in the poly(dA) oligo. Consequently, distortion of base stacking due to loop formation could rationalize the observed entropy increase, arising from both translation and internal degrees of freedom such as bond rotation[71]. Indeed, such entropically favored unstacking between nucleotide bases has been previously reported for poly(dA) as well as between monomer A bases[71-72]. Of course, the *solvent* entropy is an essential component of this estimate and must also

be considered, since our measurements are only sensitive to entropy change of the *combined* solute + solvent system. However, solvation entropy would seem unlikely to explain the $\Delta S^0_{struct} > 0$, as compaction of the ring structure increases the overall charge density, subsequently stronger hydration forces, a more ordered water solvent environment, and thus $\Delta S^0_{solvent} < 0$[73-74]. In short, the entropy gain from base stacking dissociation would appear to dominate the overall favorable looping entropy, resulting in positive ΔS^0_{struct}. It is interesting to note that positive entropy changes are also observed in detailed molecular simulation study by Mishra et al.[75], where the presence of a ssDNA linker entropically stabilizes the folded hairpin due to more prominent base stacking upon unfolding of the hairpin[75].

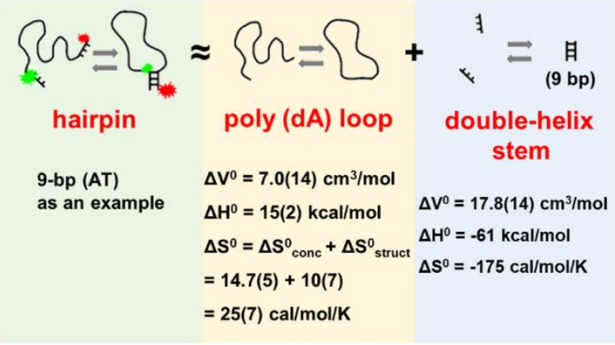

Figure 9.7 Summary of our simple additive model for deconstruction of the stem length dependent (9-bp (AT)) folding thermodynamics of a 40 A DNA hairpin.

In summary, the overall effect of the poly(dA) linker appears to be entropically favorable to hairpin folding ($\Delta S^0_{loop} > 0$). Part of this contribution arises from $\Delta S^0_{conc} > 0$ due simply to the increase in effective strand concentration for linked polymers, which results in a larger effective K_{fold} under unimolecular vs. bimolecular DNA duplexing conditions. The remainder of the entropy contribution can be attributed to conformational changes in the linker, whereby the disruption of base stacking in the poly(dA) linker relaxes the configurational confinement in translational and internal degrees of freedom during looping, resulting in $\Delta S^0_{struct} > 0$. In the end,

subtraction of $\Delta V^0_{stem} = \Delta V^0_{bp}(= +1.98(16)\ cm^3/mol/bp) \times n$ from the overall change of the free volume ΔV^0 is also plotted in Figure 9.6C to highlight the loop contribution ΔV^0_{loop}. In the context of this simple additive model, the thermodynamic properties (change in free volume, enthalpy, and entropy) of the isolated 9-bp stem and 40 A loop are schematically summarized in Figure 9.7.

9.6 Summary and conclusion

The thermodynamic properties (ΔH^0, ΔS^0 and ΔV^0) of DNA hairpin folding have been studied via smFRET spectroscopy as a function of temperature, external pressure (1-3000 bar), and base pair stem length. In the temperature dependent studies, folding of these 40A DNA hairpin constructs is found to be exothermic ($\Delta H^0 < 0$) with an entropic penalty ($\Delta S^0 < 0$), with pressure-induced unfolding experiments indicating that the DNA hairpin takes up more volume in the folded vs. unfolded state ($\Delta V^0 > 0$). With such high dynamic range in external pressure control (P_{ext} = 1 bar to 3000 bar), changes in free volume with single base pair resolution has been achieved, allowing ΔV^0 for the DNA hairpins to be linearly deconstructed into stem (ΔV^0_{bp} = +1.98(16) cm^3/mol/bp) and loop (ΔV^0_{loop} = +7.0(14) cm^3/mol) contributions by analyzing the dependence on length and complementary sequence. Based on predictions (ΔH^0_{stem} and ΔS^0_{stem}) from a nearest neighbor model, both ΔH^0 and ΔS^0 for the full DNA hairpin can thereby be deconstructed into stem and loop contributions. It is found that single strand loop formation is endothermic (ΔH^0_{loop} = +15(2) kcal/mol) and yet compensated by positive entropic gain (ΔS^0_{loop} = +25(7) cal/mol/K), where the looping endothermicity can be attributed to the disruption of base stacking in the poly(dA) linker. In the context of a simple additive thermodynamic model, this positive ΔS^0_{loop} can be further deconstructed into contributions due to unimolecular enhancement

in the effective strand concentration (ΔS^0_{conc} = +14.7(5) cal/mol/K), with the remainder attributed to structural changes in the loop (ΔS^0_{struct} = +10(7) cal/mol/K) arising from the disruption of base stacking relaxing external (i.e., translational) and internal (i.e., hindered rotational) constraints.

9.7 References

1. Heremans, K.; Smeller, L. Protein Structure and Dynamics at High Pressure. *Biochim. Biophys. Acta, Protein Struct. Mol. Enzymol.* **1998,** *1386*, 353-370.

2. Smeller, L. Pressure–Temperature Phase Diagrams of Biomolecules. *Biochim. Biophys. Acta, Protein Struct. Mol. Enzymol.* **2002,** *1595*, 11-29.

3. Mozhaev, V. V.; Heremans, K.; Frank, J.; Masson, P.; Balny, C. High Pressure Effects on Protein Structure and Function. *Proteins* **1996,** *24*, 81-91.

4. Meersman, F.; Daniel, I.; Bartlett, D. H.; Winter, R.; Hazael, R.; McMillan, P. F. High-Pressure Biochemistry and Biophysics. *Rev. Mineral. Geochem.* **2013,** *75*, 607-648.

5. Somero, G. N. Adaptations to High Hydrostatic Pressure. *Annu. Rev. Physiol.* **1992,** *54*, 557-577.

6. Zhang, J.; Peng, X.; Jonas, A.; Jonas, J. NMR Study of the Cold, Heat, and Pressure Unfolding of Ribonuclease A. *Biochemistry* **1995,** *34*, 8631-8641.

7. Jonas, J.; Ballard, L.; Nash, D. High-Resolution, High-Pressure NMR Studies of Proteins. *Biophys. J.* **1998,** *75*, 445-452.

8. Schroer, M. A.; Paulus, M.; Jeworrek, C.; Krywka, C.; Schmacke, S.; Zhai, Y.; Wieland, D. C. F.; Sahle, C. J.; Chimenti, M.; Royer, C. A.; Garcia-Moreno, B.; Tolan, M.; Winter, R. High-Pressure SAXS Study of Folded and Unfolded Ensembles of Proteins. *Biophys. J.* **2010,** *99*, 3430-3437.

9. Fujisawa, T.; Kato, M.; Inoko, Y. Structural Characterization of Lactate Dehydrogenase Dissociation under High Pressure Studied by Synchrotron High-Pressure Small-Angle X-ray Scattering. *Biochemistry* **1999,** *38*, 6411-6418.

10. Krywka, C.; Sternemann, C.; Paulus, M.; Tolan, M.; Royer, C.; Winter, R. Effect of Osmolytes on Pressure-Induced Unfolding of Proteins: A High-Pressure SAXS Study. *ChemPhysChem* **2008,** *9*, 2809-2815.

11. Patra, S.; Anders, C.; Erwin, N.; Winter, R. Osmolyte Effects on the Conformational Dynamics of a DNA Hairpin at Ambient and Extreme Environmental Conditions. *Angew. Chem. Int. Ed.* **2017,** *56*, 5045-5049.

12. Smeller, L.; Fidy, J.; Heremans, K. Protein Folding, Unfolding and Aggregation. Pressure Induced Intermediate States on the Refolding Pathway of Horseradish Peroxidase. *J. Phys.: Condens. Matter* **2004,** *16*, S1053-S1058.

13. Silva, J. L.; Oliveira, A. C.; Gomes, A. M. O.; Lima, L. M. T. R.; Mohana-Borges, R.; Pacheco, A. B. F.; Foguel, D. Pressure Induces Folding Intermediates that are Crucial for Protein–DNA Recognition and Virus Assembly. *Biochim. Biophys. Acta, Protein Struct. Mol. Enzymol.* **2002,** *1595*, 250-265.

14. Patra, S.; Anders, C.; Schummel, P. H.; Winter, R. Antagonistic Effects of Natural Osmolyte Mixtures and Hydrostatic Pressure on the Conformational Dynamics of a DNA Hairpin Probed at the Single-Molecule Level. *Phys. Chem. Chem. Phys.* **2018,** *20*, 13159-13170.

15. Bikard, D.; Loot, C.; Baharoglu, Z.; Mazel, D. Folded DNA in Action: Hairpin Formation and Biological Functions in Prokaryotes. *Microbiol. Mol. Biol. Rev.* **2010,** *74*, 570-588.

16. Nicholson, D. A.; Sengupta, A.; Sung, H.-L.; Nesbitt, D. J. Amino Acid Stabilization of Nucleic Acid Secondary Structure: Kinetic Insights from Single-Molecule Studies. *J. Phys. Chem. B* **2018,** *122*, 9869-9876.

17. Nakano, S.-i.; Yamaguchi, D.; Tateishi-Karimata, H.; Miyoshi, D.; Sugimoto, N. Hydration Changes upon DNA Folding Studied by Osmotic Stress Experiments. *Biophys. J.* **2012,** *102*, 2808-2817.

18. Patra, S.; Schuabb, V.; Kiesel, I.; Knop, J.-M.; Oliva, R.; Winter, R. Exploring the Effects of Cosolutes and Crowding on the Volumetric and Kinetic Profile of the Conformational Dynamics of a Poly dA Loop DNA Hairpin: a Single-Molecule FRET Study. *Nucleic Acids Res.* **2018,** *47*, 981-996.

19. Baltierra-Jasso, L. E.; Morten, M. J.; Laflör, L.; Quinn, S. D.; Magennis, S. W. Crowding-Induced Hybridization of Single DNA Hairpins. *J. Am. Chem. Soc.* **2015,** *137*, 16020-16023.

20. Stiehl, O.; Weidner-Hertrampf, K.; Weiss, M. Kinetics of Conformational Fluctuations in DNA Hairpin-Loops in Crowded Fluids. *New J. Phys.* **2013,** *15*, 113010.

21. Knowles, D. B.; LaCroix, A. S.; Deines, N. F.; Shkel, I.; Record, M. T. Separation of Preferential Interaction and Excluded Volume Effects on DNA Duplex and Hairpin Stability. *Proc. Natl. Acad. Sci. U.S.A.* **2011,** *108*, 12699-12704.

22. Varani, G. Exceptionally Stable Nucleic Acid Hairpins. *Annu. Rev. Biophys.* **1995,** *24*, 379-404.

23. John SantaLucia, J.; Hicks, D. The Thermodynamics of DNA Structural Motifs. *Annu. Rev. Biophys.* **2004,** *33*, 415-440.

24. SantaLucia, J.; Allawi, H. T.; Seneviratne, P. A. Improved Nearest-Neighbor Parameters for Predicting DNA Duplex Stability. *Biochemistry* **1996,** *35*, 3555-3562.

25. SantaLucia, J. A Unified View of Polymer, Dumbbell, and Oligonucleotide DNA Nearest-Neighbor Thermodynamics. *Proc. Natl. Acad. Sci. U.S.A.* **1998,** *95*, 1460-1465.

26. Rauzan, B.; McMichael, E.; Cave, R.; Sevcik, L. R.; Ostrosky, K.; Whitman, E.; Stegemann, R.; Sinclair, A. L.; Serra, M. J.; Deckert, A. A. Kinetics and Thermodynamics of DNA, RNA, and Hybrid Duplex Formation. *Biochemistry* **2013,** *52*, 765-772.

27. Tekmen, M.; Müller, J. D. High-Pressure Cell for Fluorescence Fluctuation Spectroscopy. *Rev. Sci. Instrum.* **2004,** *75*, 5143-5148.

28. Beimborn, J. C.; Hall, L. M. G.; Tongying, P.; Dukovic, G.; Weber, J. M. Pressure Response of Photoluminescence in Cesium Lead Iodide Perovskite Nanocrystals. *J. Phys. Chem. C* **2018,** *122*, 11024-11030.

29. Fiore, J. L.; Kraemer, B.; Koberling, F.; Edmann, R.; Nesbitt, D. J. Enthalpy-Driven RNA Folding: Single-Molecule Thermodynamics of Tetraloop−Receptor Tertiary Interaction. *Biochemistry* **2009,** *48*, 2550-2558.

30. Sengupta, A.; Sung, H.-L.; Nesbitt, D. J. Amino Acid Specific Effects on RNA Tertiary Interactions: Single-Molecule Kinetic and Thermodynamic Studies. *J. Phys. Chem. B* **2016,** *120*, 10615-10627.

31. Vieweger, M.; Holmstrom, Erik D.; Nesbitt, David J. Single-Molecule FRET Reveals Three Conformations for the TLS Domain of Brome Mosaic Virus Genome. *Biophys. J.* **2015,** *109*, 2625-2636.

32. Sung, H.-L.; Nesbitt, D. J. Novel Heat-Promoted Folding Dynamics of the *yybP-ykoY* Manganese Riboswitch: Kinetic and Thermodynamic Studies at the Single-Molecule Level. *J. Phys. Chem. B* **2019,** *123*, 5412-5422.

33. Fiore, J. L.; Hodak, J. H.; Piestert, O.; Downey, C. D.; Nesbitt, D. J. Monovalent and Divalent Promoted GAAA Tetraloop-Receptor Tertiary Interactions from Freely Diffusing Single-Molecule Studies. *Biophys. J.* **2008,** *95*, 3892-3905.

34. Fiegland, L. R.; Garst, A. D.; Batey, R. T.; Nesbitt, D. J. Single-Molecule Studies of the Lysine Riboswitch Reveal Effector-Dependent Conformational Dynamics of the Aptamer Domain. *Biochemistry* **2012,** *51*, 9223-9233.

35. Macgregor Jr., R. B. Effect of Hydrostatic Pressure on Nucleic Acids. *Biopolymers* **1998,** *48*, 253-263.

36. Roche, J.; Royer Catherine, A. Lessons from Pressure Denaturation of Proteins. *J. Royal Soc. Interface* **2018,** *15*, 20180244.

37. Roche, J.; Caro, J. A.; Norberto, D. R.; Barthe, P.; Roumestand, C.; Schlessman, J. L.; Garcia, A. E.; García-Moreno E., B.; Royer, C. A. Cavities Determine the Pressure Unfolding of Proteins. *Proc. Natl. Acad. Sci. U.S.A.* **2012,** *109*, 6945-6950.

38. Nucci, N. V.; Fuglestad, B.; Athanasoula, E. A.; Wand, A. J. Role of Cavities and Hydration in the Pressure Unfolding of T_4 Lysozyme. *Proc. Natl. Acad. Sci. U.S.A.* **2014,** *111*, 13846-13851.

39. Rashin, A. A.; Iofin, M.; Honig, B. Internal Cavities and Buried Waters in Globular Proteins. *Biochemistry* **1986,** *25*, 3619-3625.

40. Najaf-Zadeh, R.; Wu, J. Q.; Macgregor, R. B. Effect of Cations on the Volume of the Helix-Coil Transition of Poly[d(A-T)]. *Biochim. Biophys. Acta, Gene Struct. Expression* **1995,** *1262*, 52-58.

41. Rayan, G.; Macgregor, R. B. Pressure-Induced Helix–Coil Transition of DNA Copolymers is Linked to Water Activity. *Biophys. Chem.* **2009,** *144*, 62-66.

42. Rayan, G.; Macgregor, R. B. A Look at the Effect of Sequence Complexity on Pressure Destabilisation of DNA Polymers. *Biophys. Chem.* **2015,** *199*, 34-38.

43. Lane, A. N.; Jenkins, T. C. Thermodynamics of Nucleic Acids and Their Interactions with Ligands. *Annu. Rev. Biophys.* **2001,** *33*, 255-306.

44. McConnell, T. S.; Cech, T. R. A Positive Entropy Change for Guanosine Binding and for the Chemical Step in the Tetrahymena Ribozyme Reaction. *Biochemistry* **1995,** *34*, 4056-4067.

45. Mikulecky, P. J.; Feig, A. L. Cold Denaturation of the Hammerhead Ribozyme. *J. Am. Chem. Soc.* **2002,** *124*, 890-891.

46. Lumry, R.; Rajender, S. Enthalpy–Entropy Compensation Phenomena in Water Solutions of Proteins and Small Molecules: A Ubiquitous Properly of Water. *Biopolymers* **1970,** *9*, 1125-1227.

47. Schmid, R.; Miah, A. M.; Sapunov, V. N. A New Table of the Thermodynamic Quantities of Ionic Hydration: Values and Some applications (Enthalpy–Entropy Compensation and Born Radii). *Phys. Chem. Chem. Phys.* **2000,** *2*, 97-102.

48. Wu, J. Q.; Macgregor Jr., R. B. Pressure Dependence of the Helix–Coil Transition Temperature of Poly[d(G-C)]. *Biopolymers* **1995,** *35*, 369-376.

49. Allemand, J.-F.; Cocco, S.; Douarche, N.; Lia, G. Loops in DNA: An Overview of Experimental and Theoretical Approaches. *Eur. Phys. J. E* **2006,** *19*, 293-302.

50. Hanke, A.; Metzler, R. Entropy Loss in Long-Distance DNA Looping. *Biophys. J.* **2003,** *85*, 167-173.

51. Goddard, N. L.; Bonnet, G.; Krichevsky, O.; Libchaber, A. Sequence Dependent Rigidity of Single Stranded DNA. *Phys. Rev. Lett.* **2000,** *85*, 2400-2403.

52. Plumridge, A.; Meisburger, S. P.; Andresen, K.; Pollack, L. The Impact of Base Stacking on the Conformations and Electrostatics of Single-Stranded DNA. *Nucleic Acids Res.* **2017,** *45*, 3932-3943.

53. Ke, C.; Humeniuk, M.; S-Gracz, H.; Marszalek, P. E. Direct Measurements of Base Stacking Interactions in DNA by Single-Molecule Atomic-Force Spectroscopy. *Phys. Rev. Lett.* **2007,** *99*, 018302.

54. Mosayebi, M.; Romano, F.; Ouldridge, T. E.; Louis, A. A.; Doye, J. P. K. The Role of Loop Stacking in the Dynamics of DNA Hairpin Formation. *J. Phys. Chem. B* **2014,** *118*, 14326-14335.

55. Buhot, A.; Halperin, A. Effects of Stacking on the Configurations and Elasticity of Single-Stranded Nucleic Acids. *Phys. Rev. E* **2004,** *70*, 020902.

56. Yancey, P. H.; Blake, W. R.; Conley, J. Unusual Organic Osmolytes in Deep-Sea Animals: Adaptations to Hydrostatic Pressure and Other Perturbants. *Comp. Biochem. Physiol., Part A Mol. Integr. Physiol.* **2002,** *133*, 667-676.

57. Yancey, P. H.; Gerringer, M. E.; Drazen, J. C.; Rowden, A. A.; Jamieson, A. Marine Fish May be Biochemically Constrained from Inhabiting the Deepest Ocean Depths. *Proc. Natl. Acad. Sci. U.S.A.* **2014,** *111*, 4461-4465.

58. Holmstrom, E. D.; Dupuis, N. F.; Nesbitt, D. J. Kinetic and Thermodynamic Origins of Osmolyte-Influenced Nucleic Acid Folding. *J. Phys. Chem. B* **2015,** *119*, 3687-3696.

59. Svoboda, P.; Cara, A. D. Hairpin RNA: A Secondary Structure of Primary Importance. *Cell. Mol. Life Sci.* **2006,** *63*, 901-908.

60. Alden, C. J.; Kim, S.-H. Solvent-accessible surfaces of nucleic acids. *Journal of Molecular Biology* **1979,** *132*, 411-434.

61. Pal, S.; Maiti, P. K.; Bagchi, B.; Hynes, J. T. Multiple Time Scales in Solvation Dynamics of DNA in Aqueous Solution: The Role of Water, Counterions, and Cross-Correlations. *The Journal of Physical Chemistry B* **2006,** *110*, 26396-26402.

62. Auffinger, P.; Hashem, Y. Nucleic Acid Solvation: From Outside to Insight. *Curr. Opin. Struct. Biol.* **2007,** *17*, 325-333.

63. Kuhn, W. Über die Gestalt fadenförmiger Moleküle in Lösungen. *Kolloid-Zeitschrift* **1934,** *68*, 2-15.

64. Kuhn, W.; Kuhn, H. Die Frage nach der Aufrollung von Fadenmolekeln in strömenden Lösungen. *Helv. Chim. Acta* **1943,** *26*, 1394-1465.

65. Vologodskii, A., *Biophysics of DNA*. Cambridge University Press: Cambridge, 2015.

66. Doi, M.; See, H., *Introduction to Polymer Physics*. Oxford Univesity Press: New York, U.S.A., 1996.

67. Chi, Q.; Wang, G.; Jiang, J. The Persistence Length and Length per Base of Single-Stranded DNA Obtained from Fluorescence Correlation Spectroscopy Measurements Using Mean Field Theory. *Physica A* **2013,** *392*, 1072-1079.

68. Kuznetsov, S. V.; Shen, Y.; Benight, A. S.; Ansari, A. A Semiflexible Polymer Model Applied to Loop Formation in DNA Hairpins. *Biophysical Journal* **2001,** *81*, 2864-2875.

69. Murphy, M. C.; Rasnik, I.; Cheng, W.; Lohman, T. M.; Ha, T. Probing Single-Stranded DNA Conformational Flexibility Using Fluorescence Spectroscopy. *Biophysical Journal* **2004,** *86*, 2530-2537.

70. Seol, Y.; Skinner, G. M.; Visscher, K.; Buhot, A.; Halperin, A. Stretching of Homopolymeric RNA Reveals Single-Stranded Helices and Base-Stacking. *Phys. Rev. Lett.* **2007,** *98*, 158103.

71. Searle, M. S.; Williams, D. H. On the Stability of Nucleic Acid Structures in Solution: Enthalpy - Entropy Compensations, Internal Rotations and Reversibility. *Nucleic Acids Res.* **1993,** *21*, 2051-2056.

72. Brahms, J.; Michelson, A. M.; Van Holde, K. E. Adenylate Oligomers in Single- and Double-Strand Conformation. *J. Mol. Biol.* **1966,** *15*, 467-488.

73. Huber, R. G.; Fuchs, J. E.; von Grafenstein, S.; Laner, M.; Wallnoefer, H. G.; Abdelkader, N.; Kroemer, R. T.; Liedl, K. R. Entropy from State Probabilities: Hydration Entropy of Cations. *The Journal of Physical Chemistry B* **2013,** *117*, 6466-6472.

74. Marcus, Y. Thermodynamics of Ion Hydration and its Interpretation in Terms of a Common Model. *Pure Appl. Chem.* **1987,** *59*, 1093.

75. Mishra, G.; Giri, D.; Li, M. S.; Kumar, S. Role of Loop Entropy in the Force Induced Melting of DNA Hairpin. *J. Chem. Phys.* **2011,** *135*, 035102.

Chapter 10

High Pressure Single-Molecule FRET Studies of the Lysine Riboswitch: Cationic and Osmolytic Effects on Pressure Induced Denaturation

---

10.1 Abstract

Deep sea biology is known to thrive at pressures up to ≈ 1 kbar, which motivates fundamental biophysical studies of biomolecules under such extreme environments. In this work, the conformational equilibrium of the lysine riboswitch has been systematically investigated by single molecule FRET (smFRET) microscopy at pressures up to 1500 bar. The lysine riboswitch preferentially unfolds with increasing pressure, which signals an increase in free volume ($\Delta V^0 > 0$) upon reverse folding of the biopolymer. Indeed, the effective lysine binding constant increases quasi-exponentially with pressure rise, which implies a significant weakening of the riboswitch-ligand interaction in a high-pressure environment. The effects of monovalent/divalent cations and osmolytes on folding are also explored to acquire additional insights into cellular mechanisms for adapting to high pressures. For example, we find that although Mg^{2+} greatly stabilizes folding of the lysine riboswitch ($\Delta\Delta G^0 < 0$), there is negligible impact on changes in free volume ($\Delta\Delta V^0 \approx 0$) and thus any pressure induced denaturation effects. Conversely, osmolytes (commonly at high concentrations in deep sea marine species) such as the trimethylamine N-oxide (TMAO) significantly reduce free volumes ($\Delta\Delta V^0 < 0$) and thereby diminish pressure-induced denaturation. We speculate that, besides stabilizing RNA structure, enhanced levels of TMAO in cells might increase the dynamic range for competent riboswitch

*This chapter is adapted from: Sung, H.-L.; Nesbitt, D. J. High Pressure Single-Molecule FRET Studies of the Lysine Riboswitch: Cationic and Osmolytic Effects on Pressure Induced Denaturation. *Phys. Chem. Chem. Phys.* **2020**, *22*, 15853-15866.

folding by suppressing the pressure-induced denaturation response. This in turn could offer biological advantage for vertical migration of deep-sea species, with impacts on food searching in a resource limited environment.

10.2 Introduction

The effective free volume of a biomolecule can vary substantially upon folding, mainly due to changes in accessibility of hydrophilic regions and compactness of the resulting water configuration[1-4]. Consequently, the equilibrium between each conformation can be modulated by pressure, according to Gibbs free energy: $\Delta G^0 = \Delta U^0 - T\Delta S^0 + P\Delta V^0$.[5-6] Although pressure is often a relatively benign variable in biology, pressure dependence of folding is extremely important to deep sea marine species, as a result of the rapid increase of hydraulic pressure with ocean depth (≈ 1 bar every 10 meters). In fact, multiple organisms have been found thriving in the deep sea and some even at the bottom of the Mariana Trench[7], where pressure at the deepest point is P ≈ 1.1 kbar. It is thus of considerable interest to investigate not only the biophysical response of biomolecules to pressure fluctuations, but also the molecular strategies developed by deep sea organisms to accommodate extreme pressures and changes in pressure by vertical migration. As an explicit focus of this work, we combine single molecule fluorescence microscopy tools in a high pressure apparatus to explore the folding dynamics of RNA riboswitches.

As a simple test construct for such studies, riboswitches are noncoding mRNA elements that can regulate their shape and gene expression in response to the specific presence of small molecular ligands.[8-10] The aptamer domain of a riboswitch structurally changes to selectively

capture a specific ligand molecule(s), with which the gene expression platform may toggle between "on" and "off" conformations and thus result in disparate regulatory outcomes. In order to optimize gene regulation, therefore, the folding equilibrium of a riboswitch must be delicately modulated by a multitude of external variables such as external pressure, temperature, and concentrations of monovalent/divalent cations and osmolytes. Although external pressure might seem only a relatively small perturbation, typical free volume changes associated with DNA hairpin formation with only 7-10 bp (say, $\Delta V^0 \approx 25$ mL/mol) translate into free energy changes of ≈ 0.6 kcal/mol $\approx$ kT at 1 kbar pressures common to deep ocean marine life[11]. To date, pressure-dependent studies of nucleic acid folding have been largely limited to secondary structure formation,[11-17] with studies of higher order (tertiary) interactions only for the DNA G-quadruplex[18-20] and RNA tetraloop-tetraloop receptor (TL-TLR).[21] This leaves the highly diverse arena of RNA riboswitch tertiary structure motifs largely uninvestigated and ripe for further exploration as a function of external hydrostatic pressure. In the present work, we have chosen the lysine riboswitch[22] (see Figure 10.1) as a model system to study the pressure dependent effects on ligand binding and tertiary folding, both of which are among the most important conformational transitions in biologically functional RNA.

To achieve these goals, we have recently converted our single molecule confocal FRET (smFRET) apparatus into a novel tool for biomolecular folding studies at high pressure (see Figure 10.2)[11, 16-17, 23]. The present high pressure smFRET measurements are performed in a square (50 μm x 50 μm) quartz capillary sample cell, which due to relatively small surface area of the inner capillary can sustain pressures up to 5 kbar without shattering[11]. Such a large dynamic range of pressures enables us to obtain precise measurement of free volume differences

upon nucleic acid folding (ΔV^0), as well as changes in these free volumes ($\Delta\Delta V^0$) in response to various cationic and osmolytic buffer conditions.

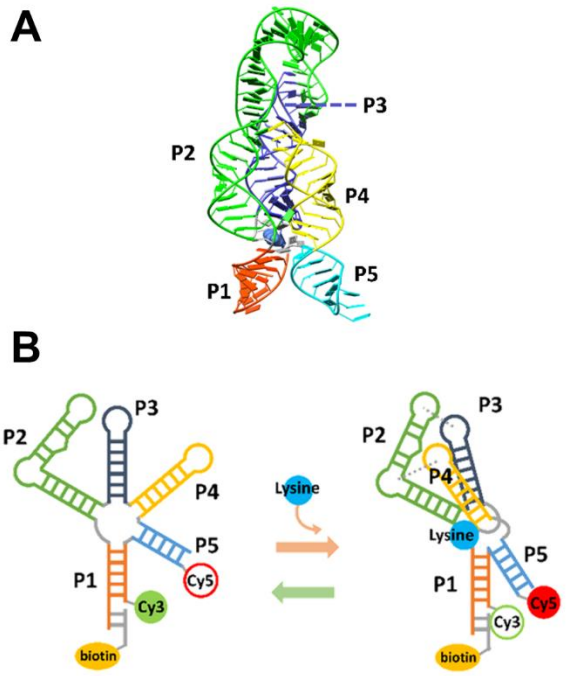

Figure 10.1 Single molecule FRET construct design for studying ligand-induced lysine riboswitch folding. (A) Crystal structure of the lysine riboswitch. (PDB: 4ERJ) (B) Schematic representation of lysine riboswitch folding and the energy transfer between Cy3 and Cy5 in each conformation. (Left: unfolded; right: folded)

The basic organization of this paper is as follows. Key aspects of the i) high pressure confocal experimental apparatus, ii) construct design and preparation, and iii) sample data analysis are presented in Sec. 10.3.1-3, followed by a detailed pressure dependent studies under a variety of buffer conditions. Specifically, since both solvent and solute, in addition to the biomolecule itself, can contribute significantly to the folding thermodynamics,[24-26] the pressure-dependent response of the lysine riboswitch has been systematically studied as a function of three classes of solutes: i) ligand (lysine), ii) monovalent (Na^+) and divalent (Mg^{2+}) cations, and

iii) osmolyte (trimethylamine *N*-oxide, TMAO) concentrations, as presented in Sec 10.4.1-4 First of all, as the cognate ligand, lysine plays an obviously central role in lysine riboswitch folding, which from previous detailed kinetic analyses[27] has been shown to be triggered by a single lysine in a "induced-fit" mechanism, whereby the ligand first binds and then folds.[27-28] Secondly, nucleic acids interact strongly with cations, due to its polyanionic nature of the RNA polymer. Thus, cationic solute species as Na^+ and Mg^{2+} can not only result in compaction of a folded (or unfolded) nucleic acid structure, but also significantly alter the hydration shell through partial Debye shielding of the Coulomb interactions[29-30]. Thirdly, TMAO is an osmolyte commonly found in marine species[31-32], with increasing accumulations in deep sea fish and amphipods.[33-34] Moreover, TMAO has been shown to act as a chemical chaperone[35] to stabilize protein[36-37] and nucleic acids[38-39] structures at ambient pressures, and to preserve enzyme activity at high pressures[40-41]. These suggest TMAO to be a crucial "piezolyte" with which to counteract pressure induced denaturation effects. Indeed, in the present work, we find that an increase in TMAO results in a novel preferential *stabilization* of the folded riboswitch conformation at high pressure ($\Delta\Delta V^0 < 0$), thereby counterbalancing the above-noted tendency for RNA to be *destabilized* with increasing pressure, as discussed further in Sec. 10.5. Finally, the paper presents summary results, possible directions for future investigation, and concluding remarks in Sec 10.6.

10.3 Experiment

10.3.1 High pressure capillary sample cell and pressure control

These high pressure smFRET experiments are made possible by introduction of a high pressure glass capillary sample cell[11, 17, 23] into a time correlated single photon counting confocal

microscope (see Figure 10.2).[42] Specifically, for the sample cell we use square capillary tubing made from fused silica, with ≈ 360 μm and ≈ 50 μm outer and inner sidewall lengths, respectively (Polymicro, Phoenix, AZ). Due to the small surface area of the inner capillary, the cell can sustain repeated high internal pressure cycling up to 5 kbar without fracturing. Moreover, the wall thickness (≈ 155 μm) and relatively flat interior and exterior surfaces of the square capillary mimic a standard cover slip and thereby optimize the excitation/collection photon efficiencies for fluorescence studies.

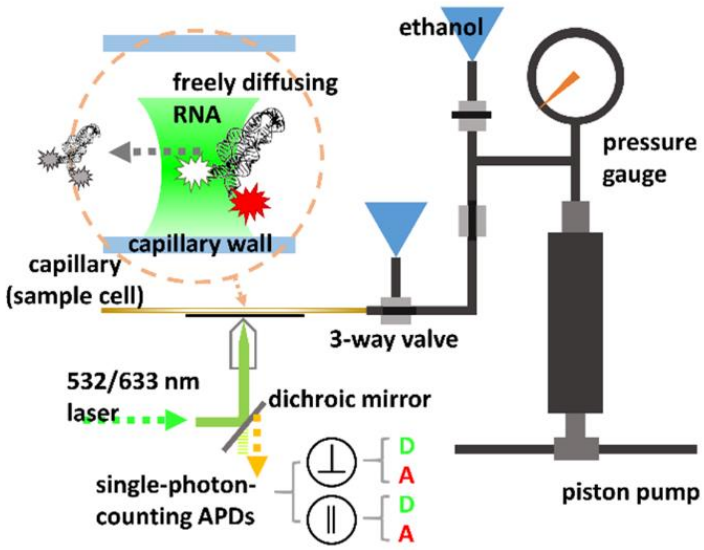

Figure 10.2 High pressure smFRET diffusing experiment setup.

To prepare a sample for high pressure smFRET study, one end of the capillary is first glued to a modified stainless-steel pressure plug (High Pressure Equipment, Erie, PA). A small section of the opaque hydrocarbon polymer coating of the capillary is then removed by low temperature propane flame oxidation to create a clear optical window for fluorescence excitation and detection. We load the sample by capillary forces, simply immersing one end into the sample

solution; once the capillary is filled, its free end (far from the pressure plug) is sealed by momentary heating with an oxy-propane torch. Prior to coupling the cell to the high pressure system, the open end of the capillary is dipped into low viscosity silicone oil to create a thin, immiscible liquid layer. This prevents any contamination of the sample from the pressure-transmitting ethanol and yet still conducts pressure effectively from the hydraulic press (*vide infra*) to the single molecule detection volume. More detailed description of sample cell preparation and alignment of the excitation/fluorescence microscope can be found in our previous work[11].

The source of high pressure is a manually operated piston screw pump (High Pressure Equipment) which can generate and deliver pressures up to 5 kilobars. The pressure generator is connected to the sample cell and a Bourdon pressure gauge via high pressure stainless steel tubing with 1/4" O.D. and 1/16” I.D. (High Pressure Equipment, rated at 100,000 psi), with the entire manifold using ethanol as the pressure-transmitting fluid. Prior to high pressure experimentation, any residual air bubbles in the manifold are removed by repeatedly venting and flushing the high pressure valves. The end-point absence of any residual air bubble is unambiguously evidenced by dramatic increase in the pressurizing efficiency with manual displacement of the piston screw pump.

10.3.2 RNA lysine riboswitch construct and sample preparation

The crystal structure of the *B. subtilis lysC* riboswitch aptamer is shown in Figure 10.1A[22]. According to previous structural characterizations of the ligand-bound and ligand-free *lysC* aptamer domain[22, 43-44], the lysine induced conformational change (Figure 10.1B) mostly likely involves a change in the relative orientation of the P1 and P5 helices in response to ligand binding at the five-way aptamer junction. Therefore, to optimize smFRET contrast in the

construct design, the Cy3 and Cy5 dyes are attached at the distal ends of P1 and P5, respectively (Figure 10.1B).[27] The three-strand lysine riboswitch smFRET construct is specifically illustrated in Figure 10.1B, with detailed RNA oligomer designs and synthesis methods available from our previous lysine riboswitch studies under ambient pressure conditions.[27] In anticipation of future smFRET studies, we have also incorporated an additional biotin modification at the extended P1 stem for tethering the RNA construct onto BSA-biotin/streptavidin modified surfaces, which will restrict free diffusion and enable much longer observation times for studies of single molecule kinetics. For maximum simplicity in these early high-pressure experiments, however, we have chosen to *not* tether the construct to the surface. This allows the RNA riboswitch construct to freely diffuse in the capillary cell through the laser beam focus, for which detection/sorting fluorescence photon "bursts" ($\tau \sim 1$ ms duration) through dichroic filters onto avalanche photodiodes permit statistical probing of the instantaneous biomolecular conformations by smFRET.

In preparation for smFRET sample solutions, the stock RNA solution is diluted in imaging buffer to ~ 50 pM, i.e., sufficiently low that each fluorescence burst results exclusively from only one doubly-labeled construct diffusing through the confocal volume. The imaging buffer contains i) 50 mM hemipotassium HEPEs buffer (pH 7.5), ii) Trolox/PCA/PCD oxygen scavenger cocktail to catalytically remove oxygen, iii) 25 mM KCl, 100 mM NaCl and 0.5 mM $MgCl_2$ to provide background salt, and iv) sufficient lysine, TMAO, additional NaCl and $MgCl_2$ to achieve the desired experimental conditions.

10.3.3 Single-molecule FRET spectroscopy and data analysis

The high pressure smFRET experiment is based on a homebuilt inverted confocal microscope setup with details described in previous work (Figure 10.2)[42]. In short, a water

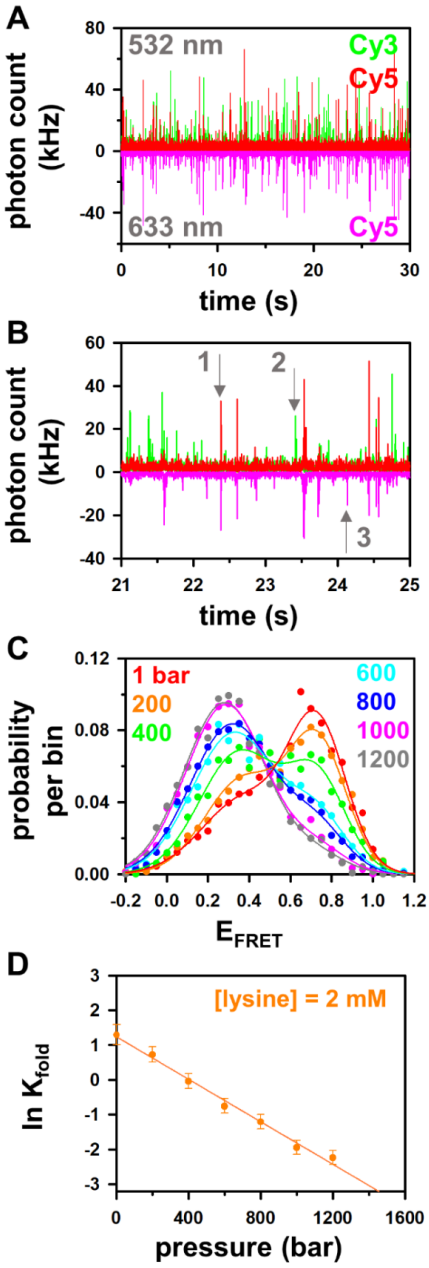

Figure 10.3 Sample data and analysis. (A) Representative time-resolved fluorescence trajectories. The green and red signals plotted upward correspond to Cy3 and Cy5 fluorescence channels, respectively. The pink traces from 633 nm alternating laser excitation (ALEX) is plotted downward for direct comparison to conform the presence (or absence) of the Cy5 labeling. (B) Detailed fluorescent traces displaying individual fluorescent events: (1) folded doubly labeled, (2) Cy3-only and (3) Cy5-only labeled construct. (C) Sample E_{FRET} histogram of the lysine riboswitch folding with [lysine] = 2.0 mM at increasing pressure. Each set of data is fit to a two-Gaussian function where the high and low E_{FRET} populations correspond to folded and unfolded conformations of the lysine riboswitch respectively. (D) The $\ln(K_{fold})$ vs P plot where the slope yields the free volume change during folding ΔV^0.

immersion objective with 1.2 NA tightly focuses the collimated incident beam into a nearly diffraction limited spot ($1/e^2$ radius = 310(30) nm). The resulting fluorescent photons are collected through the same objective, sorted into spatially distinct color/polarization channels with dichroic filters/polarization cubes before being detected by an array of four single-photon counting avalanche photodiodes. Since the double fluorophore labelling efficiency is < 100%, alternating laser excitation methods (ALEX) with interleaving green and red laser pulses are used to rigorously ensure that only bursts from doubly-labeled RNA constructs are included in the FRET energy transfer efficiency (E_{FRET}) distributions.[27, 45] Sample fluorescence traces are exhibited in Figure 10.3A and Fig. 10.3B, with the ALEX signal plotted downward (pink) to distinguish it from the upward FRET (green/red) emission channels. By way of example, the series of photon events flagged by arrows in Figure 10.3B and numbered from 1 to 3 can be unambiguously sorted into fluorescent bursts corresponding to 1) doubly labeled, 2) Cy3 only and 3) Cy5 only RNA constructs, respectively.

Integrated over the full burst diffusion time, the E_{FRET} value ($E_{FRET} = I_A/(I_A + I_D)$) for each event from doubly-labeled DNA is computed and used to generate a E_{FRET} histogram (Figure 10.3C). The lysine riboswitch histogram clearly reveals two distinct populations with low E_{FRET} (~ 0.3) and high E_{FRET} (~ 0.7) states, which corresponds well with predictions for unfolded and folded conformations, respectively.[27] Therefore, data are fit to a two-Gaussian distribution function with the center and width of the high E_{FRET} peak floating globally (Figure 10.3C).[27, 45] As a function of hydrostatic external pressure, the unfolded population clearly increases while the folded population decreases (see Figure 10.3C). The relative abundance of the two states can be quantified by taking the ratio of the areas under the two fitted Gaussian functions to obtain the riboswitch equilibrium constant for folding. Note that under saturating

lysine/salt concentrations, the maximum fraction of free diffusing riboswitch constructs folded is only 71(8) % of the value obtained from direct single-molecule observation of an immobilized construct (see Figure 10.4). This fraction is in good agreement with previous reported values of 67(3) % in earlier riboswitch studies restricted to a narrower range of [lysine] due to time resolution limits.[27] As shown previously, such discrepancies between the diffusing and immobilized measurements occur because a small fraction (28(4) %) of the constructs are stuck in long lived misfolded states, with only 72(4) % actively undergoing conformational transitions.[27] Thus, accurate extraction of single molecule equilibrium constants (K_{fold}) is

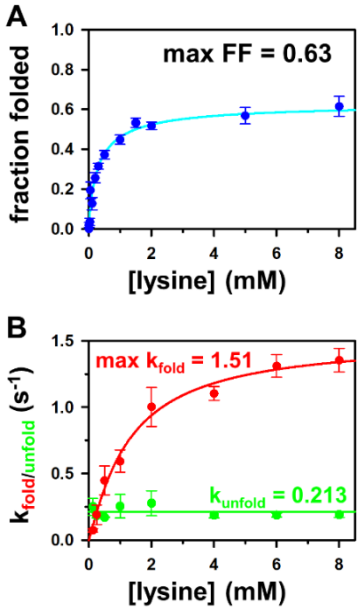

Figure 10.4 Lysine dependent folding at the ambient pressure obtained from smFRET (A) diffusing and (B) surface tether experiments. Data of fraction folded and k_{fold} are fit to the Hill equation with floating Hill coefficients n = 0.93(16) and 1.12(17), respectively, consistent with the expected ligand binding stoichiometry from crystal structure data. In smFRET diffusing experiments, the max folded fraction is observed as 0.63(6) at saturating [lysine]. In surface tether experiments where the lysine-dependent folding and unfolding rates can be obtained by prolonged observation of the fluorescence signals from a single construct at a time, the k_{unfold} is found independent of [lysine] as 0.213(14) s^{-1} and the k_{fold} is determined as 1.51(13) s^{-1} at saturating [lysine], leading to the steady state folded fraction as 0.88(9). The difference in fraction folded (29(8) %) between the diffusing and surface tether measurements is made up by the subpopulaion of constructs that are incapable of folding (28(4) %) from the previous raster scanned image.

obtained after correction for the inactive non-folding subpopulations,[46-47] with these corrected values used in all further analyses.

10.4 Results and analysis

10.4.1 Pressure-induced denaturation of the lysine riboswitch

The systematic decrease in the folded (high E_{FRET} state) construct population as a function of increasing pressure (Figure 10.3C) clearly indicates that folding of the lysine riboswitch is energetically disfavored at high pressure. We can quantitatively express the pressure dependence of this folding equilibrium constant from[5]

$$\left(\frac{\partial lnK_{fold}}{\partial P}\right)_T = \frac{-\Delta V^0}{RT}, \qquad \text{Eq. 10.1}$$

where R is the gas constant and ΔV^0 denotes the change in effective free volume upon folding: $\Delta V^0 = V_{fold} - V_{unfold}$. The pressure induced denaturation we see experimentally signifies that $\Delta V^0 > 0$, e.g. the effective free volume *increases* upon folding. Such a free volume change can be further quantified by a $\ln(K_{fold})$ vs pressure "van't Hoff" plot (Figure 10.3D), for which Eq. 10.1 predicts a slope of $-\Delta V^0/RT$. In Figure 10.3D, the free volume change of lysine riboswitch folding at [lysine] = 2 mM is extracted from a linear least squares fit to be $\Delta V^0 = +75(3)$ mL/mol.

The positive sign of this free volume change may seem at first counterintuitive. The folded RNA state is generally thought to be more compact in size, but such intuitions are only valid for the solute and ignore the complete solute + solvent system. The positive ΔV^0 values therefore arise from changes not just in the biopolymer solute itself but in the effective volume of the surrounding solvent and solvent accessibility[1-4]. For example, unfolded RNA presents a less shielded polyanionic conformation to the solvent, which therefore becomes more hydrated due to

larger solvent-exposed surface area. This could in general result in a more highly ordered hydration shell with smaller effective volume and therefore a $\Delta V^0 > 0$ upon refolding[48-49]. Alternatively, folding with more tertiary/higher order contacts can create hydrophobic voids that exclude water molecules, which would also contribute to the folded state occupying an effectively larger volume with $\Delta V^0 > 0$.[2] We note that a similarly counterintuitive effects also occur in high pressure studies of protein folding, which routinely indicate pressure induced denaturation effects consistent with $\Delta V^0 > 0$.[4-5] One clear take home message from the anomalous sign of ΔV^0 for nucleic acid and proteins is that coupled solute + solvent dynamics must play an exceedingly important synergistic role and cannot be ignored.

It is also worth noting that these $\Delta V^0 \approx 75(3)$ mL/mol free volume changes in the lysine riboswitch are an order of magnitude larger than the $\Delta V^0 \approx 5$ to 9 mL/mol values obtained from bulk fluorescence studies of the RNA tetraloop-tetraloop receptor (TL-TLR) at high pressures over a series of buffer conditions.[21] However, given that multiple tertiary structure formations are involved in lysine riboswitch folding, these differences become much easier to rationalize[22]. Indeed, the lysine riboswitch construct is a much more complex RNA folding motif than the simple TL-TLR system, with a multi-helix junction connecting 5 mutually interacting stem-loops. Moreover, the lysine riboswitch also has a larger molecular size (~ 6 kDa) comparable to that of a small protein. Thus, the ΔV^0 values measured for the lysine riboswitch are in fact comparable with values measured for small proteins (≈ 50-150 mL/mol) over a similar range of molecule weights (10-20 kDa).[50-51]

10.4.2 Pressure-dependent effects on ligand-induced folding of the lysine riboswitch

Binding of the cognate ligand lysine to the 5-way junction promotes the folded state of the riboswitch and thus brings stem 1 and stem 5 in close proximity (Figure 10.1B).[27] The

association of a lysine molecule has been previously identified to be crucial for conformational change of the lysine riboswitch through an "induced-fit" (i.e., bind-then-fold), mechanism,[27] suggesting a well-defined ligand-bound folded conformation.[28] We are therefore naturally interested in the role of ligand in promoting or decreasing the pressure stability of the well-established ligand-riboswitch interaction. The pressure dependence of lysine riboswitch folding has been studied as a function of [lysine] from 0.5 to 8 mM. Since lysine (side chain pKa = 10.5) is already positively charged in our buffer (pH ~ 7.5), this could in principle influence the riboswitch stability due to Debye shielding effects in the Na^+ and Mg^{2+} cation studies reported below. To specifically isolate the ligand-aptamer interactions from the less ligand-specific effects due to the positive charge of lysine, the dynamic range of lysine concentrations explored has

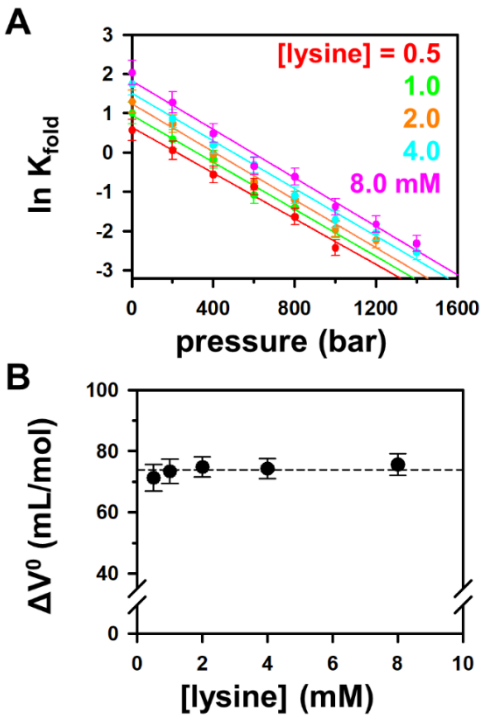

Figure 10.5 Pressure dependence of folding at series of ligand (lysine) concentrations. (A) $\ln(K_{fold})$ vs P plot where the parallel lines indicate constant ΔV^0. (B) The insensitivity of folding ΔV^0 to lysine concentration where the error bars are visually magnified by two with the vertical break.

therefore been restricted to < 10 mM, i.e., more than an order of magnitude lower than typical [Na^+] values (> 100 mM) previously shown necessary to promote nucleic acid stability.[42, 52]

The pressure dependence of K_{fold} as a function of [lysine] is displayed as a logarithmic plot in Figure 10.5A, with each set of data well fit to a linear function predicted by Eq. 10.1. By visual inspection, the slopes remain relatively unaffected, while the intercepts all vertically shift upwards with increasing [lysine]. Stated alternatively, the presence of lysine significantly stabilizes the folding of the lysine riboswitch, and yet with negligible effect on any change in the free volume ($\Delta\Delta V^0 \approx 0$). The results are more quantitatively summarized in Table 10.1, where ΔV^0 is plotted in Figure 10.5B as a function of [lysine]. Figure 10.5B demonstrates the remarkable insensitivity of ΔV^0 to lysine concentrations (note the break in the vertical axis, visually magnifying any such lysine dependences by a factor of two).

[lysine] (mM)	**0.5**	**1.0**	**2.0**	**4.0**	**8.0**
ΔV^0 (mL/mol)	**71(4)**	**73(3)**	**75(3)**	**74(3)**	**76(3)**

Table 10.1 ΔV^0 obtained at increasing [lysine]

For ligand-induced riboswitch folding, the dissociation constant is a common measure of the ligand-RNA interaction strength,[53] where K_d is equivalent to the lysine concentration at the point of 50% folding, i.e., where [folded] ≈ [unfolded] and thus $\ln(K_{fold}) = 0$. One should note that K_d represents an apparent dissociation constant, since the actual ligand binding and riboswitch folding event (which triggers the FRET change) could in principle be decoupled and separated in time.[28] Conveniently restated, we can therefore empirically determine the

corresponding 50% pressures ($P_{50\%}$) for which [lysine] equals K_d from the data in Figure 10.5A, obtained from the intersection of each least squares fit with $\ln(K_{fold}) = 0$. For example, the x-intercept for [lysine] = 0.5 mM corresponds to $P_{50\%} \approx 221$ bar (see Figure 10.5A), which implies that at 221 bar applied pressure, the lysine riboswitch is 50% unfolded and thus $K_d \approx 0.5$ mM. In this fashion, the results in Figure 10.5A can be more usefully replotted as K_d vs applied pressure (see Figure 10.6), where we have included the value ($K_d = 0.31(10)$ mM) determined from concentration dependent folding at ambient pressure (see Figure 10.4). Interestingly, Figure 10.6 reveals that the dissociation constant K_d increases dramatically and indeed roughly *exponentially* as a function of increasing pressure. On the one hand, this result follows immediately from the fact that the plots in Figure 10.5A are linear and free energies scale as the logarithm of equilibrium constants. On the other hand, our simple restatement of the data in terms of the apparent lysine K_d suggests a subtler interpretation – that external pressure weakens the apparent binding/binding-induced folding of lysine to the riboswitch. Furthermore, this behavior predicts that weakening of the RNA-ligand interaction becomes exponentially more significant at higher

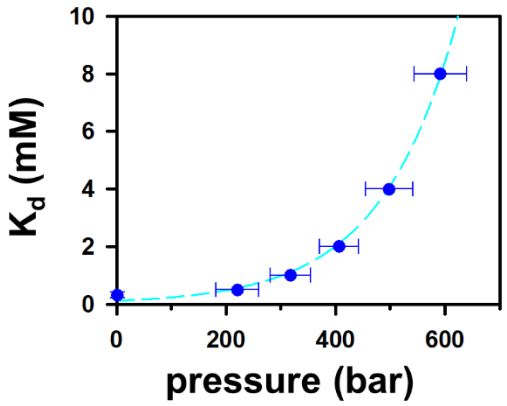

Figure 10.6 Pressure effects on apparent K_d of lysine binding. K_d increases exponentially with pressures, suggesting riboswitch-ligand interactions are efficiently weakened at high pressures.

pressure. For example, at the bottom of the Mariana Trench (≈ 1.1 kbar), Figure 10.6 predicts that K_d will be *increased by 3 orders of magnitude* (≈ 300 mM), signaling much higher [lysine] required to achieve biochemically competent folding of the riboswitch. Due to such strong denaturation influences, one anticipates the need for deep sea organisms to develop adaptive mechanisms to counteract pressure in order to maintain correct biochemical function,[31-32] a point to which we will return and discuss further in Sec 10.5.3.

10.4.3 Cation effects on pressure dependent folding of the lysine riboswitch

Nucleic acids are highly negatively charged polymers, with one phosphate group per nucleotide and which therefore interact strongly with solute cations. It has been well established that mono- and divalent cations are crucial to stabilizing the native structure of a nucleic acid riboswitch, with tertiary interactions in the riboswitch folding particularly sensitive to physiologically important multivalent cations such as Mg^{2+}.[29-30, 54-57] We thus are naturally interested in both monovalent and divalent cation effects on the pressure dependent response of the lysine riboswitch. To explore the monovalent cation effects, the pressure dependence on riboswitch folding is first studied as a function of $[Na^+]$ at constant divalent ($[Mg^{2+}]$ = 0.5 mM) and ligand ([lysine] = 0.5 mM) concentrations (Figure 10.7A). Interestingly, over the

$[Na^+]$ (mM)	125	250	500
ΔV^0 (mL/mol)	71(4)	72(5)	76(6)
$[Mg^{2+}]$ (mM)	0.5	1.0	1.5
ΔV^0 (mL/mol)	71(4)	69(6)	72(6)

Table 10.2 ΔV^0 obtained at increasing monovalent (Na^+)/divalent (Mg^{2+}) cation concentrations.

physiologically relevant scale of [Na^+] from 100 to 500 mM, the effects are quite similar to that of lysine, i.e., with the slopes in Figure 10.7A predicting essentially negligible dependence of free volume change on Na^+. Indeed, the slopes are indistinguishable within experimental uncertainty, which from the above lysine analysis indicates that i) ΔV^0 is independent of Na^+ over physiological range and ii) the dependence of K_{fold} on pressure is insensitive to [Na^+] from ambient up to 1 kbar. These ΔV^0 results are quantitatively summarized in Figure 10.7B and Table 10.2, with the data confirming that both the folding equilibrium constant and its pressure-dependent response remain relatively constant over the range of physiologically relevant [Na^+].

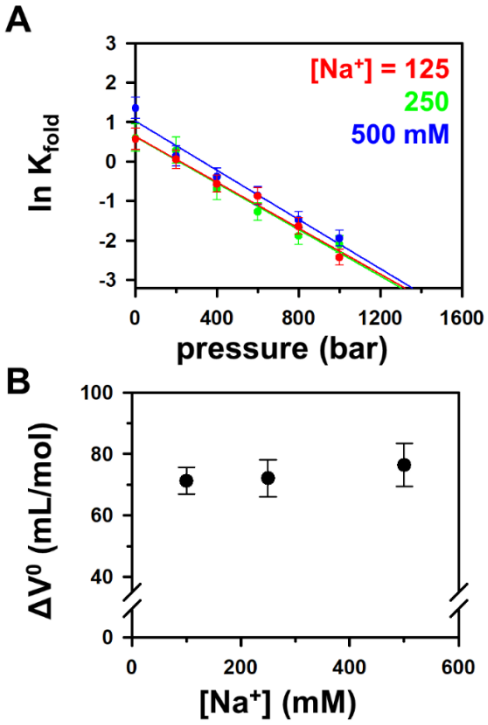

Figure 10.7 Pressure dependence of folding at series of Na^+ concentrations. (A) ln(K_{fold}) vs P plot where folding shows negligible dependence on [Na^+]. (B) [Na^+] (in)dependence of ΔV^0.

We next turn to the effects of divalent Mg^{2+} on this pressure dependent riboswitch folding. Once again, the slopes (see Figure 10.8) in each of the plots of ln(K_{fold}) vs P plots are

equal within experimental uncertainty. This is equivalent to the statement that there is no Mg^{2+} dependence to free volume changes observed upon folding of the lysine riboswitch, as more quantitatively captured in the nearly horizontal data plot in Figure 10.8B. This contrasts, however, with the monovalent Na^+ results in that there are very significant effects on K_{fold} due to the presence of Mg^{2+} even at ambient pressure (Figure 10.8A). Note that the range of [Mg^{2+}] studied is nearly 3 orders of magnitudes lower than [Na^+], again indicating much stronger Mg^{2+} stabilization effects on RNA tertiary structures and consistent with many previous studies.[29-30, 44, 58] In the ln(K_{fold}) vs pressure plots in Figure 10.8A, the least squares fits reveal ΔV^0 to remain nearly constant (as echoed in Figure 10.8B, Table 10.2), while the significant upward vertical shifts in Figure 10.8A indicate that Mg^{2+} strongly stabilizes the folded lysine riboswitch at all pressures. We note that the independence of ΔV^0 on Na^+ and Mg^{2+} demonstrated in Figure 10.7A and 10.8A is quite different from previous studies, where ΔV^0 for DNA/RNA folding was found to be sensitive to cations.[21, 59] For instance, ΔV^0 for folding of the 40A DNA hairpin is reduced from 11.5(35) mL/mol to 5.9(10) mL/mol with [Mg^{2+}] increasing from 0.3 mM to 1.0 mM ($\Delta\Delta V^0 < 0$),[59] while the ΔV^0 of TL-TLR formation increases from 5(3) mL/mol to 9(2) mL/mol with [Mg^{2+}] increasing from 0 mM to 1.0 mM ($\Delta\Delta V^0 > 0$).[21] Despite the fact that the pressure denaturation is repeatedly observed (i.e., $\Delta V^0 > 0$) for each nucleic acid structure, the *differential* cation response ($\Delta\Delta V^0$) can change sign depending on the interactions involved in the folding. A simple framework with which to understand cation effects is by charge neutralization/association between the cations and nucleic acids, resulting in a weaker hydration structure.[60] At first this would seem to predict a reduced ΔV^0 at higher cation concentrations ($\Delta\Delta V^0 < 0$) as the hydrating water molecules become less ordered.[48-49] However, just as for nucleic acid conformations, the solvent configuration is also highly dynamic during nucleic acid folding; therefore, the additional

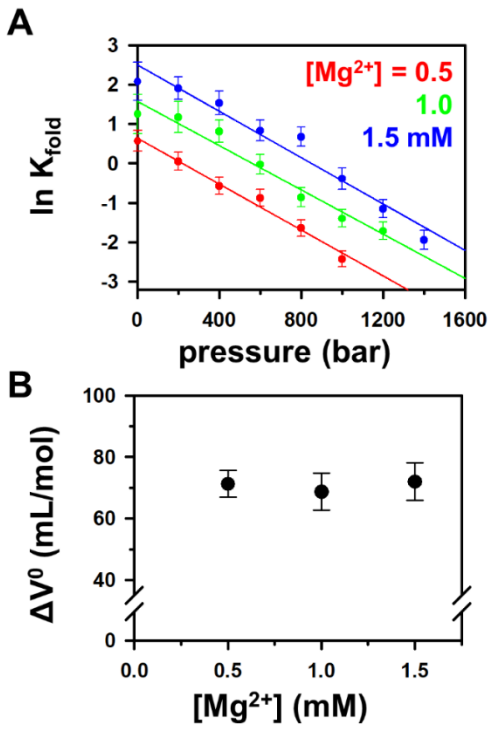

Figure 10.8 Pressure dependence of folding at series of Mg^{2+} concentrations. (A) $\ln(K_{fold})$ vs P plot where Mg^{2+} greatly promotes folding, while leaving the slopes (ΔV^0) mostly unchanged. (B) $[Mg^{2+}]$ (in)dependence of ΔV^0.

cations may preferentially interact with either the folded/unfolded state or only stay in the bulk/hydration shell during folding. As a result, the presence of cations could give rise to negative, zero or positive values of $\Delta\Delta V^0$ simply due to the redistribution of hydration at different stages of folding.[21, 59] Such cationic association along the riboswitch folding coordinate further motivates future pressure dependent analysis of the folding *kinetics*, which may provide additional physical insights with which to help interpret such cation response from a structural perspective.

Finally, the apparent lack of Na^+ influence on pressure dependent folding of the full lysine riboswitch is noteworthy, since monovalent cations have been shown to promote formation of the isolated TL-TLR folding motif at the hundred millimolar level.[30, 61] However,

multiple tertiary contacts in the *Tetrahymena thermophila* ribozyme have been shown to be unresponsive to Na^+ up to $[Na^+]$ = 1.5 M in previous X-Ray footprinting studies,[58] suggesting that Mg^{2+} can be crucial to certain tertiary folding motifs such as bending at internal loops.[58, 62] A similar metal ion dependence can also be observed in the hairpin ribozyme[63] and its four-way junction[64], where from E_{FRET} differences it appears that monovalent Na^+-induced compaction only partially folds the RNA in the absence of divalent Mg^{2+}. Indeed, even simpler tertiary folding motifs (such as the RNA kink-turn) may adopt different conformations in the presence of Na^+ vs. Mg^{2+}.[65-66] Furthermore, the importance of Mg^{2+} in the lysine riboswitch folding can be seen in the strongly $[Mg^{2+}]$-dependent K_d for lysine binding.[27, 43-44] Moreover, most of the monovalent cation effects have been studied in the absence of multivalent cations.[30] In our experiments, Na^+ must compete with 0.5 mM Mg^{2+} to interact with the lysine riboswitch and thus the results could be dominated by the more prominent Mg^{2+} effects.[67]

10.4.4 TMAO effects on the pressure dependent lysine riboswitch folding

We now return to the experimental dependence of the K_d ligand binding affinity on external pressure. Many marine organisms accumulate small organic molecules known as osmolytes inside cells to adjust cellular osmotic pressures against sea water.[34, 68] Much of these osmolytes are thought to have cytoprotective roles to stabilize biomolecular structures against environmental stressors such as temperature and pressure.[69] Indeed, the TMAO contents of fish and amphipods have been recently found to correlate strongly with ocean depth, further corroborating the protective role of TMAO against hydraulic pressure[33-34]. As a final focus of this paper, we have explored the influence of TMAO osmolyte concentration on folding of the lysine riboswitch, with the hope of gaining additional molecular insight into the mechanism of

TMAO stabilization on RNA tertiary folding of the lysine riboswitch and ligand binding under extreme pressures.

The pressure dependent data for $\ln(K_{fold})$ as a function of TMAO concentration are exhibited in Figure 10.9A. We focus first on results at ambient pressure, $P \approx 1$ bar, for which the spread in intercepts indicates a moderate TMAO free energy enhancement in folding of the lysine riboswitch over the range of physiologically relevant concentrations sampled (100 mM to 1200 mM). This modest TMAO dependent (3-4 fold) increase in K_{fold} is consistent with previously characterized stabilization effects of TMAO osmolyte on nucleic acid structures[38, 70-71]. However, it contrasts with the results obtained previously for lysine, Na^+ and Mg^{2+} cosolutes. This means that the free volume change for lysine riboswitch folding decreases significantly with TMAO osmolyte (see Figure 10.9B and Table 10.3), indeed by nearly 50% by 1.25 M. Stated alternatively, this means that the lysine riboswitch unfolds much less effectively (i.e. is more stable) at higher [TMAO], with a difference in excess of 3-4 log units in $\ln(K_{fold})$ up at the highest pressures observed.

[TMAO] (mM)	**0**	**250**	**500**	**750**	**1000**	**1250**
ΔV^0 (mL/mol)	**71(4)**	**63(4)**	**59(4)**	**54(4)**	**50(3)**	**40(2)**

Table 10.3 ΔV^0 obtained at increasing [TMAO]

The results in Figure 10.9A, B highlight two ways in which TMAO provides a protective mechanism against changes in external pressure, which could be crucially important in

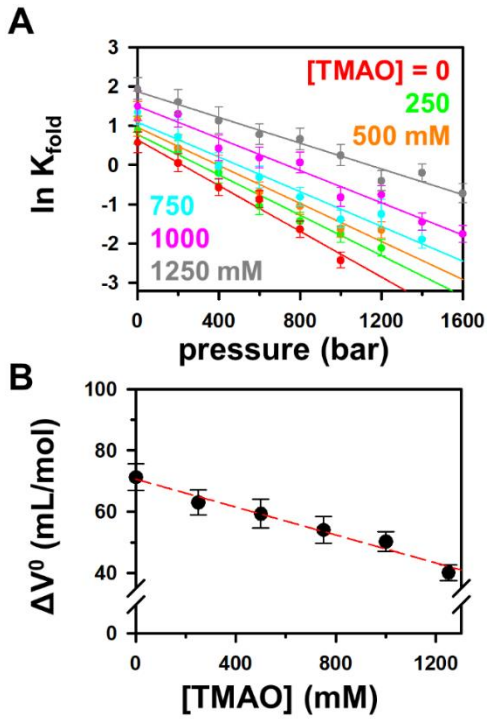

Figure 10.9 Pressure dependence of folding at series of TMAO concentrations. (A) ln(K_{fold}) vs P plot where TMAO promotes folding and effectively reduces the slope (ΔV^0). (B) [TMAO] dependence of ΔV^0. ΔV^0 decrease linearly with [TMAO] concentration.

maintaining accessibility of marine species to wider range of vertical depth profiles. Firstly, the compaction of curves in Figure 10.9A near ambient pressures indicates that TMAO increases folded lysine riboswitch stabilities only relatively modestly (≈ 3-4 fold), which could be crucial to preserving biochemical function of the riboswitch.[34, 69] This differs specifically from the more dramatic dependence of riboswitch stability on Mg^{2+}, which strongly favors riboswitch folding and thus completely switches the gene regulation on or off. Instead, TMAO at ambient pressures only shifts the equilibrium moderately toward the folded state. As a consequence, this allows the riboswitch to dynamically shift between two comparable free energy conformations and thereby still efficiently regulate gene expression.

As an important secondary effect, however, the incorporation of TMAO into the cell systematically decreases the slopes in Figure 10.9A and thus creates an exponential sensitivity of K_{fold} on pressure. As a result, what are only modest riboswitch stabilization effects under low pressure ambient conditions grow exponentially stronger at higher pressure. More quantitatively, the slopes and intercepts in Figure 10.9A indicate that [TMAO] = 1250 mM achieves an equivalent lysine riboswitch folding stability at ~ 800 bar as obtained at ambient pressures in the complete absence of TMAO. This may signal an elegant strategy behind controlled build-up of osmolytes such as TMAO in cells. Specifically, it promotes biomolecular folding under high pressures and yet also maintains the requisite "on-off" two-state riboswitch sensitivity to lysine over a wider range of ocean depth profiles and external pressures.

10.5 Discussion

10.5.1 Pressure denaturation of lysine riboswitch folding

The pressure dependence of our biomolecular folding is dominated by the positive free volume difference between the folded and unfolded conformations ($\Delta V^0 = V^0_{fold} - V^0_{unfold} \approx +74$ mL/mol), which according to Le Chatelier's principle, predicts pressure-induced denaturation.[5] The physical reason why $\Delta V^0 > 0$ for the lysine riboswitch is not immediately obvious, since folded conformations of biopolymers are generally considered to be more compact. However, one must remember that measured ΔV^0 values represent changes for the entire solute + solvent system, for which the solvent can contribute significantly to the overall ΔV^0.[1-4] For instance, solvent voids can be generated due to formation of hydrophobic contacts upon folding, which can decrease the solvent accessible volume and result in a net outward displacement of the solvent ($\Delta V^0 > 0$).[2] Alternatively, the unfolded RNA conformation can expose the polyanionic

backbone to more solvent (water) and thus can form a more compact hydration shell.[48-49] Since a more highly ordered hydration structure for the unfolded conformation takes up less volume,[48-49] this could translate into an increase in free volume ($\Delta V^0 > 0$) as the riboswitch folds and partially disrupts these water contacts. The potential for competition between solute vs solvent volume changes makes unambiguous deconstruction of the contributions to ΔV^0 challenging. However, it is the case that pressure-induced denaturation effects (which require $\Delta V^0 > 0$) have been noted in ensemble studies of many other protein and nucleic acid systems.[4, 72]

Pressure-induced denaturation of the lysine riboswitch is clearly indicated in each of the $\ln(K_{fold})$ vs. pressure plots in Figure 10.5-9, where negative slopes correspond to $\Delta V^0 > 0$ (Eq. 10.1). Interestingly, an increase in [lysine] stabilizes the folded conformation predominantly by parallel translation of the curves with negligible changes in the slope, consistent with $\Delta\Delta V^0 \approx 0$ (Figure 10.5). What makes this particularly interesting is that it had been previously shown that the lysine riboswitch folding follows an "induced-fit" (bind-then-fold) mechanism and therefore its folded state is well characterized as ligand-bound[27-28]. This would imply that any [lysine] changes must therefore correlate with ligand binding to the unfolded conformation. As a result, the fact that $\Delta\Delta V^0$ with respect to lysine is experimentally small could reflect that the unfolded conformation is dominated by one of the two ligand-bound or ligand-free association states. This looks not to be the case, however, as a dissociation constant K_D = 1.7(5) mM for the unfolded conformation has been determined from previous single molecule kinetic studies.[27] which predicts both ligand-bound and ligand-free states to be significantly present at [lysine] ≈ 0.5-8 mM. Thus, the measured independence of ΔV^0 on [lysine] indicates the volumes of the ligand-bound and ligand-free unfolded states to be experimentally indistinguishable. It is also worth

noting that the uncertainties in ΔV^0 are < 5 mL/mol, i.e., less than 1/3 the volume of a single water molecule.

From the pressure dependent folding data in Figure 10.5, we obtain the apparent dissociation constant K_d for lysine and the corresponding 50% folding pressures ($P_{50\%}$) with which to characterize the pressure dependent riboswitch-ligand interaction. Since ΔV^0 is approximately independent of [lysine], K_d increases nearly exponentially with P (Figure 10.6), clearly demonstrating that external pressure impedes cognate ligand-induced folding of the lysine riboswitch. This pressure-dependent binding constant for lysine decreases rapidly, with K_d predicted at the bottom of the Mariana Trench to be 3 orders of magnitude larger ($K_d \approx 300(60)$ mM) than at ambient pressures ($K_d \approx 0.31(10)$ mM). These results demonstrate that high pressure significantly disrupts the riboswitch-ligand interaction, which in deep sea species must therefore be compensated by some other protective mechanism (e.g., osmotic enhancement) in order to maintain cellular function. Finally, we note that these smFRET burst fluorescence studies only report on the *apparent* dissociation constant K_d through observation of overall riboswitch folding. More specifically, we cannot rule out whether the increase in K_d occurs by a i) pressure-dependent decrease in ligand affinity or ii) pressure-dependent efficiency of the resulting ligand-promoted conformational change, although such questions should be addressed by single molecule kinetic studies on tethered constructs.

10.5.2 Cationic effects on the lysine riboswitch

The equilibrium for lysine riboswitch folding exhibits only a quite modest dependence on $[Na^+]$ under both ambient and high-pressure conditions. Not only is the free volume change ΔV^0 effectively independent of $[Na^+]$, but the riboswitch folding equilibrium constant (K_{fold}) is largely

constant over the entire physiologically relevant range ($[Na^+]$ = 100-250 mM). Since charge neutralization and Debye shielding is an essential prerequisite for RNA forming compact structures[55, 73], this is a bit surprising. Indeed, although monovalent cations are found to be less effective than divalent cations in stabilizing RNA tertiary structure, they are often still able to promote RNA folding at sufficiently high concentrations.[30, 46, 73] However, as discussed in Sec. 10.4.3, not all tertiary contacts in a full ribozyme can be effectively promoted by monovalent cations alone,[58, 63-65] suggesting Mg^{2+} to be essential for RNA structure formation.[62] Moreover, these Na^+ dependent studies have been explored in the presence of $[Mg^{2+}]$ = 0.5 mM in order to effectively promote the lysine binding.[27, 43] It is unclear how Mg^{2+} competes with Na^+ to neutralize/solvate the RNA; thus the overall monovalent cation effects may still be dominated by Mg^{2+}, which is known to interact strongly with RNA.[67]

By way of contrast, Mg^{2+} is known to strongly promote RNA structure formation and has been shown in previous studies to be essential for lysine riboswitch folding,[22, 27, 43] primarily in promoting tertiary contacts and pre-organizing the ligand binding site.[44] It is thus not surprising that Mg^{2+} strongly stabilizes the folded lysine riboswitch, as evidenced by strong upward displacement of the semilogarithmic plots in Figure 10.8A. Instead, it is the parallel nature of these curves as a function of Mg^{2+} (which implies an Mg^{2+}-independent change in ΔV^0) that becomes most noteworthy. Interestingly, although only a limited nucleic acid systems have been studied as a function of external pressure, ΔV^0 values for nucleic acid folding have been found to be small and $[Mg^{2+}]$ sensitive.[21, 59] For example, ΔV^0 for secondary structure formation in a DNA 40A hairpin is *reduced* from 11.5(35) mL/mol to 5.9(10) mL/mol between $[Mg^{2+}]$ = 0.3 mM - 1.0 mM,[59] while ΔV^0 for folding of the tetraloop-receptor tertiary interaction motif is *increased* from 5(3) mL/mol - 9(2) mL/mol between $[Mg^{2+}]$ = 0.0 - 1.0 mM.[21] As described in Sec. 10.4.3,

such sign reversals in $\Delta\Delta V^0$ may result from preferential interaction of Mg^{2+} with folded vs. unfolded RNA conformations. This again provides additional motivation for high pressure kinetic studies at the single molecule level, which would permit further thermodynamic deconstruction of these equilibrium constants into forward (folding) and reverse (unfolding) rate constants over a transition state barrier.

Despite an RNA construct-dependent sign of $\Delta\Delta V^0$ with respect to divalent cation concentration, the data in Figure 10.8A make clear that Mg^{2+} strongly stabilizes lysine riboswitch folding. In principle, this additional stabilization could also be used to protect lysine riboswitches from pressure-induced denaturation under deep sea conditions. However, the riboswitch gene regulatory mechanism relies on efficient, high dynamic range "switching" between on- and off-states of comparable free energy, triggered by presence or absence of the cognate ligand.[9] Therefore, overzealous stabilization of one of the two conformations by Mg^{2+} would shift this equilibrium and therefore be less desirable for robust riboswitch competency. This could represent yet another reason why marine species do not accumulate divalent salts to modulate their cellular osmotic pressure, as these species could significantly perturb riboswitch equilibria and therefore biomolecular function.[34, 69]

10.5.3 Osmolytic protection against pressure denaturation

As described in Sec. 10.4 and above, common monovalent (Na^+) and divalent (Mg^{2+}) cations exert a negligible influence on free volume changes ($\Delta\Delta V^0 \approx 0$) due to lysine riboswitch folding. As a result, modulation of cation concentrations should have little impact on riboswitch folding equilibria as a function of external pressure. Instead, marine species have evolved to accumulate small highly polar organic molecules ("osmolytes") to help achieve the correct

osmotic balance between cellular and external environments.[31] Unlike inorganic cations, these osmolytes do not significantly alter biomolecular folding equilibria and may also protect the cell from multiple environmental stressors such as temperature and pressure.[69] Trimethyl amine oxide (TMAO) is one of the most common of these osmolytes, empirically known to be crucial for survival of organisms at extreme deep sea pressures.[33] Indeed, TMAO concentrations in fish and amphipods increasing quasi linearly with ocean depth up to as high as [TMAO] ≈ 0.5 M.[33-34] TMAO has explicitly been shown to protect proteins and DNA helices from pressure-induced denaturation,[59, 74] while effects on the stability of RNA tertiary folding under pressure have remained largely unexplored. Although the precise biological mechanism for protection against high external hydrostatic pressure in deep sea bacteria is still unclear, our current study of TMAO pressure-induced denaturation of the lysine riboswitch highlights some useful principles for identifying potential "piezolytes," which can hope to counteract external pressure effects by not only stabilizing biomolecular folding of the riboswitch but also reducing pressure sensitivity to riboswitch folding formation by control of $\Delta\Delta V^0$.

From pressure dependent plots of $\ln(K_{fold})$ vs. [TMAO] (see Figure 10.9A), the folded lysine riboswitch is stabilized (i.e., K_{fold} *increases* with [TMAO]) all the way down to ambient pressure (1 bar). There are three closely related predictions and corollaries from Figure 10.9A that bear emphasizing, all arising from the simple observation in Figure 10.9B of a *negative* $\Delta\Delta V^0$. 1) First and foremost is that the pressure dependence becomes *weaker* (i.e., the slopes become *shallower*) with increasing [TMAO]. 2) The corollary is that increasing [TMAO] does not shift folding equilibria as dramatically at low vs. high pressure conditions. As a result, the concentration/pressure "phase space" over which $\ln(K_{fold}) \approx 0$ and thus riboswitch functionality is maximized, which can be argued is an essential characteristic of a good osmolyte. 3) The third

implication is that the ln(K_{fold}) plots naturally fan out with increasing P, and thus by control of TMAO levels, permit access to an exponentially larger dynamic range for osmolytic stabilization of the riboswitch under elevated pressure conditions. The combination of these three predictions, all fundamentally arising from $\Delta\Delta V^0 < 0$, therefore extends the biochemically functional range of the lysine riboswitch for gene regulation over a greater dynamic range of pressures.

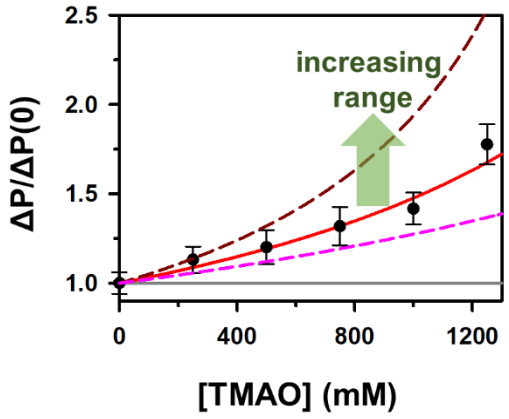

Figure 10.10 Accessible pressure range for the lysine riboswitch as a function of [TMAO], normalized to the corresponding pressure range at [TMAO] = 0. The grey solid line corresponds the pressure range without osmolyte effects. The red solid line represents predictions from the fit of the [TMAO] dependence of ΔV^0 with m = -0.0228(18) mL mol^{-1} mM^{-1}. The dashed lines indicate effects due to the uncertainty in m on the pressure range as a function of [osmolyte]: 50% larger (dark red) and 50% smaller (pink) m values.

We attempt to capture this point in Figure 10.10, based on the pressure range over which the lysine riboswitch properly functions. We can roughly estimate this range as $\Delta P = P_{max}-P_{min}$ whereby K_{fold} changes by some small factor κ, which based on elementary thermodynamics of reversible work ($P \approx \Delta(\Delta G^0)/\Delta V^0$), translates into $\Delta P \approx 2RTln(\kappa)/\Delta V^0$. Next, we least squares fit the [TMAO] dependence of $\Delta(\Delta V^0)$ in Figure 10.9B to a simple linear function $\Delta V^0(0)$ + m[osmolyte] ($\Delta V^0(0)$ = 70.6(13) mL/mol, slope m = -0.0228(18) mL/mol/mM). The explicit influence of TMAO on pressure dependent folding can therefore be plotted as ΔP for finite

[TMAO] normalized to ΔP(0) at [TMAO] = 0, which from Figure 10.10 can be seen to increase nearly 70% over [TMAO] = 0.00 M -1.25 M. Finally, it is worth noting that this normalization process yields results conveniently independent of the arbitrary choice of κ. The results, however, do indicate the correct sensitivity to the experimentally fitted slopes, which predict an enhanced pressure range (ΔP/ΔP(0) > 1) for negative values of m. The sensitivity of the pressure range to the osmolyte effects (m) is also illustrated in Figure 10.10 with dark red and pink curves corresponding to + 50% and – 50% m value of TMAO.

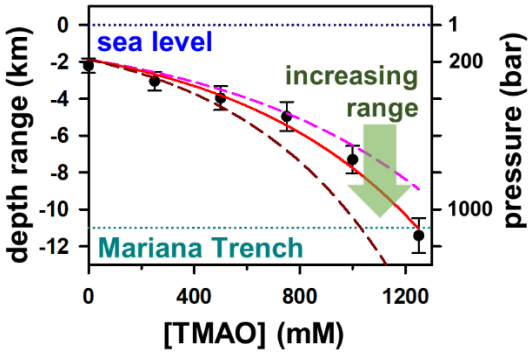

Figure 10.11 Iso-K_d curve as a function of both pressure (depth in the ocean) and [TMAO] where K_d = 0.5 mM. K_d is maintained by [TMAO] = 1250 mM with Δ(ocean depth) > 9 km. Data fit to a negative exponential growth function (red), indicating the TMAO effects are even stronger at high concentrations. The dashed lines indicate the effects of changes in slope magnitude on the iso-K_d curve: + 50% (dark red) and − 50% (pink).

Since the environmental factors such as temperature, salinity and dissolved oxygen remain largely constant under deep sea conditions,[75] pressure represents the major limitation for deep sea organisms to migrate and survive at different depths. The data allow us to put this simple model on a more rigorous mathematical footing. For example, we can determine from Figure 10.9A the 50% pressure ($P_{50\%}$) at each [TMAO] for an experimentally convenient value of the apparent dissociation constant (e.g., at $K_{fold} \approx 1$, for which $K_d \approx$ [lysine] ≈ 0.5 mM). We

can then use $\Delta G^0(P) = \Delta G^0(P=0) + P\Delta V^0 = -RT\ln(K_{fold}) \approx 0$ to plot in Figure 10.11 a constant K_d ("iso-K_d") curve of accessible deep sea ocean pressures ($P \approx \Delta G^0(P = 0)/ \Delta V^0$), which reveals a dramatic exponential increase in the accessible pressure range with increasing [TMAO]. Specifically, Figure 10.11 makes clear that a constant riboswitch-ligand affinity (K_d = 0.5 mM) can be maintained over a 900 bar pressure increase (≈ 9000 m vertical migration) by control of TMAO cellular concentrations between 0-1.25 M, with the TMAO stabilization effects becoming exponentially more significant at higher pressures. As a result, the sensitivity to the negative slope (m) is quite high, with the results for m and ± 50% of m indicated as dashed lines in Figure 10.11.

It is worth noting that the maximum [TMAO] values in this study are close to the theoretical upper bound of osmolyte concentration (~1.2 M, sea water) for marine species which tend to achieve either isosmotic or hypoosmotic conditions. Thus, the actual [TMAO] must in fact be lower due to additional salts, metabolites and other osmolytes required for cellular function. Our results therefore support the previous hypothesis[33] that fish may be constrained from inhabiting the deepest part of the sea below ~8500 m due to these limits on TMAO (~ 0.5 M). However, despite this crucial role in promoting biomolecule stability, the fact that fish are found at ~7000 m with only 0.5 M TMAO indicates [TMAO] can not be the sole factor for deep sea species to survive high pressures. Indeed, genetic adaptation for deep sea organisms can facilitate utilization of more pressure resistant protein and nucleic acid structures[76] as well as synergies between TMAO and other osmolytes/cosolutes to increase biomolecular stability. One important example would be that of "macromolecular crowding," which can not only stabilize biomolecule structures but also increase the effective concentration/activity of TMAO by taking up intracellular space.[77]

As a final comment, we can attempt a linear deconstruction of these free volume changes (ΔV^0) into solvent voids (ΔV^0_{void}) plus solvent hydration effects ($\Delta V^0_{hydration}$).[1, 3, 17] The relatively constant values of E_{FRET} values that we observe as a function of [TMAO] supports that TMAO does not significantly change the lysine riboswitch conformation nor the overall compactness of the folded state. This in turn suggests that $\Delta V^0_{void} \approx$ constant, from which the linear dependence of $\ln(K_{fold})$ on [TMAO] in Figure 10.9B could be entirely ascribed to hydration contributions ($\Delta V^0_{hydration}$) linearly proportional to [TMAO]. Indeed, TMAO has been found in previous studies to be excluded from the surfaces of proteins and RNA tertiary folding motifs[78-80] and also to greatly enhance the water structure[81], thereby reducing the effective volume of the bulk water.[48-49] It is likely that since TMAO tend to orient the water molecules in the bulk, it reduces the effective volume difference between water molecules in the solvation shell of RNA and in the bulk, and consequently mitigate the pressure effects by reducing $\Delta V^0_{hydration}$. The linear decrease of ΔV^0 (Figure 10.9B) which expands a wide range of [TMAO] can be simply explained by the fact that TMAO primarily affects the bulk water instead of the hydration shell surrounding the RNA.[80] Indeed, it has been found in previous molecular dynamics simulations that one hydrated TMAO is in close contact with 25 water molecules,[81] suggesting the bulk water (55.5 M) could be sufficiently ordered by the saturation [TMAO] at ~ 2.2 M. The dynamic range explored in this study for [TMAO] is still far from this saturation limit and thus might expect a linear decrease in ΔV^0 with increasing [TMAO]. It is also worth noting that since TMAO tends to remain strongly hydrated in the bulk water and interact only indirectly with RNA/protein,[78-80] the sign of these TMAO effects ($\Delta\Delta V^0 < 0$) is likely to be more universal and system-independent, making it an ideal piezolyte with which to protect biomolecular structures from pressure-induced denaturation.

10.6 Summary and conclusion

The pressure dependence of lysine riboswitch folding has been investigated at the single molecule level with smFRET spectroscopy and up to P ≈ 1500 bar pressures. The lysine riboswitch unfolds readily at increasing pressure, with a change in free volume determined from linear pressure van't Hoff plots to be $\Delta V^0 = V_{fold} - V_{unfold} \approx 75(3)$ mL/mol. These data can be replotted as an apparent lysine riboswitch dissociation constant K_d as a function of P, which reveals the riboswitch-ligand interaction to be weakened quasi-exponentially with increasing pressure. While monovalent Na^+ effects on the free volume change are found to be negligible, the presence of divalent Mg^{2+} greatly stabilizes the folded lysine riboswitch at all pressures, with only negligible changes in ΔV^0 for both Mg^{2+} and Na^+ cations. By way of contrast, TMAO, a known piezolyte, is found to increase pressure stability of the riboswitch by simultaneously promoting folding (increase in K_{fold}) and reducing the folding-induced change in free volume ($\Delta\Delta V^0 < 0$). We argue that the latter influence of TMAO on free volume can play a crucial role in migration of deep sea species to different ocean depth layers of water in search of sparse resources. Moreover, we introduce an empirical deconstruction of the overall free volume change (ΔV^0) into solvent void formation (ΔV^0_{void}) and changes in the hydration layer ($\Delta V^0_{hydration}$) upon folding. The insensitivity of observed E_{FRET} values suggests that TMAO does not significantly alter the folded riboswitch conformation and thus that ΔV^0_{void} remains approximately constant over a variety of osmolyte conditions. If this is true, our deconstruction would identify the sign of $\Delta V^0 > 0$ to be due to changes in hydration effects. Furthermore, since TMAO is known to be excluded from biomolecular surfaces and to enhance the formation of ordered water, this would be consistent with a linear reduction in ΔV^0 by TMAO over a wide range of concentration due to

greater ordering of the bulk water structure and thereby lesser importance of RNA hydration effects.

10.7 References

1. Chalikian, T. V.; Breslauer, K. J. On Volume Changes Accompanying Conformational Transitions of Biopolymers. *Biopolymers* **1996,** *39*, 619-626.

2. Roche, J.; Caro, J. A.; Norberto, D. R.; Barthe, P.; Roumestand, C.; Schlessman, J. L.; Garcia, A. E.; García-Moreno E., B.; Royer, C. A. Cavities Determine the Pressure Unfolding of Proteins. *Proc. Natl. Acad. Sci. U.S.A.* **2012,** *109*, 6945-6950.

3. Nucci, N. V.; Fuglestad, B.; Athanasoula, E. A.; Wand, A. J. Role of Cavities and Hydration in the Pressure Unfolding of T_4 Lysozyme. *Proc. Natl. Acad. Sci. U.S.A.* **2014,** *111*, 13846-13851.

4. Roche, J.; Royer Catherine, A. Lessons from Pressure Denaturation of Proteins. *J. Royal Soc. Interface* **2018,** *15*, 20180244.

5. Mozhaev, V. V.; Heremans, K.; Frank, J.; Masson, P.; Balny, C. High Pressure Effects on Protein Structure and Function. *Proteins* **1996,** *24*, 81-91.

6. Meersman, F.; Daniel, I.; Bartlett, D. H.; Winter, R.; Hazael, R.; McMillan, P. F. High-Pressure Biochemistry and Biophysics. *Rev. Mineral. Geochem.* **2013,** *75*, 607-648.

7. Epping, E. Life in an Oceanic Extreme. *Nat. Geosci.* **2013,** *6*, 252-253.

8. Mironov, A. S.; Gusarov, I.; Rafikov, R.; Lopez, L. E.; Shatalin, K.; Kreneva, R. A.; Perumov, D. A.; Nudler, E. Sensing Small Molecules by Nascent RNA: A Mechanism to Control Transcription in Bacteria. *Cell* **2002,** *111*, 747-756.

9. Garst, A. D.; Edwards, A. L.; Batey, R. T. Riboswitches: Structures and Mechanisms. *Cold Spring Harb. Perspect. Biol.* **2011,** *3*.

10. Lemay, J. F.; Penedo, J. C.; Tremblay, R.; Lilley, D. M.; Lafontaine, D. A. Folding of the Adenine Riboswitch. *Chem. Biol.* **2006,** *13*, 857-68.

11. Sung, H. L.; Nesbitt, D. J. DNA Hairpin Hybridization under Extreme Pressures: A Single-Molecule FRET Study. *J Phys Chem B* **2020,** *124*, 110-120.

12. Wu, J. Q.; Macgregor Jr., R. B. Pressure Dependence of the Helix–Coil Transition Temperature of Poly[d(G-C)]. *Biopolymers* **1995,** *35*, 369-376.

13. Najaf-Zadeh, R.; Wu, J. Q.; Macgregor, R. B. Effect of Cations on the Volume of the Helix-Coil Transition of Poly[d(A-T)]. *Biochim. Biophys. Acta, Gene Struct. Expression* **1995,** *1262*, 52-58.

14. Rayan, G.; Macgregor, R. B. Pressure-Induced Helix–Coil Transition of DNA Copolymers is Linked to Water Activity. *Biophys. Chem.* **2009,** *144*, 62-66.

15. Rayan, G.; Macgregor, R. B. A Look at the Effect of Sequence Complexity on Pressure Destabilisation of DNA Polymers. *Biophys. Chem.* **2015,** *199*, 34-38.

16. Patra, S.; Anders, C.; Erwin, N.; Winter, R. Osmolyte Effects on the Conformational Dynamics of a DNA Hairpin at Ambient and Extreme Environmental Conditions. *Angew. Chem. Int. Ed.* **2017,** *56*, 5045-5049.

17. Patra, S.; Anders, C.; Schummel, P. H.; Winter, R. Antagonistic Effects of Natural Osmolyte Mixtures and Hydrostatic Pressure on the Conformational Dynamics of a DNA Hairpin Probed at the Single-Molecule Level. *Phys. Chem. Chem. Phys.* **2018,** *20*, 13159-13170.

18. Fan, H. Y.; Shek, Y. L.; Amiri, A.; Dubins, D. N.; Heerklotz, H.; Macgregor, R. B.; Chalikian, T. V. Volumetric Characterization of Sodium-Induced G-Quadruplex Formation. *J. Am. Chem. Soc.* **2011,** *133*, 4518-4526.

19. Takahashi, S.; Sugimoto, N. Effect of Pressure on Thermal Stability of G-Quadruplex DNA and Double-Stranded DNA Structures. *Molecules* **2013,** *18*, 13297-13319.

20. Arns, L.; Knop, J.-M.; Patra, S.; Anders, C.; Winter, R. Single-Molecule Insights into the Temperature and Pressure Dependent Conformational Dynamics of Nucleic Acids in the Presence of Crowders and Osmolytes. *Biophys. Chem.* **2019,** *251*, 106190.

21. Downey, C. D.; Crisman, R. L.; Randolph, T. W.; Pardi, A. Influence of Hydrostatic Pressure and Cosolutes on RNA Tertiary Structure. *J. Am. Chem. Soc.* **2007,** *129*, 9290-9291.

22. Garst, A. D.; Héroux, A.; Rambo, R. P.; Batey, R. T. Crystal Structure of the Lysine Riboswitch Regulatory mRNA Element. *J. Biol. Chem.* **2008,** *283*, 22347-22351.

23. Schneider, S.; Paulsen, H.; Reiter, K. C.; Hinze, E.; Schiene-Fischer, C.; Hübner, C. G. Single Molecule FRET Investigation of Pressure-Driven Unfolding of Cold Shock Protein A. *J. Chem. Phys.* **2018,** *148*, 123336.

24. Ben-Naim, A. Solvent Effects on Protein Association and Protein Folding. *Biopolymers* **1990,** *29*, 567-596.

25. Mikulecky, P. J.; Feig, A. L. Heat Capacity Changes in RNA Folding: Application of Perturbation Theory to Hammerhead Ribozyme Cold Denaturation. *Nucleic Acids Res.* **2004,** *32*, 3967-3976.

26. Sung, H.-L.; Nesbitt, D. J. Novel Heat-Promoted Folding Dynamics of the *yybP-ykoY* Manganese Riboswitch: Kinetic and Thermodynamic Studies at the Single-Molecule Level. *J. Phys. Chem. B* **2019,** *123*, 5412-5422.

27. Fiegland, L. R.; Garst, A. D.; Batey, R. T.; Nesbitt, D. J. Single-Molecule Studies of the Lysine Riboswitch Reveal Effector-Dependent Conformational Dynamics of the Aptamer Domain. *Biochemistry* **2012,** *51*, 9223-9233.

28. Sung, H.-L.; Nesbitt, D. J. Single-Molecule FRET Kinetics of the Mn^{2+} Riboswitch: Evidence for Allosteric Mg^{2+} Control of "Induced-Fit" vs "Conformational Selection" Folding Pathways. *J. Phys. Chem. B* **2019,** *123*, 2005-2015.

29. Tan, Z.-J.; Chen, S.-J. Nucleic Acid Helix Stability: Effects of Salt Concentration, Cation Valence and Size, and Chain Length. *Biophys. J.* **2006,** *90*, 1175-1190.

30. Fiore, J. L.; Holmstrom, E. D.; Fiegland, L. R.; Hodak, J. H.; Nesbitt, D. J. The Role of Counterion Valence and Size in GAAA Tetraloop–Receptor Docking/Undocking Kinetics. *J. Mol. Biol.* **2012,** *423*, 198-216.

31. Yancey, P.; Clark, M.; Hand, S.; Bowlus, R.; Somero, G. Living with Water Stress: Evolution of Osmolyte Systems. *Science* **1982,** *217*, 1214-1222.

32. Yancey, P. H.; Blake, W. R.; Conley, J. Unusual Organic Osmolytes in Deep-Sea Animals: Adaptations to Hydrostatic Pressure and Other Perturbants. *Comp. Biochem. Physiol., Part A Mol. Integr. Physiol.* **2002,** *133*, 667-676.

33. Yancey, P. H.; Gerringer, M. E.; Drazen, J. C.; Rowden, A. A.; Jamieson, A. Marine Fish May be Biochemically Constrained from Inhabiting the Deepest Ocean Depths. *Proc. Natl. Acad. Sci. U.S.A.* **2014,** *111*, 4461-4465.

34. Downing, A. B.; Wallace, G. T.; Yancey, P. H. Organic Osmolytes of Amphipods from Littoral to Hadal Zones: Increases with Depth in Trimethylamine N-Oxide, Scyllo-Inositol and Other Potential Pressure Counteractants. *Deep Sea Res.* **2018,** *138*, 1-10.

35. Bennion, B. J.; Daggett, V. Counteraction of Urea-Induced Protein Denaturation by Trimethylamine *N*-Oxide: A Chemical Chaperone at Atomic Resolution. *Proc. Natl. Acad. Sci. U. S. A.* **2004,** *101*, 6433-6438.

36. Street, T. O.; Bolen, D. W.; Rose, G. D. A Molecular Mechanism for Osmolyte-Induced Protein Stability. *Proc. Natl. Acad. Sci. U.S.A.* **2006,** *103*, 13997-14002.

37. Canchi, D. R.; García, A. E. Cosolvent Effects on Protein Stability. *Annual Review of Physical Chemistry* **2013,** *64*, 273-293.

38. Holmstrom, E. D.; Dupuis, N. F.; Nesbitt, D. J. Kinetic and Thermodynamic Origins of Osmolyte-Influenced Nucleic Acid Folding. *J. Phys. Chem. B* **2015,** *119*, 3687-3696.

39. Lambert, D.; Leipply, D.; Draper, D. E. The Osmolyte TMAO Stabilizes Native RNA Tertiary Structures in the Absence of Mg^{2+}: Evidence for a Large Barrier to Folding from Phosphate Dehydration. *J. Mol. Biol.* **2010,** *404*, 138-157.

40. Yancey, P. H.; Siebenaller, J. F. Trimethylamine Oxide Stabilizes Teleost and Mammalian Lactate Dehydrogenases Against Inactivation by Hydrostatic Pressure and Trypsinolysis. *J. Exp. Biol.* **1999,** *202*, 3597-3603.

41. Yancey, P. H.; Fyfe-Johnson, A. L.; Kelly, R. H.; Walker, V. P.; Auñón, M. T. Trimethylamine Oxide Counteracts Effects of Hydrostatic Pressure on Proteins of Deep-Sea Teleosts. *Journal of Experimental Zoology* **2001,** *289*, 172-176.

42. Sengupta, A.; Sung, H.-L.; Nesbitt, D. J. Amino Acid Specific Effects on RNA Tertiary Interactions: Single-Molecule Kinetic and Thermodynamic Studies. *J. Phys. Chem. B* **2016,** *120*, 10615-10627.

43. Blouin, S.; Chinnappan, R.; Lafontaine, D. A. Folding of the Lysine Riboswitch: Importance of Peripheral Elements for Transcriptional Regulation. *Nucleic Acids Res.* **2010,** *39*, 3373-3387.

44. McCluskey, K.; Boudreault, J.; St-Pierre, P.; Perez-Gonzalez, C.; Chauvier, A.; Rizzi, A.; Beauregard, P. B.; Lafontaine, D. A.; Penedo, J. C. Unprecedented Tunability of Riboswitch Structure and Regulatory Function by Sub-Millimolar Variations in Physiological Mg2+. *Nucleic Acids Res.* **2019,** *47*, 6478-6487.

45. Vieweger, M.; Holmstrom, Erik D.; Nesbitt, David J. Single-Molecule FRET Reveals Three Conformations for the TLS Domain of Brome Mosaic Virus Genome. *Biophys. J.* **2015,** *109*, 2625-2636.

46. Fiore, J. L.; Hodak, J. H.; Piestert, O.; Downey, C. D.; Nesbitt, D. J. Monovalent and Divalent Promoted GAAA Tetraloop-Receptor Tertiary Interactions from Freely Diffusing Single-Molecule Studies. *Biophys. J.* **2008,** *95*, 3892-3905.

47. Fiore, J. L.; Kraemer, B.; Koberling, F.; Edmann, R.; Nesbitt, D. J. Enthalpy-Driven RNA Folding: Single-Molecule Thermodynamics of Tetraloop−Receptor Tertiary Interaction. *Biochemistry* **2009,** *48*, 2550-2558.

48. Barbosa, R. d. C.; Barbosa, M. C. Hydration Shell of the TS-Kappa Protein: Higher Density than Bulk Water. *Physica A* **2015,** *439*, 48-58.

49. Merzel, F.; Smith, J. C. Is the First Hydration Shell of Lysozyme of Higher Density than Bulk Water? *Proc. Natl. Acad. Sci. U.S.A.* **2002,** *99*, 5378-5383.

50. Royer, C. A. Revisiting Volume Changes in Pressure-Induced Protein Unfolding. *Biochim. Biophys. Acta, Protein Struct. Mol. Enzymol.* **2002,** *1595*, 201-209.

51. Rouget, J.-B.; Aksel, T.; Roche, J.; Saldana, J.-L.; Garcia, A. E.; Barrick, D.; Royer, C. A. Size and Sequence and the Volume Change of Protein Folding. *J. Am. Chem. Soc.* **2011,** *133*, 6020-6027.

52. Nicholson, D. A.; Sengupta, A.; Sung, H.-L.; Nesbitt, D. J. Amino Acid Stabilization of Nucleic Acid Secondary Structure: Kinetic Insights from Single-Molecule Studies. *J. Phys. Chem. B* **2018,** *122*, 9869-9876.

53. Furukawa, K.; Gu, H.; Sudarsan, N.; Hayakawa, Y.; Hyodo, M.; Breaker, R. R. Identification of Ligand Analogues that Control c-di-GMP Riboswitches. *ACS Chem, Biol.* **2012,** *7*, 1436-1443.

54. Bowman, J. C.; Lenz, T. K.; Hud, N. V.; Williams, L. D. Cations in Charge: Magnesium Ions in RNA Folding and Catalysis. *Curr. Opin. Struct. Biol.* **2012,** *22*, 262-272.

55. Draper, D. E.; Grilley, D.; Soto, A. M. Ions and RNA Folding. *Annu. Rev. Biophys.* **2005,** *34*, 221-243.

56. Draper, D. E. RNA Folding: Thermodynamic and Molecular Descriptions of the Roles of Ions. *Biophys. J.* **2008,** *95*, 5489-5495.

57. Schroeder, Kersten T.; Daldrop, P.; Lilley, David M. J. RNA Tertiary Interactions in a Riboswitch Stabilize the Structure of a Kink Turn. *Structure* **2011,** *19*, 1233-1240.

58. Shcherbakova, I.; Gupta, S.; Chance, M. R.; Brenowitz, M. Monovalent Ion-Mediated Folding of the *Tetrahymena thermophila* Ribozyme. *J. Mol. Biol.* **2004,** *342*, 1431-1442.

59. Patra, S.; Schuabb, V.; Kiesel, I.; Knop, J.-M.; Oliva, R.; Winter, R. Exploring the Effects of Cosolutes and Crowding on the Volumetric and Kinetic Profile of the Conformational Dynamics of a Poly dA Loop DNA Hairpin: a Single-Molecule FRET Study. *Nucleic Acids Res.* **2018,** *47*, 981-996.

60. Tsukida, N.; Muranaka, H.; Ide, M.; Maeda, Y.; Kitano, H. Effect of Neutralization of Poly(acrylic acid) on the Structure of Water Examined by Raman Spectroscopy. *J. Phys. Chem. B* **1997,** *101*, 6676-6679.

61. Holmstrom, E. D.; Fiore, J. L.; Nesbitt, D. J. Thermodynamic Origins of Monovalent Facilitated RNA Folding. *Biochemistry* **2012,** *51*, 3732-3743.

62. Schlatterer, J. C.; Kwok, L. W.; Lamb, J. S.; Park, H. Y.; Andresen, K.; Brenowitz, M.; Pollack, L. Hinge Stiffness Is a Barrier to RNA Folding. *J. Mol. Biol.* **2008,** *379*, 859-870.

63. Wilson, T. J.; Lilley, D. M. J. Metal Ion Binding and the Folding of the Hairpin Ribozyme. *RNA* **2002,** *8*, 587-600.

64. Hohng, S.; Wilson, T. J.; Tan, E.; Clegg, R. M.; Lilley, D. M. J.; Ha, T. Conformational Flexibility of Four-way Junctions in RNA. *J. Mol. Biol.* **2004,** *336*, 69-79.

65. Goody, T. A.; Melcher, S. E.; Norman, D. G.; Lilley, D. M. J. The Kink-Turn Motif in RNA is Dimorphic, and Metal Ion-Dependent. *RNA* **2004,** *10*, 254-264.

66. Huang, L.; Lilley, D. M. J. The Kink Turn, a Key Architectural Element in RNA Structure. *J. Mol. Biol.* **2016,** *428*, 790-801.

67. Shiman, R.; Draper, D. E. Stabilization of RNA Tertiary Structure by Monovalent Cations. *J. Mol. Biol.* **2000,** *302*, 79-91.

68. Forster, R.; Goldstein, L. Intracellular Osmoregulatory Role of Amino Acids and Urea in Marine Elasmobranchs. *Am. J. Physiol.* **1976,** *230*, 925-931.

69. Yancey, P. H. Organic Osmolytes as Compatible, Metabolic and Counteracting Cytoprotectants in High Osmolarity and Other Stresses. *J. Exp. Biol.* **2005,** *208*, 2819-2830.

70. Gluick, T. C.; Yadav, S. Trimethylamine N-Oxide Stabilizes RNA Tertiary Structure and Attenuates the Denaturating Effects of Urea. *J. Am. Chem. Soc.* **2003,** *125*, 4418-4419.

71. Lambert, D.; Draper, D. E. Effects of Osmolytes on RNA Secondary and Tertiary Structure Stabilities and RNA-Mg^{2+} Interactions. *J. Mol. Biol.* **2007,** *370*, 993-1005.

72. Macgregor Jr., R. B. Effect of Hydrostatic Pressure on Nucleic Acids. *Biopolymers* **1998,** *48*, 253-263.

73. Heilman-Miller, S. L.; Thirumalai, D.; Woodson, S. A. Role of Counterion Condensation in Folding of the *Tetrahymena* Ribozyme. I. Equilibrium Stabilization by Cations. *J. Mol. Biol.* **2001,** *306*, 1157-1166.

74. Krywka, C.; Sternemann, C.; Paulus, M.; Tolan, M.; Royer, C.; Winter, R. Effect of Osmolytes on Pressure-Induced Unfolding of Proteins: A High-Pressure SAXS Study. *ChemPhysChem* **2008,** *9*, 2809-2815.

75. Childress, J. J.; Seibel, B. A. Life at Stable Low Oxygen Levels: Adaptations of Animals to Oceanic Oxygen minimum Layers. *J. Exp. Biol.* **1998,** *201*, 1223-1232.

76. Morita, T. Structure-Based Analysis of High Pressure Adaptation of α-Actin. *J. Biol. Chem.* **2003,** *278*, 28060-28066.

77. Ellis, R. J. Macromolecular Crowding: Obvious but Underappreciated. *Trends in Biochemical Sciences* **2001,** *26*, 597-604.

78. Canchi, D. R.; Jayasimha, P.; Rau, D. C.; Makhatadze, G. I.; Garcia, A. E. Molecular Mechanism for the Preferential Exclusion of TMAO from Protein Surfaces. *J. Phys. Chem. B* **2012,** *116*, 12095-12104.

79. Ma, J.; Pazos, I. M.; Gai, F. Microscopic Insights into the Protein-Stabilizing Effect of Trimethylamine *N*-Oxide (TMAO). *Proc. Natl. Acad. Sci. U.S.A.* **2014,** *111*, 8476-8481.

80. Pincus, D. L.; Hyeon, C.; Thirumalai, D. Effects of Trimethylamine N-Oxide (TMAO) and Crowding Agents on the Stability of RNA Hairpins. *J. Am. Chem. Soc.* **2008,** *130*, 7364-7372.

81. Zou, Q.; Bennion, B. J.; Daggett, V.; Murphy, K. P. The Molecular Mechanism of Stabilization of Proteins by TMAO and Its Ability to Counteract the Effects of Urea. *J. Am. Chem. Soc.* **2002,** *124*, 1192-1202.

Chapter 11

Single-Molecule Kinetic Studies of DNA Hybridization Under Extreme Pressures

---

11.1 Abstract

Pressure may perturb biomolecular function by altering equilibrium structures and folding dynamics. Its influences are particularly important to deep sea organisms, as maximum pressures reach up to ≈ 1100 bar at the bottom of the ocean as a result of the rapid increase in hydraulic pressure (1 bar every 10 meters) under water. In this work, DNA hybridization kinetics has been studied at the single molecule level under external pressure control (P_{max} ≈ 1500 bar), realized by incorporating a mechanical hydraulic capillary sample cell into a confocal fluorescence microscope. We find that the DNA hairpin construct unfolds ("denatures") with increasing pressure by simultaneously *decelerating* and *accelerating* the unimolecular rate constants for *folding* and *unfolding*, respectively. The single molecule kinetics is then investigated via pressure dependent van't Hoff analysis to infer changes in the thermodynamic molar volume, which unambiguously reveals that the effective DNA plus solvent volume *increases* ($\Delta V^0 > 0$) along the folding coordinate. Cation effects on the pressure dependent kinetics are also explored as a function of monovalent [Na^+]. In addition to stabilizing the overall DNA secondary structure, sodium ions at low concentrations are also found to weaken any pressure dependence for the folding kinetics, but with these effects quickly saturating at physiologically relevant levels of [Na^+]. In particular, the activation volumes for the DNA

*This chapter is adapted from: Sung, H.-L.; Nesbitt, D. J. Single-Molecule Kinetic Studies of DNA Hybridization Under Extreme Pressures. *Phys. Chem. Chem. Phys.* **2020**, *22*, 23491-23501.

dehybridization ($\Delta V^{\ddagger}_{unfold}$) are significantly reduced with increasing [Na^{+}], suggesting that sodium cations help DNA adopt a more fold-like transition state configuration.

11.2 Introduction

Most biochemical studies are performed under ambient pressures (≈ 1 bar = 100,000 Pascal), though this is far from conventional conditions for marine organisms inhabiting the deepest parts of the ocean (≈ 1100 bar).[1-2] Indeed, although experimental results obtained at atmospheric pressure are of obvious relevance to life on the surface of the earth, one could argue that most biochemistry studies sample only a quite limited wedge of naturally occurring pressures in biology. Extreme pressure effects on biological systems turn out to be of immense importance to marine life due to the rapid increase of hydraulic pressure (1 bar per 10 meters) under water.[3] As one particularly relevant biophysical impact, molecules such as proteins and nucleic acids may lose the thermodynamic stability of their native folded state under increasing pressure,[4-7] with such pressure-induced changes in conformation known as pressure denaturation.[8-9] Marine organisms, especially those deep-sea species, therefore must evolve and adopt protective mechanisms to stabilize biomolecular structures and maintain biochemical function in order to counteract extreme pressure changes due to change in depth profile.[3, 10]

DNA occurs in biology primarily in the form of a double helix configuration. Previous studies have shown the pressure response of DNA secondary structures may vary, depending heavily on the sequence and buffer condition.[6] While majority of the relatively long/stable DNA double helices are found with increasing melting temperature at higher pressure,[11-12] folding of the DNA with shorter complementary regions is constantly shown to be destabilized by elevating pressure.[13-15] Since the structure determines the biomolecular function, such a pressure

denaturation phenomenon of nucleic acid structures is regarded to have a potentially enormous impact on cellular function in deep sea marine species. Moreover, nucleic acid structure is in fact dynamic rather than static,[16-17] the destabilization effects of pressure therefore may not be fully captured by previous equilibrium observations. A predictive understanding of such pressure induced changes in conformational structure clearly requires new tools for exploring not just the *equilibria* but also the *kinetics* of nucleic acid hybridization/dehybridization, in particular under the impact of high hydraulic pressures relevant to deep sea life. In order to make such kinetic studies of nucleic acid conformational dynamics possible at the single molecule level, we have coupled together two powerful techniques, i) confocal single molecule Förster resonance energy transfer (smFRET) with ii) a high-pressure generating system in a small quartz capillary cell. The goal of the present study is to report first results on folding/unfolding kinetics of nucleic acids at the single molecule level, with pressure as an external control variable up to ≈ 5 kilobar.[7, 15]

The present work builds on previous experimental studies of pressure dependent nucleic acid RNA and DNA folding under equilibrium conditions, made accessible via freely diffusing smFRET methods at the single molecule level.[7, 13-15] Specifically, these previous studies investigated doubly dye-labeled nucleic acid constructs freely diffusing in solution, with FRET energy transfer efficiencies (E_{FRET}) sampled one molecule at a time and single molecule E_{FRET} distributions statistically revealing the equilibrium ratio between folded and unfolded states (K_{eq} = [folded]/[unfolded]) and its dependence on external pressure and temperature.[7, 13-15] In the present work, DNA constructs are tethered onto the inner surface of a square quartz high pressure capillary cell (Figure 11.1) instead of freely diffusing in solution. By virtue of this tethering, we can locate the nucleic acid constructs by piezo scanning a focused laser beam in a

confocal microscope and thereby interrogate single molecule fluorescence signals over an extended temporal window.[18-19] Since the photon stream changes color as a function of nucleic acid conformation, the resulting time dependent E_{FRET} "trajectories" contain valuable statistical information on the folded and unfolded dwell time distributions[19-20] which allow us to explore nucleic acid conformational kinetics as a function of pressure.

The organization of this paper is as follows. Sec. 11.3 provides a brief description of the combined high pressure experimental apparatus and single molecule microscope. This is followed by a presentation in Sec 11.4A, B of folding and unfolding kinetic results and analysis as a function of external hydraulic pressure, for which the pressure dependent folding/unfolding kinetics provides detailed quantitative information on the differential molar volumes ($\Delta V^{\ddagger}_{fold}$, $\Delta V^{\ddagger}_{unfold}$) for accessing the transition state from a pressure dependent van't Hoff analysis. We turn in Sec 11.4C to the impact of "ion atmosphere" on the overall (ΔV^{0}) and transition state ($\Delta V^{\ddagger}$) molar volume changes, which exhibit a strong sensitivity to monovalent Na^{+} but only a

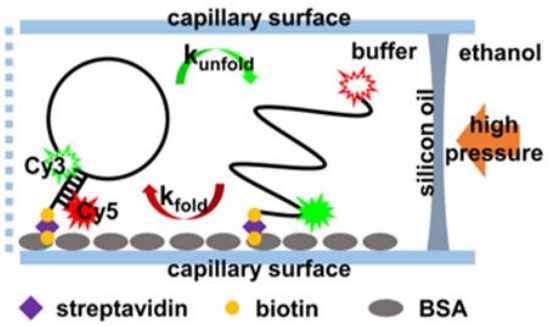

Figure 11.1 Schematic presentation of the surface tethered smFRET experiment performed in a pressurized capillary sample holder. The doubly dye-labeled DNA hairpin construct is immobilized on the capillary surface through biotin-streptavidin interactions. The energy transfer efficiency (E_{FRET}) in the folded (left) and unfolded (right) conformations correspond to high E_{FRET} (≈ 0.8) and low E_{FRET} (≈ 0.1) fluorescence states, respectively. Prior to each experiment, a thin layer of silicon oil is introduced inside the capillary cell to prevent contamination of the aqueous sample region by the pressure transmitting fluid (ethanol).

surprisingly weak dependence on divalent Mg^{2+} deemed crucial for nucleic acid achievement of the correct secondary structure. In Sec. 11.5, we discuss the reasons and simple models for such pressure and cationic dependent behaviors, followed in Sec. 11.6 by a summary of the conclusions and directions for further work.

11.3 Experiment

11.3.1 Single molecule FRET microscopy under external hydraulic pressure

Details of our high pressure smFRET experimental apparatus can be found in previous work;[7, 15] we focus herein on modifications required for the present studies of single molecule nucleic acid folding kinetics. In brief, a confocal microscope with a high NA objective is coupled to a high-pressure sample cell fabricated from a fused-silica capillary with a square 50 μm × 50 μm cross section of the inner cell (Polymicro, Phoenix, AZ), where the capillary can sustain pressures up to ≈ 5 kilobar without fracturing. (Note: company names are reported for completeness and not intended as commercial product support) Moreover, the flat interior surface and uniform thickness (≈ 155 μm) of the high pressure capillary cell closely approximates that of a standard microscope coverslip configuration, therefore maximizing the excitation/collection efficiency for a high NA (1.2) fluorescence measurement. The aqueous sample is pressurized by a manual screw pump (High Pressure Equipment, Erie, PA) through stainless steel tubing (High Pressure Equipment), with ethanol as pressure transmitting fluid to increase pressurization efficiency. Before connection to the ethanol-filled pressure generating system, one end of the capillary is sealed by a propane/oxygen torch, while the other open end is dipped into low viscosity silicon oil to create a thin liquid membrane (≈ 50 μm thickness) inside the sample cell (Figure 11.1) to prevent diffusion of ethanol into the microscopy region. During

the smFRET experiment, the dye-labeled construct is excited by laser excitation through a high NA = 1.2 water immersion microscope objective, with the resulting fluorescence photons collected through the same objective and sorted with dichroic filters before detection on single-photon counting avalanche photodiodes. The time resolved E_{FRET} trajectory is then calculated from the resulting fluorescent signals (Figure 11.2) and used in the kinetics analysis described in Sec. 11.4A.

11.3.2 Sample Preparation and Single Molecule Tethering

The doubly dye-labeled and biotinylated DNA hairpin construct has been purchased in HPLC purified form (Integrated DNA Technologies, Coralville, IA) and is used as is.[15, 20] The full DNA sequence and dye labeling sites are indicated as follows: 5'-Cy5-TCTTCAGT-A_{40}-Cy3-ACTGAAGA-A10-biotin-3'. Specifically, the construct contains an 8 base pair complimentary sequence separated by a 40-(dA) linker (Figure 11.1). The labeling of Cy3 and Cy5 results in two distinct E_{FRET} states corresponding to the folded/hybridized ($E_{FRET} \approx 0.8$) and unfolded/dehybridized ($E_{FRET} \approx 0.1$) conformations.[15, 20] To extend the observation time of fluorescent signals from a single construct, the DNA hairpins are immobilized on the surface of the capillary cell through biotin-streptavidin interactions (Figure 11.1).[18-19] We note that the DNA hairpin is chosen in these first high pressure single molecule kinetic measurements due mainly to the fact that not only it has been widely studied as a model system of nucleic acid secondary structure formation, but also its folding kinetics as well as equilibrium have been extensively characterized at the single molecule level[15, 20-22]. While the incorporation of the poly(dA) linker simplifies the DNA duplexing from a bimolecular to unimolecular process, it may also contribute to the folding kinetics and thermodynamics in addition to the duplex formation. Despite the hairpin folding thermodynamic being previously shown to be largely

dominated by complementary base paring[15], it is worth noting that the linker effects on the kinetics remain uncharacterized at high pressure.

Preparation of the DNA-decorated surface is achieved by sequentially flushing the capillary cell with the following in order: (i) 10 mg/mL bovine serum albumin (BSA) with 10% biotinylation for surface passivation, (ii) 200 μg/mL streptavidin solution for surface immobilization, and (iii) ≈ 25 pmol/L biotinylated DNA hairpin constructs. Prior to each smFRET experiment, the sample holder is flushed by the imaging buffer containing (i) 50 mmol/L hemipotassium HEPES buffer (pH 7.5), (ii) Trolox/protocatechuate 3,4-dioxygenase

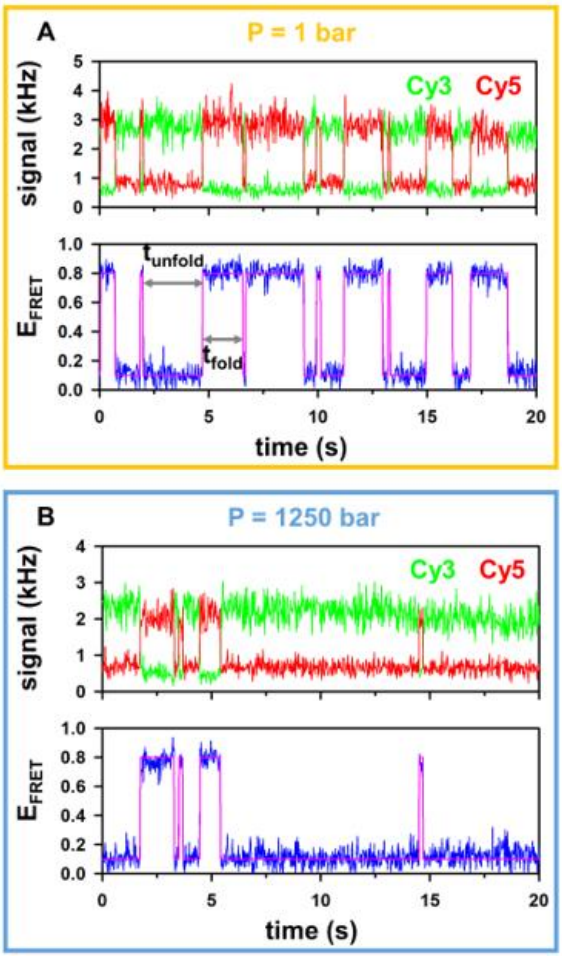

Figure 11.2 Sample time-resolved fluorescent signals (upper panels) and corresponding E_{FRET} trajectories (lower panels) at (A) 1 bar and (B) 1250 bar. Background $[Na^+]$ = 50 mmol/L.

(PCD)/protocatechuate (PCA) oxygen scavenger cocktail to catalytically remove oxygen and thereby increase dye photostability, and (iii) sufficient NaCl and $MgCl_2$ to achieve desired monovalent (Na^+)/divalent (Mg^{2+}) cation concentrations. We note that 25 mmol/L of background K^+ from the HEPES buffer is always presented in the pressure dependent experiments.

11.4 Results and analysis

11.4.1 Kinetic origin of DNA hairpin unfolding with increasing pressure

The prolonged observation of a single DNA construct one at a time allows us to obtain the time dependent fluorescence signals from Cy3/Cy5 and calculate the resulting E_{FRET} trajectory (Figure 11.2). At ambient (≈ 1 bar) pressures (Figure 11.2A), the correlation between Cy3 and Cy5 fluorescence indicates the DNA hairpin actively switches between the folded and unfolded conformations, corresponding to $E_{FRET} \approx 0.8$ and 0.1, respectively.[15, 20] As the pressure increases to 1250 bar (Figure 11.2B), the DNA hairpin clearly spends more time in the low E_{FRET} conformation, indicating that the DNA hybridization equilibrium is shifted toward the denatured (i.e. unfolded) state with increasing pressure. This is completely consistent with results reported in freely diffusing smFRET studies of the similar constructs under equilibrium conditions.[13, 15]

However, the present tethered studies contain much richer information on the folding/unfolding kinetics, which can be extracted by the dwell time analysis with in-house software and thresholding methods as previously described.[18-19, 23] Specifically, the well separated E_{FRET} distributions for the DNA hairpin allow us to unambiguously distinguish between folded/unfolded conformational states with a temporal resolution of 25 ms (Figure 11.2A, B). The resulting cumulative distribution functions (CDFs) of dwell time in each of the states are well-fit to a single exponential decay model, as clearly demonstrated by the semi-

logarithmic plots in Figure 11.3. Thus, both the folding and unfolding of the DNA hairpin appear to follow simple first order kinetics,[20] with the DNA hairpin folding dynamics described by first order rate constants k_{fold} and k_{unfold}, respectively. In Figure 11.3A, the CDF slope for the unfolded (red) dwell times is greater than for the folded (green) dwell times, suggesting $k_{fold} > k_{unfold}$, and therefore the DNA hairpin spends more time in the folded conformation at ambient pressure with folding equilibrium constant $K_{eq} = k_{fold}/k_{unfold} > 1$. At the high pressure (1250 bar, Figure 11.3B), the CDF logarithmic decays reveal a dramatic decrease in k_{fold} accompanied by a simultaneous increase in k_{unfold}. Thus, the kinetic origins of pressure induced denaturation of the DNA hairpin is therefore by *deceleration* and *acceleration* of the folding and unfolding rate constants, respectively.

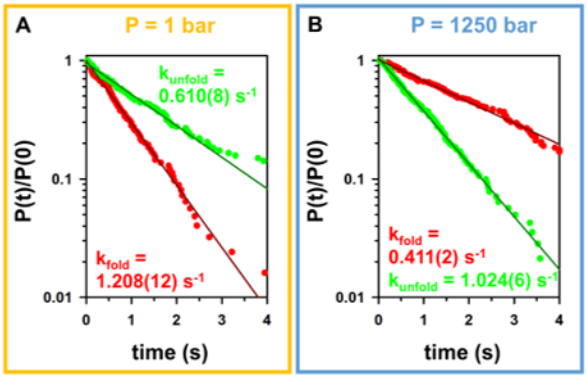

Figure 11.3 Sample cumulative distribution functions of dwell time at (A) 1 bar and (B) 1250 bar. Background $[Na^+]$ = 50 mmol/L.

11.4.2 Volumetric characterization of pressure-dependent DNA (un)folding

If we associate the purely single exponential kinetic behavior (Figure 11.3) with a single rate limiting transition state, the rate constant k can be expressed by the Eyring equation[24]

$$k = \nu e^{-\frac{\Delta G^{\ddagger}}{RT}}, \qquad \text{Eq. 11.1}$$

where ν is the attempt frequency to reach the transition state barrier. Since the pressure dependence of the folding/unfolding rate constants and equilibrium constants originates from

changes in molar volume along the folding path,[4-5] a more quantitative evaluation can be obtained by van't Hoff analysis of the folding/unfolding rate constants at a series of increasing pressures (Figure 11.4A).:[4-5]

$$\left(\frac{\partial lnk}{\partial P}\right)_T = \frac{-\Delta V^{\ddagger}}{RT}, \qquad \text{Eq. 11.2}$$

where $\Delta V^{\ddagger}_{fold}$ ($\Delta V^{\ddagger}_{unfold}$) represents the activation volume equivalent to volume change from the unfolded (folded) conformation to the transition state: $\Delta V^{\ddagger}_{fold} = V_{TS} - V_{unfold}$ ($\Delta V^{\ddagger}_{unfold} = V_{TS} - V_{fold}$). As shown in Figure 11.4, $\ln(k_{fold})$ decreases linearly as a function of increasing pressure, with the negative slope indicating an increase in volume for the DNA hairpin to reach the transition state barrier from the unfolded state ($\Delta V^{\ddagger}_{fold}$ = +22.1(16) mL/mol). Conversely, $\ln(k_{unfold})$ increases linearly as a function of pressure, with a slope corresponding to a negative $\Delta V^{\ddagger}_{unfold}$ = −10.3(6) mL/mol, indicating that the fully folded conformation expands further in molar volume from the transition conformation. Simply summarized, the volumetric analysis of the pressure dependent rate constants reveals that the molar volume of the DNA hairpin increases monotonically along the hybridization path: $V_{unfold} < V_{TS} < V_{fold}$.

Moreover, the conventional pressure-dependent folding equilibrium behavior can be reconstructed simply through the relation $K_{eq} = k_{fold}/k_{unfold}$ (Figure 11.4B). The results are consistent with previous observations of $\ln(K_{eq})$ linearly decreasing as a function of increasing pressure[13, 15] predicted by[4-5]

$$\left(\frac{\partial lnK_{eq}}{\partial P}\right)_T = \frac{-\Delta V^{0}}{RT}. \qquad \text{Eq. 11.3}$$

The corresponding overall molar volume change upon DNA hairpin folding is found to be ΔV^0 = +33.7(13) mL/mol, which is in excellent agreement with the present pressure dependent kinetic analysis predictions of $\Delta V^0 = \Delta V^{\ddagger}_{fold} + (-\Delta V^{\ddagger}_{unfold})$ = +32.4(17) mL/mol. It is worth noting that this overall change in molar volume is substantially higher than found from previous high

pressure burst fluorescence studies under equilibrium conditions (ΔV^0 = +23(2) mL/mol), which was obtained at a higher (75 vs. 50 mmol/L) sodium ion (Na^+) concentration.[15] Indeed, this provides a first indication of the substantial sensitivity to monovalent cations in the pressure dependences of both kinetic rates and equilibrium constants for DNA hybridization. By way of confirmation, we have determined the overall molar volume change upon hybridization under similar buffer conditions ([Na^+] = 75 mmol/L) to be ΔV^0 = +25.9(19) mL/mol, which is now in good agreement with previous published results. Detailed studies for the dependence of these molar volumes on monovalent and divalent cation conditions are described below.

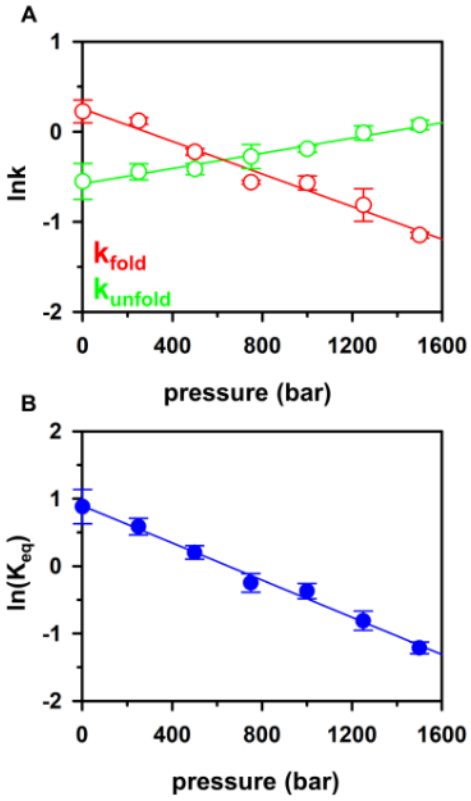

Figure 11.4 Pressure dependent van't Hoff analysis of DNA hairpin folding. (A) Folding (k_{fold}) and unfolding (k_{unfold}) rate constants, and (B) folding equilibrium constant (K_{eq}) as a function of increasing pressure. Note that k_{fold} and k_{unfold} are each scaled to 1 Hz (s^{-1}) to permit taking logarithms of unitless quantities. The slope of these plots can be used to infer changes in the molar volume with uncertainties (≈ 1 to 2 mL/mol) at ≈ 5 to 10% of a single H_2O molecule volume (V ≈ 18 mL/mol). Background [Na^+] = 50 mmol/L.

11.4.3 Effects of Na^+ on pressure dependent folding kinetics

With one phosphate group per nucleotide, DNA is highly negatively charged under pH neutral conditions; therefore cations are essential to facilitate the formation of a more compact folded DNA configuration.[25-26] Moreover, charge screening and neutralization can have significant impacts on the hydration structure,[27] which in turn can alter the effective molar volume of the biomolecule plus solvent system and ultimately pressure dependences for the folding/unfolding kinetics.[28-29] In this section, pressure dependent equilibrium and kinetic rate constants of DNA hairpin folding are systematically investigated to explore the impact of monovalent Na^+ cations.

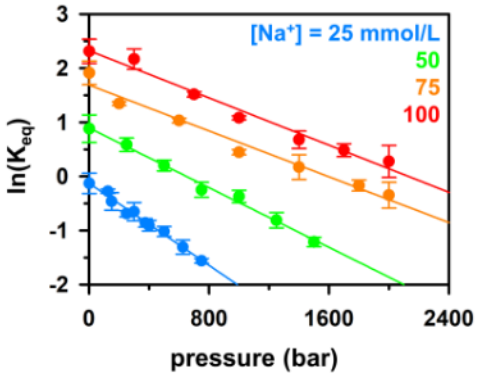

Figure 11.5 Pressure dependent folding equilibrium constants (K_{eq}) as a function of Na^+ concentration, expressed as a van't Hoff pressure analysis, whereby the slope of these plots can be used to infer changes in the molar volume with uncertainties (≈ 1 to 2 mL/mol) at ≈ 5 to 10% of a single H_2O molecule volume (V ≈ 18 mL/mol).

Firstly, the pressure dependence of the equilibrium constant K_{eq} as a function of $[Na^+]$ is displayed as a semi-logarithmic plot in Figure 11.5. Under all conditions explored, the overall trend reveals linear decrease in $\ln(K_{eq})$ with elevated applied pressure, which by Eq. 11.3 predicts a positive $\Delta V^0 > 0$. However, there are two quite noticeable changes in $K_{eq}(P)$ with increasing $[Na^+]$: i) $\ln(K_{eq})$ systematically shifts upward, reflecting that sodium significantly promotes folding of the DNA hairpin under all pressures; ii) the $\ln(K_{eq})$ vs P slopes become

$[Na^+]$ (mmol/L)	25	50	75	100
ΔV^0 (mL/mol)	46.4(19)	33.7(13)	25.9(19)	26.7(17)

Table 11.1 Na^+ dependence of overall molar volume changes (ΔV^0) for the single molecule DNA hairpin construct in the absence of divalent cation (i.e., $[Mg^{2+}] = 0$).

shallower with increasing $[Na^+]$, indicating an overall reduction in ΔV^0 and thus pressure sensitivity for DNA hairpin folding. From linear least squares fits, the resulting $[Na^+]$ dependent change in molar volume values are summarized in Table 11.1, which illustrate that ΔV^0 decreases systematically with increasing $[Na^+]$ up to 75 mmol/L values but eventually saturates at $[Na^+] \approx 75$ to 100 mmol/L. Note that ΔV^0 obtained at $[Na^+] = 75$ mmol/L is experimentally

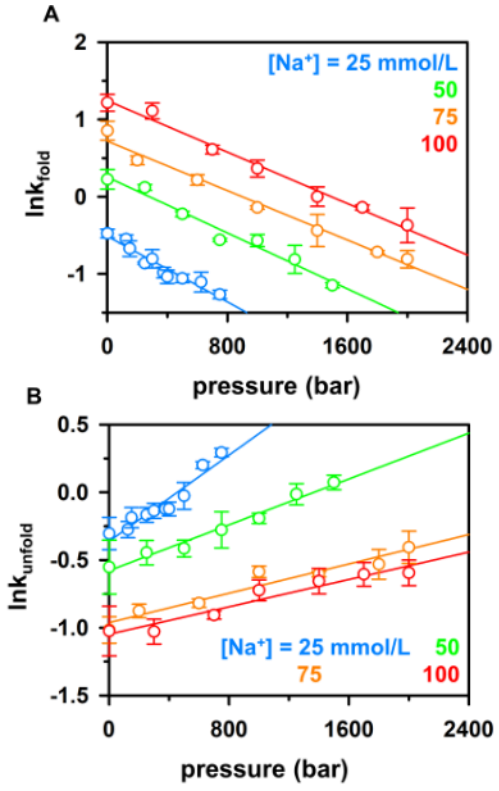

Figure 11.6 Pressure dependent van't Hoff analysis of (A) folding (k_{fold}) and (B) unfolding (k_{unfold}) rate constants for a series of monovalent Na^+ concentrations.

$[Na^+]$ (mmol/L)	25	50	75	100
$\Delta V^{\ddagger}_{fold}$ (mL/mol)	26(2)	22.1(16)	19.6(11)	20.4(10)
$\Delta V^{\ddagger}_{unfold}$ (mL/mol)	-19(2)	-10.3(6)	-6.6(7)	-6.2(7)

Table 11.2 Na^+ dependence of $\Delta V^{\ddagger}_{fold}$ and $\Delta V^{\ddagger}_{unfold}$ molar volume changes for the single molecule DNA hairpin construct in the absence of divalent cation (i.e., $[Mg^{2+}] = 0$).

indistinguishable from the previous diffusion smFRET equilibrium measurements under the same salt conditions (25.9(19) vs. 23(2) mL/mol),[15] confirming that surface tethering has negligible impact on folding equilibrium properties for the DNA hairpin construct.[30-31]

Secondly, access to dwell time analysis in a surface tethered smFRET experiment also permits $[Na^+]$ dependent kinetic information to be obtained from the single-molecule E_{FRET} trajectories. The resulting pressure dependent rate constants k_{fold} and k_{unfold} from cumulative distribution functions are presented in Figure 11.6A and Figure 11.6B, respectively, as a function of $[Na^+]$. In these semi-logarithmic plots, the clear upward and downward vertical shifts in k_{fold} and k_{unfold} reveal that Na^+ promotes DNA hairpin folding by simultaneously increasing k_{fold} and decreasing $k_{unfold,}$ respectively.[20] The plots for $\ln(k_{fold})$ vs. pressure in Figure 11.6A are well fit to a series of nearly parallel lines with negative slopes, confirming that k_{fold} decreases at increasing pressure and $\Delta V^{\ddagger}_{fold} > 0$ for all $[Na^+]$ conditions explored (Eq. 11.2). The steepening of slopes for lowest $[Na^+]$ reflects a larger $\Delta V^{\ddagger}_{fold}$ at $[Na^+] < 75$ mmol/L, which then quickly decreases to a saturation value independent of increasing $[Na^+]$ (see also Table 11.2). Conversely, as evident from the positive slopes in Figure 11.6B, $\ln(k_{unfold})$ increases rapidly with increasing pressure, consistent with a negative $\Delta V^{\ddagger}_{unfold} < 0$. Moreover, the sensitivity of k_{unfold} to pressure and cation concentration is now clearly evident in the steeper slopes at low $[Na^+] < 75$ mmol/L, revealing a

much more significant Na^+ dependence of $\Delta V^{\ddagger}_{unfold}$ in the low sodium regime. Similar to $\Delta V^{\ddagger}_{fold}$, as $[Na^+]$ increases, the magnitude of $\Delta V^{\ddagger}_{unfold}$ decreases and gradually reaches a saturation value at $[Na^+] \approx 75$ mmol/L. By way of summary, *increasing* $[Na^+]$ lowers the sensitivity of both k_{fold} and k_{unfold} to pressure by reduction in the magnitude of $\Delta V^{\ddagger}_{fold}$ and $\Delta V^{\ddagger}_{unfold}$, respectively, with much stronger effects observed for the latter. However, as $[Na^+]$ increases above ≈ 75 mmol/L, monovalent cation effects on the pressure dependent rate constants appear to saturate for both $\Delta V^{\ddagger}_{fold}$ and $\Delta V^{\ddagger}_{unfold}$.

11.5 Discussion

11.5.1 Effective volume of the DNA hairpin increases along the folding path

The surface tether smFRET experiments (Figure 11.1) performed in the high pressure capillary sample cell allow us to probe the kinetics of DNA hairpin folding with pressure as a controlled external variable up to ≈ 5 kilobar.[7, 15] The E_{FRET} time trajectories are calculated from the resulting time-dependent Cy3/Cy5 fluorescent signals (Figure 11.2) and analyzed by conventional thresholding methods to obtain dwell time distributions of the folded and unfolded states (Figure 11.3).[18-19, 23] First of all, visual inspection of the E_{FRET} trajectories (Figure 11.2) clearly reveals that with increasing pressure, the DNA hairpin spends more time in the unfolded (low E_{FRET}) conformation. Such DNA unfolding at elevated pressures is commonly referred to as pressure denaturation,[8-9] which had been routinely observed in multiple protein[4-5] and nucleic acid[7, 32-34] systems in previous high pressure equilibrium measurements. Pressure denaturation indicates that the thermodynamic volume of the system is larger for the folded vs unfolded conformations ($\Delta V^0 = V_{fold} - V_{unfold} > 0$) and therefore according to Le Chatelier's principle, folding is disfavored at high pressures (Eq. 11.3).[35] Though still a topic of intense discussion,

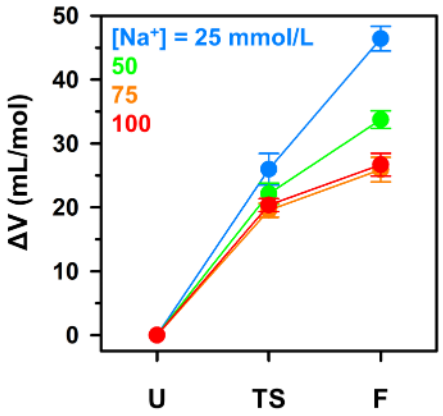

Figure 11.7 Effective volume change along the folding coordinate as a function of increasing [Na^+], with volume of the unfolded state (V_{unfold}) arbitrarily designated as the reference zero.

such a volume increase due to folding is commonly ascribed to a corresponding change in hydration structure for the surrounding solvating water molecules.[4, 35] In essence, the total system volume can decrease with DNA unfolding, since the volume occupied by water in this temperature range decreases with greater ordering of the solvent molecules.[28-29] This greater ordering and thus decreased volume can occur upon DNA unfolding by exposing greater surface area and thus orienting more water molecules due for example to stronger Coulombic interactions with the phosphate anion backbone. An alternate mechanism proposed for $\Delta V > 0$ behavior would be the formation of water-excluding hydrophobic voids upon folding,[36] which would then effectively induce the folded DNA to displace a greater molar volume in solution.

In the kinetic analysis, Figure 11.4A explicitly reveals the origin of this pressure-induced denaturation as a simultaneous decrease in k_{fold} and increase in k_{unfold}. Such kinetic response implies that the effective transition state volume must be smaller than the fully folded state, yet larger than the unfolded state ($V_{unfold} < V_{TS} < V_{fold}$). In Figure 11.7, the volumes of each of the three conformations are displayed with V_{unfold} referenced to zero, clearly revealing that the volume of the DNA hairpin increases monotonically along the folding coordinate. Similar trends

have also been observed in some protein systems with pressure-jump[37-38] and high pressure ZZ-exchange NMR[39] studies. Indeed, it is not surprising that the transition state adopts an intermediate volume between the folded and unfolded configurational extremes. However, these experimental activation molar volumes ($\Delta V^{\ddagger}_{fold}$ and $\Delta V^{\ddagger}_{unfold}$) also contain additional information on changes in water solvation structure due to the conformational transition,[29, 35] and thus may offer insights into the influence of cations on DNA hydration as a function of the hybridization/folding coordinate,[27] as discussed in Sec. 11.5B and Sec. 11.5C.

In previous pressure dependent UV melting experiments, the majority of nucleic acid double helices are found to be stabilized by pressure,[11-12] which at first seems opposite to the recent high pressure single molecule studies with hairpins of shorter duplexing regions (< 10 base-pairs).[13-15, 21] However, a strong correlation between thermal stability and pressure response also has been previously observed in UV melting experiments,[6] suggesting pressure only destabilizes the helices with low thermal stability (e.g. T_m > 50 °C). Since the single molecule experiments are often performed under the conditions where folded and unfolded states are both sufficiently populated, the hairpins used in these single molecule studies are much less thermally stable with T_m close to the room temperature.[13-15, 21] As a result, the pressure destabilization effects ($\Delta V^0 > 0$) characterized at the single molecule level are in fact entirely consistent with previous observations in UV melting studies. Although the origin of the strong correlation between melting temperature and pressure response has not been completely understood, it can be accounted by the complex temperature-pressure dependent interactions involved in the helix-coil transition[6] such as hydration, base stacking, hydrogen bonding and Coulombic interactions, etc.[40] We note that the temperature-dependent pressure response has also been observed in previous smFRET experiments.[34]

Besides thermodynamic properties, the kinetics of helix-coil transition can be obtained by analysis of the hysteresis in UV melting/annealing curves.[41] The results again show a negative ΔV^0 for most of the duplex sequences,[42-43] while the signs of $\Delta V^{\ddagger}_{fold/unfold}$ may vary.[43] Moreover, the nearest neighbor parameters in ΔV^0 and $\Delta V^{\ddagger}_{fold/unfold}$ have been determined and the prediction agrees will with the studied duplex systems.[43] However, the same nearest neighbor analysis predicts the ΔV^0 and $\Delta V^{\ddagger}_{fold}$ of the duplex sequence in our hairpin construct to be 0.0 mL/mol (+25.9 mL/mol, as the closest value measured at $[Na^+]$ = 75 mM) and -1.5 mL/mol (+19.6 mL/mol). Although the discrepancy could partially attribute to the different buffer conditions and the poly(dA) linker, which contributes ≈ 10 mL/mol to ΔV^0,[15] the nearest neighbor analysis is not expected to correctly predict our results due simply to the fact that these parameters are derived from more thermally stable duplex structures that are mostly stabilized under high pressure. Indeed, a more sophisticated high pressure smFRET experimental setup to study the bimolecular DNA duplex formation[44] is needed to better understand the disparity between pressure effects on short and long duplex sequences. The high pressure smFRET experiment provides a powerful tool to study the pressure dependent kinetics completely free from the thermal contributions and the results obtained at low temperature may better represent the impact of extreme pressures on deep sea organisms.

11.5.2 Na^+ decreases the activation volumes for both folding and unfolding pathways

The pressure responsive DNA folding equilibrium and kinetics have been studied at increasing $[Na^+]$ to explore the monovalent cation effects (Figure 11.6). The results are quantitatively summarized in Figure 11.7, which reveals not only an strong increase in effective volume along the folding coordinate, but also that the presence of monovalent cation (Na^+) reduces these changes in volume and saturates above 75 mmol/L. Specifically, the most dramatic

effects are observed in the volume change from the transition state to the folded state ($V_{fold} - V_{TS} = -\Delta V^{\ddagger}_{unfold}$), which collapses by 3-fold from +19(2) mL/mol to +6.2(7) mL/mol as [Na^+] increases from 25 to 100 mmol/L. It is worth noting that the exceptionally large dynamic range of pressures explored in these experiments results in ΔV uncertainties down at the ≈ 1 to 2 mL/mol level. For a sense of scale, this is roughly 5 to 10% the volume of a single H_2O molecule, which in turn allows us to explore and quantify the even smaller changes in molar volume induced by the presence of monovalent cations.

In particular, there is a quite significant Na^+ dependence to the change in thermodynamic molar volume (ΔVs, Table 11.1 and Table 11.2) which provides additional confirmation that hydration water play a crucial role in pressure induced denaturation phenomena for DNA.[4, 29, 35] By way of specific physical mechanism, monovalent cation association would tend to Debye shield the highly negatively charged DNA phosphate backbone,[45-46] weakening the Coulombic interactions that align the water molecules and therefore allowing DNA to adopt a more weakly bound solvation shell with a larger effective volume.[28-29] Furthermore, such an increase in cation-induced volume changes may vary for each folding stage,[7] resulting in cation dependent changes in molar volume. In particular, since the more folded DNA hairpin has higher charge density and smaller water-exposed surface area,[47] the cations would be expected to be more readily associated with and therefore saturate the ion atmospheres of the folded vs. unfolded structures at progressively lower cation concentrations.[48-49] Alternately stated, V_{unfold} increases faster than V_{fold} with increasing [Na^+] due to preferential cation association with the unfolded state,[50-51] resulting in an overall reduction in ΔV^0 ($\Delta\Delta V^0 < 0$). Moreover, similar monovalent cation effects can also be expected with respect to changes in the transition state volume (V_{TS}),

which similarly predicts decreases in magnitudes of both $\Delta V^{\ddagger}_{fold}$ and $\Delta V^{\ddagger}_{unfold}$ with increasing $[Na^+]$.

In previous thermodynamic and kinetic characterizations of DNA duplex formation[44], increasing $[Na^+]$ is found to simultaneously decrease the relative entropies for both the unfolded and transition state, indicating that Na^+ may promote more organized DNA structures in both conformations prior to folding.[44] In the present work, the volumetric measurements clearly reveal a significant decrease in the value of $V_{fold} - V_{unfold}$ as the dominant cation response (Figure 11.7), or, if we assume a smooth dependence on folding reaction coordinate, an *increase* in molar volume between the unfolded state and the folding transition state. In this context, our high pressure volumetric analysis of the $[Na^+]$ dependence is consistent with a simple physical picture that Na^+ promotes the stability of a progressively more "folded-like" DNA structure by changes in hydration for both the unfolded, transition state, and folded configurations, an interpretation which is in good agreement with previous and current thermodynamic data.[44]

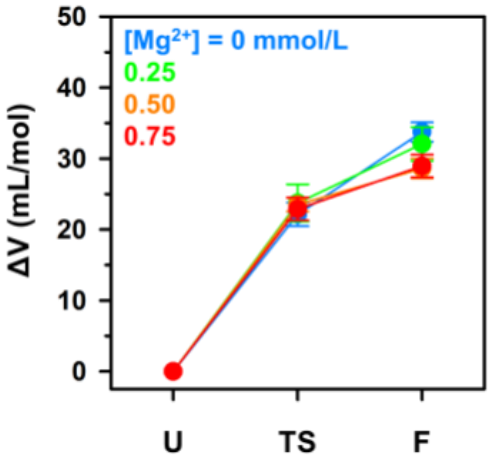

Figure 11.8 Effective volume change along the folding coordinate as a function of increasing $[Mg^{2+}]$, with volume of the unfolded state (V_{unfold}) arbitrarily designated as the reference zero. Background $[Na^+]$ = 50 mmol/L.

11.5.3 Cation-independent volume changes at physiological salt concentrations

The volumetric measurements for the DNA folding kinetics support that such monovalent cation effects saturate at ≈ 75 mmol/L for both $\Delta V^{\ddagger}_{fold}$ and $\Delta V^{\ddagger}_{unfold}$, which is comparable to physiological monovalent cation concentration conditions ($[M^+] \approx 100$ mmol/L). The results therefore predict that significant $[M^+]$ dependence in molar volume changes (ΔVs) can only be observed under low salt conditions (i.e., $[M^+] < 100$ mmol/L). Indeed, previous reports for the K^+-dependence of ΔV^0 in DNA hairpin indicate observation of folding only in the low monovalent cation regime ($[M^+] < 30$ mmol/L).[21] On the other hand, cesium ion (Cs^+) has been shown to reduce the volume changes at low concentration in previous high pressure poly[d(A-T)] melting experiments, with the effects saturating at $[Cs^+] \approx 100$ mmol/L.[11] However, we note that in the same study that the ΔV^0 dependence on Na^+ does not show evidence of any saturation up to $[Na^+] = 1$ mol/L. We believe that sodium-promoted base stacking in the DNA poly(dA) single strand may be significantly perturbing the helix-coil transition and therefore resulting in additional salt-induced volume changes upon melting.[15, 52] Clearly more high pressure data will be needed to fully explore and understand the potential salt/structure dependence of this saturation phenomenon.

Since magnesium (Mg^{2+}) is the most abundant divalent cation inside cells and known to significantly influence nucleic acid secondary and tertiary structure,[26, 53] similar volumetric analyses have been performed as a function of increasing $[Mg^{2+}] = 0$ to 0.75 mmol at background monovalent levels of $[Na^+] = 50$ mmol/L and $[K^+] = 25$ mmol/L (see SI), and the results are summarized in Figure 11.8. The background monovalent cation mimics the physiological environment of DNA folding and provide additional stability for the folded DNA hairpin to increase the pressure dynamic range of the smFRET experiments. Interestingly, the

molar volume folding landscape is only very slightly perturbed by the presence of Mg^{2+}, with $\Delta V^{\ddagger}_{fold}$ being completely independent and with only quite modest (< 5 to 10%) changes in $\Delta V^{\ddagger}_{unfold}$ as a function of $[Mg^{2+}]$. We stress that this does not mean that divalent magnesium effects on the molar volume changes are necessarily weaker than monovalent sodium. Instead, it could be that the overall cation effects are effectively saturated at background monovalent levels of $[M^{+}]$ = 75 mmol/L and that the additional magnesium is unable to achieve any further reduce in ΔV. We note that although the pressure response (ΔV) of the hairpin folding is only weakly dependent on $[Mg^{2+}]$, magnesium still strongly stabilizes the folded hairpin structure as the vertical displacements shown in Figure 11.9. To summarize, our data suggest under sufficiently high monovalent ($[M^{+}] \approx 100$ mmol/L and divalent ($[M'^{2+}] \approx 1$ mmol/L) salt conditions, the molar volume changes (ΔVs) for hybridization of the DNA hairpin saturate and depend only weakly on further increase in cation concentrations. By way of additional evidence, previous pressure dependent single molecule studies of the RNA lysine riboswitch reveal ΔV^{0} also to be independent of salt under physiological conditions ($[Na^{+}]$ = 100 to 500 mmol/L, $[Mg^{2+}]$ = 0.5 to

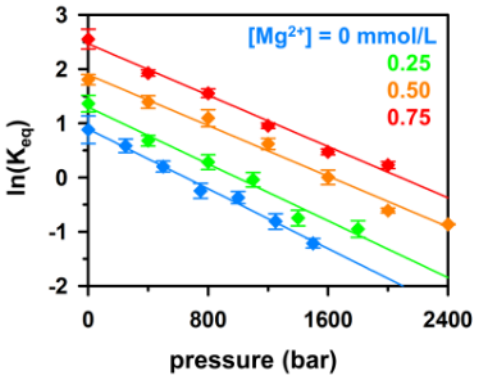

Figure 11.9 Pressure dependent folding equilibrium constants (K_{eq}) as a function of Mg^{2+} concentration, expressed as a van't Hoff pressure analysis, whereby the slope of these plots can be used to infer changes in the free volume with uncertainties (1 to 2 mL/mol) at the 5 to 10% of a single H_2O molecule volume (18 ml/mol). Background $[Na^{+}]$ = 50 mmol/L.

1.5 mmol/L).[7] Although more data are clearly needed, the results thus far encourage expectations that cationic effects on RNA folding will exhibit a similar saturation behavior as seen in DNA.

As a final comment in this subsection, we can translate these changes in molar volume landscapes (ΔV^0 and $\Delta V^{\ddagger}_{fold}$) into corresponding change in free energy landscapes. These reversible work contributions to free energy are specifically evaluated at a nominal P = 1 kilobar and plotted in Figure 11.10 against [Na^+] to highlight i) effects of pressure-induced denaturation in deep sea (≈ 10000 meter) environments, and ii) the saturation of the monovalent cation effects under physiological relevant conditions (Figure 11.10). It is worth noting that even with ΔV^0 values only slightly larger than the size of a single water molecule (V ≈ 18 mL/mol), the equivalent amount of reversible PΔV work under such deep sea pressure conditions already contributes at the level of +1 kcal/mol (≈ +2 kT) to the overall folding free energy, thereby strongly shifting the equilibrium to the unfolded conformation. Furthermore, roughly half of that

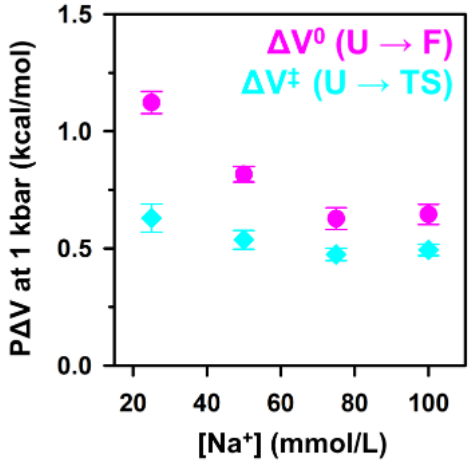

Figure 11.10 PΔV reversible work evaluated at P = 1000 bar to highlight the magnitude of free energy contributions (kT ≈ 0.6 kcal/mol) induced by deep sea pressures as a function of increasing [Na^+].

overall increase in free energy to folding is achieved by the transition state, which corresponds to a roughly three-fold deceleration in DNA hybridization rate constants under deep-sea environment vs. ambient pressure conditions.

11.5.4 Na^+ stabilization effects on DNA secondary structure revisited

In previous sections, we have mostly focused on the slopes in semi-logarithmic plots of K_{eq} or k vs P (Figure 11.5 and 11.6), whereby changes in molar volume can be directly extracted from the pressure dependence. In addition to reducing ΔVs, sodium also promotes DNA hairpin folding under all pressures explored by simultaneously increasing and decreasing k_{fold} and k_{unfold}, respectively, as shown in the vertical displacements in Figure 11.5 and Figure 11.6. For simplicity, we first focus on monovalent Na^+ effects at ambient pressure summarized in Figure 11.11, whereby the folding (ΔG^0) and activation ($\Delta G^{\ddagger}$) free energies for this DNA hairpin are plotted against $[Na^+]$. In obtaining these values, we have used standard thermodynamic and transition state expressions relating overall ($\Delta G^0 = -kT\ln[K_{eq}]$) and transition state ($\Delta G^{\ddagger} = -kT\ln[k_{fold}/\nu]$) free energies to the equilibrium and rate constants measured. ν is an approximate attempt frequency for achieving the transition state, whose precise value is irrelevant in Figure 11.11 for *changes in free energies* ($\Delta\Delta G^0$). The monotonic decrease in ΔG^0 with $[Na^+]$ confirms that the folded DNA hairpin is energetically favored by increasing monovalent cation concentration. Furthermore, such a quasilinear decrease in ΔG^0 with $[Na^+]$ is also consistent with empirical observations by Pegram et al. of cation effects on DNA folding in the low concentration regime ($[M^+] \approx 100$ mmol/L),[47] with the slopes ($\partial\Delta G^0/\partial[M^+]$) strongly correlating with strength of solute-nucleic acid interactions and the change in solvent accessible surface area (ASA) during folding (ΔASA). Indeed, cations are known to accumulate on the surface of DNA through Coulombic attraction,[45, 54-55] and in turn facilitate the formation of a more compact

structure by charge neutralization and screening effects.[25-26] Moreover, similar sodium dependence is also observed in $\Delta G^{\ddagger}$ but with ≈ 50% shallower slopes, most simply attributed to fractionally smaller $\Delta ASA^{\ddagger}$ values or molar volume changes ($\Delta V^{\ddagger}_{fold}$) at the transition state.

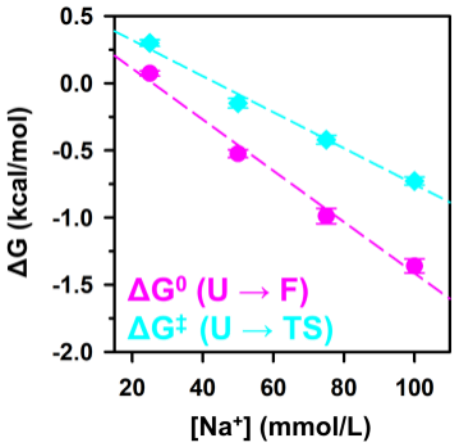

Figure 11.11 Na^+ stabilization effects on the DNA hairpin secondary structure under ambient pressure conditions.

As a parting comment, we note that the empirical relation between ΔG and $[Na^+]$ may deviate from a simple linear function at low $[Na^+] < 75$ mmol as pressure-induced denaturation becomes more significant at higher pressures (Figure 11.10). In other words, increased Na^+ could in principle *protect* the DNA structure from pressure-induced denaturation by both i) increasing the hybridization stability and ii) suppressing the pressure-induced dehybridization response. It is important to stress, however, that such effects would not necessarily make sodium (or other cations) suitable candidates to help deep sea organisms maintain cellular function at extreme pressures, due to the fact that high cation concentrations can interact strongly with biomolecules in cells and thus highly perturb their function,[56] as in dynamic gene regulation by RNA riboswitches.[7] Instead of recruiting cations, therefore, deep sea organisms accumulate high concentrations of small organic solutes (e.g. trimethylamine N-oxide, TMAO) that are much

more compatible with biomolecule structure/function[10] and can thereby counteract these pressure-induced free energy contributions primarily by reducing the pressure sensitivity to biomolecule conformation.[7, 21, 57-58]

11.6 Summary and conclusion

First high pressure kinetic studies of DNA hybridization at the single molecule level have been investigated by smFRET experiments on a doubly dye labelled DNA hairpin construct over a wide dynamic range of external pressures (1 to 1500 bar). The resulting E_{FRET} time trajectories from the prolonged observation of single tethered molecule fluorescence allows us to extract information on the unimolecular rate of DNA hairpin folding/unfolding. The folding (k_{fold}) and unfolding (k_{unfold}) rate constants are found to simultaneously decrease and increase, respectively with increasing pressure, resulting in predictions consistent with pressure-induced denaturation of DNA secondary structure and in excellent agreement with previous equilibrium high pressure studies on freely diffusing constructs. By way of pressure dependent van't Hoff analysis, the effective volume of the DNA plus solvent system is found to systematically increase along the folding coordinate ($V_{unfold} < V_{TS} < V_{fold}$), with volume sensitivities and experimental uncertainties (1 to 2 mL/mol) on the order of 5 to 10% of a single H_2O molecule. Since the cation may significantly change the hydration structure and consequently the effective volume of the DNA plus solvent system, the change in free activation volumes for both folding and unfolding ($\Delta V^{\ddagger}_{fold}$ and $\Delta V^{\ddagger}_{unfold}$) are shown to decrease at low [Na^+] and gradually reach saturation limits at [Na^+] ≈ 75 mmol/L. The more significant reduction in $\Delta V^{\ddagger}_{unfold}$ indicates a greater resemblance between V_{TS} and V_{fold}, which in turn signifies that Na^+ is able to facilitate a more folded-like transition state configuration prior to formation of the fully folded DNA

hairpin. Finally, both $\Delta V^{\ddagger}_{fold}$ and $\Delta V^{\ddagger}_{unfold}$ are approximately insensitive to monovalent (Na^{+}) and divalent (Mg^{2+}) cations under near-physiological salt concentrations, suggesting cation effects on these changes on molar volume (ΔVs) may saturate *in vivo* and therefore be insensitive to moderate intracellular cation fluctuation.

11.7 References

1. Yayanos, A. A.; Dietz, A. S.; Van Boxtel, R., Obligately Barophilic Bacterium from the Mariana Trench. *Proc. Natl. Acad. Sci. U.S.A.* **1981,** *78* (8), 5212-5215.

2. Kato, C.; Li, L.; Nogi, Y.; Nakamura, Y.; Tamaoka, J.; Horikoshi, K., Extremely Barophilic Bacteria Isolated from the Mariana Trench, Challenger Deep, at a Depth of 11,000 Meters. *Appl. Environ. Microbiol.* **1998,** *64* (4), 1510-1513.

3. Somero, G. N., Adaptations to High Hydrostatic Pressure. *Annu. Rev. Physiol.* **1992,** *54* (1), 557-577.

4. Gross, M.; Jaenicke, R., Proteins Under Pressure. *Eur. J. Biochem.* **1994,** *221* (2), 617-630.

5. Mozhaev, V. V.; Heremans, K.; Frank, J.; Masson, P.; Balny, C., High Pressure Effects on Protein Structure and Function. *Proteins* **1996,** *24* (1), 81-91.

6. Dubins, D. N.; Lee, A.; Macgregor, R. B.; Chalikian, T. V., On the Stability of Double Stranded Nucleic Acids. *J. Am. Chem. Soc.* **2001,** *123* (38), 9254-9259.

7. Sung, H.-L.; Nesbitt, D. J., High Pressure Single-Molecule FRET Studies of the Lysine Riboswitch: Cationic and Osmolytic Effects on Pressure Induced Denaturation. *Phys. Chem. Chem. Phys.* **2020,** *22* (28), 15853-15866.

8. Zipp, A.; Kauzmann, W., Pressure denaturation of metmyoglobin. *Biochemistry* **1973,** *12* (21), 4217-4228.

9. Roche, J.; Royer, C. A., Lessons from Pressure Denaturation of Proteins. *J. Royal Soc. Interface* **2018,** *15* (147), 20180244.

10. Yancey, P. H.; Blake, W. R.; Conley, J., Unusual Organic Osmolytes in Deep-Sea Animals: Adaptations to Hydrostatic Pressure and Other Perturbants. *Comp. Biochem. Physiol., Part A Mol. Integr. Physiol.* **2002,** *133* (3), 667-676.

11. Najaf-Zadeh, R.; Wu, J. Q.; Macgregor, R. B., Effect of Cations on the Volume of the Helix-Coil Transition of poly[d(A-T)]. *Biochim. Biophys. Acta, Gene Struct. Expression* **1995,** *1262* (1), 52-58.

12. Wu, J. Q.; Macgregor Jr., R. B., Pressure Dependence of the Helix–Coil Transition Temperature of poly[d(G-C)]. *Biopolymers* **1995,** *35* (4), 369-376.

13. Patra, S.; Anders, C.; Erwin, N.; Winter, R., Osmolyte Effects on the Conformational Dynamics of a DNA Hairpin at Ambient and Extreme Environmental Conditions. *Angew. Chem.* **2017,** *56* (18), 5045-5049.

14. Patra, S.; Anders, C.; Schummel, P. H.; Winter, R., Antagonistic Effects of Natural Osmolyte Mixtures and Hydrostatic Pressure on the Conformational Dynamics of a DNA Hairpin Probed at the Single-Molecule Level. *Phys. Chem. Chem. Phys.* **2018,** *20* (19), 13159-13170.

15. Sung, H.-L.; Nesbitt, D. J., DNA Hairpin Hybridization under Extreme Pressures: A Single-Molecule FRET Study. *J. Phys. Chem. B* **2020,** *124* (1), 110-120.

16. Pan, T.; Sosnick, T., RNA Folding During Transcription. *Annu. Rev. Biophys. Biomol. Struct.* **2006,** *35* (1), 161-175.

17. Mott, M. L.; Berger, J. M., DNA Replication Initiation: Mechanisms and Regulation in Bacteria. *Nat. Rev. Microbiol.* **2007,** *5* (5), 343-354.

18. Hodak, J. H.; Fiore, J. L.; Nesbitt, D. J.; Downey, C. D.; Pardi, A., Docking Kinetics and Equilibrium of a GAAA Tetraloop-Receptor Motif Probed by Single-Molecule FRET. *Proc. Natl. Acad. Sci. U.S.A.* **2005,** *102* (30), 10505-10510.

19. Sengupta, A.; Sung, H.-L.; Nesbitt, D. J., Amino Acid Specific Effects on RNA Tertiary Interactions: Single-Molecule Kinetic and Thermodynamic Studies. *J. Phys. Chem. B* **2016,** *120* (41), 10615-10627.

20. Nicholson, D. A.; Sengupta, A.; Sung, H.-L.; Nesbitt, D. J., Amino Acid Stabilization of Nucleic Acid Secondary Structure: Kinetic Insights from Single-Molecule Studies. *J. Phys. Chem. B* **2018,** *122* (43), 9869-9876.

21. Patra, S.; Schuabb, V.; Kiesel, I.; Knop, J.-M.; Oliva, R.; Winter, R., Exploring the Effects of Cosolutes and Crowding on the Volumetric and Kinetic Profile of the Conformational Dynamics of a poly dA loop DNA Hairpin: A Single-Molecule FRET Study. *Nucleic Acids Res.* **2018,** *47* (2), 981-996.

22. Tsukanov, R.; Tomov, T. E.; Masoud, R.; Drory, H.; Plavner, N.; Liber, M.; Nir, E., Detailed Study of DNA Hairpin Dynamics Using Single-Molecule Fluorescence Assisted by DNA Origami. *J. Phys. Chem. B* **2013,** *117* (40), 11932-11942.

23. Sung, H.-L.; Nesbitt, D. J., Single-Molecule FRET Kinetics of the Mn^{2+} Riboswitch: Evidence for Allosteric Mg^{2+} Control of "Induced-Fit" vs "Conformational Selection" Folding Pathways. *J. Phys. Chem. B* **2019,** *123* (9), 2005-2015.

24. Zhou, H.-X., Rate Theories for Biologists. *Q. Rev. Biophys.* **2010,** *43* (2), 219-293.

25. Record Jr., M. T., Effects of Na^{+} and Mg^{++} Ions on the Helix–Coil Transition of DNA. *Biopolymers* **1975,** *14* (10), 2137-2158.

26. Owczarzy, R.; Moreira, B. G.; You, Y.; Behlke, M. A.; Walder, J. A., Predicting Stability of DNA Duplexes in Solutions Containing Magnesium and Monovalent Cations. *Biochemistry* **2008,** *47* (19), 5336-5353.

27. Buckin, V.; Tran, H.; Morozov, V.; Marky, L. A., Hydration Effects Accompanying the Substitution of Counterions in the Ionic Atmosphere of Poly(rA)·Poly(rU) and Poly(rA)·2Poly(rU) Helices. *J. Am. Chem. Soc.* **1996,** *118* (30), 7033-7039.

28. Barbosa, R. d. C.; Barbosa, M. C., Hydration Shell of the TS-Kappa Protein: Higher Density than Bulk Water. *Physica A* **2015,** *439*, 48-58.

29. Chalikian, T. V.; Sarvazyan, A. P.; Plum, G. E.; Breslauer, K. J., Influence of Base Composition, Base Sequence, and Duplex Structure on DNA Hydration: Apparent Molar Volumes and Apparent Molar Adiabatic Compressibilities of Synthetic and Natural DNA Duplexes at 25.degree.C. *Biochemistry* **1994,** *33* (9), 2394-2401.

30. Fiore, J. L.; Kraemer, B.; Koberling, F.; Edmann, R.; Nesbitt, D. J., Enthalpy-Driven RNA Folding: Single-Molecule Thermodynamics of Tetraloop−Receptor Tertiary Interaction. *Biochemistry* **2009,** *48* (11), 2550-2558.

31. Holmstrom, E. D.; Polaski, J. T.; Batey, R. T.; Nesbitt, D. J., Single-Molecule Conformational Dynamics of a Biologically Functional Hydroxocobalamin Riboswitch. *J. Am. Chem. Soc.* **2014,** *136* (48), 16832-16843.

32. Downey, C. D.; Crisman, R. L.; Randolph, T. W.; Pardi, A., Influence of Hydrostatic Pressure and Cosolutes on RNA Tertiary Structure. *J. Am. Chem. Soc.* **2007,** *129* (30), 9290-9291.

33. Takahashi, S.; Sugimoto, N., Effect of Pressure on Thermal Stability of G-Quadruplex DNA and Double-Stranded DNA Structures. *Molecules* **2013,** *18* (11), 13297-13319.

34. Arns, L.; Knop, J.-M.; Patra, S.; Anders, C.; Winter, R., Single-Molecule Insights into the Temperature and Pressure Dependent Conformational Dynamics of Nucleic Acids in the Presence of Crowders and Osmolytes. *Biophys. Chem.* **2019,** *251*, 106190.

35. Chalikian, T. V.; Breslauer, K. J., On Volume Changes Accompanying Conformational Transitions of Biopolymers. *Biopolymers* **1996,** *39* (5), 619-626.

36. Roche, J.; Caro, J. A.; Norberto, D. R.; Barthe, P.; Roumestand, C.; Schlessman, J. L.; Garcia, A. E.; García-Moreno E., B.; Royer, C. A., Cavities Determine the Pressure Unfolding of Proteins. *Proc. Natl. Acad. Sci. U.S.A.* **2012,** *109* (18), 6945-6950.

37. Tan, C.-Y.; Xu, C.-H.; Wong, J.; Shen, J.-R.; Sakuma, S.; Yamamoto, Y.; Lange, R.; Balny, C.; Ruan, K.-C., Pressure Equilibrium and Jump Study on Unfolding of 23-kDa Protein from Spinach Photosystem II. *Biophys. J.* **2005,** *88* (2), 1264-1275.

38. Font, J.; Torrent, J.; Ribó, M.; Laurents, D. V.; Balny, C.; Vilanova, M.; Lange, R., Pressure-Jump-Induced Kinetics Reveals a Hydration Dependent Folding/Unfolding Mechanism of Ribonuclease A. *Biophys. J.* **2006,** *91* (6), 2264-2274.

39. Zhang, Y.; Kitazawa, S.; Peran, I.; Stenzoski, N.; McCallum, S. A.; Raleigh, D. P.; Royer, C. A., High Pressure ZZ-Exchange NMR Reveals Key Features of Protein Folding Transition States. *J. Am. Chem. Soc.* **2016,** *138* (46), 15260-15266.

40. Cheng, Y.-K.; Pettitt, B. M., Stabilities of Double- and Triple-strand Helical Nucleic Acids. *Prog. Biophys. Mol. Biol.* **1992,** *58* (3), 225-257.

41. Rougee, M.; Faucon, B.; Mergny, J. L.; Barcelo, F.; Giovannangeli, C.; Garestier, T.; Helene, C., Kinetics and Thermodynamics of Triple-Helix Formation: Effects of Ionic Strength and Mismatched. *Biochemistry* **1992,** *31* (38), 9269-9278.

42. Lin, M.-C.; Macgregor, R. B., Activation Volume of DNA Duplex Formation. *Biochemistry* **1997,** *36* (21), 6539-6544.

43. Dubins, D. N.; Macgregor Jr., R. B., Volumetric Properties of the Formation of Double Stranded DNA: A Nearest-Neighbor Analysis. *Biopolymers* **2004,** *73* (2), 242-257.

44. Dupuis, Nicholas F.; Holmstrom, Erik D.; Nesbitt, David J., Single-Molecule Kinetics Reveal Cation-Promoted DNA Duplex Formation Through Ordering of Single-Stranded Helices. *Biophys. J.* **2013,** *105* (3), 756-766.

45. Das, R.; Mills, T. T.; Kwok, L. W.; Maskel, G. S.; Millett, I. S.; Doniach, S.; Finkelstein, K. D.; Herschlag, D.; Pollack, L., Counterion Distribution around DNA Probed by Solution X-Ray Scattering. *Phys. Rev. Lett.* **2003,** *90* (18), 188103.

46. Tokuda, J. M.; Pabit, S. A.; Pollack, L., Protein-DNA and ion-DNA Interactions Revealed Through Contrast Variation SAXS. *Biophys. Rev.* **2016,** *8* (2), 139-149.

47. Pegram, L. M.; Wendorff, T.; Erdmann, R.; Shkel, I.; Bellissimo, D.; Felitsky, D. J.; Record, M. T., Why Hofmeister Effects of Many Salts Favor Protein Folding but not DNA Helix Formation. *Proc. Natl. Acad. Sci. U.S.A.* **2010,** *107* (17), 7716-7721.

48. Braunlin, W. H.; Bloomfield, V. A., Proton NMR Study of the Base-Pairing Reactions of d(GGAATTCC): Salt Effects on the Equilibria and Kinetics of Strand Association. *Biochemistry* **1991,** *30* (3), 754-758.

49. Spink, C. H.; Chaires, J. B., Effects of Hydration, Ion Release, and Excluded Volume on the Melting of Triplex and Duplex DNA. *Biochemistry* **1999,** *38* (1), 496-508.

50. Shiman, R.; Draper, D. E., Stabilization of RNA Tertiary Structure by Monovalent Cations. *J. Mol. Biol.* **2000,** *302* (1), 79-91.

51. Leipply, D.; Lambert, D.; Draper, D. E., Chapter 21 - Ion–RNA Interactions: Thermodynamic Analysis of the Effects of Mono- and Divalent Ions on RNA Conformational Equilibria. In *Methods in Enzymology*, Academic Press: 2009; Vol. 469, pp 433-463.

52. Goddard, N. L.; Bonnet, G.; Krichevsky, O.; Libchaber, A., Sequence Dependent Rigidity of Single Stranded DNA. *Phys. Rev. Lett.* **2000,** *85* (11), 2400-2403.

53. Sreedhara, A.; Cowan, J. A., Structural and Catalytic Roles for Divalent Magnesium in Nucleic Acid Biochemistry. *Biometals* **2002,** *15* (3), 211-223.

54. Gebala, M.; Bonilla, S.; Bisaria, N.; Herschlag, D., Does Cation Size Affect Occupancy and Electrostatic Screening of the Nucleic Acid Ion Atmosphere? *J. Am. Chem. Soc.* **2016,** *138* (34), 10925-10934.

55. McFail-Isom, L.; Sines, C. C.; Williams, L. D., DNA Structure: Cations in Charge? *Curr. Opin. Struct. Biol.* **1999,** *9* (3), 298-304.

56. Yancey, P. H., Organic Osmolytes as Compatible, Metabolic and Counteracting Cytoprotectants in High Osmolarity and Other Stresses. *J. Exp. Biol.* **2005,** *208* (15), 2819-2830.

57. Yancey, P. H.; Fyfe-Johnson, A. L.; Kelly, R. H.; Walker, V. P.; Auñón, M. T., Trimethylamine Oxide Counteracts Effects of Hydrostatic Pressure on Proteins of Deep-Sea Teleosts. *J. Exp. Zool.* **2001,** *289* (3), 172-176.

58. Krywka, C.; Sternemann, C.; Paulus, M.; Tolan, M.; Royer, C.; Winter, R., Effect of Osmolytes on Pressure-Induced Unfolding of Proteins: A High-Pressure SAXS Study. *Chem. Phys. Chem.* **2008,** *9* (18), 2809-2815.

Chapter 12

Ligand-Dependent Volumetric Characterization of Manganese Riboswitch Folding: A High-Pressure Single-Molecule Kinetic Study

---

12.1 Abstract

Nanoscopic differences in free volume result in pressure-dependent changes in free energies which can therefore impact folding/unfolding stability of biomolecules. Although such effects are typically insignificant under ambient pressure conditions, they are crucially important for deep ocean marine life, where the hydraulic pressure can be on the kbar scale or higher. In this work, single molecule FRET spectroscopy is used to study the effects of pressure on both the kinetic rates and overall thermodynamics for folding/unfolding of the manganese riboswitch. Detailed pressure-dependent analysis of the conformational kinetics allows one to extract precision changes ($\sigma \leq 4$ to 8 $Å^3$) in free volumes not only between the fully folded/unfolded conformations, but also with respect to the folding transition state of the manganese riboswitch. This permits first extraction of a novel "reversible work" free energy ($P\Delta V$) landscape, which reveals a monotonic increase in manganese riboswitch volume along the folding coordinate. Furthermore, such a tool permits exploration of pressure-dependent effects on both Mn^{2+} binding and riboswitch folding, which demonstrate that ligand attachment stabilizes the riboswitch by decreasing the volume increase upon folding. Such competition between ligand binding and pressure induced denaturation dynamics could be of significant evolutionary advantage,

*This chapter is adapted from: Sung, H.-L.; Nesbitt, D. J. Ligand-Dependent Volumetric Characterization of Manganese Riboswitch Folding: A High-Pressure Single-Molecule Kinetic Study. *J. Phys. Chem. B* **2022**, *126*, 9781-9789.

compensating a weakening in riboswitch tertiary structure with pressure mediated ligand binding and promotion of folding response.

12.2 Introduction

Structural transitions in biomolecules and the associated reorganization of the surrounding waters lead to nanoscopic changes in the overall solvent plus solute system volume.[1-2] As a result, conformational change in a biomolecule is intrinsically pressure-dependent.[3] Though such pressure effects are often negligible at ambient pressure (1 bar), these effects can become quite significant in marine biology due to rapid increase in hydraulic pressure as a function of ocean depth (0.1 bar/meter).[4] Indeed, average ocean depth already corresponds to 350 bar pressure, with the deepest regions (e.g., the Challenger Deep) in excess of 1 kbar. As a result, marine (micro)organisms can exhibit unique modes of biological function sculpted by evolution under high pressure conditions.[5-6] It is therefore of particular biophysical interest to explore pressure-dependent paradigms of biomolecular structure and function in order to understand, at the molecular level, bioadaptation of deep-sea organisms to pressure extremes.[7]

With a few exceptions,[8-9] proteins and nucleic acids are known to thermodynamically unfold/dehybridize with increasing pressure.[5, 10-12] Pressure-induced denaturation implies that the folded solute + solvent system effectively occupies more space, resulting in a positive free volume change ($\Delta V^0 > 0$) upon folding. Such an increase in volume seems initially counterintuitive, since one often thinks of biomolecular folding tending toward a state of greater compaction. The reason for such anomalous behavior is that these overall volume changes are quite modest, with solvent-excluding voids[13-15] and/or reorganization of the solvation shell[16-18]

thought to be major contributors to the volume increase upon folding. Interestingly, although pressure is known to thermodynamically destabilize the *equilibrium* folding behavior for nucleic acids and proteins, the *kinetics* of such effects has remained far less explored.[19-21] Since nucleic acid conformations are often highly dynamic,[22] with important biochemical pathways regulated by kinetic access over a barrier to a functionally new conformation (e.g., regulation of gene expression by co-transcriptional folding of riboswitches),[23-25] it is therefore of particular importance to also explore the effects of pressure on transition state barriers and the resulting folding kinetics.

Recently, high pressure single-molecule Fluorescence Resonance Energy Transfer (smFRET) studies of nucleic acid folding kinetics have become experimentally accessible, exploiting small glass capillaries as high-pressure sample cells in conjunction with confocal single photon counting fluorescence measurements.[11, 26-27] In earlier work, pulsed laser excitation through a microscope objective into solutions at high pressure have been used to measure and record the FRET energy transfer efficiency (E_{FRET}) for single RNA molecules diffusing through the confocal volume region. Though such studies have been limited to equilibrium conditions, they clearly demonstrated a systematic decrease in E_{FRET} (i.e., an increase in the unfolding fraction) with increasing pressure. In the present work, we significantly expand these equilibrium high-pressure smFRET studies by immobilizing single RNA constructs to the inside of a high pressure capillary cell, and thereby extend observation times of the fluorescence trajectories to monitor folding/unfolding kinetics at the single molecule level.[28] The resulting pressure dependent kinetic rate constant data now inform on the free volume changes associated with i) folded, ii) unfolded, and iii) transition state barrier conformations, and thus provide novel

opportunities for detailed characterization of the thermodynamic free volume along the nucleic acid folding coordinate.[29]

Specifically, this work comprises detailed study of the effects of extreme pressure on the folding/unfolding kinetics of the manganese riboswitch at the single molecule level. The folding thermodynamics and kinetics of this riboswitch have been studied previously in both ensemble and at the single molecule level under ambient pressure (1 bar) conditions,[30-33] with the present work exploring pressure-dependent *kinetics* of ligand-induced tertiary structure formation for the first time. Of particular significance is first experimental characterization of the coupling between i) pressure-dependent kinetic measurements and ii) the ligand binding event, which allows us to obtain free volume changes for accessing the transition state associated with manganese riboswitch folding. Furthermore, in the context of a simple Hill analysis,[30] we are able to separate ligand Mn^{2+} binding from riboswitch folding events and thereby obtain novel information on "reversible work" ($P\Delta V$) contributions to the free energy landscape along the conformational reaction path. These volume changes are revealed to be sensitive to the hydration structure and fractional Mn^{2+} binding with the RNA, which offers additional insights into the mechanism for ligand-induced RNA folding.

The organization of this paper is as follows. The details of sample preparation and high-pressure experiment setup are illustrated in Sec. 12.3. Sec. 12.4A demonstrates high-pressure effects on the riboswitch folding kinetics, for which increasing pressure destabilizes the riboswitch by simultaneously decreasing (increasing) the folding (unfolding) rate constants, respectively. The effects of Mn^{2+} and Mg^{2+} cations on the pressure dependent folding are then presented in Sec. 12.4B and Sec. 12.4C, respectively, which reveal that cognate ligand Mn^{2+} (and not Mg^{2+}) significantly impacts changes in free volume ($\Delta V^0_{bind} < 0$). Specifically, Mn^{2+} alters

the volumetric reversible work landscape for folding via binding of the cognate ligand to (and subsequent compaction of) the riboswitch rather than a more generic screening of anionic repulsion due to divalent cations. Finally, we briefly discuss in Sec. 12.5A/B the possible role of equilibrium vs. kinetic competition between Mn^{2+} and pressure induced changes in riboswitch volume on the evolutionary biology of deep-sea organisms.

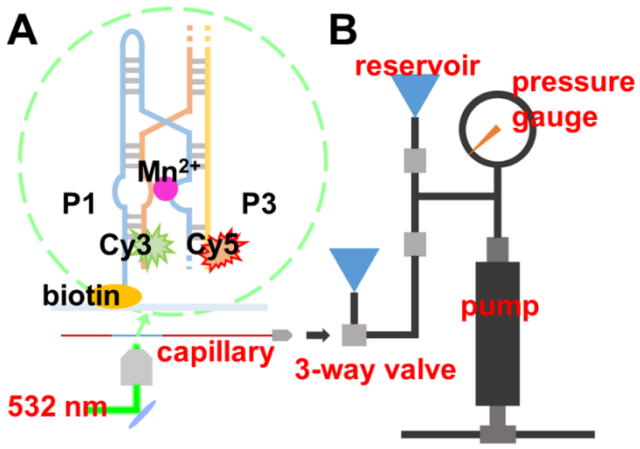

Figure 12.1 Schematic of the high pressure single molecule FRET experiment showing the instrument setup. (A) The cartoon representation of the manganese riboswitch construct in the Mn^{2+}-bound folded conformation where the loop-loop interaction between P1 and P3 stems is formed. (B) The high pressure generating system coupling to the capillary sample holder aligned with the microscope objective. The reservoirs contain ethanol as the pressure transmitting fluid throughout the high pressure tubing manifold.

12.3 Experiment

12.3.1 Single-molecule fluorescent construct design and sample preparation

The ligand-bound folded structure of the manganese riboswitch consists of an RNA four-way junction with the loop-loop interaction between P1 and P3 stems stabilized by a Mn^{2+} cation (Figure 12.1A).[33] The single-molecule FRET construct of the riboswitch is made up of three RNA oligomers, labeled with Cy3, Cy5 and biotin, respectively. The detailed RNA sequences

and the labeling positions for these oligomers can be found in previous work.[34] To assemble the ternary RNA construct, the three oligomers are heat-annealed by temperature cycling, followed by purification via high-performance liquid chromatography (HPLC) methods. The doubly-dye-labeled and biotinylated product enables surface immobilization of the RNA construct to achieve single-molecule fluorescence detection over a prolonged time window and thereby observe a sequence of multiple folding/unfolding events. Furthermore, based on a characteristic Forster length $R_0 \approx 50$ Å for the Cy3-Cy5 FRET pair, the inter-dye distances in the folded conformation can be predicted from the manganese riboswitch crystal structure to be 45 Å,[33] which is in good agreement (E_{FRET} (45 Å) ≈ 0.65) with the high $E_{FRET} \approx 0.60$ state observed. Conversely, when the manganese riboswitch unfolds, the distance between Cy3 and Cy5 increases, resulting in a reduced and easily distinguished value of $E_{FRET} \approx 0.15$ consistent with $R \geq 67$ Å.

The high-pressure sample cell is made from a glass capillary with a square cross section (75 μm/360 μm inner/outer dimensions, Polymicro).[27] Such small lateral dimensions permit higher pressure (> 2000 bar) operation, while the flat interior surface and wall thickness (143 μm) also allow the capillary to function as a conventional coverslip in standard microscope imaging. To prepare the sample, one end of the capillary is first glued into a metal plug drilled with a 450 μm diameter hole and coupled to the pressure system (Figure 12.1B). After creating an optically transparent window by oxidizing away a small 1 cm patch of the polymer coating, we immobilize the RNA molecules on the inner surface of the capillary through biotin-streptavidin interactions. To achieve this goal, we continuously flow the following solutions through the capillary in succession: 1) 10 mg/mL bovine serum albumin (BSA) with 10% biotinylation, 2) 200 μg/mL streptavidin solution, and 3) ≈ 25 pM RNA construct. The exposure time for each solution is ≈ 2 minutes, with pressure delivered through a mechanical micropipette

(Eppendorf) to flush liquid through the capillary.[29] Before any single molecule experiments, the capillary is additionally flushed with an imaging buffer containing 1) 50 mM pH 7.5 HEPES buffer, 2) enzymatic oxygen scavenger cocktail (PCD/PCA/Trolox) to catalytically remove oxygen,[35] 3) 100 mM NaCl to provide background salt, and 4) sufficient $MgCl_2$/$MnCl_2$ to achieve desired divalent cation and cognate ligand concentrations. The free end of the capillary is then sealed with an oxy-propane torch, while the metal plug end is dipped into silicon oil to create a thin pressure transmitting meniscus and prevent sample contamination.

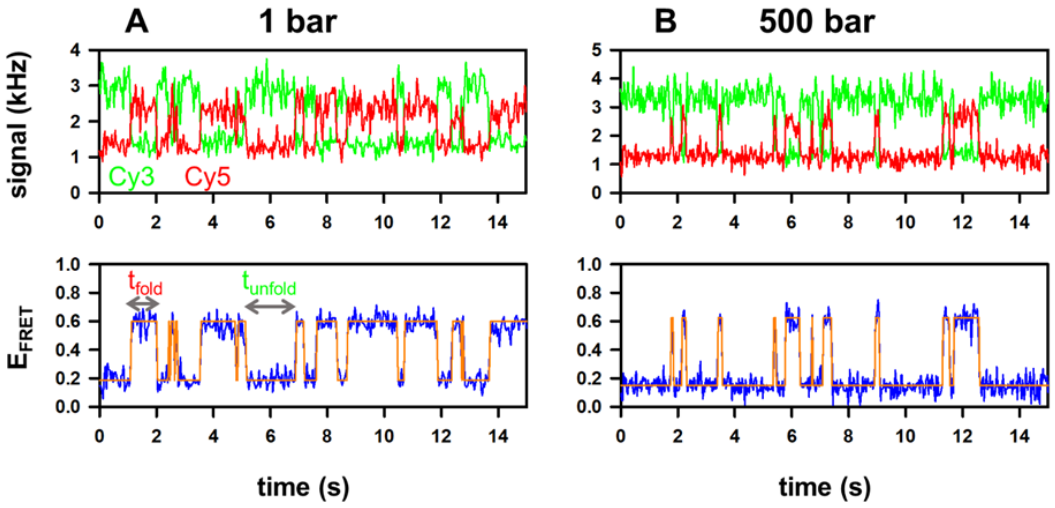

Figure 12.2 Sample fluorescence traces and the resulting time trajectories of E_{FRET} at (A) 1 bar and (B) 500 bar. The simulated traces in orange are obtained from hidden Markov modelling.

12.3.2 High pressure single-molecule FRET spectroscopy

Pressure control is achieved by a manually operated piston screw pump (High Pressure Equipment), which can deliver pressure up to 5 kilobars through high-pressure stainless steel tubing, with the entire manifold filled with ethanol as pressure transmitting fluid (Figure 12.1B).[36] We take advantage of the square cross section of the sample cell by taping it onto the surface of a coverslip, which permits ready alignment of the optical axis of the microscope

objective axis with respect to the capillary wall.[29] The details of the confocal single molecule FRET spectroscopy set up can be found in previous work.[37] To initiate an experiment, the laser is focused to a diffraction limited waist ($\omega_{x,y} \approx 260$ μm) on the inner capillary surface, with the search for single fluorescent molecule constructs conducted by raster scanning of the piezo stage. Tethering of the construct to the capillary surface permits prolonged diffraction limited observation of Cy3/Cy5 fluorescence from a single localized RNA, which in turn enables the collection of long-lived (≈ 1 min) single molecule FRET trajectories at ≈ 4 kHz photon/sec detection rates and limited by eventual photobleaching.

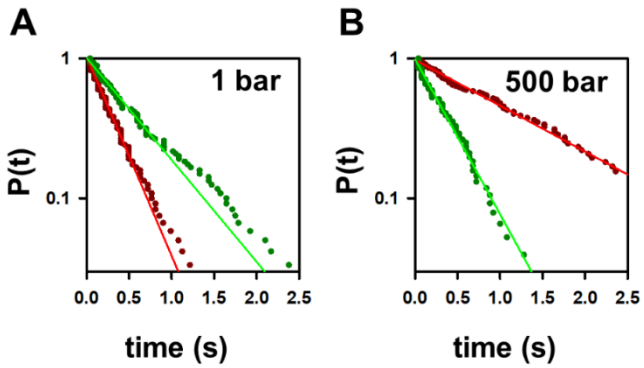

Figure 12.3 Sample dwell time distributions at (A) 1 bar and (B) 500 bar. Data are fit to a single exponential decay function to obtain folding and unfolding rate constants k_{fold} and k_{unfold}, respectively.

12.4 Results and analysis

12.4.1 Kinetic origins of manganese riboswitch unfolding at increasing pressure

Time-dependent E_{FRET} trajectories reveal that the manganese riboswitch actively switches between low and high E_{FRET} states (see sample FRET traces in Figure 12.2) corresponding to unfolded and folded conformations.[30] While the equilibrium constant K_{fold} can be readily obtained from the total timing for folded vs. unfolded events, even more valuable information on

the folding kinetics can be extracted from the distribution of dwell times. As shown in Figure 12.3, this dwell time distribution is well approximated by a single exponential decay, for which the folding/unfolding kinetics of the manganese riboswitch can be described by first order rate constants k_{fold} and k_{unfold}. The resulting dwell time analysis reveals a faster decay for the unfolded state, i.e., $k_{fold} > k_{unfold}$ under ambient (1 bar) conditions. As external hydrostatic pressure increases to 500 bar, however, the riboswitch spends significantly longer in the Cy3 vs Cy5 low E_{FRET} ("denatured") conformation, as visually evident in Figure 12.2. Such pressure dependent denaturation is consistent with previous high-pressure studies of both proteins[5, 12] and

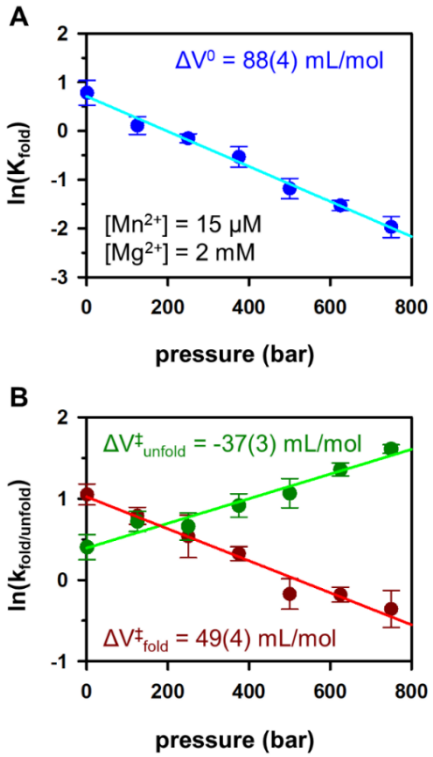

Figure 12.4 Pressure-dependent manganese riboswitch folding (A) equilibrium constant and (B) kinetics rate constant plots, where error bars represent standard deviation of the mean. In analogy to Eyring analysis of transition state barrier energies, the data are least squares fit to a single exponential function to obtain quantitative volumetric change information for ΔV^0 and $\Delta V^{\ddagger}_{fold/unfold}$. $[Mn^{2+}]$ = 15 μM; $[Mg^{2+}]$ = 2mM.

nucleic acids.[10-11] Interestingly, however, the dwell time distributions in Figure 12.3 make evident that increasing pressure kinetically results in an equilibrium preference for the unfolded Mn^{2+} riboswitch both by increase in the unfolding rate constant (k_{unfold}) and yet also a simultaneous decrease in the folding rate constant (k_{fold}).

The pressure effects on the manganese riboswitch folding equilibria can be summarized in the semi-logarithm "van't Hoff" plots of K_{fold} vs pressure (Figure 12.4A), which specifically reveal a linear decrease in $\ln(K_{fold})$ as a function of elevated pressure. We can further quantify such a pressure dependence by the simple thermodynamic relation[3, 5]

$$\left(\frac{\partial lnK_{fold}}{\partial P}\right)_T = \frac{-\Delta V^0}{RT}, \qquad \text{Eq. 12.1}$$

which allows us to relate the slope in Figure 12.4A to the change in free volume upon folding. Least squares fits to the data yield ΔV^0 = +88(4) mL/mol, with a positive sign clearly corresponding to the manganese riboswitch occupying the greater volume upon folding. The present high pressure single molecule kinetic capabilities permit a further interesting level of detail by similar volumetric analysis applied to pressure-dependence of the folding/unfolding rate constants (Figure 12.4B). Specifically, the activation free volume $\Delta V^{\ddagger}_{fold/unfold}$ for accessing the transition state barrier from the folded/unfolded conformations can be obtained from linear fits to an"Arrhenius-like" volumetric expression[5]

$$\left(\frac{\partial lnk_{fold/unfold}}{\partial P}\right)_T = \frac{-\Delta V^{\ddagger}_{fold/unfold}}{RT}. \qquad \text{Eq. 12.2}$$

where once again a positive volume change ($\Delta V^{\ddagger}_{fold}$ = 49(4) mL/mol) and reveal that the transition state (TS) takes up more volume than the fully unfolded state (U). Conversely, the corresponding volume change in the unfolding direction is negative ($\Delta V^{\ddagger}_{unfold}$ = -37(3) mL/mol),

which obviously rationalizes the observed speed up in the unfolding rate constant k_{unfold} with pressure. These results can be simply summarized as predicting a monotonic increase in the manganese riboswitch free volume along the folding coordinate, with $\Delta V_U < \Delta V_{TS} < \Delta V_F$, with uncertainties in these volume changes at the $\sigma \leq 4$ to 8 $Å^3$ level.

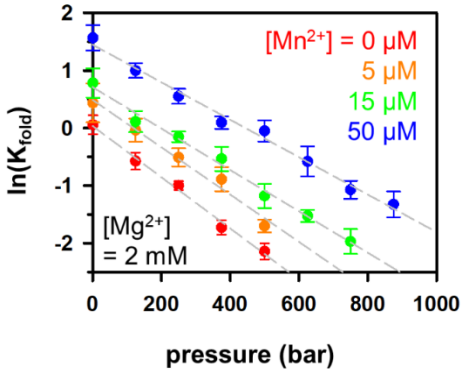

Figure 12.5 Pressure-dependent equilibrium constants (K_{fold}) for the riboswitch folding as a function of increasing [Mn^{2+}] in the presence of physiological [Mg^{2+}] = 2 mM.

12.4.2 Mn^{2+} effects on pressure dependent riboswitch folding

The manganese riboswitch responds conformationally to its cognate ligand Mn^{2+} in the regulation of gene expression, which naturally invites study of pressure dependent folding as a function of ligand concentration.[32] As evident in Figure 12.5, increasing the cognate ligand Mn^{2+} concentration promotes riboswitch folding (i.e., an increase in K_{eq}) at each pressure explored from ambient to 1000 bar. Moreover, the slopes of the van't Hoff plots are all negative ($\Delta V^0 > 0$), correctly predicting pressure induced denaturation for the manganese riboswitch at all Mn^{2+} concentration within a physiologically relevant range. At a higher level of quantification, the van't Hoff slopes in Figure 12.5 are summarized in Table 12.1, for which the ΔV^0 values exhibit a *systematic decrease* as a function of increasing Mn^{2+}. Most importantly, this implies that all positive free volume changes for manganese riboswitch folding/unfolding *are significantly*

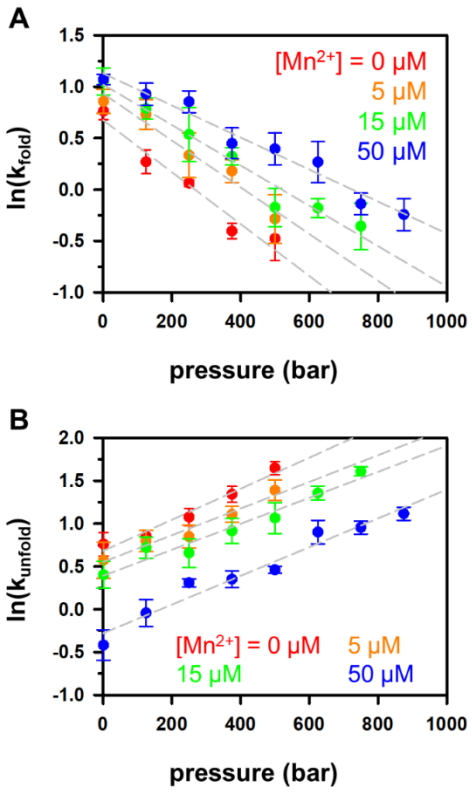

Figure 12.6 Pressure-dependent rate constants (A) k_{fold} and (B) k_{unfold} as a function of increasing $[Mn^{2+}]$ in the presence of physiological $[Mg^{2+}] = 2$ mM.

reduced by association with the cognate ligand/Mn^{2+}, a point to which we will return in Sec 12.5. Finally, we can apply a similar pressure- and Mn^{+2}-dependent analysis to the *rate constants* for manganese riboswitch folding/unfolding. As nicely summarized in Figure 12.6A/B, an increase in Mn^{2+} concentration systematically lowers the negative slopes in an Arrhenius-like pressure plot for k_{fold}, indicating a differential decrease in transition state free volume ($\Delta\Delta V^{\ddagger}_{fold} < 0$) as a function of added Mn^{2+}. On the other hand, the corresponding Arrhenius slopes in Figure 12.6B for the unfolding rate constants reveal no systematic response to Mn^{2+} concentration, indicating an approximately constant $\Delta\Delta V^{\ddagger}_{unfold}$ independent of Mn^{2+} over 0 to 50 µM. To further quantify the Mn^{2+} effects on pressure-dependent response of the riboswitch, the folding/unfolding

activation volumes ($\Delta V^{\ddagger}_{fold/unfold}$) calculated by Eq. 12.2 are summarized in Table 12.1, to which we will return as an important point of discussion in Sec. 12.5.

$[Mn^{2+}]$ \ ΔV	ΔV^0 (mL/mol)	$\Delta V^{\ddagger}_{fold}$ (mL/mol)	$\Delta V^{\ddagger}_{unfold}$ (mL/mol)
0 μM	110 (4)	61(7)	-44(4)
5 μM	100(7)	56(7)	-39(4)
15 μM	88(4)	49(4)	-37(3)
50 μM	79(3)	38(2)	-41(3)

Table 12.1 ΔV^0 and $\Delta V^{\ddagger}_{fold/unfold}$ values as a function of increasing Mn^{2+}. The reported uncertainties represent standard deviation of the mean for triplicate studies.

12.4.3 Mg^{2+} effects on the pressure dependent riboswitch folding

The manganese riboswitch has two cationic binding sites, one of which can bind with Mg+2 at physiological levels (2 mM) and another that exclusively responds to Mn^{2+} but with a much reduced affinity to Mg^{2+}. However, it has also been shown in previous single molecule studies that Mg^{2+} can promote manganese riboswitch folding with or without the cognate ligand.[30] As a parallel thrust, therefore, we have also explored Mg^{2+} and pressure-dependent manganese riboswitch folding, in order to compare the effects of cognate ligand (Mn^{2+}) vs. divalent cation (Mg^{2+}) under near physiological concentrations. As illustrated in the pressure van't Hoff plot in Figure 12.7, the presence of Mg^{2+} at constant Mn^{2+} also enhances the equilibrium stability for riboswitch folding, though requiring 1000-fold higher (i.e., mM vs μM) concentrations. Interestingly, however, the slope of this van't Hoff plot remains constant over an additional 4000 μM increase in Mg^{2+} concentration, consistent with changes in free volume being insensitive to divalent Mg^{2+} ($\Delta\Delta V^0 \approx 0$). This contrasts with the unambiguously strong

effects of Mn^{2+} on pressure-dependent denaturation, confirming that riboswitch folding contributions to $\Delta V^0 > 0$ are clearly both site- and cation-dependent.

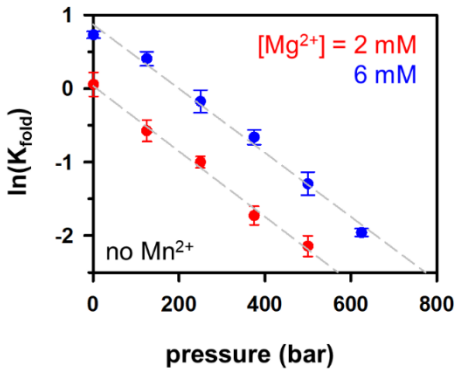

Figure 12.7 Pressure-dependent equilibrium constant (K_{fold}) data for Mn^{2+} independent-folding of the riboswitch at [Mg^{2+}] = 2mM (red) and 6 mM (blue).

Similarly, we can also deconstruct these effects by pressure-dependent investigation of the folding/unfolding kinetics. As illustrated in Figure 12.8, Mg^{2+} induced folding of the riboswitch is clearly promoted at all pressures. It is interesting to note, however, that such an effect occurs specifically by Mg^{2+} dependent increase in k_{fold}, with k_{unfold} remaining mostly unchanged, a trend entirely consistent with Mg^{2+} effects found previously at ambient pressures.[30, 34] Similar to the trends reported above for equilibrium stabilities (K_{fold}), a 4000 mM increase in Mg^{2+} has no effect on slopes in Figure 12.8, indicating no significant Mg^{2+} effects on the transition state activation volumes from either the folding or unfolding direction ($\Delta V^{\ddagger}_{fold}$ and $\Delta V^{\ddagger}_{unfold}$). Simply summarized, manganese riboswitch folding responds to much lower concentrations of the cognate ligand Mn^{2+}, with free volume changes (ΔV^0 and $\Delta V^{\ddagger}_{fold}$) decreasing significantly with Mn^{2+} but insensitive to Mg^{2+}. As a result, one concludes that Mn^{2+} effects on ΔV^0 and $\Delta V^{\ddagger}_{fold}$ result primarily from highly specific associations of the riboswitch

with the cognate ligand, as opposed to important but more generic divalent cation effects with Mg^{2+}.

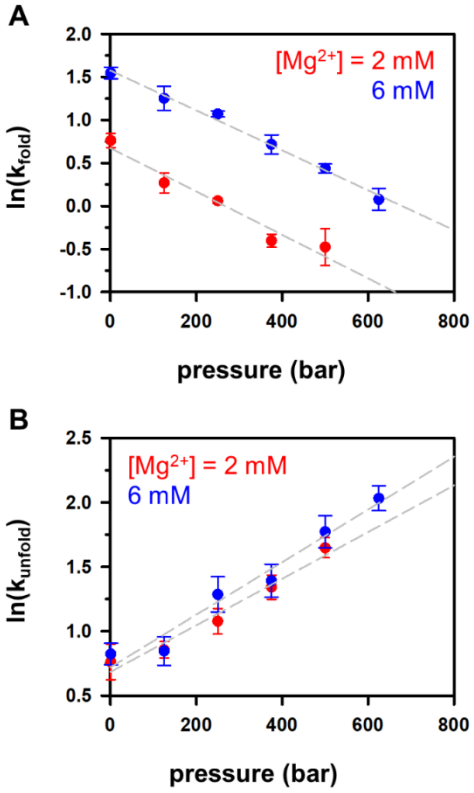

Figure 12.8 Pressure-dependent analysis of the kinetic rate constants for Mn^{2+} independent-folding of the riboswitch: (A) k_{fold} and (B) k_{unfold} at [Mg^{2+}] = 2 mM (red) and 6 mM (blue).

12.5 Discussion

12.5.1 Mn^{2+} association reduces the effective volume of the riboswitch system

The impact of Mn^{2+} on reducing both ΔV^0 and $\Delta V^{\ddagger}_{fold}$ has been demonstrated in Sec. 12.4B and shown to be a result of specific cognate ligand effects in Sec. 12.4C. Moreover, the Mn^{2+} effect on the free volume changes are most efficient at low concentration and gradually saturate with increasing concentration (see Table 12.1). These features are reminiscent of non-

cooperative binding of Mn^{2+} to the riboswitch, as characterized extensively in previous works.[30, 34] Specifically, the riboswitch folding equilibrium constant as a function of Mn^{2+} is well described by a Hill equation with apparent dissociation constant K_D = 16(5) μM, and near unity Hill coefficient of n = 1.0(3). This observation motivates an intriguing analysis by which we use these Hill parameters to convert Mn^{2+} concentration to the fractional occupation (f = 0.0-1.0) of the riboswitch by Mn^{2+}, which in turn allows us to generate free volume changes as a function of occupation and as illustrated in Figure 12.9. Interestingly, while ΔV^0 and $\Delta V^{\ddagger}_{fold}$ exhibit a pronounced linear decrease as a function of Mn^{2+} binding, $\Delta V^{\ddagger}_{unfold}$ remains approximately constant throughout the range of Mn^{2+} concentrations explored. Clearly, any Mn^{2+} dependence in the overall free volume change (ΔV^0) must be attributed to differential changes in volume between the unfolded and transition state conformations ($\Delta V^{\ddagger}_{fold}$), with Mn^{2+} association occurring predominantly prior to the transition state barrier.

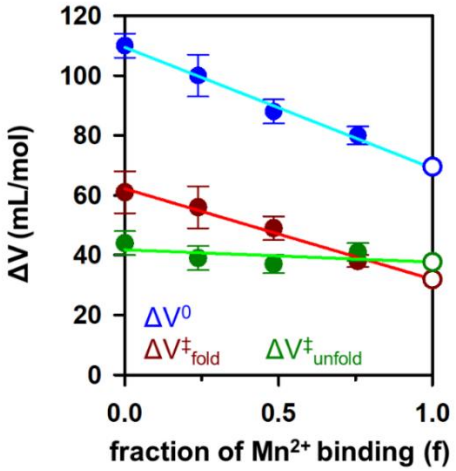

Figure 12.9 Free volume changes (ΔV^0 and $\Delta V^{\ddagger}_{fold/unfold}$) along the riboswitch folding coordinate, but plotted as a function of fractional binding of Mn^{2+} (f = 0.0 to 1.0). The fraction of Mn^{2+}-bound riboswitch is calculated from the Mn^{2+} concentrations, based on dissociation constant (K_D = 16(5) μM) and Hill coefficient (n = 1.0(3)) obtained from previous analysis for Mn^{2+}-promoted folding of the manganese riboswitch. The open circles represent the predicted volume changes from linear extrapolation to f =1.0.

Furthermore, the linear dependence of ΔV^0 on ligand binding fraction f allows us to estimate ΔV^0 = 69(2) mL/mole for folding of the fully Mn^{2+}-bound riboswitch, by simple extrapolation to f = 1.0. Since the free volume change ΔV^0 for manganese riboswitch folding in the absence of Mn^{2+} is known to be 110(4) mL/mol, we thus infer a *large negative change* in free volume for Mn^{2+} binding to the riboswitch ($\Delta V^0_{bind} \approx$ -41(4) mL/mol), i.e., approximately 40% and competitive with the overall ΔV^0 for riboswitch folding. Thus, one must conclude that Mn^{2+} association has a considerable effect on the hydration structure of the binding site.[38-40] Additionally, even though the manganese riboswitch is destabilized with increasing pressure ($\Delta V^0 > 0$), association of the cognate ligand/Mn^{2+} is favored by pressure increase ($\Delta V^0_{bind} < 0$), which in turn can compete directly with pressure-dependent denaturation effects on overall RNA folding. One possibility is that such a Mn^{2+} dependent *reduction in free volume* is due to ligand filling in "voids" formed by the folded riboswitch,[13] or ion recruitment of a more compact water structure in replacement of the loosely packed water molecules inside the confined binding pocket.[41] Although more data will be needed to deconstruct pressure dependent ligand binding from biomolecular folding behaviors, the favorable pressure response to ligand association may prove to be a universal feature of riboswitches, as well as other ligand-responsive biomolecules. This Mn^{2+} binding-induced reduction in volume ($\Delta V^0_{bind} < 0$) is significant and may be essential to maintain ligand affinity as well as biochemical function for a riboswitch under pressure.

By way of specific example, the thermophilic bacterium *T. maritima* is found in the vicinity of hydrothermal vents at the bottom of the ocean.[42] To adapt to such a high pressure and temperature environment, the aptamer domain of the *T. maritima* lysine riboswitch has evolved to contain significantly more GC interactions (38 vs 26 total GC pairs) than its *B. subtilis* counterpart[43-44] operating in a more ambient pressure/temperature range.[35] In clear contrast,

however, the sequences in the aptamer binding sites themselves remain highly conserved between these two versions of the lysine riboswitch.[45] It therefore makes sense that binding between the lysine ligand and aptamer region might be enhanced ($\Delta V^0_{bind} < 0$) rather than weakened by pressure destabilization ($\Delta V^0 > 0$), which in turn would help maintain appropriate riboswitch conformation and biochemical function under high pressure conditions.

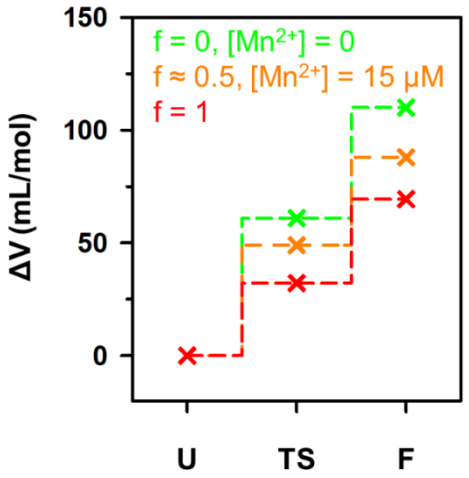

Figure 12.10 Plot of differential free volume changes (ΔV) along the riboswitch folding coordinate for a variety of Mn^{2+} conditions, with "staircase-like" structures clearly indicating a monotonic increase in volume at each folding stage. Especially noteworthy is the color-coded parsing of these volume changes with respect to Mn^{2+} binding fraction, which reveal that > 50% of this increase in riboswitch volume is achieved by the time the transition state is formed. Differential volumes are referenced to the unfolded state U at each f.

12.5.2 Insight from free volume changes along the riboswitch folding coordinate

To summarize the volumetric changes associated with manganese riboswitch folding, we have plotted in Figure 12.10 the differential free volumes (ΔV) for each of the unfolded (U), transition (TS) and folded (F) states. Even more instructively, these ΔΔV values are each displayed for a series of three Mn^{2+} occupation numbers (f = 0, 0.5, 1.0), with values for the fully ligand-bound riboswitch obtained from linear extrapolation (see Figure 12.9) to f = 1 and all free

volumes referenced to zero for the unfolded (U) conformation. From Figure 12.10, free volume changes for the manganese riboswitch *increase monotonically* with respect to the folding coordinate, i.e., $\Delta V_U < \Delta V_{TS} < \Delta V_{F)}$. Specifically, such "staircase" structure confirms a sequential increase in manganese riboswitch free volume as it folds. Furthermore, such structure is clearly responsible for the simultaneous increase (and decrease) in k_{unfold} (and k_{fold}) as a function of applied hydrostatic pressure, respectively, as reported in Sec. 12.4A

Of particular relevance, however, is the fact that the free volume increase upon folding ($\Delta V^0 > 0$) *diminishes* significantly ($\Delta V^0_{bind} < 0$) as a function of additional Mn^{2+}, which necessarily implies that binding of Mn^{2+} to the aptamer domain decreases the overall riboswitch system volume. As mentioned above, such effects suggest that the cognate ligand replaces a less compact water network in the binding site of the manganese riboswitch.[41] More quantitatively, the magnitudes of the Mn^{2+} dependent staircase "steps" in Figure 12.10 indicate that > 50% of this "shrinkage" is already achieved by the transition state barrier, and thus dominated by regions of folding coordinate space where the riboswitch is less structured. By way of confirmation, crystallographic data for the Mn^{2+}-bound riboswitch binding pocket reveal that the majority of phosphate ions octahedrally coordinated with Mn^{2+} (including the Mn^{2+}-selective nitrogen in A41) arise from nucleotides in the P3 bulge (Figure 12.1A),.[33] From this perspective, it is not surprising that Mn^{2+} would bind to P3 prior to subsequent folding of the riboswitch, for which any loop-loop tertiary interactions between P1 and P3 stems are still largely unformed. Indeed, previous single molecule kinetic studies at $Mg^{2+} \approx 0$ explicitly reveal the folding rate constant to vanish at $Mn^{2+} \approx 0$. Stated alternatively, this implies that Mn^{2+} promotes folding of the manganese riboswitch through an induced fit (IF) "bind-then-fold" mechanism,[30] consistent with the binding/folding pathway postulated above and observed in this work.[46]

As a more subtle observation, however, previous single molecule kinetic studies also provided evidence for a *Mg^{2+} promoted* switch from an induced fit (IF) to a conformational selection (CS) "fold-then-bind" riboswitch folding mechanism.[30, 34] Specifically, addition of Mg^{2+} at physiological levels (2 mM) allows Mn^{2+} to bind with a 7-fold higher affinity, which was attributed to "preorganization" of the P3 bulge structure prior to tertiary folding of the P1, P3 domains, i.e., consistent with a conformational selection (CS) "fold-then-bind" pathway. Interestingly, for such an alternative CS pathway, binding of the Mn^{2+} ligand might be expected to occur in later stages of folding,[31] which would seem to contradict the results in the paragraph above. By way of resolution, however, we note that IF and CS folding pathways are no longer mutually exclusive in the presence of Mg^{2+}.[47-48] Indeed, these kinetic studies could not rule out *parallel contributions* from an IF "bind-then-fold" folding pathway,[30] but simply revealed that kinetics of riboswitch folding in the presence of Mg^{2+} to be insensitive to prebinding of Mn^{2+}. Specifically, the previous kinetic investigation of k_{unfold} in the presence of Mg^{2+} revealed riboswitch unfolding to occur from both Mn^{2+}-bound (f = 1) and Mn^{2+}-free (f = 0) folded conformations, with the latter now completely consistent with a parallel CS mechanism.[30, 49] By way of confirmation, one would expect the Mn^{2+} binding step required for an IF folding mechanism to primarily impact the free energy landscape region between the unfolded and the transition states, as indeed evident in Figure 12.10. Simply summarized, pressure-dependent characterization of free volume changes complements and extends the previous work by identifying the presence of an additional IF bind-then-fold pathway for riboswitch folding in the presence of Mg^{2+}. In conjunction with demonstration in these studies of remarkable sensitivity to cation association and change in hydration,[29, 36, 50-51] such high pressure characterization studies at the single molecule level (and particularly pressure-dependent single molecule kinetics) looks

well poised to improve our understanding of complex folding mechanisms by providing new and complementary information via “reversible work” PΔV free energy surfaces.

12.6 Summary and conclusions

In this work, we have demonstrated the ability to couple single molecule FRET kinetic measurements with tunable high-pressure capillary cell conditions to obtain detailed characterization of free volumes for folding of the manganese riboswitch. Based on direct measurement of the pressure-dependent folding/unfolding rate constants, the pressure-induced denaturation of the riboswitch has been unambiguously shown to arise from a simultaneous decrease (increase) in k_{fold} (k_{unfold}), respectively, as a function of increasing pressure and further signalling a sequential, monotonic increase in free volume for the manganese riboswitch along folding coordinate ($V_U < V_{TS} < V_F$). Moreover, a series of pressure-dependent studies indicate that increase in the cognate ligand Mn^{2+} lowers this free volume change upon folding (i.e. “shrinks” the riboswitch, $\Delta V_{bind} < 0$), particularly between unfolded and transition state conformations. Such a negative change in free volume ($\Delta V_{bind} < 0$) necessarily implies pressure-promoted binding of the cognate ligand, which would compete with pressure-induced destabilization of riboswitch folding ($\Delta V^0 > 0$) and in turn may help mitigate pressure induced denaturation effects in the biology of deep sea microorganisms. The study provides a novel reversible work “volumetric” characterization of the free energy folding landscape along riboswitch folding coordinate, which highlights the significance of pre-transition state effects due to Mn^{2+}. Finally, these new volumetric data provide information complementary to our previous kinetic analysis studies under ambient pressure conditions, indicating the parallel presence of

both induced fit ("bind-then-fold") and conformational selection ("fold-then-bind") components for folding of the manganese riboswitch.

12.7 References

1. Heremans, K.; Smeller, L., Protein Structure and Dynamics at High Pressure. *Biochim. Biophys. Acta, Protein Struct. Mol. Enzymol.* **1998,** *1386* (2), 353-370.

2. Mitra, L.; Rouget, J.-B.; Garcia-Moreno, B.; Royer, C. A.; Winter, R., Towards a Quantitative Understanding of Protein Hydration and Volumetric Properties. *ChemPhysChem* **2008,** *9* (18), 2715-2721.

3. Mozhaev, V. V.; Heremans, K.; Frank, J.; Masson, P.; Balny, C., High Pressure Effects on Protein Structure and Function. *Proteins* **1996,** *24* (1), 81-91.

4. Aristides Yayanos, A., Deep-Sea Piezophilic Bacteria. In *Methods in Microbiology*, Academic Press: 2001; Vol. 30, pp 615-637.

5. Gross, M.; Jaenicke, R., Proteins under Pressure. *Eur. J. Chem.* **1994,** *221* (2), 617-630.

6. Li, L.; Kato, C.; Horikoshi, K., Bacterial Diversity in Deep-Sea Sediments from Different Depths. *Biodivers. Conserv.* **1999,** *8* (5), 659-677.

7. Jannasch, H. W.; Wirsen, C. O., Variability of Pressure Adaptation in Deep sea Bacteria. *Arch. Microbiol.* **1984,** *139* (4), 281-288.

8. Najaf-Zadeh, R.; Wu, J. Q.; Macgregor, R. B., Effect of Cations on the Volume of the Helix-Coil Transition of Poly[d(A-T)]. *Biochim. Biophys. Acta Gene Regul.* **1995,** *1262* (1), 52-58.

9. Lin, M.-C.; Macgregor, R. B., Activation Volume of DNA Duplex Formation. *Biochemistry* **1997,** *36* (21), 6539-6544.

10. Downey, C. D.; Crisman, R. L.; Randolph, T. W.; Pardi, A., Influence of Hydrostatic Pressure and Cosolutes on RNA Tertiary Structure. *J. Am. Chem. Soc.* **2007,** *129* (30), 9290-9291.

11. Patra, S.; Anders, C.; Schummel, P. H.; Winter, R., Antagonistic Effects of Natural Osmolyte Mixtures and Hydrostatic Pressure on the Conformational Dynamics of a DNA Hairpin Probed at the Single-Molecule Level. *Phys. Chem. Chem. Phys.* **2018,** *20* (19), 13159-13170.

12. Ramanujam, V.; Alderson, T. R.; Pritišanac, I.; Ying, J.; Bax, A., Protein Structural Changes Characterized by High-Pressure, Pulsed Field Gradient Diffusion NMR Spectroscopy. *J. Magn. Reson.* **2020,** *312*, 106701.

13. Frye, K. J.; Royer, C. A., Probing the Contribution of Internal Cavities to the Volume Change of Protein Unfolding Under Pressure. *Protein Sci.* **1998,** *7* (10), 2217-2222.

14. Cioni, P., Role of Protein Cavities on Unfolding Volume Change and on Internal Dynamics under Pressure. *Biophys. J.* **2006,** *91* (9), 3390-3396.

15. Roche, J.; Caro, J. A.; Norberto, D. R.; Barthe, P.; Roumestand, C.; Schlessman, J. L.; Garcia, A. E.; García-Moreno E., B.; Royer, C. A., Cavities Determine the Pressure Unfolding of Proteins. *Proc. Natl. Acad. Sci. U.S.A.* **2012,** *109* (18), 6945-6950.

16. Grigera, J. R.; McCarthy, A. N., The Behavior of the Hydrophobic Effect under Pressure and Protein Denaturation. *Biophys. J.* **2010,** *98* (8), 1626-1631.

17. Royer, C.; Winter, R., Protein Hydration and Volumetric Properties. *Curr. Opin. Colloid Interface Sci.* **2011,** *16* (6), 568-571.

18. Nucci, N. V.; Fuglestad, B.; Athanasoula, E. A.; Wand, A. J., Role of Cavities and Hydration in the Pressure Unfolding of T_4 Lysozyme. *Proc. Natl. Acad. Sci. U.S.A.* **2014,** *111* (38), 13846-13851.

19. Hillson, N.; Onuchic, J. N.; García, A. E., Pressure-Induced Protein-Folding/Unfolding Kinetics. *Proc. Natl. Acad. Sci. U.S.A.* **1999,** *96* (26), 14848-14853.

20. Woenckhaus, J.; Köhling, R.; Winter, R.; Thiyagarajan, P.; Finet, S., High Pressure-Jump Apparatus for Kinetic Studies of Protein Folding Reactions Using the Small-Angle Synchrotron X-Ray Scattering Technique. *Rev. Sci. Instrum.* **2000,** *71* (10), 3895-3899.

21. Nguyen, L. M.; Roche, J., High-Pressure NMR Techniques for the Study of Protein Dynamics, Folding and Aggregation. *J. Magn. Reson.* **2017,** *277*, 179-185.

22. Mustoe, A. M.; Brooks, C. L.; Al-Hashimi, H. M., Hierarchy of RNA Functional Dynamics. *Annu. Rev. Biochem.* **2014,** *83* (1), 441-466.

23. Al-Hashimi, H. M.; Walter, N. G., RNA Dynamics: it is About Time. *Curr. Opin. Struct. Biol.* **2008,** *18* (3), 321-329.

24. Lai, D.; Proctor, J. R.; Meyer, I. M., On the Importance of Cotranscriptional RNA Structure Formation. *RNA* **2013,** *19* (11), 1461-1473.

25. Schärfen, L.; Neugebauer, K. M., Transcription Regulation Through Nascent RNA Folding. *J. Mol. Biol.* **2021,** *433* (14), 166975.

26. Schneider, S.; Paulsen, H.; Reiter, K. C.; Hinze, E.; Schiene-Fischer, C.; Hübner, C. G., Single Molecule FRET Investigation of Pressure-Driven Unfolding of Cold Shock Protein A. *J. Chem. Phys.* **2018,** *148* (12), 123336.

27. Sung, H.-L.; Nesbitt, D. J., DNA Hairpin Hybridization under Extreme Pressures: A Single-Molecule FRET Study. *J. Phys. Chem. B* **2020,** *124* (1), 110-120.

28. Hodak, J. H.; Fiore, J. L.; Nesbitt, D. J.; Downey, C. D.; Pardi, A., Docking Kinetics and Equilibrium of a GAAA Tetraloop-Receptor Motif Probed by Single-Molecule FRET. *Proc. Natl. Acad. Sci. U.S.A.* **2005,** *102* (30), 10505-10510.

29. Sung, H.-L.; Nesbitt, D. J., Single-Molecule Kinetic Studies of DNA Hybridization under Extreme Pressures. *Phys. Chem. Chem. Phys.* **2020,** *22* (41), 23491-23501.

30. Sung, H.-L.; Nesbitt, D. J., Single-Molecule FRET Kinetics of the Mn^{2+} Riboswitch: Evidence for Allosteric Mg^{2+} Control of "Induced-Fit" vs "Conformational Selection" Folding Pathways. *J. Phys. Chem. B* **2019,** *123* (9), 2005-2015.

31. Suddala, K. C.; Price, I. R.; Dandpat, S. S.; Janeček, M.; Kührová, P.; Šponer, J.; Banáš, P.; Ke, A.; Walter, N. G., Local-to-Global Signal Transduction at the Core of a Mn^{2+} Sensing Riboswitch. *Nat. Commun.* **2019,** *10* (1), 4304.

32. Dambach, M.; Sandoval, M.; Updegrove, Taylor B.; Anantharaman, V.; Aravind, L.; Waters, Lauren S.; Storz, G., The Ubiquitous *yybP-ykoY* Riboswitch is a Manganese-Responsive Regulatory Element. *Mol. Cell* **2015,** *57* (6), 1099-1109.

33. Price, Ian R.; Gaballa, A.; Ding, F.; Helmann, John D.; Ke, A., Mn^{2+}-Sensing Mechanisms of *yybP-ykoY* Orphan Riboswitches. *Mol. Cell* **2015,** *57* (6), 1110-1123.

34. Sung, H.-L.; Nesbitt, D. J., Novel Heat-Promoted Folding Dynamics of the *yybP-ykoY* Manganese Riboswitch: Kinetic and Thermodynamic Studies at the Single-Molecule Level. *J. Phys. Chem. B* **2019,** *123* (26), 5412-5422.

35. Aitken, C. E.; Marshall, R. A.; Puglisi, J. D., An Oxygen Scavenging System for Improvement of Dye Stability in Single-Molecule Fluorescence Experiments. *Biophys. J.* **2008,** *94* (5), 1826-1835.

36. Sung, H.-L.; Nesbitt, D. J., High Pressure Single-Molecule FRET Studies of the Lysine Riboswitch: Cationic and Osmolytic Effects on Pressure Induced Denaturation. *Phys. Chem. Chem. Phys.* **2020,** *22* (28), 15853-15866.

37. Sung, H.-L.; Nesbitt, D. J., Sequential Folding of the Nickel/Cobalt Riboswitch Is Facilitated by a Conformational Intermediate: Insights from Single-Molecule Kinetics and Thermodynamics. *J. Phys. Chem. B* **2020,** *124* (34), 7348-7360.

38. Sun, L.-Z.; Chen, S.-J., Predicting RNA-Metal Ion Binding with Ion Dehydration Effects. *Biophys. J.* **2019,** *116* (2), 184-195.

39. Ma, C. Y.; Pezzotti, S.; Schwaab, G.; Gebala, M.; Herschlag, D.; Havenith, M., Cation Enrichment in the Ion Atmosphere is Promoted by Local Hydration of DNA. *Phys. Chem. Chem. Phys.* **2021,** *23* (40), 23203-23213.

40. Draper, D. E., RNA Folding: Thermodynamic and Molecular Descriptions of the Roles of Ions. *Biophys. J.* **2008,** *95* (12), 5489-5495.

41. Knight, A. W.; Kalugin, N. G.; Coker, E.; Ilgen, A. G., Water Properties under Nano-Scale Confinement. *Sci. Rep.* **2019,** *9* (1), 8246.

42. Serganov, A.; Huang, L.; Patel, D. J., Structural Insights into Amino Acid Binding and Gene Control by a Lysine Riboswitch. *Nature* **2008,** *455* (7217), 1263-1267.

43. Garst, A. D.; Héroux, A.; Rambo, R. P.; Batey, R. T., Crystal Structure of the Lysine Riboswitch Regulatory mRNA Element. *J. Biol. Chem.* **2008,** *283* (33), 22347-22351.

44. Blouin, S.; Lafontaine, D. A., A Loop–Loop Interaction and a K-Turn Motif Located in the Lysine Aptamer Domain are Important for the Riboswitch Gene Regulation Control. *RNA* **2007,** *13* (8), 1256-1267.

45. Serganov, A.; Patel, D. J., Amino Acid Recognition and Gene Regulation by Riboswitches. *Biochim. Biophys. Acta Gene Regul. Mech.* **2009,** *1789* (9), 592-611.

46. Vogt, A. D.; Di Cera, E., Conformational Selection or Induced Fit? A Critical Appraisal of the Kinetic Mechanism. *Biochemistry* **2012,** *51* (30), 5894-5902.

47. Pavlović, R. Z.; Lalisse, R. F.; Hansen, A. L.; Waudby, C. A.; Lei, Z.; Güney, M.; Wang, X.; Hadad, C. M.; Badjić, J. D., From Selection to Instruction and Back: Competing Conformational Selection and Induced Fit Pathways in Abiotic Hosts. *Angew. Chem.* **2021,** *60* (36), 19942-19948.

48. Hammes, G. G.; Chang, Y.-C.; Oas, T. G., Conformational Selection or Induced Fit: A Flux Description of Reaction Mechanism. *Proc. Natl. Acad. Sci. U.S.A.* **2009,** *106* (33), 13737-13741.

49. Suddala, K. C.; Wang, J.; Hou, Q.; Walter, N. G., Mg^{2+} Shifts Ligand-Mediated Folding of a Riboswitch from Induced-Fit to Conformational Selection. *J. Am. Chem. Soc.* **2015,** *137* (44), 14075-14083.

50. Fan, H. Y.; Shek, Y. L.; Amiri, A.; Dubins, D. N.; Heerklotz, H.; Macgregor, R. B.; Chalikian, T. V., Volumetric Characterization of Sodium-Induced G-Quadruplex Formation. *J. Am. Chem. Soc.* **2011,** *133* (12), 4518-4526.

51. Patra, S.; Anders, C.; Erwin, N.; Winter, R., Osmolyte Effects on the Conformational Dynamics of a DNA Hairpin at Ambient and Extreme Environmental Conditions. *Angew. Chem.* **2017,** *56* (18), 5045-5049.

Chapter 13

Postmortem and Future Directions

13.1 Introduction

Despite extensive research and careful experiment design for each project, some may still fail and thus never make it to the literature. This chapter documents those unsuccessful attempts which I think were on the right track but need some modification.

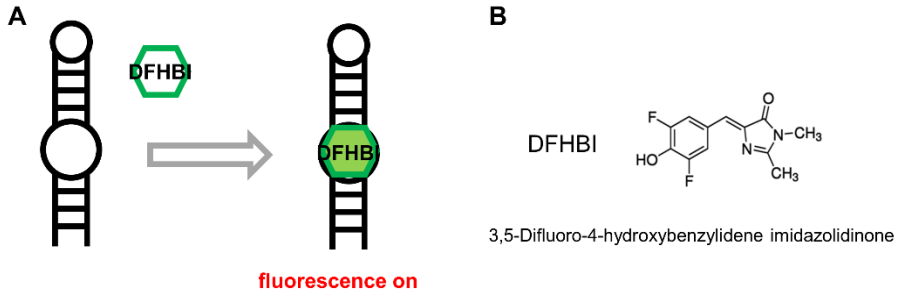

Figure 13.1 DFHBI fluorescence enhancement. (A) Cartoon representation of DFHBI binding to the Spinach2 RNA. (B) Chemical structure of DFHBI.

13.2 Label-free single molecule biosensor for TNT detection

Spinach2 is a synthetic RNA aptamer that selectively binds to DFHBI (3,5-difluoro-4-hydroxybenzylidene imidazolidinone), an analog of the GFP (green fluorescent protein) fluorophore (Figure 13.1A).[1] The benzene ring in the DFHBI can freely rotate around the single bond. If the rotation is restricted (e.g., by aptamer binding), and the molecule is fixed in planar conformation, the DFHBI fluorescence can be greatly enhanced (Figure 13.1B).[2] As a result, the Spinach2-bound DFHBI is nearly 3 orders of magnitudes brighter than the free DFHBI.

In a collaboration with Dr. Chavez-Benavides from the Air Force Research Laboratory, we received a TNT aptamer sequence obtained by SELEX (systematic evolution of ligands by

exponential enrichment),[3] an *in vitro* selection method. The structure of the TNT aptamer is a short 48-nt stem-loop with a major internal loop and several other mismatched bases (Figure 2). The simplicity of the aptamer structure in fact makes it difficult to generate a FRET construct to monitor the TNT binding. We thus came up with an alternative method to generate a fluorescence probe of TNT by coupling the TNT aptamer with the Spinach2 sequence (Figure 2). The TNT binding is expected to induce conformational change in the aptamer, and thereby stabilize the Spinach2 structure to increase DFHBI binding and thus the fluorescence.[4] The advantage is that such a Spinach2-based fluorescence probe requires no chemical modification of the nucleotide bases and that the Spinach2 sequence can be directly integrated with the TNT aptamer simply through *in vitro* transcription. Furthermore, with the common tethering strategy described in Chapter 2, the construct can be annealed with a biotinylated flagpole strand to achieved surface immobilization for single molecule fluorescence study.

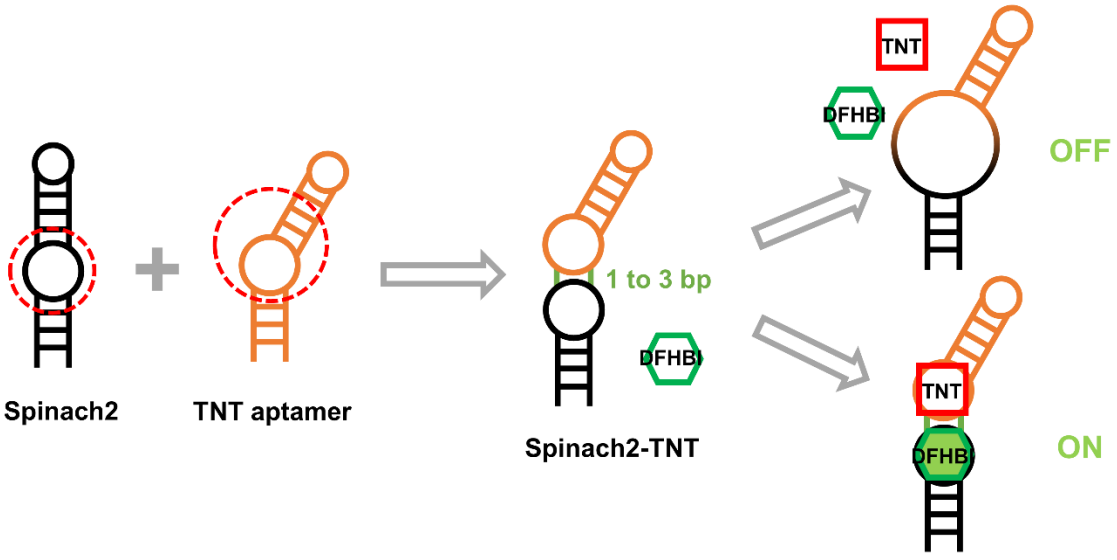

Figure 13.2 Schematic of Spinach2-TNT aptamer construct design and the resulting fluorescence enhancement by TNT/DFHBI binding.

We have synthesized the Spinach2 and Spinach2-TNT aptamers with 1 to 3 base pairs as spacer between the two RNA structures (Figure 2). Indeed, DFHBI titration reveals that

Spinach2 binds to DFHBI at the micromolar affinity level with enhanced fluorescence (Figure 13.3A). Unfortunately, however, the Spinach2-TNT aptamers never showed any significant enhanced fluorescent activity of DFHBI over a wide range of relevant DFHBI/TNT concentrations (Figure 13.3B). Our current thoughts are that, although the calculations conducted by the Chavez-Benavides group suggests TNT mainly interacts with the large internal loop in the aptamer, the rest of the aptamer stem may also participate in TNT binding. As the result, any replacement of the Spinach2 sequence may interrupt the TNT aptamer structure and reduce the TNT affinity, which is already relatively modest on the scale of riboswitches (low micromolar levels).

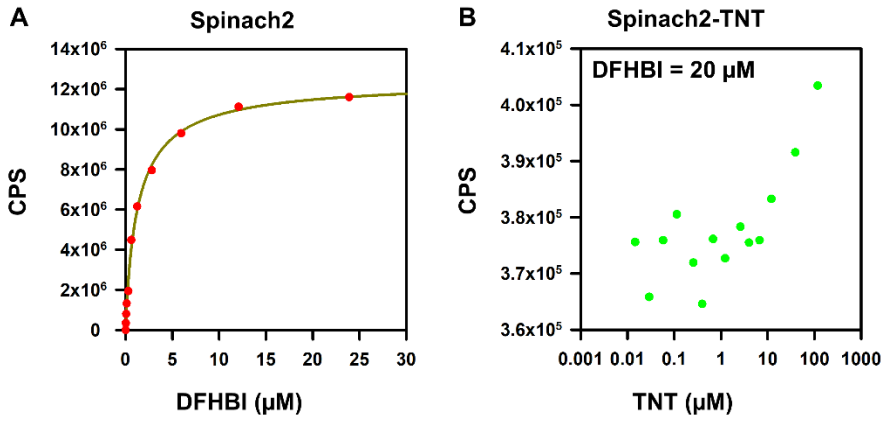

Figure 13.3 Spinach2-DFHBI fluorescence measurements. (A) DFHBI titration of Sinach2 RNA. Data are fit to the Hill equation and K_D of DFHBI is determined to be 1.3(2) μM. (B) TNT titration of Spinach2-TNT construct with saturated [DFHBI] = 20 μM. Note that despite the fluorescence increases at [TNT] > 10 μM, the count rate is way below the Spinach2 enhancement (10^5 vs 10^7 count per second) and the estimated K_D of TNT for the TNT aptamer is at low micromolar levels.

The Spinach2-TNT probe may fail partly due to lack of structural information of the TNT aptamer. However, the similar probe design can still be applied to other RNA riboswitches and aptamers with more detailed structural characterization (e.g., crystal data and SHAPE, selective 2'-hydroxyl acylation analyzed by primer extension). The aptamer-based sensor has great

potential in small molecule detection. Moreover, the rich kinetic information we could obtain from single molecule fluorescence studies may both motivate and facilitate future sensor design.

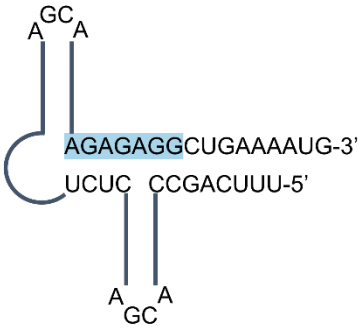

Figure 13.4 Secondary folding of the guanidine-II riboswitch in the translation-off state. The sequence color-coded in blue represents the Shine–Dalgarno (SD) sequence, a ribosome binding site.

13.3 Mimicking co-transcriptional folding by the truncated guanidine-II riboswitch

The 2^{o} structure prediction of the guanidine-II (type II guanidine riboswitch) riboswitch in its off state is illustrated in Figure 13.4,[5] where the Shine–Dalgarno (SD) sequence (in blue) forms double helix to prevent translation initiation by interrupting binding to the ribosome. In the presence of guanidine (or guanidinium to properly address cationic effects), the two terminal

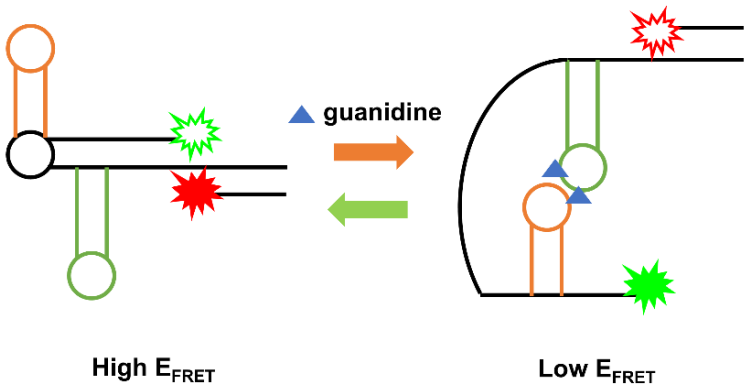

Figure 13.5 Illustration of the single molecule FRET construct design of the guanidine-II riboswitch.

loops may form a complex with 2 guanidine molecules binding in a head to head fashion and in turn trigger the double helix dissociation to activate translation (Figure 13.5).

We first generated a single molecule FRET construct to monitor the association and dissociation of the SD double helix (Figure 13.5). In the translation-off state, the terminal Cy3 and Cy5 are close in distance, resulting in a high E_{FRET} state. When the double helix is dissociated by the guanidine-induced kissing loop formation, the Cy3 and Cy5 are brought further apart. According to crystal data for the truncated kissing loop,[5] the estimated > 50 Å separation should lead to a low E_{FRET} value (< 0.5). Unfortunately, despite the single molecule diffusing data showing two distinct E_{FRET} populations, the ratio between them proved to be insensitive to guanidine concentrations (Figure 13.6).

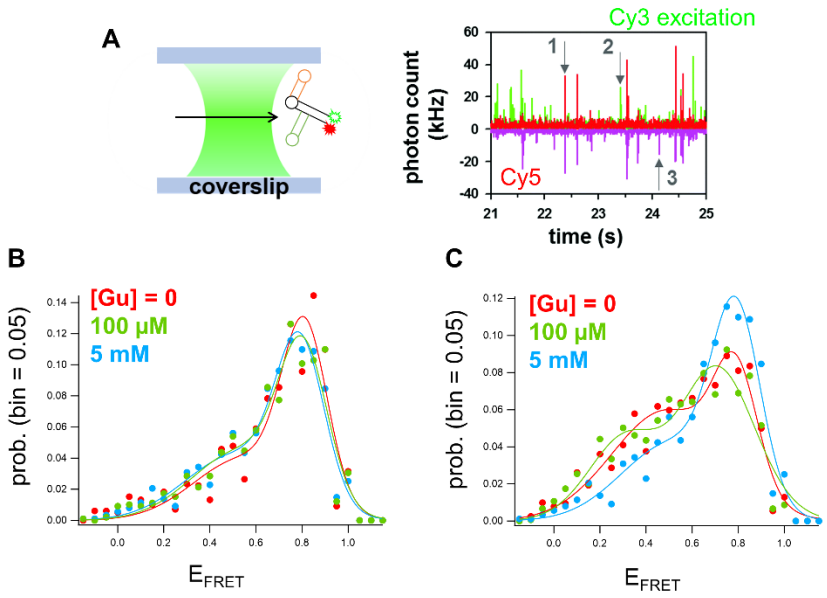

Figure 13.6 Single molecule FRET experiments of the guanidine-II riboswitch constructs. (A) illustration of the freely-diffusing experiment and data analysis. (B) E_{FRET} distribution of the full guanidine-II riboswitch at increasing guanidine concentrations. (C) E_{FRET} distribution of the truncated guanidine-II riboswitch (-2 base pairs in the SD double helix extension) at increasing guanidine concentrations.

Since the predominantly high E_{FRET} state suggests the double helix is too stable to dissociate (Figure 13.6B), we suspect the guanidine promoted kissing loop may form before the SD strand is fully extended, e.g., folding and ligand sensing during transcription. With the simple flagpole labeling strategy, we are able to synthesize a series of guanidine riboswitches with an "adjustable" 3' end to gradually reduce double helix interaction (-2 and -4 base pairs in the SD double helix extension). In the sample data (Figure 13.6C), the truncated riboswitch seems to misfold at low guanidine concentration with more prominent low E_{FRET} population yet less distinctive peak structures. As guanidine concentration increases, the E_{FRET} population becomes nearly identical to the full riboswitch (13.6B and C). We suspect that the millimolar level of guanidine may act more like a monovalent cation in stabilizing the shortened double helix. Although it is unclear why guanidine does not promote double strand dissociation, further studies on this series of truncated RNA constructs may provide a simple single molecule method to probe more deeply into the role of RNA folding during transcription.[6]

13.4 Single molecule kinetics of surface immobilized brome mosaic virus RNA

The brome mosaic virus (BMV) single molecule FRET construct was designed by a previous postdoctoral researcher Dr. Mario Vieweger.[7] He extensively characterized the salt dependent conformations of the BMV RNA construct and incorporated the single molecule FRET results with SHAPE studies to obtain even more detailed structural information.[8] In his studies, the freely diffusing single molecule FRET measurements revealed interesting 3-state folding behavior for the RNA virus.[7] However, these observations were limited to conditions where only equilibrium populations could be detected. To extend these efforts into the domain of

single molecule kinetics, therefore, I tried to re-synthesize the BMV single molecule construct with biotin labeling to achieve surface tethering capabilities.

During the construct synthesis, the 3' end labeling of Cy3 is particularly challenging. I wasn't able to achieve a reasonable labeling rate with the method of 3' oxidation, followed by the hydrazide-aldehyde reaction, as suggested in Mario's work.[7] After many unsuccessful attempts, I decided to use an alternative method to label the construct. Specifically, the BMV RNA is end-labeled with Cy3 through the enzymatic ligation with T4 RNA ligase and Cy3 modified cytidine-3',5'-bis-p (pCp-Cy3, Figure 13.7A). Such a method results in > 85% labeled RNA, as verified by HPLC analysis. Unfortunately, the resulting FRET values of the BMV RNA proved to be significantly affected. Specifically, the labeling scheme is equivalent to extension by one additional cytidine nucleotide, for which we lost sufficient contrast to resolve the three different FRET values and conformations (Figure 13.7B and C).

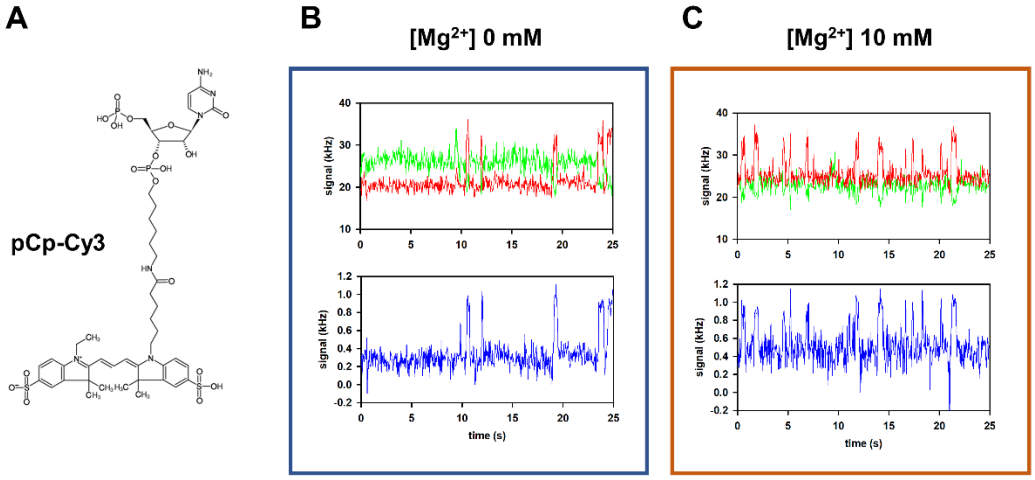

Figure 13.7 Sample fluorescence traces of the BMV virus RNA construct and the resulting E_{FRET} trajectories. (A) Chemical structure of pCp-Cy3. (B) Sample fluorescence data at $[Mg^{2+}] = 0$ mM, and (C) $[Mg^{2+}] = 10$ mM. The intermediate E_{FRET} state at high $[Mg^{2+}] = 10$ mM is indistinguishable with the low E_{FRET} state (e.g. the low E_{FRET} state at $[Mg^{2+}] = 0$ mM).

Although the original construct with the new labeling method didn't work out, we can certainly try to improve the FRET contrast by adjusting the length of the 3' extension in the BMV RNA. Moreover, I have found the ligation method consistently provides more reliable labeling with > 85% efficiency. Hence, this would appear to be an interesting and quite feasible direction for further progress.

13.5 Osmolytes and crowding effects under extreme pressures

The Nesbitt group has been long interested in the osmolyte effects on nucleic acid conformations. Previous graduate student Dr. Erik Holmstrom has characterized the kinetics and thermodynamics of nucleic folding at a series of TMAO (Trimethylamine N-oxide) and urea concentrations.[9] Interestingly, the content of TMAO (urea) in deep sea fish is found to increase (decrease) as a function of depth.[10] The anti-correlation between the two osmolytes is speculated to be part of the pressure adaption strategy for deep see marine life, since TMAO or urea is known to increase or decrease biomolecular folding, respectively.[11] This would appear to be an ideal system for studying the effects of these osmolytes on pressure dependent nucleic acid folding with our high pressure kinetic methods.

Finally, it would be a natural extension to study the effects of both crowding and osmolytes under extreme pressures, since it seems plausible that stabilization of nucleic acids by osmolytes may compete efficiently with pressure denaturation.[12] In particular, in order to confirm or refute the entropic nature of such crowding effects at elevated pressures, we need the capability for temperature dependent studies. Toward that end, we are therefore working on incorporation of reliable sample heating methods to augment our high pressure single molecule

measurements. Studies of the two-dimensional folding reaction coordinate with both temperature and pressure as external variables would provide even richer thermodynamic information on the free energy landscape for nucleic acid folding.

13.6 References

1. Paige, J. S.; Wu, K. Y.; Jaffrey, S. R., RNA Mimics of Green Fluorescent Protein. *Science* **2011,** *333* (6042), 642-646.

2. Strack, R. L.; Disney, M. D.; Jaffrey, S. R., A Superfolding Spinach2 Reveals the Dynamic Nature of Trinucleotide Repeat–Containing RNA. *Nat. Methods* **2013,** *10* (12), 1219-1224.

3. Harbaugh, S. V.; Martin, J. A.; Weinstein, J.; Ingram, G.; Kelley-Loughnane, N., Screening and Selection of Artificial Riboswitches. *Methods* **2018,** *143*, 77-89.

4. Xu, J.; Cotruvo, J. A., The *czcD* (NiCo) Riboswitch Responds to Iron(II). *Biochemistry* **2020,** *59* (15), 1508-1516.

5. Reiss, C. W.; Strobel, S. A., Structural Basis for Ligand Binding to the Guanidine-II Riboswitch. *RNA* **2017,** *23* (9), 1338-1343.

6. Meyer, I. M.; Miklós, I., Co-Transcriptional Folding is Encoded within RNA Genes. *BMC Mol. Biol.* **2004,** *5* (1), 10.

7. Vieweger, M.; Holmstrom, Erik D.; Nesbitt, David J., Single-Molecule FRET Reveals Three Conformations for the TLS Domain of Brome Mosaic Virus Genome. *Biophys. J.* **2015,** *109* (12), 2625-2636.

8. Vieweger, M.; Nesbitt, D. J., Synergistic SHAPE/Single-Molecule Deconvolution of RNA Conformation under Physiological Conditions. *Biophys. J.* **2018,** *114* (8), 1762-1775.

9. Holmstrom, E. D.; Dupuis, N. F.; Nesbitt, D. J., Kinetic and Thermodynamic Origins of Osmolyte-Influenced Nucleic Acid Folding. *J. Phys. Chem. B* **2015,** *119* (9), 3687-3696.

10. Yancey, P. H.; Gerringer, M. E.; Drazen, J. C.; Rowden, A. A.; Jamieson, A., Marine Fish May be Biochemically Constrained from Inhabiting the Deepest Ocean Depths. *Proc. Natl. Acad. Sci. U.S.A.* **2014,** *111* (12), 4461-4465.

11. Yancey, P. H.; Speers-Roesch, B.; Atchinson, S.; Reist, J. D.; Majewski, A. R.; Treberg, J. R., Osmolyte Adjustments as a Pressure Adaptation in Deep-Sea Chondrichthyan

Fishes: An Intraspecific Test in Arctic Skates (Amblyraja hyperborea) along a Depth Gradient. *Physiol. Biochem. Zool.* **2018,** *91* (2), 788-796.

12. Dupuis, N. F.; Holmstrom, E. D.; Nesbitt, D. J., Molecular-Crowding Effects on Single-Molecule RNA Folding/Unfolding Thermodynamics and Kinetics. *Proc. Natl. Acad. Sci. U.S.A.* **2014,** *111* (23), 8464-8469.

Bibliography

Chapter 1 Introduction

1. Miller, P. S., A Brief Guide to Nucleic Acid Chemistry. *Bioconjugate Chem.* **1990,** *1* (3), 187-191.

2. Minchin, S.; Lodge, J., Understanding Biochemistry: Structure and Function of Nucleic Acids. *Essays Biochem.* **2019,** *63* (4), 433-456.

3. Belmont, P.; Constant, J.-F.; Demeunynck, M., Nucleic Acid Conformation Diversity: from Structure to Function and Regulation. *Chem. Soc. Rev.* **2001,** *30* (1), 70-81.

4. Watson, J. D.; Crick, F. H. C., Molecular Structure of Nucleic Acids: A Structure for Deoxyribose Nucleic Acid. *Nature* **1953,** *171* (4356), 737-738.

5. and, P. B.; Westhof, E., Hierarchy and Dynamics of RNA Folding. *Annu. Rev. Biophys. Biomol. Struct.* **1997,** *26* (1), 113-137.

6. Schroeder, R.; Barta, A.; Semrad, K., Strategies for RNA Folding and Assembly. *Nat. Rev. Mol. Cell Biol.* **2004,** *5* (11), 908-919.

7. Cech, T. R.; Bass, B. L., Biological Catalysis by RNA. *Annu. Rev. Biochem.* **1986,** *55* (1), 599-629.

8. Kruger, K.; Grabowski, P. J.; Zaug, A. J.; Sands, J.; Gottschling, D. E.; Cech, T. R., Self-Splicing RNA: Autoexcision and Autocyclization of the Ribosomal RNA Intervening Sequence of Tetrahymena. *Cell* **1982,** *31* (1), 147-157.

9. Guerrier-Takada, C.; Gardiner, K.; Marsh, T.; Pace, N.; Altman, S., The RNA Moiety of Ribonuclease P is the Catalytic Subunit of the Enzyme. *Cell* **1983,** *35* (3, Part 2), 849-857.

10. Cech, T. R.; Zaug, A. J.; Grabowski, P. J., *In vitro* Splicing of the Ribosomal RNA Precursor of Tetrahymena: Involvement of a Guanosine Nucleotide in the Excision of the Intervening Sequence. *Cell* **1981,** *27* (3), 487-496.

11. Noller, H. F., Structure of Ribosomal RNA. *Annu. Rev. Biochem.* **1984,** *53* (1), 119-162.

12. Gefter, M. L., DNA Replication. *Annu. Rev. Biochem.* **1975,** *44* (1), 45-78.

13. Tinoco, I.; Bustamante, C., How RNA Folds. *J. Mol. Biol.* **1999,** *293* (2), 271-281.

14. Mott, M. L.; Berger, J. M., DNA Replication Initiation: Mechanisms and Regulation in Bacteria. *Nat. Rev. Microbiol.* **2007,** *5* (5), 343-354.

15. Sengupta, A.; Sung, H.-L.; Nesbitt, D. J., Amino Acid Specific Effects on RNA Tertiary Interactions: Single-Molecule Kinetic and Thermodynamic Studies. *J. Phys. Chem. B* **2016,** *120* (41), 10615-10627.

16. Nicholson, D. A.; Sengupta, A.; Sung, H.-L.; Nesbitt, D. J., Amino Acid Stabilization of Nucleic Acid Secondary Structure: Kinetic Insights from Single-Molecule Studies. *J. Phys. Chem. B* **2018,** *122* (43), 9869-9876.

17. Adams, P. L.; Stahley, M. R.; Gill, M. L.; Kosek, A. B.; Wang, J.; Strobel, S. A., Crystal Structure of a Group I Intron Splicing Intermediate. *RNA* **2004,** *10* (12), 1867-1887.

18. Wu, L.; Chai, D.; Fraser, M. E.; Zimmerly, S., Structural Variation and Uniformity among Tetraloop-Receptor Interactions and Other Loop-Helix Interactions in RNA Crystal Structures. *PLOS ONE* **2012,** *7* (11), e49225.

19. Sherwood, A. V.; Henkin, T. M., Riboswitch-Mediated Gene Regulation: Novel RNA Architectures Dictate Gene Expression Responses. *Annu. Rev. Microbiol.* **2016,** *70* (1), 361-374.

20. Pavlova, N.; Kaloudas, D.; Penchovsky, R., Riboswitch Distribution, Structure, and Function in Bacteria. *Gene* **2019,** *708*, 38-48.

21. Haller, A.; Soulière, M. F.; Micura, R., The Dynamic Nature of RNA as Key to Understanding Riboswitch Mechanisms. *Acc. Chem. Res.* **2011,** *44* (12), 1339-1348.

22. Lai, D.; Proctor, J. R.; Meyer, I. M., On the Importance of Cotranscriptional RNA Structure Formation. *RNA* **2013,** *19* (11), 1461-1473.

23. Meyer, I. M.; Miklós, I., Co-Transcriptional Folding is Encoded within RNA Genes. *BMC Mol. Biol.* **2004,** *5* (1), 10.

24. Schärfen, L.; Neugebauer, K. M., Transcription Regulation Through Nascent RNA Folding. *J. Mol. Biol.* **2021,** *433* (14), 166975.

25. Lutz, B.; Faber, M.; Verma, A.; Klumpp, S.; Schug, A., Differences between Cotranscriptional and Free Riboswitch Folding. *Nucleic Acids Res.* **2013,** *42* (4), 2687-2696.

26. Dambach, M.; Sandoval, M.; Updegrove, Taylor B.; Anantharaman, V.; Aravind, L.; Waters, Lauren S.; Storz, G., The Ubiquitous *yybP-ykoY* Riboswitch Is a Manganese-Responsive Regulatory Element. *Mol. Cell* **2015,** *57* (6), 1099-1109.

27. Price, Ian R.; Gaballa, A.; Ding, F.; Helmann, John D.; Ke, A., Mn^{2+}-Sensing Mechanisms of *yybP-ykoY* Orphan Riboswitches. *Mol. Cell* **2015,** *57* (6), 1110-1123.

28. Sung, H.-L.; Nesbitt, D. J., Novel Heat-Promoted Folding Dynamics of the *yybP-ykoY* Manganese Riboswitch: Kinetic and Thermodynamic Studies at the Single-Molecule Level. *J. Phys. Chem. B* **2019,** *123* (26), 5412-5422.

29. Krüger, H., Techniques for the Kinetic Study of Fast Reactions in Solution. *Chem. Soc. Rev.* **1982,** *11* (3), 227-255.

30. Eccleston, J. F.; Martin, S. R.; Schilstra, M. J., Rapid Kinetic Techniques. In *Methods in Cell Biology*, Academic Press: 2008; Vol. 84, pp 445-477.

31. Greenfeld, M.; Solomatin, S. V.; Herschlag, D., Removal of Covalent Heterogeneity Reveals Simple Folding Behavior for P4-P6 RNA *J. Biol. Chem.* **2011,** *286* (22), 19872-19879.

32. Bokinsky, G.; Zhuang, X., Single-Molecule RNA Folding. *Acc. Chem. Res.* **2005,** *38* (7), 566-573.

33. Kowerko, D.; König, S. L. B.; Skilandat, M.; Kruschel, D.; Hadzic, M. C. A. S.; Cardo, L.; Sigel, R. K. O., Cation-Induced Kinetic Heterogeneity of the Intron-Exon Recognition in Single Group II Introns. *Proc. Natl. Acad. Sci. U.S.A.* **2015,** *112* (11), 3403-3408.

34. Moerner, W. E.; Kador, L., Optical Detection and Spectroscopy of Single Molecules in a Solid. *Phys. Rev. Lett.* **1989,** *62* (21), 2535-2538.

35. Orrit, M.; Bernard, J., Single Pentacene Molecules Detected by Fluorescence Excitation in a p-terphenyl Crystal. *Phys. Rev. Lett.* **1990,** *65* (21), 2716-2719.

36. Ha, T.; Zhuang, X.; Kim, H. D.; Orr, J. W.; Williamson, J. R.; Chu, S., Ligand-Induced Conformational Changes Observed in Single RNA Molecules. *Proc. Natl. Acad. Sci. U.S.A.* **1999,** *96* (16), 9077-9082.

37. Zhuang, X.; Bartley, L. E.; Babcock, H. P.; Russell, R.; Ha, T.; Herschlag, D.; Chu, S., A Single-Molecule Study of RNA Catalysis and Folding. *Science* **2000,** *288* (5473), 2048-2051.

38. Hodak, J. H.; Fiore, J. L.; Nesbitt, D. J.; Downey, C. D.; Pardi, A., Docking kinetics and equilibrium of a GAAA tetraloop-receptor motif probed by single-molecule FRET. *Proc. Natl. Acad. Sci. U.S.A.* **2005,** *102* (30), 10505-10510.

39. Sung, H.-L.; Nesbitt, D. J., Single-Molecule FRET Kinetics of the Mn^{2+} Riboswitch: Evidence for Allosteric Mg^{2+} Control of "Induced-Fit" vs "Conformational Selection" Folding Pathways. *J. Phys. Chem. B* **2019,** *123* (9), 2005-2015.

40. Furukawa, K.; Ramesh, A.; Zhou, Z.; Weinberg, Z.; Vallery, T.; Winkler, Wade C.; Breaker, Ronald R., Bacterial Riboswitches Cooperatively Bind Ni^{2+} or Co^{2+} Ions and Control Expression of Heavy Metal Transporters. *Mol. Cell* **2015,** *57* (6), 1088-1098.

41. Xu, J.; Cotruvo, J. A., Reconsidering the *czcD* (NiCo) Riboswitch as an Iron Riboswitch. *ACS Bio Med Chem Au* **2022,** *2* (4), 376-385.

42. Sung, H.-L.; Nesbitt, D. J., Sequential Folding of the Nickel/Cobalt Riboswitch Is Facilitated by a Conformational Intermediate: Insights from Single-Molecule Kinetics and Thermodynamics. *J. Phys. Chem. B* **2020,** *124* (34), 7348-7360.

43. Westhof, E., Water: An Integral Part of Nucleic Acid Structure. *Annu. Rev. Biophys. Biophys. Chem.* **1988,** *17* (1), 125-144.

44. Lane, A. N.; Jenkins, T. C., Thermodynamics of Nucleic Acids and Their Interactions with Ligands. *Q. Rev. Biophys.* **2000,** *33* (3), 255-306.

45. Fiore, J. L.; Holmstrom, E. D.; Nesbitt, D. J., Entropic origin of Mg^{2+}-facilitated RNA folding. *Proc. Natl. Acad. Sci. U.S.A.* **2012,** *109* (8), 2902-2907.

46. Holmstrom, E. D.; Nesbitt, D. J., Biophysical Insights from Temperature-Dependent Single-Molecule Förster Resonance Energy Transfer. *Annu. Rev. Phys. Chem.* **2016,** *67* (1), 441-465.

47. Dupuis, N. F.; Holmstrom, E. D.; Nesbitt, D. J., Molecular-Crowding Effects on Single-Molecule RNA Folding/Unfolding Thermodynamics and Kinetics. *Proc. Natl. Acad. Sci. U.S.A.* **2014,** *111* (23), 8464-8469.

48. Sung, H.-L.; Sengupta, A.; Nesbitt, D., Smaller Molecules Crowd Better: Crowder Size Dependence Revealed by Single-Molecule FRET Studies and Depletion Force Modeling Analysis. *J. Chem. Phys.* **2021,** *154* (15), 155101.

49. Sung, H.-L.; Nesbitt, D. J., Effects of Molecular Crowders on Single-Molecule Nucleic Acid Folding: Temperature-Dependent Studies Reveal True Crowding vs Enthalpic Interactions. *J. Phys. Chem. B* **2021,** *125* (48), 13147-13157.

50. Sasahara, K.; McPhie, P.; Minton, A. P., Effect of Dextran on Protein Stability and Conformation Attributed to Macromolecular Crowding. *J. Mol. Biol.* **2003,** *326* (4), 1227-1237.

51. Kilburn, D.; Roh, J. H.; Guo, L.; Briber, R. M.; Woodson, S. A., Molecular Crowding Stabilizes Folded RNA Structure by the Excluded Volume Effect. *J. Am. Chem. Soc.* **2010,** *132* (25), 8690-8696.

52. Gnutt, D.; Ebbinghaus, S., The Macromolecular Crowding Effect – from in vitro into the Cell. *Biol. Chem.* **2016,** *397* (1), 37-44.

53. Zhou, H.-X., Rate Theories for Biologists. *Q. Rev. Biophys.* **2010,** *43* (2), 219-293.

54. Szabo, A.; Schulten, K.; Schulten, Z., First Passage time Approach to Diffusion Controlled Reactions. *J. Chem. Phys.* **1980,** *72* (8), 4350-4357.

55. Zwanzig, R.; Szabo, A.; Bagchi, B., Levinthal's Paradox. *Proc. Natl. Acad. Sci. U.S.A.* **1992,** *89* (1), 20-22.

56. Aristides Yayanos, A., Deep-Sea Piezophilic Bacteria. In *Methods in Microbiology*, Academic Press: 2001; Vol. 30, pp 615-637.

57. Cocker, J. E., Adaptations of Deep Sea Fishes. *Environ. Biol. Fishes* **1978,** *3* (4), 389-399.

58. Jannasch, H. W.; Taylor, C. D., Deep-Sea Microbiology. *Annu. Rev. Microbiol.* **1984,** *38* (1), 487-487.

59. Jannasch, H. W.; Wirsen, C. O., Variability of Pressure Adaptation in Deep Sea Bacteria. *Arch. Microbiol.* **1984,** *139* (4), 281-288.

60. Gross, M.; Jaenicke, R., Proteins under Pressure. *Eur. J. Biochem.* **1994,** *221* (2), 617-630.

61. Mozhaev, V. V.; Heremans, K.; Frank, J.; Masson, P.; Balny, C., High Pressure Effects on Protein Structure and Function. *Proteins* **1996,** *24* (1), 81-91.

62. Roche, J.; Royer, C. A., Lessons from Pressure Denaturation of Proteins. *J. R. Soc. Interface* **2018,** *15* (147), 20180244.

63. Najaf-Zadeh, R.; Wu, J. Q.; Macgregor, R. B., Effect of Cations on the Volume of the Helix-Coil Transition of poly[d(A-T)]. *Biochim. Biophys. Acta. Gene Struct. Expr.* **1995,** *1262* (1), 52-58.

64. Wu, J. Q.; Macgregor Jr., R. B., Pressure Dependence of the Helix–Coil Transition Temperature of poly[d(G-C)]. *Biopolymers* **1995,** *35* (4), 369-376.

65. Takahashi, S.; Sugimoto, N., Effect of Pressure on Thermal Stability of G-Quadruplex DNA and Double-Stranded DNA Structures. *Molecules* **2013,** *18* (11), 13297-13319.

66. Patra, S.; Anders, C.; Erwin, N.; Winter, R., Osmolyte Effects on the Conformational Dynamics of a DNA Hairpin at Ambient and Extreme Environmental Conditions. *Angew. Chem.* **2017,** *56* (18), 5045-5049.

67. Patra, S.; Anders, C.; Schummel, P. H.; Winter, R., Antagonistic Effects of Natural Osmolyte Mixtures and Hydrostatic Pressure on the Conformational Dynamics of a DNA Hairpin Probed at the Single-Molecule Level. *Phys. Chem. Chem. Phys.* **2018,** *20* (19), 13159-13170.

68. Schneider, S.; Paulsen, H.; Reiter, K. C.; Hinze, E.; Schiene-Fischer, C.; Hübner, C. G., Single Molecule FRET Investigation of Pressure-Driven Unfolding of Cold Shock Protein A. *J. Chem. Phys.* **2018,** *148* (12), 123336.

69. Sung, H.-L.; Nesbitt, D. J., DNA Hairpin Hybridization under Extreme Pressures: A Single-Molecule FRET Study. *J. Phys. Chem. B* **2020,** *124* (1), 110-120.

70. Sung, H.-L.; Nesbitt, D. J., High Pressure Single-Molecule FRET Studies of the Lysine Riboswitch: Cationic and Osmolytic Effects on Pressure Induced Denaturation. *Phys. Chem. Chem. Phys.* **2020,** *22* (28), 15853-15866.

71. Frye, K. J.; Royer, C. A., Probing the Contribution of Internal Cavities to the Volume Change of Protein Unfolding under Pressure. *Protein Sci.* **1998,** *7* (10), 2217-2222.

72. Cioni, P., Role of Protein Cavities on Unfolding Volume Change and on Internal Dynamics under Pressure. *Biophys. J.* **2006,** *91* (9), 3390-3396.

73. Roche, J.; Caro, J. A.; Norberto, D. R.; Barthe, P.; Roumestand, C.; Schlessman, J. L.; Garcia, A. E.; García-Moreno E., B.; Royer, C. A., Cavities Determine the Pressure Unfolding of Proteins. *Proc. Natl. Acad. Sci. U.S.A.* **2012,** *109* (18), 6945-6950.

74. Knight, A. W.; Kalugin, N. G.; Coker, E.; Ilgen, A. G., Water Properties under Nano-Scale Confinement. *Sci. Rep.* **2019,** *9* (1), 8246.

75. Grigera, J. R.; McCarthy, A. N., The Behavior of the Hydrophobic Effect under Pressure and Protein Denaturation. *Biophys. J.* **2010,** *98* (8), 1626-1631.

76. Royer, C.; Winter, R., Protein Hydration and Volumetric Properties. *Curr. Opin. Colloid Interface Sci.* **2011,** *16* (6), 568-571.

77. Mitra, L.; Rouget, J.-B.; Garcia-Moreno, B.; Royer, C. A.; Winter, R., Towards a Quantitative Understanding of Protein Hydration and Volumetric Properties. *ChemPhysChem* **2008,** *9* (18), 2715-2721.

78. Sung, H.-L.; Nesbitt, D. J., Single-Molecule Kinetic Studies of DNA Hybridization under Extreme Pressures. *Phys. Chem. Chem. Phys.* **2020,** *22* (41), 23491-23501.

79. Sung, H.-L.; Nesbitt, D. J., Synergism in the Molecular Crowding of Ligand-Induced Riboswitch Folding: Kinetic/Thermodynamic Insights from Single-Molecule Spectroscopy. *J. Phys. Chem. B* **2022,** *126* (34), 6419-6427.

80. Yancey, P. H.; Gerringer, M. E.; Drazen, J. C.; Rowden, A. A.; Jamieson, A., Marine Fish May be Biochemically Constrained from Inhabiting the Deepest Ocean Depths. *Proc Natl Acad Sci U S A* **2014,** *111* (12), 4461-5.

Chapter 2 Methods

1. Fiore, J. L.; Hodak, J. H.; Piestert, O.; Downey, C. D.; Nesbitt, D. J., Monovalent and Divalent Promoted GAAA Tetraloop-Receptor Tertiary Interactions from Freely Diffusing Single-Molecule Studies. *Biophys. J.* **2008,** *95* (8), 3892-3905.

2. Holmstrom, E. D.; Nesbitt, D. J., Biophysical Insights from Temperature-Dependent Single-Molecule Förster Resonance Energy Transfer. *Annu. Rev. Phys. Chem.* **2016,** *67* (1), 441-465.

3. Holmstrom, E. D.; Nesbitt, D. J., Localized Heating of Single Oligonucleotides using Infrared Light. *Biophys. J.* **2012,** *102* (3), 180a.

4. Aitken, C. E.; Marshall, R. A.; Puglisi, J. D., An Oxygen Scavenging System for Improvement of Dye Stability in Single-Molecule Fluorescence Experiments. *Biophys. J.* **2008,** *94* (5), 1826-1835.

5. Lee, N. K.; Kapanidis, A. N.; Wang, Y.; Michalet, X.; Mukhopadhyay, J.; Ebright, R. H.; Weiss, S., Accurate FRET Measurements within Single Diffusing Biomolecules Using Alternating-Laser Excitation. *Biophys. J.* **2005,** *88* (4), 2939-2953.

6. Mozhaev, V. V.; Heremans, K.; Frank, J.; Masson, P.; Balny, C., High Pressure Effects on Protein Structure and Function. *Proteins* **1996,** *24* (1), 81-91.

7. Patra, S.; Anders, C.; Erwin, N.; Winter, R., Osmolyte Effects on the Conformational Dynamics of a DNA Hairpin at Ambient and Extreme Environmental Conditions. *Angew. Chem.* **2017,** *56* (18), 5045-5049.

8. Sung, H.-L.; Nesbitt, D. J., DNA Hairpin Hybridization under Extreme Pressures: A Single-Molecule FRET Study. *J. Phys. Chem. B* **2020,** *124* (1), 110-120.

9. Sung, H.-L.; Nesbitt, D. J., Single-Molecule Kinetic Studies of DNA Hybridization under Extreme Pressures. *Phys. Chem. Chem. Phys.* **2020,** *22* (41), 23491-23501.

Chapter 3 Single Molecule FRET Kinetics of the Mn^{2+} Riboswitch: Evidence for Allosteric Mn^{2+} Control of "Induced-Fit" vs. "Conformational Selection" Folding Pathways

1. Nahvi, A.; Sudarsan, N.; Ebert, M. S.; Zou, X.; Brown, K. L.; Breaker, R. R., Genetic Control by a Metabolite Binding mRNA. *Chem. Biol.* **2002,** *9* (9), 1043-1049.

2. Tucker, B. J.; Breaker, R. R., Riboswitches as versatile gene control elements. *Curr. Opin. Struct. Biol.* **2005,** *15* (3), 342-348.

3. Breaker, R. R., Riboswitches and the RNA World. *Cold Spring Harbor Persp. Biol.* **2012,** *4* (2), 1-15.

4. Serganov, A.; Nudler, E., A Decade of Riboswitches. *Cell* **2013,** *152* (1), 17-24.

5. Roth, A.; Breaker, R. R., The Structural and Functional Diversity of Metabolite-Binding Riboswitches. *Annu. Rev. Biochem.* **2009,** *78* (1), 305-334.

6. Garst, A. D.; Edwards, A. L.; Batey, R. T., Riboswitches: Structures and mechanisms. *Cold Spring Harbor Persp. Biol.* **2011,** *3* (6), a003533.

7. Montange, R. K.; Batey, R. T., Structure of the S-adenosylmethionine riboswitch regulatory mRNA element. *Nature* **2006,** *441*, 1172.

8. Serganov, A.; Polonskaia, A.; Phan, A. T.; Breaker, R. R.; Patel, D. J., Structural basis for gene regulation by a thiamine pyrophosphate-sensing riboswitch. *Nature* **2006,** *441*, 1167.

9. Thore, S.; Leibundgut, M.; Ban, N., Structure of the Eukaryotic Thiamine Pyrophosphate Riboswitch with Its Regulatory Ligand. *Science* **2006,** *312* (5777), 1208-1211.

10. Gilbert, S. D.; Rambo, R. P.; Van Tyne, D.; Batey, R. T., Structure of the SAM-II riboswitch bound to S-adenosylmethionine. *Nat. Struct. Molec. Biol.* **2008,** *15*, 177.

11. Lu, C.; Smith, A. M.; Fuchs, R. T.; Ding, F.; Rajashankar, K.; Henkin, T. M.; Ke, A., Crystal structures of the SAM-III/SMK riboswitch reveal the SAM-dependent translation inhibition mechanism. *Nat. Struct. Molec. Biol.* **2008,** *15*, 1076.

12. Serganov, A.; Yuan, Y.-R.; Pikovskaya, O.; Polonskaia, A.; Malinina, L.; Phan, A. T.; Hobartner, C.; Micura, R.; Breaker, R. R.; Patel, D. J., Structural Basis for Discriminative Regulation of Gene Expression by Adenine- and Guanine-Sensing mRNAs. *Chem. Biol.* **2004,** *11* (12), 1729-1741.

13. Batey, R. T.; Gilbert, S. D.; Montange, R. K., Structure of a natural guanine-responsive riboswitch complexed with the metabolite hypoxanthine. *Nature* **2004,** *432*, 411.

14. Mandal, M.; Lee, M.; Barrick, J. E.; Weinberg, Z.; Emilsson, G. M.; Ruzzo, W. L.; Breaker, R. R., A Glycine-Dependent Riboswitch That Uses Cooperative Binding to Control Gene Expression. *Science* **2004,** *306* (5694), 275-279.

15. Serganov, A.; Huang, L.; Patel, D. J., Structural insights into amino acid binding and gene control by a lysine riboswitch. *Nature* **2008,** *455*, 1263.

16. Serganov, A.; Patel, D. J., Amino acid recognition and gene regulation by riboswitches. *Biochim. Biophys. Acta* **2009,** *1789* (9), 592-611.

17. Baker, J. L.; Sudarsan, N.; Weinberg, Z.; Roth, A.; Stockbridge, R. B.; Breaker, R. R., Widespread Genetic Switches and Toxicity Resistance Proteins for Fluoride. *Science* **2012,** *335* (6065), 233-235.

18. Ren, A.; Rajashankar, K. R.; Patel, D. J., Fluoride ion encapsulation by Mg^{2+} ions and phosphates in a fluoride riboswitch. *Nature* **2012,** *486*, 85.

19. Dann, C. E.; Wakeman, C. A.; Sieling, C. L.; Baker, S. C.; Irnov, I.; Winkler, W. C., Structure and Mechanism of a Metal-Sensing Regulatory RNA. *Cell* **2007,** *130* (5), 878-892.

20. Furukawa, K.; Ramesh, A.; Zhou, Z.; Weinberg, Z.; Vallery, T.; Winkler, Wade C.; Breaker, Ronald R., Bacterial Riboswitches Cooperatively Bind Ni^{2+} or Co^{2+} Ions and Control Expression of Heavy Metal Transporters. *Mol. Cell* **2015,** *57* (6), 1088-1098.

21. Price, I. R.; Gaballa, A.; Ding, F.; Helmann, J. D.; Ke, A., Mn^{2+}-Sensing Mechanisms of *yybP-ykoY* Orphan Riboswitches. *Mol. Cell* **2015,** *57* (6), 1110-1123.

22. Dambach, M.; Sandoval, M.; Updegrove, Taylor B.; Anantharaman, V.; Aravind, L.; Waters, Lauren S.; Storz, G., The Ubiquitous *yybP-ykoY* Riboswitch Is a Manganese-Responsive Regulatory Element. *Mol. Cell* **2015,** *57* (6), 1099-1109.

23. Barrick, J. E.; Corbino, K. A.; Winkler, W. C.; Nahvi, A.; Mandal, M.; Collins, J.; Lee, M.; Roth, A.; Sudarsan, N.; Jona, I., et al., New RNA motifs suggest an expanded scope for riboswitches in bacterial genetic control. *Proc. Natl. Acad. Sci. USA* **2004,** *101* (17), 6421-6426.

24. Harding, M. M.; Hsin, K.-Y., Mespeus—A Database of Metal Interactions with Proteins. In *Structural Genomics: General Applications*, Chen, Y. W., Ed. Humana Press: Totowa, NJ, 2014; pp 333-342.

25. Grubbs, R. D., Intracellular magnesium and magnesium buffering. *BioMetals* **2002,** *15* (3), 251-259.

26. Helmann, J. D., Specificity of Metal Sensing: Iron and Manganese Homeostasis in Bacillus subtilis. *J. Biol. Chem.* **2014**.

27. Chen, Y.; Li, X.; Gegenheimer, P., Ribonuclease P Catalysis Requires Mg^{2+} Coordinated to the *pro*-R_P Oxygen of the Scissile Bond. *Biochem.* **1997,** *36* (9), 2425-2438.

28. Leulliot, N.; Varani, G., Current Topics in RNA−Protein Recognition: Control of Specificity and Biological Function through Induced Fit and Conformational Capture. *Biochem.* **2001,** *40* (27), 7947-7956.

29. Boehr, D. D.; Nussinov, R.; Wright, P. E., The role of dynamic conformational ensembles in biomolecular recognition. *Nat. Chem. Biol.* **2009,** *5*, 789.

30. Stelzer, A. C.; Kratz, J. D.; Zhang, Q.; Al-Hashimi, H. M., RNA Dynamics by Design: Biasing Ensembles Towards the Ligand-Bound State. *Angew. Chem. Int. Ed.* **2010,** *49* (33), 5731-5733.

31. Haller, A.; Soulière, M. F.; Micura, R., The Dynamic Nature of RNA as Key to Understanding Riboswitch Mechanisms. *Acc. Chem. Res.* **2011,** *44* (12), 1339-1348.

32. Weikl, T. R.; Fabian, P., Conformational selection in protein binding and function. *Protein Sci.* **2014,** *23* (11), 1508-1518.

33. Kim, E.; Lee, S.; Jeon, A.; Choi, J. M.; Lee, H.-S.; Hohng, S.; Kim, H.-S., A single-molecule dissection of ligand binding to a protein with intrinsic dynamics. *Nat. Chem. Biol.* **2013,** *9*, 313.

34. Gouridis, G.; Schuurman-Wolters, G. K.; Ploetz, E.; Husada, F.; Vietrov, R.; de Boer, M.; Cordes, T.; Poolman, B., Conformational dynamics in substrate-binding domains influences transport in the ABC importer GlnPQ. *Nat. Struct. Mol. Biol.* **2014,** *22*, 57.

35. Brenner, M. D.; Scanlan, M. S.; Nahas, M. K.; Ha, T.; Silverman, S. K., Multivector Fluorescence Analysis of the *xpt* Guanine Riboswitch Aptamer Domain and the Conformational Role of Guanine. *Biochem.* **2010,** *49* (8), 1596-1605.

36. Haller, A.; Rieder, U.; Aigner, M.; Blanchard, S. C.; Micura, R., Conformational capture of the SAM-II riboswitch. *Nat. Chem. Biol.* **2011,** *7*, 393.

37. Wood, S.; Ferré-D'Amaré, A. R.; Rueda, D., Allosteric Tertiary Interactions Preorganize the c-di-GMP Riboswitch and Accelerate Ligand Binding. *ACS Chem. Biol.* **2012,** *7* (5), 920-927.

38. Haller, A.; Altman, R. B.; Soulière, M. F.; Blanchard, S. C.; Micura, R., Folding and ligand recognition of the TPP riboswitch aptamer at single-molecule resolution. *Proc. Natl. Acad. Sci. USA* **2013,** *110* (11), 4188-4193.

39. Xia, T.; Yuan, J.; Fang, X., Conformational Dynamics of an ATP-Binding DNA Aptamer: A Single-Molecule Study. *J. Phys. Chem. B* **2013,** *117* (48), 14994-15003.

40. Suddala, K. C.; Wang, J.; Hou, Q.; Walter, N. G., Mg^{2+} Shifts Ligand-Mediated Folding of a Riboswitch from Induced-Fit to Conformational Selection. *J. Am. Chem. Soc.* **2015,** *137* (44), 14075-14083.

41. Monod, J.; Changeux, J.-P.; Jacob, F., Allosteric proteins and cellular control systems. *J. Mol. Biol.* **1963,** *6* (4), 306-329.

42. Perutz, M. F., Mechanisms of cooperativity and allosteric regulation in proteins. *Q. Rev. Biophys.* **1989,** *22* (2), 139-237.

43. Peselis, A.; Gao, A.; Serganov, A., Cooperativity, allostery and synergism in ligand binding to riboswitches. *Biochimie* **2015,** *117*, 100-109.

44. Kern, D.; Zuiderweg, E. R. P., The role of dynamics in allosteric regulation. *Curr. Opin. Struct. Biol.* **2003,** *13* (6), 748-757.

45. Motlagh, H. N.; Wrabl, J. O.; Li, J.; Hilser, V. J., The ensemble nature of allostery. *Nature* **2014,** *508*, 331.

46. Thayer, K. M.; Lakhani, B.; Beveridge, D. L., Molecular Dynamics–Markov State Model of Protein Ligand Binding and Allostery in CRIB-PDZ: Conformational Selection and Induced Fit. *J. Phys. Chem. B* **2017,** *121* (22), 5509-5514.

47. Sengupta, A.; Sung, H.-L.; Nesbitt, D. J., Amino Acid Specific Effects on RNA Tertiary Interactions: Single-Molecule Kinetic and Thermodynamic Studies. *J. Phys. Chem. B* **2016,** *120* (41), 10615-10627.

48. Fiegland, L. R.; Garst, A. D.; Batey, R. T.; Nesbitt, D. J., Single-Molecule Studies of the Lysine Riboswitch Reveal Effector-Dependent Conformational Dynamics of the Aptamer Domain. *Biochem.* **2012,** *51* (45), 9223-9233.

49. Schroeder, Kersten T.; Daldrop, P.; Lilley, David M. J., RNA Tertiary Interactions in a Riboswitch Stabilize the Structure of a Kink Turn. *Structure* **2011,** *19* (9), 1233-1240.

50. Hennelly, S. P.; Novikova, I. V.; Sanbonmatsu, K. Y., The expression platform and the aptamer: cooperativity between Mg^{2+} and ligand in the SAM-I riboswitch. *Nucleic Acids Res.* **2013,** *41* (3), 1922-1935.

51. Lamichhane, R.; Daubner, G. M.; Thomas-Crusells, J.; Auweter, S. D.; Manatschal, C.; Austin, K. S.; Valniuk, O.; Allain, F. H.-T.; Rueda, D., RNA looping by PTB: Evidence using FRET and NMR spectroscopy for a role in splicing repression. *Proc. Natl. Acad. Sci. USA* **2010,** *107* (9), 4105-4110.

52. Fragata, M.; Dudekula, S., Nonlinear Enhancement of Oxygen Evolution in Thylakoid Membranes: Modeling the Effect of Light Intensity and β-Cyclodextrin Concentration. *J. Phys. Chem. B* **2005,** *109* (30), 14707-14714.

53. Moyon, N. S.; Mitra, S., Luminol Fluorescence Quenching in Biomimicking Environments: Sequestration of Fluorophore in Hydrophobic Domain. *J. Phys. Chem. B* **2011,** *115* (33), 10163-10172.

54. Leipply, D.; Draper, D. E., Dependence of RNA Tertiary Structural Stability on Mg2+ Concentration: Interpretation of the Hill Equation and Coefficient. *Biochem.* **2010,** *49* (9), 1843-1853.

55. Grilley, D.; Soto, A. M.; Draper, D. E., Mg^{2+}–RNA interaction free energies and their relationship to the folding of RNA tertiary structures. *Proc. Natl. Acad. Sci. USA* **2006,** *103* (38), 14003-14008.

56. Leipply, D.; Lambert, D.; Draper, D. E., Ion–RNA Interactions: Thermodynamic Analysis of the Effects of Mono- and Divalent Ions on RNA Conformational Equilibria. In *Methods Enzymol.*, Academic Press: 2009; Vol. 469, pp 433-463.

57. Fiore, J. L.; Holmstrom, E. D.; Fiegland, L. R.; Hodak, J. H.; Nesbitt, D. J., The Role of Counterion Valence and Size in GAAA Tetraloop–Receptor Docking/Undocking Kinetics. *J. Mol. Biol.* **2012,** *423* (2), 198-216.

58. Kim, H. D.; Nienhaus, G. U.; Ha, T.; Orr, J. W.; Williamson, J. R.; Chu, S., Mg^{2+}-dependent conformational change of RNA studied by fluorescence correlation and FRET on immobilized single molecules. *Proc. Natl. Acad. Sci. USA* **2002,** *99* (7), 4284.

59. Baird, N. J.; Inglese, J.; Ferré-D'Amaré, A. R., Rapid RNA–ligand interaction analysis through high-information content conformational and stability landscapes. *Nature Comm.* **2015,** *6,* 8898.

60. Leipply, D.; Draper, D. E., Effects of Mg^{2+} on the Free Energy Landscape for Folding a Purine Riboswitch RNA. *Biochem.* **2011,** *50* (14), 2790-2799.

61. Yamauchi, T.; Miyoshi, D.; Kubodera, T.; Nishimura, A.; Nakai, S.; Sugimoto, N., Roles of Mg^{2+} in TPP-dependent riboswitch. *FEBS Lett.* **2005,** *579* (12), 2583-2588.

62. Waters, L. S.; Sandoval, M.; Storz, G., The *Escherichia coli* MntR Miniregulon Includes Genes Encoding a Small Protein and an Efflux Pump Required for Manganese Homeostasis. *J. Bacteriol.* **2011,** *193* (21), 5887-5897.

63. Veyrier, F. J.; Boneca, I. G.; Cellier, M. F.; Taha, M.-K., A Novel Metal Transporter Mediating Manganese Export (MntX) Regulates the Mn to Fe Intracellular Ratio and *Neisseria meningitidis* Virulence. *PLoS Path.* **2011,** *7* (9), e1002261.

64. Li, C.; Tao, J.; Mao, D.; He, C., A Novel Manganese Efflux System, YebN, Is Required for Virulence by *Xanthomonas oryzae* pv. *oryzae*. *PLOS ONE* **2011,** *6* (7), e21983.

65. Winkler, W. C.; Dann III, C. E., RNA allostery glimpsed. *Nat. Struct. Mol. Biol.* **2006,** *13*, 569.

66. Mandal, M.; Breaker, R. R., Gene regulation by riboswitches. *Nature Rev. Molec. Cell Biol.* **2004,** *5*, 451.

67. Trausch, Jeremiah J.; Ceres, P.; Reyes, Francis E.; Batey, Robert T., The Structure of a Tetrahydrofolate-Sensing Riboswitch Reveals Two Ligand Binding Sites in a Single Aptamer. *Structure* **2011,** *19* (10), 1413-1423.

68. Lee, E. R.; Baker, J. L.; Weinberg, Z.; Sudarsan, N.; Breaker, R. R., An Allosteric Self-Splicing Ribozyme Triggered by a Bacterial Second Messenger. *Science* **2010,** *329* (5993), 845-848.

69. Chen, A. G. Y.; Sudarsan, N.; Breaker, R. R., Mechanism for gene control by a natural allosteric group I ribozyme. *RNA* **2011,** *17* (11), 1967-1972.

Chapter 4 Novel Heat-Promoted Folding Dynamics of the *yybP-ykoY* Manganese Riboswitch: Kinetic and Thermodynamic Studies at the Single Molecule Level

1. Mironov, A. S.; Gusarov, I.; Rafikov, R.; Lopez, L. E.; Shatalin, K.; Kreneva, R. A.; Perumov, D. A.; Nudler, E., Sensing Small Molecules by Nascent RNA: A Mechanism to Control Transcription in Bacteria. *Cell* **2002,** *111* (5), 747-756.

2. Nahvi, A.; Sudarsan, N.; Ebert, M. S.; Zou, X.; Brown, K. L.; Breaker, R. R., Genetic Control by a Metabolite Binding mRNA. *Chem. Biol.* **2002,** *9* (9), 1043-1049.

3. Tucker, B. J.; Breaker, R. R., Riboswitches as versatile gene control elements. *Curr. Opin. Struct. Biol.* **2005,** *15* (3), 342-348.

4. Serganov, A.; Nudler, E., A Decade of Riboswitches. *Cell* **2013,** *152* (1), 17-24.

5. Roth, A.; Breaker, R. R., The Structural and Functional Diversity of Metabolite-Binding Riboswitches. *Annu. Rev. Biochem.* **2009,** *78* (1), 305-334.

6. Garst, A. D.; Edwards, A. L.; Batey, R. T., Riboswitches: Structures and mechanisms. *Cold Spring Harbor Persp. Biol.* **2011,** *3* (6), a003533.

7. Brady, G. P.; Sharp, K. A., Entropy in protein folding and in protein—protein interactions. *Curr. Opin. Struct. Biol.* **1997,** *7* (2), 215-221.

8. Onuchic, J. N.; Wolynes, P. G., Theory of protein folding. *Curr. Opin. Struct. Biol.* **2004,** *14* (1), 70-75.

9. Draper, D. E., Strategies for RNA folding. *Trends Biochem. Sci.* **1996,** *21* (4), 145-149.

10. Dill, K. A., Dominant forces in protein folding. *Biochem.* **1990,** *29* (31), 7133-7155.

11. Schildkraut, C.; Lifson, S., Dependence of the melting temperature of DNA on salt concentration. *Biopolymers* **1965,** *3* (2), 195-208.

12. Donovan, J. W.; Mapes, C. J.; Davis, J. G.; Garibaldi, J. A., A differential scanning calorimetric study of the stability of egg white to heat denaturation. *J. Sci. Food Agric.* **1975,** *26* (1), 73-83.

13. Privalov, P. L., Cold Denaturation of Protein. *Crit. Rev. Biochem. Mol. Biol.* **1990,** *25* (5), 281-306.

14. Hatley, R. H. M.; Franks, F., Cold destabilisation of enzymes. *Faraday Discuss.* **1992,** *93* (0), 249-257.

15. Makhatadze, G. I.; Privalov, P. L., Contribution of Hydration to Protein Folding Thermodynamics: I. The Enthalpy of Hydration. *J. Mol. Biol.* **1993,** *232* (2), 639-659.

16. Privalov, P. L.; Makhatadze, G. I., Contribution of Hydration to Protein Folding Thermodynamics: II. The Entropy and Gibbs Energy of Hydration. *J. Mol. Biol.* **1993,** *232* (2), 660-679.

17. Kurr, M.; Huber, R.; König, H.; Jannasch, H. W.; Fricke, H.; Trincone, A.; Kristjansson, J. K.; Stetter, K. O., *Methanopyrus kandleri*, gen. and sp. nov. represents a novel group of hyperthermophilic methanogens, growing at 110°C. *Arch. Microbiol.* **1991,** *156* (4), 239-247.

18. Takai, K.; Nakamura, K.; Toki, T.; Tsunogai, U.; Miyazaki, M.; Miyazaki, J.; Hirayama, H.; Nakagawa, S.; Nunoura, T.; Horikoshi, K., Cell proliferation at 122°C and isotopically heavy CH_4 production by a hyperthermophilic methanogen under high-pressure cultivation. *Proc. Natl. Acad. Sci. USA* **2008,** *105* (31), 10949-10954.

19. Mykytczuk, N. C. S.; Foote, S. J.; Omelon, C. R.; Southam, G.; Greer, C. W.; Whyte, L. G., Bacterial growth at −15 °C; molecular insights from the permafrost bacterium *Planococcus halocryophilus* Or1. *The Isme Journal* **2013,** *7*, 1211.

20. Hurme, R.; Rhen, M., Temperature sensing in bacterial gene regulation — what it all boils down to. *Mol. Microbiol.* **1998,** *30* (1), 1-6.

21. Konkel, M. E.; Tilly, K., Temperature-regulated expression of bacterial virulence genes. *Microb. Infect.* **2000,** *2* (2), 157-166.

22. Narberhaus, F., Translational control of bacterial heat shock and virulence genes by temperature-sensing mRNAs. *RNA Biology* **2010,** *7* (1), 84-89.

23. Kortmann, J.; Narberhaus, F., Bacterial RNA thermometers: molecular zippers and switches. *Nat. Rev. Microbiol.* **2012,** *10*, 255.

24. Barrick, J. E.; Corbino, K. A.; Winkler, W. C.; Nahvi, A.; Mandal, M.; Collins, J.; Lee, M.; Roth, A.; Sudarsan, N.; Jona, I.; Wickiser, J. K.; Breaker, R. R., New RNA motifs suggest an expanded scope for riboswitches in bacterial genetic control. *Proc. Natl. Acad. Sci. USA* **2004,** *101* (17), 6421-6426.

25. Price, Ian R.; Gaballa, A.; Ding, F.; Helmann, John D.; Ke, A., Mn^{2+}-Sensing Mechanisms of *yybP-ykoY* Orphan Riboswitches. *Mol. Cell* **2015,** *57* (6), 1110-1123.

26. Dambach, M.; Sandoval, M.; Updegrove, Taylor B.; Anantharaman, V.; Aravind, L.; Waters, Lauren S.; Storz, G., The Ubiquitous *yybP-ykoY* Riboswitch Is a Manganese-Responsive Regulatory Element. *Mol. Cell* **2015,** *57* (6), 1099-1109.

27. Waters, L. S.; Sandoval, M.; Storz, G., The *Escherichia coli* MntR Miniregulon Includes Genes Encoding a Small Protein and an Efflux Pump Required for Manganese Homeostasis. *J. Bacteriol.* **2011,** *193* (21), 5887-5897.

28. Veyrier, F. J.; Boneca, I. G.; Cellier, M. F.; Taha, M.-K., A Novel Metal Transporter Mediating Manganese Export (MntX) Regulates the Mn to Fe Intracellular Ratio and *Neisseria meningitidis* Virulence. *PLoS Path.* **2011,** *7* (9), e1002261.

29. Li, C.; Tao, J.; Mao, D.; He, C., A Novel Manganese Efflux System, YebN, Is Required for Virulence by *Xanthomonas oryzae* pv. *oryzae*. *PLOS ONE* **2011,** *6* (7), e21983.

30. Haller, A.; Soulière, M. F.; Micura, R., The Dynamic Nature of RNA as Key to Understanding Riboswitch Mechanisms. *Acc. Chem. Res.* **2011,** *44* (12), 1339-1348.

31. Garst, A. D.; Batey, R. T., A switch in time: Detailing the life of a riboswitch. *Biochimica et Biophysica Acta (BBA) - Gene Regulatory Mechanisms* **2009,** *1789* (9), 584-591.

32. Sung, H.-L.; Nesbitt, D. J., Single Molecule FRET Kinetics of the Mn^{2+} Riboswitch: Evidence for Allosteric Mg^{2+} Control of "Induced Fit" vs. "Conformational Selection" Folding Pathways. *J. Phys. Chem. B* **2019**.

33. Leulliot, N.; Varani, G., Current Topics in RNA−Protein Recognition: Control of Specificity and Biological Function through Induced Fit and Conformational Capture. *Biochem.* **2001,** *40* (27), 7947-7956.

34. Fiore, J. L.; Holmstrom, E. D.; Nesbitt, D. J., Entropic origin of Mg^{2+}-facilitated RNA folding. *Proc. Natl. Acad. Sci. USA* **2012,** *109* (8), 2902-2907.

35. Sengupta, A.; Sung, H.-L.; Nesbitt, D. J., Amino Acid Specific Effects on RNA Tertiary Interactions: Single-Molecule Kinetic and Thermodynamic Studies. *J. Phys. Chem. B* **2016,** *120* (41), 10615-10627.

36. Nicholson, D. A.; Sengupta, A.; Sung, H.-L.; Nesbitt, D. J., Amino Acid Stabilization of Nucleic Acid Secondary Structure: Kinetic Insights from Single-Molecule Studies. *J. Phys. Chem. B* **2018,** *122* (43), 9869-9876.

37. Fiegland, L. R.; Garst, A. D.; Batey, R. T.; Nesbitt, D. J., Single-Molecule Studies of the Lysine Riboswitch Reveal Effector-Dependent Conformational Dynamics of the Aptamer Domain. *Biochem.* **2012,** *51* (45), 9223-9233.

38. Schroeder, Kersten T.; Daldrop, P.; Lilley, David M., RNA Tertiary Interactions in a Riboswitch Stabilize the Structure of a Kink Turn. *Structure* **2011,** *19* (9), 1233-1240.

39. Hennelly, S. P.; Novikova, I. V.; Sanbonmatsu, K. Y., The expression platform and the aptamer: cooperativity between Mg^{2+} and ligand in the SAM-I riboswitch. *Nucleic Acids Res.* **2013,** *41* (3), 1922-1935.

40. Leipply, D.; Draper, D. E., Dependence of RNA Tertiary Structural Stability on Mg^{2+} Concentration: Interpretation of the Hill Equation and Coefficient. *Biochem.* **2010,** *49* (9), 1843-1853.

41. Szabo, A.; Schulten, K.; Schulten, Z., First passage time approach to diffusion controlled reactions. *J. Chem. Phys.* **1980,** *72* (8), 4350-4357.

42. Zwanzig, R.; Szabo, A.; Bagchi, B., Levinthal's paradox. *Proc. Natl. Acad. Sci. USA* **1992,** *89* (1), 20-22.

43. Zhou, H.-X., Rate theories for biologists. *Q. Rev. Biophys.* **2010,** *43* (2), 219-293.

44. Murphy, K. P.; Xie, D.; Thompson, K. S.; Amzel, L. M.; Freire, E., Entropy in biological binding processes: Estimation of translational entropy loss. *Proteins: Struct. Funct. Bioinform.* **1994,** *18* (1), 63-67.

45. Mario, A. L., Loss of translational entropy in binding, folding, and catalysis. *Proteins: Structure, Function, and Bioinformatics* **1997,** *28* (2), 144-149.

46. Lu, B.; Wong, C. F., Direct estimation of entropy loss due to reduced translational and rotational motions upon molecular binding. *Biopolymers* **2005,** *79* (5), 277-285.

47. Mikulecky, P. J.; Feig, A. L., Cold Denaturation of the Hammerhead Ribozyme. *J. Am. Chem. Soc.* **2002,** *124* (6), 890-891.

48. Mikulecky, P. J.; Feig, A. L., Heat capacity changes in RNA folding: application of perturbation theory to hammerhead ribozyme cold denaturation. *Nucleic Acids Res.* **2004,** *32* (13), 3967-3976.

49. Cooper, A.; Johnson, C. M.; Lakey, J. H.; Nöllmann, M., Heat does not come in different colours: entropy–enthalpy compensation, free energy windows, quantum confinement, pressure perturbation calorimetry, solvation and the multiple causes of heat capacity effects in biomolecular interactions. *Biophys. Chem.* **2001,** *93* (2), 215-230.

50. Lumry, R.; Rajender, S., Enthalpy–entropy compensation phenomena in water solutions of proteins and small molecules: A ubiquitous property of water. *Biopolymers* **1970,** *9* (10), 1125-1227.

51. Schmid, R.; Miah, A. M.; Sapunov, V. N., A new table of the thermodynamic quantities of ionic hydration: values and some applications (enthalpy–entropy compensation and Born radii). *Phys. Chem. Chem. Phys.* **2000,** *2* (1), 97-102.

52. Reining, A.; Nozinovic, S.; Schlepckow, K.; Buhr, F.; Fürtig, B.; Schwalbe, H., Three-state mechanism couples ligand and temperature sensing in riboswitches. *Nature* **2013,** *499*, 355.

53. McConnell, T. S.; Cech, T. R., A positive entropy change for guanosine binding and for the chemical step in the Tetrahymena ribozyme reaction. *Biochem.* **1995,** *34* (12), 4056-4067.

54. Kuo, L. Y.; Cech, T. R., Conserved thermochemistry of guanosine nucleophile binding for structurally distinct group I ribozymes. *Nucleic Acids Res.* **1996,** *24* (19), 3722-3727.

55. Huang, L.; Serganov, A.; Patel, D. J., Structural Insights into Ligand Recognition by a Sensing Domain of the Cooperative Glycine Riboswitch. *Mol. Cell* **2010,** *40* (5), 774-786.

56. Trausch, Jeremiah J.; Ceres, P.; Reyes, Francis E.; Batey, Robert T., The Structure of a Tetrahydrofolate-Sensing Riboswitch Reveals Two Ligand Binding Sites in a Single Aptamer. *Structure* **2011,** *19* (10), 1413-1423.

57. Burnouf, D.; Ennifar, E.; Guedich, S.; Puffer, B.; Hoffmann, G.; Bec, G.; Disdier, F.; Baltzinger, M.; Dumas, P., kinITC: A New Method for Obtaining Joint Thermodynamic and Kinetic Data by Isothermal Titration Calorimetry. *J. Am. Chem. Soc.* **2012,** *134* (1), 559-565.

58. Baird, N. J.; Ferré-D'Amaré, A. R., Modulation of quaternary structure and enhancement of ligand binding by the K-turn of tandem glycine riboswitches. *RNA* **2013,** *19* (2), 167-176.

59. Gilbert, S. D.; Rambo, R. P.; Van Tyne, D.; Batey, R. T., Structure of the SAM-II riboswitch bound to S-adenosylmethionine. *Nat. Struct. Molec. Biol.* **2008,** *15*, 177.

60. Ren, A.; Rajashankar, K. R.; Patel, D. J., Fluoride ion encapsulation by Mg^{2+} ions and phosphates in a fluoride riboswitch. *Nature* **2012,** *486*, 85.

61. Ren, A.; Patel, D. J., c-di-AMP binds the *ydaO* riboswitch in two pseudo-symmetry–related pockets. *Nat. Chem. Biol.* **2014,** *10*, 780.

62. Ren, A.; Rajashankar, K. R.; Patel, D. J., Global RNA Fold and Molecular Recognition for a *pfl* Riboswitch Bound to ZMP, a Master Regulator of One-Carbon Metabolism. *Structure* **2015,** *23* (8), 1375-1381.

63. Stoddard, C. D.; Gilbert, S. D.; Batey, R. T., Ligand-dependent folding of the three-way junction in the purine riboswitch. *RNA* **2008,** *14* (4), 675-684.

64. Wickiser, J. K.; Cheah, M. T.; Breaker, R. R.; Crothers, D. M., The Kinetics of Ligand Binding by an Adenine-Sensing Riboswitch. *Biochem.* **2005,** *44* (40), 13404-13414.

65. Gao, A.; Serganov, A., Structural insights into recognition of c-di-AMP by the *ydaO* riboswitch. *Nat. Chem. Biol.* **2014,** *10*, 787.

66. Wood, S.; Ferré-D'Amaré, A. R.; Rueda, D., Allosteric Tertiary Interactions Preorganize the c-di-GMP Riboswitch and Accelerate Ligand Binding. *ACS Chem. Biol.* **2012,** *7* (5), 920-927.

67. Kang, M.; Eichhorn, C. D.; Feigon, J., Structural determinants for ligand capture by a class II $preQ_1$ riboswitch. *Proc. Natl. Acad. Sci. USA* **2014,** *111* (6), E663.

68. Wickiser, J. K.; Winkler, W. C.; Breaker, R. R.; Crothers, D. M., The Speed of RNA Transcription and Metabolite Binding Kinetics Operate an FMN Riboswitch. *Mol. Cell* **2005,** *18* (1), 49-60.

69. Baird, N. J.; Ferré-D'Amaré, A. R., Idiosyncratically tuned switching behavior of riboswitch aptamer domains revealed by comparative small-angle X-ray scattering analysis. *RNA* **2010,** *16* (3), 598-609.

70. Batey, R. T.; Gilbert, S. D.; Montange, R. K., Structure of a natural guanine-responsive riboswitch complexed with the metabolite hypoxanthine. *Nature* **2004,** *432*, 411.

71. Gilbert, S. D.; Stoddard, C. D.; Wise, S. J.; Batey, R. T., Thermodynamic and Kinetic Characterization of Ligand Binding to the Purine Riboswitch Aptamer Domain. *J. Mol. Biol.* **2006,** *359* (3), 754-768.

72. Edwards, A. L.; Reyes, F. E.; Héroux, A.; Batey, R. T., Structural basis for recognition of S-adenosylhomocysteine by riboswitches. *RNA* **2010,** *16* (11), 2144-2155.

73. Pikovskaya, O.; Polonskaia, A.; Patel, D. J.; Serganov, A., Structural principles of nucleoside selectivity in a 2'-deoxyguanosine riboswitch. *Nat. Chem. Biol.* **2011,** *7*, 748.

74. Wilson, R. C.; Smith, A. M.; Fuchs, R. T.; Kleckner, I. R.; Henkin, T. M.; Foster, M. P., Tuning Riboswitch Regulation through Conformational Selection. *J. Mol. Biol.* **2011,** *405* (4), 926-938.

75. Müller, M.; Weigand, J. E.; Weichenrieder, O.; Suess, B., Thermodynamic characterization of an engineered tetracycline-binding riboswitch. *Nucleic Acids Res.* **2006,** *34* (9), 2607-2617.

76. Li, Y.; Bevilacqua, P. C.; Mathews, D.; Turner, D. H., Thermodynamic and activation parameters for binding of a pyrene-labeled substrate by the Tetrahymena ribozyme: docking is not diffusion-controlled and is driven by a favorable entropy change. *Biochem.* **1995,** *34* (44), 14394-14399.

77. Kulshina, N.; Edwards, T. E.; Ferré-D'Amaré, A. R., Thermodynamic analysis of ligand binding and ligand binding-induced tertiary structure formation by the thiamine pyrophosphate riboswitch. *RNA* **2010,** *16* (1), 186-196.

78. Ali, S. F.; Duhart, H. M.; Newport, G. D.; Lipe, G. W.; Slikker, W., Manganese-induced reactive oxygen species: Comparison between Mn^{+2} and Mn^{+3}. *Neurodegeneration* **1995,** *4* (3), 329-334.

79. Brenneman, K. A.; Cattley, R. C.; Ali, S. F.; Dorman, D. C., Manganese-induced developmental neurotoxicity in the CD rat: is oxidative damage a mechanism of action? *Neurotoxicology* **1999,** *20* (2-3), 477-487.

80. Sairam, R. K.; Deshmukh, P. S.; Shukla, D. S., Tolerance of Drought and Temperature Stress in Relation to Increased Antioxidant Enzyme Activity in Wheat. *J. Agron. Crop Sci.* **1997,** *178* (3), 171-178.

81. Sairam, R. K.; Srivastava, G. C.; Saxena, D. C., Increased Antioxidant Activity under Elevated Temperatures: A Mechanism of Heat Stress Tolerance in Wheat Genotypes. *Biol. Plant.* **2000,** *43* (2), 245-251.

82. Lushchak, V. I.; Bagnyukova, T. V., Temperature increase results in oxidative stress in goldfish tissues. 2. Antioxidant and associated enzymes. *Comp. Biochem. Physiol. C* **2006,** *143* (1), 36-41.

Chapter 5 Sequential Folding of the Nickel/Cobalt Riboswitch is Facilitated by a Conformational Intermediate: Insights from Single-Molecule Kinetics and Thermodynamics

1. Barrick, J. E.; Breaker, R. R., The Distributions, Mechanisms, and Structures of Metabolite-Binding Riboswitches. *Genome Biol.* **2007,** *8* (11), R239.

2. Garst, A. D.; Edwards, A. L.; Batey, R. T., Riboswitches: Structures and Mechanisms. *Cold Spring Harb. Perspect. Biol.* **2011,** *3* (6), a003533.

3. Nudler, E.; Mironov, A. S., The Riboswitch Control of Bacterial Metabolism. *Trends Biochem. Sci.* **2004,** *29* (1), 11-17.

4. Winkler, W. C.; Breaker, R. R., Regulation of Bacterial Gene Expression by Riboswitches. *Annu. Rev. Microbiol.* **2005,** *59* (1), 487-517.

5. McCown, P. J.; Corbino, K. A.; Stav, S.; Sherlock, M. E.; Breaker, R. R., Riboswitch Diversity and Distribution. *RNA* **2017,** *23* (7), 995-1011.

6. Valko, M.; Morris, H.; Cronin, M. T. D., Metals, Toxicity and Oxidative Stress. *Curr. Med. Chem.* **2005,** *12* (10), 1161-1208.

7. Jaishankar, M.; Tseten, T.; Anbalagan, N.; Mathew, B. B.; Beeregowda, K. N., Toxicity, Mechanism and Health Effects of Some Heavy Metals. *Interdiscip. Toxicol.* **2014,** *7* (2), 60-72.

8. Andreini, C.; Bertini, I.; Cavallaro, G.; Holliday, G. L.; Thornton, J. M., Metal Ions in Biological Catalysis: from Enzyme Databases to General Principles. *J. Biol. Inorg. Chem.* **2008,** *13* (8), 1205-1218.

9. Hausinger, R. P., Nickel Utilization by Microorganisms. *Microbiol. Rev.* **1987,** *51* (1), 22-42.

10. Chen, P. R.; He, C., Selective Recognition of Metal Ions by Metalloregulatory Proteins. *Curr. Opin. Chem. Biol.* **2008,** *12* (2), 214-221.

11. Reyes-Caballero, H.; Campanello, G. C.; Giedroc, D. P., Metalloregulatory Proteins: Metal Selectivity and Allosteric Switching. *Biophys. Chem.* **2011,** *156* (2), 103-114.

12. Pyle, A., Metal ions in the structure and function of RNA. *J. Biol. Inorg. Chem.* **2002,** *7* (7), 679-690.

13. Saunders, A. M.; DeRose, V. J., Beyond Mg^{2+}: Functional Interactions Between RNA and Transition Metals. *Curr. Opin. Chem. Biol.* **2016,** *31*, 153-159.

14. Price, Ian R.; Gaballa, A.; Ding, F.; Helmann, John D.; Ke, A., Mn^{2+}-Sensing Mechanisms of *yybP-ykoY* Orphan Riboswitches. *Mol. Cell* **2015,** *57* (6), 1110-1123.

15. Dambach, M.; Sandoval, M.; Updegrove, Taylor B.; Anantharaman, V.; Aravind, L.; Waters, Lauren S.; Storz, G., The Ubiquitous *yybP-ykoY* Riboswitch Is a Manganese-Responsive Regulatory Element. *Mol. Cell* **2015,** *57* (6), 1099-1109.

16. Furukawa, K.; Ramesh, A.; Zhou, Z.; Weinberg, Z.; Vallery, T.; Winkler, Wade C.; Breaker, Ronald R., Bacterial Riboswitches Cooperatively Bind Ni^{2+} or Co^{2+} Ions and Control Expression of Heavy Metal Transporters. *Mol. Cell* **2015,** *57* (6), 1088-1098.

17. Anton, A.; Große, C.; Reißmann, J.; Pribyl, T.; Nies, D. H., CzcD Is a Heavy Metal Ion Transporter Involved in Regulation of Heavy Metal Resistance in *Ralstonia* sp. Strain CH34. *J. Bacteriol.* **1999,** *181* (22), 6876-6881.

18. Große, C.; Anton, A.; Hoffmann, T.; Franke, S.; Schleuder, G.; Nies, D. H., Identification of a Regulatory Pathway that Controls the Heavy-Metal Resistance System Czc via Promoter czcNp in *Ralstonia metallidurans*. *Arch. Microbiol.* **2004,** *182* (2), 109-118.

19. Bouzat, J. L.; Hoostal, M. J., Evolutionary Analysis and Lateral Gene Transfer of Two-Component Regulatory Systems Associated with Heavy-Metal Tolerance in Bacteria. *J. Mol. Evol.* **2013,** *76* (5), 267-279.

20. Frieda, K. L.; Block, S. M., Direct Observation of Cotranscriptional Folding in an Adenine Riboswitch. *Science* **2012,** *338* (6105), 397-400.

21. Watters, K. E.; Strobel, E. J.; Yu, A. M.; Lis, J. T.; Lucks, J. B., Cotranscriptional Folding of a Riboswitch at Nucleotide Resolution. *Nat. Struct. Mol. Biol.* **2016,** *23* (12), 1124-1131.

22. Tolić-Nørrelykke, S. F.; Engh, A. M.; Landick, R.; Gelles, J., Diversity in the Rates of Transcript Elongation by Single RNA Polymerase Molecules. *J. Biol. Chem.* **2004,** *279* (5), 3292-3299.

23. Wickiser, J. K.; Winkler, W. C.; Breaker, R. R.; Crothers, D. M., The Speed of RNA Transcription and Metabolite Binding Kinetics Operate an FMN Riboswitch. *Mol. Cell* **2005,** *18* (1), 49-60.

24. Lemay, J.-F.; Desnoyers, G.; Blouin, S.; Heppell, B.; Bastet, L.; St-Pierre, P.; Massé, E.; Lafontaine, D. A., Comparative Study between Transcriptionally- and Translationally-Acting Adenine Riboswitches Reveals Key Differences in Riboswitch Regulatory Mechanisms. *PLoS Genet.* **2011,** *7* (1), e1001278.

25. Lutz, B.; Faber, M.; Verma, A.; Klumpp, S.; Schug, A., Differences Between Cotranscriptional and Free Riboswitch Folding. *Nucleic Acids Res.* **2013,** *42* (4), 2687-2696.

26. Zhuang, X.; Bartley, L. E.; Babcock, H. P.; Russell, R.; Ha, T.; Herschlag, D.; Chu, S., A Single-Molecule Study of RNA Catalysis and Folding. *Science* **2000,** *288* (5473), 2048-2051.

27. Roy, R.; Hohng, S.; Ha, T., A Practical Guide to Single-Molecule FRET. *Nat. Methods* **2008,** *5* (6), 507-516.

28. Guo, Z.; Karunatilaka, K. S.; Rueda, D., Single-Molecule Analysis of Protein-Free U2–U6 snRNAs. *Nat. Struct. Mol. Biol.* **2009,** *16* (11), 1154-1159.

29. McCluskey, K.; Boudreault, J.; St-Pierre, P.; Perez-Gonzalez, C.; Chauvier, A.; Rizzi, A.; Beauregard, P. B.; Lafontaine, D. A.; Penedo, J. C., Unprecedented Tunability of

Riboswitch Structure and Regulatory Function by Sub-Millimolar Variations in Physiological Mg^{2+}. *Nucleic Acids Res.* **2019,** *47* (12), 6478-6487.

30. Lu, M.; Ma, X.; Castillo-Menendez, L. R.; Gorman, J.; Alsahafi, N.; Ermel, U.; Terry, D. S.; Chambers, M.; Peng, D.; Zhang, B., et al., Associating HIV-1 Envelope Glycoprotein Structures with States on the Virus Observed by smFRET. *Nature* **2019,** *568* (7752), 415-419.

31. Fiore, J. L.; Holmstrom, E. D.; Nesbitt, D. J., Entropic origin of Mg^{2+}-Facilitated RNA Folding. *Proc. Natl. Acad. Sci. U.S.A.* **2012,** *109* (8), 2902-2907.

32. Nicholson, D. A.; Sengupta, A.; Sung, H.-L.; Nesbitt, D. J., Amino Acid Stabilization of Nucleic Acid Secondary Structure: Kinetic Insights from Single-Molecule Studies. *J. Phys. Chem. B* **2018,** *122* (43), 9869-9876.

33. Holmstrom, E. D.; Nesbitt, D. J., Biophysical Insights from Temperature-Dependent Single-Molecule Förster Resonance Energy Transfer. *Annu. Rev. Phys. Chem.* **2016,** *67* (1), 441-465.

34. Sung, H.-L.; Nesbitt, D. J., Novel Heat-Promoted Folding Dynamics of the yybP-ykoY Manganese Riboswitch: Kinetic and Thermodynamic Studies at the Single-Molecule Level. *J. Phys. Chem. B* **2019,** *123* (26), 5412-5422.

35. Vogt, A. D.; Pozzi, N.; Chen, Z.; Di Cera, E., Essential Role of Conformational Selection in Ligand Binding. *Biophys. Chem.* **2014,** *186*, 13-21.

36. Suddala, K. C.; Wang, J.; Hou, Q.; Walter, N. G., Mg^{2+} Shifts Ligand-Mediated Folding of a Riboswitch from Induced-Fit to Conformational Selection. *J. Am. Chem. Soc.* **2015,** *137* (44), 14075-14083.

37. Sung, H.-L.; Nesbitt, D. J., Single-Molecule FRET Kinetics of the Mn^{2+} Riboswitch: Evidence for Allosteric Mg^{2+} Control of "Induced-Fit" vs "Conformational Selection" Folding Pathways. *J. Phys. Chem. B* **2019,** *123* (9), 2005-2015.

38. Serganov, A.; Yuan, Y.-R.; Pikovskaya, O.; Polonskaia, A.; Malinina, L.; Phan, A. T.; Hobartner, C.; Micura, R.; Breaker, R. R.; Patel, D. J., Structural Basis for Discriminative Regulation of Gene Expression by Adenine- and Guanine-Sensing mRNAs. *Chem. Biol.* **2004,** *11* (12), 1729-1741.

39. Garst, A. D.; Héroux, A.; Rambo, R. P.; Batey, R. T., Crystal Structure of the Lysine Riboswitch Regulatory mRNA Element. *J. Biol. Chem.* **2008,** *283* (33), 22347-22351.

40. Serganov, A.; Huang, L.; Patel, D. J., Coenzyme Recognition and Gene Regulation by a Flavin Mononucleotide Riboswitch. *Nature* **2009,** *458* (7235), 233-237.

41. Sengupta, A.; Sung, H.-L.; Nesbitt, D. J., Amino Acid Specific Effects on RNA Tertiary Interactions: Single-Molecule Kinetic and Thermodynamic Studies. *J. Phys. Chem. B* **2016,** *120* (41), 10615-10627.

42. Holmstrom, E. D.; Nesbitt, D. J., Single-Molecule Fluorescence Resonance Energy Transfer Studies of the Human Telomerase RNA Pseudoknot: Temperature-/Urea-Dependent Folding Kinetics and Thermodynamics. *J. Phys. Chem. B* **2014,** *118* (14), 3853-3863.

43. Sung, H.-L.; Nesbitt, D. J., DNA Hairpin Hybridization under Extreme Pressures: A Single-Molecule FRET Study. *J. Phys. Chem. B* **2020,** *124* (1), 110-120.

44. Fiore, J. L.; Holmstrom, E. D.; Fiegland, L. R.; Hodak, J. H.; Nesbitt, D. J., The Role of Counterion Valence and Size in GAAA Tetraloop–Receptor Docking/Undocking Kinetics. *J. Mol. Biol.* **2012,** *423* (2), 198-216.

45. Qin, F.; Auerbach, A.; Sachs, F., A Direct Optimization Approach to Hidden Markov Modeling for Single Channel Kinetics. *Biophys. J.* **2000,** *79* (4), 1915-1927.

46. Andrec, M.; Levy, R. M.; Talaga, D. S., Direct Determination of Kinetic Rates from Single-Molecule Photon Arrival Trajectories Using Hidden Markov Models. *J. Phys. Chem. A* **2003,** *107* (38), 7454-7464.

47. Schröder, G. F.; Grubmüller, H., Maximum Likelihood Trajectories from Single Molecule Fluorescence Resonance Energy Transfer Experiments. *J. Chem. Phys.* **2003,** *119* (18), 9920-9924.

48. McKinney, S. A.; Joo, C.; Ha, T., Analysis of Single-Molecule FRET Trajectories Using Hidden Markov Modeling. *Biophys. J.* **2006,** *91* (5), 1941-1951.

49. Forsén, S.; Linse, S., Cooperativity: over the Hill. *Trends Biochem. Sci.* **1995,** *20* (12), 495-497.

50. Schroeder, Kersten T.; Daldrop, P.; Lilley, David M. J., RNA Tertiary Interactions in a Riboswitch Stabilize the Structure of a Kink Turn. *Structure* **2011,** *19* (9), 1233-1240.

51. Fiegland, L. R.; Garst, A. D.; Batey, R. T.; Nesbitt, D. J., Single-Molecule Studies of the Lysine Riboswitch Reveal Effector-Dependent Conformational Dynamics of the Aptamer Domain. *Biochemistry* **2012,** *51* (45), 9223-9233.

52. Draper, D. E.; Grilley, D.; Soto, A. M., Ions and RNA Folding. *Annu. Rev. Biophys. Biomol. Struct.* **2005,** *34* (1), 221-243.

53. Woodson, S. A., Metal Ions and RNA Folding: a Highly Charged Topic with a Dynamic Future. *Curr. Opin. Chem. Biol.* **2005,** *9* (2), 104-109.

54. Goody, T. A.; Melcher, S. E.; Norman, D. G.; Lilley, D. M. J., The Kink-Turn motif in RNA is Dimorphic, and Metal Ion-Dependent. *RNA* **2004,** *10* (2), 254-264.

55. Hohng, S.; Wilson, T. J.; Tan, E.; Clegg, R. M.; Lilley, D. M. J.; Ha, T., Conformational Flexibility of Four-way Junctions in RNA. *J. Mol. Biol.* **2004,** *336* (1), 69-79.

56. Holmstrom, E. D.; Fiore, J. L.; Nesbitt, D. J., Thermodynamic Origins of Monovalent Facilitated RNA Folding. *Biochemistry* **2012,** *51* (18), 3732-3743.

57. Irudayam, S. J.; Henchman, R. H., Entropic Cost of Protein−Ligand Binding and Its Dependence on the Entropy in Solution. *J. Phys. Chem. B* **2009,** *113* (17), 5871-5884.

58. Zhou, H.-X.; Gilson, M. K., Theory of Free Energy and Entropy in Noncovalent Binding. *Chem. Rev.* **2009,** *109* (9), 4092-4107.

59. Kramers, H. A., Brownian Motion in a Field of Force and the Diffusion Model of Chemical Reactions. *Physica* **1940,** *7* (4), 284-304.

60. Grote, R. F.; Hynes, J. T., The Stable States Picture of Chemical Reactions. II. Rate Constants for Condensed and Gas Phase Reaction Models. *J. Chem. Phys.* **1980,** *73* (6), 2715-2732.

61. Szabo, A.; Schulten, K.; Schulten, Z., First Passage Time Approach to Diffusion Controlled Reactions. *J. Chem. Phys.* **1980,** *72* (8), 4350-4357.

62. Zwanzig, R.; Szabo, A.; Bagchi, B., Levinthal's Paradox. *Proc. Natl. Acad. Sci. U.S.A.* **1992,** *89* (1), 20-22.

63. Weiss, J. N., The Hill Equation Revisited: Uses and Misuses. *FASEB J.* **1997,** *11* (11), 835-841.

64. Leipply, D.; Draper, D. E., Dependence of RNA Tertiary Structural Stability on Mg^{2+} Concentration: Interpretation of the Hill Equation and Coefficient. *Biochemistry* **2010,** *49* (9), 1843-1853.

65. Goldbeter, A.; Koshland, D. E., An Amplified Sensitivity Arising from Covalent Modification in Biological Systems. *Proc. Natl. Acad. Sci. U.S.A.* **1981,** *78* (11), 6840-6844.

66. Ralston, D. M.; O'Halloran, T. V., Ultrasensitivity and Heavy-Metal Selectivity of the Allosterically Modulated MerR Transcription Complex. *Proc. Natl. Acad. Sci. U.S.A.* **1990,** *87* (10), 3846-3850.

67. Xu, J.; Cotruvo, J. A., The czcD (NiCo) Riboswitch Responds to Iron(II). *Biochemistry* **2020,** *59* (15), 1508-1516.

68. Minton, A. P., Macromolecular Crowding and Molecular Recognition. *J. Mol. Recognit.* **1993,** *6* (4), 211-214.

69. Zhou, H.-X.; Rivas, G.; Minton, A. P., Macromolecular Crowding and Confinement: Biochemical, Biophysical, and Potential Physiological Consequences. *Annu. Rev. Biophys.* **2008,** *37* (1), 375-397.

70. Reynolds, C. H.; Holloway, M. K., Thermodynamics of Ligand Binding and Efficiency. *ACS Med. Chem. Lett.* **2011,** *2* (6), 433-437.

71. Marchand, A.; Rosu, F.; Zenobi, R.; Gabelica, V., Thermal Denaturation of DNA G-Quadruplexes and Their Complexes with Ligands: Thermodynamic Analysis of the Multiple States Revealed by Mass Spectrometry. *J. Am. Chem. Soc.* **2018,** *140* (39), 12553-12565.

72. Gallicchio, E.; Kubo, M. M.; Levy, R. M., Entropy−Enthalpy Compensation in Solvation and Ligand Binding Revisited. *J. Am. Chem. Soc.* **1998,** *120* (18), 4526-4527.

Chapter 6 Smaller Molecules Crowd Better: Crowder Size Dependence Revealed by Single-Molecule FRET Studies and Depletion Force Modeling Analysis

1. Caprara, M. G.; Nilsen, T. W., RNA: Versatility in Form and Function. *Nat. Struct. Biol.* **2000,** *7* (10), 831-833.

2. Brion, P.; Westhof, E., Hierarchy and Dynamics of RNA Folding. *Annu. Rev. Biophys. Biomol. Struct.* **1997,** *26* (1), 113-137.

3. Draper, D. E.; Grilley, D.; Soto, A. M., Ions and RNA Folding. *Annu. Rev. Biophys. Biomol. Struct.* **2005,** *34* (1), 221-243.

4. Fulton, A. B., How Crowded is the Cytoplasm? *Cell* **1982,** *30* (2), 345-347.

5. Ellis, R. J., Macromolecular Crowding: Obvious but Underappreciated. *Trends Biochem. Sci.* **2001,** *26* (10), 597-604.

6. Minton, A. P., The Influence of Macromolecular Crowding and Macromolecular Confinement on Biochemical Reactions in Physiological Media. *J. Biol. Chem.* **2001,** *276* (14), 10577-10580.

7. Zhou, H.-X.; Rivas, G.; Minton, A. P., Macromolecular Crowding and Confinement: Biochemical, Biophysical, and Potential Physiological Consequences. *Annu. Rev. Biophys.* **2008,** *37* (1), 375-397.

8. Nakano, S.-i.; Karimata, H.; Ohmichi, T.; Kawakami, J.; Sugimoto, N., The Effect of Molecular Crowding with Nucleotide Length and Cosolute Structure on DNA Duplex Stability. *J. Am. Chem. Soc.* **2004,** *126* (44), 14330-14331.

9. Zheng, K.-w.; Chen, Z.; Hao, Y.-h.; Tan, Z., Molecular Crowding Creates an Essential Environment for the Formation of Stable G-Quadruplexes in Long Double-Stranded DNA. *Nucleic Acids Res.* **2010,** *38* (1), 327-338.

10. Knowles, D. B.; LaCroix, A. S.; Deines, N. F.; Shkel, I.; Record, M. T., Separation of Preferential Interaction and Excluded Volume Effects on DNA Duplex and Hairpin Stability. *Proc. Natl. Acad. Sci. U.S.A.* **2011,** *108* (31), 12699-12704.

11. Dupuis, N. F.; Holmstrom, E. D.; Nesbitt, D. J., Molecular-Crowding Effects on Single-Molecule RNA Folding/Unfolding Thermodynamics and Kinetics. *Proc. Natl. Acad. Sci. U.S.A.* **2014,** *111* (23), 8464-8469.

12. Paudel, B. P.; Rueda, D., Molecular Crowding Accelerates Ribozyme Docking and Catalysis. *J. Am. Chem. Soc.* **2014,** *136* (48), 16700-16703.

13. Baltierra-Jasso, L. E.; Morten, M. J.; Laflör, L.; Quinn, S. D.; Magennis, S. W., Crowding-Induced Hybridization of Single DNA Hairpins. *J. Am. Chem. Soc.* **2015,** *137* (51), 16020-16023.

14. Minton, A. P., Excluded Volume as a Determinant of Macromolecular Structure and Reactivity. *Biopolymers* **1981,** *20* (10), 2093-2120.

15. Kilburn, D.; Roh, J. H.; Guo, L.; Briber, R. M.; Woodson, S. A., Molecular Crowding Stabilizes Folded RNA Structure by the Excluded Volume Effect. *J. Am. Chem. Soc.* **2010,** *132* (25), 8690-8696.

16. Soranno, A.; Koenig, I.; Borgia, M. B.; Hofmann, H.; Zosel, F.; Nettels, D.; Schuler, B., Single-Molecule Spectroscopy Reveals Polymer Effects of Disordered Proteins in Crowded Environments. *Proc. Natl. Acad. Sci. U. S. A.* **2014,** *111* (13), 4874-4879.

17. Bai, J.; Liu, M.; Pielak, G. J.; Li, C., Macromolecular and Small Molecular Crowding Have Similar Effects on α-Synuclein Structure. *ChemPhysChem* **2017,** *18* (1), 55-58.

18. Das, N.; Sen, P., Size-dependent Macromolecular Crowding Effect on the Thermodynamics of Protein Unfolding Revealed at the Single Molecular Level. *Int. J. Biol. Macromol.* **2019,** *141*, 843-854.

19. Cho, S. S.; Reddy, G.; Straub, J. E.; Thirumalai, D., Entropic Stabilization of Proteins by TMAO. *J. Phys. Chem. B* **2011,** *115* (45), 13401-13407.

20. Denesyuk, N. A.; Thirumalai, D., Crowding Promotes the Switch from Hairpin to Pseudoknot Conformation in Human Telomerase RNA. *J. Am. Chem. Soc.* **2011,** *133* (31), 11858-11861.

21. Denesyuk, N. A.; Thirumalai, D., Entropic Stabilization of the Folded States of RNA Due to Macromolecular Crowding. *Biophys. Rev.* **2013,** *5* (2), 225-232.

22. Kang, H.; Pincus, P. A.; Hyeon, C.; Thirumalai, D., Effects of Macromolecular Crowding on the Collapse of Biopolymers. *Phys. Rev. Lett.* **2015,** *114* (6), 068303.

23. Hilaire, M. R.; Abaskharon, R. M.; Gai, F., Biomolecular Crowding Arising from Small Molecules, Molecular Constraints, Surface Packing, and Nano-Confinement. *J. Phys. Chem. Lett.* **2015,** *6* (13), 2546-2553.

24. Lebowitz, J. L.; Helfand, E.; Praestgaard, E., Scaled Particle Theory of Fluid Mixtures. *J. Chem. Phys.* **1965,** *43* (3), 774-779.

25. Sharp, K. A., Analysis of the Size Dependence of Macromolecular Crowding Shows That Smaller is Better. *Proc. Natl. Acad. Sci. U.S.A.* **2015,** *112* (26), 7990-7995.

26. Holmstrom, E. D.; Dupuis, N. F.; Nesbitt, D. J., Kinetic and Thermodynamic Origins of Osmolyte-Influenced Nucleic Acid Folding. *J. Phys. Chem. B* **2015,** *119* (9), 3687-3696.

27. Culik, R. M.; Abaskharon, R. M.; Pazos, I. M.; Gai, F., Experimental Validation of the Role of Trifluoroethanol as a Nanocrowder. *J. Phys. Chem. B* **2014,** *118* (39), 11455-11461.

28. Verma, P. K.; Kundu, A.; Cho, M., How Molecular Crowding Differs from Macromolecular Crowding: A Femtosecond Mid-Infrared Pump–Probe Study. *J. Phys. Chem. Lett.* **2018,** *9* (22), 6584-6592.

29. Ydoshida, K.; Yamaguchi, T., Low-frequency Raman Spectroscopy of Aqueous Solutions of Aliphatic Alcohols. *Z. Naturforsch. A* **2001,** *56* (8), 529-536.

30. Roney, A. B.; Space, B.; Castner, E. W.; Napoleon, R. L.; Moore, P. B., A Molecular Dynamics Study of Aggregation Phenomena in Aqueous n-Propanol. *J. Phys. Chem. B* **2004,** *108* (22), 7389-7401.

31. Chodzińska, A.; Zdziennicka, A.; Jańczuk, B., Volumetric and Surface Properties of Short Chain Alcohols in Aqueous Solution–Air Systems at 293 K. *J. Solution Chem.* **2012,** *41* (12), 2226-2245.

32. Fiore, J. L.; Holmstrom, E. D.; Fiegland, L. R.; Hodak, J. H.; Nesbitt, D. J., The Role of Counterion Valence and Size in GAAA Tetraloop–Receptor Docking/Undocking Kinetics. *J. Mol. Biol.* **2012,** *423* (2), 198-216.

33. Fiore, J. L.; Holmstrom, E. D.; Nesbitt, D. J., Entropic Origin of Mg^{2+}-Facilitated RNA Folding. *Proc. Natl. Acad. Sci. U.S.A.* **2012,** *109* (8), 2902-2907.

34. Sengupta, A.; Sung, H.-L.; Nesbitt, D. J., Amino Acid Specific Effects on RNA Tertiary Interactions: Single-Molecule Kinetic and Thermodynamic Studies. *J. Phys. Chem. B* **2016,** *120* (41), 10615-10627.

35. Sung, H.-L.; Nesbitt, D. J., Novel Heat-Promoted Folding Dynamics of the yybP-ykoY Manganese Riboswitch: Kinetic and Thermodynamic Studies at the Single-Molecule Level. *J. Phys. Chem. B* **2019,** *123* (26), 5412-5422.

36. Asakura, S.; Oosawa, F., On Interaction between Two Bodies Immersed in a Solution of Macromolecules. *J. Chem. Phys.* **1954,** *22* (7), 1255-1256.

37. Marenduzzo, D.; Finan, K.; Cook, P. R., The Depletion Attraction: an Underappreciated Force Driving Cellular Organization. *J. Cell Biol.* **2006,** *175* (5), 681-686.

38. Trokhymchuk, A.; Henderson, D., Depletion Forces in Bulk and in Confined Domains: From Asakura–Oosawa to Recent Statistical Physics Advances. *Curr. Opin. Colloid Interface Sci.* **2015,** *20* (1), 32-38.

39. Aitken, C. E.; Marshall, R. A.; Puglisi, J. D., An Oxygen Scavenging System for Improvement of Dye Stability in Single-Molecule Fluorescence Experiments. *Biophys. J.* **2008,** *94* (5), 1826-1835.

40. Sung, H.-L.; Nesbitt, D. J., Sequential Folding of the Nickel/Cobalt Riboswitch Is Facilitated by a Conformational Intermediate: Insights from Single-Molecule Kinetics and Thermodynamics. *J. Phys. Chem. B* **2020,** *124* (34), 7348-7360.

41. Cate, J. H.; Gooding, A. R.; Podell, E.; Zhou, K.; Golden, B. L.; Kundrot, C. E.; Cech, T. R.; Doudna, J. A., Crystal Structure of a Group I Ribozyme Domain: Principles of RNA Packing. *Science* **1996,** *273* (5282), 1678-1685.

42. Sung, H.-L.; Nesbitt, D. J., Single-Molecule FRET Kinetics of the Mn2+ Riboswitch: Evidence for Allosteric Mg2+ Control of "Induced-Fit" vs "Conformational Selection" Folding Pathways. *J. Phys. Chem. B* **2019,** *123* (9), 2005-2015.

43. Hodak, J. H.; Fiore, J. L.; Nesbitt, D. J.; Downey, C. D.; Pardi, A., Docking Kinetics and Equilibrium of a GAAA Tetraloop-Receptor Motif Probed by Single-Molecule FRET. *Proc. Natl. Acad. Sci. U. S. A.* **2005,** *102* (30), 10505.

44. Sung, H.-L.; Nesbitt, D. J., Single-Molecule Kinetic Studies of DNA Hybridization Under Extreme Pressures. *Phys. Chem. Chem. Phys.* **2020,** *22* (41), 23491-23501.

45. Zhou, H.-X., Rate Theories for Biologists. *Quarterly Reviews of Biophysics* **2010,** *43* (2), 219-293.

46. Gorensek-Benitez, A. H.; Smith, A. E.; Stadmiller, S. S.; Perez Goncalves, G. M.; Pielak, G. J., Cosolutes, Crowding, and Protein Folding Kinetics. *J. Phys. Chem. B* **2017,** *121* (27), 6527-6537.

47. Kilburn, D.; Roh, J. H.; Behrouzi, R.; Briber, R. M.; Woodson, S. A., Crowders Perturb the Entropy of RNA Energy Landscapes to Favor Folding. *J. Am. Chem. Soc.* **2013,** *135* (27), 10055-10063.

48. Shelton, V. M.; Sosnick, T. R.; Pan, T., Applicability of Urea in the Thermodynamic Analysis of Secondary and Tertiary RNA Folding. *Biochemistry* **1999,** *38* (51), 16831-16839.

49. Devanand, K.; Selser, J. C., Asymptotic behavior and long-range interactions in aqueous solutions of poly(ethylene oxide). *Macromolecules* **1991,** *24* (22), 5943-5947.

50. Mitchison, T. J., Colloid Osmotic Parameterization and Measurement of Subcellular Crowding. *Mol. Biol. Cell* **2019,** *30* (2), 173-180.

51. Lee, H.-C.; Jiang, H.-R., Directed aggregation of carbon nanotube on curved surfaces by polymer induced depletion attraction. *AIP Adv.* **2017,** *7* (12), 125228.

52. McKenzie, D. S., Polymers and Scaling. *Phys. Rep.* **1976,** *27* (2), 35-88.

53. Pietronero, L., Critical Dimensionality and Exponent of the "True" Self-Avoiding Walk. *Phys. Rev. B* **1983,** *27* (9), 5887-5889.

54. Leung, B. O.; Yang, Z.; Wu, S. S. H.; Chou, K. C., Role of Interfacial Water on Protein Adsorption at Cross-Linked Polyethylene Oxide Interfaces. *Langmuir* **2012,** *28* (13), 5724-5728.

55. Leng, C.; Hung, H.-C.; Sun, S.; Wang, D.; Li, Y.; Jiang, S.; Chen, Z., Probing the Surface Hydration of Nonfouling Zwitterionic and PEG Materials in Contact with Proteins. *ACS Appl. Mater. Interfaces* **2015,** *7* (30), 16881-16888.

56. Money, N. P., Osmotic Pressure of Aqueous Polyethylene Glycols: Relationship between Molecular Weight and Vapor Pressure Deficit. *Plant Physiol.* **1989,** *91* (2), 766-769.

57. Gonzalez-Tello, P.; Camacho, F.; Blazquez, G., Density and Viscosity of Concentrated Aqueous Solutions of Polyethylene Glycol. *J. Chem. Eng. Data* **1994,** *39* (3), 611-614.

Chapter 7 The Effects of Molecular Crowders on Single Molecule Nucleic Acid Folding: Temperature Dependent Studies Reveal True Crowding vs. Enthalpic Interactions

1. Fulton, A. B., How Crowded is the Cytoplasm? *Cell* **1982,** *30* (2), 345-347.

2. Ellis, R. J., Macromolecular Crowding: Obvious but Underappreciated. *Trends Biochem. Sci.* **2001,** *26* (10), 597-604.

3. Minton, A. P., The Influence of Macromolecular Crowding and Macromolecular Confinement on Biochemical Reactions in Physiological Media. *J. Biol. Chem.* **2001,** *276* (14), 10577-10580.

4. Gnutt, D.; Ebbinghaus, S., The Macromolecular Crowding Effect – from *in vitro* into the Cell. *Biol. Chem.* **2016,** *397* (1), 37-44.

5. Minton, A. P., Excluded Volume as a Determinant of Macromolecular Structure and Reactivity. *Biopolymers* **1981,** *20* (10), 2093-2120.

6. Gnutt, D.; Gao, M.; Brylski, O.; Heyden, M.; Ebbinghaus, S., Excluded-Volume Effects in Living Cells. *Angew. Chem.* **2015,** *54* (8), 2548-2551.

7. Cheung, M. S.; Klimov, D.; Thirumalai, D., Molecular Crowding Enhances Native State stability and Refolding Rates of Globular Proteins. *Proc. Natl. Acad. Sci. U.S.A.* **2005,** *102* (13), 4753.

8. Zheng, K.-w.; Chen, Z.; Hao, Y.-h.; Tan, Z., Molecular Crowding Creates an Essential Environment for the Formation of Stable G-Quadruplexes in Long Double-Stranded DNA. *Nucleic Acids Res.* **2009,** *38* (1), 327-338.

9. Miyoshi, D.; Sugimoto, N., Molecular Crowding Effects on Structure and Stability of DNA. *Biochimie* **2008,** *90* (7), 1040-1051.

10. Tokuriki, N.; Kinjo, M.; Negi, S.; Hoshino, M.; Goto, Y.; Urabe, I.; Yomo, T., Protein Folding by the Effects of Macromolecular Crowding. *Protein Sci.* **2004,** *13* (1), 125-133.

11. Denos, S.; Dhar, A.; Gruebele, M., Crowding Effects on the Small, Fast-Folding Protein λ_{6-85}. *Faraday Discuss.* **2012,** *157* (0), 451-462.

12. Politou, A.; Temussi, P. A., Revisiting a Dogma: the Effect of Volume Exclusion in Molecular Crowding. *Curr. Opin. Struct. Biol.* **2015,** *30*, 1-6.

13. Blümmel, J.; Perschmann, N.; Aydin, D.; Drinjakovic, J.; Surrey, T.; Lopez-Garcia, M.; Kessler, H.; Spatz, J. P., Protein Repellent Properties of Covalently Attached PEG Coatings on Nanostructured SiO2-Based Interfaces. *Biomaterials* **2007,** *28* (32), 4739-4747.

14. Schulz, A.; Woolley, R.; Tabarin, T.; McDonagh, C., Dextran-Coated Silica Nanoparticles for Calcium-Sensing. *Analyst* **2011,** *136* (8), 1722-1727.

15. Kilburn, D.; Roh, J. H.; Guo, L.; Briber, R. M.; Woodson, S. A., Molecular Crowding Stabilizes Folded RNA Structure by the Excluded Volume Effect. *J. Am. Chem. Soc* **2010,** *132* (25), 8690-8696.

16. Sasahara, K.; McPhie, P.; Minton, A. P., Effect of Dextran on Protein Stability and Conformation Attributed to Macromolecular Crowding. *J. Mol. Biol.* **2003,** *326* (4), 1227-1237.

17. Dupuis, N. F.; Holmstrom, E. D.; Nesbitt, D. J., Molecular-Crowding Effects on Single-Molecule RNA Folding/Unfolding Thermodynamics and Kinetics. *Proc. Natl. Acad. Sci. U.S.A.* **2014,** *111* (23), 8464.

18. Minton, A. P., Models for Excluded Volume Interaction between an Unfolded Protein and Rigid Macromolecular Cosolutes: Macromolecular Crowding and Protein Stability Revisited. *Biophys. J.* **2005,** *88* (2), 971-985.

19. Christiansen, A.; Wittung-Stafshede, P., Synthetic Crowding Agent Dextran Causes Excluded Volume Interactions Exclusively to Tracer Protein Apoazurin. *FEBS Lett.* **2014,** *588* (5), 811-814.

20. Kilburn, D.; Behrouzi, R.; Lee, H.-T.; Sarkar, K.; Briber, R. M.; Woodson, S. A., Entropic Stabilization of Folded RNA in Crowded Solutions Measured by SAXS. *Nucleic Acids Res.* **2016,** *44* (19), 9452-9461.

21. Halpin, J. C.; Huang, B.; Sun, M.; Street, T. O., Crowding Activates Heat Shock Protein 90. *J. Biol. Chem.* **2016,** *291* (12), 6447-6455.

22. Mukherjee, S.; Waegele, M. M.; Chowdhury, P.; Guo, L.; Gai, F., Effect of Macromolecular Crowding on Protein Folding Dynamics at the Secondary Structure Level. *J. Mol. Biol.* **2009,** *393* (1), 227-236.

23. Benton, L. A.; Smith, A. E.; Young, G. B.; Pielak, G. J., Unexpected Effects of Macromolecular Crowding on Protein Stability. *Biochem.* **2012,** *51* (49), 9773-9775.

24. Senske, M.; Törk, L.; Born, B.; Havenith, M.; Herrmann, C.; Ebbinghaus, S., Protein Stabilization by Macromolecular Crowding through Enthalpy Rather Than Entropy. *J. Am. Chem. Soc* **2014,** *136* (25), 9036-9041.

25. Das, N.; Sen, P., Shape-Dependent Macromolecular Crowding on the Thermodynamics and Microsecond Conformational Dynamics of Protein Unfolding Revealed at the Single-Molecule Level. *J. Phys. Chem. B* **2020,** *124* (28), 5858-5871.

26. Miyoshi, D.; Nakao, A.; Sugimoto, N., Molecular Crowding Regulates the Structural Switch of the DNA G-Quadruplex. *Biochem.* **2002,** *41* (50), 15017-15024.

27. Knowles, D. B.; LaCroix, A. S.; Deines, N. F.; Shkel, I.; Record, M. T., Separation of Preferential Interaction and Excluded Volume Effects on DNA Duplex and Hairpin Stability. *Proc. Natl. Acad. Sci. U.S.A.* **2011,** *108* (31), 12699.

28. Nakano, S.-i.; Miyoshi, D.; Sugimoto, N., Effects of Molecular Crowding on the Structures, Interactions, and Functions of Nucleic Acids. *Chem. Rev.* **2014,** *114* (5), 2733-2758.

29. Fiore, J. L.; Holmstrom, E. D.; Nesbitt, D. J., Entropic Origin of Mg^{2+}-Facilitated RNA Folding. *Proc. Natl. Acad. Sci. U.S.A.* **2012,** *109* (8), 2902.

30. Sung, H.-L.; Nesbitt, D. J., Novel Heat-Promoted Folding Dynamics of the *yybP-ykoY* Manganese Riboswitch: Kinetic and Thermodynamic Studies at the Single-Molecule Level. *J. Phys. Chem. B* **2019,** *123* (26), 5412-5422.

31. Nicholson, D. A.; Sengupta, A.; Sung, H.-L.; Nesbitt, D. J., Amino Acid Stabilization of Nucleic Acid Secondary Structure: Kinetic Insights from Single-Molecule Studies. *J. Phys. Chem. B* **2018,** *122* (43), 9869-9876.

32. Sung, H.-L.; Nesbitt, D. J., DNA Hairpin Hybridization under Extreme Pressures: A Single-Molecule FRET Study. *J. Phys. Chem. B* **2020,** *124* (1), 110-120.

33. Fiore, J. L.; Kraemer, B.; Koberling, F.; Edmann, R.; Nesbitt, D. J., Enthalpy-Driven RNA Folding: Single-Molecule Thermodynamics of Tetraloop−Receptor Tertiary Interaction. *Biochem.* **2009,** *48* (11), 2550-2558.

34. Aitken, C. E.; Marshall, R. A.; Puglisi, J. D., An Oxygen Scavenging System for Improvement of Dye Stability in Single-Molecule Fluorescence Experiments. *Biophys. J.* **2008,** *94* (5), 1826-1835.

35. Sengupta, A.; Sung, H.-L.; Nesbitt, D. J., Amino Acid Specific Effects on RNA Tertiary Interactions: Single-Molecule Kinetic and Thermodynamic Studies. *J. Phys. Chem. B* **2016,** *120* (41), 10615-10627.

36. Sung, H.-L.; Nesbitt, D. J., Sequential Folding of the Nickel/Cobalt Riboswitch Is Facilitated by a Conformational Intermediate: Insights from Single-Molecule Kinetics and Thermodynamics. *J. Phys. Chem. B* **2020,** *124* (34), 7348-7360.

37. Holmstrom, E. D.; Nesbitt, D. J., Biophysical Insights from Temperature-Dependent Single-Molecule Förster Resonance Energy Transfer. *Annu. Rev. Phys. Chem.* **2016,** *67* (1), 441-465.

38. Sung, H.-L.; Nesbitt, D. J., Single-Molecule Kinetic Studies of DNA Hybridization Under Extreme Pressures. *Phys. Chem. Chem. Phys.* **2020,** *22* (41), 23491-23501.

39. Fiore, J. L.; Holmstrom, E. D.; Fiegland, L. R.; Hodak, J. H.; Nesbitt, D. J., The Role of Counterion Valence and Size in GAAA Tetraloop–Receptor Docking/Undocking Kinetics. *J. Mol. Biol.* **2012,** *423* (2), 198-216.

40. Baltierra-Jasso, L. E.; Morten, M. J.; Laflör, L.; Quinn, S. D.; Magennis, S. W., Crowding-Induced Hybridization of Single DNA Hairpins. *J. Am. Chem. Soc* **2015,** *137* (51), 16020-16023.

41. Patra, S.; Schuabb, V.; Kiesel, I.; Knop, J.-M.; Oliva, R.; Winter, R., Exploring the Effects of Cosolutes and Crowding on the Volumetric and Kinetic Profile of the Conformational Dynamics of a Poly dA Loop DNA Hairpin: a Single-Molecule FRET Study. *Nucleic Acids Res.* **2018,** *47* (2), 981-996.

42. Vander Meulen, K. A.; Davis, J. H.; Foster, T. R.; Record, M. T.; Butcher, S. E., Thermodynamics and Folding Pathway of Tetraloop Receptor-Mediated RNA Helical Packing. *J. Mol. Biol.* **2008,** *384* (3), 702-717.

43. Sung, H.-L.; Sengupta, A.; Nesbitt, D., Smaller Molecules Crowd Better: Crowder Size Dependence Revealed by Single-Molecule FRET Studies and Depletion Force Modeling Analysis. *J. Chem. Phys.* **2021,** *154* (15), 155101.

44. Greene, R. F.; Pace, C. N., Urea and Guanidine Hydrochloride Denaturation of Ribonuclease, Lysozyme, *α*-Chymotrypsin, and *b*-Lactoglobulin. *J. Biol. Chem.* **1974,** *249* (17), 5388-5393.

45. Holmstrom, E. D.; Dupuis, N. F.; Nesbitt, D. J., Kinetic and Thermodynamic Origins of Osmolyte-Influenced Nucleic Acid Folding. *J. Phys. Chem. B* **2015,** *119* (9), 3687-3696.

46. Yi, Q.; Scalley, M. L.; Simons, K. T.; Gladwin, S. T.; Baker, D., Characterization of the Free Energy Spectrum of Peptostreptococcal Protein L. *Fold. Des.* **1997,** *2* (5), 271-280.

47. Shelton, V. M.; Sosnick, T. R.; Pan, T., Applicability of Urea in the Thermodynamic Analysis of Secondary and Tertiary RNA Folding. *Biochem.* **1999,** *38* (51), 16831-16839.

48. Auton, M.; Bolen, D. W., Predicting the Energetics of Osmolyte-Induced Protein Folding/Unfolding. *Proc. Natl. Acad. Sci. U.S.A.* **2005,** *102* (42), 15065.

49. Wartell, R. M.; Benight, A. S., Thermal Denaturation of DNA Molecules: A Comparison of Theory with Experiment. *Phys. Rep.* **1985,** *126* (2), 67-107.

50. Privalov, P. L., Thermodynamics of Protein Folding. *J. Chem. Thermodyn.* **1997,** *29* (4), 447-474.

51. Dupuis, Nicholas F.; Holmstrom, Erik D.; Nesbitt, David J., Single-Molecule Kinetics Reveal Cation-Promoted DNA Duplex Formation Through Ordering of Single-Stranded Helices. *Biophys. J.* **2013,** *105* (3), 756-766.

52. Zhou, H.-X., Rate Theories for Biologists. *Q. Rev. Biophys.* **2010,** *43* (2), 219-293.

53. Szabo, A.; Schulten, K.; Schulten, Z., First Passage Time Approach to Diffusion Controlled Reactions. *J. Chem. Phys.* **1980,** *72* (8), 4350-4357.

54. Paudel, B. P.; Rueda, D., Molecular Crowding Accelerates Ribozyme Docking and Catalysis. *J. Am. Chem. Soc* **2014,** *136* (48), 16700-16703.

55. Tyrrell, J.; Weeks, K. M.; Pielak, G. J., Challenge of Mimicking the Influences of the Cellular Environment on RNA Structure by PEG-Induced Macromolecular Crowding. *Biochem.* **2015,** *54* (42), 6447-6453.

56. Sharma, G. S.; Mittal, S.; Singh, L. R., Effect of Dextran 70 on the Thermodynamic and Structural Properties of Proteins. *Int. J. Biol. Macromol.* **2015,** *79*, 86-94.

57. Malik, A.; Kundu, J.; Mukherjee, S. K.; Chowdhury, P. K., Myoglobin Unfolding in Crowding and Confinement. *J. Phys. Chem. B* **2012,** *116* (43), 12895-12904.

58. Dunitz, J. D., Win Some, Lose Some: Enthalpy-Entropy Compensation in Weak Intermolecular Interactions. *Chem. Biol.* **1995,** *2* (11), 709-712.

59. Eftink, M. R.; Anusiem, A. C.; Biltonen, R. L., Enthalpy-Entropy Compensation and Heat Capacity Changes for Protein-Ligand Interactions: General Thermodynamic Models and Data for the Binding of Nucleotides to Ribonuclease A. *Biochem.* **1983,** *22* (16), 3884-3896.

Chapter 8 Synergism in the Molecular Crowding of Ligand-Induced Riboswitch Folding: Kinetic/Thermodynamic Insights from Single Molecule FRET Spectroscopy

1. Fulton, A. B., How Crowded is the Cytoplasm? *Cell* **1982,** *30* (2), 345-347.

2. Minton, A. P., Excluded Volume as a Determinant of Macromolecular Structure and Reactivity. *Biopolymers* **1981,** *20* (10), 2093-2120.

3. Ellis, R. J., Macromolecular Crowding: Obvious but Underappreciated. *Trends Biochem. Sci.* **2001,** *26* (10), 597-604.

4. Minton, A. P., The Influence of Macromolecular Crowding and Macromolecular Confinement on Biochemical Reactions in Physiological Media. *J. Biol. Chem.* **2001,** *276* (14), 10577-10580.

5. Nakano, S.-i.; Miyoshi, D.; Sugimoto, N., Effects of Molecular Crowding on the Structures, Interactions, and Functions of Nucleic Acids. *Chem. Rev.* **2014,** *114* (5), 2733-2758.

6. Cheung, M. S.; Klimov, D.; Thirumalai, D., Molecular Crowding Enhances Native State Stability and Refolding Rates of Globular Proteins. *Proc. Natl. Acad. Sci. U.S.A.* **2005,** *102* (13), 4753-4758.

7. Gnutt, D.; Ebbinghaus, S., The Macromolecular Crowding Effect – from in vitro into the Cell. *Biol. Chem.* **2016,** *397* (1), 37-44.

8. Zhou, H.-X.; Rivas, G.; Minton, A. P., Macromolecular Crowding and Confinement: Biochemical, Biophysical, and Potential Physiological Consequences. *Annu. Rev. Biophys.* **2008,** *37* (1), 375-397.

9. Rivas, G.; Minton, A. P., Macromolecular Crowding In Vitro, In Vivo, and In Between. *Trends Biochem. Sci.* **2016,** *41* (11), 970-981.

10. Politou, A.; Temussi, P. A., Revisiting a Dogma: the Effect of Volume Exclusion in Molecular Crowding. *Curr. Opin. Struct. Biol.* **2015,** *30*, 1-6.

11. Minton, A. P., Models for Excluded Volume Interaction between an Unfolded Protein and Rigid Macromolecular Cosolutes: Macromolecular Crowding and Protein Stability Revisited. *Biophys. J.* **2005,** *88* (2), 971-985.

12. Sasahara, K.; McPhie, P.; Minton, A. P., Effect of Dextran on Protein Stability and Conformation Attributed to Macromolecular Crowding. *J. Mol. Biol.* **2003,** *326* (4), 1227-1237.

13. Dupuis, N. F.; Holmstrom, E. D.; Nesbitt, D. J., Molecular-Crowding Effects on Single-Molecule RNA Folding/Unfolding Thermodynamics and Kinetics. *Proc. Natl. Acad. Sci. U.S.A.* **2014,** *111* (23), 8464-8469.

14. Sung, H.-L.; Sengupta, A.; Nesbitt, D., Smaller Molecules Crowd Better: Crowder Size Dependence Revealed by Single-Molecule FRET Studies and Depletion Force Modeling Analysis. *Chem. Phys.* **2021,** *154* (15), 155101.

15. Kilburn, D.; Roh, J. H.; Guo, L.; Briber, R. M.; Woodson, S. A., Molecular Crowding Stabilizes Folded RNA Structure by the Excluded Volume Effect. *J. Am. Chem. Soc.* **2010,** *132* (25), 8690-8696.

16. Nudler, E.; Mironov, A. S., The Riboswitch Control of Bacterial Metabolism. *Trends Biochem. Sci.* **2004,** *29* (1), 11-17.

17. Mironov, A. S.; Gusarov, I.; Rafikov, R.; Lopez, L. E.; Shatalin, K.; Kreneva, R. A.; Perumov, D. A.; Nudler, E., Sensing Small Molecules by Nascent RNA: A Mechanism to Control Transcription in Bacteria. *Cell* **2002,** *111* (5), 747-756.

18. Fiegland, L. R.; Garst, A. D.; Batey, R. T.; Nesbitt, D. J., Single-Molecule Studies of the Lysine Riboswitch Reveal Effector-Dependent Conformational Dynamics of the Aptamer Domain. *Biochemistry* **2012,** *51* (45), 9223-9233.

19. Marton Menendez, A.; Nesbitt, D. J., Lysine-Dependent Entropy Effects in the *B. subtilis* Lysine Riboswitch: Insights from Single-Molecule Thermodynamic Studies. *J. Phys. Chem. B* **2021**.

20. Zimmerman, S. B.; Harrison, B., Macromolecular Crowding Increases Binding of DNA Polymerase to DNA: an Adaptive Effect. *Proc. Natl. Acad. Sci. U.S.A.* **1987,** *84* (7), 1871-1875.

21. Ralston, G. B., Effects of "Crowding" in Protein Solutions. *J. Chem. Educ.* **1990,** *67* (10), 857.

22. Qu, Y.; Bolen, D. W., Efficacy of Macromolecular Crowding in Forcing Proteins to Fold. *Biophys. Chem.* **2002,** *101-102*, 155-165.

23. Tokuriki, N.; Kinjo, M.; Negi, S.; Hoshino, M.; Goto, Y.; Urabe, I.; Yomo, T., Protein Folding by the Effects of Macromolecular Crowding. *Protein Sci.* **2004,** *13* (1), 125-133.

24. Batra, J.; Xu, K.; Qin, S.; Zhou, H.-X., Effect of Macromolecular Crowding on Protein Binding Stability: Modest Stabilization and Significant Biological Consequences. *Biophys. J.* **2009,** *97* (3), 906-911.

25. Sung, H.-L.; Nesbitt, D. J., Effects of Molecular Crowders on Single-Molecule Nucleic Acid Folding: Temperature-Dependent Studies Reveal True Crowding vs Enthalpic Interactions. *J. Phys. Chem. B* **2021,** *125* (48), 13147-13157.

26. Sung, H.-L.; Nesbitt, D. J., Single-Molecule FRET Kinetics of the Mn^{2+} Riboswitch: Evidence for Allosteric Mg^{2+} Control of “Induced-Fit” vs “Conformational Selection” Folding Pathways. *J. Phys. Chem. B* **2019,** *123* (9), 2005-2015.

27. Fiore, J. L.; Holmstrom, E. D.; Nesbitt, D. J., Entropic Origin of Mg^{2+}-Facilitated RNA Folding. *Proc. Natl. Acad. Sci. U.S.A.* **2012,** *109* (8), 2902-2907.

28. Garst, A. D.; Héroux, A.; Rambo, R. P.; Batey, R. T., Crystal Structure of the Lysine Riboswitch Regulatory mRNA Element *J. Biol. Chem.* **2008,** *283* (33), 22347-22351.

29. Sung, H.-L.; Nesbitt, D. J., High Pressure Single-Molecule FRET Studies of the Lysine Riboswitch: Cationic and Osmolytic Effects on Pressure Induced Denaturation. *Phys. Chem. Chem. Phys.* **2020,** *22* (28), 15853-15866.

30. Sudarsan, N.; Wickiser, J. K.; Nakamura, S.; Ebert, M. S.; Breaker, R. R., An mRNA Structure in Bacteria That Controls Gene Expression by Binding Lysine. *Genes Dev.* **2003,** *17* (21), 2688-2697.

31. Aitken, C. E.; Marshall, R. A.; Puglisi, J. D., An Oxygen Scavenging System for Improvement of Dye Stability in Single-Molecule Fluorescence Experiments. *Biophys. J.* **2008,** *94* (5), 1826-1835.

32. Nicholson, D. A.; Sengupta, A.; Nesbitt, D. J., Chirality-Dependent Amino Acid Modulation of RNA Folding. *J. Phys. Chem. B* **2020,** *124* (51), 11561-11572.

33. McKinney, S. A.; Joo, C.; Ha, T., Analysis of Single-Molecule FRET Trajectories Using Hidden Markov Modeling. *Biophys. J.* **2006,** *91* (5), 1941-1951.

34. Sung, H.-L.; Nesbitt, D. J., Sequential Folding of the Nickel/Cobalt Riboswitch Is Facilitated by a Conformational Intermediate: Insights from Single-Molecule Kinetics and Thermodynamics. *J. Phys. Chem. B* **2020,** *124* (34), 7348-7360.

35. Sung, H.-L.; Nesbitt, D. J., Novel Heat-Promoted Folding Dynamics of the *yybP-ykoY* Manganese Riboswitch: Kinetic and Thermodynamic Studies at the Single-Molecule Level. *J. Phys. Chem. B* **2019,** *123* (26), 5412-5422.

36. Privalov, P. L., Thermodynamics of Protein Folding. *J. Chem. Thermodyn.* **1997,** *29* (4), 447-474.

37. Winzor, D. J.; Jackson, C. M., Interpretation of the Temperature Dependence of Equilibrium and Rate Constants. *J. Mol. Recognit.* **2006,** *19* (5), 389-407.

38. Zhou, H.-X., Rate Theories for Biologists. *Q. Rev. Biophys.* **2010,** *43* (2), 219-293.

39. Sengupta, A.; Sung, H.-L.; Nesbitt, D. J., Amino Acid Specific Effects on RNA Tertiary Interactions: Single-Molecule Kinetic and Thermodynamic Studies. *J. Phys. Chem. B* **2016,** *120* (41), 10615-10627.

40. Szabo, A.; Schulten, K.; Schulten, Z., First Passage Time Approach to Diffusion Controlled Reactions. *Chem. Phys.* **1980,** *72* (8), 4350-4357.

41. Pegram, L. M.; Wendorff, T.; Erdmann, R.; Shkel, I.; Bellissimo, D.; Felitsky, D. J.; Record, M. T., Why Hofmeister Effects of Many Salts Favor Protein Folding But Not DNA Helix Formation. *Proc. Natl. Acad. Sci. U.S.A.* **2010,** *107* (17), 7716-7721.

42. Courtenay, E. S.; Capp, M. W.; Record Jr., M. T., Thermodynamics of Interactions of Urea and Guanidinium Salts with Protein Surface: Relationship Between Solute Effects on Protein Processes and Changes in Water-Accessible Surface Area. *Protein Sci.* **2001,** *10* (12), 2485-2497.

43. Capp, M. W.; Pegram, L. M.; Saecker, R. M.; Kratz, M.; Riccardi, D.; Wendorff, T.; Cannon, J. G.; Record, M. T., Interactions of the Osmolyte Glycine Betaine with Molecular Surfaces in Water: Thermodynamics, Structural Interpretation, and Prediction of m-Values. *Biochemistry* **2009,** *48* (43), 10372-10379.

44. McCluskey, K.; Boudreault, J.; St-Pierre, P.; Perez-Gonzalez, C.; Chauvier, A.; Rizzi, A.; Beauregard, P. B.; Lafontaine, D. A.; Penedo, J. C., Unprecedented Tunability of Riboswitch Structure and Regulatory Function by Sub-Millimolar Variations in Physiological Mg^{2+}. *Nucleic Acids Res.* **2019,** *47* (12), 6478-6487.

45. Suddala, K. C.; Wang, J.; Hou, Q.; Walter, N. G., Mg^{2+} Shifts Ligand-Mediated Folding of a Riboswitch from Induced-Fit to Conformational Selection. *J. Am. Chem. Soc.* **2015,** *137* (44), 14075-14083.

46. Paudel, B. P.; Rueda, D., Molecular Crowding Accelerates Ribozyme Docking and Catalysis. *J. Am. Chem. Soc.* **2014,** *136* (48), 16700-16703.

47. Kilburn, D.; Roh, J. H.; Behrouzi, R.; Briber, R. M.; Woodson, S. A., Crowders Perturb the Entropy of RNA Energy Landscapes to Favor Folding. *J. Am. Chem. Soc.* **2013,** *135* (27), 10055-10063.

48. Knowles, D. B.; LaCroix, A. S.; Deines, N. F.; Shkel, I.; Record, M. T., Separation of Preferential Interaction and Excluded Volume Effects on DNA Duplex and Hairpin Stability. *Proc. Natl. Acad. Sci. U.S.A.* **2011,** *108* (31), 12699-12704.

Chapter 9 DNA Hairpin Hybridization under Extreme Pressures: A Single-Molecule FRET Study

1. Heremans, K.; Smeller, L. Protein Structure and Dynamics at High Pressure. *Biochim. Biophys. Acta, Protein Struct. Mol. Enzymol.* **1998,** *1386*, 353-370.

2. Smeller, L. Pressure–Temperature Phase Diagrams of Biomolecules. *Biochim. Biophys. Acta, Protein Struct. Mol. Enzymol.* **2002,** *1595*, 11-29.

3. Mozhaev, V. V.; Heremans, K.; Frank, J.; Masson, P.; Balny, C. High Pressure Effects on Protein Structure and Function. *Proteins* **1996,** *24*, 81-91.

4. Meersman, F.; Daniel, I.; Bartlett, D. H.; Winter, R.; Hazael, R.; McMillan, P. F. High-Pressure Biochemistry and Biophysics. *Rev. Mineral. Geochem.* **2013,** *75*, 607-648.

5. Somero, G. N. Adaptations to High Hydrostatic Pressure. *Annu. Rev. Physiol.* **1992,** *54*, 557-577.

6. Zhang, J.; Peng, X.; Jonas, A.; Jonas, J. NMR Study of the Cold, Heat, and Pressure Unfolding of Ribonuclease A. *Biochemistry* **1995,** *34*, 8631-8641.

7. Jonas, J.; Ballard, L.; Nash, D. High-Resolution, High-Pressure NMR Studies of Proteins. *Biophys. J.* **1998,** *75*, 445-452.

8. Schroer, M. A.; Paulus, M.; Jeworrek, C.; Krywka, C.; Schmacke, S.; Zhai, Y.; Wieland, D. C. F.; Sahle, C. J.; Chimenti, M.; Royer, C. A.; Garcia-Moreno, B.; Tolan, M.; Winter, R. High-Pressure SAXS Study of Folded and Unfolded Ensembles of Proteins. *Biophys. J.* **2010,** *99*, 3430-3437.

9. Fujisawa, T.; Kato, M.; Inoko, Y. Structural Characterization of Lactate Dehydrogenase Dissociation under High Pressure Studied by Synchrotron High-Pressure Small-Angle X-ray Scattering. *Biochemistry* **1999,** *38*, 6411-6418.

10. Krywka, C.; Sternemann, C.; Paulus, M.; Tolan, M.; Royer, C.; Winter, R. Effect of Osmolytes on Pressure-Induced Unfolding of Proteins: A High-Pressure SAXS Study. *ChemPhysChem* **2008,** *9*, 2809-2815.

11. Patra, S.; Anders, C.; Erwin, N.; Winter, R. Osmolyte Effects on the Conformational Dynamics of a DNA Hairpin at Ambient and Extreme Environmental Conditions. *Angew. Chem. Int. Ed.* **2017,** *56*, 5045-5049.

12. Smeller, L.; Fidy, J.; Heremans, K. Protein Folding, Unfolding and Aggregation. Pressure Induced Intermediate States on the Refolding Pathway of Horseradish Peroxidase. *J. Phys.: Condens. Matter* **2004,** *16*, S1053-S1058.

13. Silva, J. L.; Oliveira, A. C.; Gomes, A. M. O.; Lima, L. M. T. R.; Mohana-Borges, R.; Pacheco, A. B. F.; Foguel, D. Pressure Induces Folding Intermediates that are Crucial for Protein–DNA Recognition and Virus Assembly. *Biochim. Biophys. Acta, Protein Struct. Mol. Enzymol.* **2002,** *1595*, 250-265.

14. Patra, S.; Anders, C.; Schummel, P. H.; Winter, R. Antagonistic Effects of Natural Osmolyte Mixtures and Hydrostatic Pressure on the Conformational Dynamics of a DNA Hairpin Probed at the Single-Molecule Level. *Phys. Chem. Chem. Phys.* **2018,** *20*, 13159-13170.

15. Bikard, D.; Loot, C.; Baharoglu, Z.; Mazel, D. Folded DNA in Action: Hairpin Formation and Biological Functions in Prokaryotes. *Microbiol. Mol. Biol. Rev.* **2010,** *74*, 570-588.

16. Nicholson, D. A.; Sengupta, A.; Sung, H.-L.; Nesbitt, D. J. Amino Acid Stabilization of Nucleic Acid Secondary Structure: Kinetic Insights from Single-Molecule Studies. *J. Phys. Chem. B* **2018,** *122*, 9869-9876.

17. Nakano, S.-i.; Yamaguchi, D.; Tateishi-Karimata, H.; Miyoshi, D.; Sugimoto, N. Hydration Changes upon DNA Folding Studied by Osmotic Stress Experiments. *Biophys. J.* **2012,** *102*, 2808-2817.

18. Patra, S.; Schuabb, V.; Kiesel, I.; Knop, J.-M.; Oliva, R.; Winter, R. Exploring the Effects of Cosolutes and Crowding on the Volumetric and Kinetic Profile of the Conformational Dynamics of a Poly dA Loop DNA Hairpin: a Single-Molecule FRET Study. *Nucleic Acids Res.* **2018,** *47*, 981-996.

19. Baltierra-Jasso, L. E.; Morten, M. J.; Laflör, L.; Quinn, S. D.; Magennis, S. W. Crowding-Induced Hybridization of Single DNA Hairpins. *J. Am. Chem. Soc.* **2015,** *137*, 16020-16023.

20. Stiehl, O.; Weidner-Hertrampf, K.; Weiss, M. Kinetics of Conformational Fluctuations in DNA Hairpin-Loops in Crowded Fluids. *New J. Phys.* **2013,** *15*, 113010.

21. Knowles, D. B.; LaCroix, A. S.; Deines, N. F.; Shkel, I.; Record, M. T. Separation of Preferential Interaction and Excluded Volume Effects on DNA Duplex and Hairpin Stability. *Proc. Natl. Acad. Sci. U.S.A.* **2011,** *108*, 12699-12704.

22. Varani, G. Exceptionally Stable Nucleic Acid Hairpins. *Annu. Rev. Biophys.* **1995,** *24*, 379-404.

23. John SantaLucia, J.; Hicks, D. The Thermodynamics of DNA Structural Motifs. *Annu. Rev. Biophys.* **2004,** *33*, 415-440.

24. SantaLucia, J.; Allawi, H. T.; Seneviratne, P. A. Improved Nearest-Neighbor Parameters for Predicting DNA Duplex Stability. *Biochemistry* **1996,** *35*, 3555-3562.

25. SantaLucia, J. A Unified View of Polymer, Dumbbell, and Oligonucleotide DNA Nearest-Neighbor Thermodynamics. *Proc. Natl. Acad. Sci. U.S.A.* **1998,** *95*, 1460-1465.

26. Rauzan, B.; McMichael, E.; Cave, R.; Sevcik, L. R.; Ostrosky, K.; Whitman, E.; Stegemann, R.; Sinclair, A. L.; Serra, M. J.; Deckert, A. A. Kinetics and Thermodynamics of DNA, RNA, and Hybrid Duplex Formation. *Biochemistry* **2013,** *52*, 765-772.

27. Tekmen, M.; Müller, J. D. High-Pressure Cell for Fluorescence Fluctuation Spectroscopy. *Rev. Sci. Instrum.* **2004,** *75*, 5143-5148.

28. Beimborn, J. C.; Hall, L. M. G.; Tongying, P.; Dukovic, G.; Weber, J. M. Pressure Response of Photoluminescence in Cesium Lead Iodide Perovskite Nanocrystals. *J. Phys. Chem. C* **2018,** *122*, 11024-11030.

29. Fiore, J. L.; Kraemer, B.; Koberling, F.; Edmann, R.; Nesbitt, D. J. Enthalpy-Driven RNA Folding: Single-Molecule Thermodynamics of Tetraloop−Receptor Tertiary Interaction. *Biochemistry* **2009,** *48*, 2550-2558.

30. Sengupta, A.; Sung, H.-L.; Nesbitt, D. J. Amino Acid Specific Effects on RNA Tertiary Interactions: Single-Molecule Kinetic and Thermodynamic Studies. *J. Phys. Chem. B* **2016,** *120*, 10615-10627.

31. Vieweger, M.; Holmstrom, Erik D.; Nesbitt, David J. Single-Molecule FRET Reveals Three Conformations for the TLS Domain of Brome Mosaic Virus Genome. *Biophys. J.* **2015,** *109*, 2625-2636.

32. Sung, H.-L.; Nesbitt, D. J. Novel Heat-Promoted Folding Dynamics of the *yybP-ykoY* Manganese Riboswitch: Kinetic and Thermodynamic Studies at the Single-Molecule Level. *J. Phys. Chem. B* **2019,** *123*, 5412-5422.

33. Fiore, J. L.; Hodak, J. H.; Piestert, O.; Downey, C. D.; Nesbitt, D. J. Monovalent and Divalent Promoted GAAA Tetraloop-Receptor Tertiary Interactions from Freely Diffusing Single-Molecule Studies. *Biophys. J.* **2008,** *95*, 3892-3905.

34. Fiegland, L. R.; Garst, A. D.; Batey, R. T.; Nesbitt, D. J. Single-Molecule Studies of the Lysine Riboswitch Reveal Effector-Dependent Conformational Dynamics of the Aptamer Domain. *Biochemistry* **2012,** *51*, 9223-9233.

35. Macgregor Jr., R. B. Effect of Hydrostatic Pressure on Nucleic Acids. *Biopolymers* **1998,** *48*, 253-263.

36. Roche, J.; Royer Catherine, A. Lessons from Pressure Denaturation of Proteins. *J. Royal Soc. Interface* **2018,** *15*, 20180244.

37. Roche, J.; Caro, J. A.; Norberto, D. R.; Barthe, P.; Roumestand, C.; Schlessman, J. L.; Garcia, A. E.; García-Moreno E., B.; Royer, C. A. Cavities Determine the Pressure Unfolding of Proteins. *Proc. Natl. Acad. Sci. U.S.A.* **2012,** *109*, 6945-6950.

38. Nucci, N. V.; Fuglestad, B.; Athanasoula, E. A.; Wand, A. J. Role of Cavities and Hydration in the Pressure Unfolding of T_4 Lysozyme. *Proc. Natl. Acad. Sci. U.S.A.* **2014,** *111*, 13846-13851.

39. Rashin, A. A.; Iofin, M.; Honig, B. Internal Cavities and Buried Waters in Globular Proteins. *Biochemistry* **1986,** *25*, 3619-3625.

40. Najaf-Zadeh, R.; Wu, J. Q.; Macgregor, R. B. Effect of Cations on the Volume of the Helix-Coil Transition of Poly[d(A-T)]. *Biochim. Biophys. Acta, Gene Struct. Expression* **1995,** *1262*, 52-58.

41. Rayan, G.; Macgregor, R. B. Pressure-Induced Helix–Coil Transition of DNA Copolymers is Linked to Water Activity. *Biophys. Chem.* **2009,** *144*, 62-66.

42. Rayan, G.; Macgregor, R. B. A Look at the Effect of Sequence Complexity on Pressure Destabilisation of DNA Polymers. *Biophys. Chem.* **2015,** *199*, 34-38.

43. Lane, A. N.; Jenkins, T. C. Thermodynamics of Nucleic Acids and Their Interactions with Ligands. *Annu. Rev. Biophys.* **2001,** *33*, 255-306.

44. McConnell, T. S.; Cech, T. R. A Positive Entropy Change for Guanosine Binding and for the Chemical Step in the Tetrahymena Ribozyme Reaction. *Biochemistry* **1995,** *34*, 4056-4067.

45. Mikulecky, P. J.; Feig, A. L. Cold Denaturation of the Hammerhead Ribozyme. *J. Am. Chem. Soc.* **2002,** *124*, 890-891.

46. Lumry, R.; Rajender, S. Enthalpy–Entropy Compensation Phenomena in Water Solutions of Proteins and Small Molecules: A Ubiquitous Properly of Water. *Biopolymers* **1970,** *9*, 1125-1227.

47. Schmid, R.; Miah, A. M.; Sapunov, V. N. A New Table of the Thermodynamic Quantities of Ionic Hydration: Values and Some applications (Enthalpy–Entropy Compensation and Born Radii). *Phys. Chem. Chem. Phys.* **2000,** *2*, 97-102.

48. Wu, J. Q.; Macgregor Jr., R. B. Pressure Dependence of the Helix–Coil Transition Temperature of Poly[d(G-C)]. *Biopolymers* **1995,** *35*, 369-376.

49. Allemand, J.-F.; Cocco, S.; Douarche, N.; Lia, G. Loops in DNA: An Overview of Experimental and Theoretical Approaches. *Eur. Phys. J. E* **2006,** *19*, 293-302.

50. Hanke, A.; Metzler, R. Entropy Loss in Long-Distance DNA Looping. *Biophys. J.* **2003,** *85*, 167-173.

51. Goddard, N. L.; Bonnet, G.; Krichevsky, O.; Libchaber, A. Sequence Dependent Rigidity of Single Stranded DNA. *Phys. Rev. Lett.* **2000,** *85*, 2400-2403.

52. Plumridge, A.; Meisburger, S. P.; Andresen, K.; Pollack, L. The Impact of Base Stacking on the Conformations and Electrostatics of Single-Stranded DNA. *Nucleic Acids Res.* **2017,** *45*, 3932-3943.

53. Ke, C.; Humeniuk, M.; S-Gracz, H.; Marszalek, P. E. Direct Measurements of Base Stacking Interactions in DNA by Single-Molecule Atomic-Force Spectroscopy. *Phys. Rev. Lett.* **2007,** *99*, 018302.

54. Mosayebi, M.; Romano, F.; Ouldridge, T. E.; Louis, A. A.; Doye, J. P. K. The Role of Loop Stacking in the Dynamics of DNA Hairpin Formation. *J. Phys. Chem. B* **2014,** *118*, 14326-14335.

55. Buhot, A.; Halperin, A. Effects of Stacking on the Configurations and Elasticity of Single-Stranded Nucleic Acids. *Phys. Rev. E* **2004,** *70*, 020902.

56. Yancey, P. H.; Blake, W. R.; Conley, J. Unusual Organic Osmolytes in Deep-Sea Animals: Adaptations to Hydrostatic Pressure and Other Perturbants. *Comp. Biochem. Physiol., Part A Mol. Integr. Physiol.* **2002,** *133*, 667-676.

57. Yancey, P. H.; Gerringer, M. E.; Drazen, J. C.; Rowden, A. A.; Jamieson, A. Marine Fish May be Biochemically Constrained from Inhabiting the Deepest Ocean Depths. *Proc. Natl. Acad. Sci. U.S.A.* **2014,** *111*, 4461-4465.

58. Holmstrom, E. D.; Dupuis, N. F.; Nesbitt, D. J. Kinetic and Thermodynamic Origins of Osmolyte-Influenced Nucleic Acid Folding. *J. Phys. Chem. B* **2015,** *119*, 3687-3696.

59. Svoboda, P.; Cara, A. D. Hairpin RNA: A Secondary Structure of Primary Importance. *Cell. Mol. Life Sci.* **2006,** *63*, 901-908.

60. Alden, C. J.; Kim, S.-H. Solvent-accessible surfaces of nucleic acids. *Journal of Molecular Biology* **1979,** *132*, 411-434.

61. Pal, S.; Maiti, P. K.; Bagchi, B.; Hynes, J. T. Multiple Time Scales in Solvation Dynamics of DNA in Aqueous Solution: The Role of Water, Counterions, and Cross-Correlations. *The Journal of Physical Chemistry B* **2006,** *110*, 26396-26402.

62. Auffinger, P.; Hashem, Y. Nucleic Acid Solvation: From Outside to Insight. *Curr. Opin. Struct. Biol.* **2007,** *17*, 325-333.

63. Kuhn, W. Über die Gestalt fadenförmiger Moleküle in Lösungen. *Kolloid-Zeitschrift* **1934,** *68*, 2-15.

64. Kuhn, W.; Kuhn, H. Die Frage nach der Aufrollung von Fadenmolekeln in strömenden Lösungen. *Helv. Chim. Acta* **1943,** *26*, 1394-1465.

65. Vologodskii, A., *Biophysics of DNA*. Cambridge University Press: Cambridge, 2015.

66. Doi, M.; See, H., *Introduction to Polymer Physics*. Oxford Univesity Press: New York, U.S.A., 1996.

67. Chi, Q.; Wang, G.; Jiang, J. The Persistence Length and Length per Base of Single-Stranded DNA Obtained from Fluorescence Correlation Spectroscopy Measurements Using Mean Field Theory. *Physica A* **2013,** *392*, 1072-1079.

68. Kuznetsov, S. V.; Shen, Y.; Benight, A. S.; Ansari, A. A Semiflexible Polymer Model Applied to Loop Formation in DNA Hairpins. *Biophysical Journal* **2001,** *81*, 2864-2875.

69. Murphy, M. C.; Rasnik, I.; Cheng, W.; Lohman, T. M.; Ha, T. Probing Single-Stranded DNA Conformational Flexibility Using Fluorescence Spectroscopy. *Biophysical Journal* **2004,** *86*, 2530-2537.

70. Seol, Y.; Skinner, G. M.; Visscher, K.; Buhot, A.; Halperin, A. Stretching of Homopolymeric RNA Reveals Single-Stranded Helices and Base-Stacking. *Phys. Rev. Lett.* **2007,** *98*, 158103.

71. Searle, M. S.; Williams, D. H. On the Stability of Nucleic Acid Structures in Solution: Enthalpy - Entropy Compensations, Internal Rotations and Reversibility. *Nucleic Acids Res.* **1993,** *21*, 2051-2056.

72. Brahms, J.; Michelson, A. M.; Van Holde, K. E. Adenylate Oligomers in Single- and Double-Strand Conformation. *J. Mol. Biol.* **1966,** *15*, 467-488.

73. Huber, R. G.; Fuchs, J. E.; von Grafenstein, S.; Laner, M.; Wallnoefer, H. G.; Abdelkader, N.; Kroemer, R. T.; Liedl, K. R. Entropy from State Probabilities: Hydration Entropy of Cations. *The Journal of Physical Chemistry B* **2013,** *117*, 6466-6472.

74. Marcus, Y. Thermodynamics of Ion Hydration and its Interpretation in Terms of a Common Model. *Pure Appl. Chem.* **1987,** *59*, 1093.

75. Mishra, G.; Giri, D.; Li, M. S.; Kumar, S. Role of Loop Entropy in the Force Induced Melting of DNA Hairpin. *J. Chem. Phys.* **2011,** *135*, 035102.

Chapter 10 High Pressure Single-Molecule FRET Studies of the Lysine Riboswitch: Cationic and Osmolytic Effects on Pressure Induced Denaturation

1. Chalikian, T. V.; Breslauer, K. J. On Volume Changes Accompanying Conformational Transitions of Biopolymers. *Biopolymers* **1996,** *39*, 619-626.

2. Roche, J.; Caro, J. A.; Norberto, D. R.; Barthe, P.; Roumestand, C.; Schlessman, J. L.; Garcia, A. E.; García-Moreno E., B.; Royer, C. A. Cavities Determine the Pressure Unfolding of Proteins. *Proc. Natl. Acad. Sci. U.S.A.* **2012,** *109*, 6945-6950.

3. Nucci, N. V.; Fuglestad, B.; Athanasoula, E. A.; Wand, A. J. Role of Cavities and Hydration in the Pressure Unfolding of T_4 Lysozyme. *Proc. Natl. Acad. Sci. U.S.A.* **2014,** *111*, 13846-13851.

4. Roche, J.; Royer Catherine, A. Lessons from Pressure Denaturation of Proteins. *J. Royal Soc. Interface* **2018,** *15*, 20180244.

5. Mozhaev, V. V.; Heremans, K.; Frank, J.; Masson, P.; Balny, C. High Pressure Effects on Protein Structure and Function. *Proteins* **1996,** *24*, 81-91.

6. Meersman, F.; Daniel, I.; Bartlett, D. H.; Winter, R.; Hazael, R.; McMillan, P. F. High-Pressure Biochemistry and Biophysics. *Rev. Mineral. Geochem.* **2013,** *75*, 607-648.

7. Epping, E. Life in an Oceanic Extreme. *Nat. Geosci.* **2013,** *6*, 252-253.

8. Mironov, A. S.; Gusarov, I.; Rafikov, R.; Lopez, L. E.; Shatalin, K.; Kreneva, R. A.; Perumov, D. A.; Nudler, E. Sensing Small Molecules by Nascent RNA: A Mechanism to Control Transcription in Bacteria. *Cell* **2002,** *111*, 747-756.

9. Garst, A. D.; Edwards, A. L.; Batey, R. T. Riboswitches: Structures and Mechanisms. *Cold Spring Harb. Perspect. Biol.* **2011,** *3*.

10. Lemay, J. F.; Penedo, J. C.; Tremblay, R.; Lilley, D. M.; Lafontaine, D. A. Folding of the Adenine Riboswitch. *Chem. Biol.* **2006,** *13*, 857-68.

11. Sung, H. L.; Nesbitt, D. J. DNA Hairpin Hybridization under Extreme Pressures: A Single-Molecule FRET Study. *J Phys Chem B* **2020,** *124*, 110-120.

12. Wu, J. Q.; Macgregor Jr., R. B. Pressure Dependence of the Helix–Coil Transition Temperature of Poly[d(G-C)]. *Biopolymers* **1995,** *35*, 369-376.

13. Najaf-Zadeh, R.; Wu, J. Q.; Macgregor, R. B. Effect of Cations on the Volume of the Helix-Coil Transition of Poly[d(A-T)]. *Biochim. Biophys. Acta, Gene Struct. Expression* **1995,** *1262*, 52-58.

14. Rayan, G.; Macgregor, R. B. Pressure-Induced Helix–Coil Transition of DNA Copolymers is Linked to Water Activity. *Biophys. Chem.* **2009,** *144*, 62-66.

15. Rayan, G.; Macgregor, R. B. A Look at the Effect of Sequence Complexity on Pressure Destabilisation of DNA Polymers. *Biophys. Chem.* **2015,** *199*, 34-38.

16. Patra, S.; Anders, C.; Erwin, N.; Winter, R. Osmolyte Effects on the Conformational Dynamics of a DNA Hairpin at Ambient and Extreme Environmental Conditions. *Angew. Chem. Int. Ed.* **2017,** *56*, 5045-5049.

17. Patra, S.; Anders, C.; Schummel, P. H.; Winter, R. Antagonistic Effects of Natural Osmolyte Mixtures and Hydrostatic Pressure on the Conformational Dynamics of a DNA Hairpin Probed at the Single-Molecule Level. *Phys. Chem. Chem. Phys.* **2018,** *20*, 13159-13170.

18. Fan, H. Y.; Shek, Y. L.; Amiri, A.; Dubins, D. N.; Heerklotz, H.; Macgregor, R. B.; Chalikian, T. V. Volumetric Characterization of Sodium-Induced G-Quadruplex Formation. *J. Am. Chem. Soc.* **2011,** *133*, 4518-4526.

19. Takahashi, S.; Sugimoto, N. Effect of Pressure on Thermal Stability of G-Quadruplex DNA and Double-Stranded DNA Structures. *Molecules* **2013,** *18*, 13297-13319.

20. Arns, L.; Knop, J.-M.; Patra, S.; Anders, C.; Winter, R. Single-Molecule Insights into the Temperature and Pressure Dependent Conformational Dynamics of Nucleic Acids in the Presence of Crowders and Osmolytes. *Biophys. Chem.* **2019,** *251*, 106190.

21. Downey, C. D.; Crisman, R. L.; Randolph, T. W.; Pardi, A. Influence of Hydrostatic Pressure and Cosolutes on RNA Tertiary Structure. *J. Am. Chem. Soc.* **2007,** *129*, 9290-9291.

22. Garst, A. D.; Héroux, A.; Rambo, R. P.; Batey, R. T. Crystal Structure of the Lysine Riboswitch Regulatory mRNA Element. *J. Biol. Chem.* **2008,** *283*, 22347-22351.

23. Schneider, S.; Paulsen, H.; Reiter, K. C.; Hinze, E.; Schiene-Fischer, C.; Hübner, C. G. Single Molecule FRET Investigation of Pressure-Driven Unfolding of Cold Shock Protein A. *J. Chem. Phys.* **2018,** *148*, 123336.

24. Ben-Naim, A. Solvent Effects on Protein Association and Protein Folding. *Biopolymers* **1990,** *29*, 567-596.

25. Mikulecky, P. J.; Feig, A. L. Heat Capacity Changes in RNA Folding: Application of Perturbation Theory to Hammerhead Ribozyme Cold Denaturation. *Nucleic Acids Res.* **2004,** *32*, 3967-3976.

26. Sung, H.-L.; Nesbitt, D. J. Novel Heat-Promoted Folding Dynamics of the *yybP-ykoY* Manganese Riboswitch: Kinetic and Thermodynamic Studies at the Single-Molecule Level. *J. Phys. Chem. B* **2019,** *123*, 5412-5422.

27. Fiegland, L. R.; Garst, A. D.; Batey, R. T.; Nesbitt, D. J. Single-Molecule Studies of the Lysine Riboswitch Reveal Effector-Dependent Conformational Dynamics of the Aptamer Domain. *Biochemistry* **2012,** *51*, 9223-9233.

28. Sung, H.-L.; Nesbitt, D. J. Single-Molecule FRET Kinetics of the Mn^{2+} Riboswitch: Evidence for Allosteric Mg^{2+} Control of "Induced-Fit" vs "Conformational Selection" Folding Pathways. *J. Phys. Chem. B* **2019,** *123*, 2005-2015.

29. Tan, Z.-J.; Chen, S.-J. Nucleic Acid Helix Stability: Effects of Salt Concentration, Cation Valence and Size, and Chain Length. *Biophys. J.* **2006,** *90*, 1175-1190.

30. Fiore, J. L.; Holmstrom, E. D.; Fiegland, L. R.; Hodak, J. H.; Nesbitt, D. J. The Role of Counterion Valence and Size in GAAA Tetraloop–Receptor Docking/Undocking Kinetics. *J. Mol. Biol.* **2012,** *423*, 198-216.

31. Yancey, P.; Clark, M.; Hand, S.; Bowlus, R.; Somero, G. Living with Water Stress: Evolution of Osmolyte Systems. *Science* **1982,** *217*, 1214-1222.

32. Yancey, P. H.; Blake, W. R.; Conley, J. Unusual Organic Osmolytes in Deep-Sea Animals: Adaptations to Hydrostatic Pressure and Other Perturbants. *Comp. Biochem. Physiol., Part A Mol. Integr. Physiol.* **2002,** *133*, 667-676.

33. Yancey, P. H.; Gerringer, M. E.; Drazen, J. C.; Rowden, A. A.; Jamieson, A. Marine Fish May be Biochemically Constrained from Inhabiting the Deepest Ocean Depths. *Proc. Natl. Acad. Sci. U.S.A.* **2014,** *111*, 4461-4465.

34. Downing, A. B.; Wallace, G. T.; Yancey, P. H. Organic Osmolytes of Amphipods from Littoral to Hadal Zones: Increases with Depth in Trimethylamine N-Oxide, Scyllo-Inositol and Other Potential Pressure Counteractants. *Deep Sea Res.* **2018,** *138*, 1-10.

35. Bennion, B. J.; Daggett, V. Counteraction of Urea-Induced Protein Denaturation by Trimethylamine *N*-Oxide: A Chemical Chaperone at Atomic Resolution. *Proc. Natl. Acad. Sci. U. S. A.* **2004,** *101*, 6433-6438.

36. Street, T. O.; Bolen, D. W.; Rose, G. D. A Molecular Mechanism for Osmolyte-Induced Protein Stability. *Proc. Natl. Acad. Sci. U.S.A.* **2006,** *103*, 13997-14002.

37. Canchi, D. R.; García, A. E. Cosolvent Effects on Protein Stability. *Annual Review of Physical Chemistry* **2013,** *64*, 273-293.

38. Holmstrom, E. D.; Dupuis, N. F.; Nesbitt, D. J. Kinetic and Thermodynamic Origins of Osmolyte-Influenced Nucleic Acid Folding. *J. Phys. Chem. B* **2015,** *119*, 3687-3696.

39. Lambert, D.; Leipply, D.; Draper, D. E. The Osmolyte TMAO Stabilizes Native RNA Tertiary Structures in the Absence of Mg^{2+}: Evidence for a Large Barrier to Folding from Phosphate Dehydration. *J. Mol. Biol.* **2010,** *404*, 138-157.

40. Yancey, P. H.; Siebenaller, J. F. Trimethylamine Oxide Stabilizes Teleost and Mammalian Lactate Dehydrogenases Against Inactivation by Hydrostatic Pressure and Trypsinolysis. *J. Exp. Biol.* **1999,** *202*, 3597-3603.

41. Yancey, P. H.; Fyfe-Johnson, A. L.; Kelly, R. H.; Walker, V. P.; Auñón, M. T. Trimethylamine Oxide Counteracts Effects of Hydrostatic Pressure on Proteins of Deep-Sea Teleosts. *Journal of Experimental Zoology* **2001,** *289*, 172-176.

42. Sengupta, A.; Sung, H.-L.; Nesbitt, D. J. Amino Acid Specific Effects on RNA Tertiary Interactions: Single-Molecule Kinetic and Thermodynamic Studies. *J. Phys. Chem. B* **2016,** *120*, 10615-10627.

43. Blouin, S.; Chinnappan, R.; Lafontaine, D. A. Folding of the Lysine Riboswitch: Importance of Peripheral Elements for Transcriptional Regulation. *Nucleic Acids Res.* **2010,** *39*, 3373-3387.

44. McCluskey, K.; Boudreault, J.; St-Pierre, P.; Perez-Gonzalez, C.; Chauvier, A.; Rizzi, A.; Beauregard, P. B.; Lafontaine, D. A.; Penedo, J. C. Unprecedented Tunability of Riboswitch Structure and Regulatory Function by Sub-Millimolar Variations in Physiological Mg2+. *Nucleic Acids Res.* **2019,** *47*, 6478-6487.

45. Vieweger, M.; Holmstrom, Erik D.; Nesbitt, David J. Single-Molecule FRET Reveals Three Conformations for the TLS Domain of Brome Mosaic Virus Genome. *Biophys. J.* **2015,** *109*, 2625-2636.

46. Fiore, J. L.; Hodak, J. H.; Piestert, O.; Downey, C. D.; Nesbitt, D. J. Monovalent and Divalent Promoted GAAA Tetraloop-Receptor Tertiary Interactions from Freely Diffusing Single-Molecule Studies. *Biophys. J.* **2008,** *95*, 3892-3905.

47. Fiore, J. L.; Kraemer, B.; Koberling, F.; Edmann, R.; Nesbitt, D. J. Enthalpy-Driven RNA Folding: Single-Molecule Thermodynamics of Tetraloop−Receptor Tertiary Interaction. *Biochemistry* **2009,** *48*, 2550-2558.

48. Barbosa, R. d. C.; Barbosa, M. C. Hydration Shell of the TS-Kappa Protein: Higher Density than Bulk Water. *Physica A* **2015,** *439*, 48-58.

49. Merzel, F.; Smith, J. C. Is the First Hydration Shell of Lysozyme of Higher Density than Bulk Water? *Proc. Natl. Acad. Sci. U.S.A.* **2002,** *99*, 5378-5383.

50. Royer, C. A. Revisiting Volume Changes in Pressure-Induced Protein Unfolding. *Biochim. Biophys. Acta, Protein Struct. Mol. Enzymol.* **2002,** *1595*, 201-209.

51. Rouget, J.-B.; Aksel, T.; Roche, J.; Saldana, J.-L.; Garcia, A. E.; Barrick, D.; Royer, C. A. Size and Sequence and the Volume Change of Protein Folding. *J. Am. Chem. Soc.* **2011,** *133*, 6020-6027.

52. Nicholson, D. A.; Sengupta, A.; Sung, H.-L.; Nesbitt, D. J. Amino Acid Stabilization of Nucleic Acid Secondary Structure: Kinetic Insights from Single-Molecule Studies. *J. Phys. Chem. B* **2018,** *122*, 9869-9876.

53. Furukawa, K.; Gu, H.; Sudarsan, N.; Hayakawa, Y.; Hyodo, M.; Breaker, R. R. Identification of Ligand Analogues that Control c-di-GMP Riboswitches. *ACS Chem, Biol.* **2012,** *7*, 1436-1443.

54. Bowman, J. C.; Lenz, T. K.; Hud, N. V.; Williams, L. D. Cations in Charge: Magnesium Ions in RNA Folding and Catalysis. *Curr. Opin. Struct. Biol.* **2012,** *22*, 262-272.

55. Draper, D. E.; Grilley, D.; Soto, A. M. Ions and RNA Folding. *Annu. Rev. Biophys.* **2005,** *34*, 221-243.

56. Draper, D. E. RNA Folding: Thermodynamic and Molecular Descriptions of the Roles of Ions. *Biophys. J.* **2008,** *95*, 5489-5495.

57. Schroeder, Kersten T.; Daldrop, P.; Lilley, David M. J. RNA Tertiary Interactions in a Riboswitch Stabilize the Structure of a Kink Turn. *Structure* **2011,** *19*, 1233-1240.

58. Shcherbakova, I.; Gupta, S.; Chance, M. R.; Brenowitz, M. Monovalent Ion-Mediated Folding of the *Tetrahymena thermophila* Ribozyme. *J. Mol. Biol.* **2004,** *342*, 1431-1442.

59. Patra, S.; Schuabb, V.; Kiesel, I.; Knop, J.-M.; Oliva, R.; Winter, R. Exploring the Effects of Cosolutes and Crowding on the Volumetric and Kinetic Profile of the Conformational Dynamics of a Poly dA Loop DNA Hairpin: a Single-Molecule FRET Study. *Nucleic Acids Res.* **2018,** *47*, 981-996.

60. Tsukida, N.; Muranaka, H.; Ide, M.; Maeda, Y.; Kitano, H. Effect of Neutralization of Poly(acrylic acid) on the Structure of Water Examined by Raman Spectroscopy. *J. Phys. Chem. B* **1997,** *101*, 6676-6679.

61. Holmstrom, E. D.; Fiore, J. L.; Nesbitt, D. J. Thermodynamic Origins of Monovalent Facilitated RNA Folding. *Biochemistry* **2012,** *51*, 3732-3743.

62. Schlatterer, J. C.; Kwok, L. W.; Lamb, J. S.; Park, H. Y.; Andresen, K.; Brenowitz, M.; Pollack, L. Hinge Stiffness Is a Barrier to RNA Folding. *J. Mol. Biol.* **2008,** *379*, 859-870.

63. Wilson, T. J.; Lilley, D. M. J. Metal Ion Binding and the Folding of the Hairpin Ribozyme. *RNA* **2002,** *8*, 587-600.

64. Hohng, S.; Wilson, T. J.; Tan, E.; Clegg, R. M.; Lilley, D. M. J.; Ha, T. Conformational Flexibility of Four-way Junctions in RNA. *J. Mol. Biol.* **2004,** *336*, 69-79.

65. Goody, T. A.; Melcher, S. E.; Norman, D. G.; Lilley, D. M. J. The Kink-Turn Motif in RNA is Dimorphic, and Metal Ion-Dependent. *RNA* **2004,** *10*, 254-264.

66. Huang, L.; Lilley, D. M. J. The Kink Turn, a Key Architectural Element in RNA Structure. *J. Mol. Biol.* **2016,** *428*, 790-801.

67. Shiman, R.; Draper, D. E. Stabilization of RNA Tertiary Structure by Monovalent Cations. *J. Mol. Biol.* **2000,** *302*, 79-91.

68. Forster, R.; Goldstein, L. Intracellular Osmoregulatory Role of Amino Acids and Urea in Marine Elasmobranchs. *Am. J. Physiol.* **1976,** *230*, 925-931.

69. Yancey, P. H. Organic Osmolytes as Compatible, Metabolic and Counteracting Cytoprotectants in High Osmolarity and Other Stresses. *J. Exp. Biol.* **2005,** *208*, 2819-2830.

70. Gluick, T. C.; Yadav, S. Trimethylamine N-Oxide Stabilizes RNA Tertiary Structure and Attenuates the Denaturating Effects of Urea. *J. Am. Chem. Soc.* **2003,** *125*, 4418-4419.

71. Lambert, D.; Draper, D. E. Effects of Osmolytes on RNA Secondary and Tertiary Structure Stabilities and RNA-Mg^{2+} Interactions. *J. Mol. Biol.* **2007,** *370*, 993-1005.

72. Macgregor Jr., R. B. Effect of Hydrostatic Pressure on Nucleic Acids. *Biopolymers* **1998,** *48*, 253-263.

73. Heilman-Miller, S. L.; Thirumalai, D.; Woodson, S. A. Role of Counterion Condensation in Folding of the *Tetrahymena* Ribozyme. I. Equilibrium Stabilization by Cations. *J. Mol. Biol.* **2001,** *306*, 1157-1166.

74. Krywka, C.; Sternemann, C.; Paulus, M.; Tolan, M.; Royer, C.; Winter, R. Effect of Osmolytes on Pressure-Induced Unfolding of Proteins: A High-Pressure SAXS Study. *ChemPhysChem* **2008,** *9*, 2809-2815.

75. Childress, J. J.; Seibel, B. A. Life at Stable Low Oxygen Levels: Adaptations of Animals to Oceanic Oxygen minimum Layers. *J. Exp. Biol.* **1998,** *201*, 1223-1232.

76. Morita, T. Structure-Based Analysis of High Pressure Adaptation of α-Actin. *J. Biol. Chem.* **2003,** *278*, 28060-28066.

77. Ellis, R. J. Macromolecular Crowding: Obvious but Underappreciated. *Trends in Biochemical Sciences* **2001,** *26*, 597-604.

78. Canchi, D. R.; Jayasimha, P.; Rau, D. C.; Makhatadze, G. I.; Garcia, A. E. Molecular Mechanism for the Preferential Exclusion of TMAO from Protein Surfaces. *J. Phys. Chem. B* **2012,** *116*, 12095-12104.

79. Ma, J.; Pazos, I. M.; Gai, F. Microscopic Insights into the Protein-Stabilizing Effect of Trimethylamine *N*-Oxide (TMAO). *Proc. Natl. Acad. Sci. U.S.A.* **2014,** *111*, 8476-8481.

80. Pincus, D. L.; Hyeon, C.; Thirumalai, D. Effects of Trimethylamine N-Oxide (TMAO) and Crowding Agents on the Stability of RNA Hairpins. *J. Am. Chem. Soc.* **2008,** *130*, 7364-7372.

81. Zou, Q.; Bennion, B. J.; Daggett, V.; Murphy, K. P. The Molecular Mechanism of Stabilization of Proteins by TMAO and Its Ability to Counteract the Effects of Urea. *J. Am. Chem. Soc.* **2002,** *124*, 1192-1202.

Chapter 11 Single-Molecule Kinetic Studies of DNA Hybridization Under Extreme Pressures

1. Yayanos, A. A.; Dietz, A. S.; Van Boxtel, R., Obligately Barophilic Bacterium from the Mariana Trench. *Proc. Natl. Acad. Sci. U.S.A.* **1981,** *78* (8), 5212-5215.

2. Kato, C.; Li, L.; Nogi, Y.; Nakamura, Y.; Tamaoka, J.; Horikoshi, K., Extremely Barophilic Bacteria Isolated from the Mariana Trench, Challenger Deep, at a Depth of 11,000 Meters. *Appl. Environ. Microbiol.* **1998,** *64* (4), 1510-1513.

3. Somero, G. N., Adaptations to High Hydrostatic Pressure. *Annu. Rev. Physiol.* **1992,** *54* (1), 557-577.

4. Gross, M.; Jaenicke, R., Proteins Under Pressure. *Eur. J. Biochem.* **1994,** *221* (2), 617-630.

5. Mozhaev, V. V.; Heremans, K.; Frank, J.; Masson, P.; Balny, C., High Pressure Effects on Protein Structure and Function. *Proteins* **1996,** *24* (1), 81-91.

6. Dubins, D. N.; Lee, A.; Macgregor, R. B.; Chalikian, T. V., On the Stability of Double Stranded Nucleic Acids. *J. Am. Chem. Soc.* **2001,** *123* (38), 9254-9259.

7. Sung, H.-L.; Nesbitt, D. J., High Pressure Single-Molecule FRET Studies of the Lysine Riboswitch: Cationic and Osmolytic Effects on Pressure Induced Denaturation. *Phys. Chem. Chem. Phys.* **2020,** *22* (28), 15853-15866.

8. Zipp, A.; Kauzmann, W., Pressure denaturation of metmyoglobin. *Biochemistry* **1973,** *12* (21), 4217-4228.

9. Roche, J.; Royer, C. A., Lessons from Pressure Denaturation of Proteins. *J. Royal Soc. Interface* **2018,** *15* (147), 20180244.

10. Yancey, P. H.; Blake, W. R.; Conley, J., Unusual Organic Osmolytes in Deep-Sea Animals: Adaptations to Hydrostatic Pressure and Other Perturbants. *Comp. Biochem. Physiol., Part A Mol. Integr. Physiol.* **2002,** *133* (3), 667-676.

11. Najaf-Zadeh, R.; Wu, J. Q.; Macgregor, R. B., Effect of Cations on the Volume of the Helix-Coil Transition of poly[d(A-T)]. *Biochim. Biophys. Acta, Gene Struct. Expression* **1995,** *1262* (1), 52-58.

12. Wu, J. Q.; Macgregor Jr., R. B., Pressure Dependence of the Helix–Coil Transition Temperature of poly[d(G-C)]. *Biopolymers* **1995,** *35* (4), 369-376.

13. Patra, S.; Anders, C.; Erwin, N.; Winter, R., Osmolyte Effects on the Conformational Dynamics of a DNA Hairpin at Ambient and Extreme Environmental Conditions. *Angew. Chem.* **2017,** *56* (18), 5045-5049.

14. Patra, S.; Anders, C.; Schummel, P. H.; Winter, R., Antagonistic Effects of Natural Osmolyte Mixtures and Hydrostatic Pressure on the Conformational Dynamics of a DNA Hairpin Probed at the Single-Molecule Level. *Phys. Chem. Chem. Phys.* **2018,** *20* (19), 13159-13170.

15. Sung, H.-L.; Nesbitt, D. J., DNA Hairpin Hybridization under Extreme Pressures: A Single-Molecule FRET Study. *J. Phys. Chem. B* **2020,** *124* (1), 110-120.

16. Pan, T.; Sosnick, T., RNA Folding During Transcription. *Annu. Rev. Biophys. Biomol. Struct.* **2006,** *35* (1), 161-175.

17. Mott, M. L.; Berger, J. M., DNA Replication Initiation: Mechanisms and Regulation in Bacteria. *Nat. Rev. Microbiol.* **2007,** *5* (5), 343-354.

18. Hodak, J. H.; Fiore, J. L.; Nesbitt, D. J.; Downey, C. D.; Pardi, A., Docking Kinetics and Equilibrium of a GAAA Tetraloop-Receptor Motif Probed by Single-Molecule FRET. *Proc. Natl. Acad. Sci. U.S.A.* **2005,** *102* (30), 10505-10510.

19. Sengupta, A.; Sung, H.-L.; Nesbitt, D. J., Amino Acid Specific Effects on RNA Tertiary Interactions: Single-Molecule Kinetic and Thermodynamic Studies. *J. Phys. Chem. B* **2016,** *120* (41), 10615-10627.

20. Nicholson, D. A.; Sengupta, A.; Sung, H.-L.; Nesbitt, D. J., Amino Acid Stabilization of Nucleic Acid Secondary Structure: Kinetic Insights from Single-Molecule Studies. *J. Phys. Chem. B* **2018,** *122* (43), 9869-9876.

21. Patra, S.; Schuabb, V.; Kiesel, I.; Knop, J.-M.; Oliva, R.; Winter, R., Exploring the Effects of Cosolutes and Crowding on the Volumetric and Kinetic Profile of the Conformational Dynamics of a poly dA loop DNA Hairpin: A Single-Molecule FRET Study. *Nucleic Acids Res.* **2018,** *47* (2), 981-996.

22. Tsukanov, R.; Tomov, T. E.; Masoud, R.; Drory, H.; Plavner, N.; Liber, M.; Nir, E., Detailed Study of DNA Hairpin Dynamics Using Single-Molecule Fluorescence Assisted by DNA Origami. *J. Phys. Chem. B* **2013,** *117* (40), 11932-11942.

23. Sung, H.-L.; Nesbitt, D. J., Single-Molecule FRET Kinetics of the Mn^{2+} Riboswitch: Evidence for Allosteric Mg^{2+} Control of "Induced-Fit" vs "Conformational Selection" Folding Pathways. *J. Phys. Chem. B* **2019,** *123* (9), 2005-2015.

24. Zhou, H.-X., Rate Theories for Biologists. *Q. Rev. Biophys.* **2010,** *43* (2), 219-293.

25. Record Jr., M. T., Effects of Na^{+} and Mg^{++} Ions on the Helix–Coil Transition of DNA. *Biopolymers* **1975,** *14* (10), 2137-2158.

26. Owczarzy, R.; Moreira, B. G.; You, Y.; Behlke, M. A.; Walder, J. A., Predicting Stability of DNA Duplexes in Solutions Containing Magnesium and Monovalent Cations. *Biochemistry* **2008,** *47* (19), 5336-5353.

27. Buckin, V.; Tran, H.; Morozov, V.; Marky, L. A., Hydration Effects Accompanying the Substitution of Counterions in the Ionic Atmosphere of Poly(rA)·Poly(rU) and Poly(rA)·2Poly(rU) Helices. *J. Am. Chem. Soc.* **1996,** *118* (30), 7033-7039.

28. Barbosa, R. d. C.; Barbosa, M. C., Hydration Shell of the TS-Kappa Protein: Higher Density than Bulk Water. *Physica A* **2015,** *439*, 48-58.

29. Chalikian, T. V.; Sarvazyan, A. P.; Plum, G. E.; Breslauer, K. J., Influence of Base Composition, Base Sequence, and Duplex Structure on DNA Hydration: Apparent Molar Volumes and Apparent Molar Adiabatic Compressibilities of Synthetic and Natural DNA Duplexes at 25.degree.C. *Biochemistry* **1994,** *33* (9), 2394-2401.

30. Fiore, J. L.; Kraemer, B.; Koberling, F.; Edmann, R.; Nesbitt, D. J., Enthalpy-Driven RNA Folding: Single-Molecule Thermodynamics of Tetraloop−Receptor Tertiary Interaction. *Biochemistry* **2009,** *48* (11), 2550-2558.

31. Holmstrom, E. D.; Polaski, J. T.; Batey, R. T.; Nesbitt, D. J., Single-Molecule Conformational Dynamics of a Biologically Functional Hydroxocobalamin Riboswitch. *J. Am. Chem. Soc.* **2014,** *136* (48), 16832-16843.

32. Downey, C. D.; Crisman, R. L.; Randolph, T. W.; Pardi, A., Influence of Hydrostatic Pressure and Cosolutes on RNA Tertiary Structure. *J. Am. Chem. Soc.* **2007,** *129* (30), 9290-9291.

33. Takahashi, S.; Sugimoto, N., Effect of Pressure on Thermal Stability of G-Quadruplex DNA and Double-Stranded DNA Structures. *Molecules* **2013,** *18* (11), 13297-13319.

34. Arns, L.; Knop, J.-M.; Patra, S.; Anders, C.; Winter, R., Single-Molecule Insights into the Temperature and Pressure Dependent Conformational Dynamics of Nucleic Acids in the Presence of Crowders and Osmolytes. *Biophys. Chem.* **2019,** *251*, 106190.

35. Chalikian, T. V.; Breslauer, K. J., On Volume Changes Accompanying Conformational Transitions of Biopolymers. *Biopolymers* **1996,** *39* (5), 619-626.

36. Roche, J.; Caro, J. A.; Norberto, D. R.; Barthe, P.; Roumestand, C.; Schlessman, J. L.; Garcia, A. E.; García-Moreno E., B.; Royer, C. A., Cavities Determine the Pressure Unfolding of Proteins. *Proc. Natl. Acad. Sci. U.S.A.* **2012,** *109* (18), 6945-6950.

37. Tan, C.-Y.; Xu, C.-H.; Wong, J.; Shen, J.-R.; Sakuma, S.; Yamamoto, Y.; Lange, R.; Balny, C.; Ruan, K.-C., Pressure Equilibrium and Jump Study on Unfolding of 23-kDa Protein from Spinach Photosystem II. *Biophys. J.* **2005,** *88* (2), 1264-1275.

38. Font, J.; Torrent, J.; Ribó, M.; Laurents, D. V.; Balny, C.; Vilanova, M.; Lange, R., Pressure-Jump-Induced Kinetics Reveals a Hydration Dependent Folding/Unfolding Mechanism of Ribonuclease A. *Biophys. J.* **2006,** *91* (6), 2264-2274.

39. Zhang, Y.; Kitazawa, S.; Peran, I.; Stenzoski, N.; McCallum, S. A.; Raleigh, D. P.; Royer, C. A., High Pressure ZZ-Exchange NMR Reveals Key Features of Protein Folding Transition States. *J. Am. Chem. Soc.* **2016,** *138* (46), 15260-15266.

40. Cheng, Y.-K.; Pettitt, B. M., Stabilities of Double- and Triple-strand Helical Nucleic Acids. *Prog. Biophys. Mol. Biol.* **1992,** *58* (3), 225-257.

41. Rougee, M.; Faucon, B.; Mergny, J. L.; Barcelo, F.; Giovannangeli, C.; Garestier, T.; Helene, C., Kinetics and Thermodynamics of Triple-Helix Formation: Effects of Ionic Strength and Mismatched. *Biochemistry* **1992,** *31* (38), 9269-9278.

42. Lin, M.-C.; Macgregor, R. B., Activation Volume of DNA Duplex Formation. *Biochemistry* **1997,** *36* (21), 6539-6544.

43. Dubins, D. N.; Macgregor Jr., R. B., Volumetric Properties of the Formation of Double Stranded DNA: A Nearest-Neighbor Analysis. *Biopolymers* **2004,** *73* (2), 242-257.

44. Dupuis, Nicholas F.; Holmstrom, Erik D.; Nesbitt, David J., Single-Molecule Kinetics Reveal Cation-Promoted DNA Duplex Formation Through Ordering of Single-Stranded Helices. *Biophys. J.* **2013,** *105* (3), 756-766.

45. Das, R.; Mills, T. T.; Kwok, L. W.; Maskel, G. S.; Millett, I. S.; Doniach, S.; Finkelstein, K. D.; Herschlag, D.; Pollack, L., Counterion Distribution around DNA Probed by Solution X-Ray Scattering. *Phys. Rev. Lett.* **2003,** *90* (18), 188103.

46. Tokuda, J. M.; Pabit, S. A.; Pollack, L., Protein-DNA and ion-DNA Interactions Revealed Through Contrast Variation SAXS. *Biophys. Rev.* **2016,** *8* (2), 139-149.

47. Pegram, L. M.; Wendorff, T.; Erdmann, R.; Shkel, I.; Bellissimo, D.; Felitsky, D. J.; Record, M. T., Why Hofmeister Effects of Many Salts Favor Protein Folding but not DNA Helix Formation. *Proc. Natl. Acad. Sci. U.S.A.* **2010,** *107* (17), 7716-7721.

48. Braunlin, W. H.; Bloomfield, V. A., Proton NMR Study of the Base-Pairing Reactions of d(GGAATTCC): Salt Effects on the Equilibria and Kinetics of Strand Association. *Biochemistry* **1991,** *30* (3), 754-758.

49. Spink, C. H.; Chaires, J. B., Effects of Hydration, Ion Release, and Excluded Volume on the Melting of Triplex and Duplex DNA. *Biochemistry* **1999,** *38* (1), 496-508.

50. Shiman, R.; Draper, D. E., Stabilization of RNA Tertiary Structure by Monovalent Cations. *J. Mol. Biol.* **2000,** *302* (1), 79-91.

51. Leipply, D.; Lambert, D.; Draper, D. E., Chapter 21 - Ion–RNA Interactions: Thermodynamic Analysis of the Effects of Mono- and Divalent Ions on RNA Conformational Equilibria. In *Methods in Enzymology*, Academic Press: 2009; Vol. 469, pp 433-463.

52. Goddard, N. L.; Bonnet, G.; Krichevsky, O.; Libchaber, A., Sequence Dependent Rigidity of Single Stranded DNA. *Phys. Rev. Lett.* **2000,** *85* (11), 2400-2403.

53. Sreedhara, A.; Cowan, J. A., Structural and Catalytic Roles for Divalent Magnesium in Nucleic Acid Biochemistry. *Biometals* **2002,** *15* (3), 211-223.

54. Gebala, M.; Bonilla, S.; Bisaria, N.; Herschlag, D., Does Cation Size Affect Occupancy and Electrostatic Screening of the Nucleic Acid Ion Atmosphere? *J. Am. Chem. Soc.* **2016,** *138* (34), 10925-10934.

55. McFail-Isom, L.; Sines, C. C.; Williams, L. D., DNA Structure: Cations in Charge? *Curr. Opin. Struct. Biol.* **1999,** *9* (3), 298-304.

56. Yancey, P. H., Organic Osmolytes as Compatible, Metabolic and Counteracting Cytoprotectants in High Osmolarity and Other Stresses. *J. Exp. Biol.* **2005,** *208* (15), 2819-2830.

57. Yancey, P. H.; Fyfe-Johnson, A. L.; Kelly, R. H.; Walker, V. P.; Auñón, M. T., Trimethylamine Oxide Counteracts Effects of Hydrostatic Pressure on Proteins of Deep-Sea Teleosts. *J. Exp. Zool.* **2001,** *289* (3), 172-176.

58. Krywka, C.; Sternemann, C.; Paulus, M.; Tolan, M.; Royer, C.; Winter, R., Effect of Osmolytes on Pressure-Induced Unfolding of Proteins: A High-Pressure SAXS Study. *Chem. Phys. Chem.* **2008,** *9* (18), 2809-2815.

Chapter 12 Ligand-Dependent Volumetric Characterization of Manganese Riboswitch Folding: A High-Pressure Single-Molecule Kinetic Study

1. Heremans, K.; Smeller, L., Protein Structure and Dynamics at High Pressure. *Biochim. Biophys. Acta, Protein Struct. Mol. Enzymol.* **1998,** *1386* (2), 353-370.

2. Mitra, L.; Rouget, J.-B.; Garcia-Moreno, B.; Royer, C. A.; Winter, R., Towards a Quantitative Understanding of Protein Hydration and Volumetric Properties. *ChemPhysChem* **2008,** *9* (18), 2715-2721.

3. Mozhaev, V. V.; Heremans, K.; Frank, J.; Masson, P.; Balny, C., High Pressure Effects on Protein Structure and Function. *Proteins* **1996,** *24* (1), 81-91.

4. Aristides Yayanos, A., Deep-Sea Piezophilic Bacteria. In *Methods in Microbiology*, Academic Press: 2001; Vol. 30, pp 615-637.

5. Gross, M.; Jaenicke, R., Proteins under Pressure. *Eur. J. Chem.* **1994,** *221* (2), 617-630.

6. Li, L.; Kato, C.; Horikoshi, K., Bacterial Diversity in Deep-Sea Sediments from Different Depths. *Biodivers. Conserv.* **1999,** *8* (5), 659-677.

7. Jannasch, H. W.; Wirsen, C. O., Variability of Pressure Adaptation in Deep sea Bacteria. *Arch. Microbiol.* **1984,** *139* (4), 281-288.

8. Najaf-Zadeh, R.; Wu, J. Q.; Macgregor, R. B., Effect of Cations on the Volume of the Helix-Coil Transition of Poly[d(A-T)]. *Biochim. Biophys. Acta Gene Regul.* **1995,** *1262* (1), 52-58.

9. Lin, M.-C.; Macgregor, R. B., Activation Volume of DNA Duplex Formation. *Biochemistry* **1997,** *36* (21), 6539-6544.

10. Downey, C. D.; Crisman, R. L.; Randolph, T. W.; Pardi, A., Influence of Hydrostatic Pressure and Cosolutes on RNA Tertiary Structure. *J. Am. Chem. Soc.* **2007,** *129* (30), 9290-9291.

11. Patra, S.; Anders, C.; Schummel, P. H.; Winter, R., Antagonistic Effects of Natural Osmolyte Mixtures and Hydrostatic Pressure on the Conformational Dynamics of a DNA Hairpin Probed at the Single-Molecule Level. *Phys. Chem. Chem. Phys.* **2018,** *20* (19), 13159-13170.

12. Ramanujam, V.; Alderson, T. R.; Pritišanac, I.; Ying, J.; Bax, A., Protein Structural Changes Characterized by High-Pressure, Pulsed Field Gradient Diffusion NMR Spectroscopy. *J. Magn. Reson.* **2020,** *312*, 106701.

13. Frye, K. J.; Royer, C. A., Probing the Contribution of Internal Cavities to the Volume Change of Protein Unfolding Under Pressure. *Protein Sci.* **1998,** *7* (10), 2217-2222.

14. Cioni, P., Role of Protein Cavities on Unfolding Volume Change and on Internal Dynamics under Pressure. *Biophys. J.* **2006,** *91* (9), 3390-3396.

15. Roche, J.; Caro, J. A.; Norberto, D. R.; Barthe, P.; Roumestand, C.; Schlessman, J. L.; Garcia, A. E.; García-Moreno E., B.; Royer, C. A., Cavities Determine the Pressure Unfolding of Proteins. *Proc. Natl. Acad. Sci. U.S.A.* **2012,** *109* (18), 6945-6950.

16. Grigera, J. R.; McCarthy, A. N., The Behavior of the Hydrophobic Effect under Pressure and Protein Denaturation. *Biophys. J.* **2010,** *98* (8), 1626-1631.

17. Royer, C.; Winter, R., Protein Hydration and Volumetric Properties. *Curr. Opin. Colloid Interface Sci.* **2011,** *16* (6), 568-571.

18. Nucci, N. V.; Fuglestad, B.; Athanasoula, E. A.; Wand, A. J., Role of Cavities and Hydration in the Pressure Unfolding of T_4 Lysozyme. *Proc. Natl. Acad. Sci. U.S.A.* **2014,** *111* (38), 13846-13851.

19. Hillson, N.; Onuchic, J. N.; García, A. E., Pressure-Induced Protein-Folding/Unfolding Kinetics. *Proc. Natl. Acad. Sci. U.S.A.* **1999,** *96* (26), 14848-14853.

20. Woenckhaus, J.; Köhling, R.; Winter, R.; Thiyagarajan, P.; Finet, S., High Pressure-Jump Apparatus for Kinetic Studies of Protein Folding Reactions Using the Small-Angle Synchrotron X-Ray Scattering Technique. *Rev. Sci. Instrum.* **2000,** *71* (10), 3895-3899.

21. Nguyen, L. M.; Roche, J., High-Pressure NMR Techniques for the Study of Protein Dynamics, Folding and Aggregation. *J. Magn. Reson.* **2017,** *277*, 179-185.

22. Mustoe, A. M.; Brooks, C. L.; Al-Hashimi, H. M., Hierarchy of RNA Functional Dynamics. *Annu. Rev. Biochem.* **2014,** *83* (1), 441-466.

23. Al-Hashimi, H. M.; Walter, N. G., RNA Dynamics: it is About Time. *Curr. Opin. Struct. Biol.* **2008,** *18* (3), 321-329.

24. Lai, D.; Proctor, J. R.; Meyer, I. M., On the Importance of Cotranscriptional RNA Structure Formation. *RNA* **2013,** *19* (11), 1461-1473.

25. Schärfen, L.; Neugebauer, K. M., Transcription Regulation Through Nascent RNA Folding. *J. Mol. Biol.* **2021,** *433* (14), 166975.

26. Schneider, S.; Paulsen, H.; Reiter, K. C.; Hinze, E.; Schiene-Fischer, C.; Hübner, C. G., Single Molecule FRET Investigation of Pressure-Driven Unfolding of Cold Shock Protein A. *J. Chem. Phys.* **2018,** *148* (12), 123336.

27. Sung, H.-L.; Nesbitt, D. J., DNA Hairpin Hybridization under Extreme Pressures: A Single-Molecule FRET Study. *J. Phys. Chem. B* **2020,** *124* (1), 110-120.

28. Hodak, J. H.; Fiore, J. L.; Nesbitt, D. J.; Downey, C. D.; Pardi, A., Docking Kinetics and Equilibrium of a GAAA Tetraloop-Receptor Motif Probed by Single-Molecule FRET. *Proc. Natl. Acad. Sci. U.S.A.* **2005,** *102* (30), 10505-10510.

29. Sung, H.-L.; Nesbitt, D. J., Single-Molecule Kinetic Studies of DNA Hybridization under Extreme Pressures. *Phys. Chem. Chem. Phys.* **2020,** *22* (41), 23491-23501.

30. Sung, H.-L.; Nesbitt, D. J., Single-Molecule FRET Kinetics of the Mn^{2+} Riboswitch: Evidence for Allosteric Mg^{2+} Control of "Induced-Fit" vs "Conformational Selection" Folding Pathways. *J. Phys. Chem. B* **2019,** *123* (9), 2005-2015.

31. Suddala, K. C.; Price, I. R.; Dandpat, S. S.; Janeček, M.; Kührová, P.; Šponer, J.; Banáš, P.; Ke, A.; Walter, N. G., Local-to-Global Signal Transduction at the Core of a Mn^{2+} Sensing Riboswitch. *Nat. Commun.* **2019,** *10* (1), 4304.

32. Dambach, M.; Sandoval, M.; Updegrove, Taylor B.; Anantharaman, V.; Aravind, L.; Waters, Lauren S.; Storz, G., The Ubiquitous *yybP-ykoY* Riboswitch is a Manganese-Responsive Regulatory Element. *Mol. Cell* **2015,** *57* (6), 1099-1109.

33. Price, Ian R.; Gaballa, A.; Ding, F.; Helmann, John D.; Ke, A., Mn^{2+}-Sensing Mechanisms of *yybP-ykoY* Orphan Riboswitches. *Mol. Cell* **2015,** *57* (6), 1110-1123.

34. Sung, H.-L.; Nesbitt, D. J., Novel Heat-Promoted Folding Dynamics of the *yybP-ykoY* Manganese Riboswitch: Kinetic and Thermodynamic Studies at the Single-Molecule Level. *J. Phys. Chem. B* **2019,** *123* (26), 5412-5422.

35. Aitken, C. E.; Marshall, R. A.; Puglisi, J. D., An Oxygen Scavenging System for Improvement of Dye Stability in Single-Molecule Fluorescence Experiments. *Biophys. J.* **2008,** *94* (5), 1826-1835.

36. Sung, H.-L.; Nesbitt, D. J., High Pressure Single-Molecule FRET Studies of the Lysine Riboswitch: Cationic and Osmolytic Effects on Pressure Induced Denaturation. *Phys. Chem. Chem. Phys.* **2020,** *22* (28), 15853-15866.

37. Sung, H.-L.; Nesbitt, D. J., Sequential Folding of the Nickel/Cobalt Riboswitch Is Facilitated by a Conformational Intermediate: Insights from Single-Molecule Kinetics and Thermodynamics. *J. Phys. Chem. B* **2020,** *124* (34), 7348-7360.

38. Sun, L.-Z.; Chen, S.-J., Predicting RNA-Metal Ion Binding with Ion Dehydration Effects. *Biophys. J.* **2019,** *116* (2), 184-195.

39. Ma, C. Y.; Pezzotti, S.; Schwaab, G.; Gebala, M.; Herschlag, D.; Havenith, M., Cation Enrichment in the Ion Atmosphere is Promoted by Local Hydration of DNA. *Phys. Chem. Chem. Phys.* **2021,** *23* (40), 23203-23213.

40. Draper, D. E., RNA Folding: Thermodynamic and Molecular Descriptions of the Roles of Ions. *Biophys. J.* **2008,** *95* (12), 5489-5495.

41. Knight, A. W.; Kalugin, N. G.; Coker, E.; Ilgen, A. G., Water Properties under Nano-Scale Confinement. *Sci. Rep.* **2019,** *9* (1), 8246.

42. Serganov, A.; Huang, L.; Patel, D. J., Structural Insights into Amino Acid Binding and Gene Control by a Lysine Riboswitch. *Nature* **2008,** *455* (7217), 1263-1267.

43. Garst, A. D.; Héroux, A.; Rambo, R. P.; Batey, R. T., Crystal Structure of the Lysine Riboswitch Regulatory mRNA Element. *J. Biol. Chem.* **2008,** *283* (33), 22347-22351.

44. Blouin, S.; Lafontaine, D. A., A Loop–Loop Interaction and a K-Turn Motif Located in the Lysine Aptamer Domain are Important for the Riboswitch Gene Regulation Control. *RNA* **2007,** *13* (8), 1256-1267.

45. Serganov, A.; Patel, D. J., Amino Acid Recognition and Gene Regulation by Riboswitches. *Biochim. Biophys. Acta Gene Regul. Mech.* **2009,** *1789* (9), 592-611.

46. Vogt, A. D.; Di Cera, E., Conformational Selection or Induced Fit? A Critical Appraisal of the Kinetic Mechanism. *Biochemistry* **2012,** *51* (30), 5894-5902.

47. Pavlović, R. Z.; Lalisse, R. F.; Hansen, A. L.; Waudby, C. A.; Lei, Z.; Güney, M.; Wang, X.; Hadad, C. M.; Badjić, J. D., From Selection to Instruction and Back: Competing Conformational Selection and Induced Fit Pathways in Abiotic Hosts. *Angew. Chem.* **2021,** *60* (36), 19942-19948.

48. Hammes, G. G.; Chang, Y.-C.; Oas, T. G., Conformational Selection or Induced Fit: A Flux Description of Reaction Mechanism. *Proc. Natl. Acad. Sci. U.S.A.* **2009,** *106* (33), 13737-13741.

49. Suddala, K. C.; Wang, J.; Hou, Q.; Walter, N. G., Mg^{2+} Shifts Ligand-Mediated Folding of a Riboswitch from Induced-Fit to Conformational Selection. *J. Am. Chem. Soc.* **2015,** *137* (44), 14075-14083.

50. Fan, H. Y.; Shek, Y. L.; Amiri, A.; Dubins, D. N.; Heerklotz, H.; Macgregor, R. B.; Chalikian, T. V., Volumetric Characterization of Sodium-Induced G-Quadruplex Formation. *J. Am. Chem. Soc.* **2011,** *133* (12), 4518-4526.

51. Patra, S.; Anders, C.; Erwin, N.; Winter, R., Osmolyte Effects on the Conformational Dynamics of a DNA Hairpin at Ambient and Extreme Environmental Conditions. *Angew. Chem.* **2017,** *56* (18), 5045-5049.

Chapter 13 Postmortem and Future Directions

1. Paige, J. S.; Wu, K. Y.; Jaffrey, S. R., RNA Mimics of Green Fluorescent Protein. *Science* **2011,** *333* (6042), 642-646.

2. Strack, R. L.; Disney, M. D.; Jaffrey, S. R., A Superfolding Spinach2 Reveals the Dynamic Nature of Trinucleotide Repeat–Containing RNA. *Nat. Methods* **2013,** *10* (12), 1219-1224.

3. Harbaugh, S. V.; Martin, J. A.; Weinstein, J.; Ingram, G.; Kelley-Loughnane, N., Screening and Selection of Artificial Riboswitches. *Methods* **2018,** *143*, 77-89.

4. Xu, J.; Cotruvo, J. A., The *czcD* (NiCo) Riboswitch Responds to Iron(II). *Biochemistry* **2020,** *59* (15), 1508-1516.

5. Reiss, C. W.; Strobel, S. A., Structural Basis for Ligand Binding to the Guanidine-II Riboswitch. *RNA* **2017,** *23* (9), 1338-1343.

6. Meyer, I. M.; Miklós, I., Co-Transcriptional Folding is Encoded within RNA Genes. *BMC Mol. Biol.* **2004,** *5* (1), 10.

7. Vieweger, M.; Holmstrom, Erik D.; Nesbitt, David J., Single-Molecule FRET Reveals Three Conformations for the TLS Domain of Brome Mosaic Virus Genome. *Biophys. J.* **2015,** *109* (12), 2625-2636.

8. Vieweger, M.; Nesbitt, D. J., Synergistic SHAPE/Single-Molecule Deconvolution of RNA Conformation under Physiological Conditions. *Biophys. J.* **2018,** *114* (8), 1762-1775.

9. Holmstrom, E. D.; Dupuis, N. F.; Nesbitt, D. J., Kinetic and Thermodynamic Origins of Osmolyte-Influenced Nucleic Acid Folding. *J. Phys. Chem. B* **2015,** *119* (9), 3687-3696.

10. Yancey, P. H.; Gerringer, M. E.; Drazen, J. C.; Rowden, A. A.; Jamieson, A., Marine Fish May be Biochemically Constrained from Inhabiting the Deepest Ocean Depths. *Proc. Natl. Acad. Sci. U.S.A.* **2014,** *111* (12), 4461-4465.

11. Yancey, P. H.; Speers-Roesch, B.; Atchinson, S.; Reist, J. D.; Majewski, A. R.; Treberg, J. R., Osmolyte Adjustments as a Pressure Adaptation in Deep-Sea Chondrichthyan Fishes: An Intraspecific Test in Arctic Skates (Amblyraja hyperborea) along a Depth Gradient. *Physiol. Biochem. Zool.* **2018,** *91* (2), 788-796.

12. Dupuis, N. F.; Holmstrom, E. D.; Nesbitt, D. J., Molecular-Crowding Effects on Single-Molecule RNA Folding/Unfolding Thermodynamics and Kinetics. *Proc. Natl. Acad. Sci. U.S.A.* **2014,** *111* (23), 8464-8469.